

日本大学博士学位論文

**RESEARCH AND DEVELOPMENT OF CONCRETE  
CONTAINING PHASE CHANGE MATERIALS (PCM)**  
相変化材料（PCM）混合コンクリートに関する研究開発

令和6年2月

**Purev-Erdene BAT-ERDENE**

## SUMMARY OF THESIS

### RESEARCH AND DEVELOPMENT OF CONCRETE CONTAINING PHASE CHANGE MATERIALS (PCM)

「相変化材料 (P C M) 混合コンクリートに関する研究開発」

Department of Architecture, Graduate School of Engineering, Nihon University  
Bat-Erdene PUREV-ERDENE

This research focuses on developing sustainable and energy-efficient building materials by integrating Phase Change Materials (PCMs) into concrete structures. The building sector's increasing energy consumption, especially in residential structures, presents a critical global concern. PCMs offer a promising solution by efficiently storing and releasing thermal energy, reducing heating and cooling loads, and promoting sustainability in construction. This innovative approach can create and maintain a comfortable thermal environment while substantially cutting energy consumption. This research comprises of eight chapters, each contributing to the development of sustainable and energy-efficient building materials.

Chapter 1 introduces PCM integration into cement structures to address rising energy consumption in the building sector.

Chapter 2 addresses the challenges of integrating PCMs into concrete structures, focusing on the development of innovative fly ash foam concrete. It utilizes several PCMs with different phase change temperature ranges without energy loss or damage. In the results of the analysis, the potential for energy savings and thermal comfort in architectural applications is identified.

Chapter 3 aims to significantly increase the energy storage and thermal storage capacity of concrete by increasing the thermal conductivity and integrating the two types of PCMs. It employs a strategy of dual combination approaches, focusing on enhancing thermal conductivity and integrating the blended PCMs, to improve the potential for reducing energy use.

Chapter 4 describes a collaborative study with a precast concrete plant that used this material and focused on addressing issues in multi-family housing using exterior insulation. Requirements included reducing the temperature rise of the concrete, maintaining the bond strength between tile and concrete, and maintaining the integrity of the PCM capsules. This study proposed the use of PCM polymer cement mortar to increase bond strength and reduce excessive temperature fluctuations.

In Chapter 5, in collaboration with the Technical University of Darmstadt, Germany, an ultralight PCM foam concrete, NRG foam, was introduced to establish an empirical model for thermal insulation and energy storage.

In Chapter 6, a comprehensive numerical simulation analysis was performed to validate the experimental data and establish a predictive model for the energy efficiency of concrete. The role of PCM in maintaining room temperature was clarified.

In Chapter 7, EnergyPlus software was used for energy analysis simulations. The effectiveness of PCM use in housing was shown to be intrinsically linked to a specific climate zone in regions where the climate closely matches the phase change temperature of the PCM material, and energy loads are significantly reduced when the phase change temperature range of the PCM matches the climate zone.

Chapter 8 summarizes the results of this study and presents challenging prospects for the future.

The results show that PCM can minimize indoor temperature fluctuations, saving energy and improving building comfort. This study contributes to future sustainable building research by proposing energy-efficient buildings using PCM concrete.

# 論文概要

## 「RESEARCH AND DEVELOPMENT OF CONCRETE CONTAINING PHASE CHANGE MATERIALS (PCM) 相変化材料 (P C M) 混合コンクリートに関する研究開発」

日本大学大学院工学研究科 博士後期課程 建築学専攻  
Bat-Erdene PUREV-ERDENE

本研究は、相変化材料 (PCM) をコンクリート構造に組み込むことにより、持続可能でエネルギー効率の高い建築材料を開発することに焦点を当てている。建築分野、特に住宅構造におけるエネルギー消費の増大は、世界的に重大な問題となっている。PCM は、熱エネルギーを効率的に貯蔵・放出し、冷暖房負荷を低減し、建築における持続可能性を促進することで、有望な解決策を提供する。この革新的なアプローチは、エネルギー消費を大幅に削減しながら、快適な温熱環境を作り出し、維持することができる。本論文は 8 つの章で構成され、それぞれが持続可能でエネルギー効率の高い建築材料の開発に貢献している。

第 1 章では、建築分野におけるエネルギー消費の増加に対処するため、セメント構造への PCM の統合について紹介した。

第 2 章では、エネルギー損失や損傷を与えることなく相変化温度範囲の異なる数種類の PCM を利用し、革新的なフライアッシュフォームコンクリートの開発を中心に、コンクリート構造物に PCM を組み込む際の課題を取り上げた。分析結果において、建築用途におけるエネルギー節約と熱的快適性の可能性を明らかにした。

第 3 章では、熱伝導率を高め、2 種類の PCM を統合することで、コンクリートのエネルギー貯蔵能力と蓄熱容量を大幅に向上させることを目指した。熱伝導率と 2 種類を混合した PCM に焦点を当てた 2 面からのアプローチを採用し、エネルギー使用量削減の可能性を確認した。

第 4 章では、本材料を用いたプレキャストコンクリート工場との共同研究について述べており、外断熱工法を使用する集合住宅における問題への対処に焦点を当てた。要求される性能には、コンクリートの温度上昇の低減、タイルとコンクリートの接着強度の維持、PCM の形状の完全性の維持が含まれる。この研究では、接着強度を高め、過度の温度変動を抑えるために PCM ポリマーセメントモルタルの使用を提案した。

第 5 章では、ドイツのダルムシュタット工科大学との共同研究により、超軽量 PCM フォームコンクリートである「NRG フォーム」を導入し、断熱とエネルギー貯蔵の実証モデルを確立した。

第 6 章では、実験データを検証し、コンクリートのエネルギー効率の予測モデルを確立するために包括的な数値シミュレーション解析を行った。室温維持における PCM の役割を明らかにした。

第 7 章では、エネルギー分析シミュレーションに「EnergyPlus」ソフトウェアを使用した。住宅における PCM 利用の有効性として、気候が PCM 材料の相変化温度と密接に一致する地域では、特定の気候帯と本質的に結びついていることを示し、PCM の相変化温度範囲が気候帯に適合する場合、エネルギー負荷が大幅に削減されることを示した。

第 8 章では、本研究の結果を総括し、今後の挑戦的な展望を示した。

本論文では、PCM が室内温度の変動を最小限に抑え、省エネルギー性能と建物の快適性を改善できることを示した。本研究の成果は、PCM コンクリートを用いた住宅のエネルギー効率の高さを明らかにし、将来の持続可能な建築材料の研究に貢献するものである。

# Contents

<b>CHAPTER 1: INTRODUCTION.....</b>	<b>1</b>
1.1.1 World Energy sources and consumption.....	2
1.1.2 Energy and Buildings.....	6
1.2 OBJEVTIVES AND STRUCTURE OF THESIS .....	10
1.2.1 Structure of thesis .....	10
1.3 LITERATRURE REVIEW OF PHASE CHANGE MATERIALS (PCM).....	14
1.3.1 Definition of PCM .....	14
1.3.2 Classification of PCM.....	14
1.3.3 PCMs incorporation in concrete .....	15
1.3.4 Main thermophysical properties of PCM.....	17
1.3.5 Foam concrete.....	18
1.3.6 Literature review of current study on Phase change material (PCM) in Japan .....	20
<b>CHAPTER 2: FLY ASH FOAM CONCRETE WITH PCM.....</b>	<b>23</b>
2.1 EXPERIMENTAL OVERVIEW.....	24
2.1.1 Introduction.....	24
2.1.2 Cementitious material .....	25
2.1.3 Fly ash.....	26
2.1.4 Microencapsulation.....	27
2.1.5 Foam & Foaming Agent.....	28
2.1.6 Superplasticizer.....	29
2.1.7 OM-10E MIXER .....	30
2.1.8 Evaluation of thermal energy storage of PCM.....	31
2.2 MIXTURE PROPERTIES .....	35
2.2.1 Experimental program .....	35
2.2.2 Constituent Materials .....	36
2.3 TEST METHODS .....	48
2.3.1 Differential Scanning Calorimetry (DSC) .....	49
2.3.2 Specific heat capacity measurements.....	69
2.3.3 Thermal conductivity test.....	74
2.3.4 Preparation of the specimens .....	76
2.3.5 Result of thermal conductivity test .....	77
2.4 HEAT CYCLES ON PRISMS AND SANDWICH PANELS.....	79



2.4.1 Experimental program .....	79
2.4.2 Preparing the specimens for heat cycling test.....	80
2.4.3 The results of heating and cooling cycles on foam concrete PCM6D samples. ....	84
2.4.4 The results of heating and cooling cycles on foam concrete PCM18D samples .....	86
2.4.5 The results of heating and cooling cycles on foam concrete PCM28D samples. ....	88
2.4.6 The results of heating and cooling cycles on foam concrete PCM43D samples .....	90
2.4.7 Microstructure analysis .....	91
2.5 CONCLUSIONS.....	92

**CHAPTER 3: ENHANCING ENERGY STORAGE CAPACITY IN CONCRETE WITH PCMS..... 96**

3.1 EXPERIMENTAL OVERVIEW.....	97
3.1.1 Introduction.....	97
3.2 MATERIAL PROPERTIES.....	98
3.2.1 Microencapsulated PCM.....	98
3.2.2 Fine aggregate .....	98
3.2.3 High density aggregate .....	99
3.2.4 Mix composition .....	100
3.3 MECHANICAL ANALYSES .....	101
3.3.1 Density test.....	101
3.3.2 Compressive strength test .....	103
3.4 THERMAL ANALYSES .....	105
3.4.1 Differential Scanning Calorimetry (DSC) .....	105
3.4.2 Specific heat capacity and Specific enthalpy measurements .....	124
3.4.3 Thermal conductivity test.....	134
3.4.4 Heat cycles test .....	135
3.4.5 Results of heat cyclic analysis .....	139
3.5 CONCLUSIONS.....	141

**CHAPTER 4: APPLICATION OF PCM TO PRECAST CONCRETE WALL PANELS.. 145**

4.1 EXPERIMENTAL OVERVIEW.....	146
4.2 RESEARCH BACKGROUND .....	146
4.3 MATERIAL PROPERTIES.....	148
4.3.1 Microencapsulated PCM.....	148
4.3.2 Fine aggregate .....	149

4.3.3 Polymers materials .....	149
4.4 MIX DESIGN OF TRAIL TEST .....	150
4.4.1 Results of relation between polymer-cement ratio and flow test of different types of polymer-modified concretes .....	152
4.4.2 Results of relation between polymer-cement ratio and water cement ratio of different types of polymer-modified concretes. ....	152
4.4.3 Compressive strength tests on different types of polymers modified concretes.....	155
4.4.4 Bending strength tests on different types of polymers modified concretes. ....	157
4.4.5 Density tests on different types of polymers modified concretes with PCM and without PCM.....	159
4.5 MIX DESIGN .....	161
4.6 MECHANICAL ANALYSIS.....	162
4.6.1 Density test.....	164
4.6.2 Compressive strength test .....	165
4.6.3 Bonding strength test .....	166
4.7 DSC AND THERMAL ANALYSIS .....	167
4.7.1 Specific heat capacity and Specific enthalpy measurements of polymer modified concrete with different types of PCM.....	170
4.7.2 Heat cyclic test analysis .....	172
4.7.3 Preparing the samples for heat cycling test.....	172
4.7.4 Thermal expansion test .....	182
4.7.5 Thermal conductivity test.....	194
4.8 CONCLUSIONS.....	195
<b>CHAPTER 5: ULTRA LIGHT WEIGHT PCM ENERGY (NRG) FOAM CONCRETE ..</b>	<b>199</b>
5.1 EXPERIMENTAL OVERVIEW.....	200
5.1 RESEARCH BACKGROUND.....	200
5.2.1 Objectives .....	201
5.2.2 Mix design .....	202
5.2.3 Production of Foam Concrete .....	202
5.2.4 Experimental findings.....	203
5.2.5 Density test.....	208
5.2.6 Compressive strength test .....	214
5.2.7 Thermal conductivity experiment .....	215
5.2.8 Mixture design tool for upscale .....	217
5.2.9 Approach for an engineering design model for NRG-Foam.....	220

5.2 CONCLUSIONS.....	227
<b>CHAPTER 6: NUMERICAL SIMULATION ANALYSIS OF PCM CONCRETE.....</b>	<b>230</b>
6.1 SIMULATION OVERVIEW .....	231
6.1.1 Introduction.....	231
6.1.2 Establishing a simulation model for temperature evolution .....	232
6.1.3 Model simulation overview .....	234
6.1.4 Model validation and heat evolution model.....	236
6.2 CONCLUSIONS .....	244
<b>CHAPTER 7: ENERGY ANALYSIS SIMULATION OF BUILDINGS WITH PCM.....</b>	<b>246</b>
7.1 SIMULATION OVERVIEW .....	247
7.1.1 Introduction.....	247
7.1.2 Model establishment .....	248
7.1.3 Environment.....	249
7.1.4 Description of the zones.....	251
7.1.5 Simulation parameters .....	252
7.1.6 General input as run period and schedules .....	253
7.1.7 Conduction through the wall.....	255
7.1.8 Setting up wall materials.....	257
7.2 TEST RESULTS .....	261
7.2.1 Comparative results in indoor temperature without heating and cooling load .....	261
7.2.2 Comparative results in indoor temperature with heating and cooling load .....	266
7.2.3 Heating and cooling loads.....	271
7.2.3 Monthly heating and cooling loads.....	276
7.3 CONCLUSIONS.....	278
<b>CHAPTER 8: CONCLUDING REMARKS .....</b>	<b>280</b>
8.1 CONCLUDING REMARKS .....	281
8.1.1 Conclusions of chapter 2.....	281
8.1.2 Conclusions of chapter 3.....	282
8.1.3 Conclusions of chapter 4.....	283
8.1.4 Conclusions of chapter 5.....	283
8.1.5 Conclusions of chapter 6.....	284
8.1.6 Conclusions of chapter 7.....	284
8.2 RECOMMENDATIONS FOR FUTURE WORK.....	285

## List of Figures

Figure 1.1.1 From 2019 to 2040, the fluctuation in the number of global energy sources [2].	2
Figure 1.1.2 From 2019 to 2050, Global primary energy consumption by region [3].	3
Figure 1.1.3 From 2010 to 2050, Global energy consumption by sector [3].	3
Figure 1.1.4 From 2019 to 2050, Global electricity consumption by sector [3].	4
Figure 1.1.5 From 2019 to 2050, Global primary energy consumption by energy source [3].	5
Figure 1.1.6 World total final consumption by sector in 2017 [4].	6
Figure 1.1.7 Breakdown of the final energy use by sectors in Japan 2018 [5].	7
Figure 1.1.8 Percentage shares of energy use in a residential building in Europe in 2019 [6].	8
Figure 1.1.9 Percentage shares of energy use in a residential building in Japan in 2020 [7].	8
Figure 1.1.10. Percentage shares of energy use in a residential building in India in 2010 [8].	9
Figure 1.2.1. Flow chart of research work.	11
Figure 1.3.1 Structure and working principle of microencapsulation.	14
Figure 1.3.2 The principle of vacuum impregnation method [8].	16
Figure 1.3.3 Direct mixing method	17
Figure 1.3.4 Potential fields of application of PCM: Temperature control and storage and supply of heat with storage density and small temperature change [11].	17
Figure 2.1.1 (a) Particle size characteristics of cement powder; (b) EDS spectrum of the cement.	25
Figure 2.1.2 (a) Particle size characteristics of fly ash powder; (b) EDS spectrum of the fly ash.	26
Figure 2.1.3 (a) Particle size characteristics of microencapsulated PCM powder (PCM6D);	27
Figure 2.1.4 Left: Foaming agent. Right: Foam generating machine.	28
Figure 2.1.5 Foam generator [2].	28
Figure 2.1.6 Superplasticizer used as water reducing agent.	29
Figure 2.1.7 OM-10E mixer and operation.	30
Figure 2.1.8 Results of DSC measurement of Pure PCM6D at various heating and cooling rates.	32
Figure 2.1.9 Results of DSC measurement of Pure PCM18D at various heating and cooling rates.	32
Figure 2.1.10 Results of DSC measurement of Pure PCM28D at various heating and cooling rates.	32
Figure 2.1.11 Results of DSC measurement of Pure PCM43D at various heating and cooling rates.	32
Figure 2.1.12 Onset, peak and temperature for the phase transition in Pure-PCM6D.	33

Figure 2.1.13 Onset, peak and temperature for the phase transition in Pure-PCM18D.....	33
Figure 2.1.14 Onset, peak and temperature for the phase transition in Pure-PCM28D.....	34
Figure 2.1.15 Onset, peak and temperature for the phase transition in Pure-PCM43D.....	34
Figure 2.2.1 Flow diagram of experimental program .....	35
Figure 2.2.2 Effect of adding PCM to compressive strength of foam concrete with PCM6D.....	39
Figure 2.2.3 Effect of adding PCM to compressive strength of foam concrete with PCM18D....	40
Figure 2.2.4 Effect of adding PCM to compressive strength of foam concrete with PCM28D....	41
Figure 2.2.5 Effect of adding PCM to compressive strength of foam concrete with PCM43D....	42
Figure 2.2.6 Effect of adding PCM6D to density of foam concrete. ....	45
Figure 2.2.7 Effect of adding PCM18D to density of foam concrete. ....	45
Figure 2.2.8 Effect of adding PCM28D to density of foam concrete. ....	46
Figure 2.2.9 Effect of adding PCM43D to density of foam concrete. ....	47
Figure 2.3.1 DSC analysis machine model Q200 .....	48
Figure 2.3.2 Results of DSC measurement of PCM6D-10% at various heating and cooling rates. .....	50
Figure 2.3.3 Results of DSC measurement of PCM6D-20% at various heating and cooling rates. .....	50
Figure 2.3.4 Results of DSC measurement of PCM6D-30% at various heating and cooling rates. .....	50
Figure 2.3.5 Results of DSC measurement of PCM18D-10% at various heating and cooling rates .....	53
Figure 2.3.6 Results of DSC measurement of PCM18D-20% at various heating and cooling rates. .....	53
Figure 2.3.7 Results of DSC measurement of PCM18D-30% at various heating and cooling rate. .....	53
Figure 2.3.8 Results of DSC measurement of PCM 28D-10% at various heating and cooling rates. .....	56
Figure 2.3.9 Results of DSC measurement of PCM 28D-20% at various heating and cooling rates. .....	56
Figure 2.3.10 Results of DSC measurement of PCM 28D-30% at various heating and cooling rates. .....	56
Figure 2.3.11 Results of DSC measurement of PCM 43D-10% at various heating and cooling rates. .....	59
Figure 2.3.12 Results of DSC measurement of PCM 43D-20% at various heating and cooling rates. .....	59

Figure 2.3.13 Results of DSC measurement of PCM 43D-30% at various heating and cooling rates. .....	59
Figure 2.3.14 Onset, peak and end temperature for the phase transition in PCM6D-10%. ....	62
Figure 2.3.15 Onset, peak and end temperature for the phase transition in PCM6D-20%. ....	62
Figure 2.3.16 Onset, peak and end temperature for the phase transition in PCM6D-30% .....	62
Figure 2.3.17 Onset, peak and end temperature for the phase transition in PCM18D-10%. ....	64
Figure 2.3.18 Onset, peak and end temperature for the phase transition in PCM18D-20%. ....	64
Figure 2.3.19 Onset, peak and end temperature for the phase transition in PCM18D-30%. ....	64
Figure 2.3.20 Onset, peak and end temperature for the phase transition in PCM28D-10%. ....	66
Figure 2.3.21 Onset, peak and end temperature for the phase transition in PCM28D-20%. ....	66
Figure 2.3.22 Onset, peak and end temperature for the phase transition in PCM28D-30%. ....	66
Figure 2.3.23 Onset, peak and end temperature for the phase transition in PCM28D-10%. ....	68
Figure 2.3.24 Onset, peak and end temperature for the phase transition in PCM28D-20%. ....	68
Figure 2.3.25 Onset, peak and end temperature for the phase transition in PCM28D-30%. ....	68
Figure 2.3.26 Results of specific heat measurements with different amount of PCMs in PCM6D. .....	70
Figure 2.3.27 Result of specific heat measurements with different amount of PCMs in PCM18D. .....	71
Figure 2.3.28 Result of specific heat measurements with different amount of PCMs in PCM28D. .....	72
Figure 2.3.29 Result of specific heat measurements with different amount of PCMs in PCM43D. .....	73
Figure 2.3.30 Thermal conductivity, FOX 200. ....	74
Figure 2.3.31 Structure of the FOX-200. ....	75
Figure 2.3.32 Thermal conductivity of PCM foam concrete as a function of PCM6D. ....	77
Figure 2.3.33 Thermal conductivity of PCM foam concrete as a function of PCM18D. ....	77
Figure 2.3.34 Conductivity of PCM foam concrete as a function of PCM28D. ....	78
Figure 2.3.35 Conductivity of PCM foam concrete as a function of PCM43D. ....	78
Figure 2.4.1 Schematization of used test setup for heating/ cooling cycles on prism. ....	79
Figure 2.4.2 Schematization of used test setup for heating/ cooling cycles on prototype 2. ....	80
Figure 2.4.3 Preparation specimens for heat cycle test .....	81
Figure 2.4.4 Preparation specimens for heat cycle test .....	82
Figure 2.4.5 Experimental condition for climate cycle test of No-PCM. ....	83
Figure 2.4.6 Experimental condition for climate cycle test of PCM6D-10%. ....	83
Figure 2.4.7 Experimental condition for climate cycle test of PCM6D-20%. ....	83

Figure 2.4.8 Experimental condition for climate cycle test of PCM6D-30%.	83
Figure 2.4.9 Experimental condition for climate cycle test of No-PCM.	85
Figure 2.4.10 Experimental condition for climate cycle test of PCM18D-10%.	85
Figure 2.4.11 Experimental condition for climate cycle test of PCM18D-20%.	85
Figure 2.4.12 Experimental condition for climate cycle test of PCM18D-30%.	85
Figure 2.4.13 Experimental condition for climate cycle test of No-PCM.	87
Figure 2.4.14 Experimental condition for climate cycle test of PCM28D-10%.	87
Figure 2.4.15 Experimental condition for climate cycle test of PCM28D-20%.	87
Figure 2.4.16 Experimental condition for climate cycle test of PCM28D-30%.	87
Figure 2.4.17 Experimental condition for climate cycle test of No-PCM.	89
Figure 2.4.18 Experimental condition for climate cycle test of PCM43D-10%.	89
Figure 2.4.19 Experimental condition for climate cycle test of PCM43D-20%.	89
Figure 2.4.20 Experimental condition for climate cycle test of PCM43D-30%.	89
Figure 2.4.21 SEM image of PCM foam concrete after 28 days of curing ( $\times 1000$ ): (A) No-PCM, magnification $\times 1000$ (B) PCM6D-10% magnification $\times 1000$ (C) PCM6D-30%, magnification $\times 1000$ .	91
.....	
Figure 3.3.1 Results of density test results on different types of concretes with and without PCMs.	101
.....	
Figure 3.3.2 Compressive strength test results on different types of concretes with and without PCM.	103
Figure 3.4.1 DSC analysis machine model Q25.	105
Figure.3.4.2 DSC curve of FC-PCM6D18D, heating and cooling process at $10^{\circ}\text{C}/\text{min}$ scanning rate.	107
.....	
Figure 3.4.3 DSC curve of FC-PCM18D28D, heating and cooling process at $10^{\circ}\text{C}/\text{min}$ scanning rate.	107
.....	
Figure 3.4.4 DSC curve of FC-PCM28D43D, heating and cooling process at $10^{\circ}\text{C}/\text{min}$ scanning rate.	107
.....	
Figure 3.4.5 DSC curve of NC-PCM6D18D, heating and cooling process at $10^{\circ}\text{C}/\text{min}$ scanning rate.	109
.....	
Figure 3.4.6 DSC curve of NC-PCM18D28D, heating and cooling process at $10^{\circ}\text{C}/\text{min}$ scanning rate.	109
.....	

Figure 3.4.7 DSC curve of NC-PCM28D143D, heating and cooling process at 10°C/min scanning rate.....	109
Figure 3.4.8 DSC curve of ND-PCM6D18D, heating and cooling process at 10°C/min scanning rate.....	111
Figure 3.4.9 DSC curve of ND-PCM18D28D, heating and cooling process at 10°C/min scanning rate.....	111
Figure 3.4.10 DSC curve of ND-PCM28D43D, heating and cooling process at 10°C/min scanning rate.....	111
Figure 3.4.11 Results of DSC measurement of FC PCM6D18D at various heating rates. ....	113
Figure 3.4.12 Results of DSC measurement of NC PCM6D18D at various heating rates. ....	113
Figure 3.4.13 Results of DSC measurement of ND PCM6D18D at various heating rates. ....	113
Figure 3.4.14 Results of DSC measurement of ND PCM6D18D at various cooling rates.....	114
Figure 3.4.15 Results of DSC measurement of NC PCM6D18D at various cooling rates. ....	114
Figure 3.4.16 Results of DSC measurement of FC PCM6D18D at various cooling rates.....	114
Figure 3.4.17 Results of DSC measurement of FC PCM18D28D at various heating rates. ....	116
Figure 3.4.18 Results of DSC measurement of NC PCM18D28D at various heating rates. ....	116
Figure 3.4.19 Results of DSC measurement of NC PCM18D28D at various heating rates. ....	116
Figure 3.4.20 Results of DSC measurement of FC PCM18D28D at various cooling rates.....	117
Figure 3.4.21 Results of DSC measurement of FC PCM18D28D at various cooling rates.....	117
Figure 3.4.22 Results of DSC measurement of FC PCM18D28D at various cooling rates.....	117
Figure 3.4.23 Results of DSC measurement of FC PCM28D43D at various heating rates. ....	119
Figure 3.4.24 Results of DSC measurement of NC PCM28D43D at various heating rates. ....	119
Figure 3.4.25 Results of DSC measurement of ND PCM28D43D at various heating rates. ....	119
Figure 3.4.26 Results of DSC measurement of FC PCM28D43D at various cooling rates.....	120
Figure 3.4.27 Results of DSC measurement of NC PCM28D43D at various cooling rates. ....	120
Figure 3.4.28 Results of DSC measurement of ND PCM28D43D at various cooling rates.....	120
Figure 3.4.29 (a) Specific heat capacity and (b) specific enthalpy of FC PCM6D18D. ....	126
Figure 3.4.30 (a) Specific heat capacity and (b) specific enthalpy of FC PCM18D28D. ....	126
Figure 3.4.31 (a) Specific heat capacity and (b) specific enthalpy of FC PCM28D43D. ....	126
Figure 3.4.32 (a) Specific heat capacity and (b) specific enthalpy of NC PCM6D18D. ....	128
Figure 3.4.33 (a) Specific heat capacity and (b) specific enthalpy of NC PCM18D28D. ....	128
Figure 3.4.34 (a) Specific heat capacity and (b) specific enthalpy of NC PCM28D43D. ....	128
Figure 3.4.35 Specific heat capacity and specific enthalpy of ND PCM6D18D. ....	130



Figure 3.4.36 Specific heat capacity and specific enthalpy of ND PCM18D28D. ....	130
Figure 3.4.37 Specific heat capacity and specific enthalpy of ND PCM28D43D. ....	130
Figure 3.4.38 Comparison graphics of Specific heat capacity and specific enthalpy of PCM6D18D .....	132
Figure 3.4.39 Comparison graphics of Specific heat capacity and specific enthalpy of PCM18D28D .....	132
Figure 3.4.40 Comparison graphics of Specific heat capacity and specific enthalpy of PCM28D43D .....	132
Figure 3.4.41 Thermal conductivity, FOX 200. ....	133
Figure 3.4.42 Thermal conductivity of different types of PCM concretes.....	134
Figure 3.4.43 Heat cycling program.....	135
Figure 3.4.44 Heat cyclic analysis of different types of PCM6D18D on the surface side of prototype. ....	136
Figure 3.4.45 Heat cyclic analysis of different types of PCM6D18D on the backside of prototype. .....	136
Figure 3.4.46 Heat cyclic analysis of different types of PCM6D18D on the inside of prototype. .....	136
Figure 3.4.47 Heat cyclic analysis of different types of PCM18D28D on the surface side of prototype. ....	137
Figure 3.4.48 Heat cyclic analysis of different types of PCM18D28D on the backside of prototype. .....	137
Figure 3.4.49 Heat cyclic analysis of different types of PCM18D28D on the inside of prototype. .....	137
Figure 3.4.50 Heat cyclic analysis of different types of PCM28D43D on the surface side of prototype. ....	138
Figure 3.4.51 Heat cyclic analysis of different types of PCM28D43D on the backside of prototype. .....	138
Figure 3.4.52 Heat cyclic analysis of different types of PCM28D43D on the inside of prototype. .....	138
Figure 4.2.1 A view of PC walls with tiles bonded on site and in factory. ....	146
Figure 4.2.2 Way of applying PCM into precast concrete .....	148
Figure 4.3.1 Different types of polymers .....	149
Figure 4.4.1 Relation between polymer-cement ratio and flow test of different types of polymers modified concretes. ....	153
Figure 4.4.2 Relation between polymer-cement ratio and water cement ratio of different types of	

polymers modified concretes. ....	154
Figure 4.4.3 Effects of polymer cement ratio and different curing conditions on compressive strength test of samples without PCM. ....	156
Figure 4.4.4 Effects of polymer cement ratio and different curing conditions on compressive strength test of samples with PCM. ....	156
Figure 4.4.5 Effects of polymer cement ratio and different curing conditions on bending strength test of samples without PCM. ....	158
Figure 4.4.6 Effects of polymer cement ratio and different curing conditions on bending strength test of samples with PCM. ....	158
Figure 4.4.7 Effects of polymer cement ratio and different curing condition on density test....	160
Figure 4.6.1 Density test on PCM modified concretes with different PCMs.....	164
Figure 4.6.2 Compressive strength analysis on different types of PCMs. ....	165
Figure 4.6.3 Adhesive strength analysis on different types of PCMs. ....	166
Figure 4.7.1 DSC curve of PCM6D, heating and cooling process at various heating rates.....	168
Figure 4.7.2 DSC curve of PCM18D, heating and cooling process at various heating rates.....	168
Figure 4.7.3 DSC curve of PCM28D, heating and cooling process at various heating rates.....	168
Figure 4.7.4 DSC curve of PCM43D, heating and cooling process at various heating rates.....	168
Figure 4.7.5 (a) Specific heat capacity and (b) specific enthalpy of PCM6D.....	171
Figure 4.7.6 (a) Specific heat capacity and (b) specific enthalpy of PCM18D.....	171
Figure 4.7.7 (a) Specific heat capacity and (b) specific enthalpy of PCM28D.....	171
Figure 4.7.8 Specific heat capacity and (b) specific enthalpy of PCM43D. ....	171
Figure 4.7.9 Heat cycling program.....	172
Figure 4.7.10 Preparation procedure of prototype setup. ....	173
Figure 4.7.11 Finished procedure. ....	173
Figure 4.7.12 Heat cyclic analysis of different types of PCM6D on surface side of prototype..	175
Figure 4.7.13 Heat cyclic analysis of different types of PCM6D on backside of prototype.....	175
Figure 4.7.14 Heat cyclic analysis of different types of PCM6D on inside of prototype. ....	175
Figure 4.7.15 Heat cyclic analysis of different types of PCM18D on surface of prototype. ....	177
Figure 4.7.16 Heat cyclic analysis of different types of PCM18D on backside of prototype....	177
Figure 4.7.17 Heat cyclic analysis of different types of PCM18D on inside of prototype. ....	177
Figure 4.7.18 Heat cyclic analysis of different types of PCM28D on surface side of prototype. ....	179
Figure 4.7.19 Heat cyclic analysis of different types of PCM28D on inside of prototype. ....	179
Figure 4.7.20 Heat cyclic analysis of different types of PCM28D on backside of prototype....	179
Figure 4.7.21 Heat cyclic analysis of different types of PCM43D on surface side of prototype.	

.....	181
Figure 4.7.22 Heat cyclic analysis of different types of PCM43D on backside of prototype.....	181
Figure 4.7.23 Heat cyclic analysis of different types of PCM43D on inside of prototype. ....	181
Figure 4.7.24 Test program of lamp heating test.....	182
Figure 4.7.25 A view of lamp heating test.....	182
Figure 4.7.26 Thermal expansion analysis of No-PCM with white tile.....	184
Figure 4.7.27 Thermal expansion analysis of No-PCM with black tile.....	184
Figure 4.7.28 Strain measurement test on sample No-PCM with white tile (L:S.side R:B.side)..	185
Figure 4.7.29 Strain measurement test on sample No-PCM with black tile (L:S.side R:B.side)	185
Figure 4.7.30 The results of max and min strain measurement test (No-PCM L: White tile R:Black tile) .....	185
Figure 4.7.31 Thermal expansion analysis of PCM6D with white tile.....	186
Figure 4.7.32 Thermal expansion analysis of PCM6D with black tile.....	186
Figure 4.7.33 Strain measurement test on sample PCM6D with white tile L:S.side R:B.side)..	187
Figure 4.7.34 Strain measurement test on sample PCM6D with black tile L:S.side R:B.side)..	187
Figure 4.7.35 The results of max and min strain measurement test (PCM6D L: White tile R:Black tile) .....	187
Figure 4.7.36 Thermal expansion analysis of PCM18D with white tile .....	188
Figure 4.7.37 Thermal expansion analysis of PCM18D with black tile .....	188
Figure 4.7.38 Strain measurement test on sample PCM18D with white tile ( L:S.side R:B.side).	189
Figure 4.7.39 Strain measurement test on sample PCM18D with black tile ( L:S.side R:B.side).	189
Figure 4.7.40 The results of max and min strain measurement test (PCM18D L: White tile R:Black tile) .....	189
Figure 4.7.41 Thermal expansion analysis of PCM28D with white tile .....	190
Figure 4.7.42 Thermal expansion analysis of PCM28D with black tile .....	190
Figure 4.7.43 Strain measurement test on sample PCM28D with white tile ( L:S.side R:B.side).	191
Figure 4.7.44 Strain measurement test on sample PCM28D with black tile ( L:S.side R:B.side).	191
Figure 4.7.45 The results of max and min strain measurement test (PCM28D L: White tile R: Black tile) .....	191
Figure 4.7.46 Thermal expansion analysis of PCM43D with white tile .....	192
Figure 4.7.47 Thermal expansion analysis of PCM43D with black tile .....	192
Figure 4.7.48 Strain measurement test on sample PCM43D with white tile (L:S.side R: B.side).	193
Figure 4.7.49 Strain measurement test on sample PCM43D with black tile (L:S.side R: B.side).	193
Figure 4.7.50 The results of max and min strain measurement test (PCM43D L: White tile R: Black tile) .....	193

Figure 4.7.51 Thermal conductivity results on polymer modified concrete .....	194
Figure 5.1.1 The main idea of NRG foam [1] .....	201
Figure 5.1.2 The mixtures of NRG foam with Nextek24 PCM with 10% collapsed foam structure. .....	204
Figure 5.1.3 The mixtures of NRG foam with Nextek24 PCM with 10% after increasing accelerator. .....	204
Figure 5.1.4 Density results of NRG foam.....	208
Figure 5.1.5 Compressive strength test of NRG foam. ....	214
Figure 5.1.6 Compressive strength test results.....	214
Figure 5.1.7 Thermal conductivity machine (left) and test specimen wrapped in foil with a thermocouple glued on (right).....	215
Figure 5.1.8 Results of thermal conductivity of NRG foam .....	216
Figure 5.1.9. Calculation sheet of the NRG-Foam mix design using the example of 20 volume percent PCM and a dry bulk density of 200 kg/m <sup>3</sup> → Target value is the dry bulk density.....	217
Figure 5.1.10. Calculation sheet of the NRG-Foam mix design using the example of 20 volume percent PCM and a dry bulk density of 200 kg/m <sup>3</sup> → Target value is the porosity.....	218
Figure 5.1.11. Flowchart for the GRG solution approach of the mixture design tool. ....	219
Figure 5.1.12. Calculated NRG-Foam porosity as a function of dry bulk density.....	219
Figure 5.1.13. Schematic representation of the average particle spacing of the PCM particles in the binder glue as ribbon thickness $R_P$ . ....	220
Figure 5.1.14. Particle size distribution of encapsulated Nextek 24D PCM.....	221
Figure 5.1.15. $R_P$ -Value of microencapsulated PCM from Nextek 24D as function of PCM percentage in NRG-Paste. ....	221
Figure 5.1.16. Schematic representation of the average distance of air bubbles in the NRG-Paste as ribbon thickness $R_F$ . ....	222
Figure 5.1.17. Average pore size distribution of NRG-Foam based on 3D $\mu$ XCT scans.....	223
Figure 5.1.18. $R_F$ -Value of NRG-Foam as a function of NRG-Foam porosity. ....	224
Figure 5.1.19. Ribbon thickness of the NRG-Foam $R_F$ as a function of the ribbon thickness of the NRG-Paste $R_P$ . ....	225
Figure 5.1.20. Approach for an engineering design model based on the limiting function for NRG- Foam stability $R_F = f(R_P)$ . ....	226
Figure 6.1.1 Schematic of the heat evolution model and parameter definitions on DSC model	232
Figure 6.1.2 Schematic of the basic model and parameter definitions heat evolution model.....	234
Figure 6.1.3 Schematic of the the heat transfer model and parameter definitions. ....	235
Figure 6.1.4 Heat cyclic results for different amounts of PCM6D (solid line represents	

experimental testing, dashed line represents simulation results. ....	238
Figure 6.1.5 Heat cyclic results for different types of PCM-30% (solid line represents experimental testing, dashed line represents simulation results). ....	240
Figure 6.1.6 Heat cyclic prediction results for PCM6D-30% with varying particle sizes. ....	241
Figure 6.1.7 Heat cyclic prediction results for different amounts of PCM6D. ....	242
Figure 6.1.8 Simulation results of DSC for PCM18D-30% at three different heating rates. ....	243
Figure 7.1.1: Calculation model Southeast side .....	248
Figure 7.1.2 Calculation model Southeast side .....	248
Figure 7.1.3 Location of the house. Source: Energy Plus screenshot .....	249
Figure 7.1.4 Annual temperature in Tokyo (2019).....	250
Figure 7.1.5 January weather in Tokyo involves considerations of both temperature and solar radiation .....	250
Figure 7.1.6 August weather in Tokyo involves considerations of both temperature and solar radiation .....	250
Figure 7.1.7 Description of the zones (a) Zone 1: Basement (b) Zone 2: Living room.....	251
Figure 7.1.8 Description of the zones. Source Energy Plus.....	251
Figure 7.1.9 Object: Run period. Source: Energy Plus .....	253
Figure 7.1.10 Occupancy schedule. Source: Energy Plus Schedule database .....	254
Figure 7.1.11 Ventilation schedule. Source: Energy Plus Schedule database .....	254
Figure 7.1.12 Specific heat of No-PCM.....	258
Figure 7.1.13 Specific heat of PCM6D .....	258
Figure 7.1.14 Specific heat of PCM18D .....	258
Figure 7.1.15 Enthalpy of PCM6D (Heating) .....	259
Figure 7.1.16 Enthalpy of PCM6D (Cooling).....	259
Figure 7.1.17 Enthalpy of PCM18D (Heating) .....	260
Figure 7.1.18 Enthalpy of PCM18D (Cooling).....	260
Figure 7.1.19 Enthalpy of PCM6D Source: Energy plus .....	260
Figure 7.1.20 Enthalpy of PCM18D Source: Energy plus .....	260
Figure 7.2.1 Indoor simulation of the gypsum wall in January.....	262
Figure 7.2.2 Indoor simulation of the gypsum wall in August.....	262
Figure 7.2.3 Indoor simulation of the No-PCM wall in January.....	262
Figure 7.2.4 Indoor simulation of the No-PCM wall in August.....	262
Figure 7.2.5 Indoor simulation of the PCM6D-30% wall in January .....	263
Figure 7.2.6 Indoor simulation of the PCM6D-30% wall in August .....	263
Figure 7.2.7 Indoor simulation of the PCM18D-30% wall in January .....	263

Figure 7.2.8 Indoor simulation of the PCM18D-30% wall in August .....	263
Figure 7.2.9 Indoor simulation comparison of gypsum wall and No-PCM wall in January .....	264
Figure 7.2.10 Indoor simulation comparison of gypsum wall and No-PCM wall in August.....	264
Figure 7.2.11 Indoor simulation comparison of No-PCM wall and PCM6D-30% wall in January .....	264
Figure 7.2.12 Indoor simulation comparison of No-PCM wall and PCM6D-30% wall in August .....	264
Figure 7.2.13 Indoor simulation comparison of No-PCM wall and PCM18D-30% wall in January .....	265
Figure 7.2.14 Indoor simulation comparison of No-PCM wall and PCM18D-30% wall in August .....	265
Figure 7.2.15 Indoor simulation comparison of PCM6D-30% wall and PCM18D-30% wall in January .....	265
Figure 7.2.16 Indoor simulation comparison of PCM6D-30% wall and PCM18D-30% wall in August .....	265
Figure 7.2.17 Indoor simulation with the air conditioning of the gypsum wall in January .....	267
Figure 7.2.18 Indoor simulation with the air conditioning of the gypsum wall in August .....	267
Figure 7.2.19 Indoor simulation with the air conditioning of No-PCM wall in January .....	267
Figure 7.2.20 Indoor simulation with the air conditioning of No-PCM wall in August .....	267
Figure 7.2.21 Indoor simulation with the air conditioning of PCM6D-30% wall in January.....	268
Figure 7.2.22 Indoor simulation with the air conditioning of PCM6D-30% wall in August.....	268
Figure 7.2.23 Indoor simulation with the air conditioning of PCM18D-30% wall in January...268	268
Figure 7.2.24 Indoor simulation with the air conditioning of PCM18D-30% wall in August....	268
Figure 7.2.25 Indoor simulation comparison with the air conditioning of gypsum and No-PCM in January .....	269
Figure 7.2.26 Indoor simulation comparison with the air conditioning of gypsum and No-PCM in August .....	269
Figure 7.2.27 Indoor simulation comparison with the air conditioning of PCM6D-30% and No-PCM in January.....	270
Figure 7.2.28 Indoor simulation comparison with the air conditioning of PCM6D-30% and No-PCM August.....	270
Figure 7.2.29 Indoor simulation comparison with the air conditioning of PCM18D-30% and No-PCM January.....	270
Figure 7.2.30 Indoor simulation comparison with the air conditioning of PCM18D-30% and No-PCM in August.....	270

Figure 7.2.31 Indoor simulation comparison with the air conditioning of PCM6D-30% &PCM18D-30% in January .....	271
Figure 7.2.32 Indoor simulation comparison with the air conditioning of PCM6D-30% &PCM18D-30% in August. ....	271
Figure 7.2.33 Air-conditioning load of the gypsum wall building in January .....	272
Figure 7.2.34 Air-conditioning load of the gypsum wall building in August .....	272
Figure 7.2.35 Air-conditioning load of the No-PCM wall building in January .....	272
Figure 7.2.36 Air-conditioning load of the No-PCM wall building in August .....	272
Figure 7.2.37 Air-conditioning load of the PCM6D-30% wall building in January .....	273
Figure 7.2.38 Air-conditioning load of the PCM6D-30% wall building in August .....	273
Figure 7.2.39 Air-conditioning load of the PCM18D-30% wall building in January .....	273
Figure 7.2.40 Air-conditioning load of the PCM18D-30% wall building in August .....	273
Figure 7.2.41 Air-conditioning load of gypsum wall building and No-PCM wall building in January .....	274
Figure 7.2.42 Air-conditioning load of gypsum wall building and No-PCM wall building in August .....	274
Figure 7.2.43 Air-conditioning load of No-PCM wall building and PCM6D-30% wall building in January .....	274
Figure 7.2.44 Air-conditioning load of No-PCM wall building and PCM6D-30% wall building in August .....	274
Figure 7.2.45 Air-conditioning load of No-PCM wall building and PCM18D-30% wall building January .....	275
Figure 7.2.46 Air-conditioning load of No-PCM wall building and PCM18D-30% wall building in August .....	275
Figure 7.2.47 Air-conditioning load of PCM6D-30% wall building and PCM18D-30% wall building in January .....	275
Figure 7.2.48 Air-conditioning load of PCM6D-30% wall building and PCM18D-30% wall building in August .....	275
Figure 7.2.49 Monthly division air-conditioning load .....	276
Figure 7.2.50 Air-conditioning load percentage of PCM6D-10% in No-PCM standard .....	277
Figure 7.2.51 Air-conditioning load percentage of PCM6D-20% in No-PCM standard .....	277
Figure 7.2.52 Air-conditioning load percentage of PCM6D-30% in No-PCM standard .....	277

## List of tables

Table 1-1 The advantages and disadvantages of the thermal properties of the PCM.....	15
Table 2-1 Chemical composition of fly ash.....	26
Table 2-2 Different studied encapsulated PCMs with their size, melting point and heat of fusion .....	27
Table 2-3 Specification of OM mixer.....	30
Table 2-4 Pure PCM enthalpy, onset and end temperatures for different PCM sample.....	31
Table 2-5 Mix proportion for foam concrete adding PCM .....	37
Table 2-6 Result of compressive strength of foam concrete .....	38
Table 2-7 Density control in PCM concretes. ....	43
Table 2-8 Enthalpy variation and standpoint temperatures scanning rates varying from 10°C/min to 0.5°C/min (6D).....	51
Table 2-9 Enthalpy variation and standpoint temperatures scanning rates varying from 10°C/min to 0.5°C/min (18D).....	54
Table 2-10 Enthalpy variation and standpoint temperatures scanning rates varying from 10°C/min to 0.5°C/min (28D).....	57
Table 2-11 Enthalpy variation and standpoint temperatures scanning rates varying from 10°C/min to 0.5°C/min (43D).....	60
Table 3-1 Thermo physical properties of various microencapsulated PCMs.....	98
Table 3-2 Chemical composition of silica sand (No.5).....	99
Table 3-3 Physical properties of silica sand (No.5).....	99
Table 3-4 Chemical composition of aggregate.....	99
Table 3-5 Physical properties of aggregate. ....	99
Table 3-6 Mix composition of foam concrete. ....	100
Table 3-7 Mix composition of ordinary concrete. ....	100
Table 3-8 Mix composition of high-density concrete. ....	101
Table 3-9 Enthalpy variation and standpoint temperatures scanning rates varying from 10°C/min to 0.5°C/min. ....	121
Table 3-10 Enthalpy variation and standpoint temperatures scanning rates varying from 10°C/min	



to 0.5°C/min. ....	122
Table 3-11 Enthalpy variation and standpoint temperatures scanning rates varying from 10°C/min to 0.5°C/min. ....	123
Table 4-1 Thermo physical properties of various microencapsulated PCMs. ....	148
Table 4-2 Chemical composition of silica sand (No.5). ....	149
Table 4-3 Physical properties of silica sand (No.5). ....	149
Table 4-4 Mix design of polymer modified concrete with PCMs. ....	150
Table 4-5 Mix design of polymer modified concrete with PCMs. ....	151
Table 4-6 Mix compositions. ....	161
Table 4-7 Mechanical results of No-PCM and PCM6D. ....	162
Table 4-8 Mechanical results of PCM18D, PCM28D and PCM43D. ....	163
Table 4-9 Enthalpy variation and standpoint temperatures scanning rates varying from 10°C/min to 0.5°C/min. ....	169
Table 5-1 Mix designs of the NRG foam. ....	202
Table 5-2 The results of volume measurement for reference NRG-foam samples ....	205
Table 5-3 7 days density test of NRG foam samples with No-PCM. ....	209
Table 5-4 28 days density test of NRG foam samples with No-PCM. ....	210
Table 5-5 7 days density test of NRG foam samples with 5% PCM. ....	211
Table 5-6 28 days density test of NRG foam samples with 5% PCM. ....	211
Table 5-7 7 days density test of NRG foam samples with 10% PCM. ....	212
Table 5-8 28 days density test of NRG foam samples with 10% PCM. ....	213
Table 5-9. Relationship between R <sub>P</sub> -value and R <sub>F</sub> -value. ....	224
Table 6-1. Inputs Parameters for simulation Process. ....	233
Table 7-1 Simulation parameters. ....	252
Table 7-2 Characteristic of the structure materials of the calculation model ....	253
Table 7-3 Thermal conductivity of PCM concrete ....	257
Table 7-4 Density of concrete PCM concrete ....	257
Table 7-5 Phase change behavior of PCM concrete ....	257
Table 7-6 Specific Heat of No-PCM ....	236
Table 7-6 Specific Heat of PCM6D ....	236
Table 7-6 Specific Heat of PCM18D ....	236

**CHAPTER 1**  
**INTRODUCTION**

## 1.1 INTRODUCTION

### 1.1.1 World Energy sources and consumption

First, what energy do we have in today's world? There are two types of energy sources: renewable and non-renewable. The renewable energy sources include solar, wind, geothermal energy from the heat inside the earth, hydropower from flowing water, ocean (in the form of wave and tide), and biomass from plants. While non-renewable one comprises petroleum, hydrocarbon gas liquids, natural gas, coal, and nuclear energy [1].

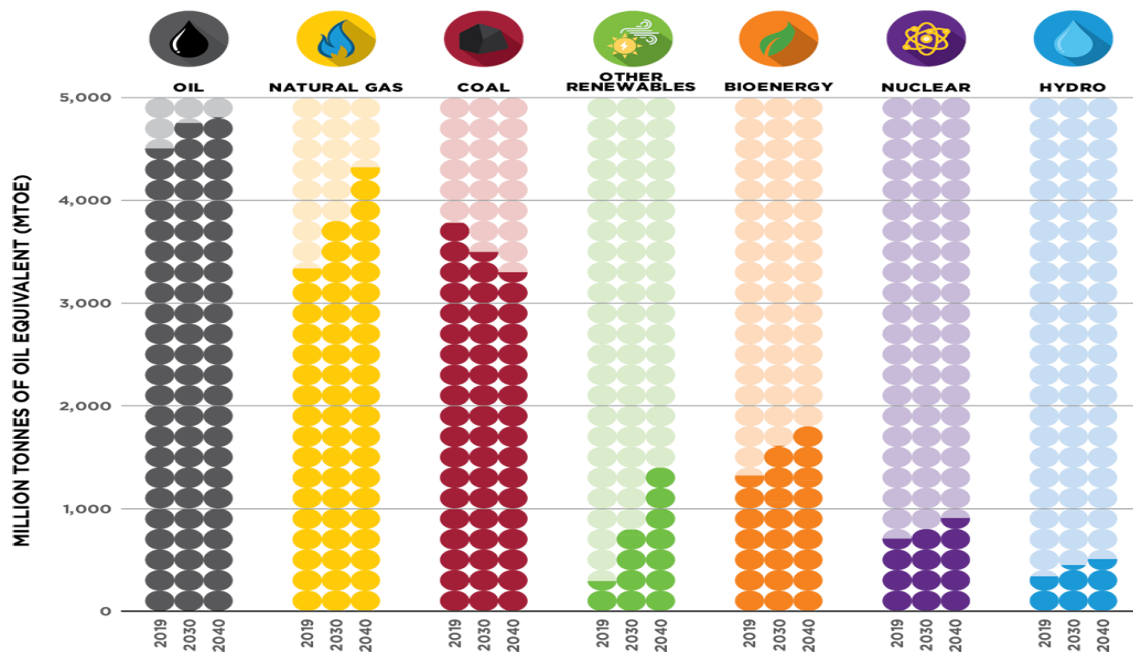


Figure 1.1.1 From 2019 to 2040, the fluctuation in the number of global energy sources [2].

As of 2019, the global population stood at 7.7 billion. However, projections indicate that this figure is expected to surge to approximately 9 billion by the year 2040. In light of this anticipation, despite the presence of readily available energy resources (details provided in the graph below), the demand for energy continues to rise and is predicted to double over the course of two decades, driven by an improvement in living standards. Notably, as countries like India and China transition their populations out of poverty, there is a corresponding increase in electricity consumption among their citizens. While the United States has been a significant consumer of oil in recent years, China now leads the world in electricity consumption. Other nations also play a part in this energy consumption landscape, with their ranking's contingent upon the types of energy resources they utilize.

### Global primary energy consumption by region (2010-2050)

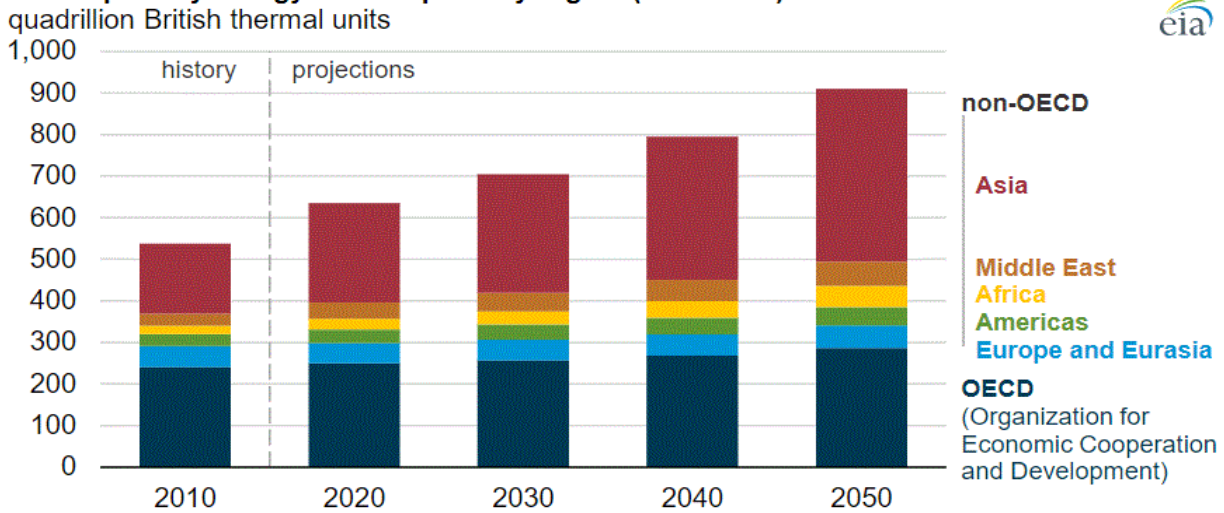


Figure 1.1.2 From 2019 to 2050, Global primary energy consumption by region [3].

Another source also approved that the need for whole world energy consumption tends to sustainably climb from over 500 quadrillion (by British thermal units) to 900 quadrillion from 2010 until 2050. According to the Energy information administration (EIA), the energy consumption will nearly be 2040 years. The 6 different colors of sources below the table show us the energy demand forecast over 3 decades from 2020. Many developing nations in the Asian continent who are not registered at Organization for Economic Cooperation and Development (OECD) rather increase the energy consumption greatly.

### Global energy consumption by sector (2010-2050)

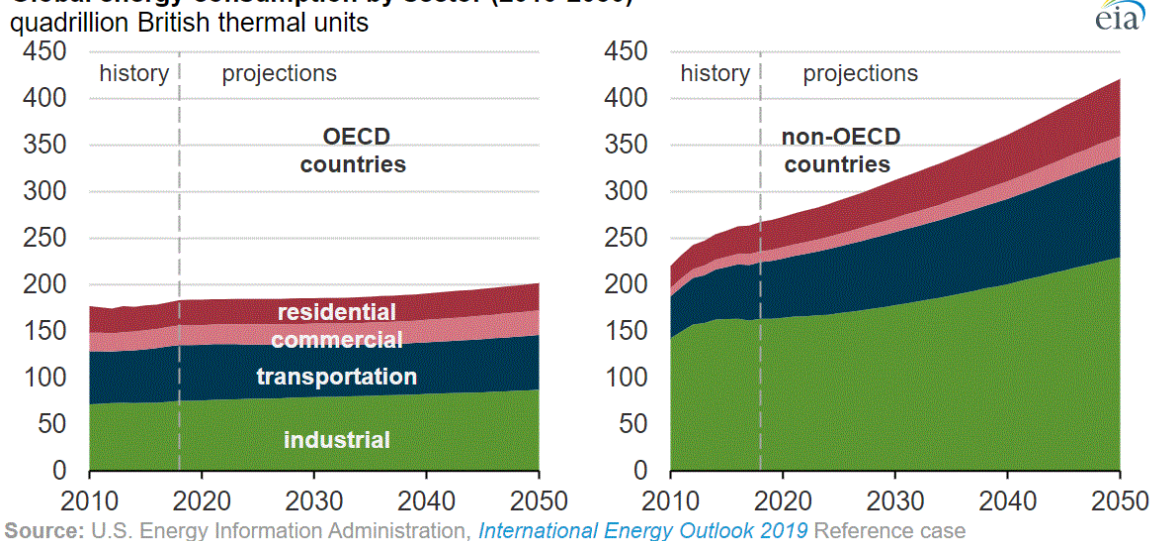


Figure 1.1.3 From 2010 to 2050, Global energy consumption by sector [3].

The largest share of energy consumption, divided by sectors, is attributed to the industrial sector, encompassing activities such as refining, mining, manufacturing, agriculture, and construction. In essence, this sector accounts for roughly half of the total energy usage from 2010 to 2050. It is anticipated that as industrial production continues to expand, energy input in this sector will witness a minimum 30% increase over the course of three decades.

The second most significant contributor to energy demand, namely the transportation sector, is expected to experience a notable surge of approximately 40% in energy consumption over the 30-year period starting in 2020. It's worth highlighting the non-OECD countries in this context, as their energy consumption is projected to escalate by a substantial 80% during the same timeframe. This increase can be attributed to heightened tourism and freight shipping activities, which are set to consume more energy compared to developed OECD countries.

Energy usage in buildings designated for residential and commercial purposes is forecasted to rise by 65%, climbing from 91 quadrillion to 139 quadrillion BTUs. While this increase is slightly lower than that of the transportation sector, factors such as urban concentration and increased access to electricity will contribute significantly to the growth in energy consumption.

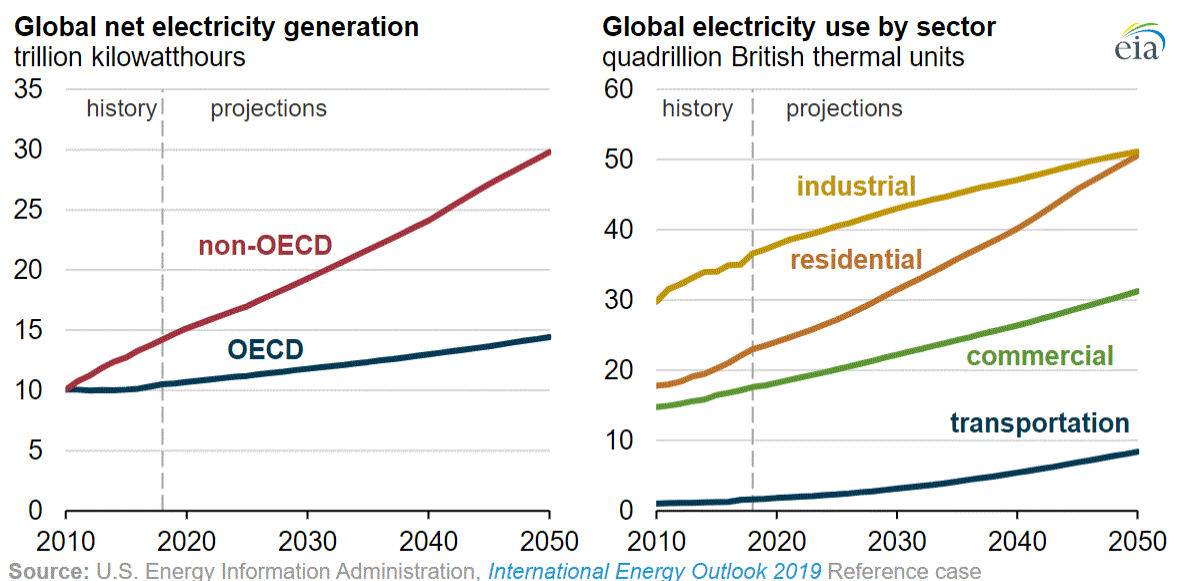


Figure 1.1.4 From 2019 to 2050, Global electricity consumption by sector [3].

From 2018 to 2050, the growing energy consumption across various end-uses is expected to drive a significant 79% increase in electricity generation. This increase can be attributed to several factors, including the rising population and the migration of people into urban residential areas in Asian countries. As individuals' living standards improve, there will be a notable surge in energy consumption related to personal electronic devices and appliances.

Furthermore, the transportation sector will play a significant role in this escalation of electricity

consumption. This increase will be facilitated by a higher number of daily commuters utilizing electric vehicles for their personal transportation needs, along with the expansion of public rail systems.

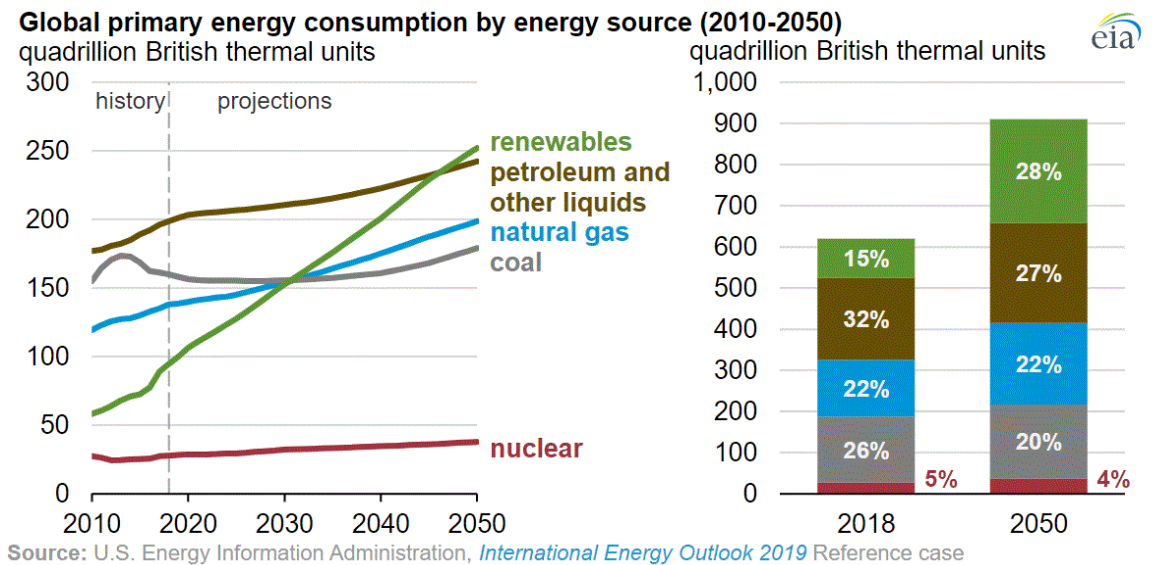


Figure 1.1.5 From 2019 to 2050, Global primary energy consumption by energy source [3].

Between 2018 and 2050, the demand for electricity generation will see an urgent need for a significant increase. To address this demand, renewable energy sources such as solar, wind, and hydroelectric power will emerge as highly favorable and cost-effective alternatives. In this Reference case scenario, renewables are projected to surpass petroleum and other liquid fuels to become the predominant energy source. Over this 32-year period, global renewable energy consumption is expected to grow at a rate of 3.1% annually. This growth rate outpaces natural gas consumption, which is anticipated to increase by 1.1%, as well as petroleum and other liquids at 0.6%, and coal at a slower rate of 0.4%.

The global consumption of natural gas will increase significantly, driven by a 40% share of the world's population. This will result in a total consumption of 200 quadrillion Btu by 2050. Natural gas will not only be used for electricity generation but will also have high demand in the industrial sector, particularly in industries such as chemical and primary metals manufacturing, as well as oil and natural gas extraction.

Liquid fuel consumption worldwide is projected to grow by more than 20% from 2018 to 2050, reaching a total consumption of 240 quadrillion Btu by the end of the period. Demand for energy in OECD countries is expected to remain at current levels throughout the project period, while non-OECD countries will experience substantial growth of up to 45%.

### 1.1.2 Energy and buildings

Electricity in buildings serves various purposes, including heating during winter, cooling in summer, air conditioning, ventilation systems, lighting, and powering a wide range of home and industrial appliances. Among these uses, electricity and heat are the primary and direct forms of energy consumption. Electricity serves multiple functions, encompassing heating, cooling, lighting, air conditioning, and more, while heat is primarily used for heating purposes.

It's worth noting that the building sector accounts for a significant portion of global final energy consumption. Specifically, less than half of the total final energy consumption (precisely 37%) is attributed to industries, with 21% allocated to the residential sector, and an additional 29% to transportation in global statistics. This highlights that the building sector garners significant attention from researchers aiming to reduce overall energy consumption. Figure 1.2.6 illustrates the world's total final consumption by sector.

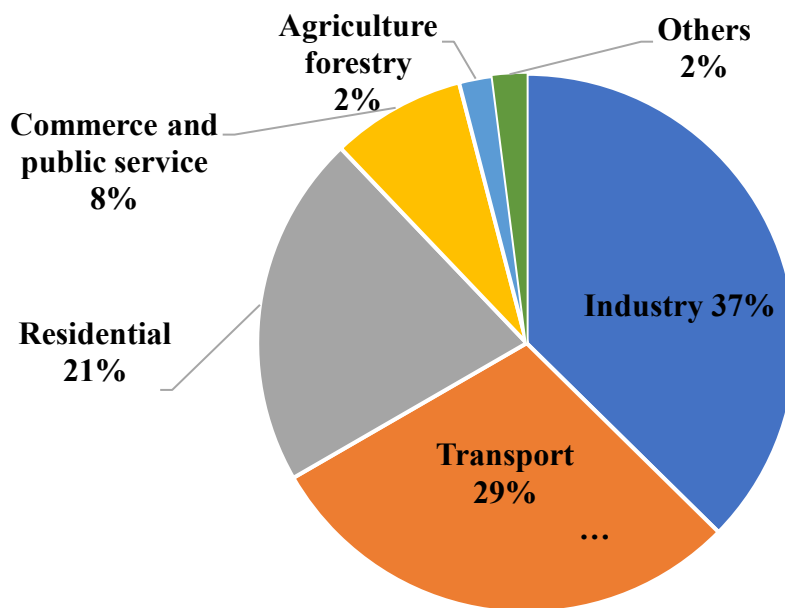


Figure 1.1.6 World total final consumption by sector in 2017 [4].

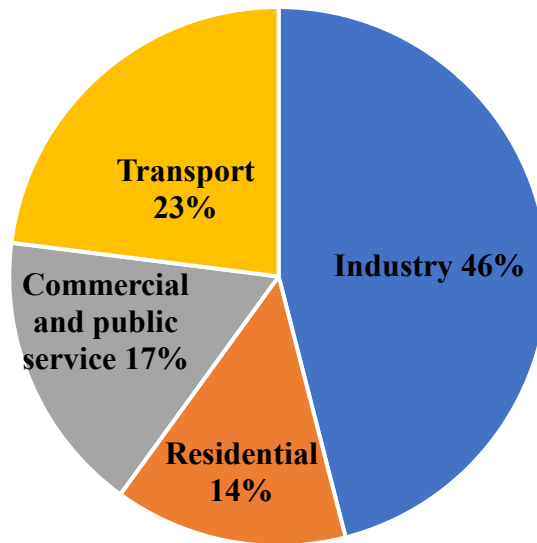


Figure 1.1.7 Breakdown of the final energy use by sectors in Japan 2018 [5].

The energy consumption of buildings varies significantly based on several factors, including climatic conditions, the building's intended use (residential or commercial), architectural design, and construction materials. For instance, buildings located in cold climate regions typically have higher energy consumption for heating, while those in tropical areas consume more energy for cooling. Commercial high-rise buildings and business centers in urban areas have elevated energy usage due to extensive lighting and large-screen advertisements, surpassing the energy consumed by residential lighting.

The pie chart below illustrates the distribution of energy consumption across different end-users in selected cities within European countries and regions, specifically for residential buildings in 2019. It demonstrates that the most substantial portion of energy consumption is attributed to space heating.



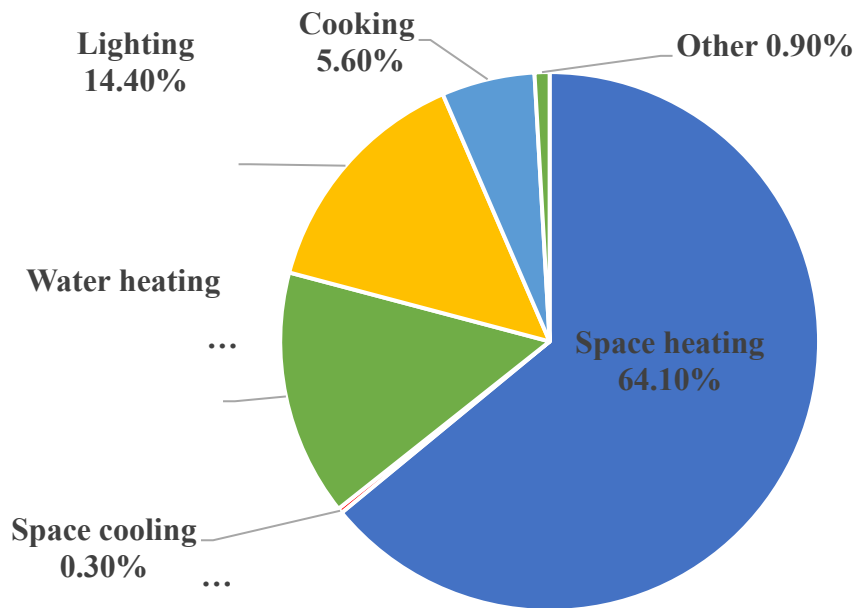


Figure 1.1.8 Percentage shares of energy use in a residential building in Europe in 2019[6].

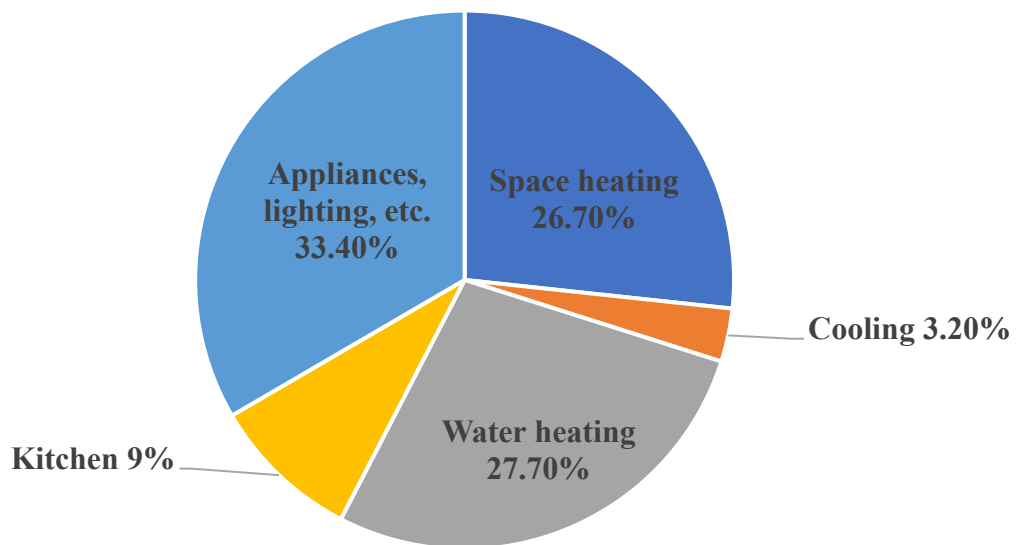


Figure 1.1.9 Percentage shares of energy use in a residential building in Japan in 2020 [7].

Source: The Institute of Energy Economics, Japan, 2020 EDMC Handbook of Energy and Economic Statistics in Japan

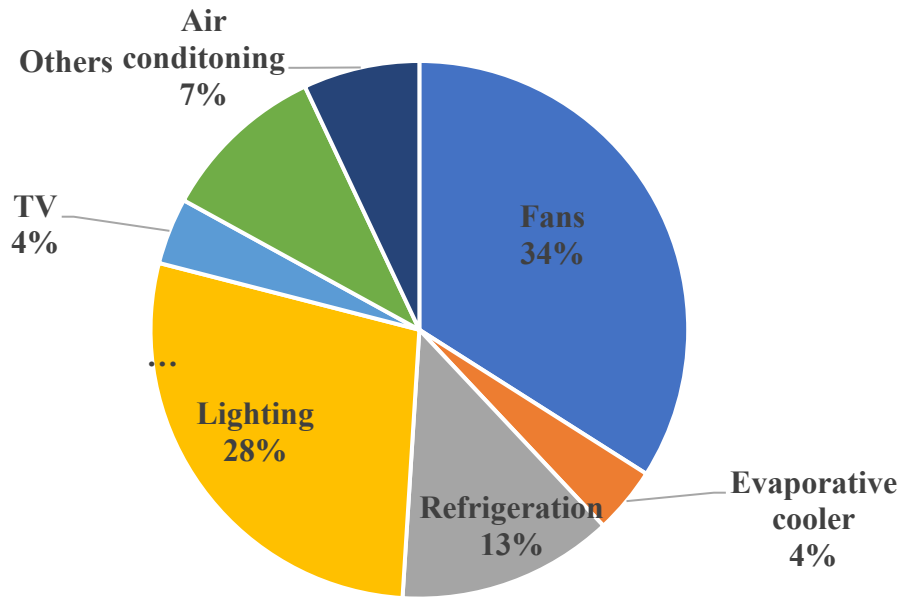


Figure 1.1.10. Percentage shares of energy use in a residential building in India in 2010 [8].

Analyzing the upper pie chart, it's evident that heating, cooling, and ventilation together account for the largest portion of energy consumption within buildings, surpassing all other purposes of energy consumption. To significantly reduce this percentage, the introduction of more advanced and efficient technologies in air conditioning, ventilation, and cooling systems is essential to enhance people's comfort inside buildings and contribute to global energy conservation efforts. The successful adoption of low-energy air conditioning innovations, once experienced by users, would lead to a reduction in energy consumption and a decrease in fossil fuel emissions simultaneously. Additionally, it's clear that buildings represent the most significant share of fossil fuel consumption worldwide.

## 1.2 OBJECTIVES AND STRUCTURE OF THESIS

### 1.2.1 Structure of thesis

This research focuses on the development of sustainable and energy-efficient building materials by incorporating phase change materials (PCMs) into concrete structures. PCM concrete offer a promising solution by efficiently storing and releasing thermal energy, reducing heating and cooling loads, and promoting sustainability in construction. This innovative approach can create and maintain a comfortable thermal environment while significantly reducing energy consumption. This thesis is structured into eight chapters, each contributing to the development of sustainable and energy-efficient building materials.

**Chapter 1** presents the integration of PCM into cement structures to address the increasing energy consumption in the building sector.

**Chapter 2** addresses the challenges of integrating PCM into concrete structures, focusing on the development of innovative fly ash foam concrete that utilizes several types of PCM with different phase change temperature ranges without energy loss or damage. In the findings, the potential for energy savings and thermal comfort in building applications is highlighted.

**In Chapter 3**, aimed to significantly increase the energy storage and thermal storage capacity of concrete by increasing the thermal conductivity and integrating the two types of PCMs. A two-pronged approach focusing on thermal conductivity and the two mixed PCMs was adopted to improve the potential for energy use reduction.

**Chapter 4** describes a collaborative study with a precast concrete plant that used this material and focused on addressing issues in multi-family housing using exterior insulation. Requirements included reducing the temperature rise of the concrete, maintaining the bond strength between tile and concrete, and maintaining the integrity of the PCM geometry. This study proposed the use of PCM polymer cement mortar to increase bond strength and reduce excessive temperature fluctuations.

**In Chapter 5**, in collaboration with the Technical University of Darmstadt, Germany, an ultralight PCM foam concrete, NRG foam, was introduced to establish an empirical model for thermal insulation and energy storage.

**In Chapter 6**, a comprehensive numerical simulation analysis was performed to validate the experimental data and establish a predictive model for the energy efficiency of concrete. The role of PCM in maintaining room temperature was clarified.

In Chapter 7, Energy Plus software was used for energy analysis simulations. It was shown that the effectiveness of PCM use in housing is intrinsically linked to the specific climate zone in regions where the climate closely matches the phase change temperature of the PCM material, and that energy loads are significantly reduced when the phase change temperature range of the PCM matches the climate zone.

Chapter 8 summarizes the results of this study and presents challenging prospects for the future. The results of this extensive exploration are promising: PCM concrete has great potential to revolutionize building materials if optimized with the right PCM materials and design.

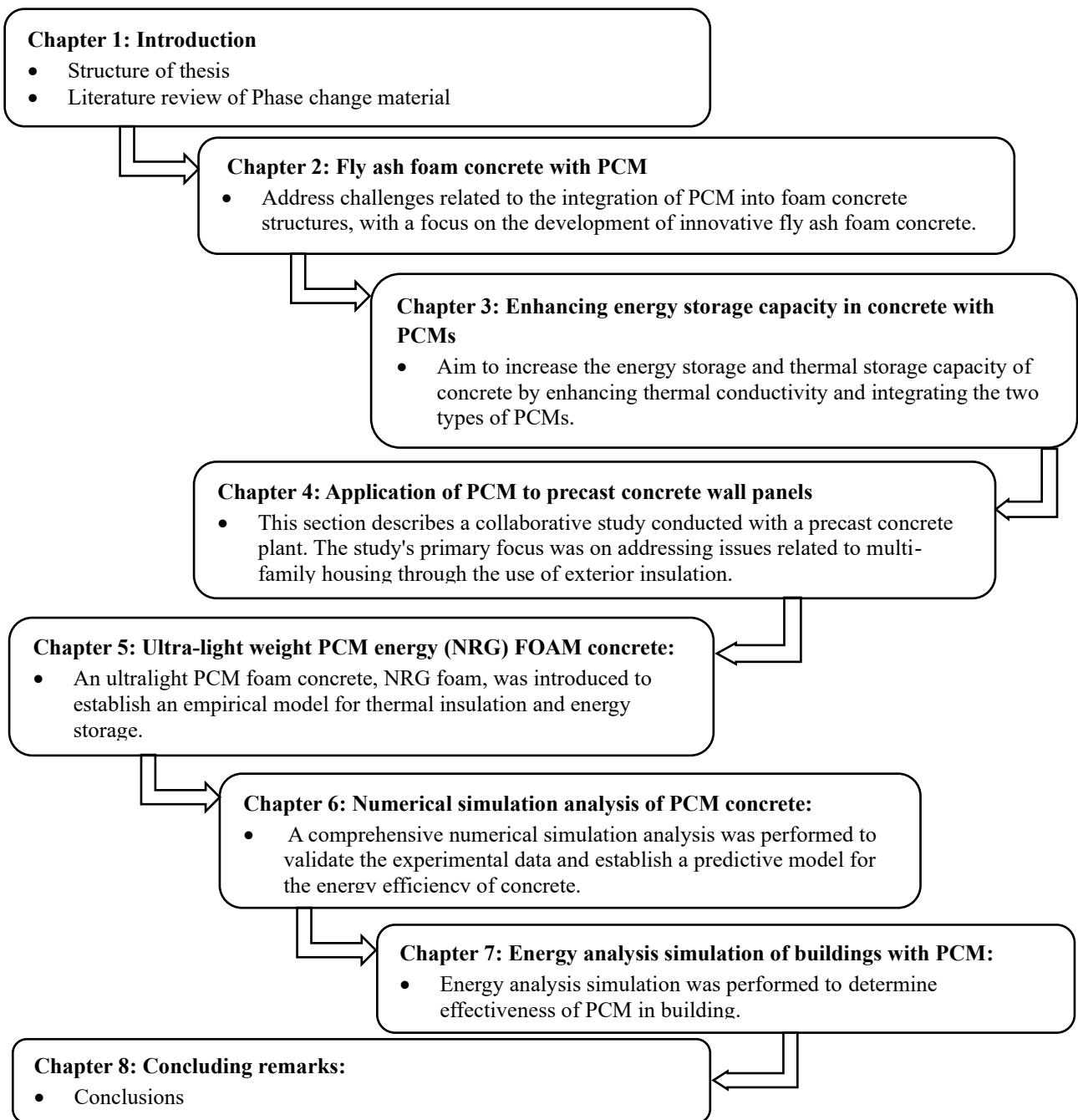


Figure 1.2.1. Flow chart of research work.

## REFERENCES

- [1] Rinkesh, “What are different alternative sources of energy.” [Online]. Available: <https://www.conserve-energy-future.com/family-survive-two-weeks-without-power.php>
- [2] M. Preparation *et al.*, “A Smart Epoxy Composite Based on Phase Change”, doi: 10.3390/molecules24050916.
- [3] T. C. Ling and C. S. Poon, “Use of phase change materials for thermal energy storage in concrete: An overview,” *Constr Build Mater*, vol. 46, pp. 55–62, 2013, doi: 10.1016/j.conbuildmat.2013.04.031.
- [4] P. Prabhu, N. Shinde, and P. Patil, “Review of phase change materials for thermal energy storage applications97,” *International Journal of Engineering Research and Applications (IJERA)*, vol. 2, no. 3, pp. 871–875, 2012.
- [5] A. R. Sakulich and D. P. Bentz, “Incorporation of phase change materials in cementitious systems via fine lightweight aggregate,” *Constr Build Mater*, vol. 35, pp. 483–490, 2012, doi: 10.1016/j.conbuildmat.2012.04.042.
- [6] Q. Xie, L. Yang, F. Hu, W. Hao, S. Yin, and L. Zhang, “Degradation behavior of concrete after freeze-thaw cycles and then exposure to high temperatures,” *Advances in Materials Science and Engineering*, vol. 2019, 2019, doi: 10.1155/2019/9378935.
- [7] C. Castellón, M. Medrano, J. Roca, M. Nogués, A. Castell, and L. F. Cabeza, “Use of Microencapsulated Phase Change Materials in Building Applications,” *Ashrae*, 2008.
- [8] M. Hunger, A. G. Entrop, I. Mandilaras, H. J. H. Brouwers, and M. Founti, “The behavior of self-compacting concrete containing micro-encapsulated Phase Change Materials,” *Cem Concr Compos*, vol. 31, no. 10, pp. 731–743, 2009, doi: 10.1016/j.cemconcomp.2009.08.002.
- [9] T. Lee, D. W. Hawes, D. Banu, and D. Feldman, “Control aspects of latent heat storage and recovery in concrete,” *Solar Energy Materials and Solar Cells*, vol. 62, no. 3, pp. 217–237, 2000, doi: 10.1016/S0927-0248(99)00128-2.
- [10] D. W. Hawes, D. Banu, and D. Feldman, “The stability of phase change materials in concrete,” *Solar Energy Materials and Solar Cells*, vol. 27, no. 2, pp. 103–118, 1992, doi: 10.1016/0927-0248(92)90113-4.
- [11] D. W. Hawes, D. Feldman, and D. Banu, “Latent heat storage in building materials,” *Energy Build*, vol. 20, no. 1, pp. 77–86, 1993, doi: 10.1016/0378-7788(93)90040-2.
- [12] T. Lee, D. W. Hawes, D. Banu, and D. Feldman, “Control aspects of latent heat storage and recovery in concrete,” *Solar Energy Materials and Solar Cells*, vol. 62, no. 3, pp. 217–237, 2000, doi: 10.1016/S0927-0248(99)00128-2.
- [13] 永瀬伸子, “少子化の要因 : 就業環境か価値観の変化かNo Title,” 「ジャーナル」, vol. 49, no. 1, p. 11, 2008.
- [14] N. Uddin, F. Fouad, U. K. Vaidya, A. Khotpal, and J. C. Serrano-Perez, “Structural characterization of hybrid Fiber reinforced Polymer (FRP)-Autoclave Aerated Concrete (AAC) panels,” *Journal of Reinforced Plastics and Composites*, vol. 25, no. 9, pp. 981–999, 2006, doi: 10.1177/0731684406065090.
- [15] Brady, G. R. A. Watts, and R. Jones, “Specification for Foamed Concrete,” *TRL Limited*, p. 78, 2001.
- [16] Z. Pan, F. Hiromi, and T. Wee, “Preparation of high performance foamed concrete from cement,

- sand and mineral admixtures,” *Journal Wuhan University of Technology, Materials Science Edition*, vol. 22, no. 2, pp. 295–298, 2007, doi: 10.1007/s11595-005-2295-4.
- [17] T. H. Wee, S. B. Daneti, and T. Tamilselvan, “Effect of w/c ratio on air-void system of foamed concrete and their influence on mechanical properties,” *Magazine of Concrete Research*, vol. 63, no. 8, pp. 583–595, 2011, doi: 10.1680/mac.2011.63.8.583.
- [18] Y. H. M. Amran, N. Farzadnia, and A. A. A. Ali, “Properties and applications of foamed concrete; A review,” *Constr Build Mater*, vol. 101, no. May 2017, pp. 990–1005, 2015, doi: 10.1016/j.conbuildmat.2015.10.112.
- [19] M. R. Jones and A. McCarthy, “Utilising unprocessed low-lime coal fly ash in foamed concrete,” *Fuel*, vol. 84, no. 11, pp. 1398–1409, 2005, doi: 10.1016/j.fuel.2004.09.030.
- [20] X. Zhao *et al.*, “Addendum: Zhao, X.; et al. Properties of foamed mortar prepared with granulated blast-furnace slag. *Materials* 2015, 8(2), 462-473,” *Materials*, vol. 8, no. 7, pp. 3958–3959, 2015, doi: 10.3390/ma8073958.
- [21] A. S. Tarasov, E. P. Kearsley, A. S. Kolomatskiy, and H. F. Mostert, “Heat evolution due to cement hydration in foamed concrete,” *Magazine of Concrete Research*, vol. 62, no. 12, pp. 895–906, 2010, doi: 10.1680/mac.2010.62.12.895.
- [22] J. Sathya Narayanan and K. Ramamurthy, “Development of solid, foam concrete interlocking blocks and studies on short masonry specimens,” *Masonry International*, vol. 26, no. 1, pp. 7–16, 2013.
- [23] M. A. O. Mydin and Y. C. Wang, “Mechanical properties of foamed concrete exposed to high temperatures,” *Constr Build Mater*, vol. 26, no. 1, pp. 638–654, 2012, doi: 10.1016/j.conbuildmat.2011.06.067.
- [24] Z. Zhang, J. L. Provis, A. Reid, and H. Wang, “Mechanical, thermal insulation, thermal resistance and acoustic absorption properties of geopolymer foam concrete,” *Cem Concr Compos*, vol. 62, pp. 97–105, 2015, doi: 10.1016/j.cemconcomp.2015.03.013.
- [25] 算手法の提案潜熱蓄熱建材の実装形態を考慮した計, 准教授・博士 (工学) 東京大学大学院工学系研究科, and A. Prof, “日本建築学会技術報告集 第 25 巻 第 60 号, 735-740, 2019 年 6 月,” *AIJ J. Technol. Des*, vol. 25, no. 60, pp. 735–740, 2019, doi: 10.3130/aijt.25.735.
- [26] Y. Kusama and Y. Ishidoya, “Effects of construction position of PCM layer on energy conservation and environmental improvement,” *AIJ Journal of Technology and Design*, vol. 22, no. 52, pp. 1027–1030, Oct. 2016, doi: 10.3130/aijt.22.1027.
- [27] S. Ji *et al.*, “Study on introduction effects of phase change building materials used in wooden houses (part 1): Verification on heat storage effect of phase change building materials by laid position using real-scale experimental room in winter,” *AIJ Journal of Technology and Design*, vol. 26, no. 64, pp. 1025–1030, Oct. 2020, doi: 10.3130/aijt.26.1025.
- [28] S. M. Md Suman Mia, Yuya Takahashi, Tetsuya Ishida, and Koichi Tsuchiya, “Thermal and Mechanical Properties of Porous Cementitious Composites Using Phase-Change Materials with Different Microstructures,” *The 4th International Conference On Green Civil and Environmental Engineering*, 2023.

## 1.3 LITERATURE REVIEW OF PHASE CHANGE MATERIALS (PCM)

### 1.3.1 Definition of PCM

Phase change materials (PCMs) fall under the category of thermal energy storage materials (TES). They utilize a phase transition process, typically shifting from a solid to a liquid state within a specific temperature range to store latent energy, or reversing from a liquid to a solid state to release the stored energy. This phase change mechanism allows these materials to maximize their energy storage capacity while experiencing minimal volume changes. Unlike concrete and many other materials, which primarily exhibit sensible heat storage (energy storage due to temperature increases), PCMs exhibit latent heat storage during a phase change. In this process, the temperature remains constant while energy is absorbed during the melting phase and stored until the material reverts to a solid state. At this point, the stored energy is released into the surrounding environment, as depicted in Figure 1.3.1. These unique characteristics make PCMs highly promising for integration into building systems.

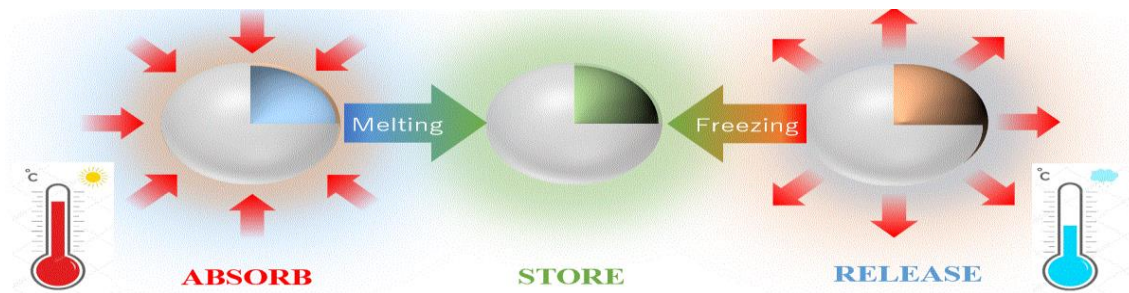


Figure 1.3.1 Structure and working principle of microencapsulation.

### 1.3.2 Classification of PCM

Phase change materials (PCMs) commonly employed in concrete can be categorized into three main principles: inorganic, organic, and eutectics [2][3]. From a concrete design perspective, it's crucial to determine which type of PCMs is appropriate for specific concrete applications because different PCMs possess distinct melting/transition temperatures and chemical properties. Here are the general characteristics of organic, inorganic, and eutectic PCMs.

#### a. Organic PCM

Organic PCMs can be categorized as either paraffin or non-paraffin. Paraffin PCMs have found extensive use due to their high heat latent, a range of phase-change temperatures, supercooling, low vapor pressure in a molten state, and good chemical stability. Paraffin wax is composed of a mixture of predominantly straight-chain alkanes ( $\text{CH}_3\text{-(CH}_2\text{)-CH}_3$ ) [4]. The crystallization of the ( $\text{CH}_3$ )-chain releases a significant amount of latent heat [5]. Both the melting point and latent heat of fusion

increase with chain length [5]. Paraffin is a suitable heat of fusion storage material due to its availability across a wide temperature range [6]. Numerous previous studies have successfully demonstrated the widespread use of organic paraffin with a phase change temperature in concrete [6]. Paraffin is one of the most common PCMs used in concrete because it is inert in an alkaline environment, chemically stable, and cost-effective. However, paraffin does have drawbacks, including flammability and low thermal conductivity in its solid state.

**b. Inorganic PCM**

Inorganic phase change materials (PCM) can be categorized into metallic and salt hydrate materials. These inorganic PCMs have potential applications in certain building materials due to their excellent thermal conductivity and high volumetric heat storage capacity [7]. These properties make them advantageous for specific applications. However, inorganic PCMs, especially salt hydrates, have certain unfavorable characteristics, including significant volume changes and supercooling during the solid-liquid transition. As a result, hydrated salts are often not considered suitable materials for incorporation into concrete [3].

Table 1-1 The advantages and disadvantages of the thermal properties of the PCM.

Material name	Type	Melting point (°C)	Melting heat (J/g)	Advantages	Disadvantages
Heptadecane	Organic	27.5	224	No corrosion,	Low energy storage
n-octadecene	Organic	19	240	high chemical stability, no sub-cooling degree	density, volatile, large volumetric change
Hexadecenoic acid	Organic	62.9	54.3		
Paraffin C17	Organic	21.7	231		
CaCl <sub>2</sub> ·6H <sub>2</sub> O	Inorganic	29	180	High energy storage density, good flame retardant, low price	Sub-cooling degree, severe corrosion, phase separation, poor thermal stability
Na <sub>2</sub> SO <sub>4</sub> ·10H <sub>2</sub> O	Inorganic	32.4	250.8		

**1.3.3 PCMs incorporation in concrete**

There are three distinct techniques for incorporating phase change materials (PCMs) into concrete:

1. Immersion: This technique involves immersing porous concretes or mortars in melted (liquid) PCM.
2. Impregnation: Impregnation entails saturating porous aggregates with PCM.
3. Direct mixing: In this approach, microencapsulated PCM is directly mixed into the concrete mix during the concrete mixing process.



Previous research has shown that the method of PCM incorporation in concrete significantly impacts the thermal and mechanical properties of PCM-concrete.

### 1.3.3.1 Immersion technique

This technique involves immersing liquid phase change material (PCM) into the open spaces within a dried cementitious composite. Its effectiveness relies on several factors, including the permeability and absorption capacity of the porous medium, the operating temperature, and the specific type of PCM used. The process prioritizes the absorption capacity of cement-based materials, followed by the type of PCM, and the required heating degrees to achieve quality saturation in porous concrete [3]. This technique is particularly suitable for concrete bricks, blocks, or wallboards that can absorb significant amounts of PCM. However, it has certain drawbacks, such as potential leakage issues, especially after undergoing various thermal cycles. These issues can have implications for both the environment and the flammability of the final product [8]. Experimental research related to this technique has been conducted by [9][10][11].

### 1.3.3.2 Impregnation technique

The impregnation technique involves immersing a porous matrix in liquid phase change material (PCM) in its melted state. Once the PCM has soaked into the gaps within the matrix, vacuum treatment is applied, and then the matrix is removed to cool down [12]. Its principle is shown in Figure 1.3.2.

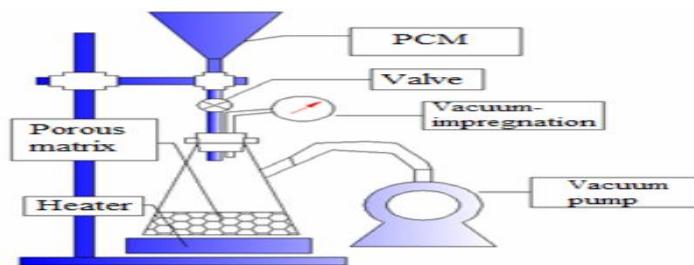


Figure 1.3.2 The principle of vacuum impregnation method [8]

### 1.3.3.3 Direct mixing technique

The direct mixing technique involves incorporating phase change materials (PCMs) into concrete during the mixing process [8]. To prevent leakage and enhance fire resistance, the PCMs are first encapsulated within a chemically and physically stable shell. It's important to note that microencapsulated PCMs (M-PCMs) might reduce the mechanical properties of concrete, particularly when particles are broken during mixing or when high dosages are used. This method has been studied for its application in both Portland cement concrete and geopolymer concrete (GPC).

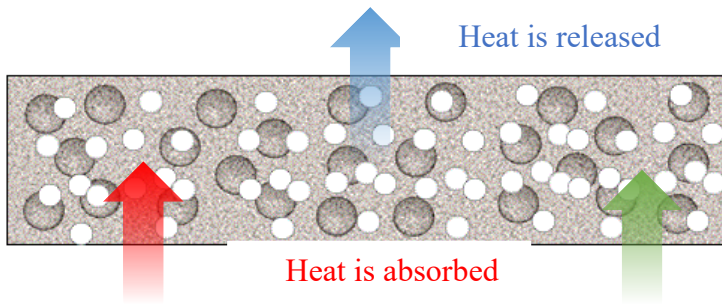


Figure 1.3.3 Direct mixing method

### 1.3.4 Main thermophysical properties of PCM

Figure 1.3.4 presents the general applications of phase change materials (PCMs) in thermal energy storage (TES). These applications involve temperature control and the storage/release of heat while maintaining minimal temperature fluctuations [11]. The figure demonstrates how heat can be absorbed and stored as latent heat without significant changes in the material's temperature, which is a fundamental characteristic of PCMs discussed in Chapter 2,3,4. This property makes PCMs suitable for TES applications where precise temperature control is required.

One of the key advantages of PCMs is their ability to store heat efficiently through latent heat with minimal temperature change, as indicated on the vertical "stored heat axis" within an allowed temperature range where the phase change occurs. It's important to note that the behavior of typical PCMs varies slightly from current PCMs. For typical PCMs, the preferred melting-peak temperature and the isothermal phase-change process's melting temperature range have been altered, as shown in Figure 1.3.4.

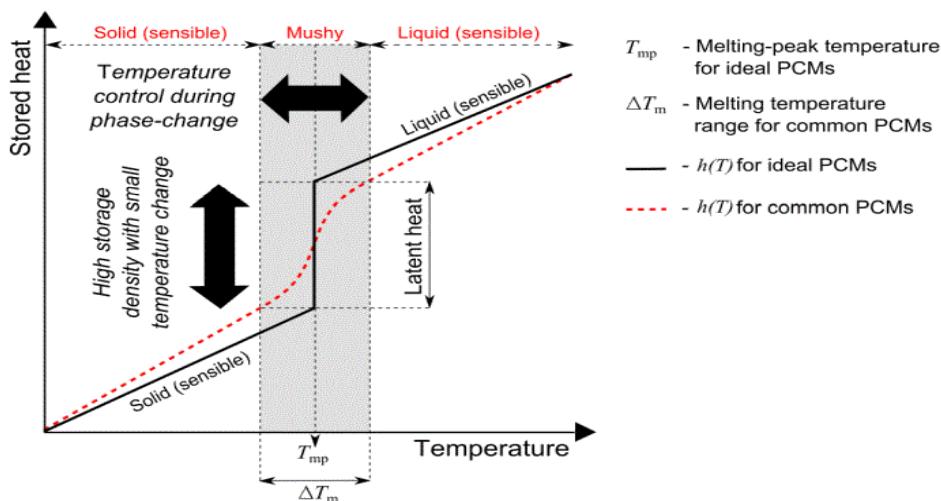


Figure 1.3.4 Potential fields of application of PCM: Temperature control and storage and supply of heat with storage

density and small temperature change [11].

### **1.3.5 Foam concrete**

#### **1.3.5.1 Definition of foam concrete**

Foam concrete is a lightweight construction material consisting of fine sand, cement, stable foam, and water. Its density is determined by millions of small, uniform air bubbles formed during the drying process. This material offers numerous advantages, including being non-flammable, waterproof, and providing sound and thermal insulation. Unlike traditional concrete, foam concrete lacks aggregates, with its unique property lying in its ability to absorb moisture through a foaming agent, enabling smooth cement hydration. Its cellular structure, created by incorporating uniform air bubbles, distinguishes foam concrete, making it similar to other cellular materials. Production involves adding foam to a cement slurry, aerating it to form bubbles, and allowing the cement to set around them. Foam concrete properties vary widely, with mixes tailored to specific requirements, offering diverse physical characteristics.

#### **1.3.5.2 Density**

Density plays a crucial role in foam concrete properties and applications. Achieving a specific density level is a critical concern for various foam concrete uses because density significantly affects mechanical, thermal, transport, and durability properties. Foam concrete can exhibit a wide range of densities, with porosities varying from over 90 percent to as low as 10 percent of the total volume. Consequently, dry density measurements of foam concrete can range from as low as 140 kg/m<sup>3</sup> to more than 1900 kg/m<sup>3</sup> [13] [14]. In the majority of foam concrete mixtures, dry density measurements typically fall within the range of 400 to 1600 kg/m<sup>3</sup> [15]. The primary factor controlling density is the volume of foam used in the mixture. To a lesser extent, the proportions and particle densities of fillers and binders can also influence the final density of the solidified cement paste. It's worth noting that the moisture content of a sample can significantly impact the measured density of foam concrete.

#### **1.3.5.3 Mechanical Properties**

The compressive strength of foam concrete is highly dependent on its porosity. Low-density foam concrete mixes with a density of 160 kg/m<sup>3</sup> typically exhibit compressive strengths as low as 0.04 MPa, whereas mixes with a higher density of 1600 kg/m<sup>3</sup> can achieve compressive strengths of up to 25 MPa. For mixes with similar compositions but varying porosities, there are generally consistent relationships between strength and porosity. However, for a given density, widely diverse values of compression strength are reported for mixes of different compositions [16]. 1600 kg/m<sup>3</sup> mix may

have compressive strength as low as 2 MPa, or as high as 60 MPa [17]. This variation may be attributed to differences in the intrinsic strength of the cement paste, as well as the presence of flaws in the matrix on account of the air void system. The ratio between splitting tensile strength and compressive strength of foam concrete mix may typically be between 0.06 and 0.10 [18]. Tensile strength may be increased in the order of 50 [19] to 100% with the use of reinforcing fibers.

#### **1.3.5.4 Thermal Properties**

The thermal conductivity of lightweight concrete typically follows a logarithmic relationship with its oven-dry density. In the case of foam concrete, it may exhibit slightly better thermal resistance compared to other types of lightweight concrete. This improved thermal resistance is attributed to the characteristics of the air-void system within foam concrete.

The presence of a homogeneous matrix with relatively thin cell walls in foam concrete creates a tortuous path for heat transfer by conduction. Additionally, the low interconnectivity of air voids in foam concrete helps suppress convection and radiative heat transfer. These combined factors contribute to the enhanced thermal resistance of foam concrete, making it an effective choice for applications requiring good insulation properties [20].

In comparison, the thermal conductivity of normal density concrete typically falls in the range of approximately 1.1 to 1.4 W/m·K. Foam concrete, with its lower thermal conductivity values, is a more effective insulating material, making it suitable for various applications where good insulation properties are required [15]. The volumetric heat capacity of foam concrete increases with density. Here are the calculated values for foam concrete at different dry densities: 350 kg/m<sup>3</sup> dry density: Approximately 916 kJ/m<sup>3</sup>·K (equivalent to 2.62 kJ/kg·K), 400 kg/m<sup>3</sup> dry density: Approximately 967 kJ/m<sup>3</sup>·K (equivalent to 2.42 kJ/kg·K), 800 kg/m<sup>3</sup> dry density: Approximately 1479 kJ/m<sup>3</sup>·K (equivalent to 1.85 kJ/kg·K) and 1200 kg/m<sup>3</sup> dry density: Approximately 1998 kJ/m<sup>3</sup>·K (equivalent to 1.67 kJ/kg·K)[21]. In comparison, normal density concrete typically has a specific heat ranging from approximately 0.79 to 0.92 kJ/kg·K, corresponding to approximately 1900 to 2200 kJ/m<sup>3</sup>·K. [22]. Foam concrete's characteristics, including its low thermal conductivity and high heat capacity, result in the material changing temperature slowly. This means it has a low thermal diffusivity, which is an important property for resistance to extreme heat and fire [23]. As the density of foam concrete increases, its thermal diffusivity also increases. For foam concrete with densities ranging from 583 to 1370 kg/m<sup>3</sup>, thermal diffusivity was reported to increase from 0.27 to 0.34 mm<sup>2</sup>/s [24]. This difference in thermal diffusivity contributes to foam concrete's ability to withstand high temperatures and provides advantages in fire resistance.

### 1.3.6 Literature review of current study on Phase change material (PCM) in Japan

Researchers mostly involves the incorporation PCM into plaster board [25] [26], insulation materials and wooden house etc. For example, Taniguchi et al.[27] specifically investigated the thermal properties of wooden houses incorporating PCM. Their study examined the optimal placement of PCM under the floor finishing material, revealing notable enhancements in heat absorption and dissipation efficiency. Furthermore, Serikawa et al.[25] conducted a study on an insulation box with PCM to introduce calculation methods for PCM behavior. However, only few researchers were dealing with PCM concrete [28]. Applying PCM into concrete without any damage and energy loss can be one of the major challenges. In our study, we dealt with problems and found solutions to improve the thermal storage capacity of PCM concrete.

### REFERENCES

- [1] Rinkesh, “What are different alternative sources of energy.” [Online]. Available: <https://www.conserve-energy-future.com/family-survive-two-weeks-without-power.php>
- [2] M. Preparation *et al.*, “A Smart Epoxy Composite Based on Phase Change”, doi: 10.3390/molecules24050916.
- [3] T. C. Ling and C. S. Poon, “Use of phase change materials for thermal energy storage in concrete: An overview,” *Constr Build Mater*, vol. 46, pp. 55–62, 2013, doi: 10.1016/j.conbuildmat.2013.04.031.
- [4] P. Prabhu, N. Shinde, and P. Patil, “Review of phase change materials for thermal energy storage applications97,” *International Journal of Engineering Research and Applications (IJERA)*, vol. 2, no. 3, pp. 871–875, 2012.
- [5] A. R. Sakulich and D. P. Bentz, “Incorporation of phase change materials in cementitious systems via fine lightweight aggregate,” *Constr Build Mater*, vol. 35, pp. 483–490, 2012, doi: 10.1016/j.conbuildmat.2012.04.042.
- [6] Q. Xie, L. Yang, F. Hu, W. Hao, S. Yin, and L. Zhang, “Degradation behavior of concrete after freeze-thaw cycles and then exposure to high temperatures,” *Advances in Materials Science and Engineering*, vol. 2019, 2019, doi: 10.1155/2019/9378935.
- [7] C. Castellón, M. Medrano, J. Roca, M. Nogués, A. Castell, and L. F. Cabeza, “Use of Microencapsulated Phase Change Materials in Building Applications,” *Ashrae*, 2008.
- [8] M. Hunger, A. G. Entrop, I. Mandilaras, H. J. H. Brouwers, and M. Founti, “The behavior of self-compacting concrete containing micro-encapsulated Phase Change Materials,” *Cem Concr Compos*, vol. 31, no. 10, pp. 731–743, 2009, doi: 10.1016/j.cemconcomp.2009.08.002.
- [9] T. Lee, D. W. Hawes, D. Banu, and D. Feldman, “Control aspects of latent heat storage and recovery in concrete,” *Solar Energy Materials and Solar Cells*, vol. 62, no. 3, pp. 217–237, 2000, doi: 10.1016/S0927-0248(99)00128-2.
- [10] D. W. Hawes, D. Banu, and D. Feldman, “The stability of phase change materials in concrete,” *Solar Energy Materials and Solar Cells*, vol. 27, no. 2, pp. 103–118, 1992, doi: 10.1016/0927-

0248(92)90113-4.

- [11] D. W. Hawes, D. Feldman, and D. Banu, “Latent heat storage in building materials,” *Energy Build*, vol. 20, no. 1, pp. 77–86, 1993, doi: 10.1016/0378-7788(93)90040-2.
- [12] T. Lee, D. W. Hawes, D. Banu, and D. Feldman, “Control aspects of latent heat storage and recovery in concrete,” *Solar Energy Materials and Solar Cells*, vol. 62, no. 3, pp. 217–237, 2000, doi: 10.1016/S0927-0248(99)00128-2.
- [13] 永瀬伸子, “少子化の要因：就業環境か価値観の変化かNo Title,” 「ジャーナル」, vol. 49, no. 1, p. 11, 2008.
- [14] N. Uddin, F. Fouad, U. K. Vaidya, A. Khotpal, and J. C. Serrano-Perez, “Structural characterization of hybrid Fiber reinforced Polymer (FRP)-Autoclave Aerated Concrete (AAC) panels,” *Journal of Reinforced Plastics and Composites*, vol. 25, no. 9, pp. 981–999, 2006, doi: 10.1177/0731684406065090.
- [15] Brady, G. R. A. Watts, and R. Jones, “Specification for Foamed Concrete,” *TRL Limited*, p. 78, 2001.
- [16] Z. Pan, F. Hiromi, and T. Wee, “Preparation of high performance foamed concrete from cement, sand and mineral admixtures,” *Journal Wuhan University of Technology, Materials Science Edition*, vol. 22, no. 2, pp. 295–298, 2007, doi: 10.1007/s11595-005-2295-4.
- [17] T. H. Wee, S. B. Daneti, and T. Tamilselvan, “Effect of w/c ratio on air-void system of foamed concrete and their influence on mechanical properties,” *Magazine of Concrete Research*, vol. 63, no. 8, pp. 583–595, 2011, doi: 10.1680/macr.2011.63.8.583.
- [18] Y. H. M. Amran, N. Farzadnia, and A. A. A. Ali, “Properties and applications of foamed concrete; A review,” *Constr Build Mater*, vol. 101, no. May 2017, pp. 990–1005, 2015, doi: 10.1016/j.conbuildmat.2015.10.112.
- [19] M. R. Jones and A. McCarthy, “Utilising unprocessed low-lime coal fly ash in foamed concrete,” *Fuel*, vol. 84, no. 11, pp. 1398–1409, 2005, doi: 10.1016/j.fuel.2004.09.030.
- [20] X. Zhao *et al.*, “Addendum: Zhao, X.; et al. Properties of foamed mortar prepared with granulated blast-furnace slag. *Materials* 2015, 8(2), 462-473,” *Materials*, vol. 8, no. 7, pp. 3958–3959, 2015, doi: 10.3390/ma8073958.
- [21] A. S. Tarasov, E. P. Kearsley, A. S. Kolomatskiy, and H. F. Mostert, “Heat evolution due to cement hydration in foamed concrete,” *Magazine of Concrete Research*, vol. 62, no. 12, pp. 895–906, 2010, doi: 10.1680/macr.2010.62.12.895.
- [22] J. Sathya Narayanan and K. Ramamurthy, “Development of solid, foam concrete interlocking blocks and studies on short masonry specimens,” *Masonry International*, vol. 26, no. 1, pp. 7–16, 2013.
- [23] M. A. O. Mydin and Y. C. Wang, “Mechanical properties of foamed concrete exposed to high temperatures,” *Constr Build Mater*, vol. 26, no. 1, pp. 638–654, 2012, doi: 10.1016/j.conbuildmat.2011.06.067.
- [24] Z. Zhang, J. L. Provis, A. Reid, and H. Wang, “Mechanical, thermal insulation, thermal resistance and acoustic absorption properties of geopolymer foam concrete,” *Cem Concr Compos*, vol. 62, pp. 97–105, 2015, doi: 10.1016/j.cemconcomp.2015.03.013.
- [25] 算手法の提案潜熱蓄熱建材の実装形態を考慮した計, 准教授・博士 (工学) 東京大学大学院工学系研究科, and A. Prof, “日本建築学会技術報告集 第 25 巻 第 60 号, 735-740, 2019 年 6 月,” *AIJ J. Technol. Des*, vol. 25, no. 60, pp. 735–740, 2019, doi:

10.3130/ajjt.25.735.

- [26] Y. Kusama and Y. Ishidoya, “Effects of construction position of PCM layer on energy conservation and environmental improvement,” *AIJ Journal of Technology and Design*, vol. 22, no. 52, pp. 1027–1030, Oct. 2016, doi: 10.3130/ajjt.22.1027.
- [27] S. Ji *et al.*, “Study on introduction effects of phase change building materials used in wooden houses (part 1): Verification on heat storage effect of phase change building materials by laid position using real-scale experimental room in winter,” *AIJ Journal of Technology and Design*, vol. 26, no. 64, pp. 1025–1030, Oct. 2020, doi: 10.3130/ajjt.26.1025.
- [28] S. M. Md Suman Mia, Yuya Takahashi, Tetsuya Ishida, and Koichi Tsuchiya, “Thermal and Mechanical Properties of Porous Cementitious Composites Using Phase-Change Materials with Different Microstructures,” *The 4th International Conference On Green Civil and Environmental Engineering*, 2023.

# **CHAPTER 2**

## **FLY ASH FOAM CONCRETE WITH PCM**



## **2.1 EXPERIMENTAL OVERVIEW**

This chapter is structured into four different sections, each section dedicated to exploring foam concrete with different PCMs. Initial section deals with mix design and mechanical properties. We examine how varying quantities of PCM and different admixtures impact the consistency, stability, and overall strength of these concrete mixes. Second section deals with thermal properties such as latent heat and specific heat capacity of PCM foam concrete. We meticulously analyzed the thermal behavior of the concrete concerning different heating and cooling rates. Third section deals with thermal conductivity analysis. The fourth and final section evaluates the heat cycle performance of PCM foam concretes.

### **2.1.1 Introduction**

Phase change materials (PCMs) have the remarkable ability to absorb and release substantial amounts of energy as they undergo phase transitions. This unique property makes PCMs highly suitable for various applications related to thermal energy storage, and they play a critical role in reducing energy consumption within building environments. In order to incorporate PCMs into building materials, the two commonly used methods for PCM integration are direct impregnation and microencapsulation. The first, direct impregnation method, involves absorbing PCMs into porous aggregates, but it can lead to PCM leakage and reduced thermal storage capacity [1]. In second method, microencapsulation, addresses this issue by covering PCMs in protective shells, maintaining their properties during heating and cooling cycle[2]. However, microcapsules of PCMs have a significant drawback as they crack during the mixing process. Because the protective shell of PCM is composed of polymer with limited mechanical stiffness, microencapsulated PCMs can be damaged. Numerous studies have reported that a certain number of PCM microcapsules were damaged [3], [4], [5].[6] who evaluated the durability of self-compacting concrete incorporating microencapsulated PCMs, observed large numbers of broken microcapsules. From their findings, it can be suggested that microencapsulated PCM is a sensitive soft material and has lower density than the concrete that contains high density aggregates. PCM microcapsules can be easily damaged by shear stress when mixed with conventional concrete containing high density raw materials. Such damage result in substantial energy loss.

To address this issue and prevent the damage of PCM shells during the mixing process, two factors need to be considered. First, using low density materials, such as foam and fly ash, in concrete composites could help prevent cracking. Unlike conventional concrete, foamed concrete typically signifies lightweight concrete characterized by a notably reduced density, high porosity, and low

thermal conductivity [7], [8], [9], [10]. Because of its substantial amount of air voids and lightweight, foamed concrete can be as an effective insulation material for external walls [1], [10], [11]. Second, choosing an appropriate mixer also helps prevent cracking. It is also important to use an appropriate mixer to avoid such damage, and OM mixer is claimed to be the most suitable option because, instead of stirring blades, it has a flexible rubber ball which ensures that the PCM particles are mixed homogeneously without any damage [12].

This research assesses the energy-saving potential of integrating microencapsulated PCMs into fly ash foam concrete, investigating extensively material properties and thermal behavior. Our experiments contribute to understanding phase change phenomena and have practical implications for enhancing indoor comfort and reducing cooling and heating energy demand.

### 2.1.2 Cementitious material

Rapid Hardening Cement (RHC) is also called high early strength cement. The main difference between the rapid hardening cement and ordinary Portland cement is the lime content. A large proportion of lime is the distinguishing feature of rapid hardening cement.

The 3 days strength of rapid hardening cement is equivalent to the 7 days strength of OPC when the water-cement ratio for both the cement is taken to be the same. The increased rate of strength is because of a higher proportion of tri-calcium silicate (C3S) contained in RHC along with finer grinding of the cement clinker. Though the rate at which RHC gains strength is higher than the rate at which OPC gains strength, the ultimate strength is only we materials used as substance materials for foam concrete were investigated and are shown in Figure. 2.1.1. As it can be seen, the dehydrated particles are debris, with debris lying of particles in the microstructure of cement as well as chemical elements of the cement (Figure 2.1.1).

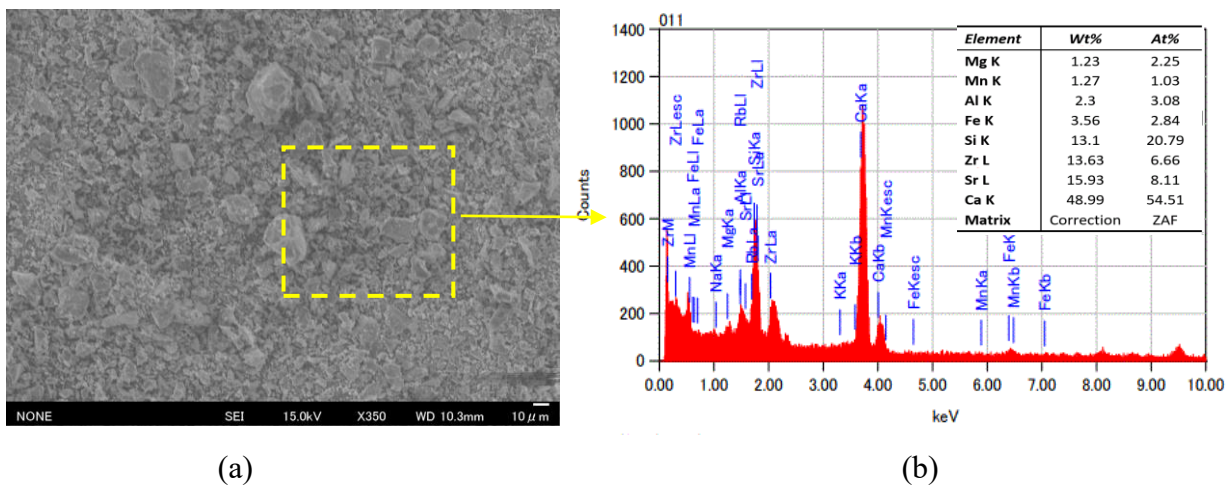


Figure 2.1.1 (a) Particle size characteristics of cement powder; (b) EDS spectrum of the cement.

### 2.1.3 Fly ash

Fly ash is a by-product of burning pulverized coal in thermal power plants and is used as a raw material for admixtures and fly ash cement. JIS defines it as "JIS A 6201 fly ash for concrete [13]" By using high-quality fly ash, unit water volume is reduced, workability is improved, hydration calorific value is reduced, long-term strength and durability, water tightness, chemical resistance and chemical resistance are improved. Fly ash has been used as the raw material of foamed concrete. Such as, it can be added to foamed concrete mixes as cement replacement and replacing fine aggregate. [14] reported that he enhanced the consistency and mix stability contributed to long-term strength. The additional beneficial effect of using fine fly ash has reduced the heat of hydration, which is important as foamed concrete has high thermal insulation characteristics [14]. Table 2-1. Shows the chemical composition of fly ash. Figure 2.1.2 shows SEM/EDS observations that Sr L, Si K and Zr L were the constituents and less of Fe k, k k, Mn K and Mg K.

Table 2-1 Chemical composition of fly ash

	SiO <sub>2</sub>	Al <sub>2</sub> O <sub>3</sub>	Fe <sub>2</sub> O <sub>3</sub>	CaO	MgO	Glass	p(g/cm <sup>3</sup> )	Ig.loss	Surface Area cm <sup>2</sup> /g
Japan FA (JIS2)	64.5	23.9	4.8	5.3	1.5	77.1	2.26	2.10	3880

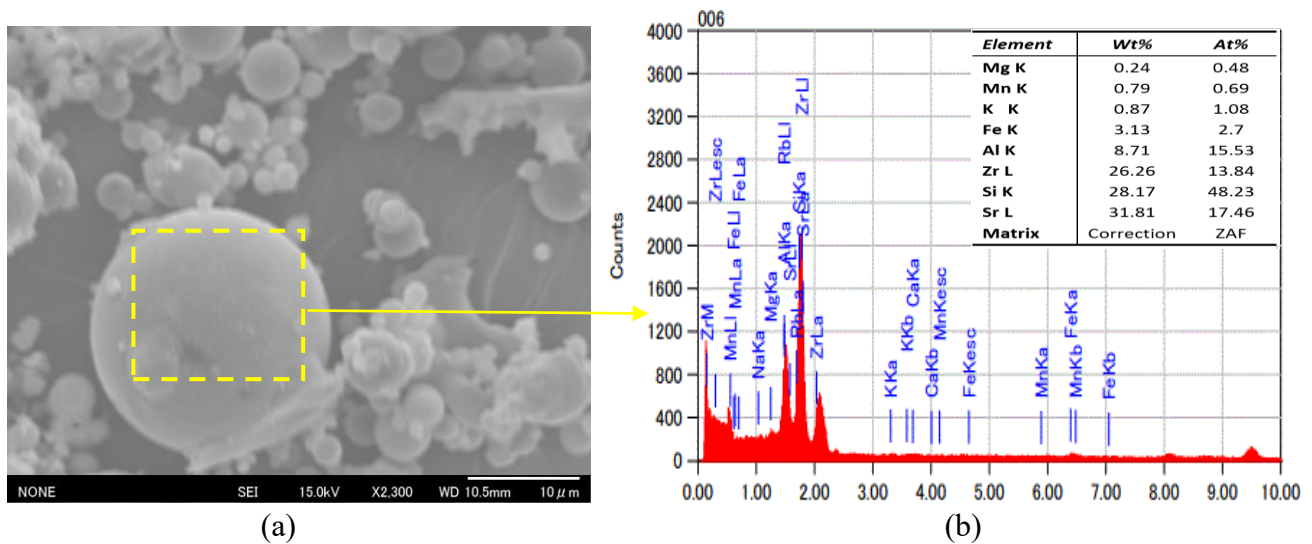


Figure 2.1.2 (a) Particle size characteristics of fly ash powder; (b) EDS spectrum of the fly ash.

### 2.1.4 Microencapsulation

Four types of encapsulated PCMs are studied. These included 6D, 18D, D28 and D43. All encapsulated PCMs are micro-encapsulated free wax:  $\leq 2.5\%$  PCM and solid content: 97.0-100.0. These four are spray-dried and powders. Their sizes were provided by the manufacturers and were determined as well by using optical microscopy (Table 2-3)[15]. In the latter, a PCM sample was placed on a disk and the single PCM particles were measured along perpendicular axes ( $n = 500$ ).

Table 2-2 Different studied encapsulated PCMs with their size, melting point and heat of fusion

Material	Nature	Size $\mu\text{m}$	Melting ( $^{\circ}\text{C}$ )	Heat of fusion (J/g)	Solid content %
<b>PCM6D</b>	Dry	15.0-30.0	4 to 8	181	97.0-100.0
<b>PCM18D</b>	Dry	15.0-30.0	16 to 20	215	97.0-100.0
<b>PCM28D</b>	Dry	15.0-30.0	26 to 30	189	97.0-100.0
<b>PCM43D</b>	Dry	15.0-30.0	41 to 45	235	97.0-100.0

The EDS/SEM analysis of pure microencapsulated PCM has a strong peak appeared in the elemental analysis of the PCM is the Zr L element and less of K K, Cu K, and Ti K.

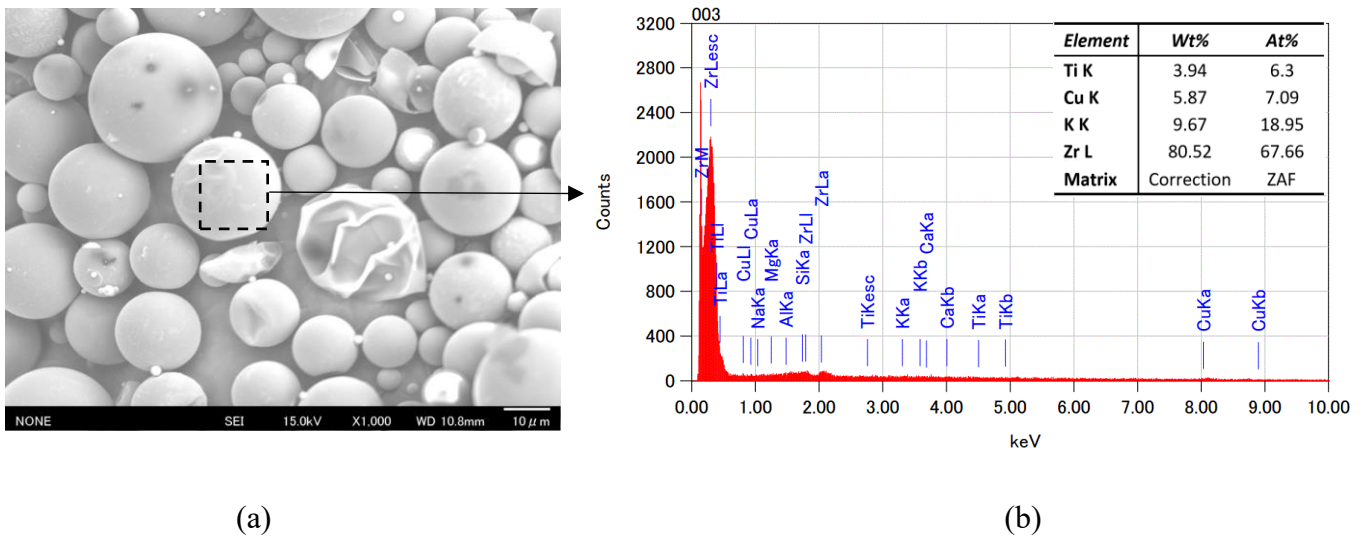


Figure 2.1.3 (a) Particle size characteristics of microencapsulated PCM powder (PCM6D); (b) EDS spectrum of the (PCM6D).

### 2.1.5 Foam & Foaming Agent

The foam concentrate used in this experimental study is Crete Foam Drexel brand as shown in Figure 2.2.4 and is synthetic based type. They offer a much longer shelf life, have no obnoxious and perform well under a variety of conditions. Foam plays a vital role in foamed concrete, when it is added into the mix; it increases the concrete volume significantly hence decreasing the weight of the mix. The foam usually forms the bubbles or voids in the concrete. When the foam evaporates, the bubbles tend to create voids. So, understanding how bubbles form and evaporate as the concrete hardens is a very important issue to be dealt with. The ratio of foam concentrates to water used was 1:50. Foam generating machines as shown in Figure 2.1.4, are used to get the foam output as shown in Figure 2.1.5. The process of producing foam was very simple; foam concentrate and water were placed in the pressure container and mixed gently for some time. Then the machine is connected to power and switched on to develop pressure inside the container to produce foam. Foam generating machine has the feature of generating low and high density of the foam.



Figure 2.1.4 Left: Foaming agent. Right: Foam generating machine.

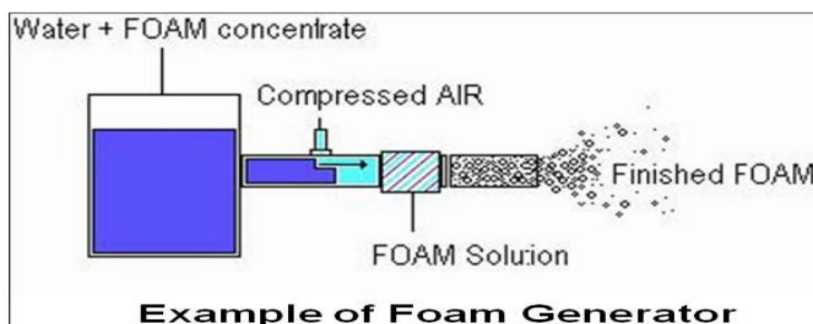


Figure 2.1.5 Foam generator [16]

## 2.1.6 Superplasticizer

MIGHTY 3000H superplasticizer agent manufactured by Kao corporation used in this experimental study. Superplasticizer is a water-reducing admixture capable of producing large water reduction or great flowability without causing undue set retardation or entrainment of air in mortar or concrete. An admixture is a mixture of two or more components.

The main of using a superplasticizer is to avoid particles from segregating. Segregation is the action or state of setting someone or something apart from others. Superplasticizers are used to improve the quality of concrete mixtures. The weak characteristics of concrete are improved by superplasticizers.



Figure 2.1.6 Superplasticizer used as water reducing agent

### 2.1.7 OM-10E MIXER

The OM mixer is a device that does not have a stirring blade and has a flexible rubber ball mounted on a rocking board[17]. It is a diffusion mixing method that can accelerate a mixture and swing it in a random direction in a short time. Is an epoch-making mixer. The standard OM mixer uses an epoch-making mechanism that does not use stirring blades and has a highly viscous resin/coating agent such as epoxy, as well as various powders and granules of materials with extremely different specific gravity, fragile raw materials, and metal powder materials. The materials are suitable for mixing additives and dispersion mixing of fiber materials such as G / R / C (alkoxy resistant glass fiber reinforced cement) and water moss peat (Petemos), damaging the mixture (breakage of particles, bending of fibers). It has excellent performance as soft mixing without giving. Besides, the process up to the granulation of various industrial waste such as desulfurized gypsum, EP ash, and dust collection can be performed with this machine, making the equipment extremely easy.

Table 2-3 Specification of OM mixer [17]

Model	Capacity (L)	Drive type	Power (v/kW)	Weight	Dimensions (W×D×Hmm)
OM- 10E	10	Electric motor	100/0.5	140	810x660x1100

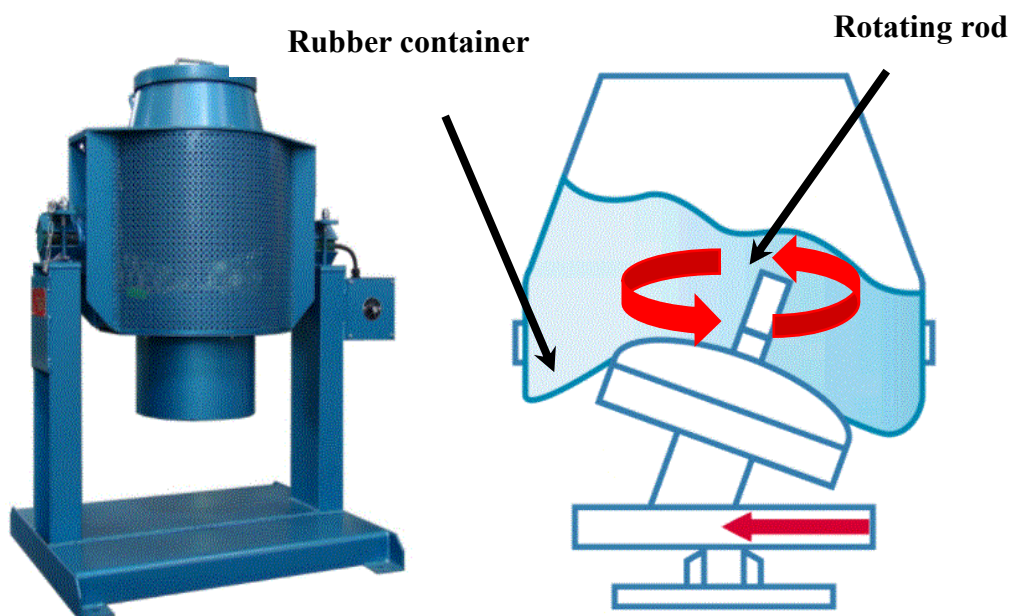


Figure 2.1.7 OM-10E mixer and operation



## 2.1.8 Evaluation of thermal energy storage of PCM

The DSC calorimeter submits the sample to controlled temperatures and records the corresponding heat fluxes, thus provides information about temperatures and enthalpies associated with the phase changes. From the heat flux, the specific heat as a function of temperature can be obtained, and the enthalpy is determined by integration procedures.

### 2.1.8.1 DSC procedure for pure microencapsulated PCMs

The calorimetry measurements were taken with a TA device with a temperature accuracy of  $\pm 0.1$  C. It measures the difference in the heat flow rate between samples and insert reference as a function of time and temperature. The melting and freezing behaviors of the PCM were analyzed by a DSC model Q200 at a high-tech plaza in Koriyama city, Fukushima Prefecture. The temperature was measured at the sample platform with a thermocouple. The sample sizes were between 5 and 10 mg and were encapsulated with Pans [18](container of the sample material) and Lids (cap of the container). The samples were weighted by an analytical ultra-micro balance model: MC25. Then the samples were sealed in the pan by using an encapsulating press. An empty aluminum crucible was used as a reference in all measurements. To accurately measure the transition temperature, it is recommended [19], [20] that the samples are scanned with a low heating/cooling rate. Once the sample is measured with a low heating rate, conducting an experiment with a higher heating/cooling rate is suggested to measure the value of the enthalpy. The effect of the thermal cycles and heating/cooling rates on the phase change processes and specific enthalpy values was examined. In this way, different heating/cooling rates of 10°C/min, 5°C/min, 2°C/min, 1°C/min and 0.5°C/min were considered. The results of DSC test are shown in below table 2-4 and Figure 2.1.8- 2.1.15.

Table 2-4 Pure PCM enthalpy, onset and end temperatures for different PCM sample.

Designation	Melting				Freezing			
	Onset temp. (°C)	End Temp. (°C)	Enthalpy (J/g)	Peak Temp. (°C)	Onset temp. (°C)	End Temp. (°C)	Enthalpy (J/g)	Peak Temp. (°C)
PCM6D	-8.34	16.1	73.25	6.11	4.82	14.21	72.97	2.98
PCM18D	0.7	33.15	170.2	19.49	14.97	-3.32	177.5	7.71
PCM28D	9.13	40.85	181.3	28.13	27.10	6.69	183.1	20.46
PCM43D	16.17	58.55	218.8	44.53	42.61	20.35	214.8	28.99



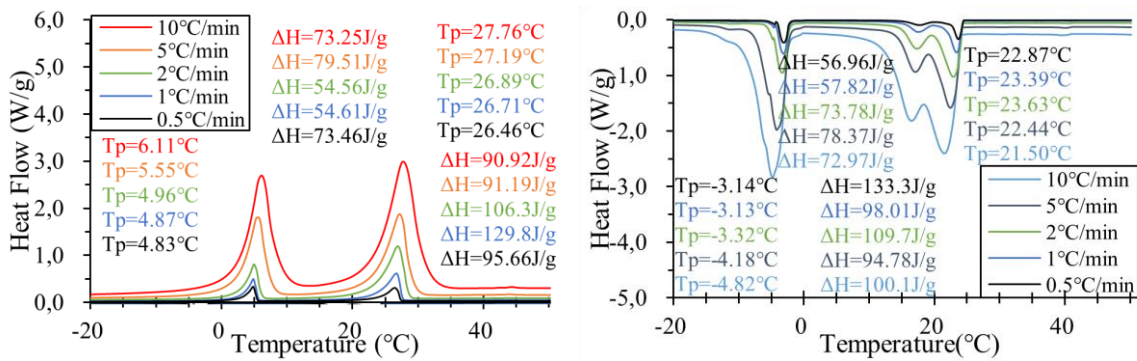


Figure 2.1.8 Results of DSC measurements of Pure PCM6D at various heating and cooling rates.

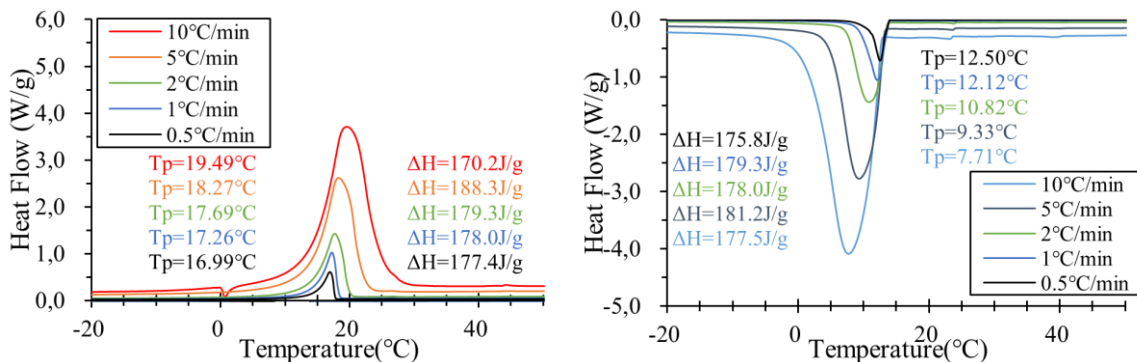


Figure 2.1.9 Results of DSC measurements of Pure PCM18D at various heating and cooling rates.

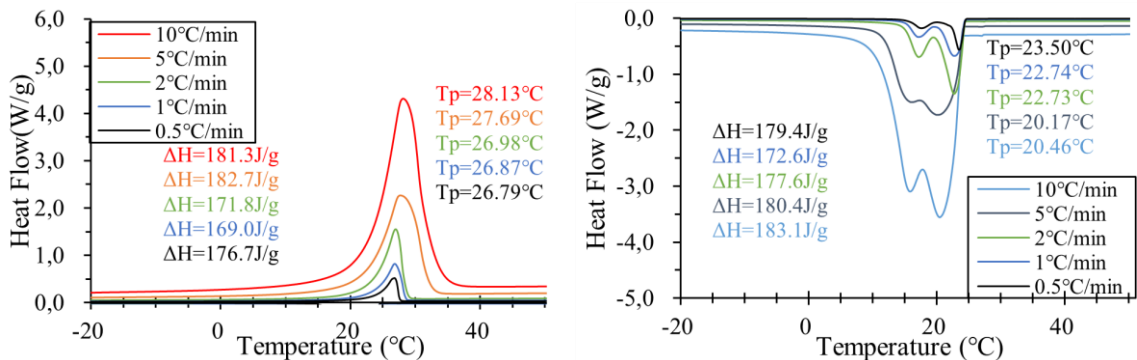


Figure 2.1.10 Results of DSC measurements of Pure PCM28D at various heating and cooling rates.

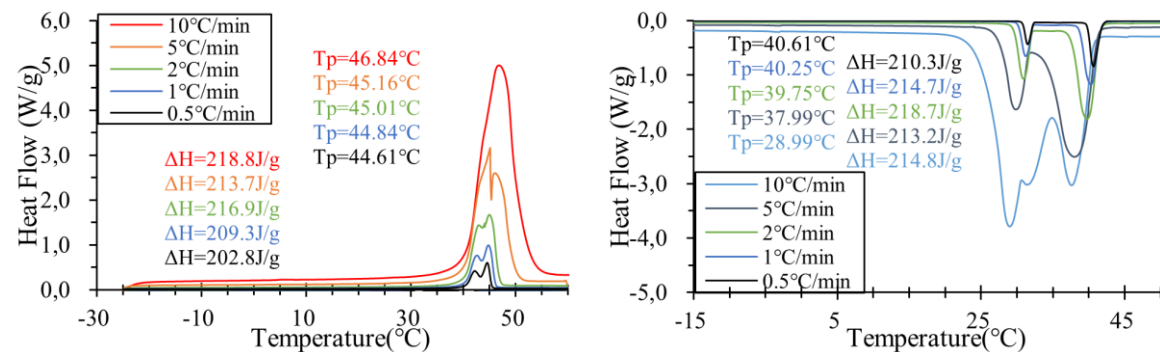


Figure 2.1.11 Results of DSC measurements of Pure PCM43D at various heating and cooling rates.

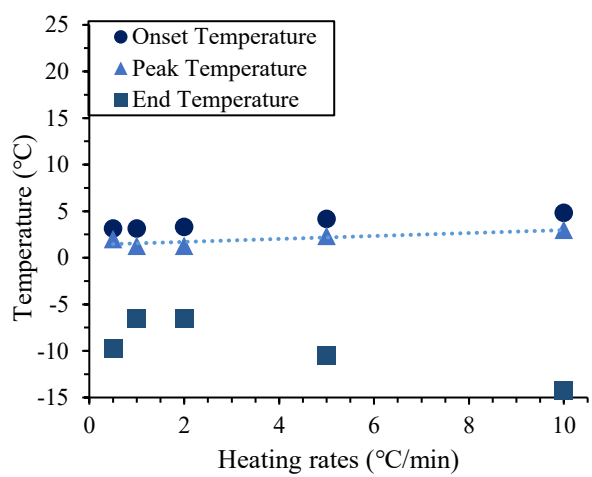
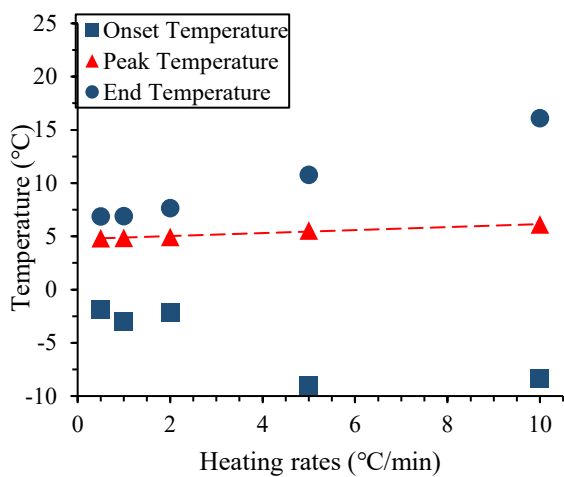


Figure 2.1.12 Onset, peak and temperature for the phase transition in Pure-PCM6D.

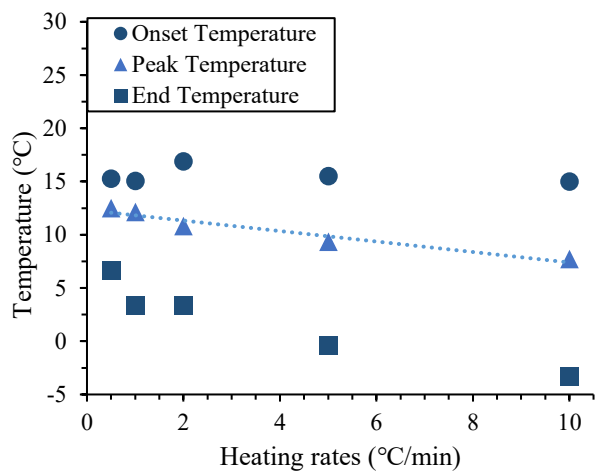
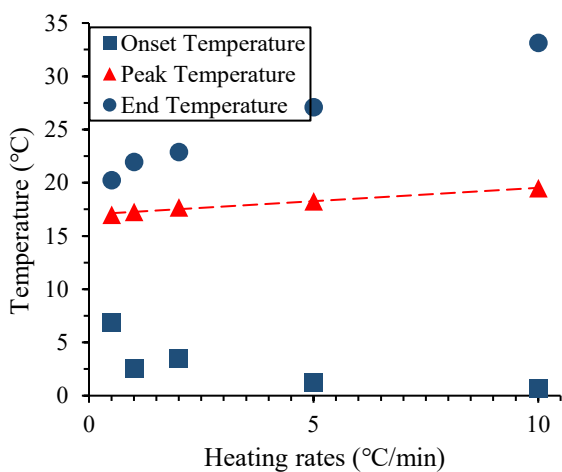


Figure 2.1.13 Onset, peak and temperature for the phase transition in Pure-PCM18D.

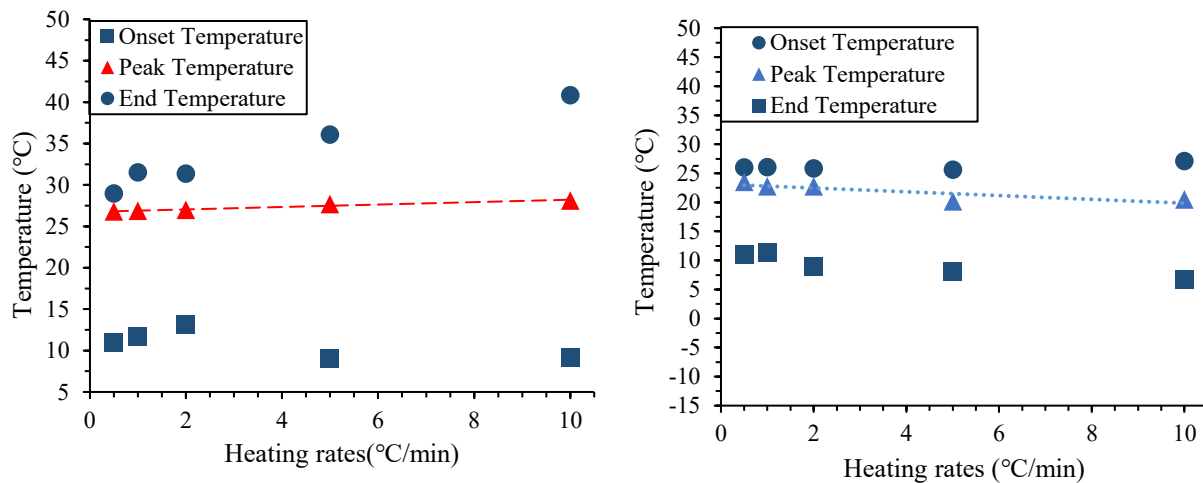


Figure 2.1.14 Onset, peak and temperature for the phase transition in Pure-PCM28D.

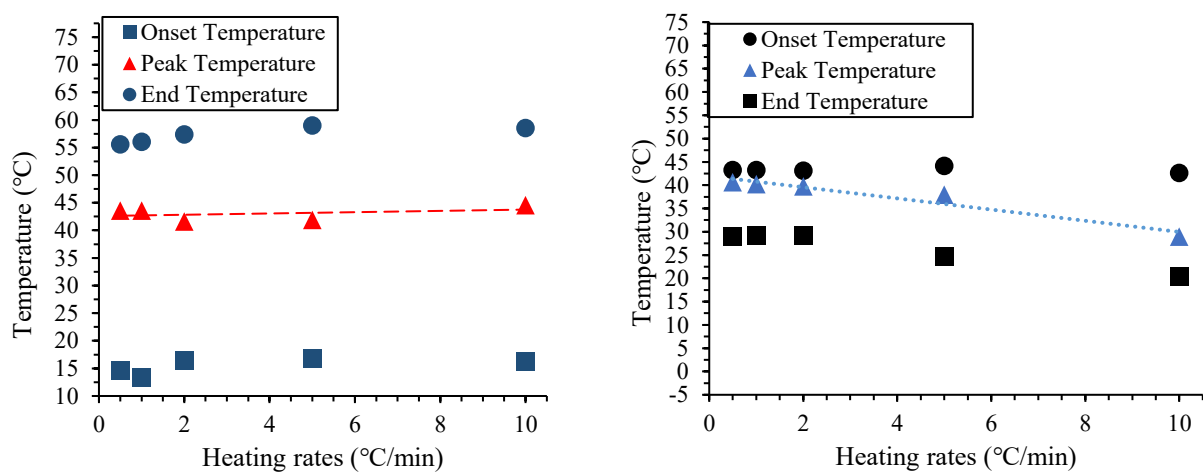


Figure 2.1.15 Onset, peak and temperature for the phase transition in Pure-PCM43D.

## 2.2 MIXTURE PROPORTIONS

### 2.2.1 Experimental program

In this chapter, the introduction of the experimental works such as the materials used, mix design, mixing procedure, preparation and the testing procedure is presented. At the initial stage of this experiment, different trial mixes were conducted to determine an optimum mix proportion by keeping the strength constant. At the second stage of this experiment, the optimum mix proportion was used to carry out PCM foam mortar. And then PCM was replaced by different cement ratios such as 10%, 20% and 30% in the foam mortar. After the replacement flow and air content tests had been done, another compressive strength and density tests were conducted. As the final stage, the experimental result was concluded.

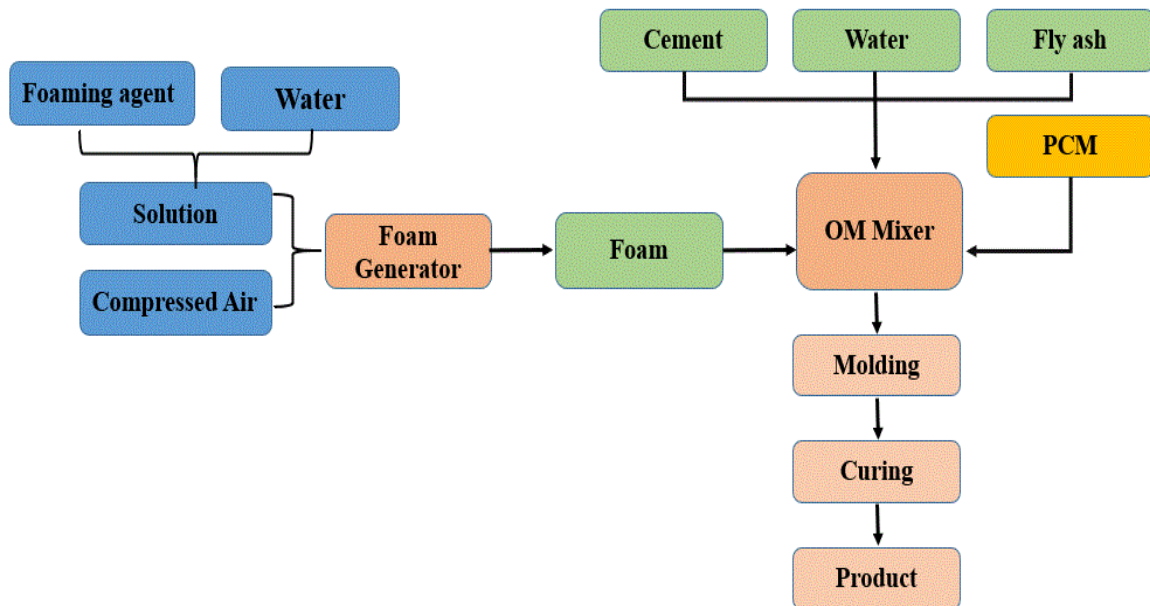


Figure 2.2.1 Flow diagram of experimental program

### **2.2.2 Mix composition**

The foamed concrete has been produced by using the following constituents of cementitious material (rapid hardening cement & fly ash), superplasticizer, water and foaming agent.

There is no standard method for proportioning foamed concrete, but it is a specified target density that becomes a prime design criterion. On the basis of target plastic density, a theoretical mix design is to be formulated and trial tests are undertaken and the results from the trial tests are used as mix design for the foamed concrete. The target densities for the foam concrete are 800-1050 kg/m<sup>3</sup>, for various compositions of cement and fly ash. In order to reach target densities and light weight, sand was not used as an aggregate. The amount of foam affects the dry density of concrete as the amount of foam increases and the density of the mix decreases.

According to a survey, one of the big concerns was that a compressive strength of foam concrete was lower than that of ordinary concrete. Therefore, in order to improve the compressive strength of foam concrete, rapid hardening cement (R.C), ordinary cement (N.C), silica fume and superplasticizer were used as the main and additional ingredients. In order to determine optimal mix composition, series of trial test were conducted. Based on the tests' results, the optimal mix composition and curing temperature were chosen. Moreover, PCM was replaced by cement to make light weight ratio for the chosen mix composition, the exact data of which is shown in Table 2-5.

Table 2-5 Mix proportions for foam concrete with PCM6D,18D,28D and 43D.

<b>Mix Designation</b>	<b>Cement (kg)</b>	<b>Fly ash (kg)</b> <b>10%</b>	<b>W/C (Lit)</b> <b>0.3</b>	<b>PCM (kg)</b> <b>10-30%</b>	<b>SP (kg)</b> <b>1%</b>	<b>SF (kg)</b> <b>10%</b>	<b>Foam (gram)</b>
<b>Reference</b>	4.5	0.45	1.35	0	0.045	0.45	800
<b>PCM 6D (10%)</b>	3.15	0.45	0.945	0.45	0.045	0.45	1200
<b>PCM 6D (20%)</b>	2.7	0.45	0.81	0.9	0.045	0.45	1500
<b>PCM 6D (30%)</b>	2.25	0.45	0.675	1.35	0.045	0.45	1800
<b>PCM 18D (10%)</b>	3.15	0.45	0.945	0.45	0.045	0.45	990
<b>PCM 18D (20%)</b>	2.7	0.45	0.81	0.9	0.045	0.45	1350
<b>PCM 18D (30%)</b>	2.25	0.45	0.675	1.35	0.045	0.45	1400
<b>PCM 28D (10%)</b>	3.15	0.45	0.945	0.45	0.045	0.45	860
<b>PCM 28D (20%)</b>	2.7	0.45	0.81	0.9	0.045	0.45	1150
<b>PCM 28D (30%)</b>	2.25	0.45	0.675	1.35	0.045	0.45	1244
<b>PCM 43D (10%)</b>	3.15	0.45	0.945	0.45	0.045	0.45	820
<b>PCM 43D (20%)</b>	2.7	0.45	0.81	0.9	0.045	0.45	1120
<b>PCM 43D (30%)</b>	2.25	0.45	0.675	1.35	0.045	0.45	1700

Table 2-6 Result of compressive strength of foam concrete.

(Compressive Strength test)									
Mix	%	Curing	Foam (gram)	Period	Fresh	Compressive Strength (MPa)			Coefficient Variation (%)
Designation					Density (kg/m <sup>3</sup> )	1	2	Average	
NO-PCM	0	40°C H-95%	240	3	1044	5.1	10.0	7.6	3.3
				7	1044	10.9	7.8	9.4	4.1
				14	1044	10.9	7.8	9.4	4.2
				28	1044	14.0	12.0	13.0	5.9
PCM6D	10	40°C H-95%	300	3	955	5.7	5.3	5.5	2.9
				7	955	6.6	4.6	5.6	2.9
				14	955	7.5	5.5	6.5	3.3
				28	955	7.2	6.5	6.9	3.5
PCM6D	20	40°C H-95%	1670	3	1092	4.2	4.6	4.4	2.2
				7	1092	4.9	5.0	5.0	2.5
				14	1092	4.9	5.0	5.0	2.5
				28	1092	5.5	5.9	5.7	2.8
PCM6D	30	40°C H-96%	2100	3	1062	2.9	2.2	2.6	1.2
				7	1062	2.8	3.0	2.9	1.4
				14	1062	3.1	2.9	3.0	1.5
				28	1062	3.7	3.2	3.5	1.7
PCM18D	10	40°C H-97%	1150	3	1003	7.1	6.3	6.7	3.3
				7	1003	7.6	7.0	7.3	3.6
				14	1003	5.1	10.1	7.6	3.7
				28	1003	8.1	8.5	8.3	4.1
PCM18D	20	40°C H-98%	1500	3	1098	4.2	4.2	4.2	2.1
				7	1098	5.6	3.8	4.7	2.3
				14	1098	4.5	6.0	5.3	2.6
				28	1098	4.4	6.7	5.6	2.7
PCM18D	30	40°C H-99%	2020	3	1050	2.8	2.2	2.5	1.2
				7	1050	4.3	3.7	4.0	1.9
				14	1050	4.4	4.1	4.3	2.0
				28	1050	4.1	4.5	4.3	2.0

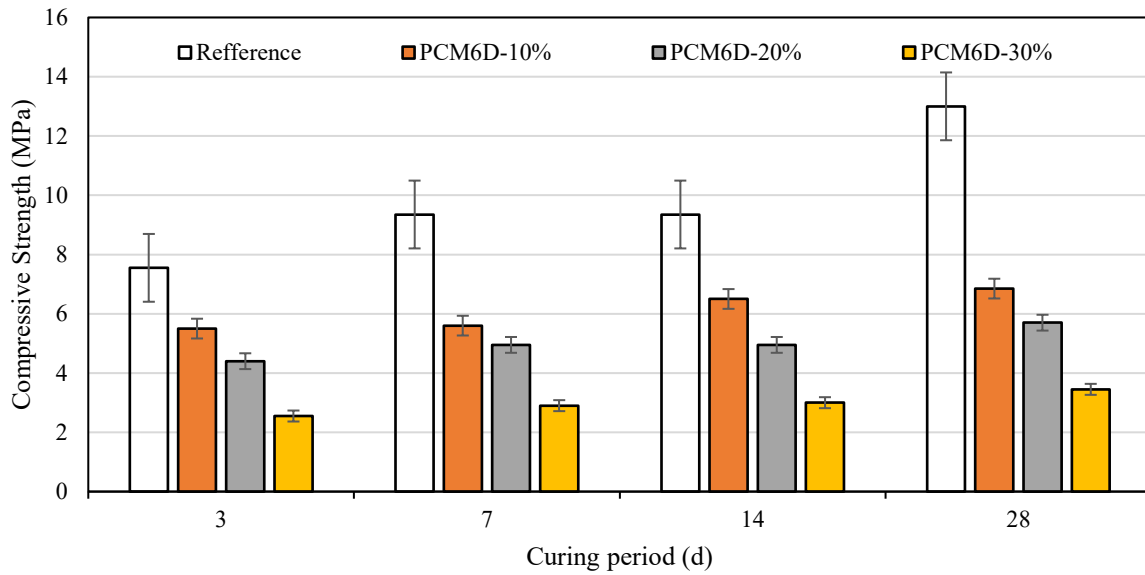


Figure 2.2.2 Effect of adding PCM to compressive strength of foam concrete with PCM6D.

The compressive strength tests were conducted under curing temperature of 40°C H-95%. 4 types of PCMs were used, which were PCM6D, PCM18D, PCM28D and PCM43D. As seen from Figure 2.2.2 to Figure 2.2.5, all types of PCMs were added respectively to replace 10-30% of the unit weight of cement in the foam concrete. Table 2-6 contains the compressive strength values of the various mixture proportions and compressive strength reduction values and those were compared with the mix design of PCM-0%.

On day 3, there was a significant difference between the compressive strength of concrete with and without PCM. As seen in Figure 2.2.2, when PCM was added to replace 10%- 30% of cement, adding the PCM significantly reduced the compressive strength of concrete. Compressive strength of PCM6D was recorded as 5.5 MPa, 4.4 MPa, 2.6 MPa and respectively whereas concrete without PCM revealed 7.55 MPa on the same day. The decrease in the strength of PCM6D concrete compared with that without PCM was around 27.5%, 41.7% and 65.5% respectively, after replacing cements by 10-30%. A dramatical change was observed on day 28, being recorded at 6.9 MPa, 5.7 MPa and 3.5 MPa, whereas NO-PCM concrete revealed 13 MPa on the same day. The decrease in strength of PCM6D concrete compared with those of without PCM was around 46.9%, 56.1% and 73.1% respectively, after replacing cements by 10-30%. On the other hand, the compressive strength increased from day 3 to day 28 around without PCM: 41.9%, PCM-10%: 20.2%, PCM-20%: 22.8% and PCM-30%: 25.7%.



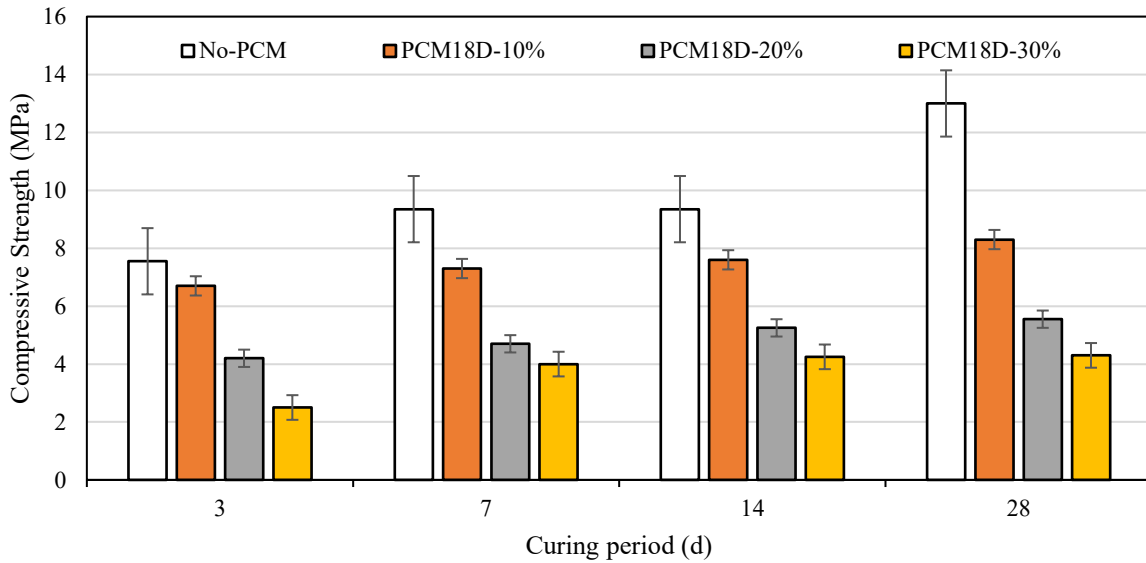


Figure 2.2.3 Effect of adding PCM to compressive strength of foam concrete with PCM18D.

On day 3, there was a significant difference between the compressive strength of concrete with and without PCM. As seen in Figure 2.2.3, when PCM was added to replace 10%- 30% of cement, adding the PCM significantly reduced the compressive strength of concrete. Compressive strength of PCM18D was recorded as 6.7 MPa, 4.2 MPa, 2.5 MPa respectively, whereas concrete without PCM revealed 7.55 MPa at the same day. The decrease in strength of PCM18D concrete compared with those of without PCM were around 11.1%, 44.3% and 66.8% respectively, after replacing cements from 10 to 30%. Dramatical change was observed on day 28 when it was noticed as 8.3 MPa, 5.6 MPa and 4.3 MPa, while the concrete without PCM revealed 13 MPa on the same day. The strengths of PCM18D concrete showed a remarkable decrease of around 36.1%, 56.9% and 66.9% respectively compared with those of without PCM, after replacing the cements by 10-30%. On the other hand, the compressive strength increased from day 3 to day 28; the percentages were like: for concrete without PCM: 41.9%; PCM-10%: 19.2%; PCM-20%: 37.3%; and PCM-30%: 41.6%, respectively.

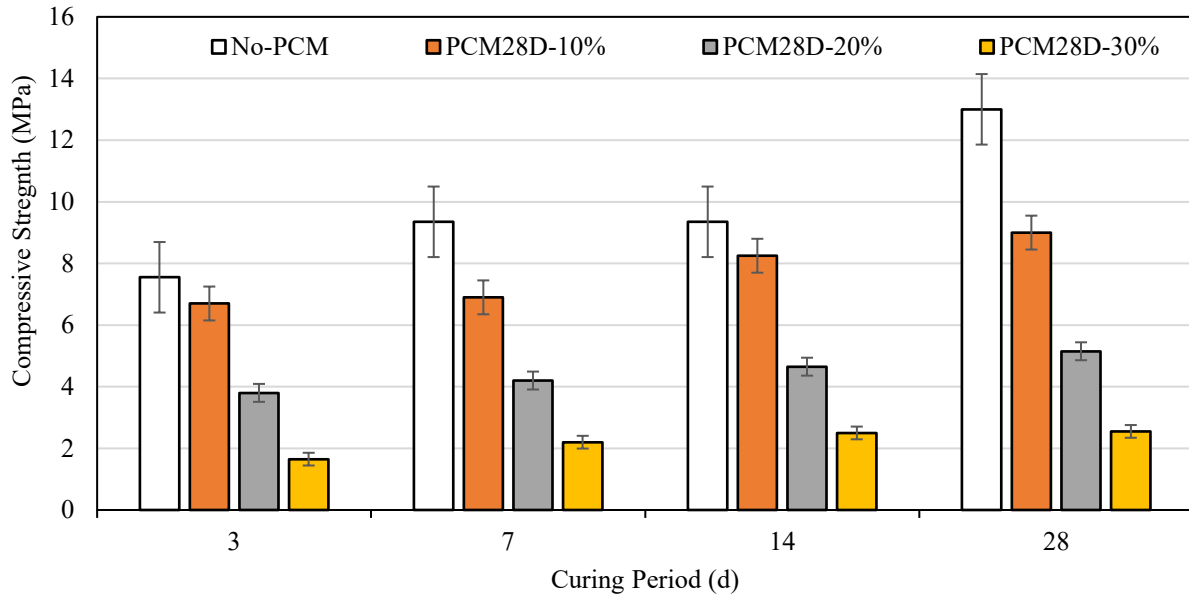


Figure 2.2.4 Effect of adding PCM to compressive strength of foam concrete with PCM28D.

On day 3, there was a significant difference between the compressive strength of concrete with and without PCM. As seen in Figure. 2.2.4, when PCM was added to replace 10%- 30% of cement, adding the PCM significantly reduced the compressive strength of concrete. Compressive strength of PCM28D concrete was recorded as 6.7 MPa, 3.8 MPa, 1.7 MPa respectively, whereas concrete without PCM revealed 7.55 MPa at the same day. The decrease in strength of PCM28D concrete compared with those of without PCM were around 11.2%, 49.6% and 77.4% respectively, after replacing cements by 10-30%. Dramatical change was observed on day 28 when it was noticed as 9 MPa, 5.5 MPa and 2.6 MPa, while concrete without PCM revealed 13 MPa at the same day. The strength of PCM28D concrete showed a remarkable decrease around 30.7%, 57.6% and 80% respectively, compared with those of without PCM, after replacing cements by 10-30%. On the other hand, the compressive strength increased from day 3 to day 28, the percentages are like: for concrete without PCM: 41.9%; PCM-10%: 25.5%; PCM-20%: 26.9%; and PCM-30%: 34.6% respectively.

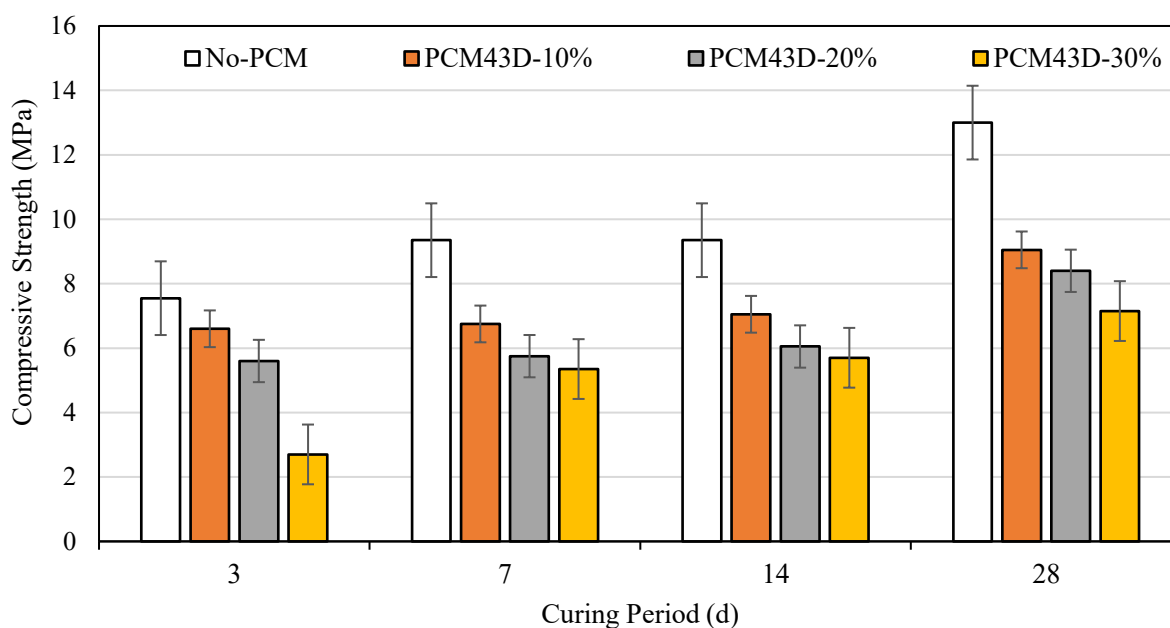


Figure 2.2.5 Effect of adding PCM to compressive strength of foam concrete with PCM43D.

On day 3, there was a significant difference between the compressive strength of concrete with and without PCM. As seen in Figure 2.2.5, when PCM was added to replace 10%- 30% of cement, adding the PCM significantly reduced the compressive strength of concrete. Compressive strength of PCM28D concrete was recorded as 6.6 MPa, 5.6 MPa, 2.7 MPa respectively, whereas concrete without PCM revealed 7.55 MPa at the same day. The decrease in strength of PCM28D concrete compared with those of without PCM were around 12.5%, 25.8% and 64.2% respectively, after replacing cements by 10-30%. Dramatical change was observed on day 28 when it was noticed as 9.1 MPa, 8.4 MPa and 7.2 MPa, while concrete without PCM revealed 13 MPa at the same day. The strength of PCM28D concrete showed a remarkable decrease around 30%, 35.3% and 44.6% respectively, compared with those of without PCM, after replacing cements by 10-30%. On the other hand, the compressive strength increased from day 3 to day 28, the percentages are like: for concrete without PCM: 41.9%; PCM-10%: 27.4%; PCM-20%: 33.3%; and PCM-30%: 62.5% respectively.

Two main reasons for the decrease in the compressive strength are as follows: First, the results show that the increase in the PCM added to PCM foam concrete causes higher foam volume. A larger amount of foam creates higher porosity, causing a decrease in compressive strength that PCM foam concrete displays. Furthermore, an increasing amount of PCM results in a significant decrease in the compressive strength of PCM foam concrete due to low mechanical properties of PCM. PCM behaves

more like voids rather than aggregates and can be easily broken under compressive force. According to [21], the retardation of the hydration process is evident in cement mortars with PCM was reported; it is also reported that PCM's interacts with the C-S-H formation adversely impacts the strength [22], [23], [24].

Table 2-7 Density control in PCM foam concretes.

(Density control)							
Mix Designation	%	Curing	Period	Fresh density (kg/m <sup>3</sup> )	Dry density (kg/m <sup>3</sup> )	Consistency (%)	Stability (%)
<b>NO-PCM</b>	0	40°C H-95%	3	1044	1021	1.0	1.0
			7	1044	1016	1.0	1.0
			14	1044	1012	1.0	1.0
			28	1044	1008	1.0	1.0
<b>PCM6D-10%</b>	10	40°C H-95%	3	955	955	1.0	1.0
			7	955	910	1.0	1.0
			14	955	895	1.0	1.1
			28	955	871	1.0	1.1
<b>PCM6D-20%</b>	20	40°C H-95%	3	1092	1004	1.1	1.1
			7	1092	898	1.1	1.2
			14	1092	867	1.1	1.3
			28	1092	840	1.1	1.3
<b>PCM6D-30%</b>	30	40°C H-95%	3	1062	928	1.1	1.1
			7	1062	773	1.1	1.4
			14	1062	770	1.1	1.4
			28	1062	730	1.1	1.5
<b>PCM18D-10%</b>	10	40°C H-95%	3	1003	1086	1.0	0.9
			7	1003	1031	1.0	1.0
			14	1003	1027	1.0	1.0
			28	1003	1000	1.0	1.0
<b>PCM18D-20%</b>	20	40°C H-95%	3	1098	1031	1.1	1.1
			7	1098	1008	1.1	1.1
			14	1098	992	1.1	1.1
			28	1098	965	1.1	1.1
<b>PCM18D-30%</b>	30	40°C H-95%	3	1050	957	1.1	1.1
			7	1050	871	1.1	1.2
			14	1050	839	1.1	1.3
			28	1050	826	1.1	1.3

(Density control)							
Mix Designation	%	Curing	Period	Fresh density (kg/m <sup>3</sup> )	Dry density (kg/m <sup>3</sup> )	Consistency (%)	Stability (%)
PCM28D	10	40°C H-95%	3	3	937	7.2	6.2
			7	7	937	5.2	8.6
			14	14	937	8.2	8.3
			28	28	937	8.5	9.5
PCM28D	20	40°C H-95%	1500	3	1050	3.6	4
			7	7	1050	4	4.4
			14	14	1050	3.9	5.4
			28	28	1050	4.8	5.5
PCM28D	30	40°C H-95%	1750	3	1020	1.9	1.4
			7	7	1020	2.2	2.2
			14	14	1020	2.2	2.8
			28	28	1020	2.5	2.6
PCM43D	10	40°C H-95%	800	3	919	5.2	8
			7	7	919	7.3	6.2
			14	14	919	7.1	7
			28	28	919	8.1	10
PCM43D	20	40°C H-95%	950	3	1050	4.2	7
			7	7	1050	6.3	5.2
			14	14	1050	6.1	6
			28	28	1050	7.3	9.5
PCM43D	30	40°C H-95%	1700	3	1050	2.4	3
			7	7	1050	5.3	5.4
			14	14	1050	5.9	5.5
			28	28	1050	7.7	6.6

It can be seen from Table 2-7 that PCM concrete densities were stabilized to be close to the target densities. It shows that the foam was able to mix with mortar thoroughly without collapsing when the OM mixer was used. Stability of foam concrete is the ratio of fresh density to hardened density. Therefore, stability of foam concrete depends on the quality of foam used. Consistency is the ratio of fresh density to the designated density. Consistency depends on the amount of foam added to the foam concrete mix. The density of foam concrete depends on the stability and consistency of the mix, and the strength of foam concrete depends on density, as such the stability and consistency of FC mix affects the strength of foam concrete.

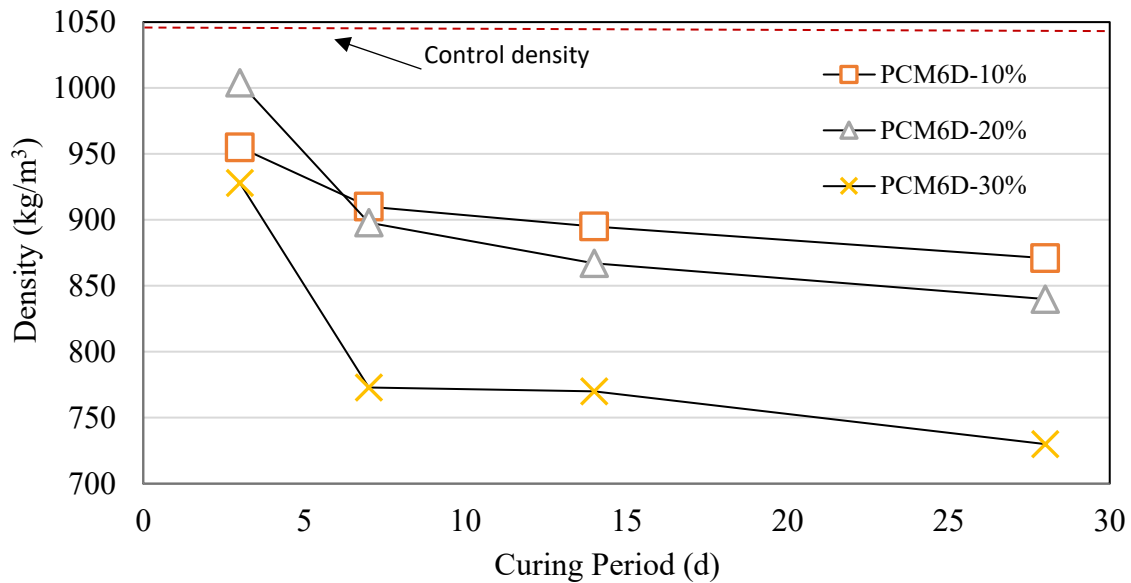


Figure 2.2.6 Effect of adding PCM6D to density of foam concrete.

Density test was done in PCM foam concrete of 3, 7, 14 and 28 days. The control wet density of all of PCM concretes was 1050 kg/m<sup>3</sup>. Figure 2.3.6 was a test result of PCM concrete density that used PCM18D by 10-30% on 3, 7, 14 and 28 days. As the PCM amount of addition got greater the density of concrete got less in opposite. The testing of concrete's density that was cured in a 40°C, H-95% in chamber. Figure 2.3.6 revealed the value of all percent of PCM18D foam concrete density of value 1086-730 kg/m<sup>3</sup>. The highest density of PCM18D concrete was 1086 kg/m<sup>3</sup> or PCM18D-10% at day 3 while the lowest density was 826 kg/m<sup>3</sup> or PCM-30% at day 28. The density showed a drop from day 3 to day 28, percentages are like: for concrete PCM6D-10%: 8.7%; PCM6D-20%: 13.6%; PCM6D-30%: 21.3% respectively.

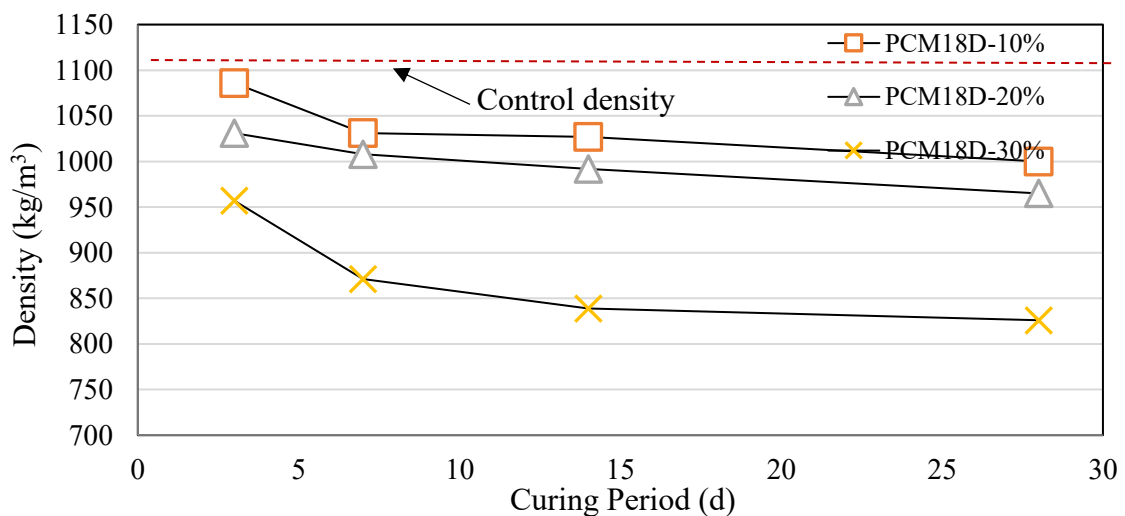


Figure 2.2.7 Effect of adding PCM18D to density of foam concrete.

The control wet density of all of PCM concretes was 1050 kg/m<sup>3</sup>. Figure 2.3.7 was a test result of PCM concrete density that used PCM18D by 10-30% on 3, 7, 14 and 28 days. As the PCM amount of addition got greater the density of concrete got less in opposite. The testing of concrete's density that was cured in a 40°C, H-95% in chamber. Figure 2.3.7 revealed the value of all percent of PCM18D foam concrete density of value 1086-826 kg/m<sup>3</sup>. The highest density of PCM18D concrete was 1086 kg/m<sup>3</sup> or PCM18D-10% at day 3 while the lowest density was 826 kg/m<sup>3</sup> or PCM-30% at day 28. The density showed a drop from day 3 to day 28, percentages are like: for concrete PCM18D-30%: 7.9%; PCM6D-20%: 6.4%; PCM6D-30%: 13.6% respectively.

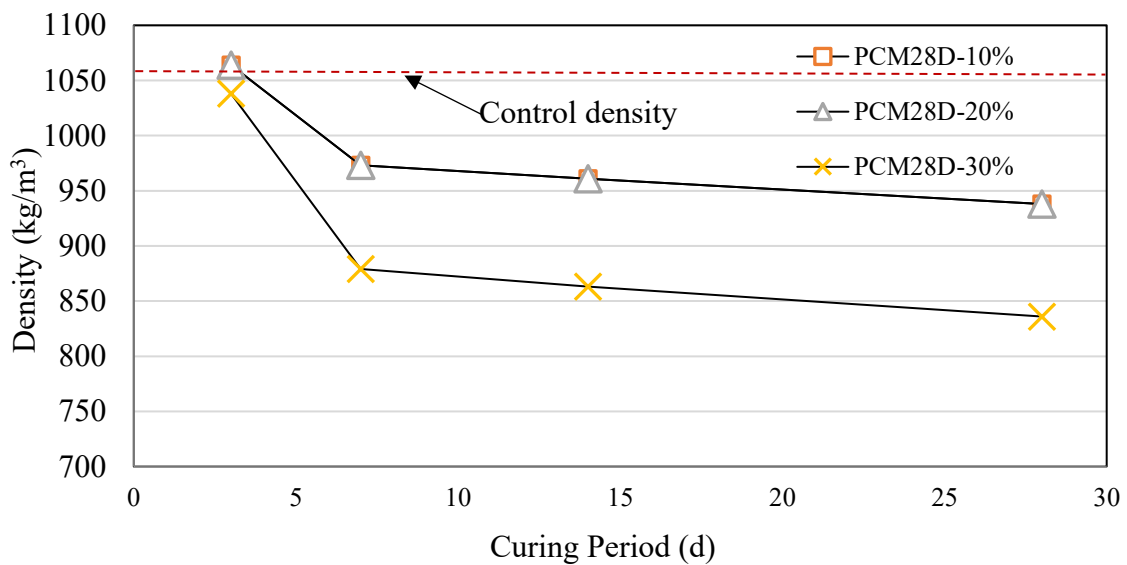


Figure 2.2.8 Effect of adding PCM28D to density of foam concrete.

The control wet density of all of PCM concretes was 1050 kg/m<sup>3</sup>. Figure 2.3.8 was a test result of PCM concrete density that used PCM by 10-30% on 3, 7, 14 and 28 days. As the PCM amount of addition got greater the density of concrete got less in opposite. The testing of concrete's density that was cured in a 40°C, H-95% in chamber. Figure 2.3.8 revealed the value of all percent of PCM28D foam concrete density of value 1064-836 kg/m<sup>3</sup>. The highest density of PCM28D concrete was 1064 kg/m<sup>3</sup> or PCM28D-20% at day 3 while the lowest density was 836 kg/m<sup>3</sup> or PCM-30% at day 28. The density showed a drop from day 3 to day 28, percentages are like: for concrete PCM28D-10%: 14.5%; PCM28D-20%: 11.8%; PCM28D-30%: 19.46% respectively.

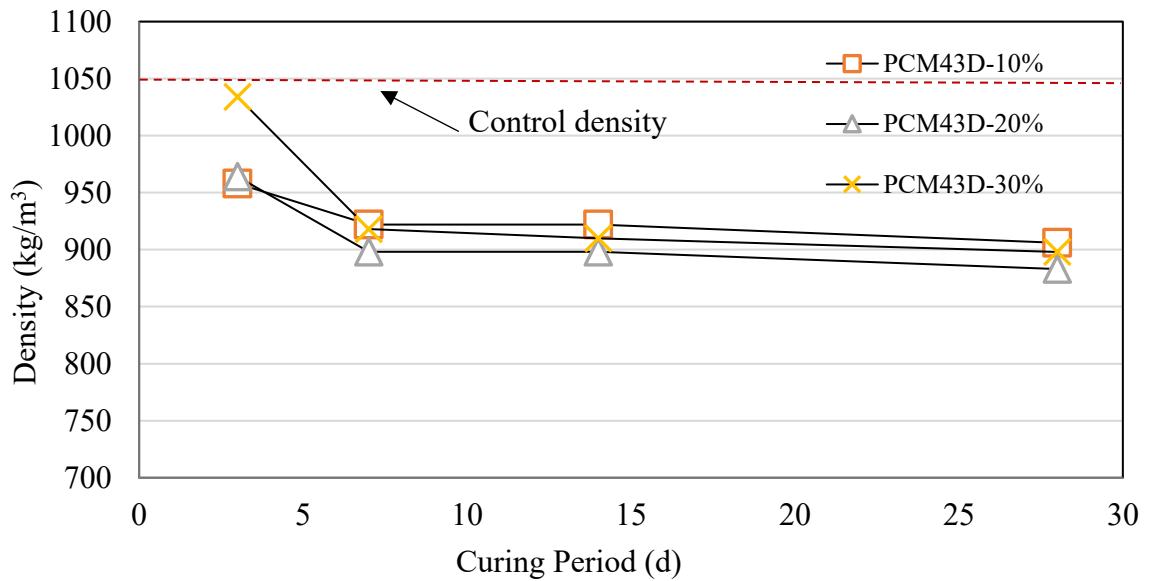


Figure 2.2.9 Effect of adding PCM43D to density of foam concrete.

The control wet density of all of PCM concretes was 1050 kg/m<sup>3</sup>. Figure 2.3.9 was a test result of PCM concrete density that used PCM by 10-30% on 3, 7, 14 and 28 days. As the PCM amount of addition got greater the density of concrete got less in opposite. The testing of concrete's density that was cured in a 40°C, H-95% in chamber. Figure 2.3.9 revealed the value of all percent of PCM43D foam concrete density of value 1034-883 kg/m<sup>3</sup>. The highest density of PCM43D concrete was 1034 kg/m<sup>3</sup> or PCM43D-30% at day 3 while the lowest density was 883 kg/m<sup>3</sup> or PCM-20% at day 28. The density showed a drop from day 3 to day 28, percentages are like: for concrete PCM43D-10%: 5.4%; PCM43D-20%: 8.4%; PCM43D-30%: 13.5% respectively.

The findings indicated that with an increase in the quantity of PCM, the density of the foamed concrete decreases. This was attributed to comparatively the lower specific gravity of PCM in comparison to other components in foamed concrete [25].



## 2.3 TEST METHODS

### 2.3.1 Differential Scanning Calorimetry (DSC)

The calorimetry measurements were taken with a TA device with a temperature accuracy of  $\pm 0.1^\circ\text{C}$ . It measures the difference in the heat flow rate between samples and insert reference as a function of time and temperature. The melting and freezing behaviors of the PCM were analyzed by a DSC model Q200 at a high-tech plaza in Koriyama city, Fukushima Prefecture. The temperature was measured at the sample platform with a thermocouple. The sample sizes were between 5 and 10 mg and were encapsulated with Pans (container of the sample material) and Lids (cap of the container). The samples were weighted by an analytical ultra-micro balance model: MC25. Then the samples were sealed in the pan by using an encapsulating press. An empty aluminum crucible was used as a reference in all measurements.

The 4 materials were analyzed, and each sample endured five full cycles. The DSC peaks for each composite PCM were evaluated for the second cycle of heating/cooling curves in terms of latent heat storage studies and phase change temperatures. Evaluation of the resulting DSC curves was performed through Proteus analysis v.6.0.0 Software. Phase change enthalpy and temperature were obtained from the DSC heat flux signal response by integration. The peak temperatures of heating and cooling have been considered as the representative temperature of a phase change transition.



Figure 2.3.1 DSC analysis machine model Q200.

### 2.3.1.1 Results of DSC measurements of PCM6D at various heating and cooling rates

The effect of heating/cooling rates was discussed based on the collected results of heating/cooling cycles for each sample.

The experimental results for PCM6D-10% to PCM6D-30% of foam concrete with different heating/cooling rates are shown at Figure 2.3.2 to Figure 2.3.4. The peak temperatures in the thermograms of the heating process consistently increased with the heating rate surged. Conversely, for cooling cases, the coldest temperatures appeared when dropping down the cooling rates. Initially, on one side of the PCM6D-10% of the heating process at 0.5°C/min to 10°C/min as shown in Figure 2.3.2. The first latent heat ( $\Delta h$ ) increased by 5.1% and the second latent heat decreased by 20.9%. On the other side of the PCM6D-10% for the cooling process in the first latent heat ( $\Delta h$ ) decreased by 19.47% and the second latent heat ( $\Delta h$ ) increased by 14.07% respectively.

Moreover, for the PCM6D-20% of the heating process at 0.5°C/min to 10°C/min is displayed in Figure 2.3.3. The first latent heat peak ( $\Delta h$ ) decreased by 6.9% and the second latent heat peak increased by 5.8%. Conversely, both peaks of cooling processes of latent heat ( $\Delta h$ ) on the PCM6D-10% increased by 10.2%. and 26% respectively.

Furthermore, for the PCM6D-30% of heating process from 0.5°C/min to 10°C/min as shown in Figure 2.3.4. The first latent heat pick ( $\Delta h$ ) was almost no difference where shift was between 0.5°C/min and 10°C/min and The Second latent heat pick increased by 4.6%. Conversely, For the PCM6D-10% of the cooling process the first pick of latent heat ( $\Delta h$ ) decreased around 24.23%. and the second peak of latent heat ( $\Delta h$ ) increased by 16.9%.

Overall, two peaks were noticed in the cooling rates in the results of PCM6D foam concrete, regardless of the amount of PCM. It could be suggested that the two peaks have different reasons. The smaller peak could have been caused by the polymer shell transition of the PCM material itself whereas the larger peak might have been caused by the phase change of the paraffin material. If so, this is in line with [26].

The DSC results of PCM6D foam concretes for all scanning rates above mentioned were summarized in Table 2-8.

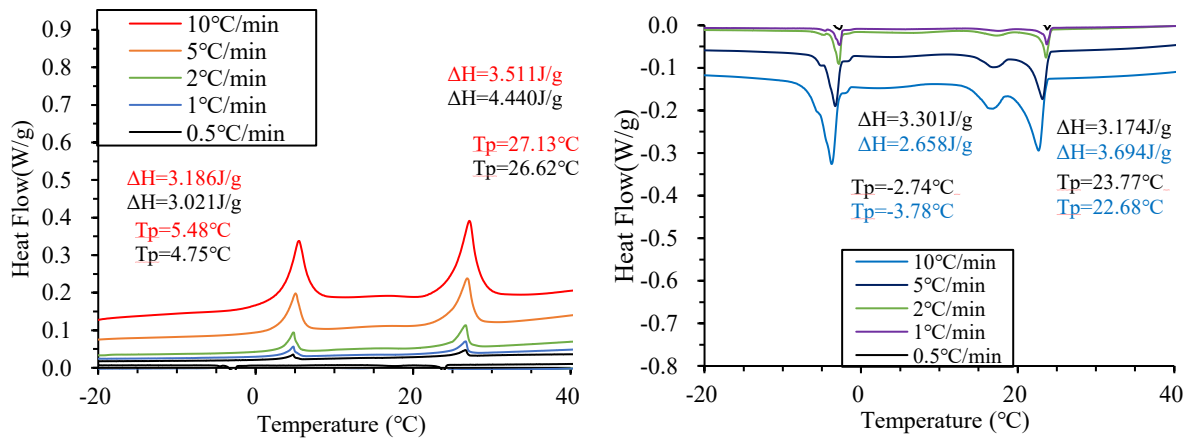


Figure 2.3.2 Results of DSC measurements of PCM6D-10% at various heating and cooling rates.

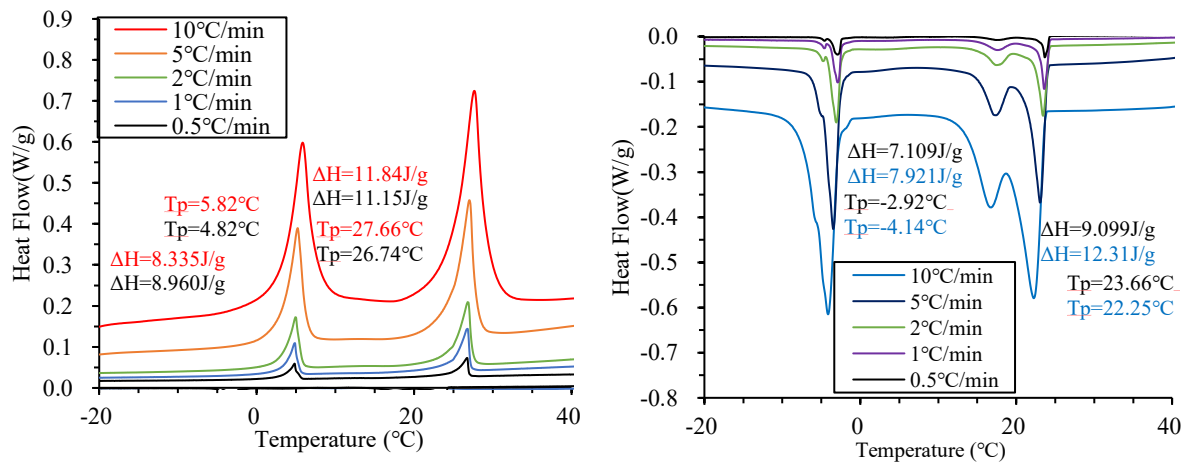


Figure 2.3.3 Results of DSC measurements of PCM6D-20% at various heating and cooling rates.

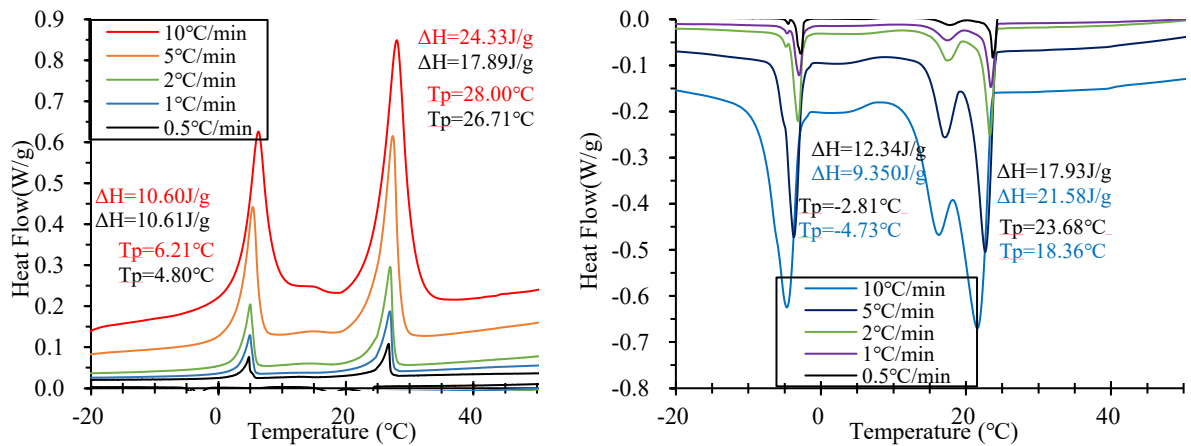


Figure 2.3.4 Results of DSC measurements of PCM6D-30% at various heating and cooling rates.

Table 2-8 Enthalpy variation and standpoint temperatures scanning rates varying from 10°C/min to 0.5°C/min of PCM6D.

Designation		Melting				Freezing				
		Onset Temp (°C)	End Temp (°C)	Peak enthalpy (J/g)	Peak Temp (°C)	Onset Temp (°C)	End Temp (°C)	Peak enthalpy (J/g)	Peak Temp (°C)	
6 D	Pure	10°C/min	-8.34	16.10	73.25	6.11	4.82	2.98	72.97	-14.21
		5°C/min	-9.04	10.78	79.51	5.55	4.18	2.34	78.37	-10.53
		2°C/min	-2.14	7.65	54.56	4.96	3.32	1.28	73.78	-6.49
		1°C/min	-3.01	6.90	54.61	4.87	3.13	1.28	57.82	-6.53
		0.5°C/min	-1.90	6.87	73.46	4.83	3.14	2.00	56.96	-9.71
	10%	10°C/min	-6.40	9.57	3.19	5.48	-1.31	-11.26	3.69	-3.78
		5°C/min	-4.55	10.04	3.01	5.05	-0.27	-8.60	3.83	-3.32
		2°C/min	-6.75	7.72	3.10	4.81	12.24	-8.02	3.65	-2.80
		1°C/min	-7.21	7.37	3.23	4.80	13.97	-8.14	3.54	-2.74
		0.5°C/min	-4.55	6.68	3.02	4.75	6.92	-7.36	3.17	-2.74
	20%	10°C/min	-4.32	10.5	8.34	5.82	-0.38	-13.23	7.92	-4.14
		5°C/min	-6.98	9.69	9.10	5.20	5.75	-10.69	8.52	-3.48
		2°C/min	-4.09	7.84	7.71	4.92	-0.96	-10.57	6.82	-3.10
		1°C/min	-3.85	7.49	8.10	4.84	0.31	-9.76	6.70	-2.88
		0.5°C/min	-8.60	7.03	8.96	4.82	7.26	-7.79	7.11	-2.92
30%	10°C/min	-6.98	12.93	10.60	6.21	-1.42	-13.35	9.35	-4.73	
	5°C/min	-6.86	9.81	11.54	5.36	-0.96	-9.87	9.55	-3.74	
	2°C/min	-9.64	7.61	10.85	4.95	11.06	-12.19	11.25	-3.16	
	1°C/min	-7.21	7.61	11.76	4.94	0.08	-8.37	8.44	-3.03	
	0.5°C/min	-6.98	6.33	10.61	4.8	10.15	-11.15	12.34	-2.81	

### 2.3.1.2 Results of DSC measurements of PCM18D at various heating and cooling rates

The effect of heating/cooling rates was discussed, with the basis on results collected at heating/cooling cycle on each sample.

The experimental results for from PCM18D-10% to PCM18D-30% of foam concrete different heating/cooling rates are shown from Figure 2.3.5 to Figure 2.3.7. The peak temperatures in the thermograms of the heating process were consistently with increased as the heating rate. Conversely, in the case of cooling, the peak temperatures decrease with increased cooling rates. For the PCM18D-10% of heating process from 0.5°C/min to 10°C/min as shown. The latent heat ( $\Delta h$ ) was no difference between the rate 0.5°C/min and 10°C/min. Conversely, For the PCM6D-10% of the cooling process of latent heat ( $\Delta h$ ) increased by 1.1%.

For the PCM18D-20% of heating process from 0.5°C/min to 10°C/min as shown in Figure 4-66. The first latent heat pick ( $\Delta h$ ) increased around 2.7%. Conversely, For the PCM6D-10% of the cooling process of latent heat ( $\Delta h$ ) increased by 15.2%.

For the PCM18D-30% of heating process from 0.5°C/min to 10°C/min as shown.

The first latent heat pick ( $\Delta h$ ) increased by 21.95%. Conversely, For the PCM18D-10% of the cooling process the first pick of latent heat ( $\Delta h$ ) increased by 33.98%.

Overall, it can be stated that the PCM peak response shifts in the direction of the imposed flux: the higher the peaks for heating and lower peak temperature for cooling. The DSC results of PCM18D foam concretes for all scanning rates above mentioned were summarized in Table 2-9.

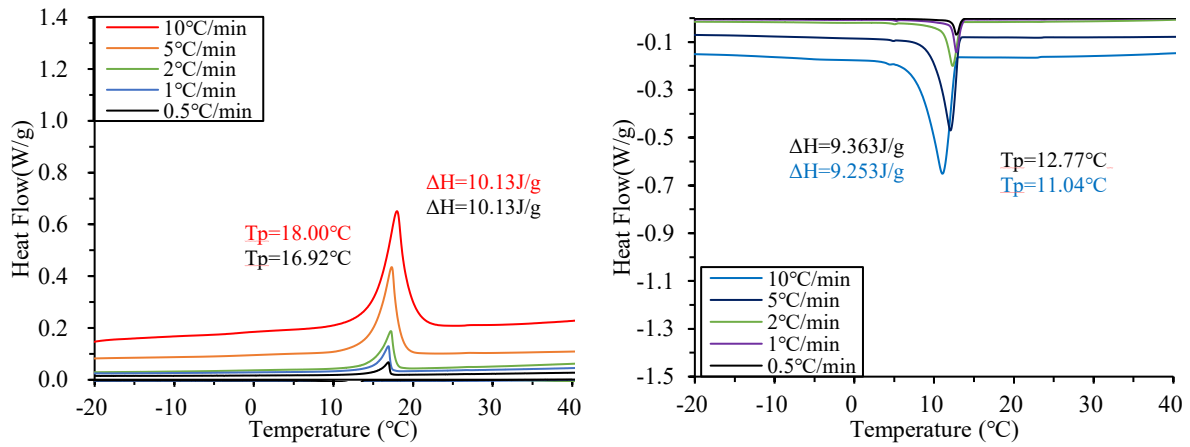


Figure 2.3.5 Results of DSC measurements of PCM18D-10% at various heating and cooling rates

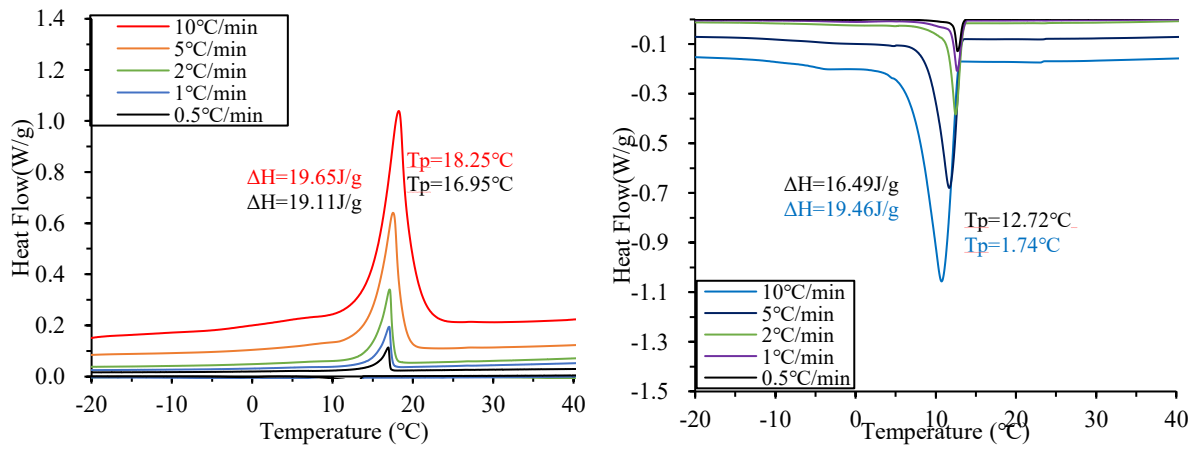


Figure 2.3.6 Results of DSC measurements of PCM18D-20% at various heating and cooling rates.

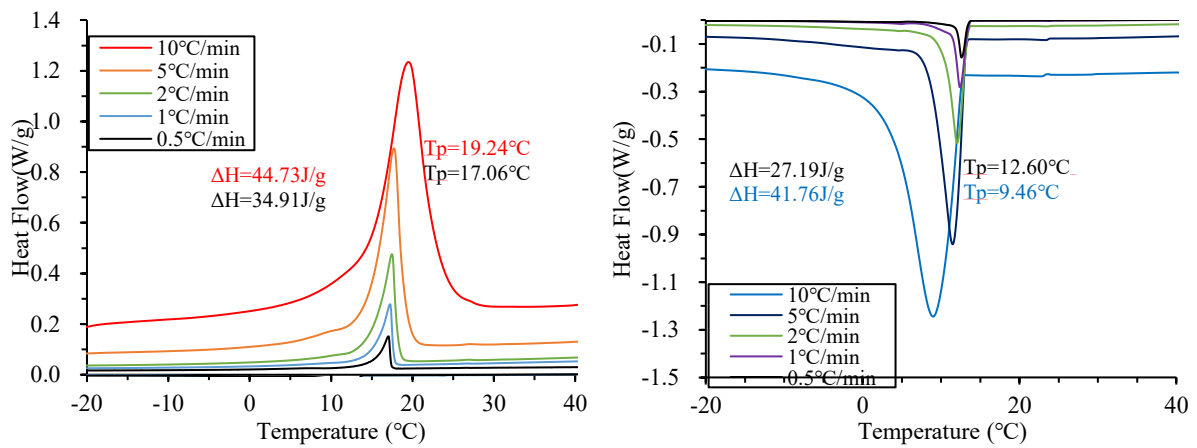


Figure 2.3.7 Results of DSC measurements of PCM18D-30% at various heating and cooling rate.

Table 2-9 Enthalpy variation and standpoint temperatures scanning rates varying from 10°C/min to 0.5°C/min of PCM18D.

Designation		Melting				Freezing				
		Onset Temp (°C)	End Temp (°C)	Peak enthalpy (J/g)	Peak Temp (°C)	Onset Temp (°C)	End Temp (°C)	Peak enthalpy (J/g)	Peak Temp (°C)	
18 D	Pure	10°C/min	0.70	33.15	170.2	19.49	14.97	7.71	177.50	-3.32
		5°C/min	1.21	27.11	188.3	18.27	15.50	9.33	181.20	-0.39
		2°C/min	3.51	22.90	179.3	17.69	16.89	10.82	178.00	3.36
		1°C/min	2.57	21.97	178	17.26	15.05	12.12	179.30	3.36
		0.5°C/min	6.84	20.24	177.4	16.99	15.26	12.50	175.80	6.60
	10%	10°C/min	4.25	24.97	10.13	18.00	13.28	-0.03	9.36	11.04
		5°C/min	4.02	22.43	11.46	17.32	14.09	-6.40	10.13	12.06
		2°C/min	4.94	20.23	9.86	17.22	14.21	-7.44	10.44	12.32
		1°C/min	3.90	19.30	10.90	16.92	14.78	-0.03	12.06	12.79
		0.5°C/min	4.48	18.60	10.13	16.92	14.09	0.43	9.25	12.77
	20%	10°C/min	6.33	25.55	19.65	18.25	13.05	-3.16	19.46	10.74
		5°C/min	0.43	21.15	21.78	17.54	14.09	-1.08	19.11	11.68
		2°C/min	-3.39	18.72	21.83	17.11	13.86	-9.41	20.89	12.47
		1°C/min	-3.85	19.30	22.37	17.04	13.97	-9.06	19.11	12.66
		0.5°C/min	2.98	18.60	19.11	16.95	14.32	2.28	19.46	12.72
30%	10°C/min	-8.72	29.26	44.73	19.24	13.16	-14.04	41.76	9.46	
	5°C/min	-7.10	22.31	38.66	17.74	13.51	-14.39	38.28	11.48	
	2°C/min	-0.73	20.92	37.70	17.46	13.86	-8.37	37.24	12.04	
	1°C/min	-1.19	19.99	35.31	17.26	14.44	-6.63	32.49	12.40	
	0.5°C/min	-4.32	18.6	34.91	17.06	14.21	-5.82	27.19	12.60	

### 2.3.1.3 Results of DSC measurements of PCM28D at various heating and cooling rates

The effect of heating/cooling rates was discussed, with the basis on results collected at heating/cooling cycle on each sample.

The experimental results for from PCM28D-10% to PCM28D-30% of foam concrete different heating/cooling rates are shown from Figure 2.3.8 to Figure 2.3.10. The peak temperatures in the thermograms of the heating process were consistently increased with the heating rate. Conversely, in the case of cooling, the peak temperatures decrease with increased cooling rates. For the PCM28D-10% of heating process from 0.5°C/min to 10°C/min as shown in Figure 4-68. The latent heat ( $\Delta h$ ) decreased by 14.76%. Conversely, For the PCM28D-10% of the cooling process of latent heat ( $\Delta h$ ) increased by 22.9%.

For the PCM28D-20% of heating process from 0.5°C/min to 10°C/min was shown. Figure 4-69. The first latent heat pick ( $\Delta h$ ) decreased by 8.7%. Conversely, for the PCM6D-10% of the cooling process of latent heat ( $\Delta h$ ) increased around 11.8%.

For the PCM28D-30% of heating process from 0.5°C/min to 10°C/min was shown in Figure 4-70. The first latent heat pick ( $\Delta h$ ) increased by 9.3%. Conversely, For the PCM28D-10% of the cooling process the first pick of latent heat ( $\Delta h$ ) increased by 12.3%.

Overall, it can be stated that the PCM peak response shifts in the direction of the imposed flux: the higher the peaks for heating and lower peak temperature for cooling. The DSC results of PCM28D foam concretes for all scanning rates above mentioned were summarized in Table 2-10.



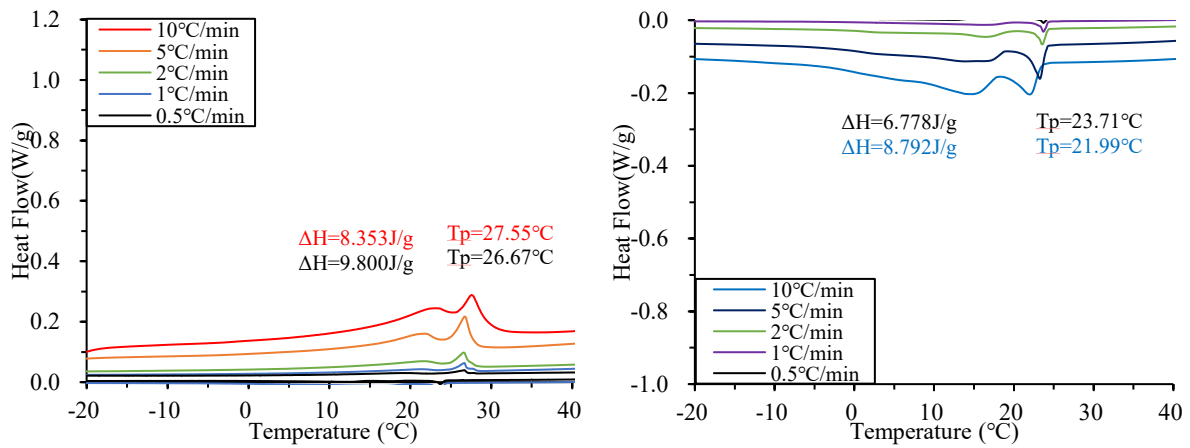


Figure 2.3.8 Results of DSC measurements of PCM 28D-10% at various heating and cooling rates.

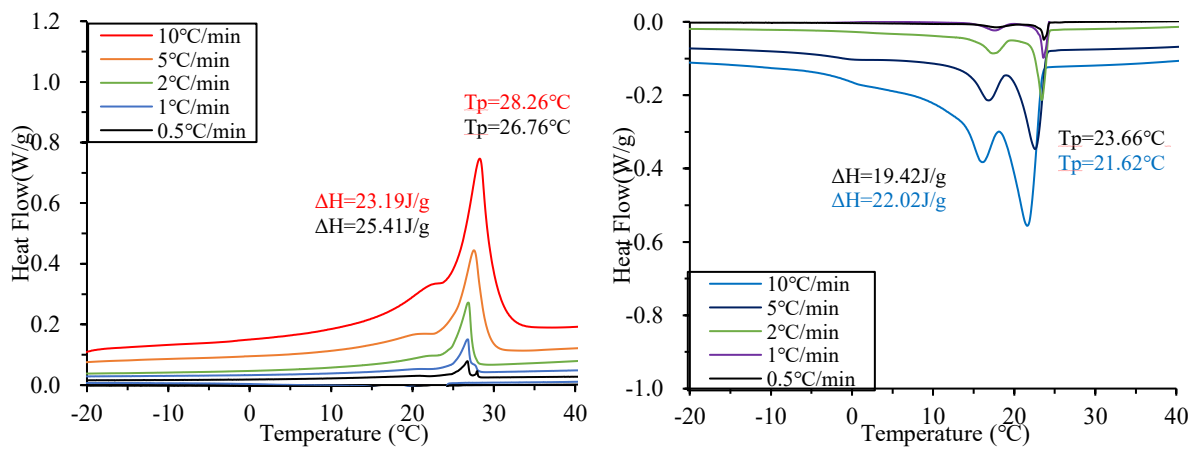


Figure 2.3.9 Results of DSC measurements of PCM 28D-20% at various heating and cooling rates.

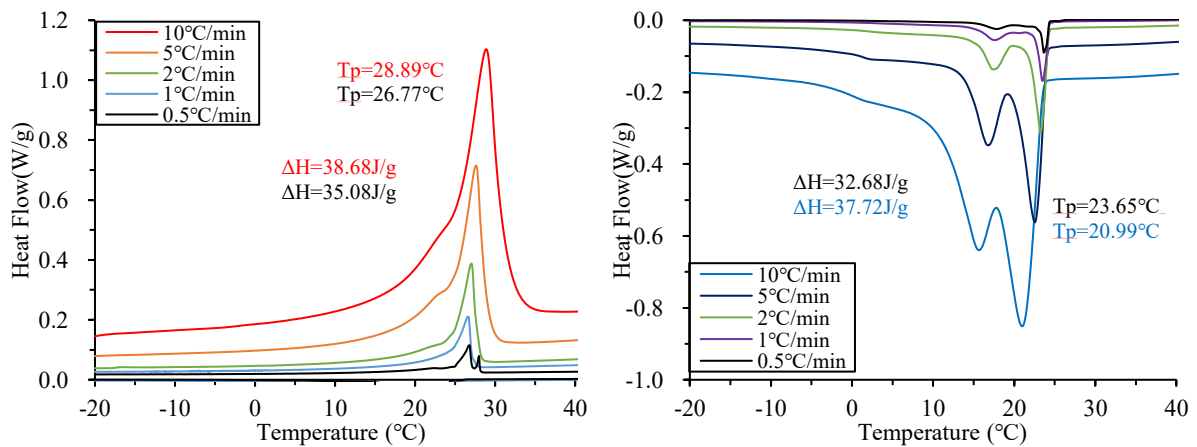


Figure 2.3.10 Results of DSC measurements of PCM 28D-30% at various heating and cooling rates.

Table 2-10 Enthalpy variation and standpoint temperatures scanning rates varying from 10°C/min to 0.5°C/min of PCM28D.

Designation		Melting				Freezing				
		Onset Temp (°C)	End Temp (°C)	Peak enthalpy (J/g)	Peak Temp (°C)	Onset Temp (°C)	End Temp (°C)	Peak enthalpy (J/g)	Peak Temp (°C)	
28D	Pure	10°C/min	9.13	40.85	181.3	28.13	27.10	20.46	183.10	6.69
		5°C/min	9.01	36.09	182.7	27.69	25.59	20.17	180.40	8.16
		2°C/min	13.19	31.37	171.8	26.98	25.83	22.73	177.60	8.92
		1°C/min	11.72	31.51	169	26.87	26.04	22.74	172.60	11.27
		0.5°C/min	11.05	28.98	176.7	26.79	26.00	23.50	179.40	11.05
	10%	10°C/min	0.20	34.93	8.35	27.55	24.51	-12.07	8.79	21.99
		5°C/min	-11.50	31.80	11.07	26.72	25.67	-14.16	11.16	23.25
		2°C/min	-12.19	29.95	12.10	26.59	26.48	-13.12	11.27	23.57
		1°C/min	-5.24	29.37	10.57	26.66	26.13	-8.60	9.61	23.69
		0.5°C/min	-7.10	28.45	9.80	26.67	26.25	-5.01	6.78	23.71
	20%	10°C/min	-1.42	37.82	23.19	28.26	24.86	-9.64	22.02	21.62
		5°C/min	-7.91	31.57	23.31	27.52	24.74	-12.65	22.03	22.56
		2°C/min	-5.48	29.60	26.56	26.85	24.97	-10.45	23.27	23.40
		1°C/min	2.74	29.37	22.05	26.80	26.13	-3.85	19.71	23.60
		0.5°C/min	-3.39	28.68	25.41	26.76	26.59	-11.61	19.42	23.66
	30%	10°C/min	0.08	37.36	38.68	28.89	24.62	-10.11	37.72	20.99
		5°C/min	-1.77	33.54	38.40	27.62	27.40	-9.76	37.45	22.56
		2°C/min	-0.73	30.76	37.51	27.01	26.01	-9.53	37.38	23.24
		1°C/min	3.44	29.83	36.24	26.62	26.48	-5.36	34.73	23.49
		0.5°C/min	3.21	29.26	35.08	26.77	26.94	-4.32	32.68	23.65

#### **2.3.1.4 Results of DSC measurements of PCM43D at various heating and cooling rates**

The effect of heating/cooling rates was discussed, with the basis on results collected at heating/cooling cycle on each sample.

The experimental results for from PCM43D-10% to PCM43D-30% of foam concrete different heating/cooling rates are shown from Figure 2.3.11 to 2.3.13. The peak temperatures in the thermograms of the heating process were consistently being increased with the heating rate. Conversely, in the case of cooling, the peak temperatures decrease with increased cooling rates. For the PCM43D-10% of heating process from 0.5°C/min to 10°C/min as shown in Figure 2.4.11. The latent heat ( $\Delta h$ ) decreased around 26.9%. Conversely, For the PCM43D-10% of the cooling process of latent heat ( $\Delta h$ ) increased by 20.8%.

For the PCM43D-20% of heating process from 0.5°C/min to 10°C/min as shown in Figure 2.4.11. The first latent heat pick ( $\Delta h$ ) decreased by 18.14%. Conversely, for the PCM43D-10% of the cooling process of latent heat ( $\Delta h$ ) increased by 19.3%.

For the PCM43D-30% of heating process from 0.5°C/min to 10°C/min was shown in Figure 2.4.12. The first latent heat pick ( $\Delta h$ ) increased by 1.3%. Conversely, for the PCM43D-10% of the cooling process the first pick of latent heat ( $\Delta h$ ) was increased around 24.5%.

Overall, it can be stated that the PCM peak response shifts in the direction of the imposed flux: the higher the peaks for heating and lower peak temperature for cooling. The DSC results of PCM43D foam concretes for all scanning rates above mentioned were summarized in Table 2-11.

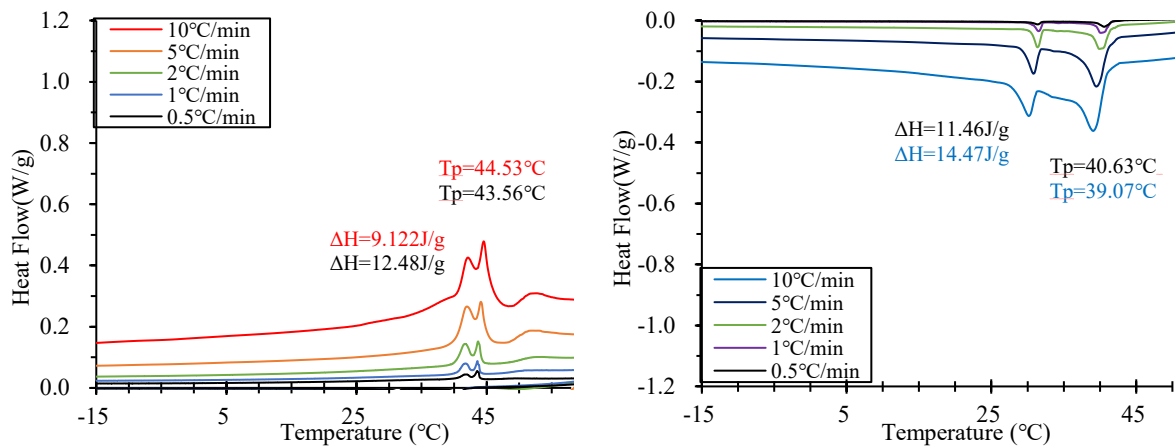


Figure 2.3.11 Results of DSC measurements of PCM 43D-10% at various heating and cooling rates.

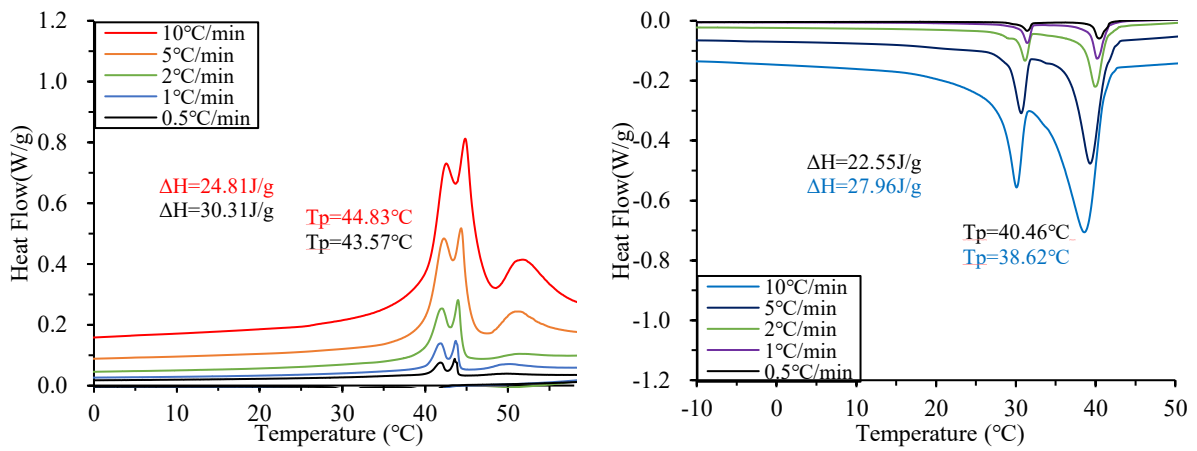


Figure 2.3.12 Results of DSC measurements of PCM 43D-20% at various heating and cooling rates.

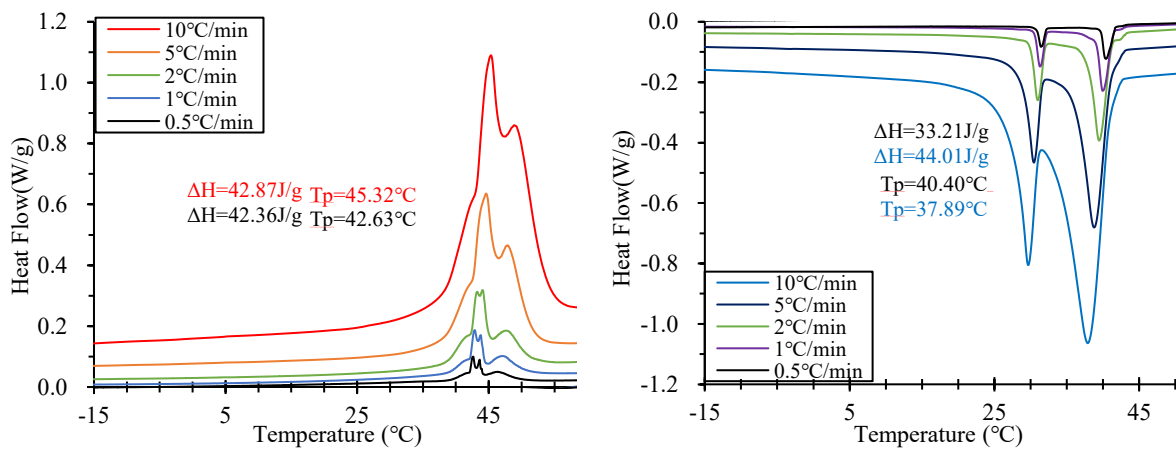


Figure 2.3.13 Results of DSC measurements of PCM 43D-30% at various heating and cooling rates.

Table 2-11 Enthalpy variation and standpoint temperatures scanning rates varying from 10°C/min to 0.5°C/min of PCM43D.

Designation		Melting				Freezing				
		Onset Temp (°C)	End Temp (°C)	Peak enthalpy (J/g)	Peak Temp (°C)	Onset Temp (°C)	End Temp (°C)	Peak enthalpy (J/g)	Peak Temp (°C)	
43D	Pure	10°C/min	16.17	58.55	218.8	44.53	42.61	28.99	214.80	20.35
		5°C/min	16.75	59.01	213.7	41.88	44.11	37.99	213.20	24.75
		2°C/min	16.41	57.39	216.9	41.57	43.08	39.75	218.70	29.25
		1°C/min	13.43	56.00	209.3	43.58	43.24	40.25	214.70	29.24
		0.5°C/min	14.55	55.54	202.8	43.56	43.23	40.61	210.30	28.98
	10%	10°C/min	16.17	58.55	9.12	44.53	42.69	0.20	14.47	39.07
		5°C/min	16.75	59.01	8.21	41.88	43.61	11.77	12.15	39.52
		2°C/min	16.41	57.39	12.80	41.57	43.84	6.56	13.16	39.93
		1°C/min	37.24	56.00	6.72	43.58	43.73	11.77	11.59	40.14
		0.5°C/min	14.55	55.54	12.48	43.56	44.31	12.58	11.46	40.63
	20%	10°C/min	27.29	58.43	24.81	44.83	43.61	12.47	27.96	38.62
		5°C/min	26.59	59.12	25.43	44.33	43.61	10.27	28.76	39.32
		2°C/min	25.32	59.47	21.82	43.96	44.54	13.28	27.72	39.98
		1°C/min	22.08	59.47	25.34	43.67	44.07	11.77	27.22	40.19
		0.5°C/min	11.54	56.23	30.31	43.57	45.23	10.50	22.55	40.46
	30%	10°C/min	28.91	58.89	42.87	45.32	42.80	10.15	44.01	37.89
		5°C/min	24.39	58.31	44.46	44.60	43.84	12.82	42.57	38.78
		2°C/min	24.97	59.24	44.95	44.08	43.73	11.66	44.43	39.49
		1°C/min	27.52	59.12	44.21	42.86	44.42	20.69	39.53	39.97
		0.5°C/min	24.51	58.31	42.36	42.63	44.31	16.29	33.21	40.40

### 2.3.1.5 Results of onset, peak and temperature for phase transition in PCM6D

The DSC curves of the samples (from PCM6D-10% to PCM6D-30%) for heating and cooling processes are shown in Figure 2.3.14 to Figure 2.3.16. The onset and end temperatures, corresponding to the start and end of the phase change, were identified from the intersections of the baseline with the inflection points. For example, PCM6D-10% during heating, the melting process started at about  $-6.40^{\circ}\text{C}$  and ended at  $9.5^{\circ}\text{C}$ . In the experiments, where heat was removed from the sample, the freezing process started at about  $-1.31^{\circ}\text{C}$  and ended at  $-11.26^{\circ}\text{C}$  (of  $10^{\circ}\text{C}/\text{min}$  range). Moreover, the peak melting temperatures of samples (PCM6D-10%) occurred almost in the same position in comparison to the other PCM samples.

As seen in figures from Figure 2.3.14 to Figure 2.3.16, it is interesting to remark that the overall differences between the heating/cooling rates are smaller as the rate decreases, with an almost negligible behavior being observed at the heating/cooling rate of  $0.5^{\circ}\text{C}/\text{min}$ . An example of such a case for the PCM6D-10% sample is presented in Figure 2.3.14, where a negligible shift is generally observed in the case of  $0.5^{\circ}\text{C}/\text{min}$  rate, in opposition to the observable situation for  $10^{\circ}\text{C}/\text{min}$  (Figure 2.4.14). It should be noted that the DSC fluxes have been normalized to their peaks in order to facilitate the simultaneous observation of the shape of the thermograms for  $0.5^{\circ}\text{C}/\text{min}$  and  $10^{\circ}\text{C}/\text{min}$ .

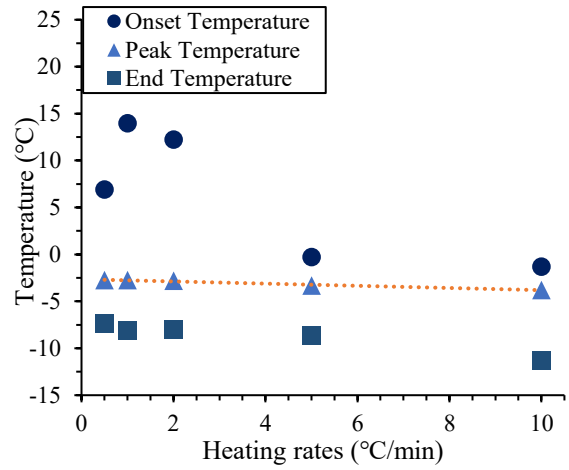
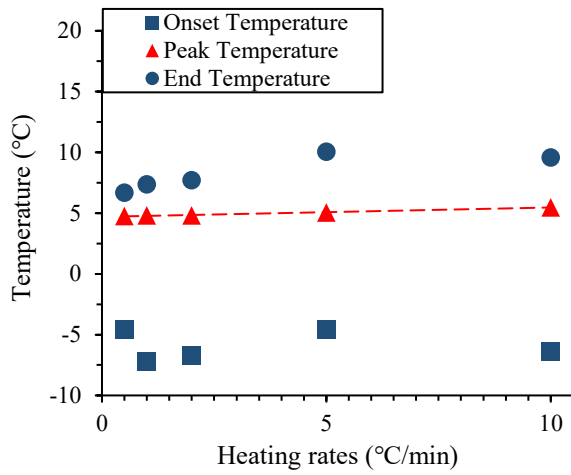


Figure 2.3.14 Onset, peak and end temperature for the phase transition in PCM6D-10%.

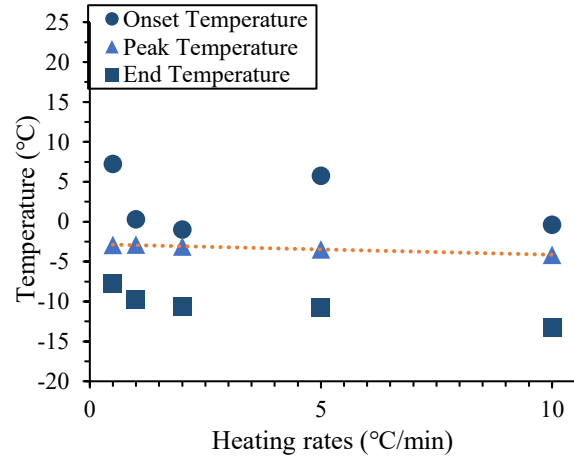
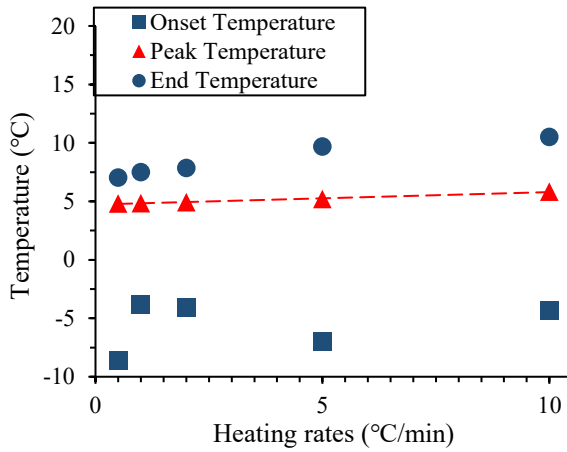


Figure 2.3.15 Onset, peak and end temperature for the phase transition in PCM6D-20%.

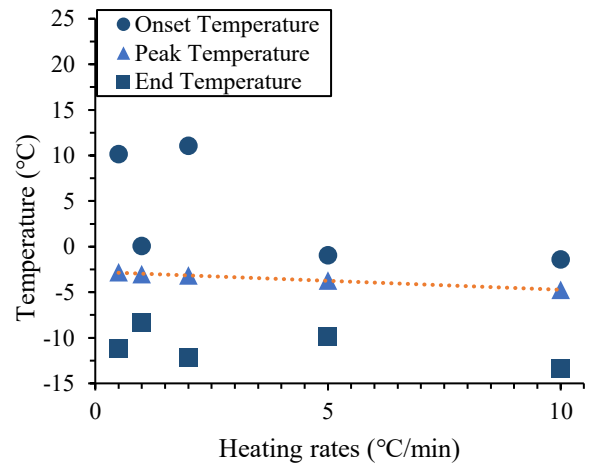
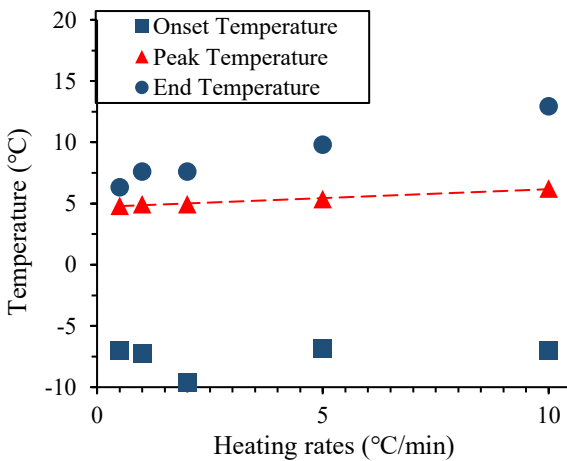


Figure 2.3.16 Onset, peak and end temperature for the phase transition in PCM6D-30%

### 2.3.1.6 Results of onset, peak and temperature for phase transition in PCM18D

The DSC curves of the samples (from PCM18D-10% to PCM18D-30%) for heating and cooling processes are shown in Figure 2.4.17 to Figure 2.4.19. The onset and end temperatures, corresponding to the start and end of the phase change, were identified from the intersections of the baseline with the inflection points. For example, PCM18D-10% during heating, the melting process started at about 4.25°C and ended at 24.97°C. In the experiments where heat was removed from the sample, the freezing process started at about 13.28°C and ended at -0.03 of 10°C/min range). Moreover, the peak melting temperatures of samples (PCM6D-10%) occurred almost in the same position in comparison to the other PCM samples.

As seen in figures from Figure 2.3.17 to Figure 2.3.19, it is interesting to remark that the overall differences between the heating/cooling rates are smaller as the rate decreases, with an almost negligible behavior being observed at the heating/cooling rate of 0.5°C/min. An example of such a case for the PCM18D-10% sample is presented in Figure 2.4.17, where a negligible shift is generally observed in the case of 0.5°C/min rate, in opposition to the observable situation for 10°C/min (Figure 2.4.17). It should be noted that the DSC fluxes have been normalized to their peaks in order to facilitate the simultaneous observation of the shape of the thermograms for 0.5°C/min and 10°C/min.



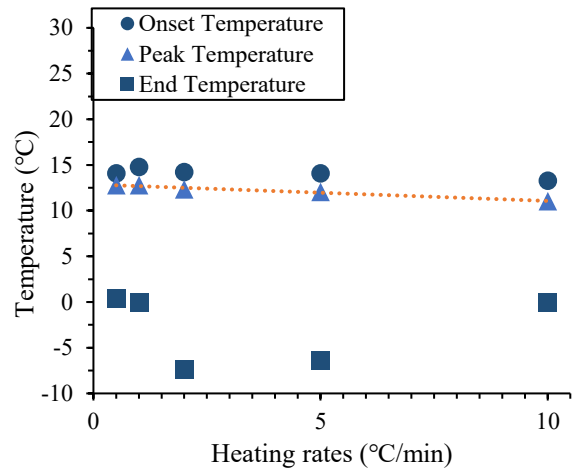
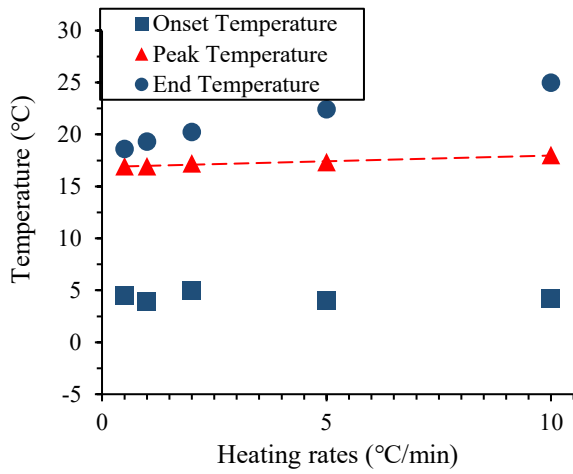


Figure 2.3.17 Onset, peak and end temperature for the phase transition in PCM18D-10%.

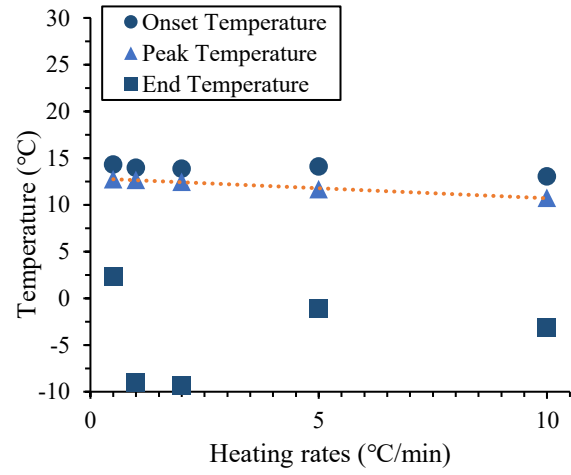
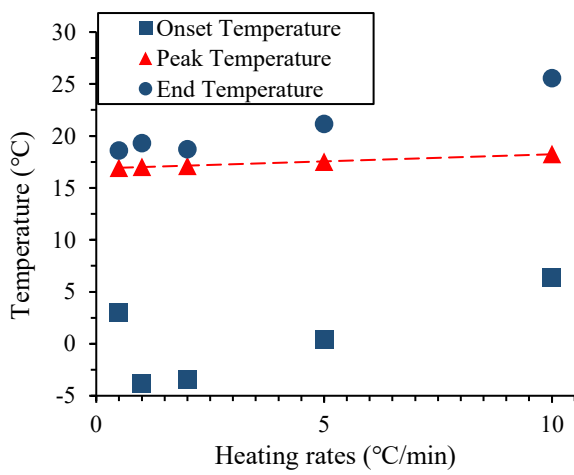


Figure 2.3.18 Onset, peak and end temperature for the phase transition in PCM18D-20%.

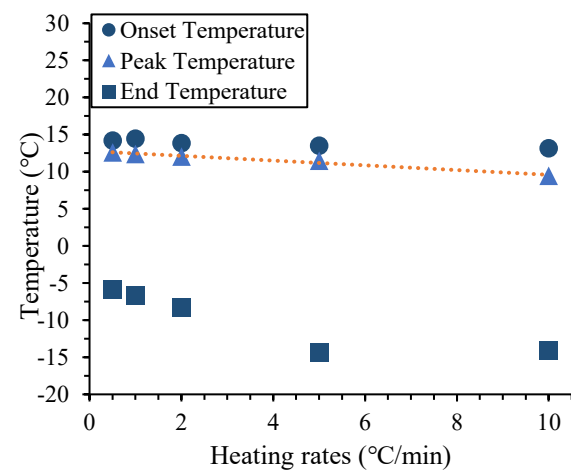
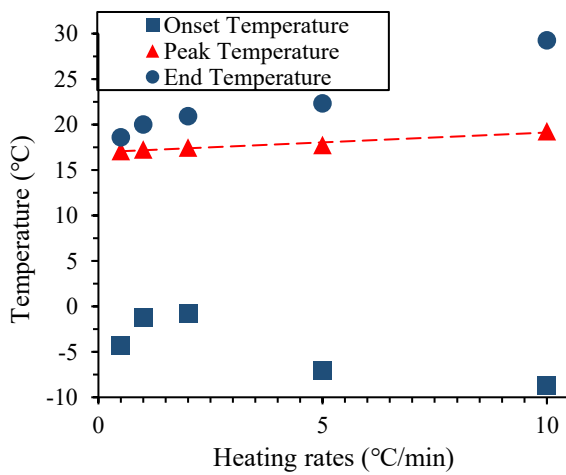


Figure 2.3.19 Onset, peak and end temperature for the phase transition in PCM18D-30%.

### 2.3.1.7 Results of onset, peak and temperature for phase transition in PCM28D

The DSC curves of the samples (from PCM28D-10% to PCM28D-30%) for heating and cooling processes are shown in Figure 2.3.20 to Figure 2.3.22. The onset and end temperatures, corresponding to the start and end of the phase change, were identified from the intersections of the baseline with the inflection points. For example, PCM28D-10% during heating, the melting process started at about 0.20°C and ended at 34.93°C. In the experiments where heat was removed from the sample, the freezing process started at about 24.51°C and ended at -12.07 of 10°C/min range). Moreover, the peak melting temperatures of samples (PCM6D-10%) occurred almost in the same position in comparison to the other PCM samples.

As seen in figures from Figure 2.3.20 to Figure 2.3.22, it is interesting to remark that the overall differences between the heating/cooling rates are smaller as the rate decreases, with an almost negligible behavior being observed at the heating/cooling rate of 0.5°C/min. An example of such a case for the PCM28D-30% sample is presented in Figure 2.4.22 where a negligible shift is generally observed in the case of 0.5°C/min rate, in opposition to the observable situation for 10°C/min (Figure 2.4.22). It should be noted that the DSC fluxes have been normalized to their peaks in order to facilitate the simultaneous observation of the shape of the thermograms for 0.5°C/min and 10°C/min.

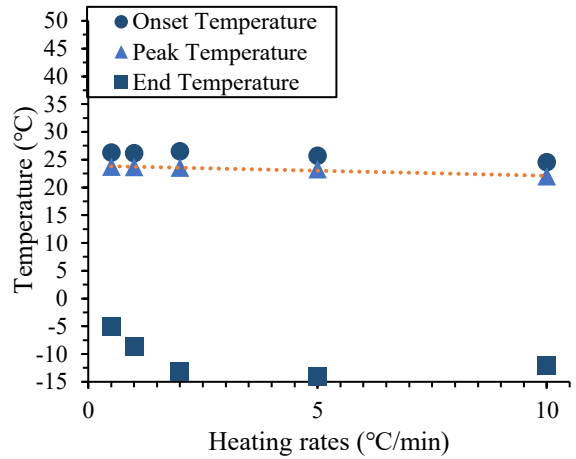
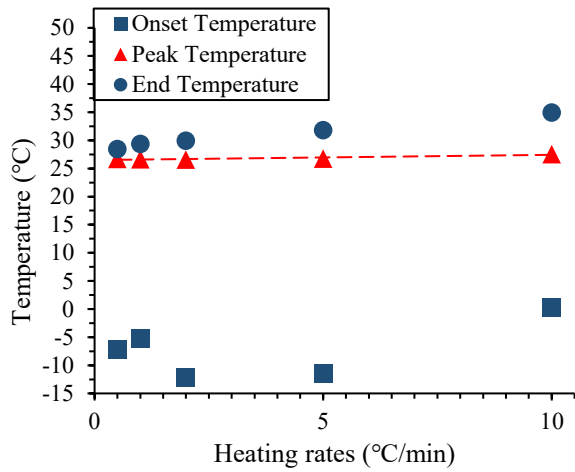


Figure 2.3.20 Onset, peak and end temperature for the phase transition in PCM28D-10%.

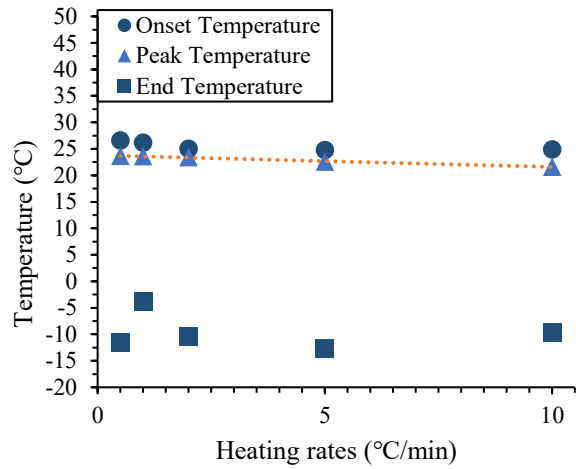
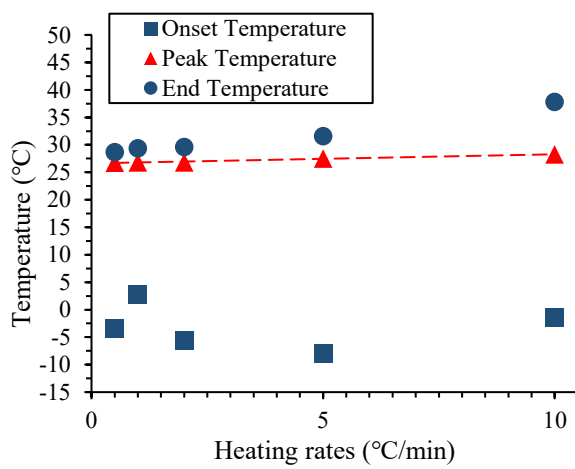


Figure 2.3.21 Onset, peak and end temperature for the phase transition in PCM28D-20%.

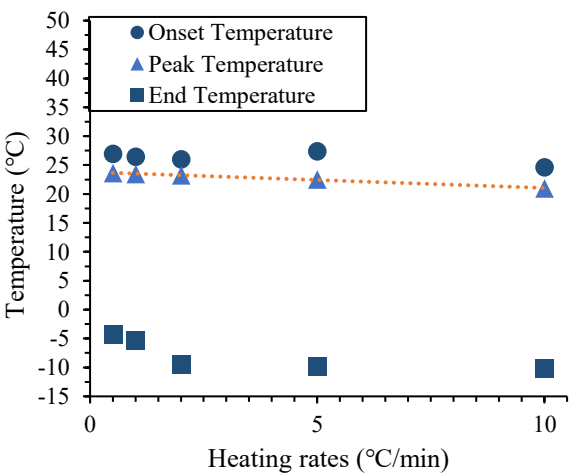
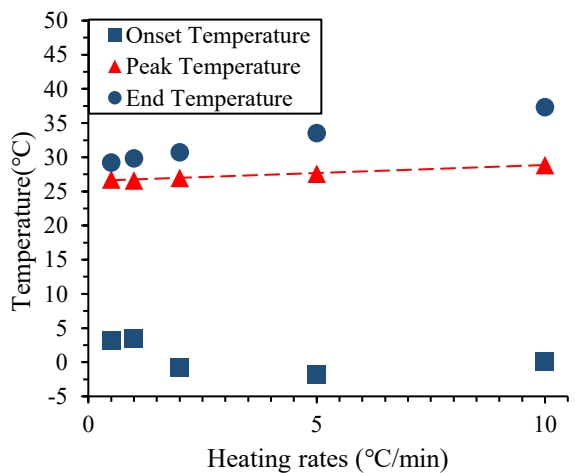


Figure 2.3.22 Onset, peak and end temperature for the phase transition in PCM28D-30%.

### 2.3.1.8 Results of onset, peak and temperature for phase transition in PCM43D

The DSC curves of the samples (from PCM43D-10% to PCM43D-30%) for heating and cooling processes are shown in Figure 2.3.23 to Figure 2.3.25. The onset and end temperatures, corresponding to the start and end of the phase change, were identified from the intersections of the baseline with the inflection points. For example, PCM43D-10% during heating, the melting process started at about 16.17 °C and ended at 58.55 °C. In the experiments where heat was removed from the sample, the freezing process started at about 42.69 °C and ended at 0.2 °C of 10°C/min range). Moreover, the peak melting temperatures of samples (PCM6D-10%) occurred almost in the same position in comparison to the other PCM samples.

It is further interesting to remark, that the overall differences from Figure 2.3.23 to Figure 2.3.25 for each rate heating/cooling are smaller as the rate decreases, with an almost negligible behavior being observed at the heating/cooling rate of 0.5°C/min. An example of such a case for the PCM43D-30% sample is presented in Figure 2.3.25, where a negligible shift is generally observed in the case of 0.5°C/min rate, in opposition to the observable situation for 10°C/min (Figure 2.3.25). It should be noted that the DSC fluxes have been normalized to their peaks in order to facilitate the simultaneous observation of the shape of the thermograms for 0.5°C/min and 10°C/min.

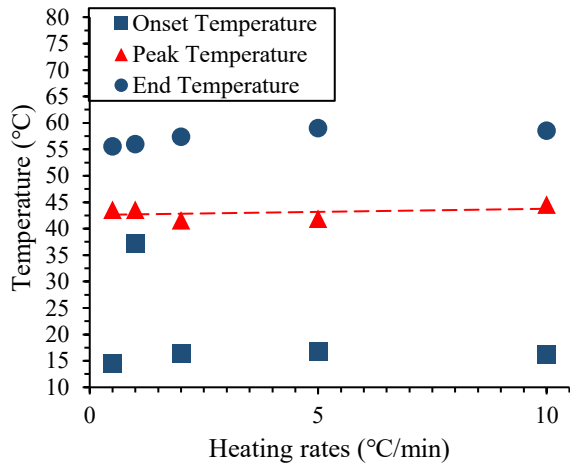


Figure 2.3.23 Onset, peak and end temperature for the phase transition in PCM43D-10%.

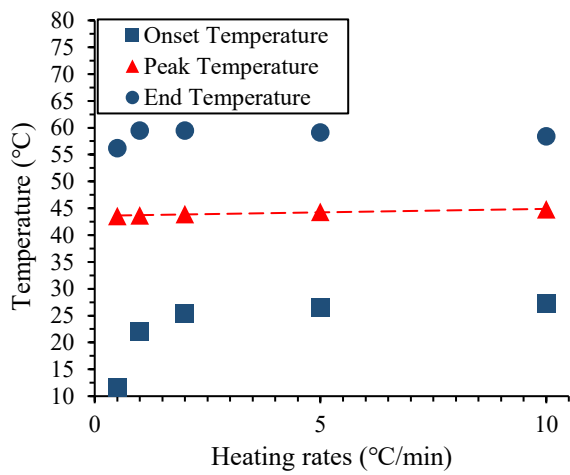
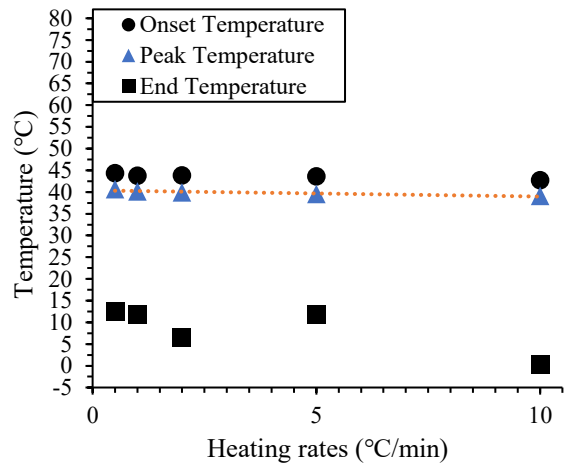


Figure 2.3.24 Onset, peak and end temperature for the phase transition in PCM43D-20%.

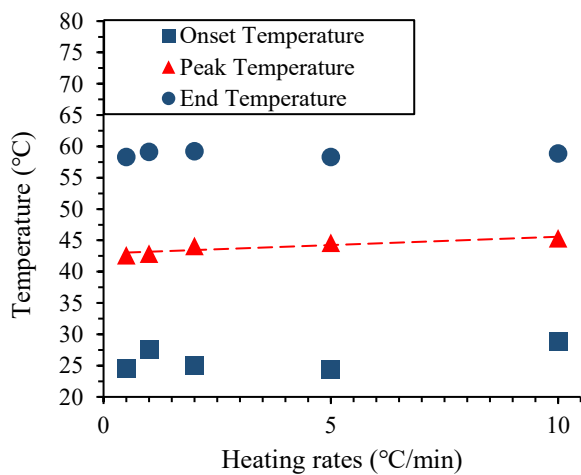
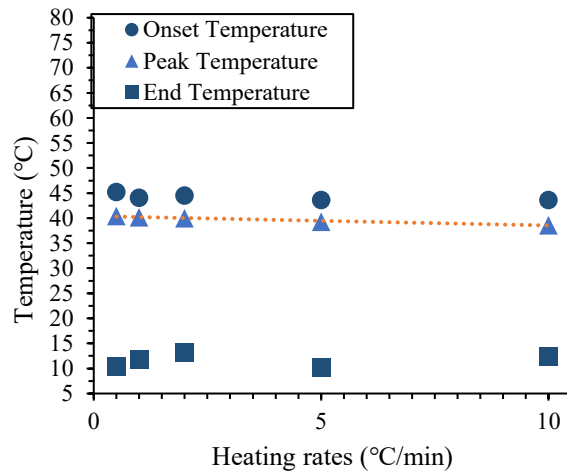
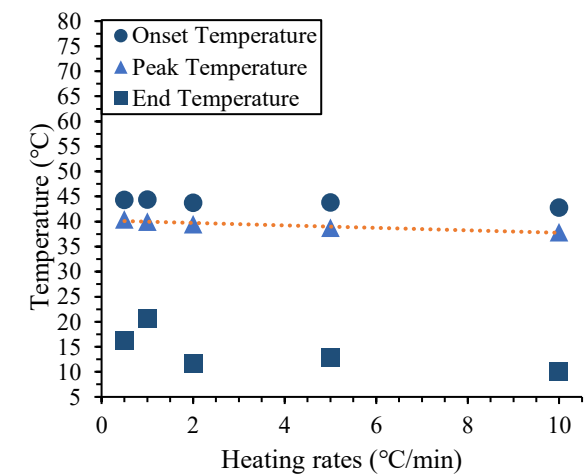


Figure 2.3.25 Onset, peak and end temperature for the phase transition in PCM43D-30%.



### 2.3.2 Specific heat capacity measurements

The specific heat capacity is referred to the amount of energy required to raise the temperature of 1 gram of substance by 1°C or 1K with units quoted as (J/g°C). Also designed as  $C_p$ , specific heat capacity can be quantitatively measured using a DSC as it is obtained at constant pressure.

The schematic DSC, specific heat capacity plots are shown from Figure 2.3.26 to 2.3.29. The specific heat capacity curve can be obtained by removing the baseline part of the DSC and consequently, the specific enthalpy in the unit weight of PCM can be obtained by dividing the integrated area of specific heat capacity curve with a temperature rising rate. This value can be calculated automatically by the software. Dynamic DSC tests were performed for all PCM foam concrete samples, considering a heating rate of 10°C/min. The effect of the heating rate between -10°C to 40°C was investigated for all PCM foam concrete samples.

#### 2.3.2.1 Results of specific heat capacity measurements

The specific heat capacity measurements yielded the following results:

For PCM6D-10%: Two distinct peaks were observed. The first peak occurred at 5.56°C, with a specific heat ( $C_p$ ) of 0.79 J/g°C. The second peak was at 27.60°C, with a specific heat capacity of 0.90 J/g°C, which was the lowest among the tested PCM foam concrete mixtures. For PCM6D-30%: Similar to PCM6D-10%, this mixture also exhibited two peaks. The first peak was at 5.64°C, with a specific heat of 2.16 J/g°C. The second peak occurred at 28.21°C, with a specific heat capacity of 2.91 J/g°C, which was the highest among the tested PCM concrete mixtures.

For PCM18D-10%: The lowest specific heat ( $C_p$ ) was observed in this mixture. The peak temperature was at 17°C, and the specific heat was 1.62 J/g°C. For PCM18D-30%: This mixture exhibited the highest specific heat ( $C_p$ ). The peak temperature was at 16°C, and the specific heat was 3.84 J/g°C

For PCM28D-10%: The lowest specific heat ( $C_p$ ) was recorded for this mixture, with the peak temperature at 27.79°C and a specific heat of 1.39 J/g°C. For PCM28D-30%: The highest specific heat ( $C_p$ ) was observed in this mixture, with the peak temperature at 27.38°C and a specific heat of 3.25 J/g°C.

For PCM43D-10%: The lowest specific heat ( $C_p$ ) was found in this mixture, with the peak temperature at 42.70°C and a specific heat of 1.84 J/g°C. The peak was found at 42.70°C and specific heat ( $C_p$ ) unit weight was 4.54 J/g°C. Also, the highest specific heat ( $C_p$ ) was found PCM43D-30%.

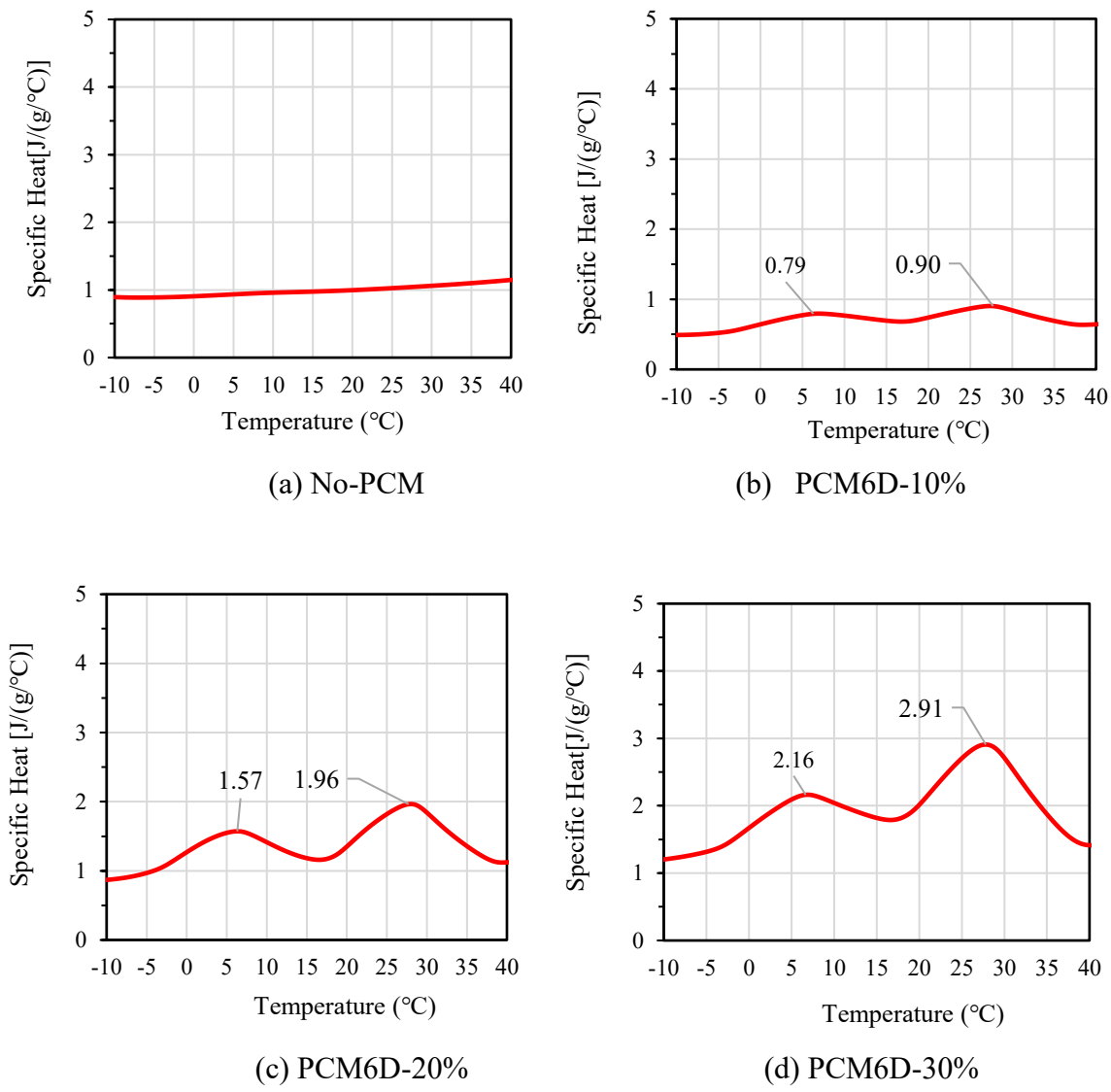
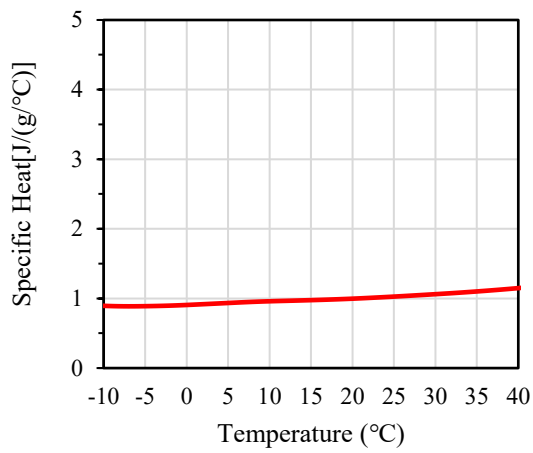
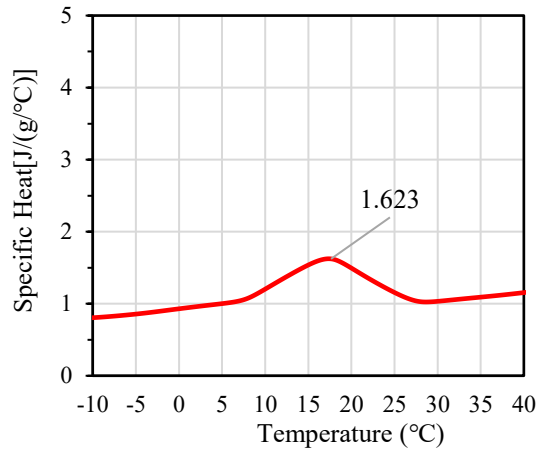


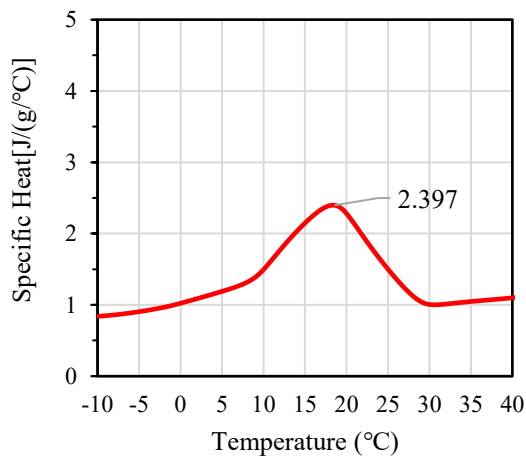
Figure 2.3.26 Results of specific heat measurements with different amount of PCMs in PCM6D.



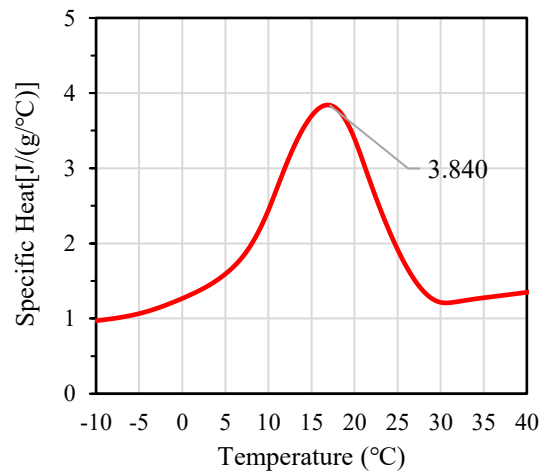
(a) No-PCM



(b) PCM18D-10%



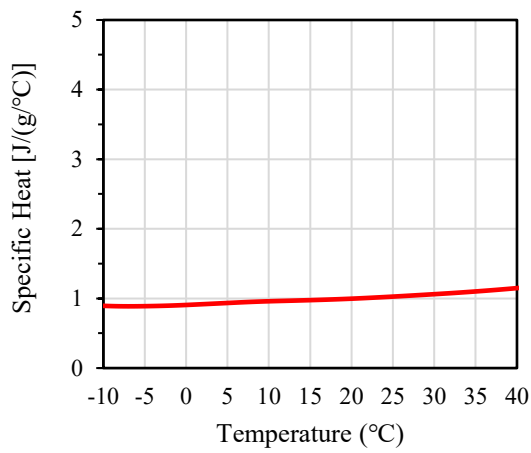
(c) PCM18D-20%



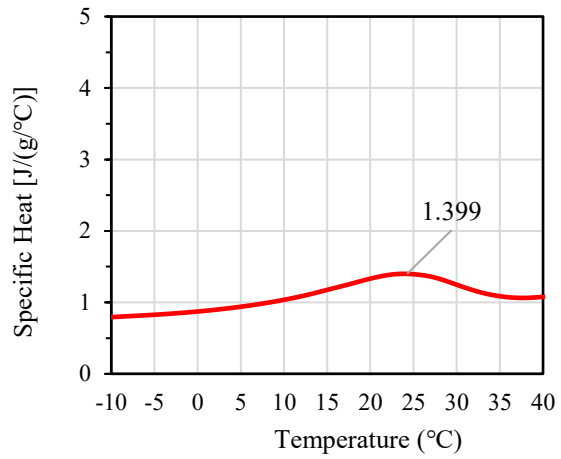
(d) PCM18D-30%

Figure 2.3.27 Result of specific heat measurements with different amount of PCMs in PCM18D.

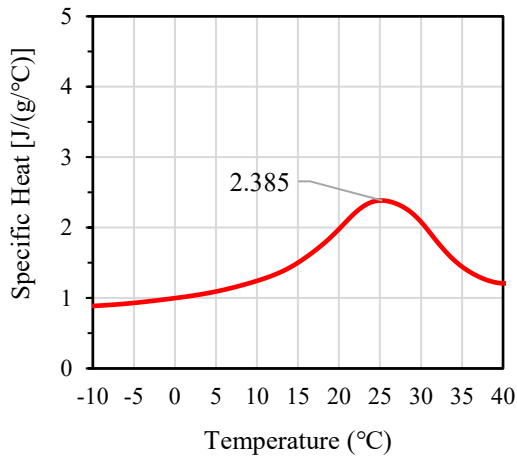




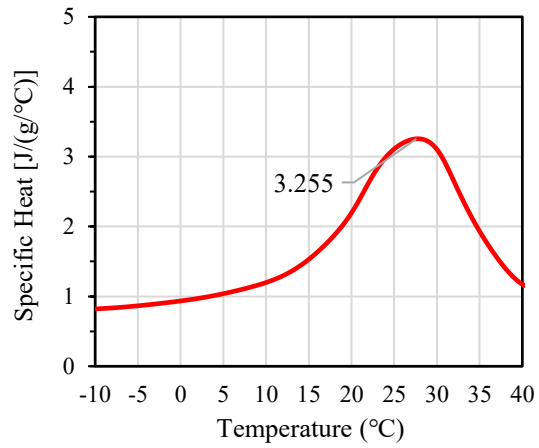
(a) No-PCM



(b) PCM28D-10%

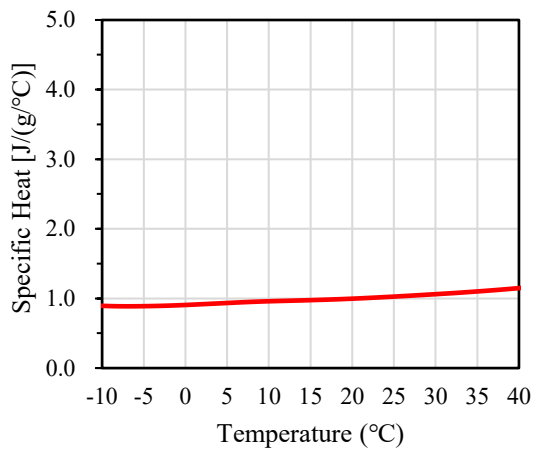


(c) PCM28D-20%

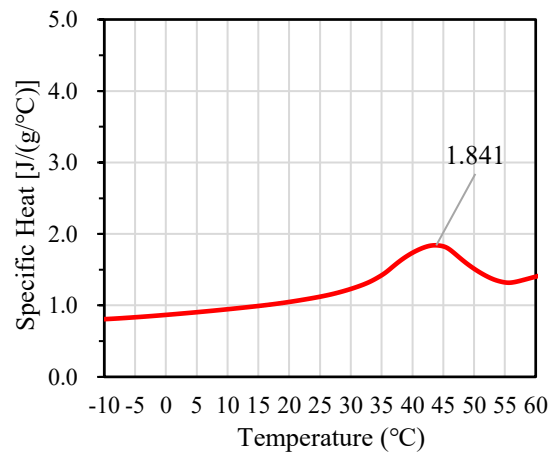


(d) PCM28D-30%

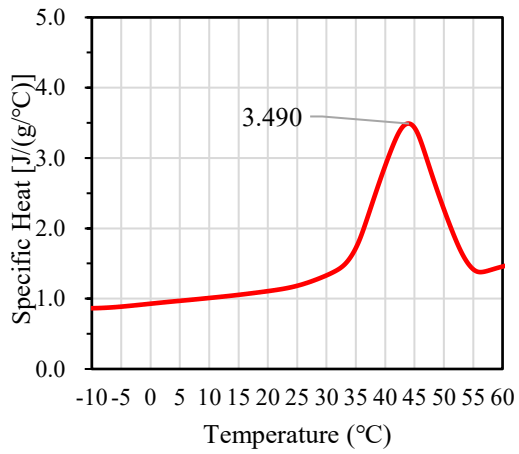
Figure 2.3.28 Result of specific heat measurements with different amount of PCMs in PCM28D.



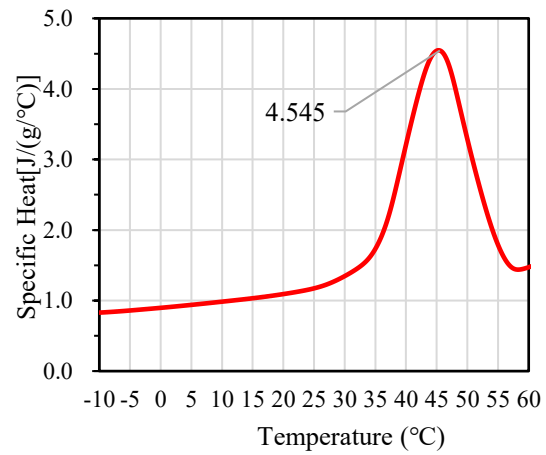
(a) No-PCM



(b) PCM43D-10%



(c) PCM43D-20%



(d) PCM43D-30%

Figure 2.3.29 Result of specific heat measurements with different amount of PCMs in PCM43D.

### 2.3.3 Thermal conductivity test

Measurement principles and used instrument the general measurement principle is based on the one-dimensional Fourier law:

$$q = -k \frac{dt}{dx}$$

[27]

where  $q$  is heat flux ( $\text{W}/\text{m}^2$ ) flowing through the sample,  $k$  its thermal conductivity ( $\text{W m}^{-1} \text{K}^{-1}$ ) and  $dt/dx$  the temperature gradient ( $\text{K m}^{-1}$ ) on the isotherm flat surface of the sample. If a flat sample is placed between two flat isothermal plates maintained at two different temperatures, and a uniform one-dimensional temperature field has been stabilized, the heat flux in the sample should be orthogonal to the sample flat faces. As a consequence, the temperature gradient can be determined by measurements of the difference between temperatures of the hot and cold plates ( $\Delta t = t_{\text{hot}} - t_{\text{cold}}$ ) and thickness of the sample  $\Delta x$ , being in this case average temperature gradient  $dt/dx$  equal to  $\Delta t / \Delta x$ . The use instrument, exploiting these principles, is the FOX-200 (Figure 2.3.30). It consists of the chamber and the base with keypad display section. All the electronics are housed in the base. Once the door of the chamber is opened, samples can be placed between two plates. The upper plate is stationary, whereas the lower one can move up and down by four independently controlled stepping motors. Four precise thickness readout digital sensors monitor the position of each corner of the lower plate. Each time a sample is inserted into the instrument and the stack is closed; the average thickness of the sample is determined within  $\pm 0.025$  mm accuracy.



Figure 2.3.30 Thermal conductivity, FOX 200.

The instrument: FOX-200 heat flow meter Heat Flow Meters (transducers) are bonded to the surfaces of both plates.

As regards the functioning of the experimental apparatus, the two parallel plates are respectively heated and cooled by two arrays of solid-state Peltier elements which, for their low mass and high-output, enable fast attainment of the temperature set-points. An advanced temperature control algorithm continuously maintains the plate temperatures and rapidly brings the system to full thermal equilibrium. Water-cooled metal heat sinks are bonded to the back sides of the Peltier elements. The waste heat is removed by a recirculating chiller system (Figure 2.3.31) which allows the Peltier elements to operate at the necessary power output. Finally, in order to prevent edge heat losses, due to the finite dimensions of the sample, the meter apparatus is equipped with a linear gradient guard, an active guard area. Before starting measurements on a sample with unknown thermal conductivity, the heat flow meter must be calibrated using a standard sample having reliable known values of thermal conductivity  $k$  (t).

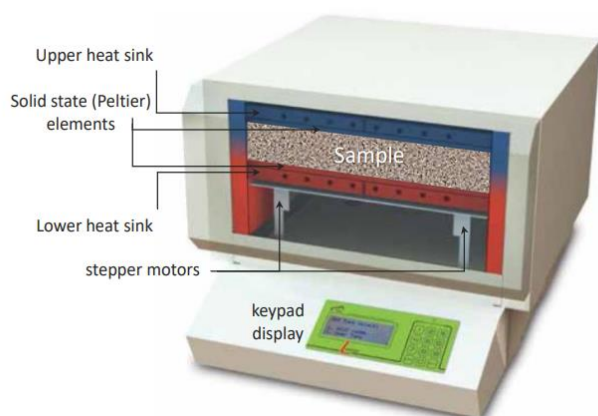


Figure 2.3.31 Structure of the FOX-200.

### **2.3.4 Preparation of the specimens**

Samples was realized by means of proper steal mold used to structure each item with the form and dimension complying with the requirement of the measurement chamber of the instrument. More precisely the specimen's dimensions are: 20cm x 20cm x 2cm, which was measured by the instrument every measurement run.

### **2.3.5 Results of thermal conductivity test**

The effect of replacement of PCM into foam concrete specimens in thermal conductivity was measured on day 28. From PCM6D-10% to PCM43D-30%, each designated mix used to measure the thermal conductivities were plotted from Figure 2.3.32 to 2.3.35. The thermal conductivity of PCM foam concrete decreases with the increasing amount of PCM substitution. Compared to reference, the reduction percentages of thermal conductivity for the composite PCM6D substitution levels of 10%, 20% and 30% were found at 44.9%, 51.39% and 53.59% respectively. Moving to Figure 2.4.4, PCM18D substitution levels were found at 41.14%, 42.65 and 51.56% respectively and then PCM28D substitution levels were found at 20.9%, 45.39% and 54.8% respectively. Next, PCM43D substitution levels were found at 24.9%, 19.13% and 27% respectively. The reduced trend of thermal conductivity with the increasing substitution level of PCM composite attributes to the low thermal conductivity from PCM6D to PCM43D composite (in the range of 0.2-0.4 W/m.K). Therefore, the thermal conductivity of PCM composites should be improved to maximize the latent heat storage efficiency of PCM.

In previous studies, it was mentioned that thermal conductivity highly depends on the density of concrete. This is in line with the suggestion of [28] who concluded that thermal conductivity increases with the higher density due to lower porosity of the sample. The density of both PCMs is lower than the No-PCM sample due to the increase in the PCM replacement, which could have resulted in the low thermal conductivity of PCM particles[29]. Another possible reason could be that the independent cell foam prevents the pores from releasing heat, resulting in lower conductivity values[1], [11], [30].

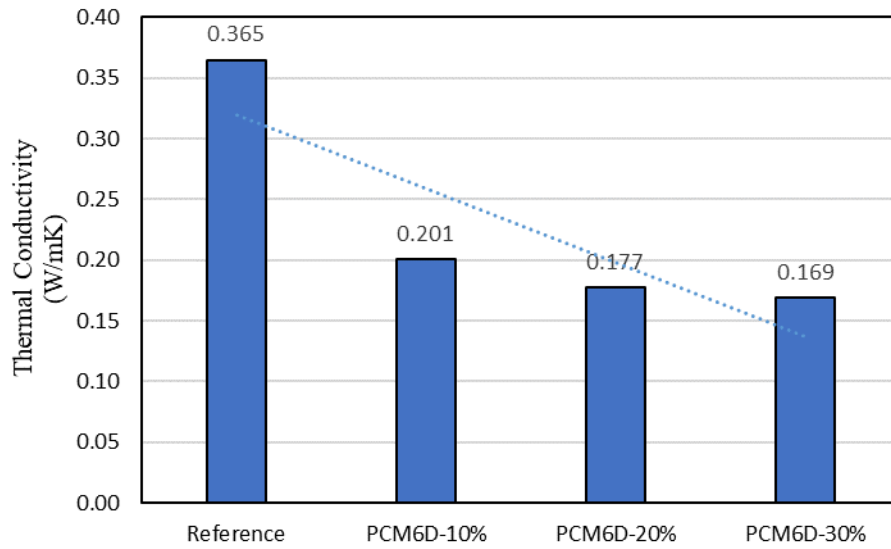


Figure 2.3.32 Thermal conductivity of PCM foam concrete as a function of PCM6D.

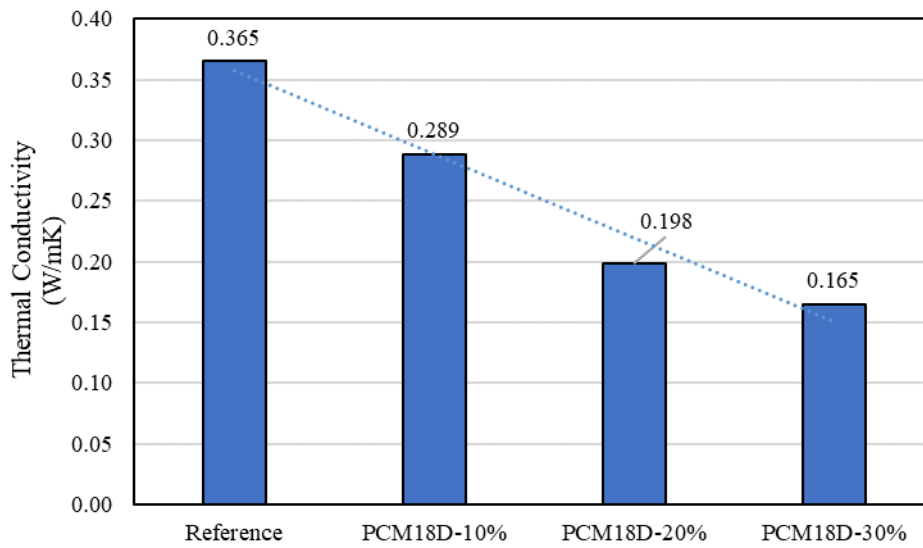


Figure 2.3.33 Thermal conductivity of PCM foam concrete as a function of PCM18D.

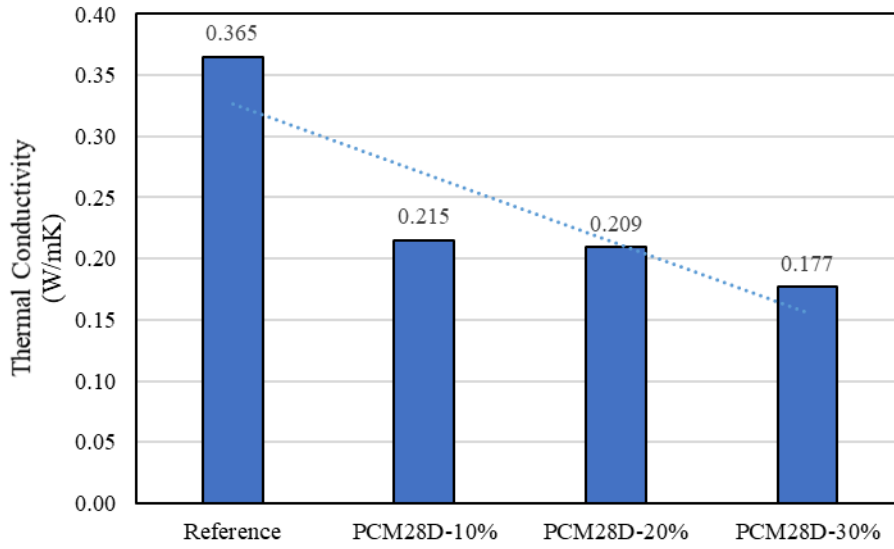


Figure 2.3.34 Conductivity of PCM foam concrete as a function of PCM28D.

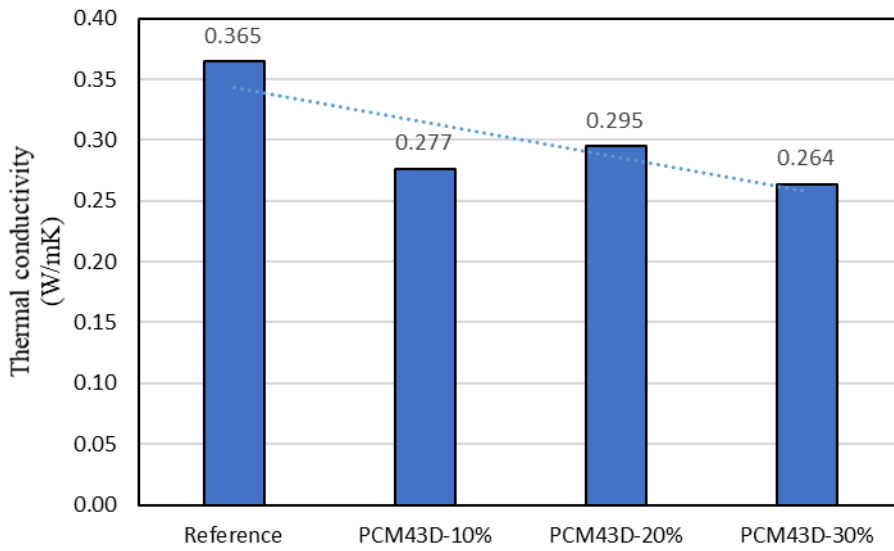


Figure 2.3.35 Conductivity of PCM foam concrete as a function of PCM43D.

## 2.4 HEAT CYCLES ON PRISMS AND SANDWICH PANELS

### 2.4.1 Experimental program

The thermal cycle test was carried out by placing the sample in a chamber with a programmable humidity and temperature (model ETAC dc-450). In this research, 4 types of PCM foam concrete were studied. The experimental program of heat cycling test shown in Figure 8, in each thermal 21-h cycle, the chamber temperature maintained at 10°C for 4-h (at rate of 2.5°C/min) and chamber temperature heated from 10°C to 50°C in 20 min (at a rate of 2.5°C/min) and maintained at 50°C for 8-h. then it cooled to 10°C in 20 min (at a rate of 2.5°C/min) and maintained at 10°C for 8-h.

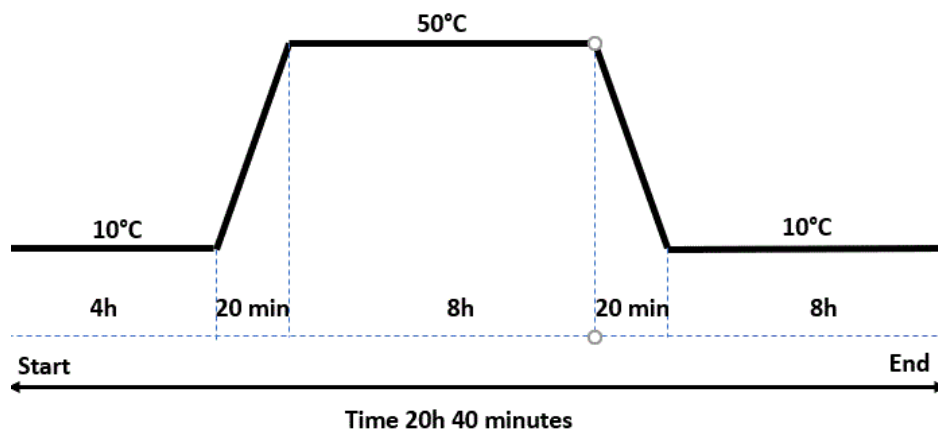


Figure 2.4.1 Schematization of used test setup for heating/ cooling cycles on prism.



## 2.4.2 Preparation of specimens for heat cyclic test

The second prototype was from inside to outside: a 20mm thick layer of PCM foam concrete specimens, and a 50mm thick of extruded polystyrene foam for 300x300x150mm. The schematic diagram of the physical models and cross-section of the model are shown in Figure 5-6. In this prototype, three thermocouples are used (Figure 2.4.2). One was put in the backside of the specimen, the other at the surface of the specimen. and then another one in the middle of the specimen was installed. The thermocouple in the middle of the specimen is used to compare with different sides of the thermocouple.

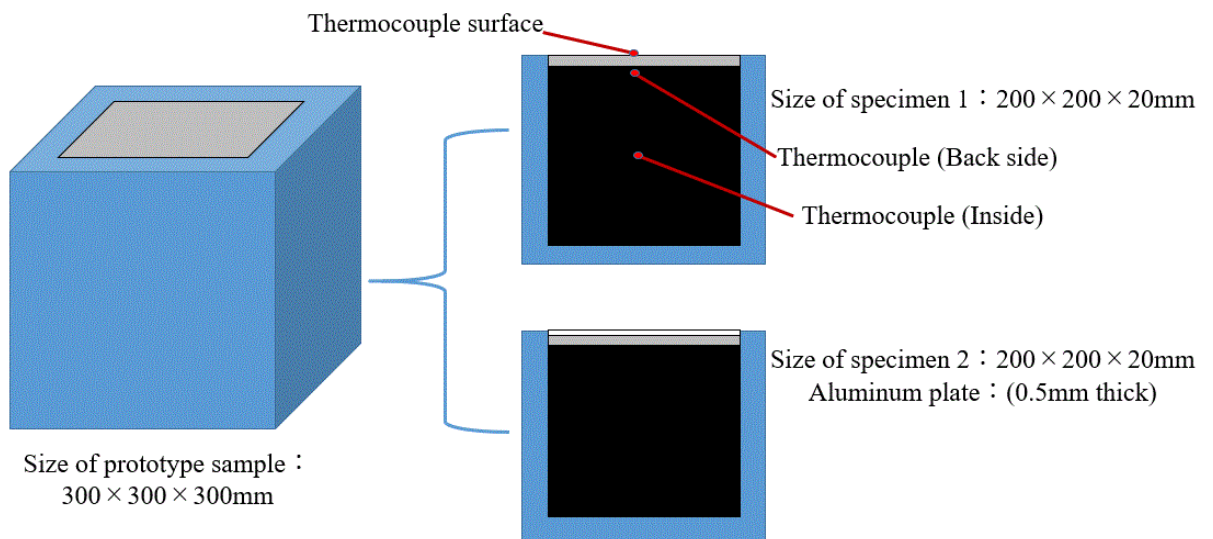


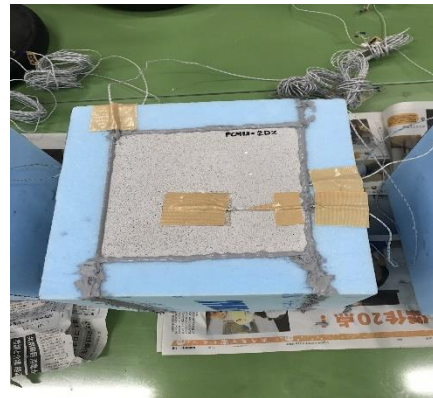
Figure 2.4.2 Schematization of used test setup for heating/ cooling cycles on prototype 2.



300x300x300 size of polystyrene box



Before installing specimens



After installing specimens



Before installing specimens



After installing specimens

Figure 2.4.3 Preparation specimens for heat cycle test

Prototype 1



Environment chamber

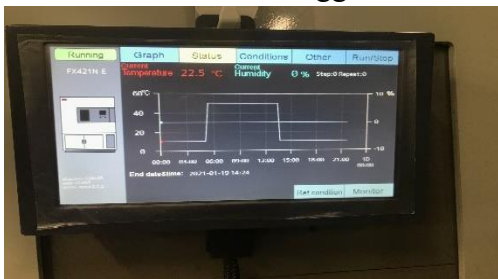
Prototype 2



Settings on environment chamber



TDS data logger



Program for heat cycle analyses



Environment chamber

Figure 2.4.4 Preparation specimens for heat cycle test

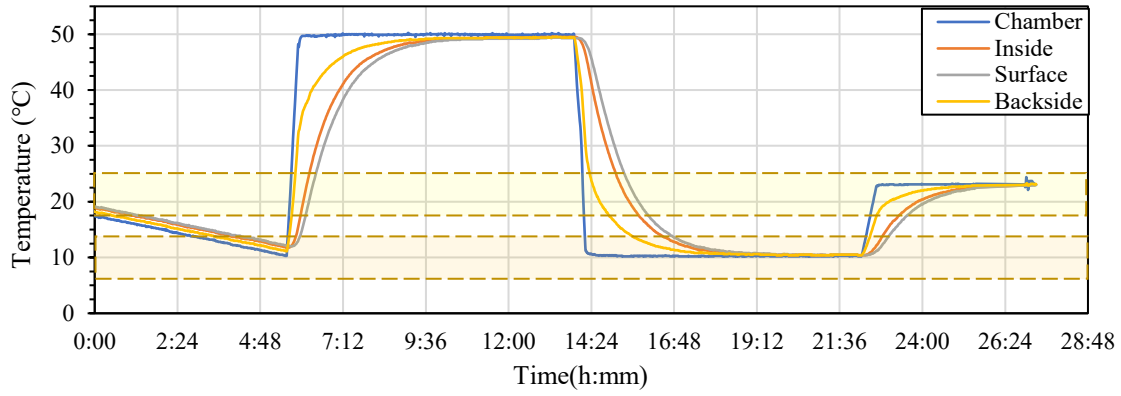


Figure 2.4.5 Experimental condition for climate cycle test of No-PCM.

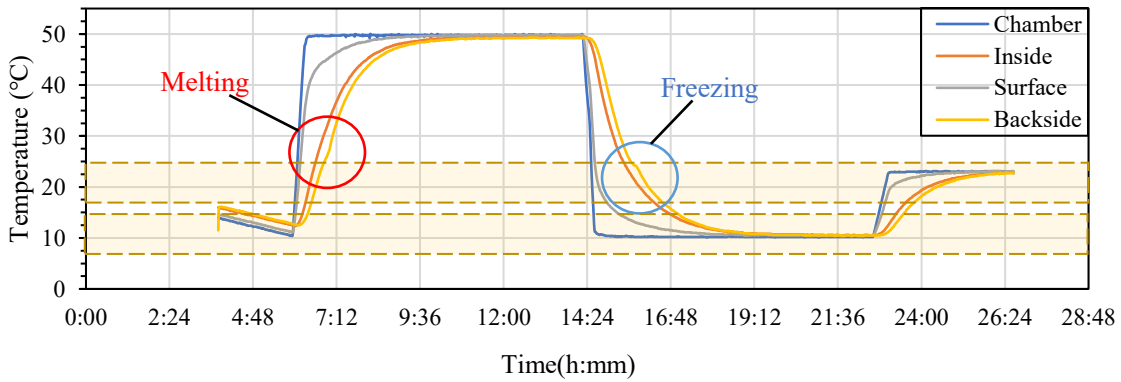


Figure 2.4.6 Experimental condition for climate cycle test of PCM6D-10%.

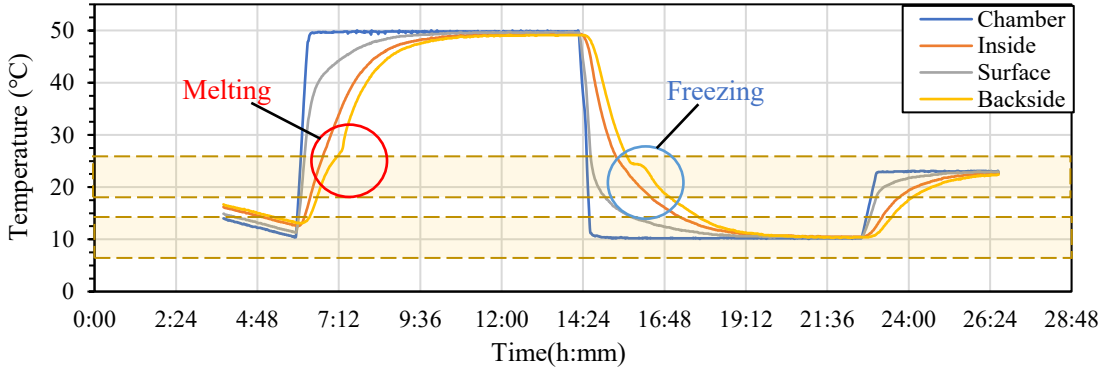


Figure 2.4.7 Experimental condition for climate cycle test of PCM6D-20%.

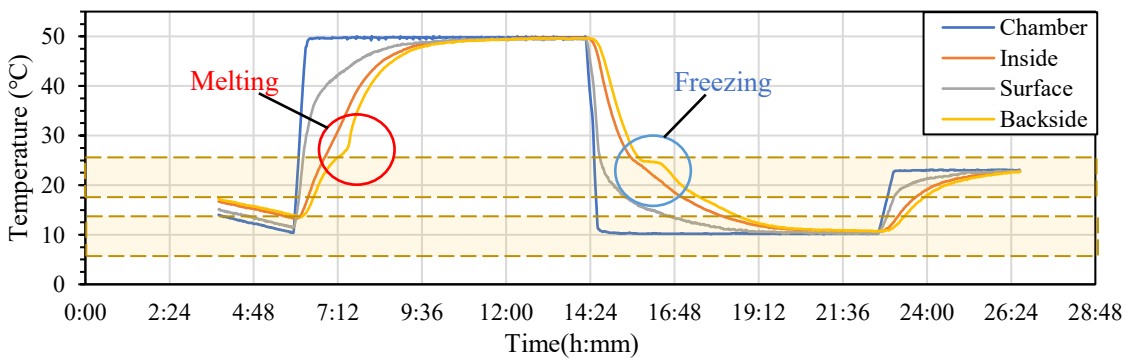


Figure 2.4.8 Experimental condition for climate cycle test of PCM6D-30%.

### **2.4.3 Test results of heating and cooling cycles on foam concrete PCM6D samples**

The melting range of PCM6D was 0-6°C. The results of heating and cooling cycles on foam concrete PCM6D samples are shown at Figure 2.4.5 to Figure 2.4.8.

PCM6D has mainly 2 melting ranges, the first one was 4-8°C and the other one 18-24°C. The temperature behavior ranges from 10°C-50°C. The cycling conditions were total 24 hour per cycle through heating and cooling for 8 hours with a heating rate of 2.5°C/min. When heat cycle test from PCM6D-10% to PCM6D-30% of foam concretes, the lowest latent heat was found at PCM6D-10%. Considering the PCM6D-10%, the temperatures increase from 4°C to 24°C, PCM foam concrete starts melting, maintains and delays the temperature for around 1 hour. Contrarily, when the temperature decreases from 24°C to 4°C, PCM foam concrete starts freezing. The temperature is delayed for around 2 hours. The highest latent heat was found at PCM6D-30%. Considering the PCM6D-30%, the temperatures increase from 4°C to 24°C, PCM foam concrete starts melting and delays the temperature for around 2 hours. Contrarily, when the temperature decreases from 24°C to 4°C, PCM foam concrete starts freezing. The temperature is delayed for around 3 hours.

After measuring the temperature of the thermal cycle surface, inside and backside of the specimens, it can be seen the clear results of melting and freezing range of the specimens. When the amount PCM increased, latent heat storage also increased. The lowest melting and freezing range mainly were the surface of the specimens. Contrarily, the highest melting and freezing range mainly was the backside of the specimens which means PCM absorbed a certain amount of energy and released large amounts of energy.



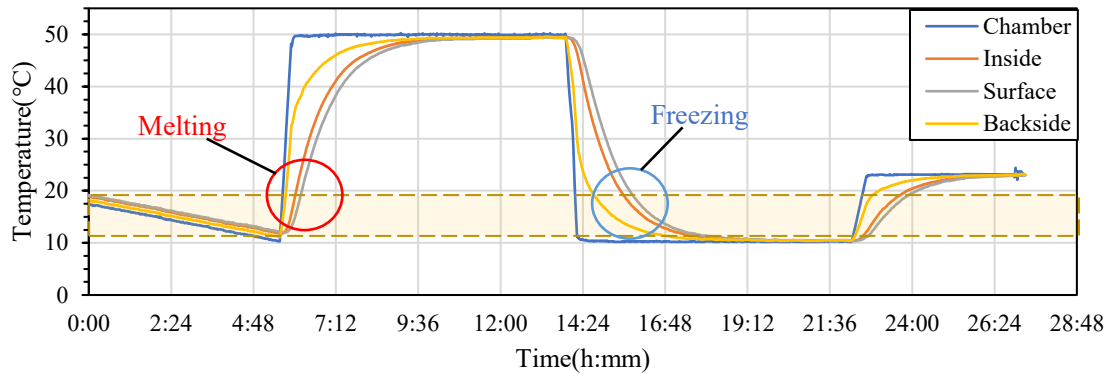


Figure 2.4.9 Experimental condition for climate cycle test of No-PCM.

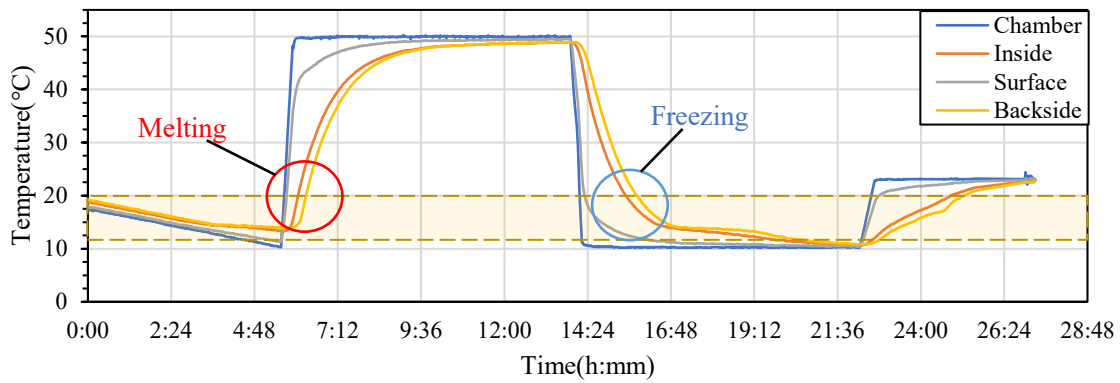


Figure 2.4.10 Experimental condition for climate cycle test of PCM18D-10%.

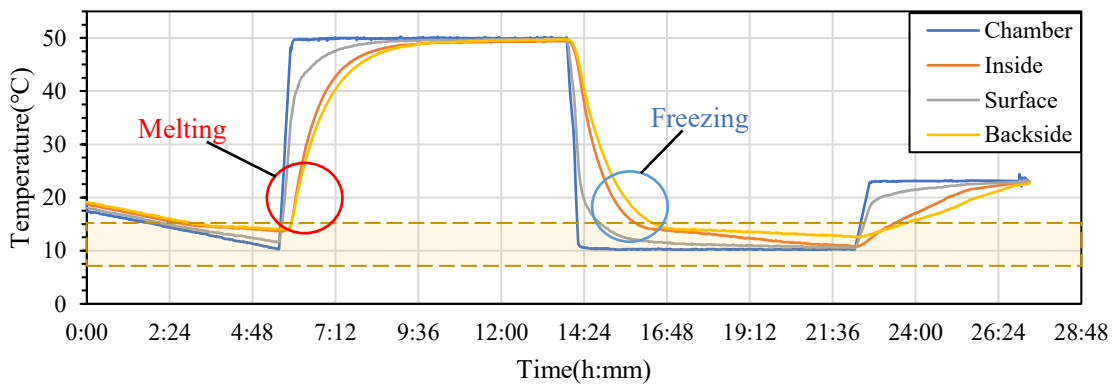


Figure 2.4.11 Experimental condition for climate cycle test of PCM18D-20%.

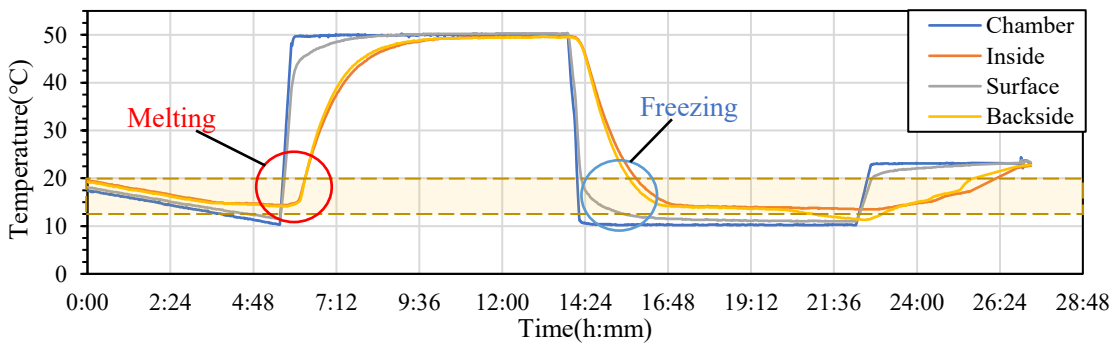


Figure 2.4.12 Experimental condition for climate cycle test of PCM18D-30%.

#### **2.4.4 Test results of heating and cooling cycles on foam concrete PCM18D samples**

The melting range of PCM18D was 16-20°C. The results of heating and cooling cycles on foam concrete PCM18D samples are shown at Figure 2.4.9 to Figure 2.4.12. The cycling conditions were total 24 hour per cycle through heating and cooling for 8 hours with a heating rate of 2.5°C/min. When heat cycle test from PCM18D-10% to PCM18D-30% of foam concretes, the lowest latent heat was found at PCM6D-10%. Considering the PCM18D-10%, the temperatures increase from 10°C to 20°C, PCM foam concrete starts melting and delays the temperature for around 3 hours. Contrarily, when the temperature decreases from 20°C to 10°C, PCM foam concrete starts freezing. The temperature is delayed for around 3 hours. The highest latent heat was found at PCM18D-30%. Considering the PCM18D-30%, the temperatures increase from 10°C to 20°C, PCM foam concrete starts melting and delays the temperature for around 3 hours. Contrarily, when the temperature decreases from 20°C to 10°C, PCM foam concrete starts freezing. The temperature is delayed for around 5 hours.

After measuring the temperature of the thermal cycle surface, inside and backside of the specimens, it can be seen the clear results of melting and freezing range of the specimens. When the amount PCM increased, latent heat storage also increased. The lowest melting and freezing range mainly were the surface of the specimens. Contrarily, the highest melting and freezing range mainly was the backside of the specimens which means PCM absorbed a certain amount of energy and released large amounts of energy.

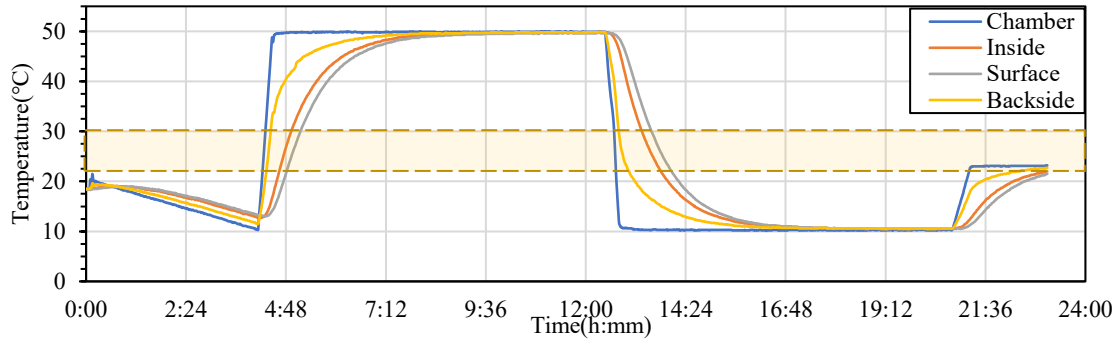


Figure 2.4.13 Experimental condition for climate cycle test of No-PCM.

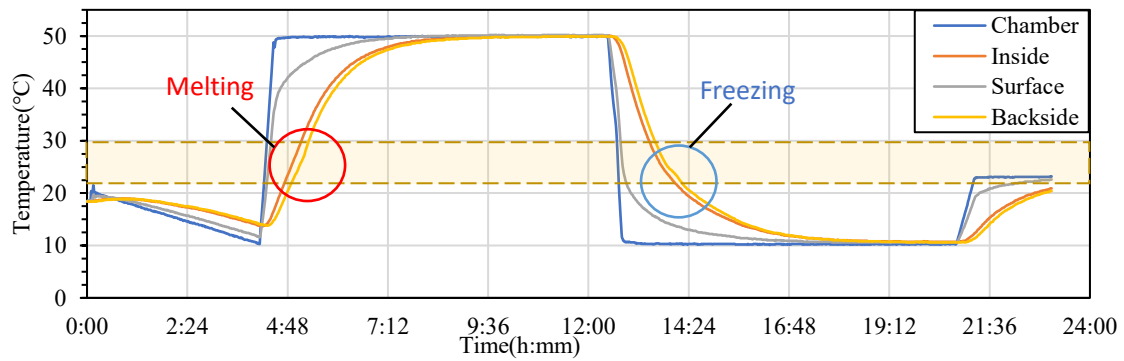


Figure 2.4.14 Experimental condition for climate cycle test of PCM28D-10%.

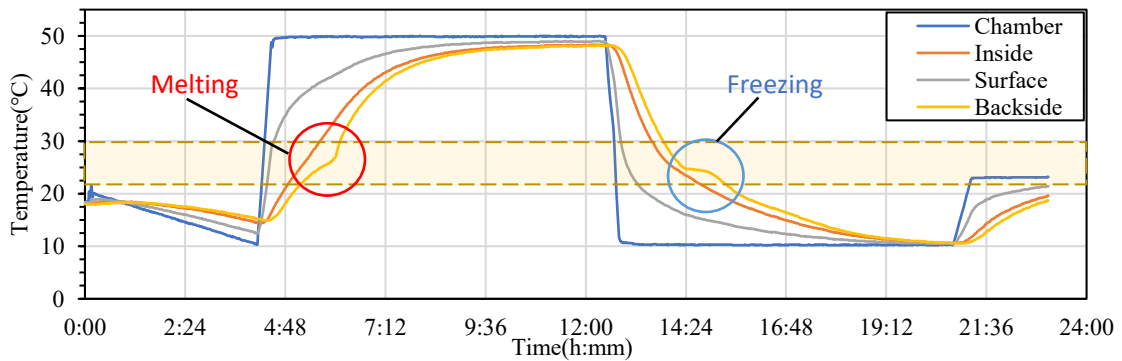


Figure 2.4.15 Experimental condition for climate cycle test of PCM28D-20%.

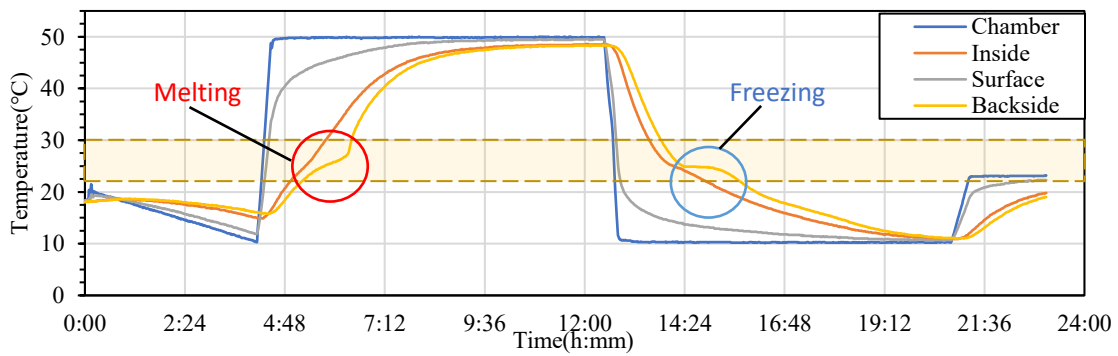


Figure 2.4.16 Experimental condition for climate cycle test of PCM28D-30%.



#### **2.4.5 Test results of heating and cooling cycles on foam concrete PCM28D samples**

The melting range of PCM28D was 26-30°C. The results of heating and cooling cycles on foam concrete PCM28D samples are shown at Fig.2.4.13 to Fig.2.4.16. The cycling conditions were total 24 hour per cycle through heating and cooling for 8 hours with a heating rate of 2.5°C/min. When heat cycle test from PCM28D-10% to PCM28D-30% of foam concretes, the lowest latent heat was found at PCM28D-10%. Considering the PCM28D-10%, the temperatures increase from 10°C to 20°C, PCM foam concrete starts melting and delays the temperature for around 2 hours. Contrarily, when the temperature decreases from 20°C to 10°C, PCM foam concrete starts freezing. The temperature is delayed for around 2 hours. The highest latent heat was found at PCM28D-30%. Considering the PCM28D-30%, the temperatures increase from 10°C to 20°C, PCM foam concrete starts melting and delays the temperature for around 6 hours. Contrarily, when the temperature decreases from 20°C to 10°C, PCM foam concrete starts freezing. The temperature is delayed for around 6 hours.

After measuring the temperature of the thermal cycle surface, inside and backside of the specimens, it can be seen the clear results of melting and freezing range of the specimens. When the amount PCM increased, latent heat storage also increased. The lowest melting and freezing range mainly were the surface of the specimens. Contrarily, the highest melting and freezing range mainly was the backside of the specimens which means PCM absorbed a certain amount of energy and released large amounts of energy.

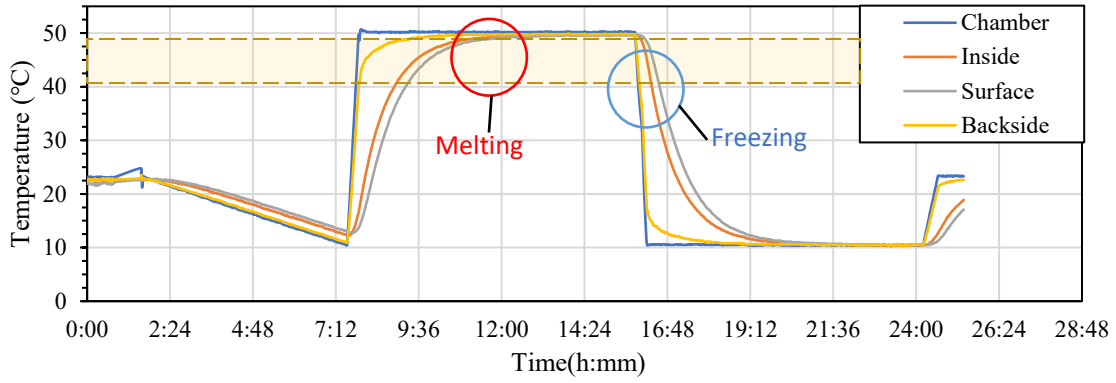


Figure 2.4.17 Experimental condition for climate cycle test of No-PCM.

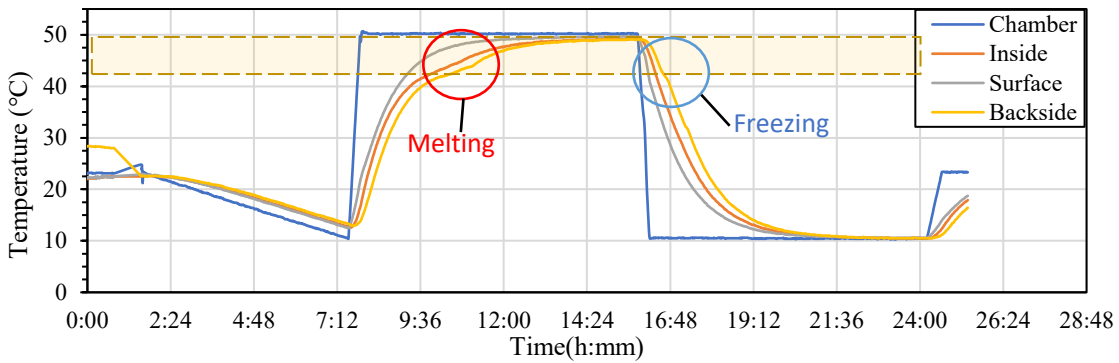


Figure 2.4.18 Experimental condition for climate cycle test of PCM43D-10%.

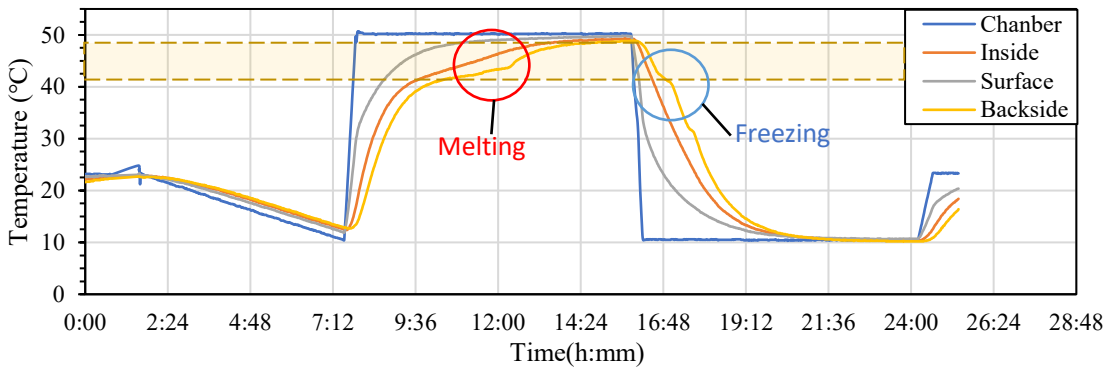


Figure 2.4.19 Experimental condition for climate cycle test of PCM43D-20%.

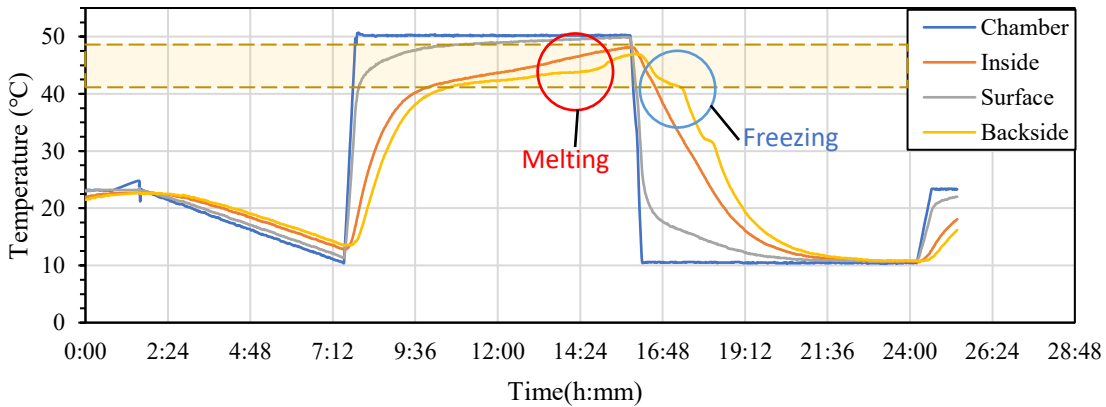


Figure 2.4.20 Experimental condition for climate cycle test of PCM43D-30%.

#### **2.4.6 Test results of heating and cooling cycles on foam concrete PCM43D samples**

The melting range of PCM43D was 26-30°C. The results of heating and cooling cycles on foam concrete PCM43D samples are shown at Figure 2.4.17 to Figure 2.4.20. The cycling conditions were total 24 hour per cycle through heating and cooling for 3 hours with a heating rate of 2.5°C/min. When heat cycle test from PCM43D-10% to PCM43D-30% of foam concretes, the lowest latent heat was found at PCM43D-10%. Considering the PCM43D-10%, the temperatures increase from 40°C to 50°C, PCM foam concrete starts melting and delays the temperature for around 8 hours. Contrarily, when the temperature decreases from 50°C to 40°C, PCM foam concrete starts freezing. The temperature is delayed for around 2 hours. The highest latent heat was found at PCM43D-30%. Considering the PCM43D-30%, the temperatures increase from 10°C to 20°C, PCM foam concrete starts melting and delays the temperature for around 8 hours. Contrarily, when the temperature decreases from 20°C to 10°C, PCM foam concrete starts freezing. The temperature is delayed for around 3 hours.

After measuring the temperature of the thermal cycle surface, inside and backside of the specimens, it can be seen the clear results of melting and freezing range of the specimens. When the amount PCM increased, latent heat storage also increased. The lowest melting and freezing range mainly were the surface of the specimens. Contrarily, the highest melting and freezing range mainly was the backside of the specimens which means PCM absorbed a certain amount of energy and released large amounts of energy.

### 2.4.7 Microstructure analysis

The observation of the microstructure of the PCM foam concrete mix by SEM produced the images of the PCM foam concrete samples. These contain (A) No-PCM, (B) PCM-10% and (C) PCM-30%, which are shown in Figure 2.4.21. The same effects can be seen for both PCM6D that from the observation both fly ash particles and PCM capsules are dispersed in the foam concrete matrix. It is said that the cementitious matrix that is composed predominantly of calcium-silica hydrate (C-S-H) and portlandite (CH) host the inert inclusion of quartz [22]. Ref. [31] said that these two phases are the main products of cement hydration. During the mixing process, the microcapsule PCMs kept their spherical shapes without any cracks or damage.

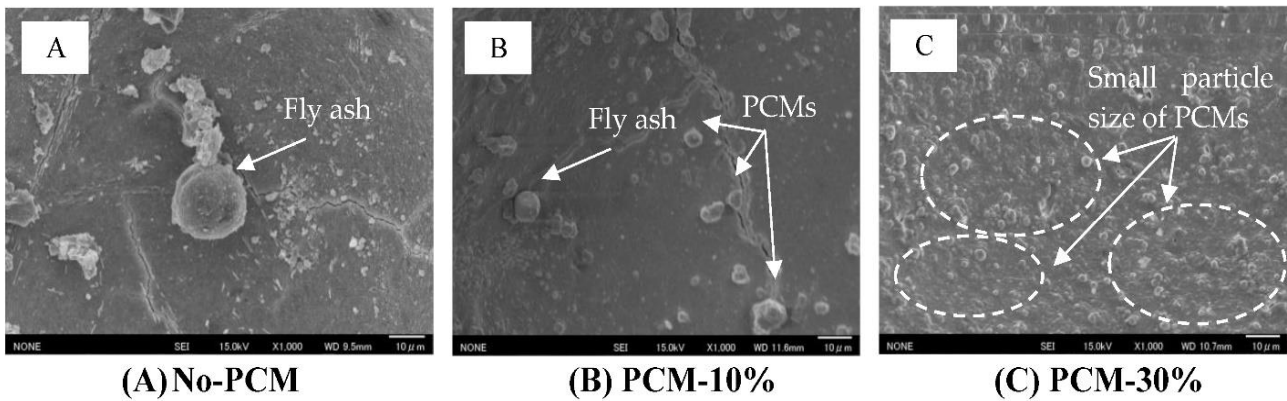


Figure 2.4.21 SEM image of PCM foam concrete after 28 days of curing ( $\times 1000$ ): (A) No-PCM, magnification  $\times 1000$  (B) PCM6D-10% magnification  $\times 1000$  (C) PCM6D-30%, magnification  $\times 1000$ .

## 2.5 CONCLUSIONS

This chapter is divided into 5 sections. The initial section deals with the design mix of foam concrete and the effect of different amount of PCMs and the effect of admixture towards to consistency, stability and strength of the mix compositions related to the objective of this study. the design mix of foam concrete and examines how different amounts of PCMs and admixtures affect the consistency, stability, and strength of the concrete mixes. It was observed that adding PCMs to replace 10% to 30% of cement led to a significant reduction in the compressive strength of the concrete. Additionally, as the amount of PCM increased, the density of the concrete decreased. The use of a special OM mixer was crucial in maintaining the integrity of the microcapsule PCMs during the mixing process. This prevented the formation of typical cracks in the PCMs within the concrete, preserving their energy storage potential.

The second section deals latent heat ( $\Delta h$ ) and specific heat capacity of PCM foam concrete. The influence of different heating/cooling rates on the thermal behavior of the PCM foam concrete has been analyzed, namely with regard to the peak temperatures on the DSC, as well as on the specific enthalpy calculated. Moreover, the impact of the heating/cooling rate on thermal behavior of the foam concrete thermal response with PCM was analyzed. When the amount PCM increased, the specific enthalpy also increased. The heat enthalpy was found in samples from PCM6D to PCM43D with the rate of 10°C/min and the melting and freezing latent heat ( $\Delta h$ ) stored in unit weight were found between 3.19 J/g and 44.01 J/g. The highest specific heat ( $C_p$ ) was found in PCM43D, with the rate of 10°C/min and specific heat ( $C_p$ ) unit weight was found between 4.54 J/g°C.

The third section deals with the thermal conductivity test. The reducing trend of thermal conductivity with the increasing substitution level of PCM composite attributes to the low thermal conductivity from PCM6D to PCM43D composites (in the range of 0.2-0.4 W/m.K).

The fourth section is about the heat cycle test. All PCMs tended to have a delayed temperature and time between 1 hour and 8 hours. The highest maintained temperature was found at PCM43D. The temperature was delayed for around 8 hours.

The fifth section is about SEM analysis, the microencapsulate PCM kept their spherical shapes without virtually any cracks or damage. The OM mixer was shown to be highly effective for mixing PCMs in the foam concrete, which is one of the fundamental findings of this research.

To conclude, PCM foam concrete has some useful characteristics such as better thermal performance and latent heat storage. The results revealed that PCMs can reduce indoor temperature fluctuations as they exhibit the potential for enhancing energy savings and thermal comfort of buildings.

## 2.6 REFERENCES

- [1] G. Hekimoğlu *et al.*, “Thermal management performance and mechanical properties of a novel cementitious composite containing fly ash/lauric acid-myristic acid as form-stable phase change material,” *Constr Build Mater*, vol. 274, p. 122105, Mar. 2021, doi: 10.1016/J.CONBUILDMAT.2020.122105.
- [2] V. V. Tyagi, S. C. Kaushik, S. K. Tyagi, and T. Akiyama, “Development of phase change materials based microencapsulated technology for buildings: A review,” *Renewable and Sustainable Energy Reviews*, vol. 15, no. 2, pp. 1373–1391, Feb. 2011, doi: 10.1016/J.RSER.2010.10.006.
- [3] L. Zhao, H. Wang, J. Luo, Y. Liu, G. Song, and G. Tang, “Fabrication and properties of microencapsulated n-octadecane with TiO<sub>2</sub> shell as thermal energy storage materials,” *Solar Energy*, vol. 127, pp. 28–35, Apr. 2016, doi: 10.1016/J.SOLENER.2016.01.018.
- [4] J. Giro-Paloma, M. Martínez, L. F. Cabeza, and A. I. Fernández, “Types, methods, techniques, and applications for microencapsulated phase change materials (MPCM): A review,” *Renewable and Sustainable Energy Reviews*, vol. 53, pp. 1059–1075, Jan. 2016, doi: 10.1016/J.RSER.2015.09.040.
- [5] F. Liu, J. Wang, and X. Qian, “Integrating phase change materials into concrete through microencapsulation using cenospheres,” *Cem Concr Compos*, vol. 80, pp. 317–325, Jul. 2017, doi: 10.1016/j.cemconcomp.2017.04.001.
- [6] M. Hunger, A. G. Entrop, I. Mandilaras, H. J. H. Brouwers, and M. Founti, “The behavior of self-compacting concrete containing micro-encapsulated Phase Change Materials,” *Cem Concr Compos*, vol. 31, no. 10, pp. 731–743, Nov. 2009, doi: 10.1016/j.cemconcomp.2009.08.002.
- [7] M. R. Ahmad, B. Chen, and S. Farasat Ali Shah, “Investigate the influence of expanded clay aggregate and silica fume on the properties of lightweight concrete,” *Constr Build Mater*, vol. 220, pp. 253–266, Sep. 2019, doi: 10.1016/J.CONBUILDMAT.2019.05.171.
- [8] O. Gencil *et al.*, “Foam Concrete Produced with Recycled Concrete Powder and Phase Change Materials,” *Sustainability (Switzerland)*, vol. 14, no. 12, Jun. 2022, doi: 10.3390/su14127458.
- [9] O. Gencil *et al.*, “Lightweight foam concrete containing expanded perlite and glass sand: Physico-mechanical, durability, and insulation properties,” *Constr Build Mater*, vol. 320, p. 126187, Feb. 2022, doi: 10.1016/J.CONBUILDMAT.2021.126187.

- [10] Q. S. Khan, M. N. Sheikh, T. J. McCarthy, M. Robati, and M. Allen, “Experimental investigation on foam concrete without and with recycled glass powder: A sustainable solution for future construction,” *Constr Build Mater*, vol. 201, pp. 369–379, Mar. 2019, doi: 10.1016/J.CONBUILDMAT.2018.12.178.
- [11] O. Gencil *et al.*, “Basalt fiber-reinforced foam concrete containing silica fume: An experimental study,” *Constr Build Mater*, vol. 326, p. 126861, Apr. 2022, doi: 10.1016/J.CONBUILDMAT.2022.126861.
- [12] P. E. Bat-Erdene and S. Pareek, “Experimental Study on the Development of Fly Ash Foam Concrete Containing Phase Change Materials (PCMs),” *Materials*, vol. 15, no. 23, Dec. 2022, doi: 10.3390/ma15238428.
- [13] “dokumen.tips\_jis-a-6201-1991”.
- [14] K. C. Brady, G. R. A. Watts, and M. R. Jones, “[BULLET HIGHWAYS AGENCY C~ Specification for foamed concrete Application Guide AG39”.
- [15] “Microtek.” Accessed: Sep. 18, 2023. [Online]. Available: <https://www.microteklabs.com/>
- [16] M. H. Thakrele, “EXPERIMENTAL STUDY ON FOAM CONCRETE,” 2014.
- [17] <https://chiyoda-machinery.co.jp/cate1/product2/>, “Oscillating OM Mixer | Chiyoda Machinery Corporation.”
- [18] Z. Andrásy and Z. Szánthó, “Thermal behaviour of materials in interrupted phase change,” *J Therm Anal Calorim*, vol. 138, no. 6, pp. 3915–3924, Dec. 2019, doi: 10.1007/s10973-019-08541-w.
- [19] B. He, V. Martin, and F. Setterwall, “Phase transition temperature ranges and storage density of paraffin wax phase change materials,” *Energy*, vol. 29, no. 11, pp. 1785–1804, 2004, doi: 10.1016/j.energy.2004.03.002.
- [20] H. Fatahi, J. Claverie, and S. Poncet, “Thermal Characterization of Phase Change Materials by Differential Scanning Calorimetry: A Review,” *Applied Sciences (Switzerland)*, vol. 12, no. 23, 2022, doi: 10.3390/app122312019.
- [21] A. Eddhahak, S. Drissi, J. Colin, S. Caré, and J. Neji, “Effect of phase change materials on the hydration reaction and kinetic of PCM-mortars,” *J Therm Anal Calorim*, vol. 117, no. 2, pp. 537–545, 2014, doi: 10.1007/s10973-014-3844-x.
- [22] M. Kheradmand, M. Azenha, J. L. B. De Aguiar, and K. J. Krakowiak, “Thermal behavior of cement based plastering mortar containing hybrid microencapsulated phase change materials,” *Energy Build*, vol. 84, pp. 526–536, 2014, doi: 10.1016/j.enbuild.2014.08.010.
- [23] X. Chen *et al.*, “Morphology prediction of portlandite: Atomistic simulations and experimental

- research,” *Appl Surf Sci*, vol. 502, Feb. 2020, doi: 10.1016/j.apsusc.2019.144296.
- [24] G. Xian, Z. Liu, Z. Wang, and X. Zhou, “Study on the Performance and Mechanisms of High-Performance Foamed Concrete,” *Materials*, vol. 15, no. 22, p. 7894, Nov. 2022, doi: 10.3390/ma15227894.
- [25] M. Kheradmand, “Incorporation of hybrid phase change materials in plastering mortars for increased energy efficiency in buildings Changing the rules of construction phasing of massive concrete structures: a new paradigm based on phase change materials (PCMs) View project Composites with hybrid phase change materials applied to the walls in buildings: Numerical approaches using ANSYS-FLUENT View project,” 2016, doi: 10.13140/RG.2.2.34299.11043.
- [26] A. Eddhahak-Ouni, J. Colin, S. Drissi, and J. Neji, “Analysis by Differential Scanning Calorimetry of concrete modified with microencapsulated phase change materials”.
- [27] R. Rajagopal, “Fourier’s Law of Heat Conduction,” 2007.
- [28] X. Huang, C. Zhu, Y. Lin, and G. Fang, “Thermal properties and applications of microencapsulated PCM for thermal energy storage: A review,” *Applied Thermal Engineering*, vol. 147. Elsevier Ltd, pp. 841–855, Jan. 25, 2019. doi: 10.1016/j.applthermaleng.2018.11.007.
- [29] P. Meshgin and Y. Xi, “Multi-scale composite models for the effective thermal conductivity of PCM-concrete,” *Constr Build Mater*, vol. 48, pp. 371–378, 2013, doi: 10.1016/J.CONBUILDMAT.2013.06.068.
- [30] L. Qiao *et al.*, “Design of monolithic closed-cell polymer foams via controlled gas-foaming for high-performance solar-driven interfacial evaporation,” *J Mater Chem A Mater*, vol. 9, no. 15, pp. 9692–9705, Apr. 2021, doi: 10.1039/d1ta01032h.
- [31] H. F. W. Taylor, “Calcined Clay Pozzolan as an Admixture to Mitigate the Alkali-Silica Reaction in Concrete,” *Cement Chemistry. 2nd Edition*, 1997.



**CHAPTER 3**  
**ENHANCING ENERGY STORAGE CAPACITY**  
**IN CONCRETE WITH PCMs**

### 3.1 EXPERIMENTAL OVERVIEW

Before this chapter, we confirmed that PCM foam concrete has capacity to reduce energy consumption. This chapter is dedicated to enhancing the energy storage capacity (TES) of concrete and comprises five key sections. The initial section examines the mechanical aspects, including the compressive strength of various concrete types blended with PCMs. The second section focuses on estimating specific enthalpy and specific heat capacity for blended PCM concretes. The third section covers heat cyclic analysis with specific enthalpy estimation and phase change temperature for all types of blended PCM concrete, crucial parameters for thermal characterization. The final section presents the chapter's conclusion.

#### 3.1.1 Introduction

To enhance the energy storage capacity (TES) of concrete, several important factors should be considered. First, it is crucial to enhance concrete ability to transfer heat effectively [1], [2]. This can be achieved by increasing thermal conductivity concrete. This is important because PCM foam concrete tends to have low thermal conductivity, which slows down heat transfer rates during phase change processes. For instance, the thermal conductivity of cement-based materials can be improved through careful optimization of mixture design. Liu, et al. [3] found that when the water-cement ratio decreased from 0.6 to 0.5, the thermal conductivity increased from 1.56 W/(m·K) to 1.81 W/(m·K). Additionally, it's worth noting that the thermal conductivity of heat transfer cement materials can be effectively modified by changing their composition [4]. Furthermore, the introduction of high-thermal-conductivity additives, such as steel fibers [5], carbon nanotube [6], graphite[7] and metal powder [8] has proven to be a successful strategy for enhancing the thermal performance of cement-based materials. For example, Liu, Kai, et al. [9] concluded that sand–iron ore sand ratio ranks the best effect on thermal conductivity.

Secondly, optimizing the amount of PCMs is vital. Furthermore, employing multiple PCMs with closely matched melting and freezing temperatures has shown significantly improve the energy storage capacity[10], [11]. For instance, Siyabi et al. [12]demonstrated better heat transfer rates in a shell-and-tube heat exchanger with multiple PCMs. Mozafari et al. [13] achieved significant improvements in thermal energy storage and recovery by using dual PCMs in a triplex tube heat exchanger. However, there is currently no reported study using the multiple PCM in concrete structure.

In our experimental work, we adopted a combination of two distinct approaches within our experimental framework. The first approach centers on improving the thermal conductivity of PCM concrete, with the expectation that this will lead to an increase in heat transfer rates during phase change processes. To accomplish this, we created different types of concrete and compared their thermal conductivity and heat storage capabilities, including foam concrete, regular concrete, and ultra-heavy concrete.

The second approach involves integrating a blend of Phase Change Materials (PCMs) into the concrete structure, with the goal of extending the duration of energy storage. This approach encompasses a variety of concrete compositions that incorporate PCMs with different melting and freezing temperatures. These compositions included scenarios with No PCM, PCM6D18D, PCM18D28D, PCM28D43D. Each type of concrete in this study contained blended PCMs.

This research dedicated to enhancing the energy storage capacity (TES) of concrete through the incorporation blended microencapsulated PCMs into different types of concretes, investigating extensively material properties and thermal behavior. Our experiments contribute to understanding phase change phenomena and have practical implications for enhancing indoor comfort and reducing cooling and heating energy demand.

### 3.2 MATERIAL PROPERTIES

#### 3.2.1 Microencapsulated PCM

Four types of encapsulated PCMs are studied. These included 6D, 18D, 28D and 43D. All encapsulated PCMs are micro-encapsulated free wax:  $\leq 2.5\%$  PCM and solid content: 97.0-100.0. Additionally, these four types of encapsulated PCMs were mixed with each other to create three different combinations: PCM6D18D, PCM18D28D, and PCM28D43D. The sizes of these PCM particles were provided by the manufacturers [14] and were also determined through microscopic analysis using optical microscopy. Their sizes were provided by the manufacturers and were determined as well by using optical microscopy (Table 3-1).

Table 3-1 Thermo physical properties of various microencapsulated PCMs.

Material	Nature	Size ( $\mu\text{m}$ )	Melting ( $^{\circ}\text{C}$ )	Heat of Fusion (J/g)	Solid Content %
PCM6D18D	Dry	15.0–30.0	0 to 30	189	97.0–100.0
PCM18D28D	Dry	15.0–30.0	10 to 30	235	97.0–100.0
PCM28D43D	Dry	15.0–30.0	30 to 50	189	97.0–100.0

#### 3.2.2 Fine aggregate

Silica sand as fine aggregate obtained on the market with dry silica sand No.5 was used in this study. The specific gravity and density of fine aggregate were 2.62 and 1.56. Table 3-2 and Table 3-3 show chemical composition and physical properties of silica sand.

Table 3-2 Chemical composition of silica sand (No.5).

	<b>SiO<sub>2</sub></b>	<b>Al<sub>2</sub>O<sub>3</sub></b>	<b>Fe<sub>2</sub>O<sub>3</sub></b>	<b>CaO</b>	<b>Na<sub>2</sub>O</b>	<b>K<sub>2</sub>O</b>	<b>TiO<sub>2</sub></b>	<b>LOI</b>
%	95.43	2.62	0.09	0.49	1.5	77.1	2.26	2.10

Table 3-3 Physical properties of silica sand (No.5).

<b>pH</b>	<b>Bulk specific Gravity (g/cm<sup>3</sup>)</b>	<b>True specific gravity (g/cm<sup>3</sup>)</b>	<b>Water Absorption (%)</b>	<b>Amount of Chloride (%)</b>
6.1	1.53	2.63	0.57	0.001

### 3.2.3 High density aggregate

The high-density aggregate is obtained by replacing natural silica sand, which is a fine aggregate, among the constituent materials of ordinary concrete used in this study described above, with high weight aggregate. The density of the weight aggregate used is 3.0~5.0g/cm<sup>3</sup> and refers to concrete with a specific gravity of 2.5~6.0 with grain size if 2.0 mm or less. Unlike ordinary concrete, it can be effective against radiation. In general, iron ore, barium ore, iron oxide powder, and barite with a high specific gravity are often used, and in particular, nuclear power is effective against radiation and  $\gamma$  rays. It is used as concrete for radiation shielding used on walls of power plants.

Table 3-4 Chemical composition of aggregate.

	<b>Fe</b>	<b>Si</b>	<b>Ca</b>	<b>Al</b>	<b>Mg</b>	<b>P</b>	<b>etc.</b>
%	81	7	3	0	6	0	3

Table 3-5 Physical properties of aggregate.

<b>pH</b>	<b>Bulk specific gravity (g/cm<sup>3</sup>)</b>	<b>True specific gravity (g/cm<sup>3</sup>)</b>	<b>Water Absorption (%)</b>	<b>Amount of chloride (%)</b>
64.5	23.9	4.8	5.3	1.5

### 3.2.4 Mix compositions

In total, we formulated 21 different mix compositions in this experiment to evaluate both thermal storage capacity and mechanical properties. Each type of concrete in this study contained blended PCMs. It included scenarios with No PCM, PCM6D18D, PCM18D28D, PCM28D43D. We quantified the blend of PCMs as a replacement for a portion of the cement in the chosen mix composition, and the specific data can be found from Table 3-6 to Table 3-8. All the samples underwent curing through water exposure at 20°C in a room with 95% humidity.

Regarding the foam concrete (FC) with blended PCMs, we didn't use a standard method for proportioning foamed concrete. Instead, our target density became the primary design criterion. The main ingredients included rapid-hardening cement, ordinary cement, silica fume, and superplasticizer. For the ordinary concrete (NC) with blended PCMs, we followed the standard JIS A 5308[15]. This material consisted of cement, water, and fine aggregate, specifically natural silica sand No. 5 (as shown in Table 3-2). As for the high-density concrete (ND) with blended PCMs, we achieved it by replacing the natural silica sand in the constituent materials of the ordinary concrete used in this study with high-weight aggregates. The presence of iron ore in these aggregates was expected to enhance thermal conductivity.

Table 3-6 Mix compositions of foam concrete.

<b>Mix Designation</b>	<b>Cement (kg)</b>	<b>Fly ash (kg)</b>	<b>W/C (Lit) 0.3</b>	<b>PCM (kg) 30%</b>	<b>SP (kg) 1%</b>	<b>SF (kg) 10%</b>	<b>Foam (gram)</b>
Reference	4.5	0.45	1.35	0	0.045	0.45	800
FC 6D18D	2.7	0.45	0.67	0.9	0.045	0.45	1500
FC 18D28D	2.7	0.45	0.67	0.9	0.045	0.45	1500
FC 28D43D	2.7	0.45	0.67	0.9	0.045	0.45	1500

Table 3-7 Mix compositions of ordinary concrete.

<b>Mix Designation</b>	<b>W/C</b>	<b>Cement (kg)</b>	<b>Water (Lit) 0.5</b>	<b>Sand (kg) 10%</b>	<b>PCM (kg) 30%</b>
Reference	0.5	0.83	0.41	1.9	0
NC 6D18D	0.5	0.83	0.4	1.1	0.18
NC 18D28D	0.5	0.83	0.4	1.1	0.18
NC 28D43D	0.5	0.83	0.4	1.1	0.18

Table 3-8 Mix compositions of high-density concrete.

Mix Designation	W/C	Cement (kg)	Water (Lit)	Aggregate	PCM	SP
				(kg) 10%	(kg) 30%	(kg) 1%
Reference	0.55	0.84	0.46	3.52	0	0.03
ND6D18D	0.3	0.84	0.25	2.06	0.18	0.02
ND18D28D	0.3	0.84	0.25	2.06	0.18	0.02
ND28D43D	0.3	0.84	0,25	2.06	0.18	0.02

### 3.3 MECHANICAL ANALYSES

#### 3.3.1 Density test

The density test results presented in Figure 3.3.1 showcase the effects of incorporating Phase Change Materials (PCMs) on three different types of concretes: ND (No-PCM), NC (No-PCM), and FC (No-PCM) over various curing periods, specifically on days 7, 14, and 28.

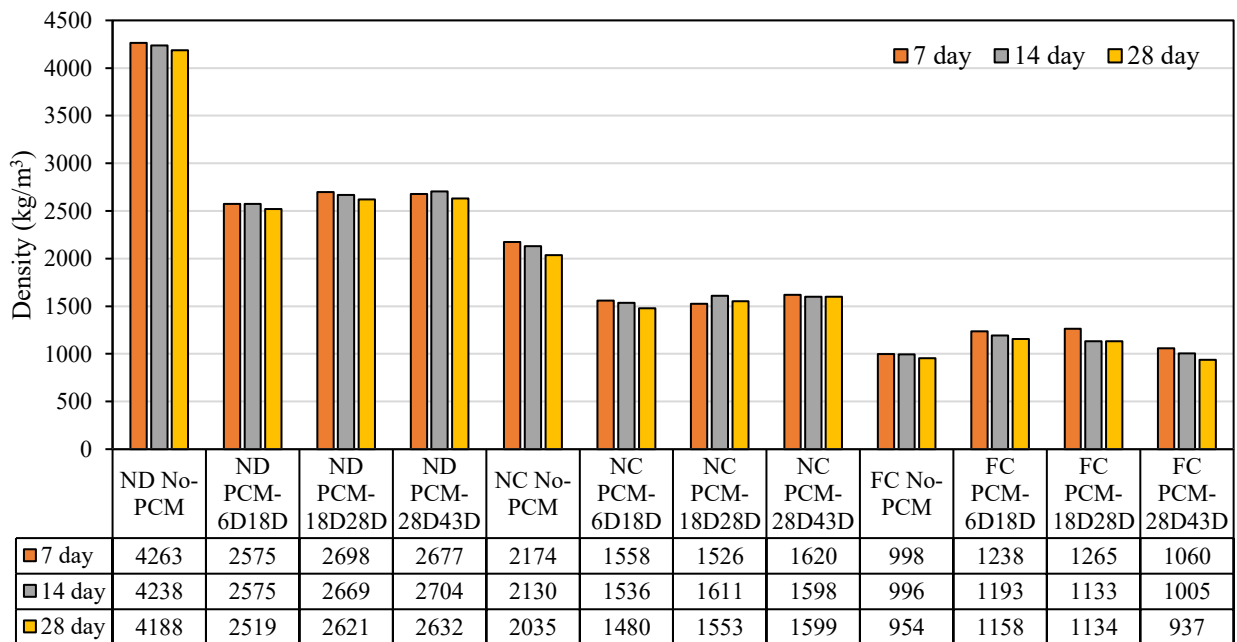


Figure 3.3.1 Results of density test results on different types of concretes with and without PCMs.

For ND concrete, both with and without PCM, the density results ranged between 2519 kg/m<sup>3</sup> and 4263 kg/m<sup>3</sup>. Notably, after adding PCMs (PCM6D18D, PCM18D28D, and PCM28D43D), the density of ND concrete experienced a significant reduction, amounting to approximately 39.5% at the 7-day mark compared to ND No-PCM. This decrease in density suggests that the incorporation of PCMs impacts the initial density of ND concrete considerably. A decrease in density was observed from 7 to 28 days and the calculated percentages variations were as follows: for ND No-PCM: 1.7%; ND PCM6D18D: 2.17%; ND PCM18D28D: 2.44% and ND PCM28D43D: 1.6%. Furthermore, ND concrete is composed of high-density aggregate, which inherently leads to a higher density compared to NC and FC.

Similar to ND concrete, NC concrete displayed a decrease in density upon the addition of PCMs (PCM6D18D, PCM18D28D, and PCM28D43D) at the 3-day, resulting in a density range between 2174 kg/m<sup>3</sup> and 1526 kg/m<sup>3</sup>. A decrease in density was observed from 3 to 28 days and the calculated percentages variations were as follows: for NC No-PCM: 6.3%; NC PCM6D18D: 5.0%; NC PCM18D28D: % and NC PCM28D43D: 1.29%. The reduction was comparable to that observed in ND concrete, demonstrating that PCMs have a similar impact on both ND and NC concrete densities.

As for FC concrete, however, showed different behavior compared to ND and NC. In the case of FC concrete with PCMs (PCM6D18D, PCM18D28D, and PCM28D43D), the density exhibited no significant reduction at the 7-day compared to FC No-PCM. This divergence from the trends observed in ND and NC concrete indicates that FC concretes are more controlled by wet density and are less affected by the addition of PCMs in terms of their initial density. A decrease in density was observed from 3 to 28 days and the calculated percentages variations were as follows: for FC No-PCM: 4.4%; FC PCM6D18D: 6.4%; FC PCM18D28D: 10.3% and FC PCM28D43D: 11.60%.

In conclusion, the study's findings suggest that the addition of PCMs has a significant impact on the density of ND and NC concretes, resulting in a substantial reduction at the 3-day which is in accordance with the result of [16], [17]. However, FC concrete, due to its unique composition, does not exhibit a similar reduction in density after PCM inclusion.

### 3.3.2 Compressive strength test

The compressive strength of each test piece was measured using the universal testing machine Hi-Actis-200L in accordance with JIS A 1108. Tests were conducted in 7d, 14d, and 28d.

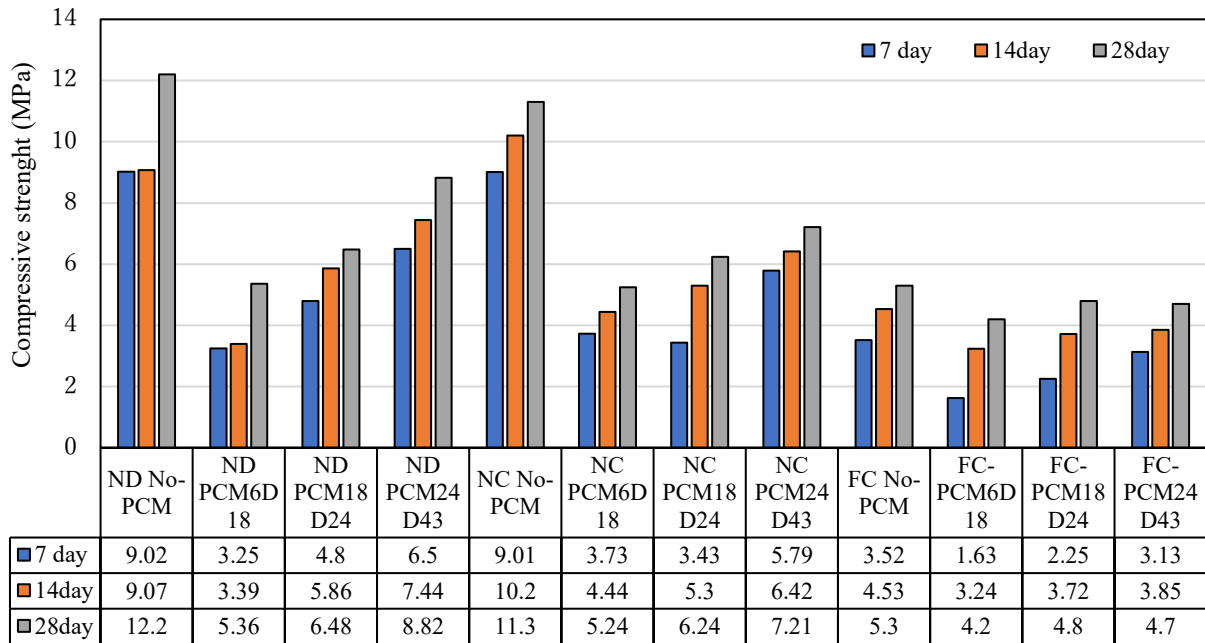


Figure 3.3.2 Compressive strength test results on different types of concretes with and without PCM.

The compressive strength test results presented in Figure 3.3.2 examine the effects of incorporating Phase Change Materials (PCMs) on three different types of concretes: ND, NC and FC over various curing periods at 7, 14, and 28 days of curing, with a temperature of 20°C and relative humidity of 90%. In these three different concretes, 30% of cement's weight in each type of concrete were substituted with PCMs.

For ND concrete, the compressive strength result of No-PCM was recorded at 9.02 MPa on day 7. In contrast, the compressive strengths of ND PCM6D18D, ND PCM18D28D and ND PCM28D43D were 3.25 MPa, 4.8 MPa and 6.5 MPa, respectively, resulting in strength decrease of 63.9%, 46.7% and 28.1%, respectively, compared to ND No-PCM. However, from day 7 to day 28, the compressive strengths of all samples increased by 26% for ND No-PCM; to 39.3% for ND PCM6D18D; to 25.9% for ND PCM18D28D; to 26.3% for ND PCM28D43D, respectively.



For NC concrete, the compressive strength result of NC No-PCM was recorded at 9.01 MPa on day 7. As opposed to this, the compressive strengths of NC PCM6D18D, NC PCM18D28D, and NC PCM28D43D were 3.7 MPa, 3.43 MPa and 5.79 MPa, with the strength decreases of 63.3%, 61.9% and 35.7%, respectively, compared to NC No-PCM. However, from day 7 to day 28, the compressive strengths of all samples increased by 20% for NC No-PCM; to 29% for NC PCM6D18D; to 45% for NC PCM18D28D; to 19% for NC PCM28D43D, respectively.

For FC concrete, the compressive strength result of FC No-PCM was recorded at 3.52 MPa on day 7. In contrast, the compressive strengths of FC PCM6D18D, FC PCM18D28D, and FC PCM28D43D were 1.63 MPa, 2.25 MPa and 3.13 MPa, with the strength decreases of 53.6%, 36% and 11%, respectively, compared to NC No-PCM. However, from day 7 to day 28, the compressive strengths of all samples increased by 64% for FC No-PCM; to 61% for FC PCM6D18D; to 46% for FC PCM18D28D; to 33% for FC PCM28D43D, respectively.

In conclusion, the incorporation of blended PCMs into concrete had a noticeable impact on compressive strength in all three types of concrete (ND, NC, and FC). As evidenced by prior research, Cui et al [18] showed that a 25% replacement of PCM led to 66.34% reduction in compressive strength compared to the control cement paste, aligning with current study's outcomes. A similar impact of adding PCM on the strength of PCM concrete was reported by [19] Although there was an initial decrease in strength when PCMs were introduced, all three types of concrete demonstrated significant improvements in compressive strength from day 7 to day 28.

### 3.4 THERMAL ANALYSIS

#### 3.4.1 Differential Scanning Calorimetry (DSC)

The calorimetry measurements were taken with a TA device with a temperature accuracy of  $\pm 0.1^\circ\text{C}$ . It measures the difference in the heat flow rate between samples and insert reference as a function of time and temperature. The melting and freezing behaviors of the PCM were analyzed by a DSC model Q25. The temperature was measured at the sample platform with a thermocouple. The sample sizes were between 5 and 10 mg and were encapsulated with Pans [20] (container of the sample material) and Lids (cap of the container). The samples were weighted by an analytical ultra-micro balance model: MC25. Then the samples were sealed in the pan by using an encapsulating press. An empty aluminum crucible was used as a reference in all measurements. To accurately measure the transition temperature, it is recommended [21], [22] that the samples are scanned with a low heating/cooling rate. Once the sample is measured with a low heating rate, conducting an experiment with a higher heating/cooling rate is suggested to measure the value of the enthalpy. The effect of the thermal cycles and heating/cooling rates on the phase change processes and specific enthalpy values was examined. In this way, different heating/cooling rates of  $10^\circ\text{C}/\text{min}$ ,  $5^\circ\text{C}/\text{min}$ ,  $2^\circ\text{C}/\text{min}$ ,  $1^\circ\text{C}/\text{min}$  and  $0.5^\circ\text{C}/\text{min}$  were considered.



Figure 3.4.1 DSC analysis machine model Q25.

### 3.4.1.1 DSC and thermal analysis results of FC-PCM

The discussion outlines the results of a Differential Scanning Calorimetry (DSC) test conducted on three different foam concrete (FC) samples, each containing a different type of blended Phase Change Material (PCM). The test involved heating and cooling scans at a rate of 10°C per minute. The results are presented in Figure 3.4.2 through Figure 3.4.4.

In the case of FC PCM6D18D, the DSC analysis revealed two melting peaks and two freezing peaks. The first melting peak was observed at 6.02°C, and the first freezing peak was found at -7.25°C. The latent heats of melting and freezing ( $\Delta h$ ) stored in unit weight were 6.02 J/g and 4.69 J/g, respectively. The second melting peak occurred at 17.9°C, with the second freezing peak at 15.7°C. The latent heats of melting and freezing for the second peak were 10.95 J/g and 7.79 J/g.

In the FC PCM18D28D sample, similar to the first, two melting peaks and two freezing peaks were observed. The first melting peak was at 17.86°C, and the first freezing peak was at 9.66°C. The corresponding latent heats of melting and freezing were 11.21 J/g and 4.06 J/g. The second melting peak was found at 26.4°C, and the second freezing peak at 21°C. The latent heats of melting and freezing for the second peak were 4.06 J/g and 4.17 J/g.

The FC PCM28D43D sample also displayed two melting peaks and two freezing peaks. The first melting peak was recorded at 26.7°C, while the first freezing peak occurred at 20.9°C. The latent heats of melting and freezing were 6.63 J/g and 5.14 J/g. The second melting peak was observed at 44.2°C, and the second freezing peak at 37.2°C. The latent heats of melting and freezing for the second peak were 9.07 J/g and 5.85 J/g.

A common observation across all three types of FC concretes containing blended PCMs was that they melted and solidified within specific temperature ranges. Notably, the first melting peak consistently exhibited a higher latent heat capacity than the second melting peak, even though the same amount of the two types of PCM was incorporated into the concrete for each case.

This observation suggests that the behavior of the blended PCMs in the FC samples is dependent on the specific type of PCM used and the corresponding temperature ranges at which phase transitions occur.

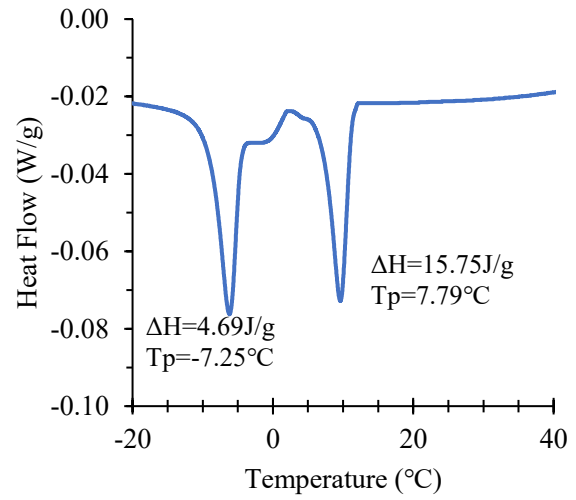
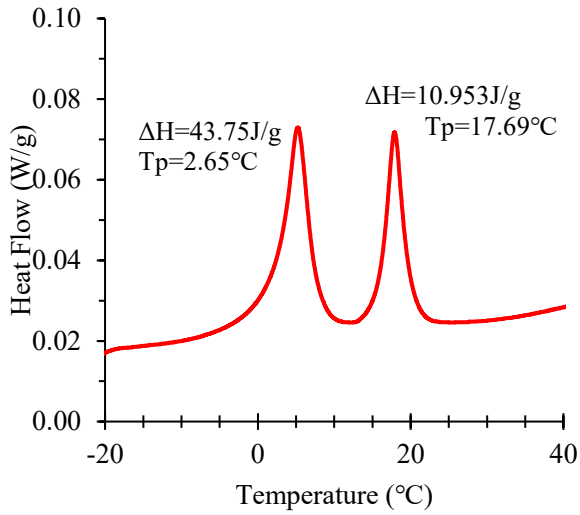


Figure 3.4.2 DSC curve of FC-PCM6D18D, heating and cooling process at  $10^\circ\text{C}/\text{min}$  scanning rate.

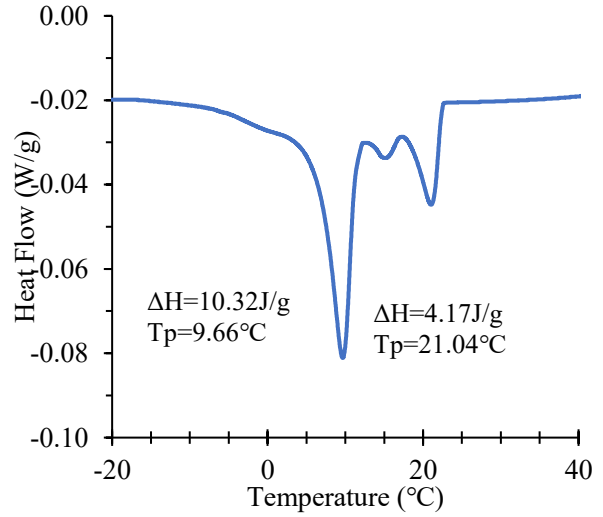
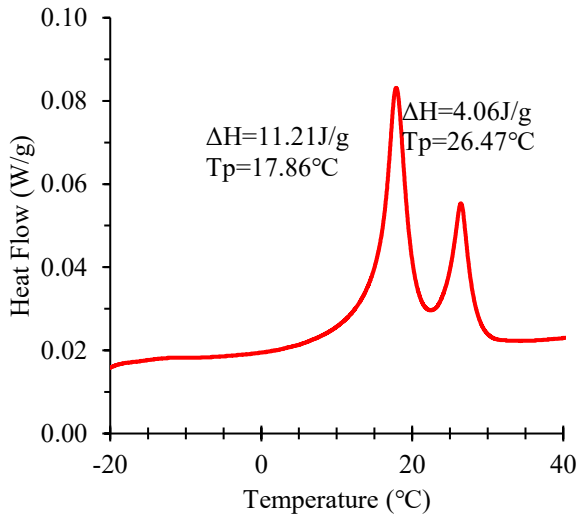


Figure 3.4.3 DSC curve of FC-PCM18D28D, heating and cooling process at  $10^\circ\text{C}/\text{min}$  scanning rate.

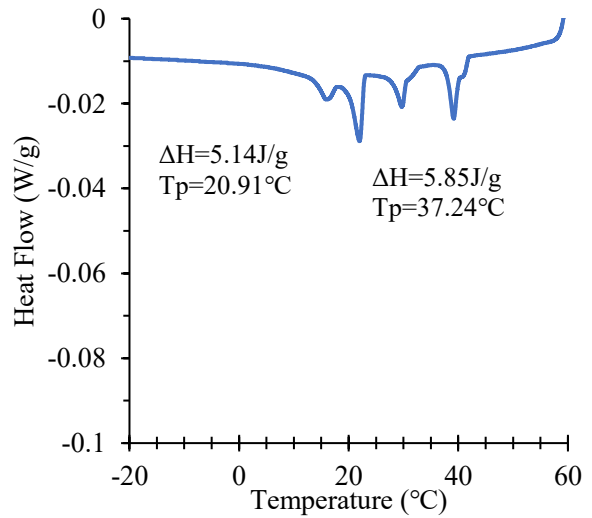
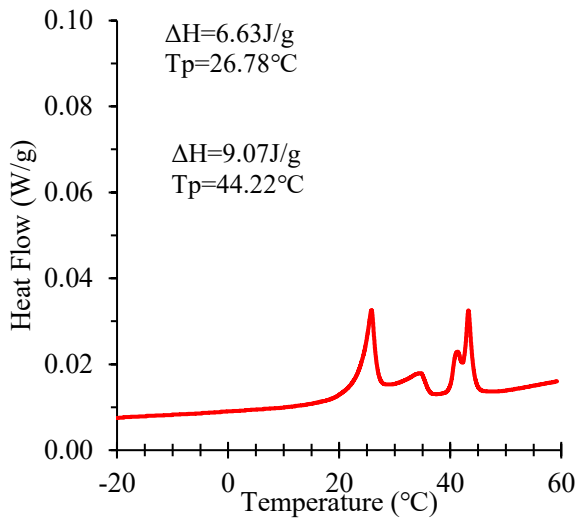


Figure 3.4.4 DSC curve of FC-PCM28D43D, heating and cooling process at  $10^\circ\text{C}/\text{min}$  scanning rate.

### 3.4.1.2 DSC and thermal analysis results of NC-PCM

The discussion outlines the results of a Differential Scanning Calorimetry (DSC) test conducted on three different foam concrete (NC) samples, each containing a different type of blended Phase Change Material (PCM). The test involved heating and cooling scans at a rate of 10°C per minute. The results are presented in Figure 3.4.5 through Figure 3.4.7.

In the case of NC PCM6D18D, the DSC analysis revealed two melting peaks and two freezing peaks. The first melting peak was observed at 4.06°C, and the first freezing peak was found at -5.15°C. The latent heats of melting and freezing ( $\Delta h$ ) stored in unit weight were 16.81 J/g and 17.03 J/g, respectively. The second melting peak occurred at 16.98°C, with the second freezing peak at 10.5°C. The latent heats of melting and freezing for the second peak were 6.33 J/g and 6.73 J/g.

In the NC PCM18D28D sample, similar to the first, two melting peaks and two freezing peaks were observed. The first melting peak was at 18°C, and the first freezing peak was at 9.77°C. The corresponding latent heats of melting and freezing were 13.99 J/g and 17.04 J/g. The second melting peak was found at 26.57°C, and the second freezing peak at 21.30°C. The latent heats of melting and freezing for the second peak were 4.08 J/g and 3.08 J/g.

The NC PCM28D43D sample also displayed two melting peaks and two freezing peaks. The first melting peak was recorded at 26.17°C, while the first freezing peak occurred at 21.47°C. The latent heats of melting and freezing were 15.15 J/g and 4.8 J/g. The second melting peak was observed at 43.77°C, and the second freezing peak at 29.17°C. The latent heats of melting and freezing for the second peak were 11.50 J/g and 12.34 J/g.

A common observation across all three types of NC concretes containing blended PCMs was that they melted and solidified within specific temperature ranges.

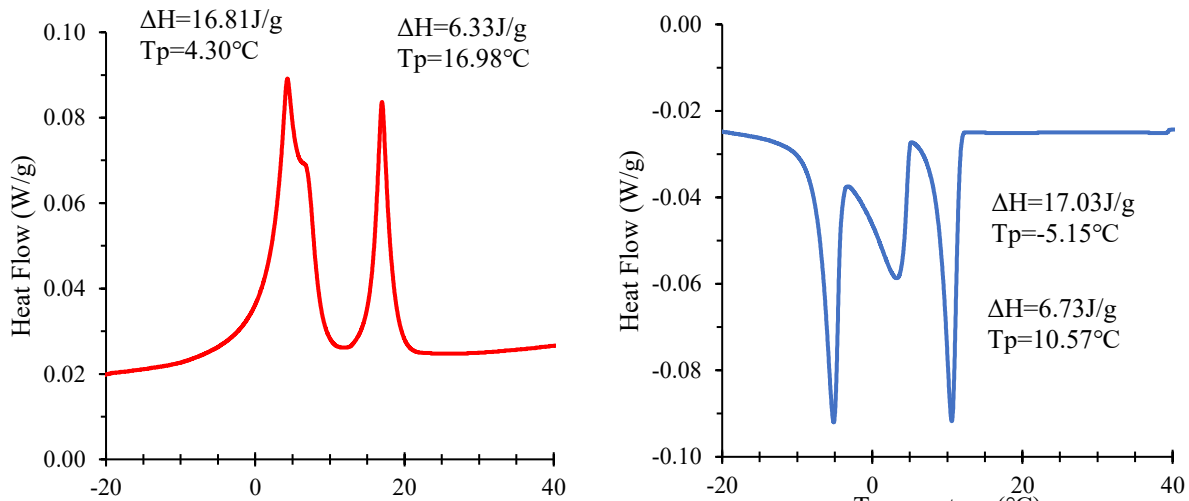


Figure 3.4.5 DSC curve of NC-PCM6D18D, heating and cooling process at  $10^\circ\text{C}/\text{min}$  scanning rate.

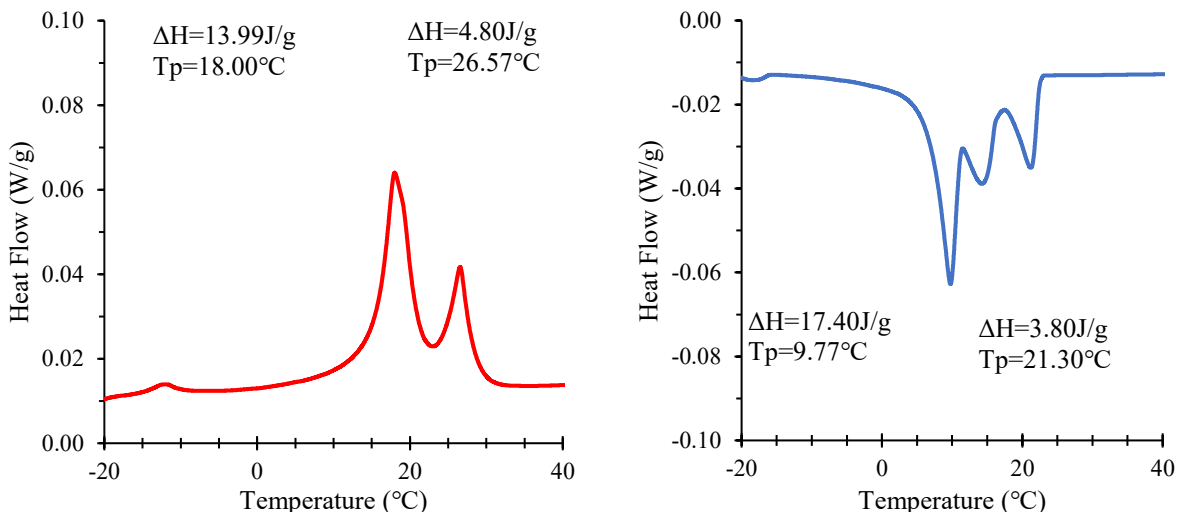


Figure 3.4.6 DSC curve of NC-PCM18D28D, heating and cooling process at  $10^\circ\text{C}/\text{min}$  scanning rate.

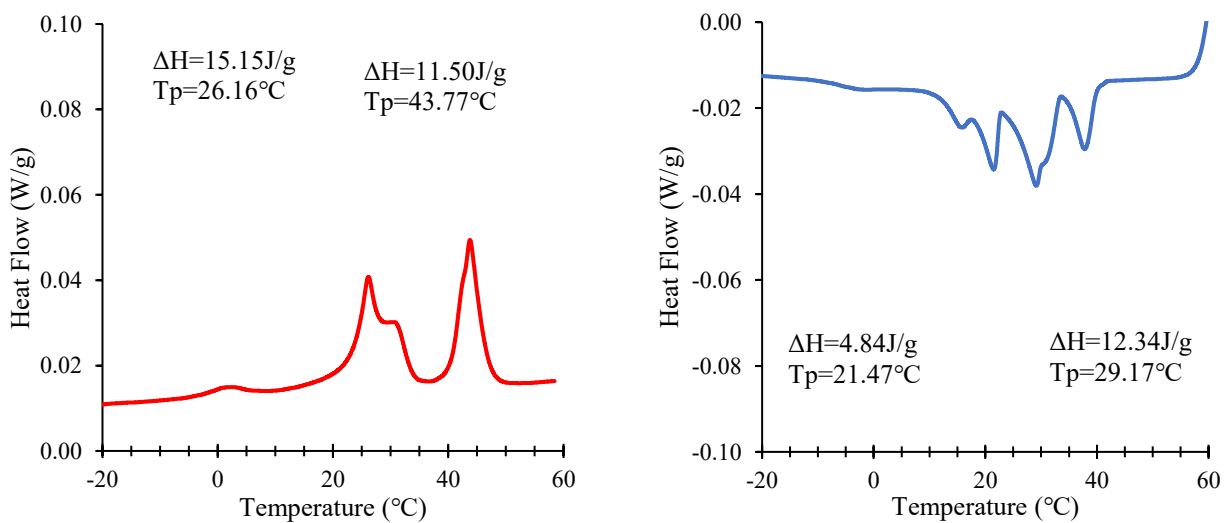


Figure 3.4.7 DSC curve of NC-PCM28D143D, heating and cooling process at  $10^\circ\text{C}/\text{min}$  scanning rate.

The discussion outlines the results of a Differential Scanning Calorimetry (DSC) test conducted on three different foam concrete (ND) samples, each containing a different type of blended Phase Change Material (PCM). The test involved heating and cooling scans at a rate of 10°C per minute. The results are presented in Figure 3.4.8 through Figure 3.4.10.

In the case of ND PCM6D18D, the DSC analysis revealed two melting peaks and two freezing peaks. The first melting peak was observed at 5.42°C, and the first freezing peak was found at -5.49°C. The latent heats of melting and freezing ( $\Delta h$ ) stored in unit weight were 3.77 J/g and 3.52 J/g, respectively. The second melting peak occurred at 17.16°C, with the second freezing peak at 10.22°C. The latent heats of melting and freezing for the second peak were 1.47 J/g and 1.5 J/g.

In the ND PCM18D28D sample, similar to the first, two melting peaks and two freezing peaks were observed. The first melting peak was at 18.74°C, and the first freezing peak was at 9.81°C. The corresponding latent heats of melting and freezing were 7.24 J/g and 9.91 J/g. The second melting peak was found at 26.32°C, and the second freezing peak at 21.25°C. The latent heats of melting and freezing for the second peak were 1.19 J/g and 1.08 J/g.

The ND PCM28D43D sample also displayed two melting peaks and two freezing peaks. The first melting peak was recorded at 26.29°C, while the first freezing peak occurred at 28.81°C. The latent heats of melting and freezing were 9.94 J/g and 12.61 J/g. The second melting peak was observed at 43.54°C, and the second freezing peak at 37.77°C. The latent heats of melting and freezing for the second peak were 6.61 J/g and 1.48 J/g.

A common observation across all three types of ND concretes containing blended PCMs was that they melted and solidified within specific temperature ranges.

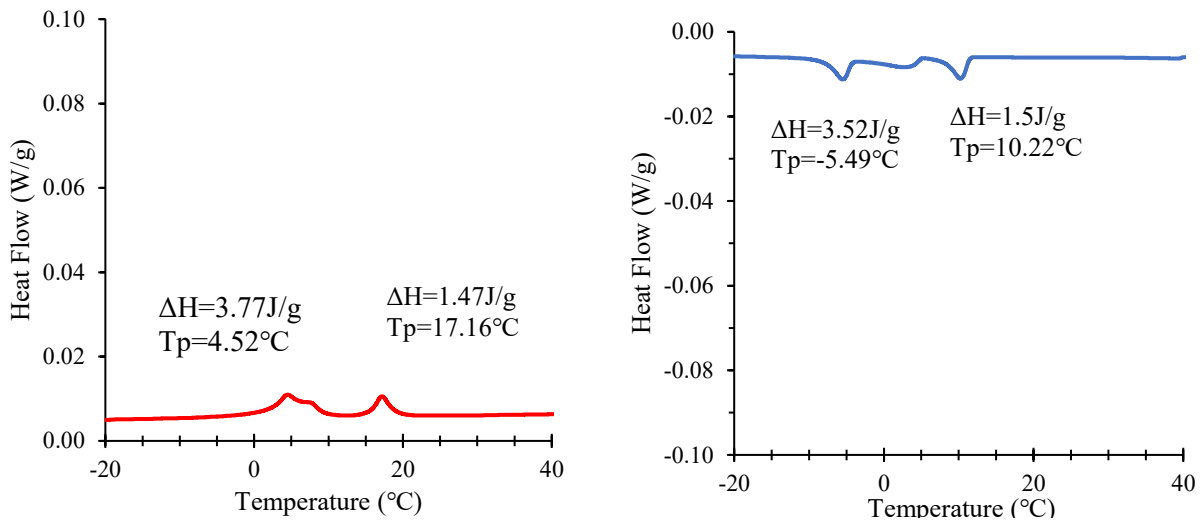


Figure 3.4.8 DSC curve of ND-PCM6D18D, heating and cooling process at  $10^\circ\text{C}/\text{min}$  scanning rate.

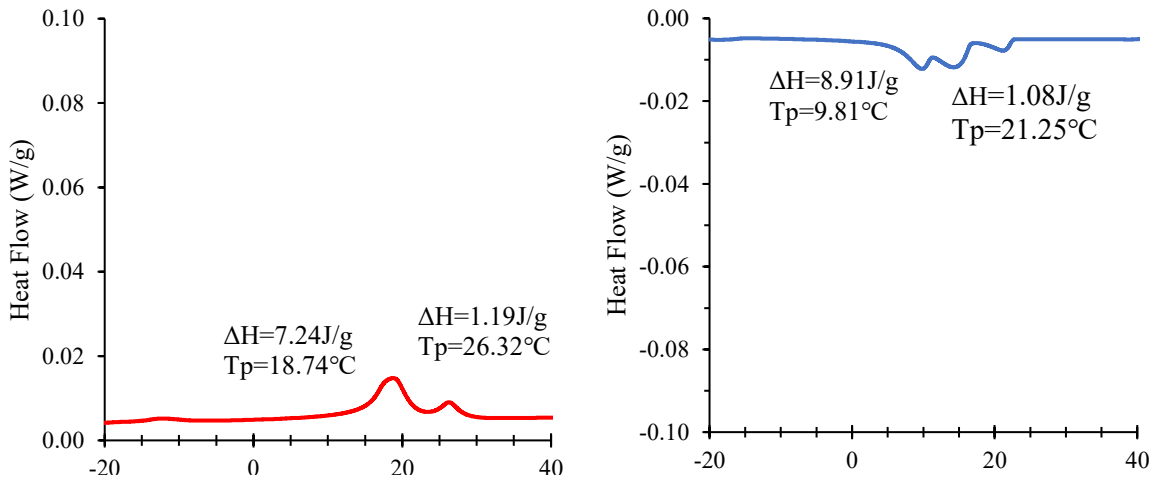


Figure 3.4.9 DSC curve of ND-PCM18D28D, heating and cooling process at  $10^\circ\text{C}/\text{min}$  scanning rate.

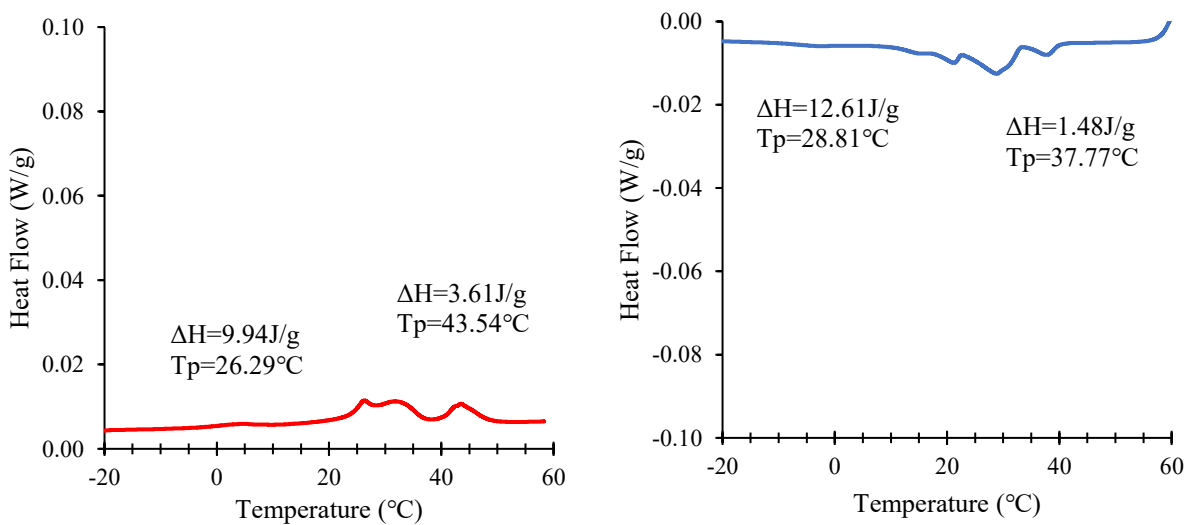


Figure 3.4.10 DSC curve of ND-PCM28D43D, heating and cooling process at  $10^\circ\text{C}/\text{min}$  scanning rate.



#### **3.4.1.4 Results of DSC measurements of PCM6D18D at various heating and cooling rates**

The impact of varying heating and cooling rates on the test results of different types of concretes containing is PCM6D18D illustrated in Figure 3.4.11 to Figure 3.4.16. These figures depict the phase changes observed at five different heating and cooling rates: 10°C/min, 5°C/min, 2°C/min, 1°C/min, and 0.5°C/min, with a specific focus on latent heat capacity, as shown on the right side.

One intriguing observation is the linear relationship between the heating rate and the variation in latent heat capacity, which remains relatively constant across different rates.

When comparing all three types of PCM6D at various heating rates (Figure 3.4.11 to Figure 3.4.13), it becomes evident that NC has, on average, a 0.8% higher latent heat capacity than FC concrete and, on average, a 78% higher capacity than ND concrete. Concerning PCM18D, NC exhibits, on average, a 20% higher latent heat capacity than FC concrete and, on average, a 74% higher capacity than ND concrete.

Similarly, when examining all three types of PCM6D at different cooling rates (Figure 3.4.14 to Figure 3.4.16), it becomes evident that NC has, on average, an 8% higher latent heat capacity than FC concrete and on average, a 78% higher capacity than ND concrete. Regarding PCM18D, NC showcases, on average, a 10% higher latent heat capacity than FC concrete and, on average, a 50% higher capacity than ND concrete.

The DSC results of PCM6D18D concretes for all scanning rates above mentioned are summarized from Table 3-10 to Table 3-12.

These comparisons highlight the significant impact of heating and cooling rates on the latent heat capacity of PCM concrete and underscore the variations in these thermal properties among different PCM types.

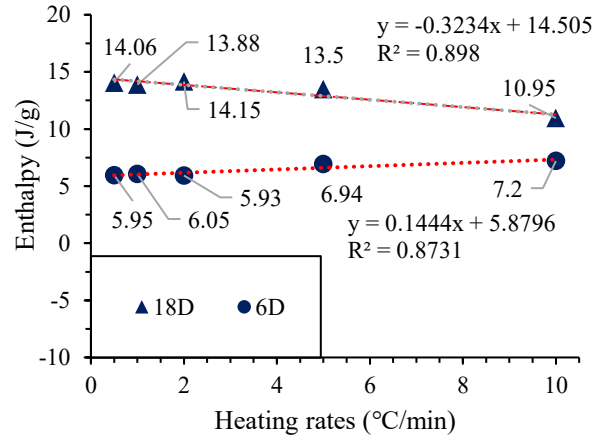
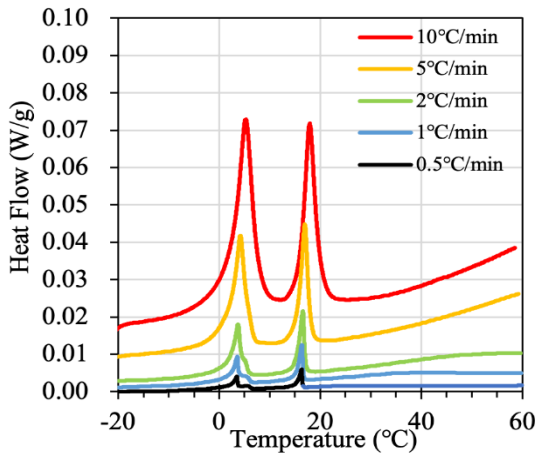


Figure 3.4.11 Results of DSC measurement of FC PCM6D18D at various heating rates.

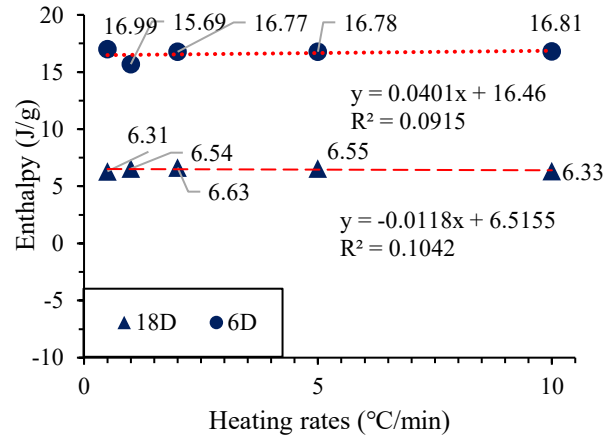
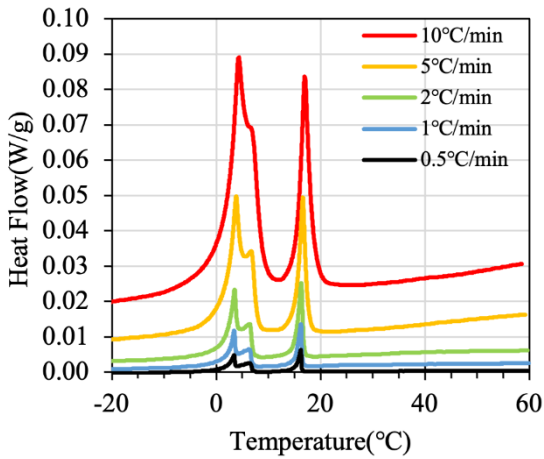


Figure 3.4.12 Results of DSC measurement of NC PCM6D18D at various heating rates.

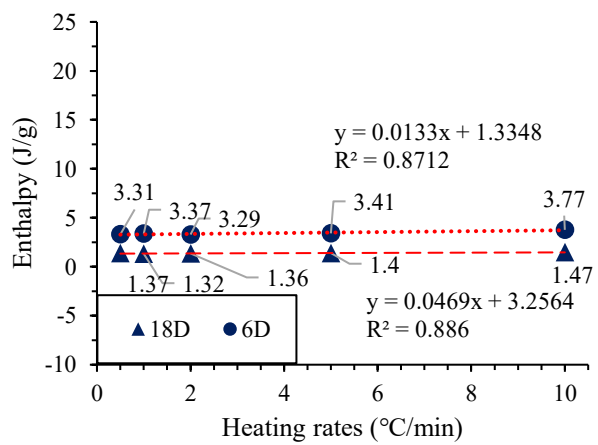
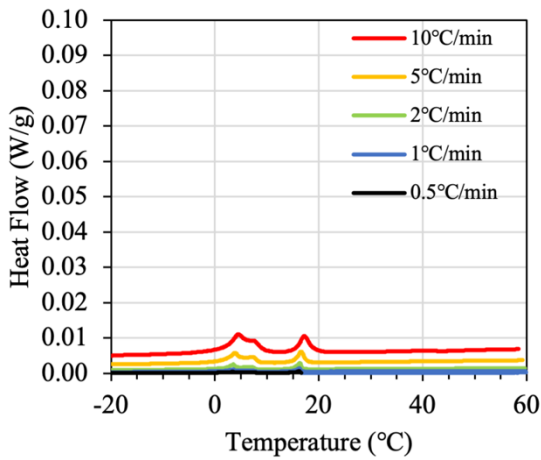


Figure 3.4.13 Results of DSC measurement of ND PCM6D18D at various heating rates.

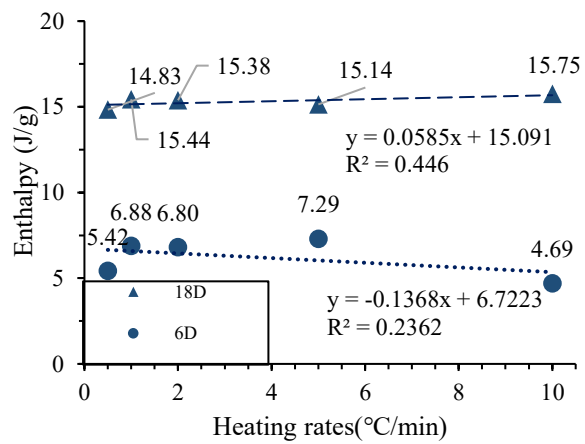
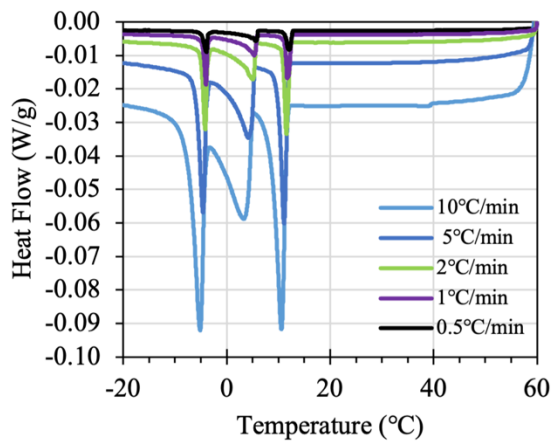


Figure 3.4.14 Results of DSC measurement of FC PCM6D18D at various cooling rates.

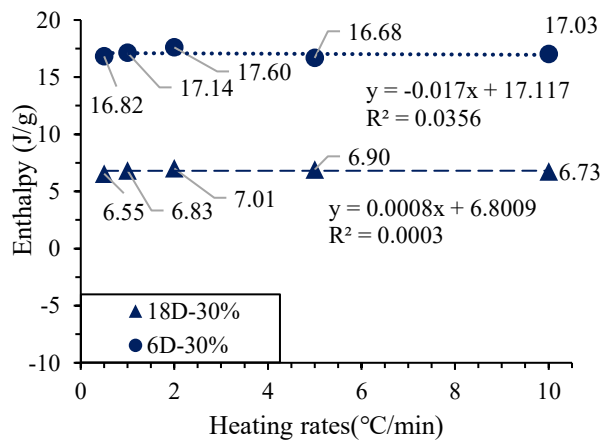
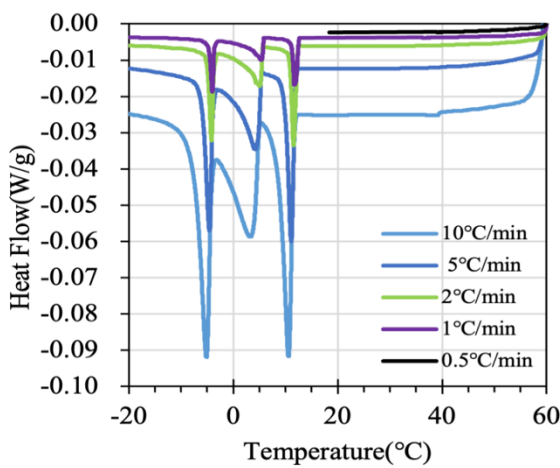


Figure 3.4.15 Results of DSC measurement of NC PCM6D18D at various cooling rates.

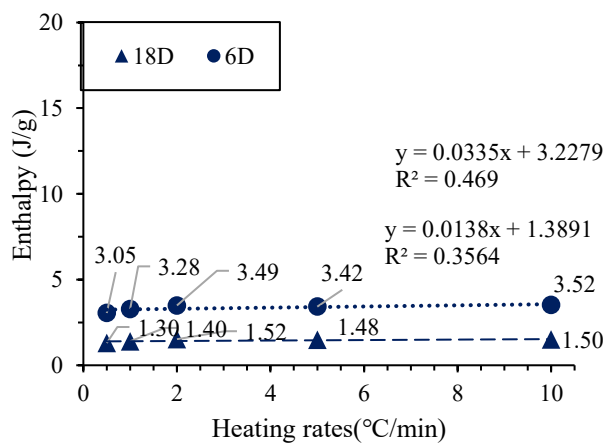
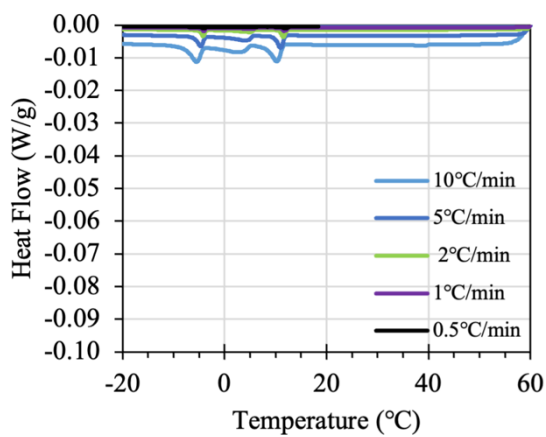


Figure 3.4.16 Results of DSC measurement of ND PCM6D18D at various cooling rates.

### 3.4.1.5 Results of DSC measurements of PCM18D28D at various heating and cooling rates

The impact of varying heating and cooling rates on the test results of different types of concretes containing is PCM18D28D illustrated in Figure 3.4.17 to Figure 3.4.22. These figures depict the phase changes observed at five different heating and cooling rates: 10°C/min, 5°C/min, 2°C/min, 1°C/min, and 0.5°C/min, with a specific focus on latent heat capacity, as shown on the right side.

One intriguing observation is the linear relationship between the heating/cooling rate and the variation in latent heat capacity, which shows a slight decrease as the heating rate and cooling rates increase.

When comparing all three types of PCM18D at various heating rates (Figure 3.4.17 to Figure 3.4.19), it becomes evident that NC has, on average, a 32% higher latent heat capacity than FC concrete and, on average, a 51% higher capacity than ND concrete. Concerning PCM28D, NC exhibits, on average, a 32% higher latent heat capacity than FC concrete and, on average, a 73% higher capacity than ND concrete.

Similarly, when examining all three types of PCM18D at different cooling rates (Figure 3.4.20 to Figure 3.4.22), it becomes evident that NC has, on average, an 44% higher latent heat capacity than FC concrete and on average, a 50% higher capacity than ND concrete. Regarding PCM28D, NC showcases, on average, a 24% higher latent heat capacity than FC concrete and, on average, a 72% higher capacity than ND concrete.

The DSC results of PCM18D28D concretes for all scanning rates above mentioned were summarized from Table 3-10 to Table 3-12.

These comparisons highlight the significant impact of heating and cooling rates on the latent heat capacity of PCM concrete and underscore the variations in these thermal properties among different PCM types.

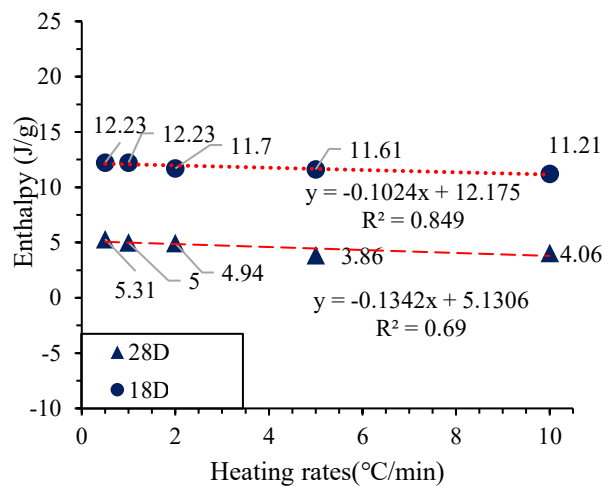
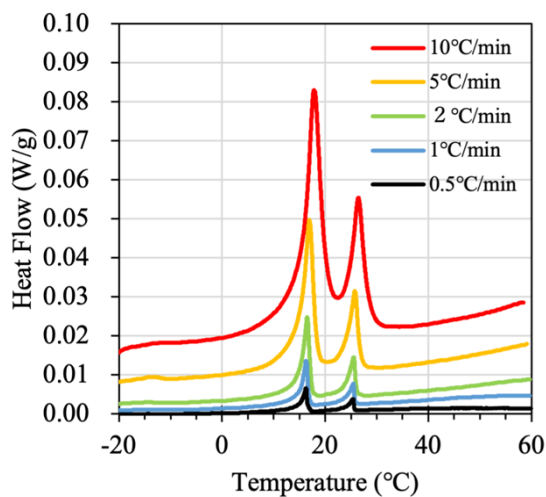


Figure 3.4.17 Results of DSC measurement of FC PCM18D28D at various heating rates.

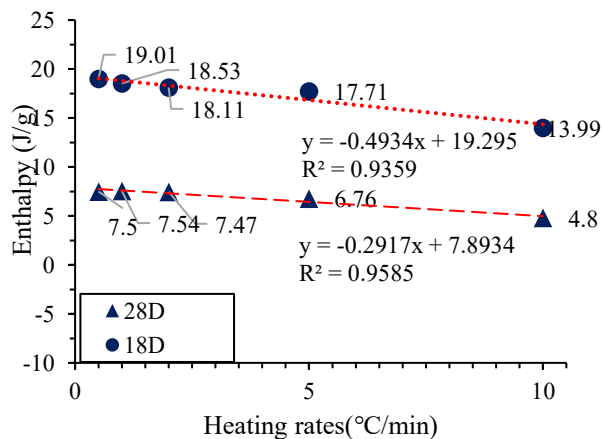
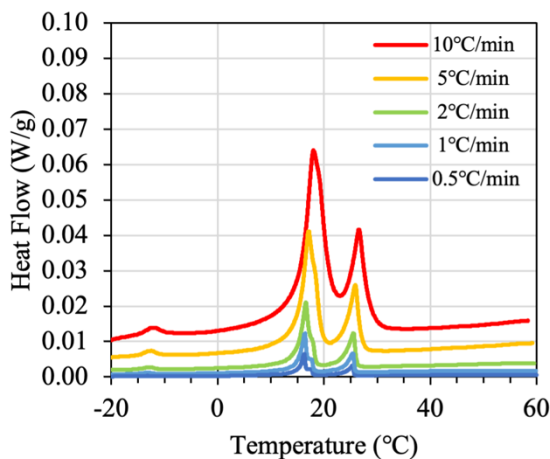


Figure 3.4.18 Results of DSC measurement of NC PCM18D28D at various heating rates.

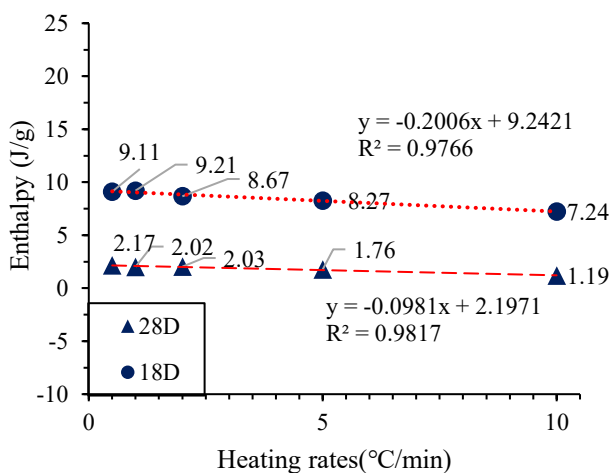
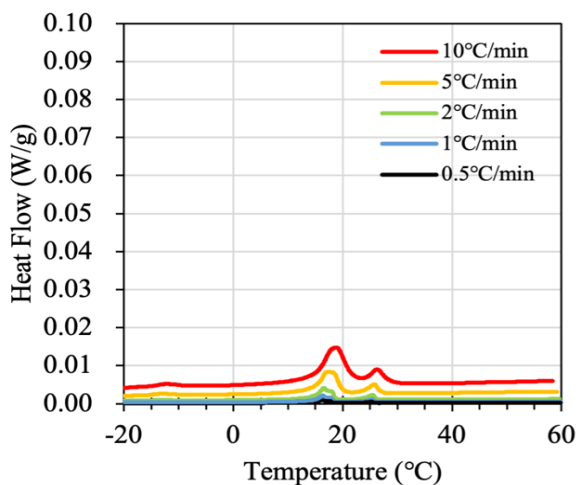


Figure 3.4.19 Results of DSC measurement of NC PCM18D28D at various heating rates.

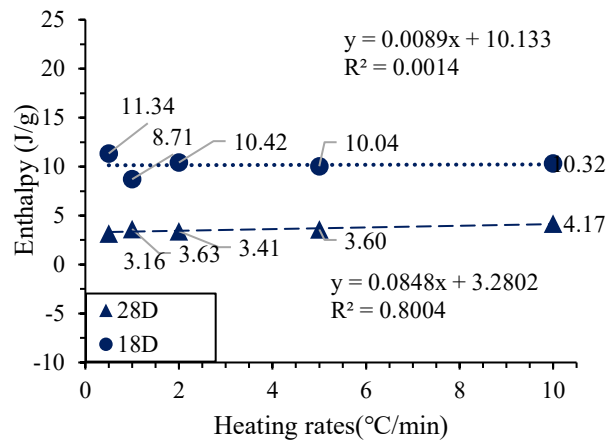
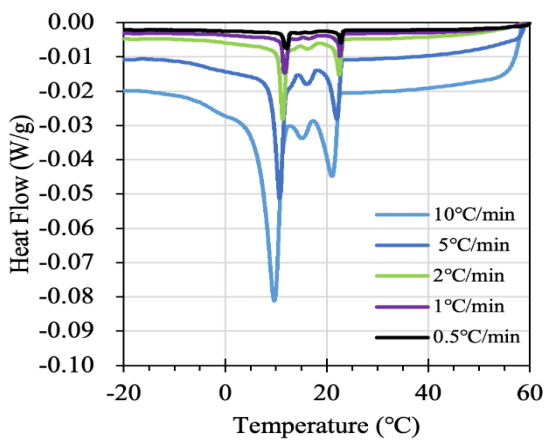


Figure 3.4.20 Results of DSC measurement of FC PCM18D28D at various cooling rates.

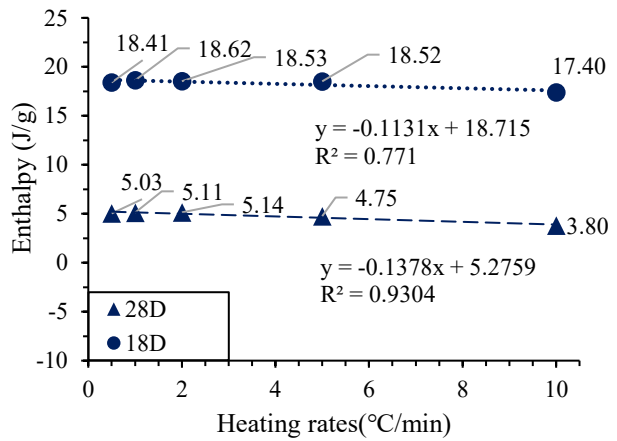
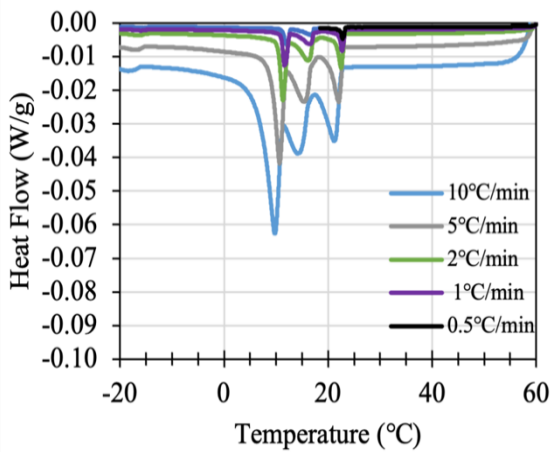


Figure 3.4.21 Results of DSC measurement of FC PCM18D28D at various cooling rates.

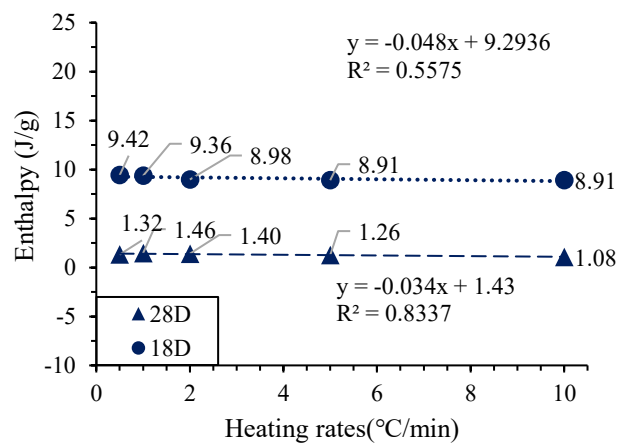
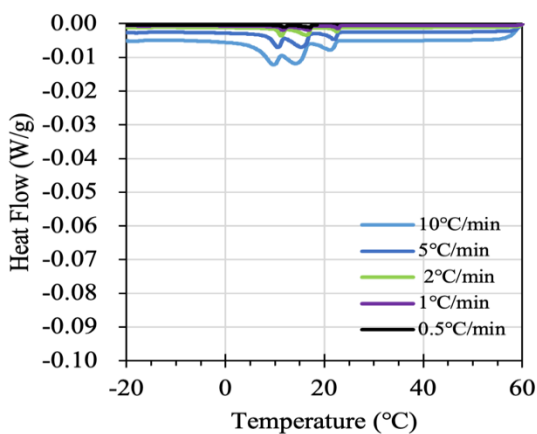


Figure 3.4.22 Results of DSC measurement of FC PCM18D28D at various cooling rates.

### 3.4.1.6 Results of DSC measurements of PCM28D43D at various heating and cooling rates

The impact of varying heating and cooling rates on the test results of different types of concretes containing PCM28D43D is illustrated in Figure 3.4.23 to Figure 3.4.28. These figures depict the phase changes observed at five different heating and cooling rates: 10°C/min, 5°C/min, 2°C/min, 1°C/min, and 0.5°C/min, with a specific focus on latent heat capacity, as shown on the right side. The

One intriguing observation is the linear relationship between the heating rate and the variation in latent heat capacity, which remains relatively constant across different rates.

When comparing all three types of PCM28D at various heating rates (Figure 3.4.23 to Figure 3.4.25), it becomes evident that NC has, on average, a 38% higher latent heat capacity than FC concrete and, on average, a 33% higher capacity than ND concrete. Concerning PCM43D, NC exhibits a value almost identical to FC concrete and, on average, a 52% higher capacity than ND concrete.

Similarly, when examining all three types of PCM43D at different cooling rates (Figure 3.4.26 to Figure 3.4.28), it becomes evident that NC has, on average, an 8% higher latent heat capacity than FC concrete and on average, a 78% higher capacity than ND concrete. Regarding PCM43D, NC showcases, on average, a 10% higher latent heat capacity than FC concrete and, on average, a 50% higher capacity than ND concrete.

The DSC results of PCM2843D concretes for all scanning rates above mentioned were summarized from Table 3-10 to Table 3-12

These comparisons highlight the significant impact of heating and cooling rates on the latent heat capacity of PCM concrete and underscore the variations in these thermal properties among different PCM types.

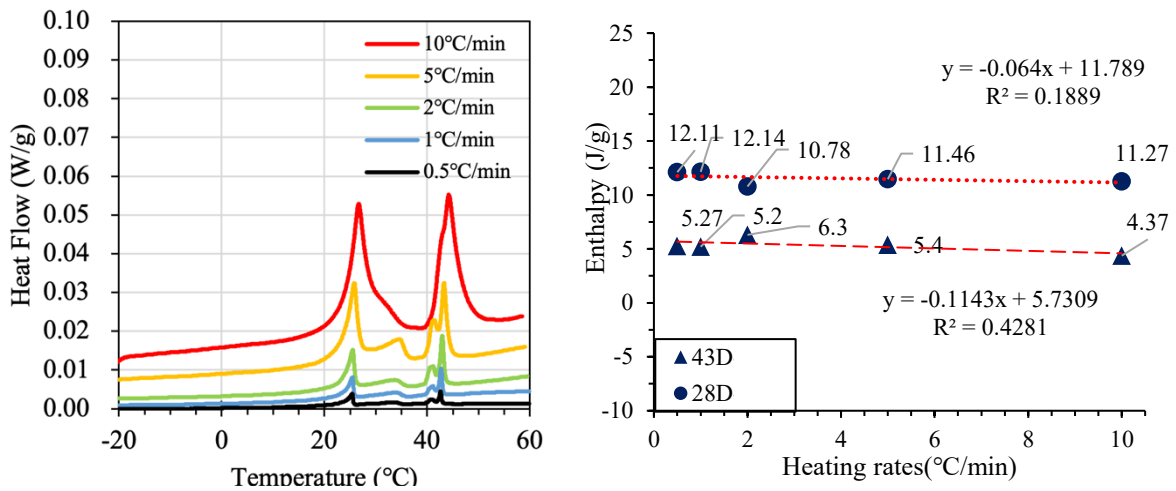


Figure 3.4.23 Results of DSC measurement of FC PCM28D43D at various heating rates.

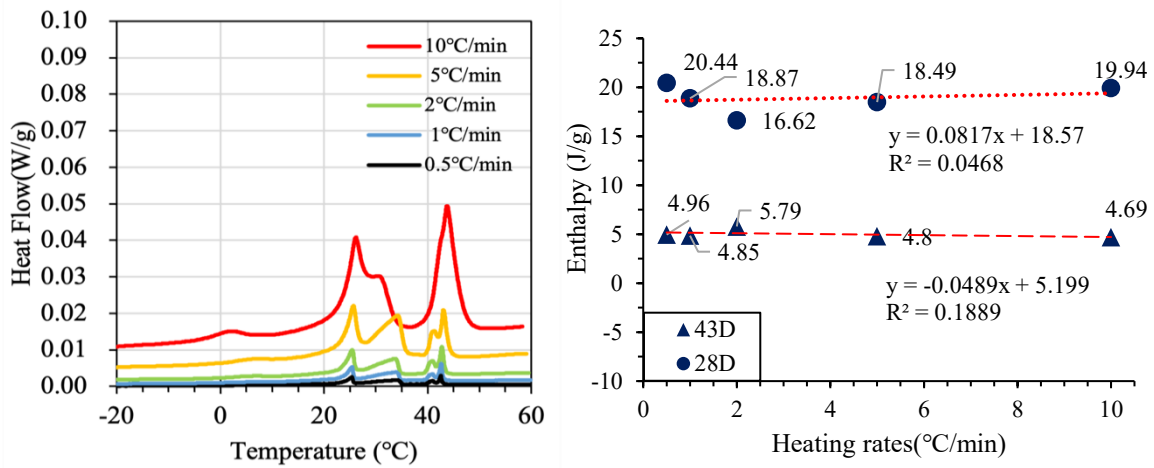


Figure 3.4.24 Results of DSC measurement of NC PCM28D43D at various heating rates.

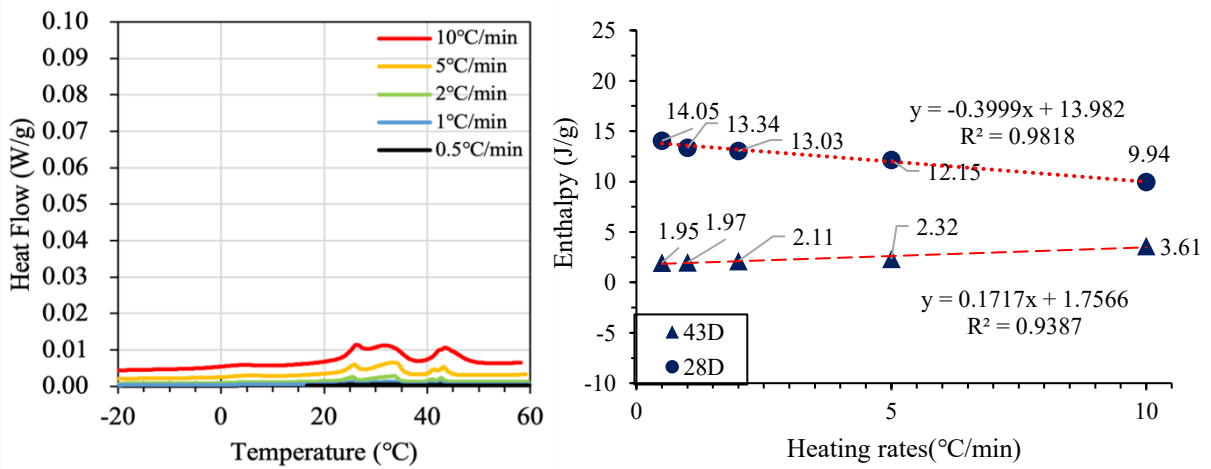


Figure 3.4.25 Results of DSC measurement of ND PCM28D43D at various heating rates.



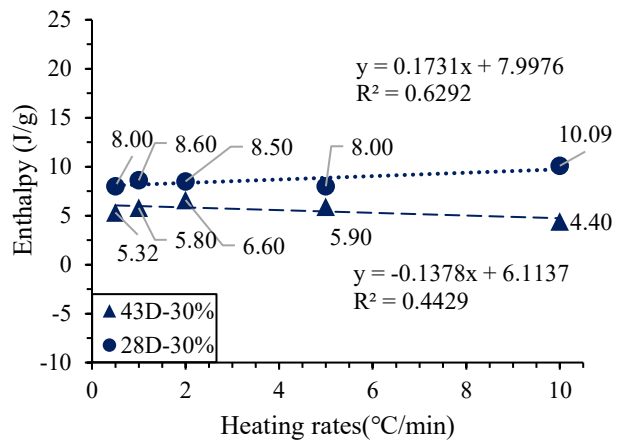
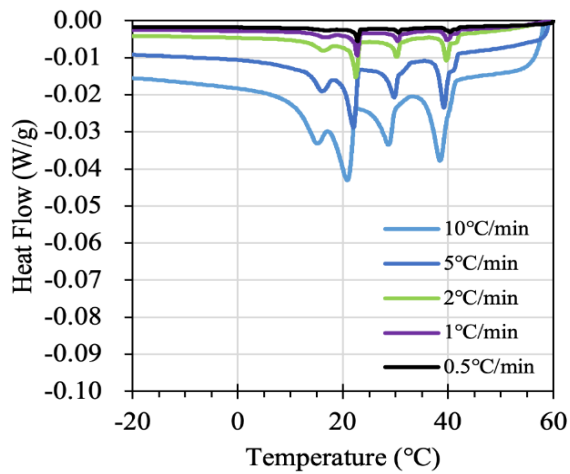


Figure 3.4.26 Results of DSC measurement of FC PCM28D43D at various cooling rates.

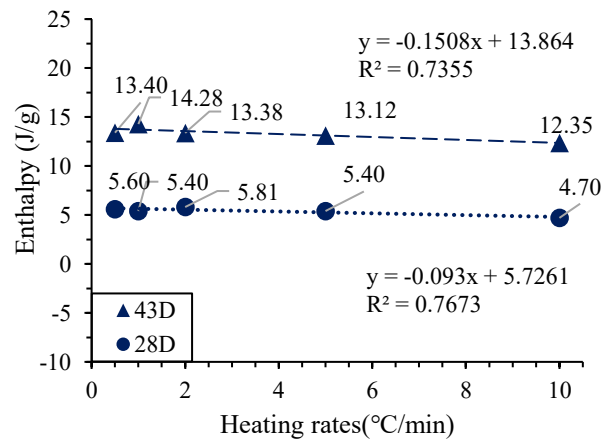
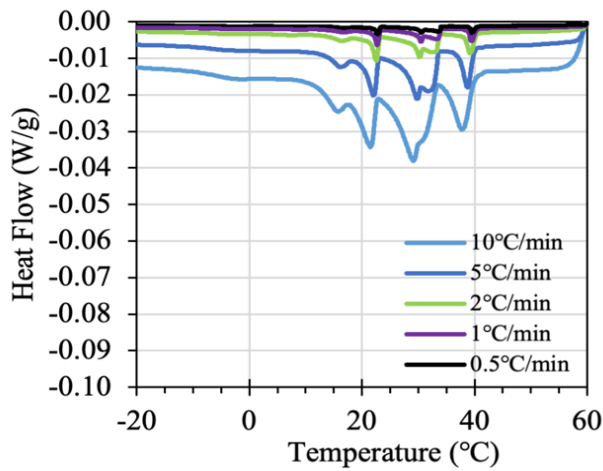


Figure 3.4.27 Results of DSC measurement of NC PCM28D43D at various cooling rates.

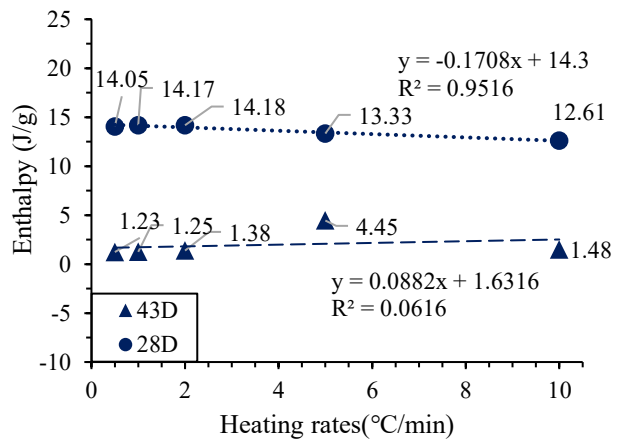
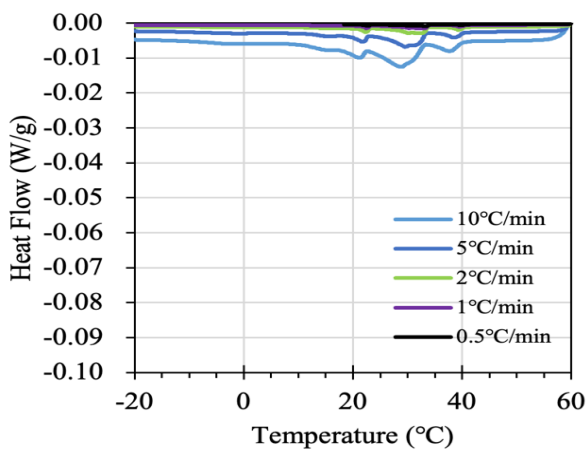


Figure 3.4.28 Results of DSC measurement of ND PCM28D43D at various cooling rates.

Table 3-9 Enthalpy variation and standpoint temperatures scanning rates varying from 10°C/min to 0.5°C/min.

Designation			Melting			Freezing		
			Onset Temp (°C)	Peak Enthalpy (J/g)	Peak Temp (°C)	Onset Temp (°C)	Peak Enthalpy (J/g)	Peak Temp (°C)
FC	6D18D	10°C/min	-1.33/14.34	43.75/10.95	2.65/17.69	-5.69/11.02	4.69/15.75	-7.25/7.79
		5°C/min	3.71/13.57	6.94/13.50	5.23/16.62	-4.79/11.71	7.29/15.14	-6.00/9.49
		2°C/min	3.61/13.64	5.93/14.15	4.65/16.08	-4.43/11.99	6.80/15.38	-5.21/16.08
		1°C/min	3.56/13.85	6.05/13.88	4.41/15.92	-4.26/12.14	6.88/15.44	-4.8/11.12
		0.5°C/min	3.56/14.11	5.95/14.06	4.27/15.84	-4.16/12.2	5.42/14.83	-4.57/11.39
	18D28D	10°C/min	15.43/24.35	11.21/4.06	17.86/26.47	11.32/22.37	10.32/4.17	9.66/21.04
		5°C/min	15.16/24.20	11.61/3.86	17.70/26.30	11.45/22.45	10.04/3.60	9.86/21.25
		2°C/min	14.92/23.72	11.70/4.94	16.53/25.56	12.30/23.10	10.42/3.41	11.31/22.45
		1°C/min	14.98/23.92	12.23/5.00	16.36/25.49	12.54/23.19	8.71/3.63	11.59/22.63
		0.5°C/min	15.15/23.86	12.23/5.31	16.30/25.42	12.75/23.07	11.34/3.16	12.01/22.71
	28D43D	10°C/min	23.76/40.87	6.63/9.07	26.78/44.22	22.48/39.22	5.14/5.85	20.91/37.24
		5°C/min	23.84/41.74	7.13/6.82	26.15/43.51	22.97/39.77	4.50/5.48	21.92/38.31
		2°C/min	23.85/41.72	6.62/6.43	25.75/42.94	23.34/40.26	9.52/3.83	22.50/39.01
		1°C/min	24.04/41.71	6.99/5.83	25.68/42.76	23.29/40.18	10.07/3.49	22.66/39.20
		0.5°C/min	23.92/41.65	9.90/5.48	25.60/42.65	23.27/40.34	10.74/3.09	22.75/39.46

Table 3-10 Enthalpy variation and standpoint temperatures scanning rates varying from 10°C/min to 0.5°C/min.

Designation			Melting			Freezing		
			Onset Temp (°C)	Peak Enthalpy (J/g)	Peak Temp (°C)	Onset Temp (°C)	Peak Enthalpy (J/g)	Peak Temp (°C)
NC	6D18D	10°C/min	1.82/15.44	16.81/6.33	4.30/16.98	-4.03/11.61	17.03/6.73	-5.15/10.57
		5°C/min	1.81/15.23	16.78/6.55	3.84/16.60	-3.85/11.92	16.68/6.90	-4.58/11.1
		2°C/min	1.89/15.10	16.77/6.63	3.54/16.32	-3.7/12.33	17.60/7.01	-4.16/11.54
		1°C/min	2.14/15.17	15.69/6.54	3.48/16.25	-3.66/12.53	17.14/6.83	-4.02/11.69
		0.5°C/min	2.15/15.33	16.99/6.31	3.46/16.24	-3.63/12.68	16.82/6.55	-3.99/12.07
	18D28D	10°C/min	15.51/24.37	13.99/4.80	18.00/26.57	11.51/22.43	17.40/3.80	9.77/21.30
		5°C/min	15.03/23.57	17.71/6.76	17.10/25.90	11.94/22.87	18.52/4.75	10.68/22.04
		2°C/min	14.93/23.51	18.11/7.47	16.59/25.56	12.23/23.14	18.53/5.14	11.30/22.48
		1°C/min	15.00/23.64	18.53/7.54	16.40/25.46	12.56/23.23	18.62/5.11	11.59/22.66
		0.5°C/min	15.15/23.74	19.01/7.50	16.33/25.43	12.75/23.29	18.41/5.03	11.99/22.75
	28D43D	10°C/min	23.14/40.34	15.15/11.50	26.16/43.77	22.59/39.94	4.84/12.34	21.47/29.17
		5°C/min	23.26/41.89	17.99/5.78	26.10/43.62	33.06/39.73	18.92/3.68	29.16/37.85
		2°C/min	23.26/41.96	17.79/5.82	25.47/42.76	23.18/40.21	20.48/3.68	22.50/39.15
		1°C/min	23.51/42.01	18.63/5.06	25.44/42.63	23.26/40.28	21.20/3.43	22.65/39.39
		0.5°C/min	23.50/42.03	20.44/4.96	25.40/42.59	34.07/40.26	20.13/3.19	22.71/39.55

Table 3-11 Enthalpy variation and standpoint temperatures scanning rates varying from 10°C/min to 0.5°C/min.

Designation			Melting			Freezing		
			Onset Temp (°C)	Peak Enthalpy (J/g)	Peak Temp (°C)	Onset Temp (°C)	Peak Enthalpy (J/g)	Peak Temp (°C)
ND	6D18D	10°C/min	1.81/15.54	3.77/1.47	4.52/17.16	-4.07/11.45	3.52/1.5	-5.49/10.22
		5°C/min	1.79/15.24	3.41/1.4	3.85/16.60	-3.84/11.84	3.42/1.48	-4.67/10.99
		2°C/min	1.98/15.17	3.29/1.36	3.57/16.33	-3.72/12.21	3.49/1.52	-4.21/11.49
		1°C/min	2.15/15.31	3.37/1.32	3.53/16.29	-3.7/12.48	3.28/1.40	-4.08/11.62
		0.5°C/min	2.19/15.32	3.31/1.37	3.46/16.26	-3.65/12.6	3.05/1.30	-4.03/12
	18D28D	10°C/min	14.96/24.40	7.24/1.19	18.74/26.32	16.62/22.49	8.91/1.08	9.81/21.25
		5°C/min	14.71/23.71	8.27/1.76	17.24/25.74	16.97/22.86	8.91/1.26	10.64/22.01
		2°C/min	14.70/23.53	8.67/2.03	16.55/25.48	17.21/23.13	8.98/1.40	11.28/22.48
		1°C/min	14.79/23.76	9.21/2.02	16.40/25.43	17.33/23.33	9.36/1.46	11.52/22.64
		0.5°C/min	15.00/23.73	9.11/2.17	16.32/25.34	17.44/23.25	9.42/1.32	17.05/22.71
	28D43D	10°C/min	23.09/40.31	9.94/3.61	26.29/43.54	32.96/39.92	12.61/1.48	28.81/37.77
		5°C/min	28.22/41.80	12.15/2.32	33.52/43.10	33.27/40.24	13.33/1.45	29.62/38.62
		2°C/min	26.64/41.95	13.03/2.11	33.47/42.73	33.60/40.53	14.18/1.38	30.12/39.30
		1°C/min	26.23/41.97	13.34/1.97	33.35/42.64	33.75/40.55	14.17/1.25	32.82/39.49
		0.5°C/min	23.02/41.98	14.05/1.95	25.39/42.58	33.85/40.76	14.05/1.23	33.30/39.90

### 3.4.2 Specific heat capacity and specific enthalpy measurements

The specific heat capacity is defined as the amount of energy required to raise the temperature of 1 gram of a substance by 1°C or 1K, with units quoted as (J/g°C). Also designated as  $C_p$ , specific heat capacity can be quantitatively measured using a DSC when obtained at constant pressure.

The specific heat capacity curve can be generated by subtracting the baseline part of the DSC, subsequently allowing the specific enthalpy, in the unit weight of PCM, to be determined by dividing the integrated area of the specific heat capacity curve by the temperature rising rate. This value can be automatically calculated by the software.

Regarding specific enthalpy, it can be obtained from calorimetry measurements. Temperature-heat capacity data pairs are measured, and interpolation is used to calculate enthalpy at the required temperature points. This method provides the highest level of certainty.

Dynamic DSC tests were conducted for all PCM foam concrete samples, considering a heating rate of 10°C/min. The effect of the heating rate ranging from 10°C to 50°C was investigated for all PCM foam concrete samples.

### 3.4.2.1 Results of specific heat capacity and specific enthalpy measurements of FC PCM concrete

The discussion presents the results of specific heat capacity and specific enthalpy tests conducted on three different foam concrete (FC) samples, each containing a different type of blended Phase Change Material (PCM). The results are presented in Figure 3.4.29- Figure 3.4.31.

In all three FC PCM concrete samples, the specific heat capacity based on specific heat enthalpy measurements displays two prominent peaks at different temperatures. These peaks indicate distinct changes in the material's heat capacity and the energy required to raise its temperature by 1°C or 1K per unit mass.

For FC PCM6D18D (Figure 3.4.29 (a)), the first peak in the specific heat capacity curve occurs at 5.7°C, with a specific heat ( $C_p$ ) of 3.9 J/g°C. The second peak emerges at 18°C, with a specific heat capacity of 3.8 J/g°C. FC PCM6D18D exhibits notable changes in heat capacity at these two distinct temperatures. In the case of FC PCM18D28D (Figure 3.4.30 (a)), the first peak in the specific heat capacity curve appears at 17.54°C, with a specific heat ( $C_p$ ) of 4.59 J/g°C. The second peak is observed at 27.3°C, with a specific heat capacity of 3.019 J/g°C. Notably, FC PCM18D28D displays the highest specific heat capacity among all FC PCM concretes, making it particularly efficient in absorbing and storing thermal energy. In contrast, FC PCM28D43D (Figure 3.4.31 (a)), exhibits the lowest specific heat capacity. Its first peak in the specific heat capacity curve occurs at 26.81°C, with a specific heat ( $C_p$ ) of 2.42 J/g°C, and the second peak is noted at 43.71°C, with a specific heat capacity of 2.78 J/g°C.

The specific enthalpy measurements, conducted within a temperature range of -30 to 60°C, allow us to understand the phase transition behavior of these materials. The specific enthalpy is assumed to be zero at -20 °C, enabling the analysis of changes in enthalpy.

For FC PCM6D18D (Figure 3.4.29 (b)), the phase transition range, characterized by substantial changes in enthalpy, occurs from 6 to 24 °C. Within this phase transition range, FC PCM6D18D exhibits a specific enthalpy of 18295 J/kg, indicating its significant capacity to absorb and release thermal energy during this phase transition. For FC PCM18D28D (Figure 3.4.30 (b)), the phase transition range is observed from 10 to 30 °C, and the specific enthalpy within this range is measured at 167785 J/kg, showcasing its substantial thermal energy storage capabilities. As for FC PCM28D43D (Figure 3.4.31 (b)), the phase transition range is noted from 30 to 50 °C, with a specific enthalpy within this range measured at 17850 J/kg. While this specific enthalpy value is lower than that of FC PCM6D18D, it still reflects the material's ability to effectively store and release thermal energy during the specified phase transition.

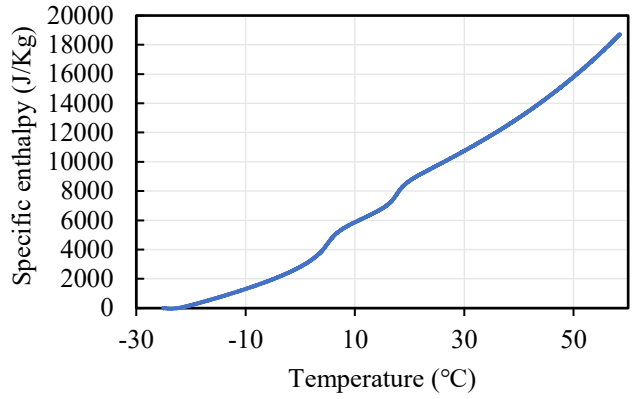
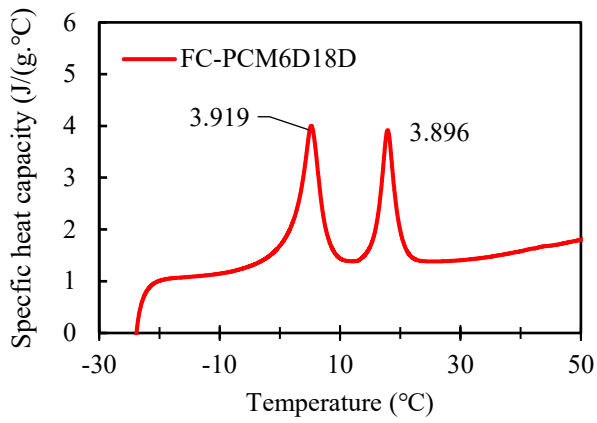


Figure 3.4.29 (a) Specific heat capacity and (b) specific enthalpy of FC PCM6D18D.

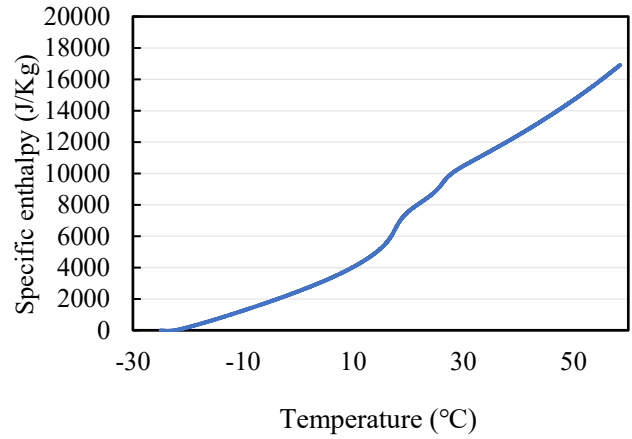
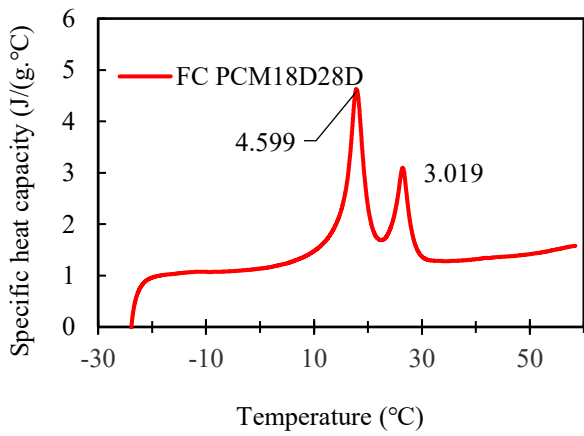


Figure 3.4.30 (a) Specific heat capacity and (b) specific enthalpy of FC PCM18D28D.

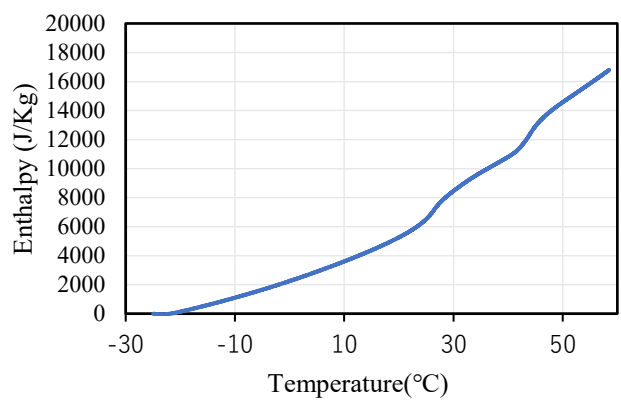
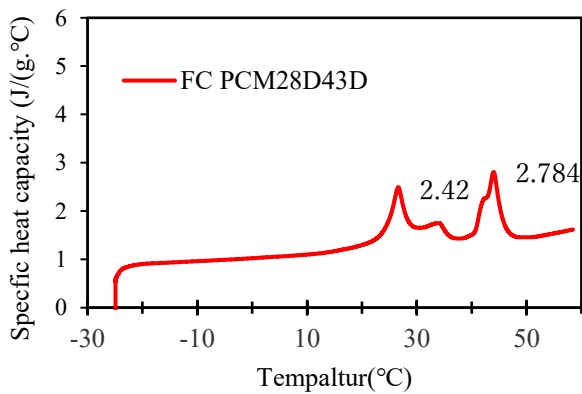


Figure 3.4.31 (a) Specific heat capacity and (b) specific enthalpy of FC PCM28D43D.

### 3.4.2.2 Results of specific heat capacity and specific enthalpy measurements of NC PCM concrete

The discussion presents the results of specific heat capacity and specific enthalpy tests conducted on three different NC samples, each containing a different type of blended Phase Change Material (PCM). The results are presented in Figure 3.4.32- Figure 3.4.34.

In all three NC PCM concrete samples, the specific heat capacity based on specific heat enthalpy measurements displays two prominent peaks at different temperatures. These peaks indicate distinct changes in the material's heat capacity and the energy required to raise its temperature by 1°C or 1K per unit mass.

For NC PCM6D18D (Figure 3.4.32 (a)), the first peak in the specific heat capacity curve occurs at 6.19°C, with a specific heat ( $C_p$ ) of 4.304 J/g°C. The second peak emerges at 18.47°C, with a specific heat capacity of 5.9 J/g°C. In the case of NC PCM18D28D (Figure 3.4.33 (a)), the first peak in the specific heat capacity curve appears at 18.9°C, with a specific heat ( $C_p$ ) of 5.3 J/g°C. The second peak is observed at 26.7°C, with a specific heat capacity of 3.4 J/g°C. Notably, NC PCM6D28D displays the highest specific heat capacity among all NC PCM concretes, making it particularly efficient in absorbing and storing thermal energy. In contrast, NC PCM28D43D (Figure 3.4.34 (a)), exhibits the lowest specific heat capacity. Its first peak in the specific heat capacity curve occurs at 25.92°C, with a specific heat ( $C_p$ ) of 3.56 J/g°C, and the second peak is noted at 47.6°C, with a specific heat capacity of 4.32 J/g°C.

The specific enthalpy measurements, conducted within a temperature range of -30 to 60°C, allow us to understand the phase transition behavior of these materials. The specific enthalpy is assumed to be zero at -20 °C, enabling the analysis of changes in enthalpy.

For NC PCM6D18D (Figure 3.4.32 (b)), the phase transition range, characterized by substantial changes in enthalpy, occurs from 6 to 24 °C. Within this phase transition range, NC PCM6D18D exhibits a specific enthalpy of 18190 J/kg, indicating its significant capacity to absorb and release thermal energy during this phase transition. For NC PCM18D28D (Figure 3.4.33 (b)), the phase transition range is observed from 10 to 30 °C, and the specific enthalpy within this range is measured at 17387 J/kg, showcasing its substantial thermal energy storage capabilities. As for NC PCM28D43D (Figure 3.4.34 (b)), the phase transition range is noted from 30 to 50 °C, with a specific enthalpy within this range measured at 19392 J/kg. While this specific enthalpy value is lower than that of NC PCM6D18D, it still reflects the material's ability to effectively store and release thermal energy during the specified phase transition.



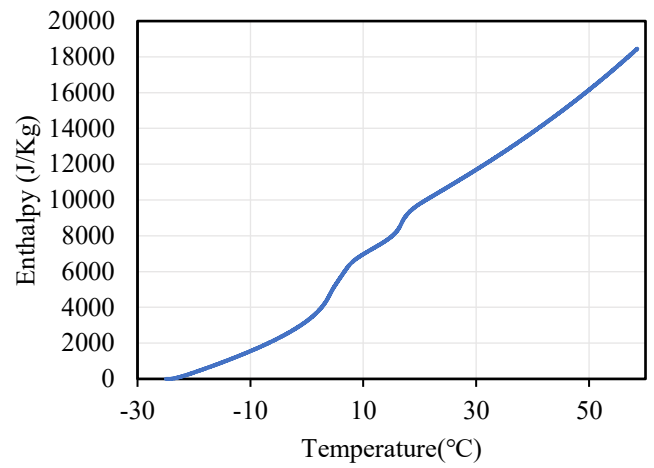
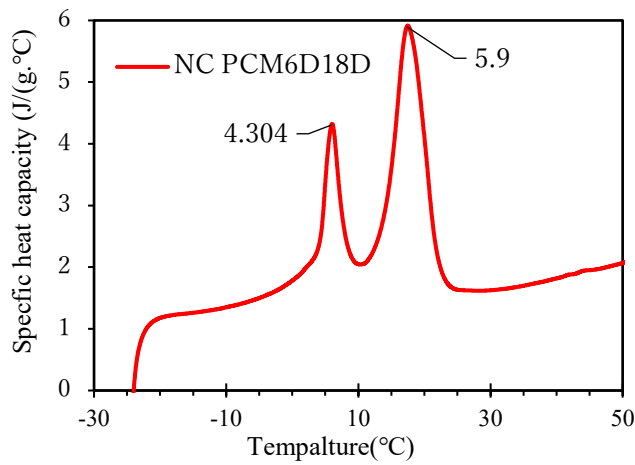


Figure 3.4.32 (a) Specific heat capacity and (b) specific enthalpy of NC PCM6D18D.

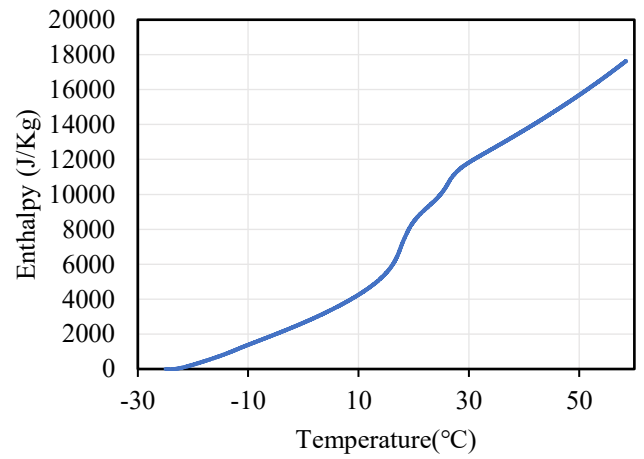
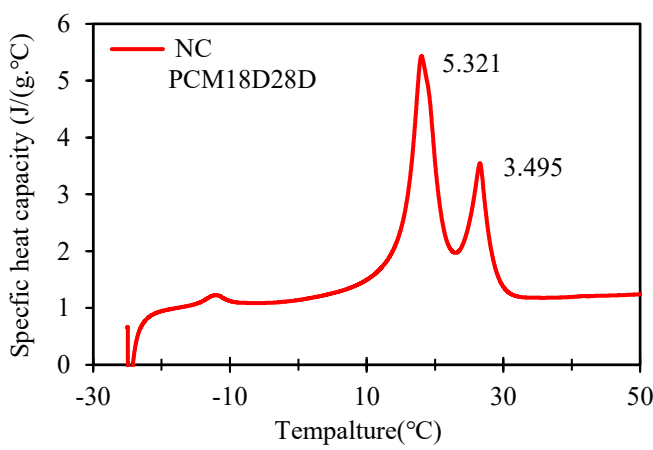


Figure 3.4.33 (a) Specific heat capacity and (b) specific enthalpy of NC PCM18D28D.

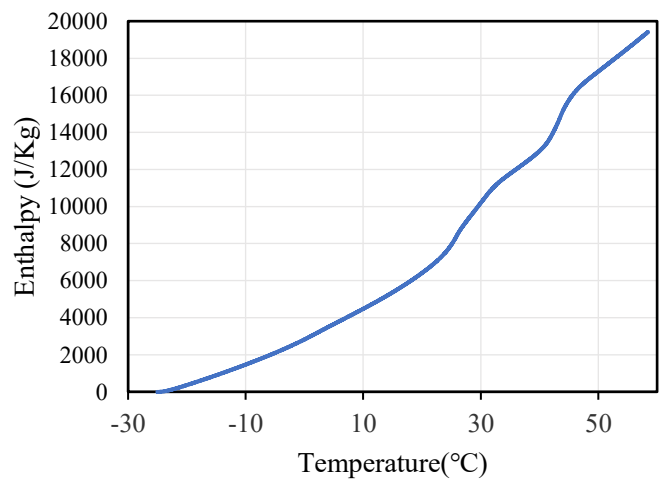
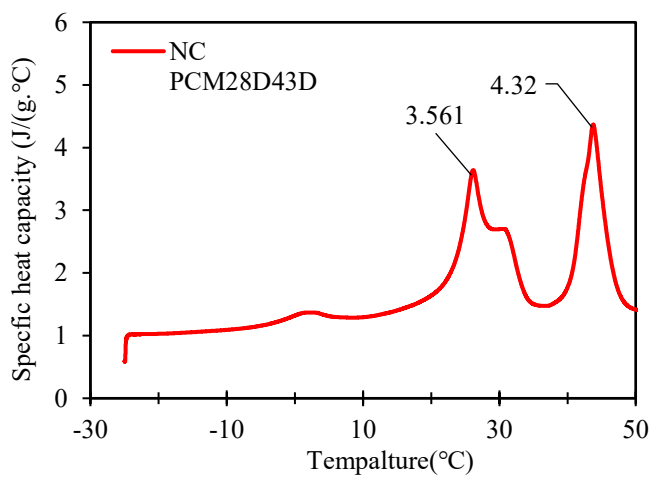


Figure 3.4.34 (a) Specific heat capacity and (b) specific enthalpy of NC PCM28D43D.

### 3.4.2.3 Results of specific heat capacity and specific enthalpy measurements of ND PCM concrete

The discussion presents the results of specific heat capacity and specific enthalpy tests conducted on three different ND samples, each containing a different type of blended Phase Change Material (PCM). The results are presented in Figure 3.4.35- Figure 3.4.37.

In all three ND PCM concrete samples, the specific heat capacity based on specific heat enthalpy measurements displays two prominent peaks at different temperatures. These peaks indicate distinct changes in the material's heat capacity and the energy required to raise its temperature by 1°C or 1K per unit mass.

For ND PCM6D18D (Figure 3.4.35 (a)), exhibits the lowest specific heat capacity. The first peak in the specific heat capacity curve occurs at 3.22°C, with a specific heat ( $C_p$ ) of 1.46 J/g°C. The second peak emerges at 16.4°C, with a specific heat capacity of 1.39 J/g°C. In the case of ND PCM18D28D (Figure 3.4.36 (a)), the first peak in the specific heat capacity curve appears at 19.68°C, with a specific heat ( $C_p$ ) of 2.6 J/g°C. The second peak is observed at 25.1°C, with a specific heat capacity of 1.5 J/g°C. Notably, ND PCM18D28D displays the highest specific heat capacity among all ND PCM concretes, making it particularly efficient in absorbing and storing thermal energy. As for ND PCM28D43D (Figure 3.4.37 (a)), Its first peak in the specific heat capacity curve occurs at 25.59°C, with a specific heat ( $C_p$ ) of 2.2 J/g°C, and the second peak is noted at 44.5°C, with a specific heat capacity of 2 J/g°C.

The specific enthalpy measurements, conducted within a temperature range of -30 to 60°C, allow us to understand the phase transition behavior of these materials. The specific enthalpy is assumed to be zero at -20 °C, enabling the analysis of changes in enthalpy.

For ND PCM6D18D (Figure 3.4.35 (b)), the phase transition range, characterized by substantial changes in enthalpy, occurs from 6 to 24 °C. Within this phase transition range, ND PCM6D18D exhibits a specific enthalpy of 9421 J/kg, indicating its significant capacity to absorb and release thermal energy during this phase transition. For ND PCM18D28D (Figure 3.4.36 (b)), the phase transition range is observed from 10 to 30 °C, and the specific enthalpy within this range is measured at 12646 J/kg, showcasing its substantial thermal energy storage capabilities. As for ND PCM28D43D (Figure 3.4.37 (b)), the phase transition range is noted from 30 to 50 °C, with a specific enthalpy within this range measured at 15355 J/kg. While this specific enthalpy value is lower than that of ND PCM6D18D, it still reflects the material's ability to effectively store and release thermal energy during the specified phase transition.

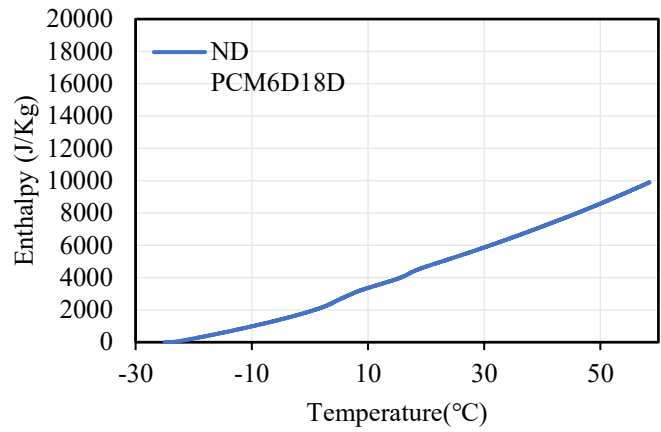
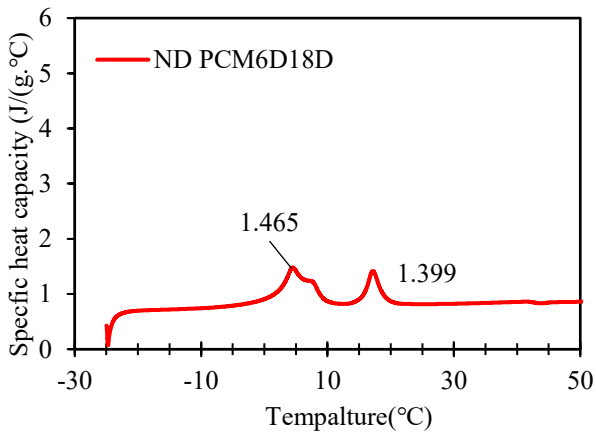


Figure 3.4.35 Specific heat capacity and specific enthalpy of ND PCM6D18D.

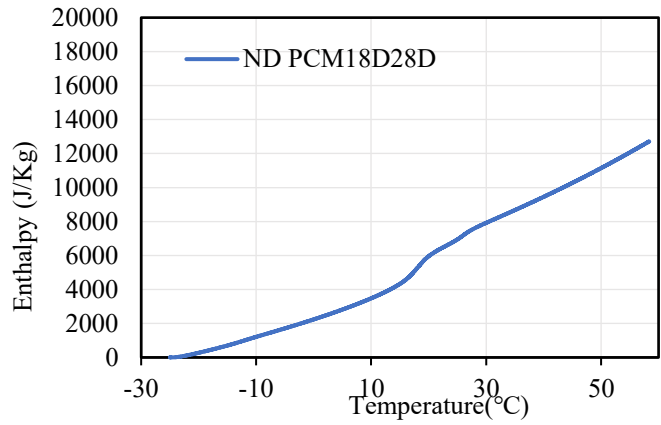
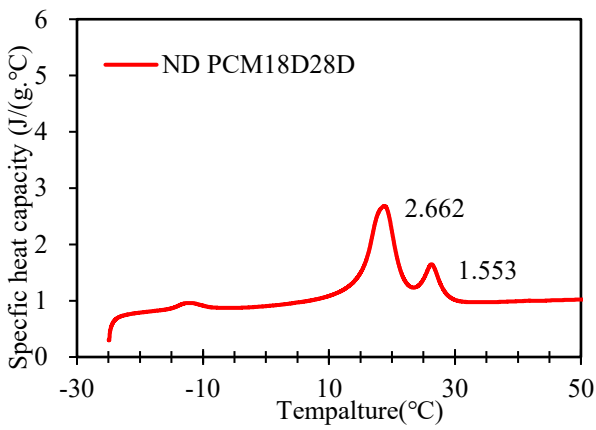


Figure 3.4.36 Specific heat capacity and specific enthalpy of ND PCM18D28D.

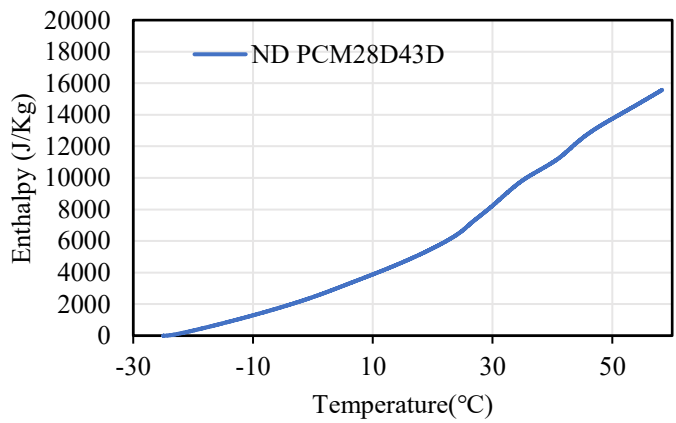
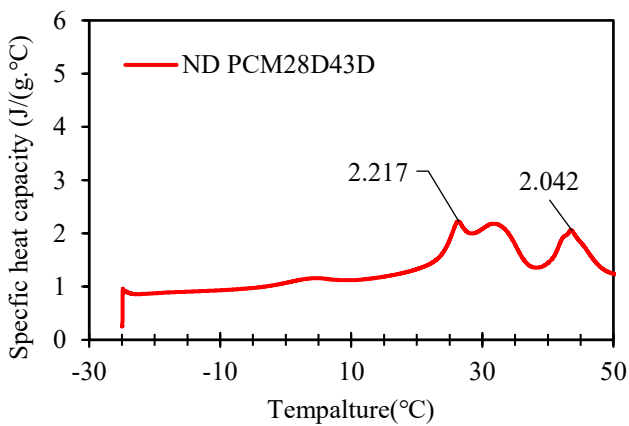


Figure 3.4.37 Specific heat capacity and specific enthalpy of ND PCM28D43D.

#### **3.4.2.4 Results of specific heat capacity and specific enthalpy measurements all three types of PCM concrete**

When comparing all three types of PCM6D18D (Figure 3.4.38), it becomes evident that NC has, on average, a 25% higher specific heat capacity than FC concrete and, on average, a 73% higher capacity than ND concrete. Regarding specific enthalpy, NC exhibits a value almost identical to FC concrete, but it is also, on average, 48% higher than ND concrete.

For the PCM18D28D variants (Figure 3.4.39), the comparison reveals that NC has, on average, a 13% higher specific heat capacity than FC concrete and approximately 52% higher capacity than ND concrete. As for specific enthalpy, NC shows around a 5% increase compared to FC concrete, and it is approximately 27.9% higher than ND concrete.

Similarly, when examining all three types of PCM28D43D (Figure 3.4.40), it becomes evident that NC boasts, on average, a 34.9% higher specific heat capacity than FC concrete and, on average, a 47% higher capacity than ND concrete. Regarding specific enthalpy, NC exhibits, on average, a 5% increase compared to FC concrete, and it is approximately 27.9% higher than ND concrete.

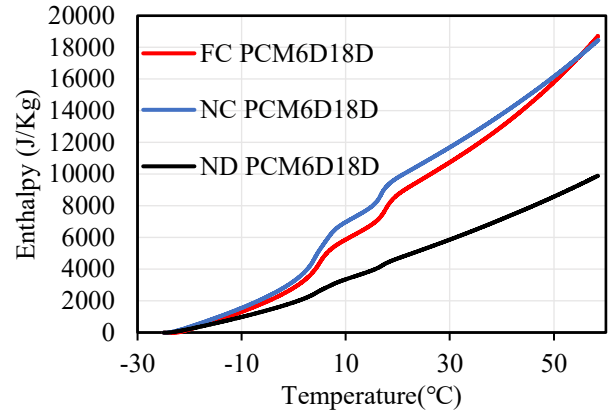
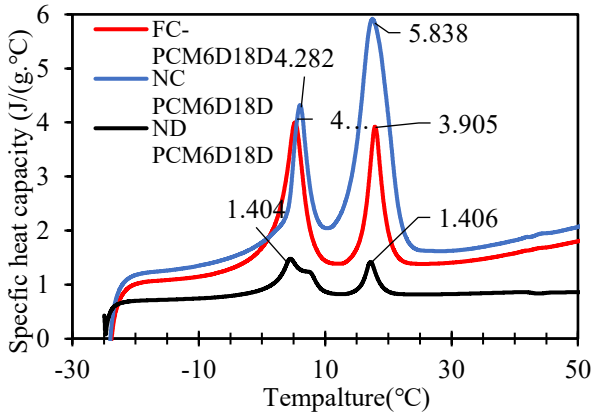


Figure 3.4.38 Comparison graphics of specific heat capacity and specific enthalpy of PCM6D18D.

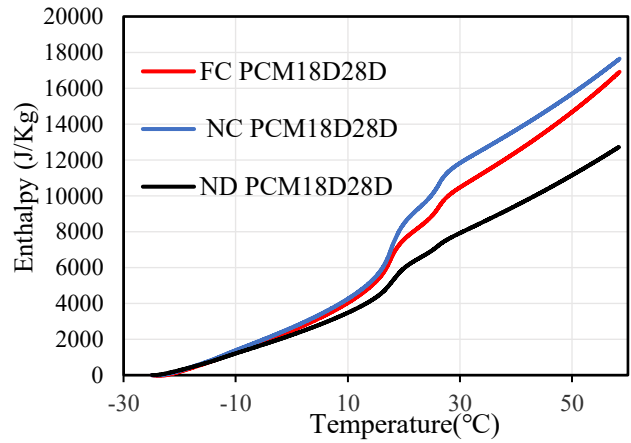
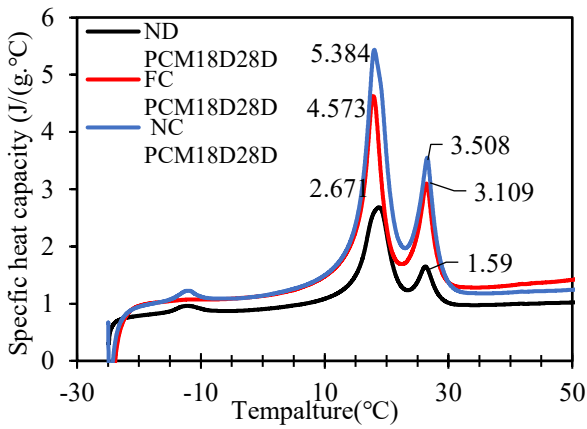


Figure 3.4.39 Comparison graphics of specific heat capacity and specific enthalpy of PCM18D28D.

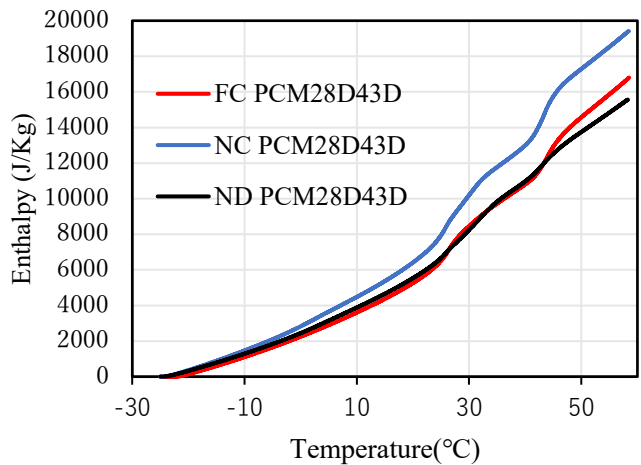
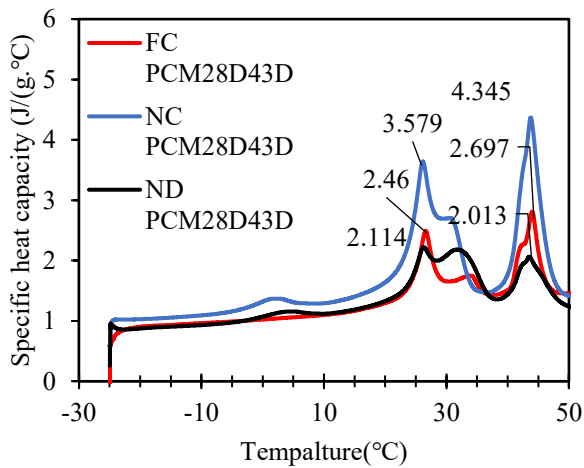


Figure 3.4.40 Comparison graphics of specific heat capacity and specific enthalpy of PCM28D43D.

### 3.4.3 Thermal conductivity test

Measurement principles and used instrument the general measurement principle is based on the one-dimensional Fourier law:

$$q = -k \frac{dt}{dx}$$

[23]

where  $q$  is heat flux ( $\text{W}/\text{m}^2$ ) flowing through the sample,  $k$  its thermal conductivity ( $\text{W m}^{-1} \text{K}^{-1}$ ) and  $dt/dx$  the temperature gradient ( $\text{K m}^{-1}$ ) on the isotherm flat surface of the sample. If a flat sample is placed between two flat isothermal plates maintained at two different temperatures, and a uniform one-dimensional temperature field has been stabilized, the heat flux in the sample should be orthogonal to the sample flat faces. As a consequence, the temperature gradient can be determined by measurements of the difference between temperatures of the hot and cold plates ( $\Delta t = t_{\text{hot}} - t_{\text{cold}}$ ) and thickness of the sample  $\Delta x$ , being in this case average temperature gradient  $dt/dx$  equal to  $\Delta t / \Delta x$ . The use instrument, exploiting these principles, is the FOX-200. It consists of the chamber and the base with keypad display section. All the electronics are housed in the base. Once the door of the chamber is opened, samples can be placed between two plates. The upper plate is stationary, whereas the lower one can move up and down by four independently controlled stepping motors. Four precise thickness readout digital sensors monitor the position of each corner of the lower plate. Each time a sample is inserted into the instrument and the stack is closed; the average thickness of the sample is determined within  $\pm 0.025$  mm accuracy.

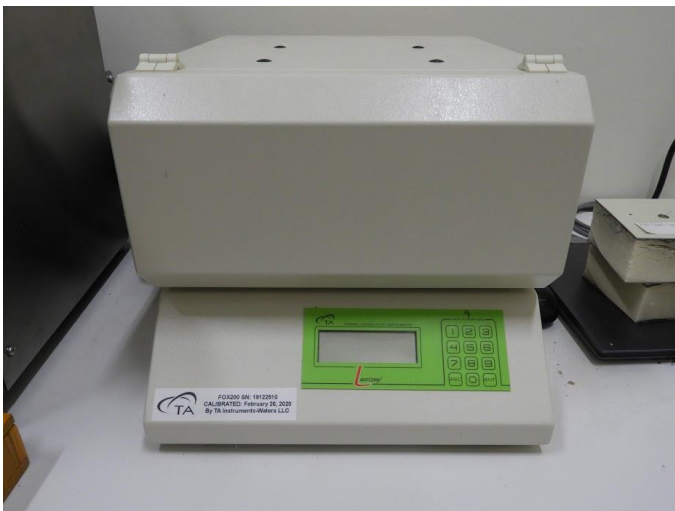


Figure 3.4.41 Thermal conductivity, FOX 200.

### 3.4.3.1 Results of thermal conductivity test

The effect of three different types of concretes with blended PCMs on thermal conductivity was measured on day 28. Figures in Figure 3.4.42 represent the thermal conductivity for FC, NC, and ND concretes, each containing blended PCMs at a 30% substitution level.

Compared to the reference concrete, the reduction percentages in thermal conductivity for the composite FC PCM6D18D, PCM18D28D, and PCM28D43D were found to be 28.5%, 39%, and 28%, respectively. Similarly, for the composite NC with PCM6D18D, PCM18D28D, and PCM28D43D, the reduction percentages in thermal conductivity compared to the reference were 39.4%, 35.1%, and 32.5%, respectively. For the composite ND with PCM6D18D, PCM18D28D, and PCM28D43D, the reduction percentages in thermal conductivity compared to the reference were 24%, 23.3%, and 21.7%, respectively.

When comparing all three types of PCM6D18D, it becomes evident that ND has thermal conductivity improved by 25% compared to FC concrete and, on average, is 21.5% higher than NC concrete. Similarly, for PCM18D28D and PCM28D43D, thermal conductivity in ND is improved by 36% and 33.2%, respectively, when compared to FC concrete, and, on average, 16.6% and 15.9% higher than NC concrete. When examining all types of FC with blended PCMs concretes and NC concretes with blended PCMs, it becomes evident that NC concretes with blended PCMs boasts, on average, a 19% higher thermal conductivity than FC concretes with blended PCMs. This is in line with the suggestion of [24] [25] who concluded that thermal conductivity increases with the higher density due to lower porosity of the sample.

Figure 3.4.42 clearly illustrates the trend that adding PCM results in a decrease in the thermal conductivity of concrete. These results indicate that enhancing the thermal conductivity of PCM composites is essential for maximizing the latent heat storage efficiency of PCMs.

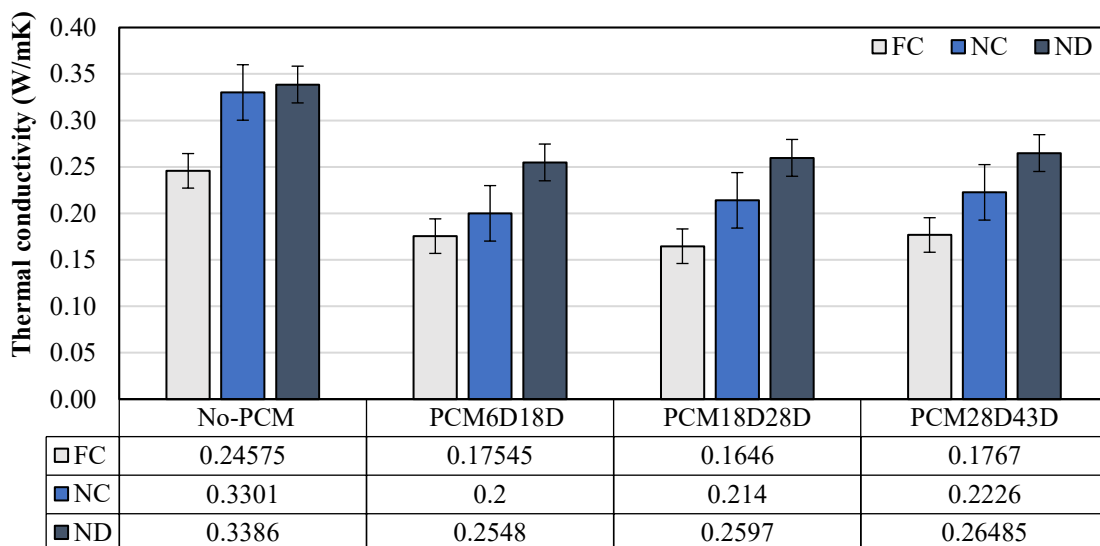


Figure 3.4.42 Thermal conductivity of different types of PCM concretes.

### 3.4.4 Heat cycles test

#### 3.4.4.1 Experimental program

The thermal cycling experiment was conducted using a specialized chamber (model ETAC dc-450) with adjustable temperature and humidity settings. Two variations of PCM foam concrete were the focus of this study. The heat cycling procedure, outlined in Figure 3.4.35, encompassed a 21-hour cycle. During each cycle, the chamber temperature remained at 10°C for a 4-hour period, achieved at a gradual rate of 2.5°C per minute. Subsequently, the temperature was raised from 10°C to 50°C in 20 minutes and maintained at 50°C for 8 hours. Afterward, the temperature was lowered back to 10°C in 20 minutes and sustained at that level for 8 hours.

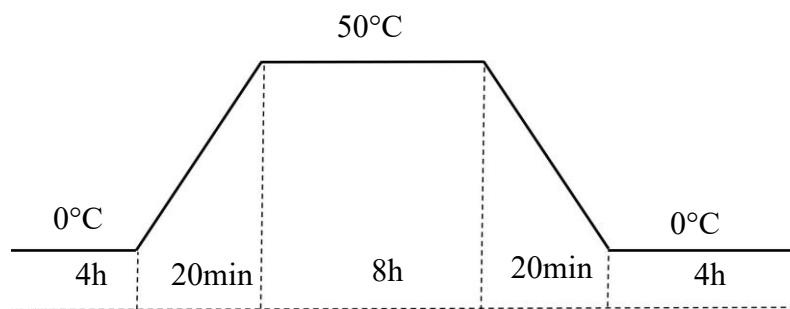


Figure 3.4.43 Heat cycling program.

#### 3.4.4.2 Preparing the specimens for heat cycling test

To evaluate the impact of PCM foam concrete when employed as a building wall material, two enclosed prototypes were constructed at a laboratory scale. The initial prototype was structured in the following sequence, from interior to exterior: a 20mm thick layer of PCM foam concrete for 200x200x20mm specimens, accompanied by a 50mm thick layer of extruded polystyrene foam for 300x300x50mm dimensions. Within this prototype setup, a total of three thermocouples were employed. One thermocouple was positioned on the backside side of the sample, another was placed on the surface, and a third was inserted in the middle of the prototype box. The mid-specimen thermocouples were utilized to facilitate comparisons with the various sides of the thermocouples.



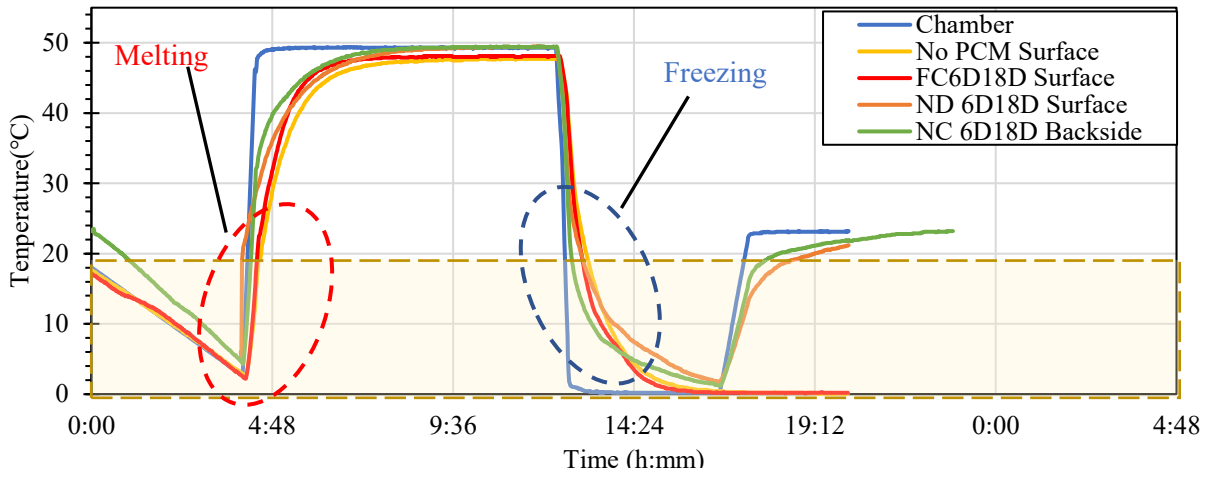


Figure 3.4.44 Heat cyclic analysis of different types of PCM6D18D on the surface side of prototype.

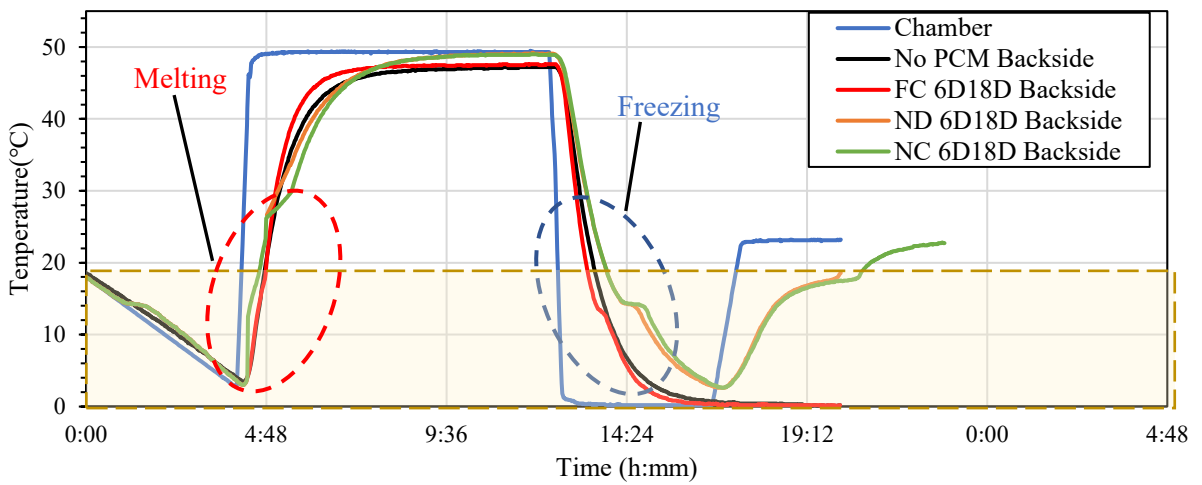


Figure 3.4.45 Heat cyclic analysis of different types of PCM6D18D on the backside of prototype.

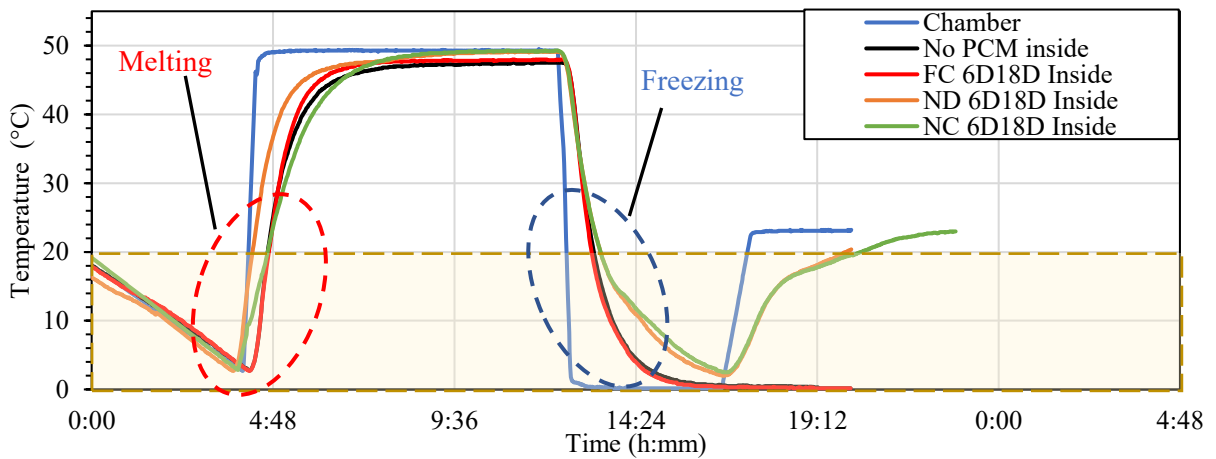


Figure 3.4.46 Heat cyclic analysis of different types of PCM6D18D on the inside of prototype.

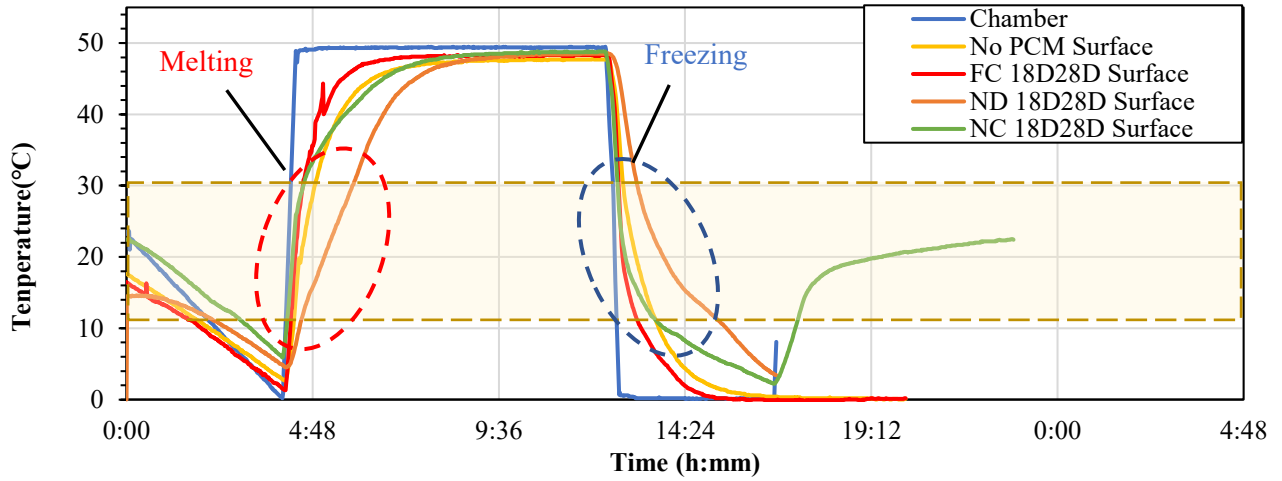


Figure 3.4.47 Heat cyclic analysis of different types of PCM18D28D on the surface side of prototype.

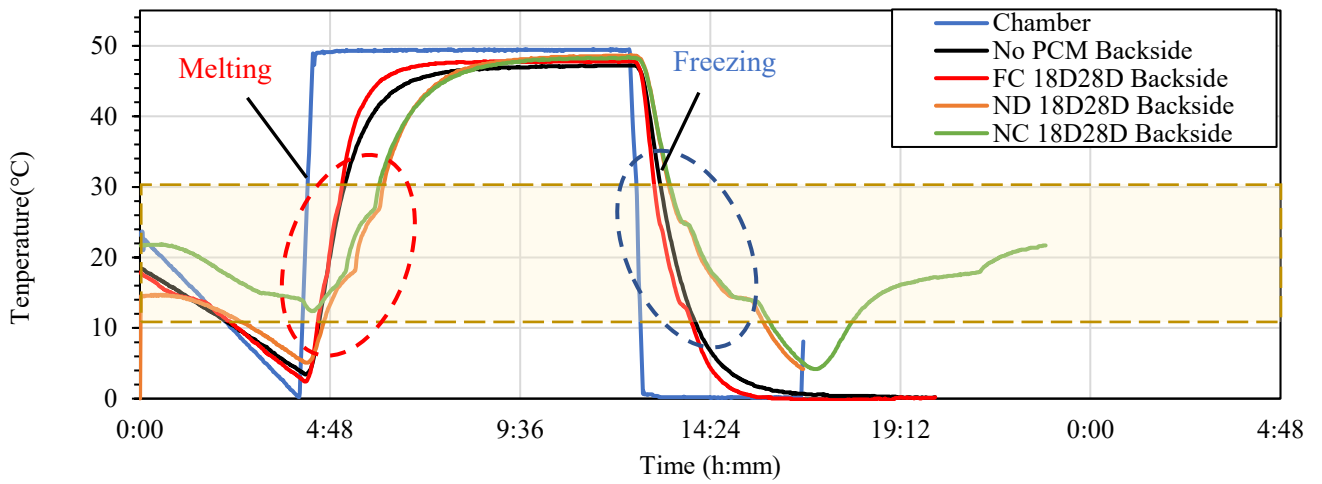


Figure 3.4.48 Heat cyclic analysis of different types of PCM18D28D on the backside of prototype.

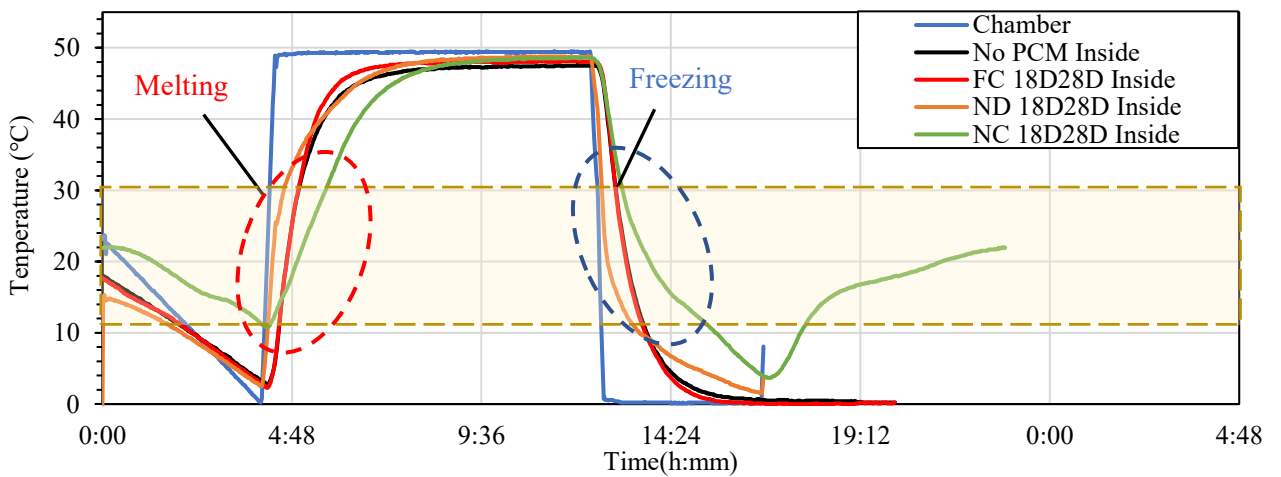


Figure 3.4.49 Heat cyclic analysis of different types of PCM18D28D on the inside of prototype.

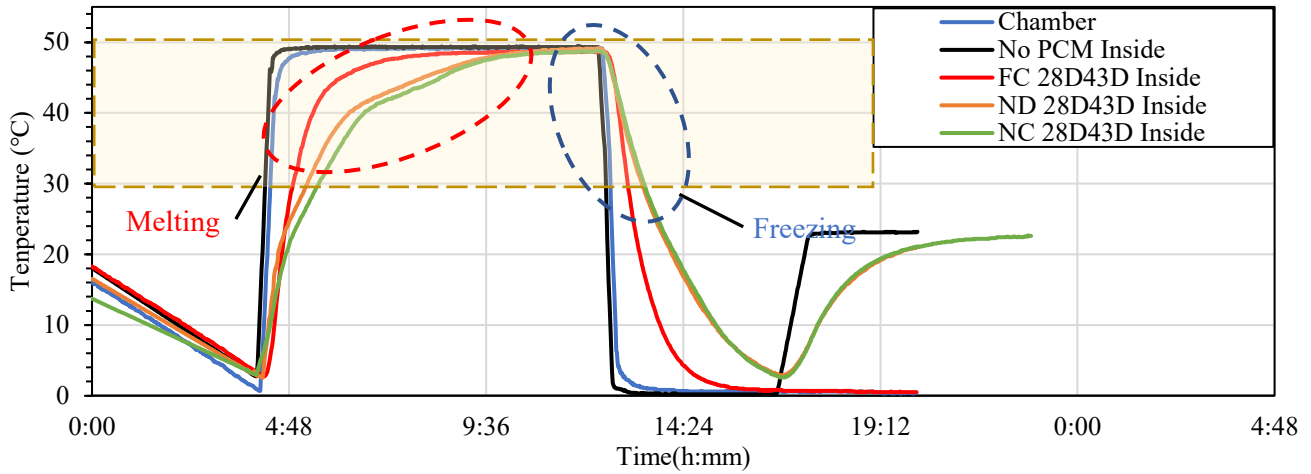


Figure 3.4.50 Heat cyclic analysis of different types of PCM28D43D on the surface side of prototype.

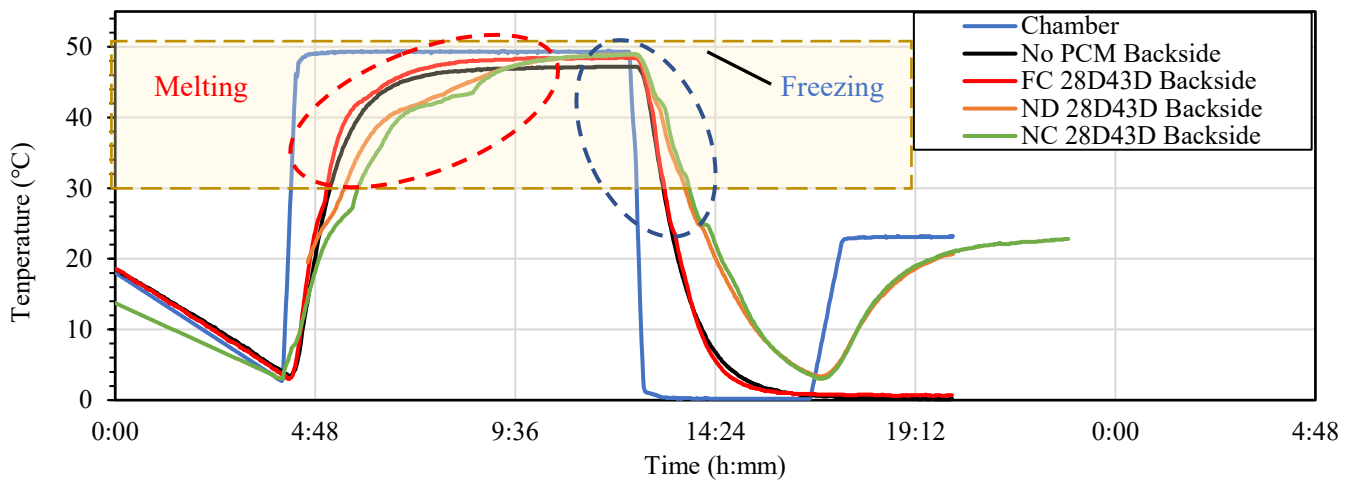


Figure 3.4.51 Heat cyclic analysis of different types of PCM28D43D on the backside of prototype.

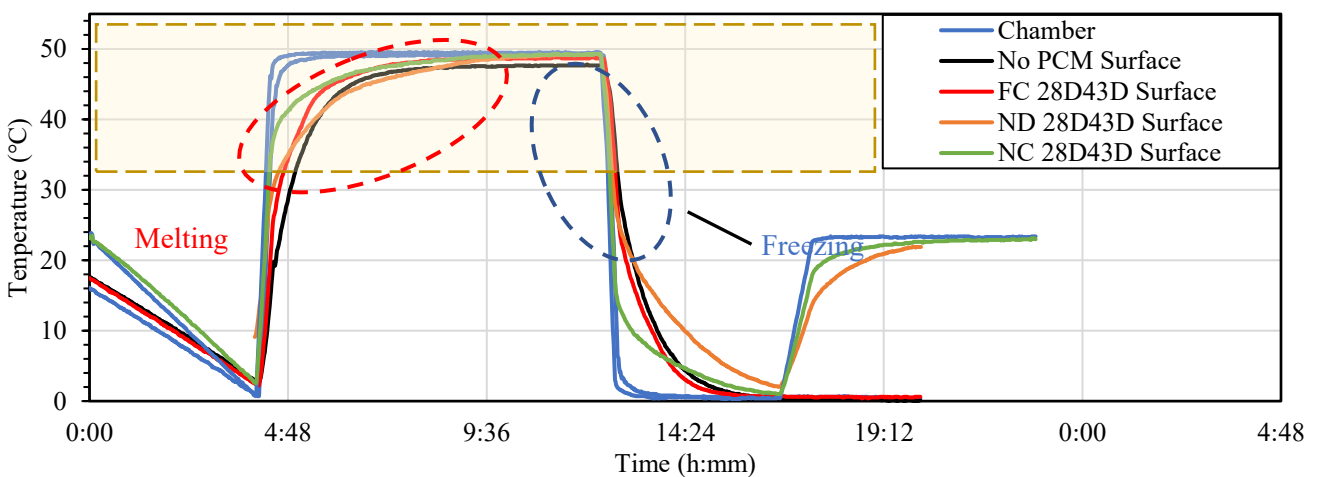


Figure 3.4.52 Heat cyclic analysis of different types of PCM28D43D on the inside side of prototype.

### 3.4.5 Results of heat cyclic analysis

The thermal performance of three types of concrete panels blended with various proportions of PCMs was assessed by analyzing temperature changes. Temperature measurements were taken at the surface, backside of the foam concrete, and the center of the prototype test room. The heat cycling conditions consisted of 24-hour cycles, with heating and cooling rates lasting for 8 hours at 2.5°C per minute. The temperature range during the heat cycling ranged between 10°C and 50°C, chosen based on the melting and freezing ranges of the two types of PCMs.

(Melting and Freezing Range: 0°C - 30°C):

Figure 3.4.44- 3.4.46 shows heat cyclic analysis of different types of concrete with PCM6D18D. The surface temperature of all samples increased dramatically up to 40°C at the beginning of the heating process, gradually reaching 50°C in about 3 hours. Meanwhile, the backside of the foam concrete panel showed a melting process, maintaining the temperature for approximately 10 minutes within the 0-30°C range. Notably, NC exhibited a clear melting curve compared to the other samples. Subsequently, the temperature of all the samples gradually increased up to 50°C. However, No-PCM, FC 6D18D, and ND6D18D experienced a more dramatic increase. Inside the prototype, the behavior was similar to No-PCM during the heating process. On the contrary, during the cooling process, the surface temperature dropped dramatically from 50°C to 20°C. Over the following 3 hours, the temperature gradually decreased to 15°C. On the backside of the foam concrete panel, all the concretes initiated freezing and began releasing heat when the temperature reached the 0-30°C range. Both NC and ND showed a similar temperature delay of around 1 hour and 30 minutes, while FC and No-PCM displayed a similar trend. Inside the prototype, NC and ND exhibited a temperature delay of around 2 hours during the cooling process.

PCM18D28D (Melting and Freezing Range: 10°C - 30°C):

Figure 3.4.47 to 3.4.49 show heat cyclic analysis of different types of concrete with PCM18D28D. The surface temperature of all the sample panels increased dramatically up to 40°C at the beginning of the heating process. A delay of about 1 hour was observed for ND compared to other samples. Subsequently, the temperature gradually increased up to 50°C in about 3 hours. On the backside of the panels, as the temperature increased from 10°C to 30°C, NC and ND began to melt and absorb heat, showing a delay of approximately 1 hour compared to No-PCM and FC. After completing the melting process, the temperature gradually increased up to 47°C in about 7 hours. Inside the prototype, as the temperature increased from 10°C to 30°C, NC began to melt and absorb heat, maintaining the room temperature for around 10 minutes. Other sample panels followed a similar trend to No-PCM. After the melting process, the temperature gradually increased to 50°C in about 3 hours. Contrarily, during the cooling process, the surface temperature dropped dramatically from 50°C to 30°C. Over the following 3 hours, the temperature gradually decreased to 10°C. On the backside of the foam concrete panel, as the temperature fell from 30°C to 10°C, all sample panels initiated freezing and

releasing heat. The temperature was delayed for approximately 2 hours compared to No-PCM, which decreased more rapidly. Although FC exhibited a heat release curve, it was relatively small, similar to No-PCM. Inside the prototype, there was a noticeable temperature difference between No-PCM and PCM28D-30%. The room temperature was maintained for around 1 hour and 30 minutes during the cooling process compared to No-PCM and FC.

PCM28D43D (Melting and Freezing Range: 30°C - 50°C):

Fig 3.4.50- 3.4.52 showed heat cyclic analysis of different types of concrete with PCM28D43D. The surface temperature of all sample panels increased dramatically up to 40°C at the beginning of the heating process, gradually reaching 50°C in about 3 hours. In contrast, No-PCM maintained a steady temperature up to 50°C. Heat was transferred to the backside of the foam concrete panel, where, as the temperature increased from 20°C to 50°C, NC and ND began to melt and absorb heat, causing a delay of approximately 4 hours. However, their temperature increased dramatically compared to No-PCM and FC. Inside the prototype, the room temperature was maintained for 3 hours and 30 minutes within the specified range. FC's temperature exhibited the highest values throughout the heating process. Conversely, during the cooling process, the surface temperature dropped dramatically from 50°C to 40°C. Over the following 3 hours, the temperature gradually decreased to 10°C, while the decrease rate in the temperature of all sample panels remained steady up to 10°C. On the backside of the foam concrete panel, as the temperature fell from 50°C to 20°C, NC and ND initiated freezing and began releasing heat. The temperature was maintained for about 68 minutes within the phase-changing range. After that, the temperature gradually decreased and reached 10°C after around 4 hours, while No-PCM decreased more rapidly. Inside the prototype, both NC and ND were effective in maintaining temperature within the phase-changing range. The temperature decreases observed in both FC and No-PCM followed a similar trend.

In conclusion, the findings suggest the potential of PCMs to enhance thermal performance in certain applications. Regarding the inside of the prototype, both types of NC and ND, except FC, were effective in maintaining temperature within the phase-changing range. However, on the surface side of the prototypes, the temperature of both types of PCM increased dramatically, although it was expected to reduce excessive temperatures. Furthermore, some differences were observed. Although FC exhibited a higher energy heat storage capacity than ND based on DSC analysis, the heat cyclic analysis showed the lowest result. This indicates that thermal conductivity plays a significant role in heat transfer. Both factors, thermal conductivity, and energy storage capacity, should be considered to enhance energy storage capacity. In the case of blended PCMs, it might be suitable to increase the melting and freezing temperature range.

### 3.5 CONCLUSIONS

This chapter focused on addressing the specific question of how to enhance energy storage capacity (TES) of concrete. Three different types of concretes with blended PCM have been studied to evaluate mechanical aspect and thermal characterization. It can be divided into 5 sections.

The initial section deals mechanical aspect including compressive strength of different types of concretes with blended PCMs. Regarding density test, that the addition of PCMs has a significant impact on the density of ND and NC concretes, resulting in a substantial reduction at the 3-day. However, FC concrete, due to its unique composition, does not exhibit a similar reduction in density after PCM inclusion. Regarding compressive strength result, the incorporation of blended PCMs into concrete had a noticeable impact on compressive strength in all three types of concrete (ND, NC, and FC). Although there was an initial decrease in strength when PCMs were introduced, all three types of concrete demonstrated significant improvements in compressive strength from day 7 to day 28.

Second section deals with specific enthalpy estimation and phase change temperature for blended PCM concretes. The influence of different heating/cooling rates on the thermal behavior of the blended PCMs has been analyzed, namely with regard to the specific enthalpy on the DSC, as well as on the specific heat capacity calculated. Moreover, the impact of the heating/cooling rate on thermal behavior of the different types of concrete thermal response with PCM was analyzed. Comparing all types of blended PCMs concretes, NC had the highest  $\Delta h$  of 16.81 J/g and 17.03 J/g for the first and second peaks, respectively. When comparing all three types concrete at various heating and cooling rates, it becomes evident that NC has, on average, a 34% higher latent heat capacity than FC concrete and, on average, a 43% higher capacity than ND concrete. Regarding specific heat capacity and specific enthalpy, it becomes evident that NC has, on average, a 25% higher specific heat capacity than FC concrete and, on average, a 73% higher capacity than ND concrete. Regarding specific enthalpy, NC exhibits a value almost identical to FC concrete, but it is also, on average, 47% higher than ND concrete.

The third section deals with the thermal conductivity test. The reducing trend of thermal conductivity with the increasing substitution PCM composite attributes to the low thermal conductivity from PCM6D18D to PCM28D43D composites (in the range of 0.16-0.33 W/m.K). When comparing all three types of PCM6D18D, it becomes evident that ND has thermal conductivity improved by 25% compared to FC concrete and, on average, is 21.5% higher than NC concrete. Similarly, for PCM18D28D and PCM28D43D, thermal conductivity in ND is improved by 36% and 33.2%, respectively, when compared to FC concrete, and, on average, 16.6% and 15.9% higher than NC concrete. When examining all types of FC with blended PCMs concretes and NC concretes with blended PCMs, it becomes evident that NC concretes with blended PCMs boasts, on average, a 19% higher thermal conductivity than FC concretes with blended PCMs.

These results indicate that enhancing the thermal conductivity of PCM composites is essential for maximizing the latent heat storage efficiency of PCMs.

The fourth section is about the heat cycle test. In order to assess the effect of PCM foam concrete, prototype was built with laboratory-scale dimensions. NC and ND tended to have a delayed temperature and time between 1 hour and 3 hours. The highest maintained temperature was found at NC. The temperature was delayed for around 3 hours and 30 min.

The findings suggest the potential of PCMs to enhance thermal performance in certain applications. Regarding the inside of the prototype, both types of NC and ND, except FC, were effective in maintaining temperature within the phase-changing range. However, on the surface side of the prototypes, the temperature of both types of PCM increased dramatically, although it was expected to reduce excessive temperatures. Furthermore, some differences were observed. Although FC exhibited a higher energy heat storage capacity than ND based on DSC analysis, the heat cyclic analysis showed the lowest result. This indicates that thermal conductivity plays a significant role in heat transfer. Both factors, thermal conductivity, and energy storage capacity, should be considered to enhance energy storage capacity. In the case of blended PCMs, it might be suitable to increase the melting and freezing temperature range.

### 3.6 REFERENCES

- [1] N. Hoivik *et al.*, “Long-term performance results of concrete-based modular thermal energy storage system,” *J Energy Storage*, vol. 24, p. 100735, Aug. 2019, doi: 10.1016/J.EST.2019.04.009.
- [2] F. Bai and C. Xu, “Performance analysis of a two-stage thermal energy storage system using concrete and steam accumulator,” *Appl Therm Eng*, vol. 31, no. 14–15, pp. 2764–2771, Oct. 2011, doi: 10.1016/J.APPLTHERMALENG.2011.04.049.
- [3] K. Liu, P. Xu, F. Wang, L. You, X. Zhang, and C. Fu, “Assessment of automatic induction self-healing treatment applied to steel deck asphalt pavement,” *Autom Constr*, vol. 133, p. 104011, Jan. 2022, doi: 10.1016/J.AUTCON.2021.104011.
- [4] Q. Li, Y. Zhang, T. Guo, and J. Fan, “Development of a new method to estimate thermal performance of multilayer radiant floor,” *Journal of Building Engineering*, vol. 33, p. 101562, Jan. 2021, doi: 10.1016/J.JOBE.2020.101562.
- [5] B. Nagy, S. G. Nehme, and D. Szagri, “Thermal Properties and Modeling of Fiber Reinforced Concretes,” *Energy Procedia*, vol. 78, pp. 2742–2747, Nov. 2015, doi: 10.1016/J.EGYPRO.2015.11.616.
- [6] H. Li, Q. Zhang, and H. Xiao, “Self-deicing road system with a CNFP high-efficiency thermal source and MWCNT/cement-based high-thermal conductive composites,” *Cold Reg Sci Technol*, vol. 86, pp. 22–35, Feb. 2013, doi:

- 10.1016/J.COLDREGIONS.2012.10.007.
- [7] I. Indacoechea-Vega, P. Pascual-Muñoz, D. Castro-Fresno, and M. A. Calzada-Pérez, “Experimental characterization and performance evaluation of geothermal grouting materials subjected to heating-cooling cycles,” 2015, doi: 10.1016/j.conbuildmat.2015.08.132.
- [8] N. S. Sundarmurti and V. Rao, “Thermal Conductivity and Diffusivity of Iron Ore Pellet Having Low Porosity,” 2002.
- [9] K. Liu, Z. Wang, C. Jin, F. Wang, and X. Lu, “An experimental study on thermal conductivity of iron ore sand cement mortar,” *Constr Build Mater*, vol. 101, pp. 932–941, Dec. 2015, doi: 10.1016/J.CONBUILDMAT.2015.10.108.
- [10] B. He, V. Martin, and F. Setterwall, “Phase transition temperature ranges and storage density of paraffin wax phase change materials,” *Energy*, vol. 29, no. 11, pp. 1785–1804, 2004, doi: 10.1016/j.energy.2004.03.002.
- [11] H. Fatahi, J. Claverie, and S. Poncet, “Thermal Characterization of Phase Change Materials by Differential Scanning Calorimetry: A Review,” *Applied Sciences (Switzerland)*, vol. 12, no. 23, 2022, doi: 10.3390/app122312019.
- [12] I. Al Siyabi, S. Khanna, T. Mallick, and S. Sundaram, “Experimental and numerical study on the effect of multiple phase change materials thermal energy storage system,” *J Energy Storage*, vol. 36, p. 102226, Apr. 2021, doi: 10.1016/J.EST.2020.102226.
- [13] M. Mozafari, A. Lee, and S. Cheng, “A novel dual-PCM configuration to improve simultaneous energy storage and recovery in triplex-tube heat exchanger,” *Int J Heat Mass Transf*, vol. 186, p. 122420, May 2022, doi: 10.1016/J.IJHEATMASSTRANSFER.2021.122420.
- [14] “Microtek.” Accessed: Sep. 18, 2023. [Online]. Available: <https://www.microteklabs.com/>
- [15] “Ready-mixed concrete,” 2019.
- [16] M. Hunger, A. G. Entrop, I. Mandilaras, H. J. H. Brouwers, and M. Founti, “The behavior of self-compacting concrete containing micro-encapsulated Phase Change Materials,” *Cem Concr Compos*, vol. 31, no. 10, pp. 731–743, Nov. 2009, doi: 10.1016/J.CEMCONCOMP.2009.08.002.
- [17] M. Fenollera, J. L. Míguez, I. Goicoechea, J. Lorenzo, and M. Á. Álvarez, “The Influence of Phase Change Materials on the Properties of Self-Compacting Concrete,” *Materials 2013, Vol. 6, Pages 3530-3546*, vol. 6, no. 8, pp. 3530–3546, Aug. 2013, doi: 10.3390/MA6083530.
- [18] H. Cui, W. Liao, S. A. Memon, B. Dong, and W. Tang, “Thermophysical and mechanical properties of hardened cement paste with microencapsulated phase change materials for energy storage,” *Materials*, vol. 7, no. 12, pp. 8070–8087, 2014, doi: 10.3390/ma7128070.



- [19] M. Fenollera, J. L. Míguez, I. Goicoechea, J. Lorenzo, and M. Á. Álvarez, “The Influence of Phase Change Materials on the Properties of Self-Compacting Concrete,” *Materials* 2013, Vol. 6, Pages 3530-3546, vol. 6, no. 8, pp. 3530–3546, Aug. 2013, doi: 10.3390/MA6083530.
- [20] Z. Andrásy and Z. Szánthó, “Thermal behaviour of materials in interrupted phase change,” *J Therm Anal Calorim*, vol. 138, no. 6, pp. 3915–3924, Dec. 2019, doi: 10.1007/s10973-019-08541-w.
- [21] B. He, V. Martin, and F. Setterwall, “Phase transition temperature ranges and storage density of paraffin wax phase change materials,” *Energy*, vol. 29, no. 11, pp. 1785–1804, 2004, doi: 10.1016/j.energy.2004.03.002.
- [22] H. Fatahi, J. Claverie, and S. Poncet, “Thermal Characterization of Phase Change Materials by Differential Scanning Calorimetry: A Review,” *Applied Sciences (Switzerland)*, vol. 12, no. 23, 2022, doi: 10.3390/app122312019.
- [23] R. Rajagopal, “Fourier’s Law of Heat Conduction,” 2007.
- [24] X. Huang, C. Zhu, Y. Lin, and G. Fang, “Thermal properties and applications of microencapsulated PCM for thermal energy storage: A review,” *Applied Thermal Engineering*, vol. 147. Elsevier Ltd, pp. 841–855, Jan. 25, 2019. doi: 10.1016/j.applthermaleng.2018.11.007.
- [25] Z. Zhang, G. Shi, S. Wang, X. Fang, and X. Liu, “Thermal energy storage cement mortar containing n-octadecane/expanded graphite composite phase change material,” 2012, doi: 10.1016/j.renene.2012.08.024.

**CHAPTER 4**  
**APPLICATION OF PCM TO PRECAST**  
**CONCRETE WALL PANELS**

## 4.1 EXPERIMENTAL OVERVIEW

This chapter is dedicated to finding solutions to reduce excessive heat in precast concrete wall panels and to enhance their overall quality and durability. The initial section investigates mechanical aspects, including the compressive strength of polymer-modified concrete with various phase change materials (PCMs). The second section is dedicated to estimating specific enthalpy and specific heat capacity for PCM polymer-modified concretes. The third section delves into heat cyclic analysis, including thermal expansion analysis for all types of PCM concrete, which are crucial parameters for thermal characterization. The final section provides the conclusion of the chapter, summarizing the key findings and insights.

## 4.2 RESEARCH BACKGROUND

This research delves into a collaborative effort undertaken with a precast concrete factory specializing in the production of PC precast concrete wall panels with attached tiles. Traditionally, the tile attachment process in the factory was a manual and time-consuming task. In an effort to improve factory efficiency, a new method was sought, which involved installing the tiles during the concrete casting process. However, this transition gave rise to specific challenges.

Reports emerged of external noise disturbances and the development of cracks in the outer walls of the structures, issues believed to be triggered by fluctuations in external temperatures and solar radiation as shown in Figure 4.2.1. The root cause of these problems appears to be the stress resulting from differences in expansion rates among the tiles, the exterior wall materials, and the foundational structure.

The core focus of this research is to address a significant issue prevalent in housing complexes that employ the exterior heat-insulated precast concrete construction method. The objective is to develop solutions that mitigate these problems and enhance the overall quality and durability of such construction.

Manufacturing status		Crack occurrence status		Bonding strength	Standard	Others
Tile installation in factory	Concrete pouring ○	Crack ×	×	98.3 ×	0.20N/mm <sup>2</sup> (0.4N/mm <sup>2</sup> )	×
	Laying insulation material △			98.5 ○	0.31N/mm <sup>2</sup> (0.2N/mm <sup>2</sup> )	×
Tile installation on site	Laying insulation material ○	No crack ○	○	98.4 ○	0.22N/mm <sup>2</sup> (0.2N/mm <sup>2</sup> )	○
	Tile installation on site ○			98.5 ○	0.28N/mm <sup>2</sup> (0.2N/mm <sup>2</sup> )	○

Figure 4.2.1 A view of PC walls with tiles bonded on site and in factory.

In order to address the issues identified, the precast concrete factory established precise criteria, which included the following:

- 1. Adhesion Strength and Durability:** Tiles or concrete used should possess an adhesion strength exceeding 0.4 MPa and exhibit durability for a minimum of 60 years.
- 2. Flow Value:** The flow value of the materials should be approximately 50 cm.
- 3. PCM Integrity:** The PCM should remain intact during the mixing process.
- 4. Temperature Reduction:** The temperature rises of the frame due to solar radiation should be reduced by half by applying PCM (Phase Change Material) concrete to the exterior side of the gable wall.
- 5. Crack Prevention:** Even when tiles and PCM concrete are cast on the precast concrete board simultaneously, they should not develop cracks. To tackle the challenges, we recommended the use of polymer-modified concrete, emphasizing several advantages associated with this choice.

To meet these specific requirements, our focus centered on two main factors. First one is to enhancing adhesion strength and other mechanical properties. The exploration of suitable materials led to the selection of polymer-modified concrete, known for its ability to improve material properties such as strength; tensile, flexural, bonding strength, adhesive forces [1], [2], [3], [4], and durability such as; water resistance, chemical resistance, freeze-thaw resistance [2], [5], [6]. This is due to the fact that polymers play a role in filling capillary pores, thereby decreasing permeability and improving mechanical properties and durability [7]. For instance, Ohama et al. [8] found almost ten times higher adhesion strength in polymer-modified mortar with ratio of 20% compared to unmodified mortar. Our choice of polymer-modified mortar was informed by its proven capabilities and the findings from the literature review.

Secondly, the study explores the integration of Phase Change Materials (PCMs) into polymer-modified concrete, expecting to reduce excessive temperature in the external wall. In general, researchers have primarily focused on applying PCMs in inner parts of wall to maintain human comfort temperature [9], [10], [11], [12]. In contrast, there are few researchers who have studied to applying PCMs on the walls' exterior surfaces showed better results. In such cases, PCM layers work more as thermal insulation, effectively reducing heat gain from outdoor environment, particularly in summer or in warmer climates [13], [14], [15], [16]. For instance, a thermal analysis in study [17] examined building bricks with PCM for use in hot weather conditions, utilizing PCMs with a melting point of 47°C. The results of these studies suggest that PCM with higher melting point could be found beneficial in external wall.

Based on the discussion above, our research involves both improving mechanical properties through polymer-modified concrete and the exploration of PCMs integration in polymer modified concrete to address temperature control of the exterior wall.

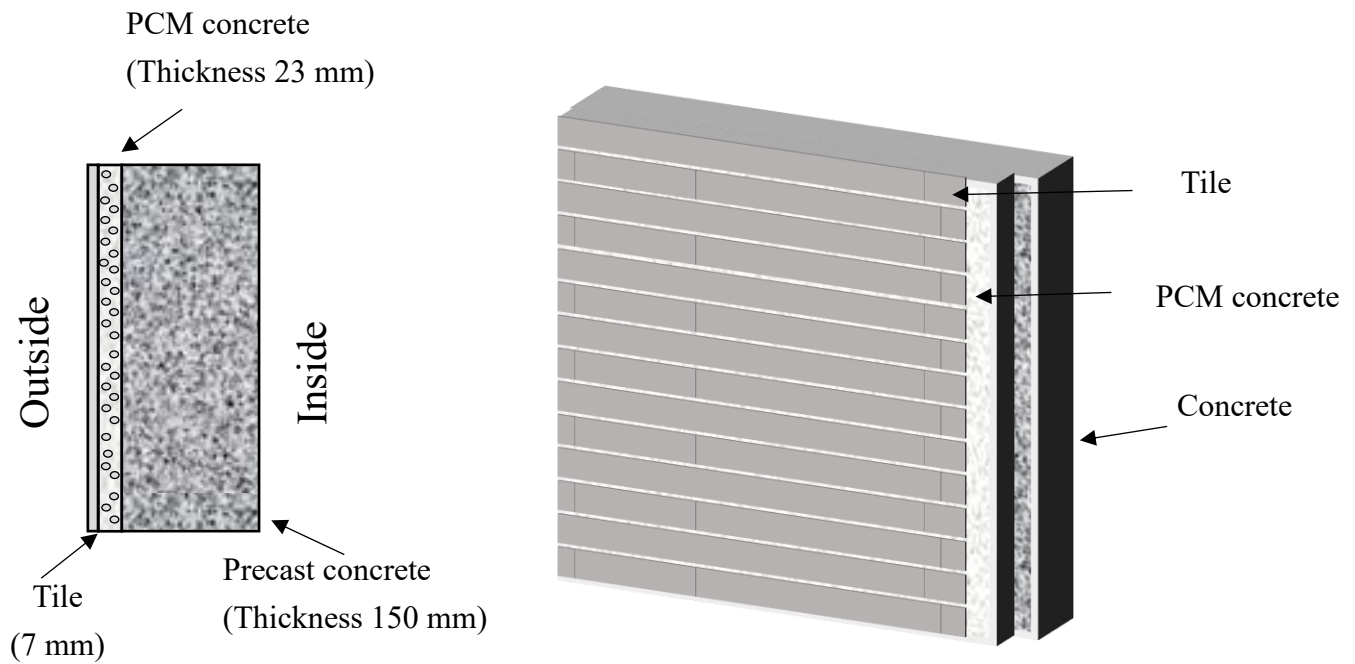


Figure 4.2.2 Way of applying PCM into precast concrete wall panels.

### 4.3 MATERIAL PROPERTIES

#### 4.3.1 Microencapsulated PCMs

Four types of encapsulated PCMs are studied. These included 6D, 18D, 28D and 43D. All encapsulated PCMs are micro-encapsulated free wax:  $\leq 2.5\%$  PCM and solid content: 97.0-100.0. Additionally, these four types of encapsulated PCMs were mixed with each other to create three different combinations: PCM6D18D, PCM18D28D, and PCM28D43D. The sizes of these PCM particles were provided by the manufacturers [18] and were also determined through microscopic analysis using optical microscopy. Their sizes were provided by the manufacturers and were determined as well by using optical microscopy (Table 4-1).

Table 4-1 Thermo physical properties of various microencapsulated PCMs.

Material	Nature	Size ( $\mu\text{m}$ )	Melting ( $^{\circ}\text{C}$ )	Heat of Fusion (J/g)	Solid Content %
PCM6D	Dry	15.0–30.0	4 to 8	181	97.0–100.0
PCM18D	Dry	15.0–30.0	16 to 20	215	97.0–100.0
PCM28D	Dry	15.0–30.0	26 to 30	189	97.0–100.0
PCM43D	Dry	15.0–30.0	41 to 45	235	97.0–100.0

### 4.3.2 Fine aggregate

Silica sand as fine aggregate obtained on the market with dry silica sand No.5 was used in this study. The specific gravity and density of fine aggregate were 2.62 and 1.56. Table 4-3 and Table 4-4 shows chemical composition of silica sand.

Table 4-2 Chemical composition of silica sand (No.5).

	<b>SiO<sub>2</sub></b>	<b>Al<sub>2</sub>O<sub>3</sub></b>	<b>Fe<sub>2</sub>O<sub>3</sub></b>	<b>CaO</b>	<b>Na<sub>2</sub>O</b>	<b>K<sub>2</sub>O</b>	<b>TiO<sub>2</sub></b>	<b>LOI</b>
%	95.43	2.62	0.09	0.49	1.5	77.1	2.26	2.10

Table 4-3 Physical properties of silica sand (No.5).

<b>pH</b>	<b>Bulk specific gravity (g/cm<sup>3</sup>)</b>	<b>True specific gravity (g/cm<sup>3</sup>)</b>	<b>Water Absorption (%)</b>	<b>Amount of chloride (%)</b>
6.1	1.53	2.63	0.57	0.001

### 4.3.3 Polymer materials

A total of five polymer types were selected, including one polymer type was chosen from styrene-butadiene rubber latex (SBR): 1. Tomax Super, and one from ethylene-vinyl acetate (EVA): 2. NS Hi-flex. Additionally, three from aqueous styrene-acrylic ester copolymer emulsions (PAE) (Figure 4.3.1): 3. PAE 6880, 4. PAE-LDM 7000, and 5. PAE-7700 Powder LDM 7000P. The selection process was based on the comprehensive evaluation of various factors, including water-cement ratio, compressive strength, bending strength, and density tests conducted during casting, all at a target flow value of 170±10 cm. The test results for each polymer type are presented below, with each sample containing a specific Phase Change Material (PCM).



Figure 4.3.1 Different types of polymers.

#### 4.4 MIX DESIGN OF TRIAL TESTS

In this research, a trial test was carried out using five different types of polymers with PCM. A total of 40 distinct mix compositions were created to identify the optimal polymer cement ratio and water cement ratio, ensuring proper adhesion to the tiles, setting speed, flowability, and the required strength.

The polymer-modified concrete employed consisted of early strength Portland cement, and fine aggregate was provided by natural dry silica sand No. 5. Silica fume was introduced to achieve the necessary strength. The mix designs can be observed in Table 4-5 and Table 4-6. As the non-volatile components of the polymers used were approximately 50%, both the solid and liquid components of the polymers were incorporated into the water and cement calculations. The weights of silica fume and PCM were determined through cement weight substitution and were deducted from the cement quantity.

Table 4-4 Mix design of polymer-modified concrete with PCMs.

<b>Mix Designation</b>	<b>Polymer-Cement Ratio (%)</b>	<b>Water Cement Ratio (%)</b>	<b>Cement (kg/m<sup>3</sup>)</b>	<b>Sand (kg/m<sup>3</sup>)</b>	<b>PCM -30% (kg)</b>	<b>SF -5% (kg)</b>
<b>SBR-Modified</b>	0	0.5	1350	1457		71.1
	5	0.45	1350	1457		71.1
	10	0.6	1350	1457		71.1
	20	0.35	1350	1457		71.1
	0	0.5	924	1457	426	71.1
	5	0.8	924	1457	426	71.1
	10	0.8	924	1457	426	71.1
	20	0.85	924	1457	426	71.1
<b>EVA-Modified</b>	0	0.5	1350	1457		71.1
	5	0.45	1350	1457		71.1
	10	0.4	1350	1457		71.1
	20	0.35	1350	1457		71.1
	0	0.92	924	1457	426	71.1
	5	0.85	924	1457	426	71.1
	10	0.75	924	1457	426	71.1
	20	0.6	924	1457	426	71.1

Table 4-5 Mix design of polymer-modified concrete with PCMs.

<b>Mix Designation</b>	<b>Polymer-Cement Ratio (%)</b>	<b>Water-Cement Ratio (%)</b>	<b>Cement (kg/m<sup>3</sup>)</b>	<b>Sand (kg/m<sup>3</sup>)</b>	<b>PCM -30% (kg)</b>	<b>SF -5% (kg)</b>
<b>PAE-68-Modified</b>	0	0.5	1350	1457		71.1
	5	0.55	1350	1457		71.1
	10	0.4	1350	1457		71.1
	20	0.35	1350	1457		71.1
	0	0.92	924	1457	426	71.1
	5	0.9	924	1457	426	71.1
	10	0.8	924	1457	426	71.1
	20	0.7	924	1457	426	71.1
<b>PAE-77-Modified</b>	0	0.5	1350	1457		71.1
	5	0.45	1350	1457		71.1
	10	0.37	1350	1457		71.1
	20	0.35	1350	1457		71.1
	0	0.92	924	1457	426	71.1
	5	0.85	924	1457	426	71.1
	10	0.72	924	1457	426	71.1
	20	0.8	924	1457	426	71.1
<b>Powder-Modified</b>	0	0.5	1350	1457		71.1
	5	0.45	1350	1457		71.1
	10	0.4	1350	1457		71.1
	20	0.37	1350	1457		71.1
	0	0.7	924	1457	426	71.1
	5	0.9	924	1457	426	71.1
	10	0.85	924	1457	426	71.1
	20	0.8	924	1457	426	71.1



#### **4.4.1 Relation between polymer-cement ratio and flow test of different types of polymer-modified concretes**

Tests were conducted in accordance with JIS A1173 [19] to measure slump of polymer modified mortar. According to Ohama et al. [20] is suggested that flow test of polymer-modified concrete should be over 171 mm. After conducting series of experiment repeatedly. We managed to keep flow of the mortar between 171 and 250. It can be seen Figure 4.4.1, the flow values for the various polymers, whether with or without PCM, were close to the specified value of  $170 \pm 10$  mm. However, for samples with PCM, adjusting the moisture content of the concrete proved challenging. For SBR and PAE7700, the flow values exceeded 200 mm, significantly surpassing the  $170 \pm 10$  mm target set for the condition.

#### **4.4.2 Relation between polymer-cement ratio and water cement ratio of different types of polymer-modified concretes**

Regarding the water-cement ratio, it was consistently approximately 40% higher for all polymers when PCM was present, compared to the water-cement ratio for polymers without PCM as shown in Figure 4.4.2. As a general pattern, a higher polymer content led to a lower water-cement ratio. Specifically, for all polymers, concretes with a 20% polymer-cement ratio and PCM had a water-cement ratio of about 80%, whereas concretes without PCM maintained a water-cement ratio of approximately 40%.

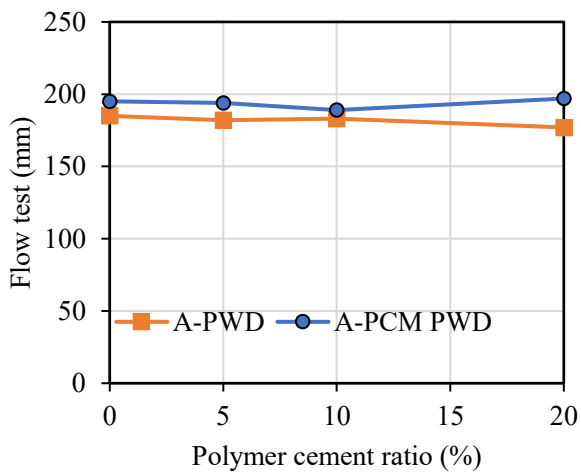
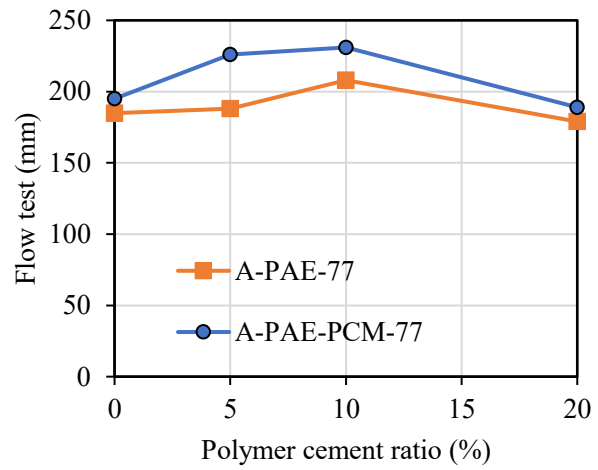
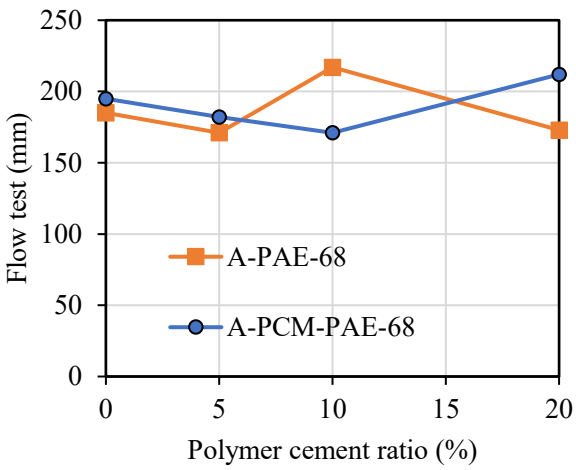
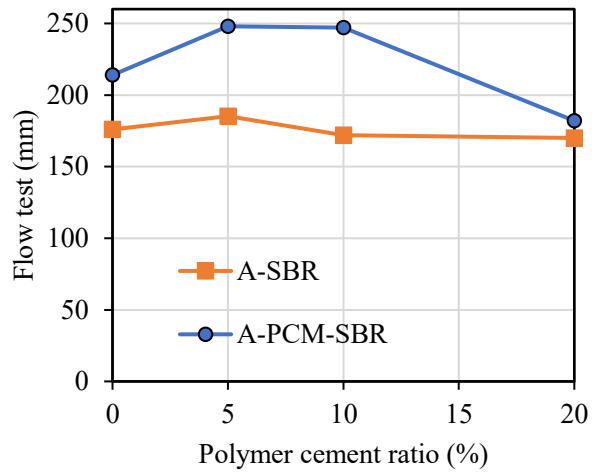
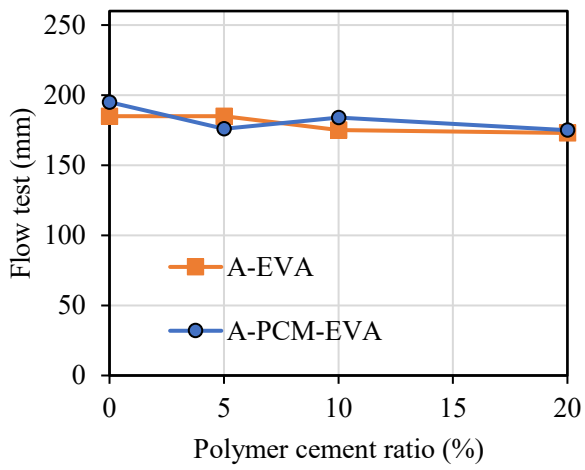


Figure 4.4.1 Relation between polymer-cement ratio and flow test of different types of polymers modified concretes.

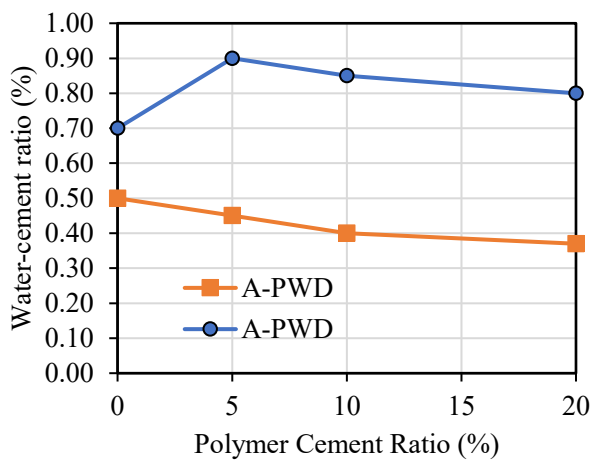
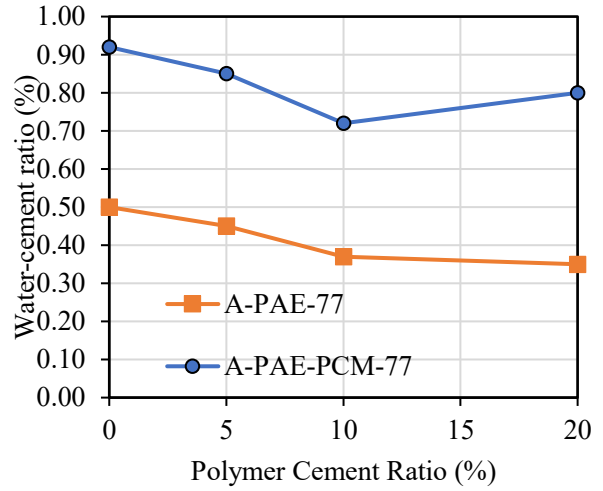
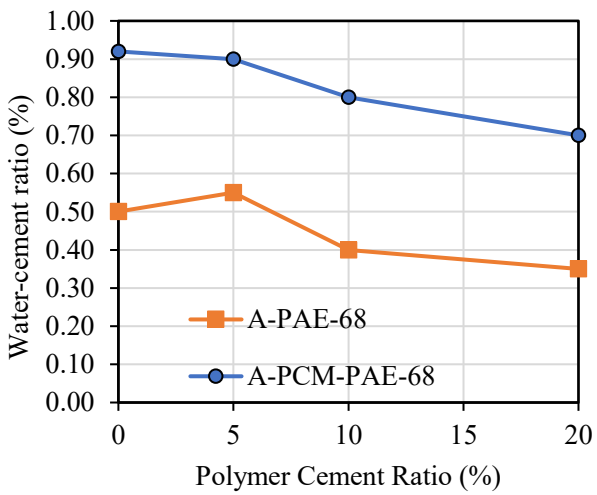
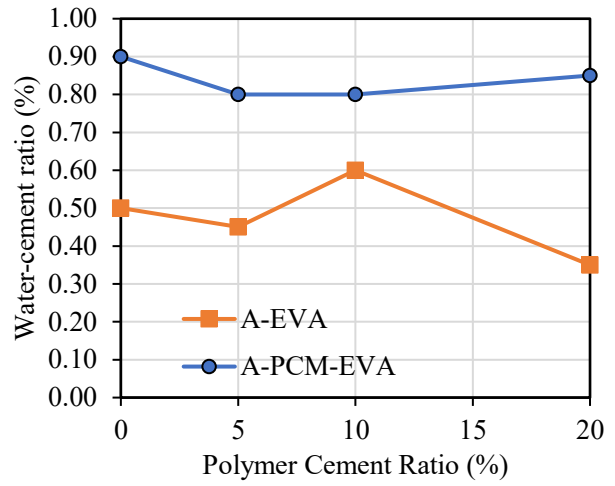
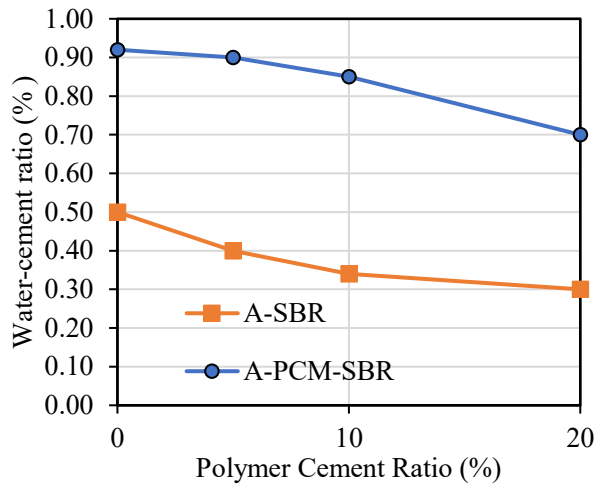


Figure 4.4.2 Relation between polymer-cement ratio and water cement ratio of different types of polymers modified concretes.

#### 4.4.3 Compressive strength tests on different types of polymers modified concretes

Tests were conducted in accordance with JIS A1172 [21] to measure strength of polymer modified mortar. The compressive strength test results highlight noteworthy variations between curing conditions in an autoclave and an environmental chamber, both with and without the presence of PCM, particularly after 1 day of curing (Figure 4.4.3- 4.4.4).

For the samples without PCM, it's evident that the compressive strength generally showed higher values when cured in the autoclave compared to the environmental chamber (Figure 4.4.3). In the autoclave curing, PAE-6880 displayed the highest strength, and its strength consistently increased with the addition of polymers, ultimately reaching the level of 20 MPa at a polymer-cement ratio of 20%. Interestingly, PAE-6880 exhibited similar behavior when cured in the environmental chamber, maintaining its compressive strength at a comparable level to the autoclave-cured samples.

In contrast, the samples with PCMs showed a dramatic reduction in compressive strength with the addition of PCMs (Figure 4.4.4). This reduction was approximately 75% compared to the samples without PCM. In the case of autoclave curing with PCM samples, only PAE-6880 and EVA demonstrated the highest compressive strength, achieving approximately 6 MPa at a polymer-cement ratio of 20%. However, in the case of environmental chamber curing, the strength of PAE-7700 and PAE-6880 increased with a higher polymer content.

Overall, both concretes containing PCM and those without PCM had higher compressive strength values when cured in the autoclave compared to the environmental chamber. Additionally, the compressive strength was consistently higher for all test samples.

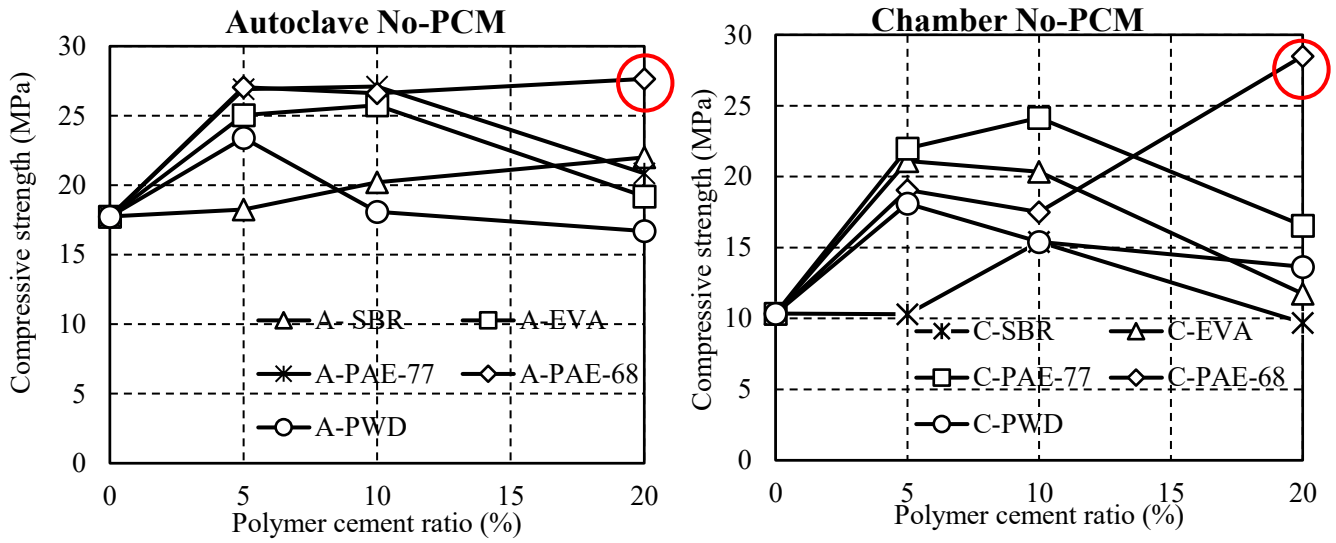


Figure 4.4.3 Effects of polymer cement ratio and different curing conditions on compressive strength test of samples without PCM.

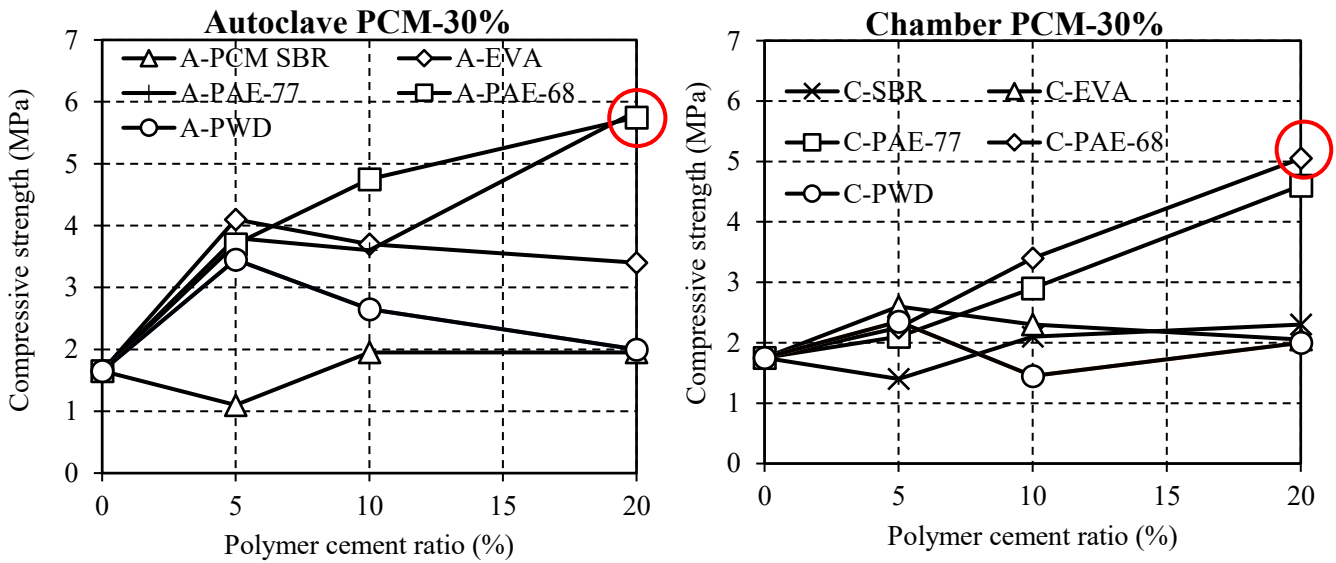


Figure 4.4.4 Effects of polymer cement ratio and different curing conditions on compressive strength test of samples with PCM.

#### 4.4.4 Bending strength tests on different curing condition

The bending strength test results highlight noteworthy variations between curing conditions in an autoclave and an environmental chamber, both with and without the presence of PCM, particularly after 1 day of curing (Figure 4.4.5- 4.4.6).

For the samples without PCM, there was no relationship between polymer content and flexural strength in terms of flexural strength, since flexural strength did not increase with increasing polymer content in autoclave curing and environmental curing. However, when comparing autoclave and environmental chamber curing, samples cured in autoclave was higher around 20-30%. In particular, the strength of PAE-7700 tended to be higher under all curing conditions.

In contrast, the samples with PCMs showed a dramatic reduction in bending strength with the addition of PCMs (Figure 4.4.6). This reduction was approximately 76% compared to the samples without PCM. In the case of autoclave curing with PCM samples, only PAE-7700 demonstrated the highest bending strength, achieving approximately 2.1 MPa at a polymer-cement ratio of 20%.

Results of flexural strength tests of various polymers containing No-PCM and PCM, comparing autoclave curing and constant temperature oven curing.

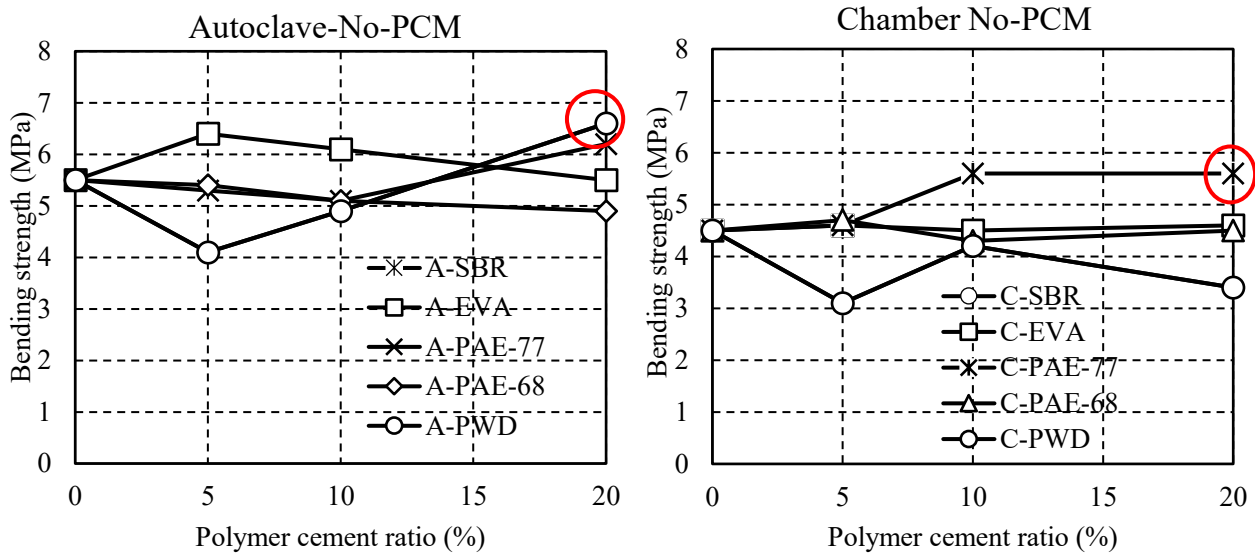


Figure 4.4.5 Effects of polymer cement ratio and different curing conditions on bending strength test of samples without PCM.

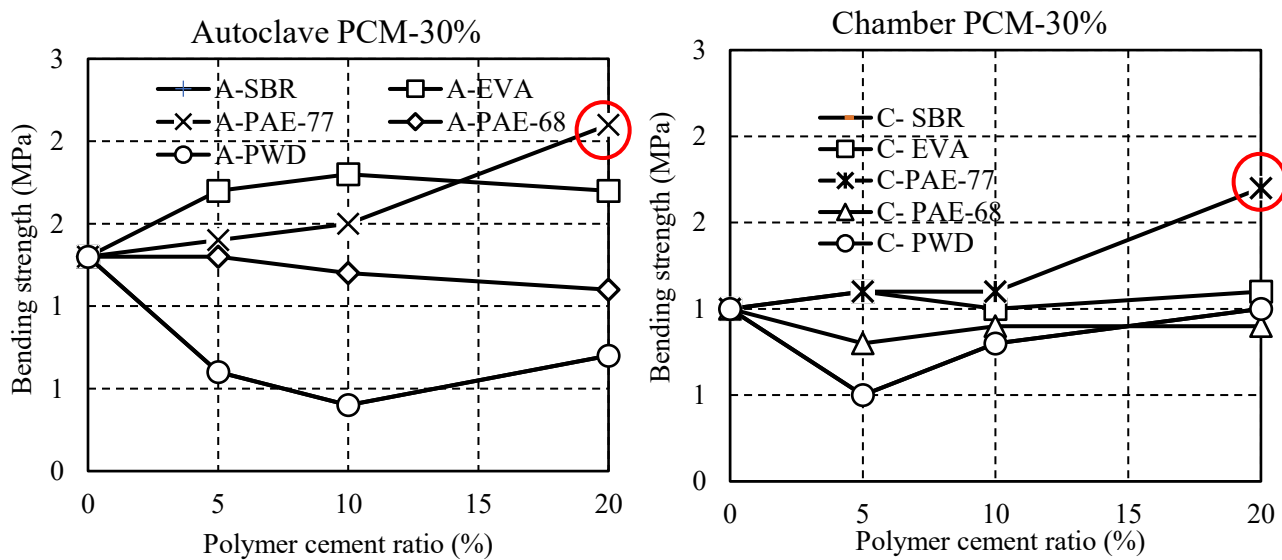


Figure 4.4.6 Effects of polymer cement ratio and different curing conditions on bending strength test of samples with PCM.

#### 4.4.5 Density tests on different types of polymers modified concretes with PCM and without PCM

The density measurement test results provided interesting insights into the effects of different polymers, polymer-cement ratios, and the presence of phase change materials (PCMs) on the density of the concrete.

For SBR, there was no significant difference in density, whether it contained PCMs or not. This suggests that the presence of SBR polymer did not substantially affect the density of the concrete.

The density of EVA concrete without PCMs decreased as the polymer content increased. This reduction in density might be attributed to the lightweight characteristics of EVA. In contrast, EVA concrete with PCMs tended to exhibit an increase in density as the polymer content increased. The introduction of PCMs, which typically have higher density compared to EVA, seemed to offset the natural lightweight nature of EVA, resulting in increased density.

For PAE-7700, the density of the concrete with PCMs remained approximately  $1600 \text{ kg/m}^3$  and did not show significant changes with varying polymer content. The concrete without PCMs in this category also displayed little density change with different polymer content.

The density measurement results for PAE-68 reveal an interesting correlation between the curing period and density. After curing in an autoclave, the density reached its highest value at  $2094 \text{ kg/m}^3$ , which was significantly higher compared to the samples cured in an environmental chamber, where the density was approximately  $500 \text{ kg/m}^3$  lower.

Notably, the density of concrete without PCMs was about  $400 \text{ kg/m}^3$  higher when PCMs were present in the mix. This suggests that the addition of PCMs led to a substantial increase in the overall density of the concrete. Furthermore, as polymer content increased, the density difference between PCM-containing concrete and No-PCM concrete was still noticeable, with about a  $200 \text{ kg/m}^3$  difference at higher polymer content.



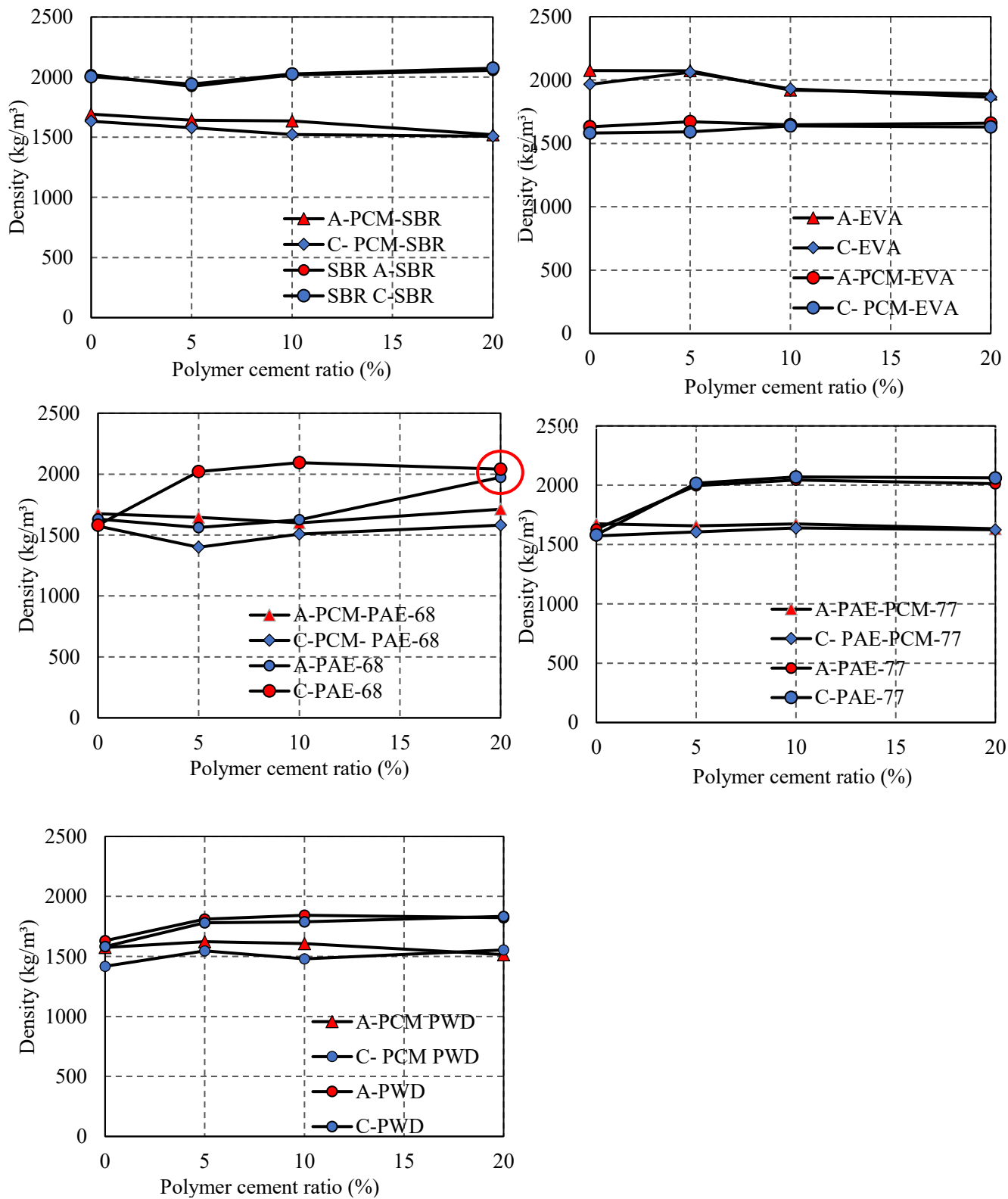


Figure 4.4.7 Effects of polymer cement ratio and different curing condition on density test.

#### 4.5 MIX DESIGN

Based on results of all these trial tests, we selected to use PAE-68 with polymer cement ratio of 20% as optimal mix composition. To tackle the challenges, we used the polymer cement concrete, emphasizing several advantages associated with this choice. Polymer cement concrete was selected for its ability to improve bonding strength, adhesive forces, and durability of the construction.

The samples used in this study were of a size measuring 40 x 40 x 160 mm. The PCM was added to the mix at a rate of 30% by mass of the cement. To prevent damage to the microcapsules of the PCM, an OM mixer was utilized, which could efficiently absorb the impact during the mixing process. The mixing procedure involved initially combining cement, silica fume, sand, and the PCM in the mixer and kneading them for a duration of 3 minutes. Subsequently, water and a high-performance AE reducer were introduced into the mixture, and mixing continued for an additional minute. Polymer was initially mixed with mixing water to achieve a concrete flow value within the range of  $170 \pm 10$  mm.

Following the mixing process, the concrete was placed in a formwork in two layers and subjected to steam curing. The curing procedure consisted of the following temperature and time stages: 23°C for 1 hour, 50°C for 3 hours, 40°C for 2 hours, and finally, 23°C for 1 hour. This meticulous curing process aimed to achieve the desired material properties and characteristics for the concrete samples used in the study.

Table 4-6 Mix compositions.

<b>Mix Designation</b>	<b>Cement (kg)</b>	<b>W/C (kg)</b> <b>0.7,0.35</b>	<b>Sand (kg)</b> <b>55%</b>	<b>PCM (kg)</b> <b>30%</b>	<b>SF (kg)</b> <b>5%</b>	<b>Polymer (kg)</b> <b>P/C 20%</b>
<b>Reference</b>	4.79	0.71	6.16	0	0.25	1.92
<b>PCM 6D</b>	2.91	1.16	5.47	1.34	0.22	1.17
<b>PCM 18D</b>	2.91	1.16	5.47	1.34	0.22	1.17
<b>PCM 28D</b>	2.91	1.16	5.47	1.34	0.22	1.17
<b>PCM 43D</b>	2.91	1.16	5.47	1.34	0.22	1.17

#### 4.6 MECHANICAL ANALYSIS

Table 4-7 Mechanical results of No-PCM and PCM6D.

Type of concrete	Curing condition	Curing period	Density (Kg/m <sup>3</sup> )	Compressive strength (MPa)	Bending strength (MPa)	Adhesion Strength (MPa)
No-PCM	Autoclave	1	2023	29.7	6.5	2.2
				29.7	7.2	
				29	6.5	
	20°C	7	1982	46.4	5.7	2.3
				47.2	5.9	
				46.7	5.9	
	20°C	14	1976	54.15	11.7	2.1
				52.3	12.7	
				52.6	11.5	
	20°C	28	1971	61.75	16.8	3
				59.05	14.6	
				60.8	14.7	
PCM-6D	Autoclave	1	1659	5.55	2.2	0.81
				5.75	2.5	
				5.9	2.6	
	20°C	7	1585	11.35	4.3	0.6
				9.4	3.7	
				11.3	3.9	
	20°C	14	1562	14.4	4.7	1.3
				14.35	4.4	
				14	4.5	
	20°C	28	1553	17.25	5.6	1.4
				15.35	6.7	
				17.25	6.6	

Table 4-8 Mechanical results of PCM18D, PCM28D and PCM43D.

Type of concrete	Curing condition	Curing period	Density (Kg/m <sup>3</sup> )	Compressive strength (MPa)	Bending strength (MPa)	Adhesion Strength (MPa)
PCM-18D	Autoclave	1	1700	6.6	2.6	0.87
				6.15	2.7	
				6.55	2.6	
	20°C	7	1590	13.55	4.4	1.26
				13.6	4.6	
				13.4	4.4	
	20°C	14	1571	16.35	5.8	1.28
				15.7	5.6	
				16.4	5.5	
	20°C	28	1567	18.1	6.3	1.31
				18.25	6.6	
				17.2	7	
PCM-28D	Autoclave	1	1686	7.7	2.6	1.07
				7.45	2.6	
				7.6	3.3	
	20°C	7	1596	14.75	5.1	1.24
				14.3	5.6	
				14.55	4.9	
	20°C	14	1578	16.45	6.6	1.28
				16.35	6	
				16.95	6.6	
	20°C	28	1570	18.85	7.4	1.4
				19.15	7.1	
				18.8	6.7	
PCM-43D	Autoclave	1	1747	10.35	3.7	1.07
				10.2	3.7	
				9.95	3.2	
	20°C	7	1682	19.55	6.2	1.31
				17.7	4.2	
				19.2	3.8	
	20°C	14	1653	22.65	6.5	1.37
				22.55	6.6	
				22.8	6.6	
	20°C	28	1642	25.95	7.8	1.55
				26.55	9.4	
				25.9	7.5	

#### 4.6.1 Density test

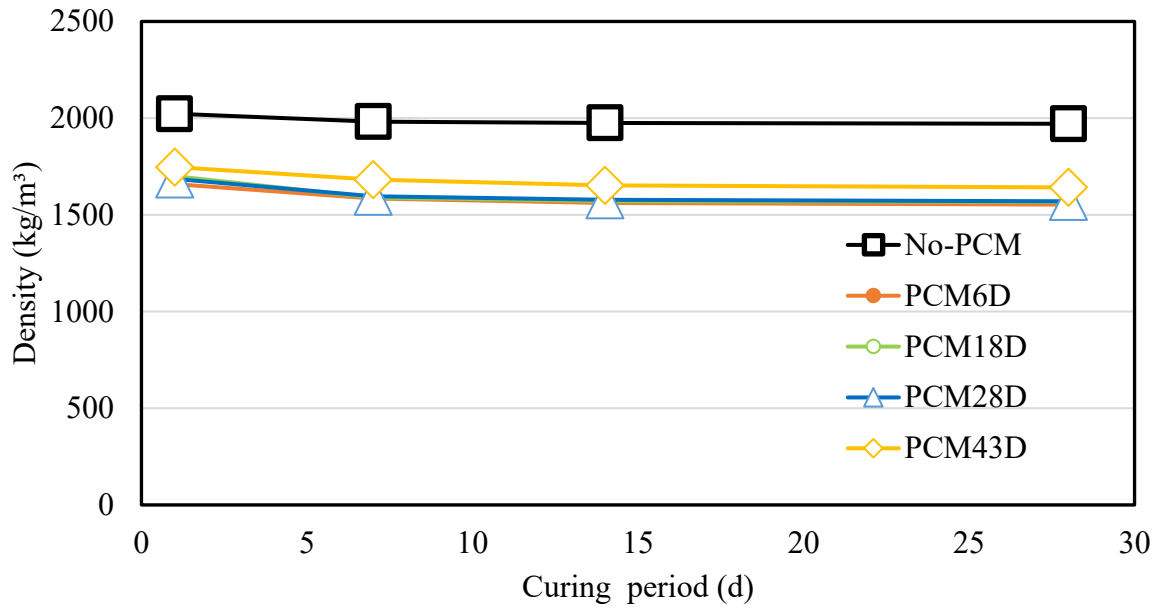


Figure 4.6.1 Density test on polymer-modified concretes with different PCMs.

##### 4.6.1.1 Results of density test on polymer-modified concrete with different PCMs

Figure 4.6.1 illustrates the density measurement test results, which highlights distinctive patterns in the density of concrete samples with and without PCMs. The density of No-PCM concrete was 2023 kg/m<sup>3</sup> after 1 day of curing, which decreased by approximately 2.5 % after 28 days. Notably, the density of No-PCM concrete was consistently remained about 16.3% higher than that of PCM-containing concrete throughout the curing period. The substantial difference in density between No-PCM and PCM-containing concretes underscores the impact of PCM presence on the overall concrete density.

The density of PCM-containing concrete followed a similar trend, with decreasing density levels observed in all PCM types from 1 day to 28 days of curing. PCM6D, PCM18D, PCM28D, and PCM43D displayed reductions in density ranging from about 6 % to 10% during the 28-day curing period. Despite the reductions, PCM-containing concretes-maintained density levels within the specified range for various PCMs. Notably, PCM43D tended to exhibit higher density compared to other PCM types, even after the 28-day curing period. The discussion of density emphasizes the influence of curing time and PCM incorporation on concrete density. The consistent variation in density levels between PCM and No-PCM concretes highlights the significance of PCM content in affecting the overall density of the concrete. Previous studies have shown comparable density reductions. For geopolymer concrete, a 13% reduction was observed following the addition 5% PCM [22]. In the case of normal mortar, a reduction of 22.39% was reported for 20% microencapsulated PCMs [23].

Comparing these outcomes concerning density, it is evident that reduction in density of Polymer modified PCM mortars is relatively low, even after replacing 30% of PCM.

#### 4.6.2 Compressive strength test

The compressive strength test results presented in Figure 4.6.2 examine the effects of incorporating PCMs on polymer-modified concrete: No-PCM, PCM6D, PCM18D and PCM43D over various curing periods at 1,7, 14, and 28 days of curing, with a temperature of 20°C and relative humidity of 90%. In these three different concretes, 30% of cement’s weight in each type of concrete were substituted with PCMs.

For No-PCM modified concrete, the compressive strength result of No-PCM was recorded at 29 MPa on day 1. In contrast, the compressive strengths of PCM6D, PCM18D PCM28D and PCM43D were 3.25 MPa, 4.8 MPa and 6.5 MPa, respectively, resulting in strength decrease of 80%, 77%, 74% and 65% respectively, compared to No-PCM polymer-modified concrete. However, from day 7 to day 28, the compressive strengths of all samples increased by 26% for No-PCM; to 52.4% for PCM6D; to 66.4% for PCM18D; to 64.4% for ND PCM28D; to 61.5% for PCM43D, respectively.

In conclusion, the incorporation of PCMs into concrete had a noticeable impact on compressive strength in all five types of concretes. PCMs are more like voids than aggregates in concrete matrix [24]. The results are in line with the conclusion of [25], who studied polymer modified concrete with PCM and reported a 77% reduction for the incorporation of 20% microencapsulated PCM. Although there was an initial decrease in strength when PCMs were introduced, all three types of concrete demonstrated significant improvements in compressive strength from day 7 to day 28.

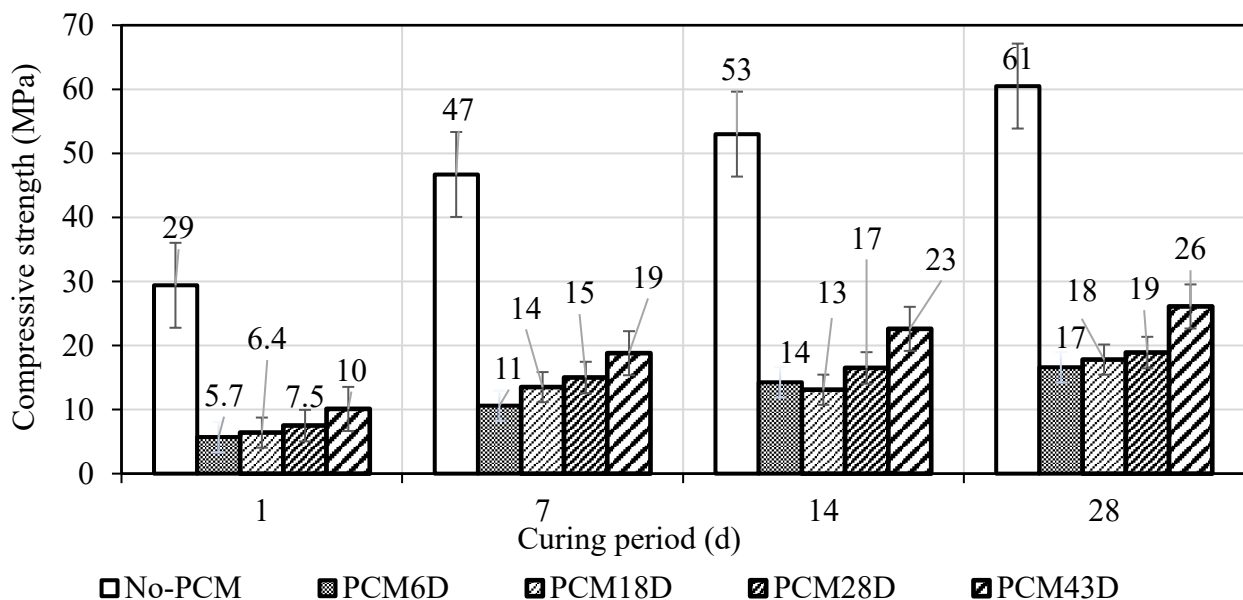


Figure 4.6.2 Compressive strength analysis on different types of PCMs.

### 4.6.3 Bonding strength test

Tests were conducted in accordance with JIS A 5557 [26] to measure the adhesion strength between tiles and concrete. The test method is outlined below: First, cut a piece of tile and concrete to the size of 40 x 40 mm, which matches the size of a steel test piece, using a tile cutter. Next, apply two-component epoxy resin adhesive to the tile and bond it to the test piece of steel. After bonding, cure the tiles in a dryer at 40°C for a minimum of 1 day. Tests were carried out with concrete curing periods ranging from day 1 to 28 days. Two tests were conducted simultaneously, and the average value was utilized as the test result.

#### 4.6.3.1 Results of adhesive strength test on polymer-modified concrete with different PCMs

The adhesive strength comparison between concrete with and without phase change materials (PCMs) reveals interesting trends throughout the curing period. Here is a summary of these observations: The adhesive strength of the concrete without PCM was consistently higher compared to that of the concrete with PCM across all curing periods. On the first day of curing, the adhesive strength for the concrete without PCM was recorded at 2.2 MPa. By day 28, the adhesive strength increased to 3 MPa, indicating a significant improvement over time. Payam et al. [27] reported a value of 2 MPa, which is consistent with these results for polymer-modified mortar without PCM.

In contrast, the adhesive strength of the concrete with PCM exhibited lower values across all curing periods. On the first day of curing, the adhesive strength ranged between 0.8 and 1 MPa for the concrete with PCM. By day 28, the adhesive strength for the concrete with PCM improved but still ranged between 1.4 and 1.55 MPa, indicating a relatively lower adhesive strength compared to the concrete without PCM.

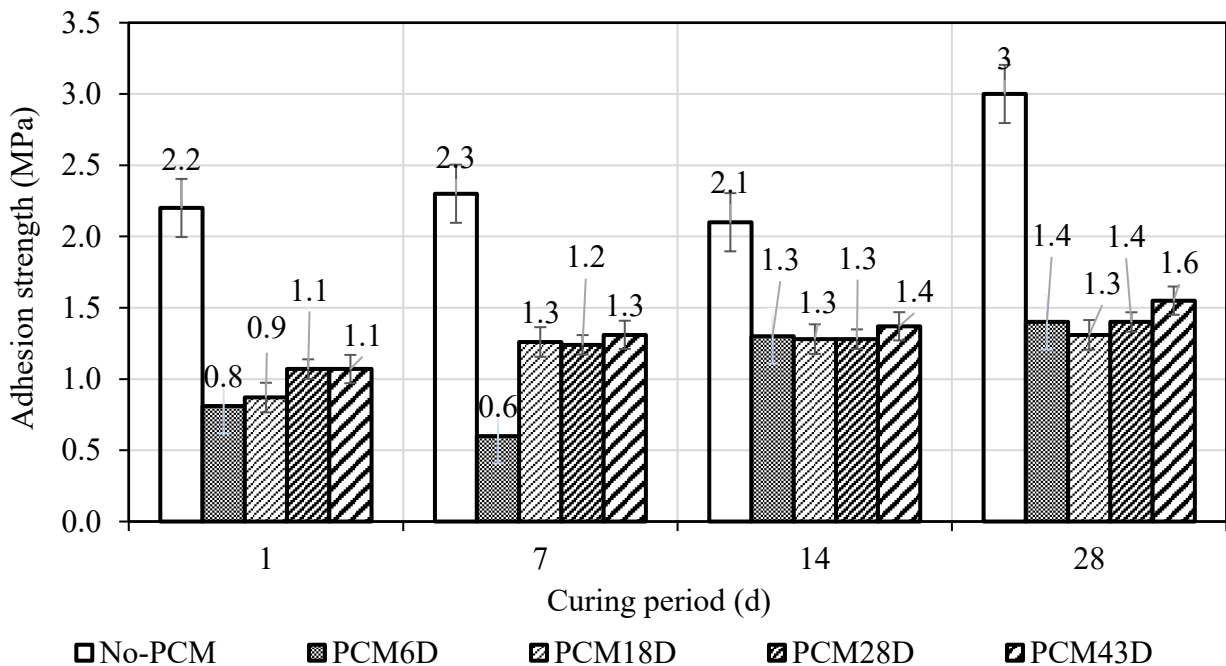


Figure 4.6.3 Adhesive strength analysis on different types of PCMs.

#### 4.7 DSC AND THERMAL ANALYSIS

DSC (Differential Scanning Calorimetry) tests were performed on four different types of polymer-modified concretes, each containing distinct types of phase change materials (PCMs): PCM6D, PCM18D, PCM28D, and PCM43D. These tests encompassed a range of heating and cooling rates, spanning from 0.5°C/min to 10°C/min, with the primary goal of determining the latent heat capacity of these materials. The DSC results of all types of polymers modified concretes for all scanning rates above mentioned were summarized in Table 4-9.

Figure 4.7.1 displays line graphs depicting the impact of these various heating and cooling rates on polymer-modified concrete with PCM6D. Notably, the slowest scanning rate, at 0.5°C/min, resulted in the lowest latent heat ( $\Delta h$ ) values. For PCM6D, this rate produced melting and freezing peaks at 4.01°C and -6.68°C, accompanied by latent heat storage values of 14.23 J/g and 14.45 J/g, respectively. Conversely, the highest latent heat values were observed for PCM28D-30% at the heating/cooling rate of 10°C/min. The melting and freezing peaks at 5.18°C and -4.51°C, accompanied by latent heat storage values of 12.45 J/g and 12.33 J/g, respectively.

Figure 4.7.2 presents line graphs illustrating the influence of heating and cooling rates on foam concrete with PCM18D. In this case, the rate of 10°C/min resulted in the lowest latent heat ( $\Delta h$ ) values for PCM18D, with melting and freezing peaks occurring at 16.55°C and -11.62°C, and latent heat storage capacities of 10.9 J/g and 9.83 J/g, respectively. The highest latent heat values were observed under the fastest heating/cooling rate of 0.5°C/min, where melting and freezing peaks appeared at 15.85°C and 14.84°C, with latent heat storage capacities of 10.9 J/g and 14.64 J/g, respectively.

Figure 4.7.3 showcases line graphs displaying the effects of heating and cooling rates on foam concrete with PCM28D. Similar to the previous tests, the slowest rate of 10°C/min yielded the lowest latent heat ( $\Delta h$ ) values for PCM28D, with melting and freezing peaks at 26.21°C and 21.68°C, along with latent heat storage capacities of 15.19 J/g and 16.45 J/g, respectively. In contrast, the heating/cooling rate of 0.5°C/min resulted in the highest latent heat values, with melting and freezing peaks at 25.11°C and 22.86°C, and latent heat storage capacities of 15.72 J/g and 16.24 J/g, respectively.

Concerning polymer-modified concrete with PCM43D, Figure 4.7.4 presents the results of heating and cooling cycles. Detailed examination of scanning rates reveals that the slowest rate of 0.5°C/min produced the lowest latent heat ( $\Delta h$ ) values for PCM43D-10%, featuring melting and freezing peaks at 42.91°C and 39.12°C, and latent heat storage capacities of 21.72 J/g and 24.16 J/g. On the other hand, the highest latent heat values for PCM43D were recorded under the heating/cooling rate of 10°C/min, with melting and freezing peaks at 44.02°C and 38.87°C, and latent heat storage capacities of 25.59 J/g and 21.26 J/g, respectively.



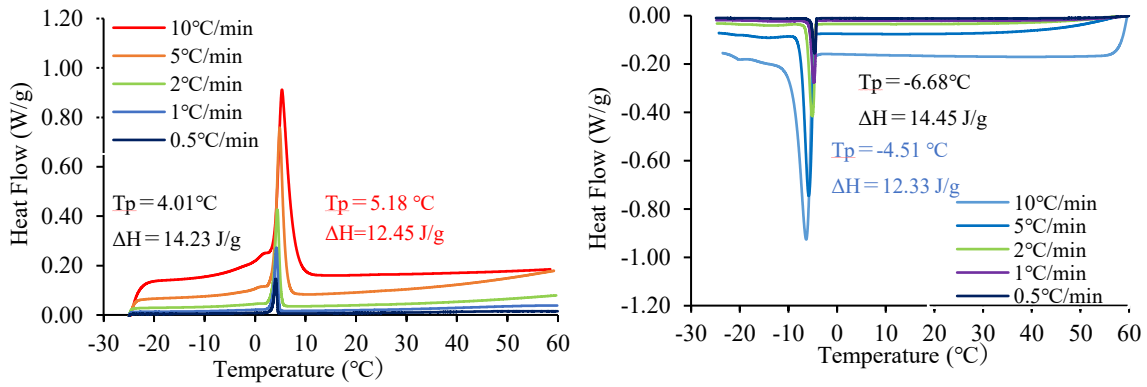


Figure 4.7.1 DSC curve of PCM6D, heating and cooling process at various heating rates.

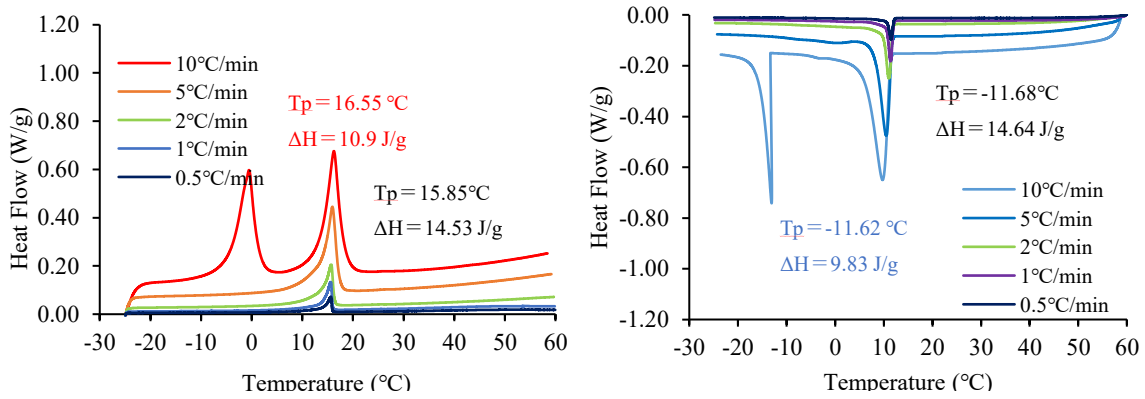


Figure 4.7.2 DSC curve of PCM18D, heating and cooling process at various heating rates.

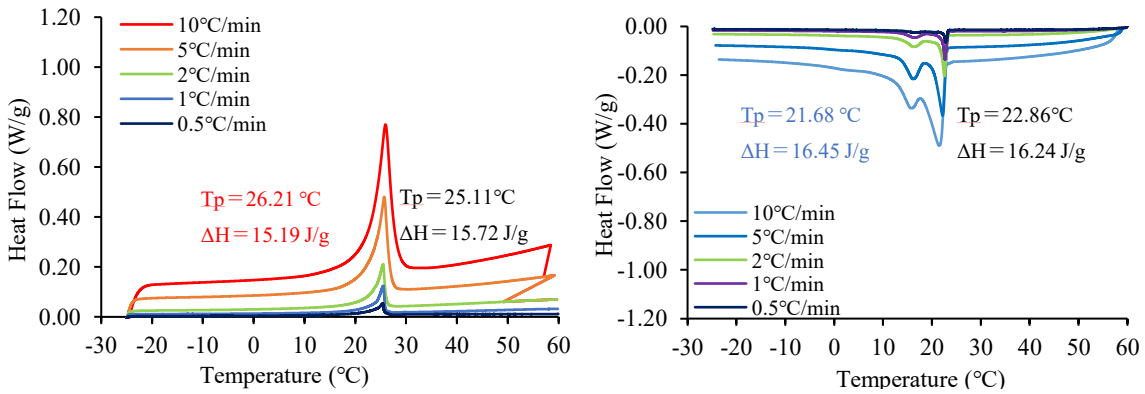


Figure 4.7.3 DSC curve of PCM28D, heating and cooling process at various heating rates.

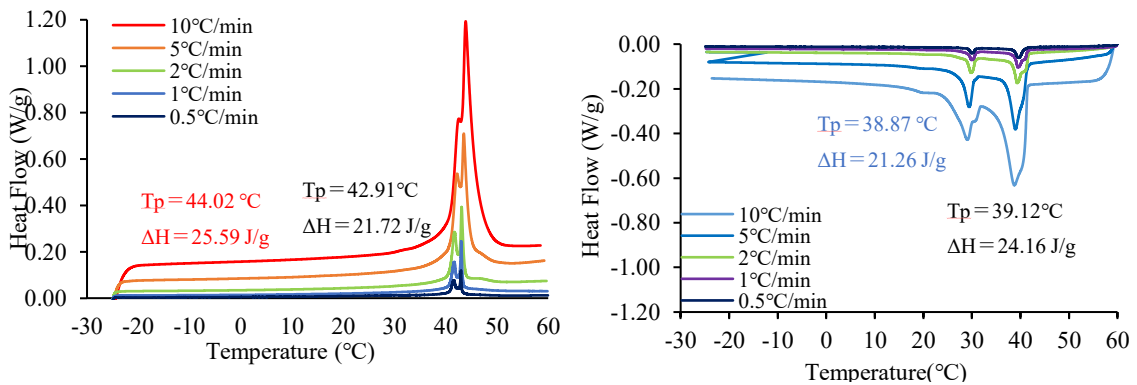


Figure 4.7.4 DSC curve of PCM43D, heating and cooling process at various heating rates.

Table 4-9 Enthalpy variation and standpoint temperatures scanning rates varying from 10°C/min to 0.5°C/min.

Designation	Melting			Freezing			
	Onset	End	Peak	Onset	End	Peak	
	Temp (°C)	Temp (°C)	Temp (°C)	Temp (°C)	Temp (°C)	Temp (°C)	
<b>6D</b>	10°C/min	3,76	3,75	5,32	-5,01	5,10	-6,34
	5 °C/min	3,65	6,12	4,89	-4,78	-4,80	-5,82
	2 °C/min	3,47	5,20	4,43	-4,45	-4,46	-5,08
	1 °C/min	3,45	4,76	4,20	-4,30	-4,30	-4,79
	0.5°C/min	14,18	15,92	15,64	12,07	12,05	11,47
<b>18D</b>	10°C/min	13,29	18,30	16,23	11,36	11,20	9,76
	5 °C/min	13,35	17,34	15,95	11,67	11,55	10,50
	2 °C/min	13,68	16,33	15,71	11,83	11,78	11,04
	1 °C/min	14,04	16,00	15,63	11,97	11,97	11,39
	0.5°C/min	14,19	15,93	15,64	12,06	12,04	11,47
<b>28D</b>	10°C/min	22,75	28,00	25,96	22,79	2,62	21,52
	5 °C/min	23,09	26,92	25,71	23,00	22,90	22,20
	2 °C/min	23,36	26,07	25,47	23,19	23,13	22,58
	1 °C/min	23,73	25,90	25,51	23,30	23,28	22,68
	0.5°C/min	23,52	25,71	25,42	23,35	23,27	22,78
<b>43D</b>	10°C/min	42,63	42,71	43,89	41,44	41,35	38,75
	5 °C/min	42,60	42,60	43,53	41,49	41,21	38,96
	2 °C/min	42,64	42,64	43,10	41,70	41,54	39,34
	1 °C/min	42,68	43,34	43,03	41,49	38,58	39,47
	0.5°C/min	42,70	43,16	42,98	41,10	40,70	39,67

#### 4.7.1 Specific heat capacity and Specific enthalpy measurements of polymer-modified concrete with different types of PCM

The discussion presents the results of specific heat capacity and specific enthalpy tests conducted on four different polymer-modified concrete with different types of PCMs. The results are presented in Figure 4.7.5- Figure 4.7.8.

In all four PCM concrete samples, the specific heat capacity based on specific heat enthalpy measurements displays peaks at different temperatures. These peaks indicate distinct changes in the material's heat capacity and the energy required to raise its temperature by 1°C or 1K per unit mass.

For PCM6D (Figure 4.7.5 (a)), the specific heat capacity curve occurs at 5.1°C, with a specific heat ( $C_p$ ) of 5.76 J/g°C. In the case of PCM18D (Figure 4.7.6 (a)), the peak in the specific heat capacity curve appears at 15.72°C, with a specific heat ( $C_p$ ) of 4.45 J/g°C. As for PCM28D (Figure 4.7.7 (a)), Its peak in the specific heat capacity curve occurs at 25.57°C, with a specific heat ( $C_p$ ) of 4.9 J/g°C. As for PCM43D (Figure 4.7.8 (a)), Its peak in the specific heat capacity curve occurs at 43°C, with a specific heat ( $C_p$ ) of 7.6 J/g°C. Notably, PCM43D displays the highest specific heat capacity among all PCM modified concretes, making it particularly efficient in absorbing and storing thermal energy.

The specific enthalpy measurements, conducted within a temperature range of -30 to 60°C, allow us to understand the phase transition behavior of these materials. The specific enthalpy is assumed to be zero at -20 °C, enabling the analysis of changes in enthalpy.

For PCM6D (Figure 4.7.5 (b)), the phase transition range, characterized by substantial changes in enthalpy, occurs from 6 to 24 °C. Within this phase transition range, PCM6D exhibits a specific enthalpy of 13356 J/kg, indicating its significant capacity to absorb and release thermal energy during this phase transition. For PCM18D (Figure 4.7.6 (b)), the phase transition range is observed from 10 to 30 °C, and the specific enthalpy within this range is measured at 15778 J/kg, showcasing its substantial thermal energy storage capabilities. As for PCM28D (Figure 4.7.7 (b)), the phase transition range is noted from 30 to 50 °C, with a specific enthalpy within this range measured at 16786 J/kg. As for PCM43D (Figure 4.7.8 (b)), the phase transition range is noted from 30 to 50 °C, with a specific enthalpy within this range measured at 16556 J/kg.

Those parameters reflect the material's ability to effectively store and release thermal energy during the specified phase transition.

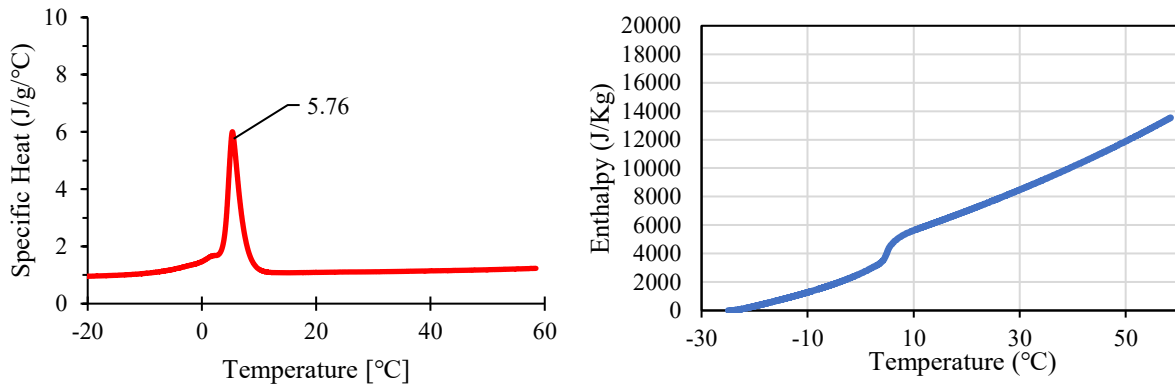


Figure 4.7.5 (a) Specific heat capacity and (b) specific enthalpy of PCM6D.

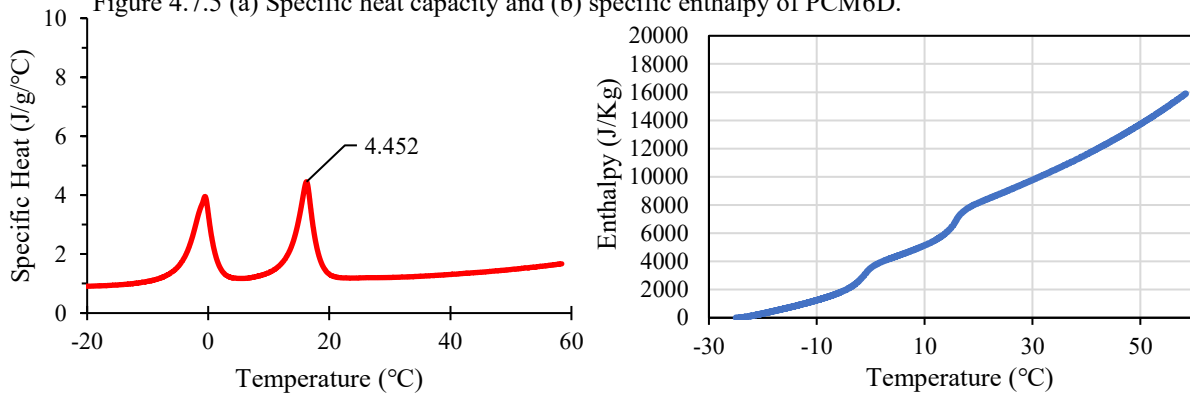


Figure 4.7.6 Specific heat capacity and (b) specific enthalpy of PCM18D.

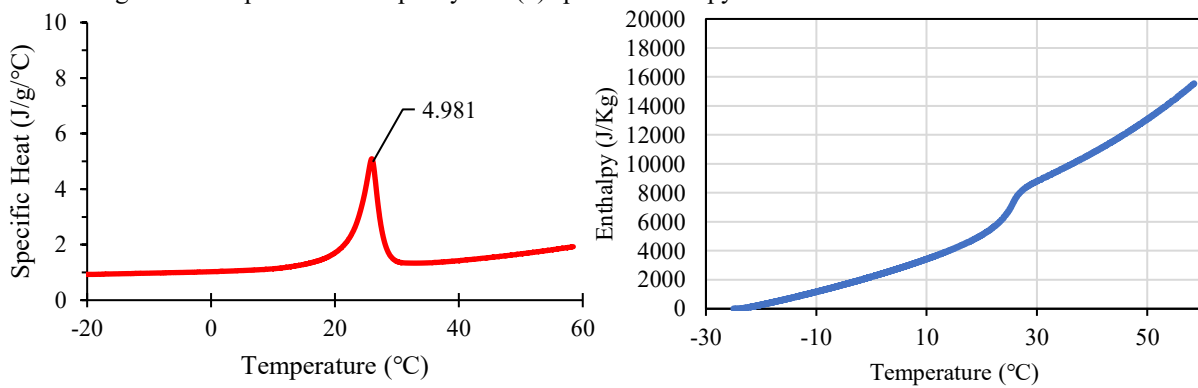


Figure 4.7.7 (a) Specific heat capacity and (b) specific enthalpy of PCM28D.

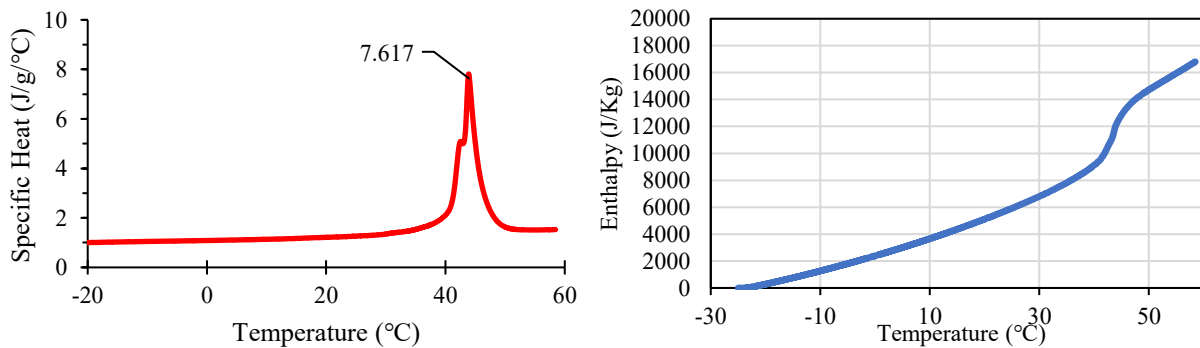


Figure 4.7.8 (a) Specific heat capacity and (b) specific enthalpy of PCM43D.

### 4.7.2 Heat cyclic test analysis

The thermal cycling experiment was conducted using a specialized chamber (model ETAC dc-450) with adjustable temperature and humidity settings. The heat cycling procedure, outlined in Figure 4.7.9, encompassed a 21-hour cycle. During each cycle, the chamber temperature remained at 10°C for a 4-hour period, achieved at a gradual rate of 2.5°C per minute. Subsequently, the temperature was raised from 10°C to 50°C in 20 minutes and maintained at 50°C for 8 hours. Afterward, the temperature was lowered back to 10°C in 20 minutes and sustained at that level for 8 hours.

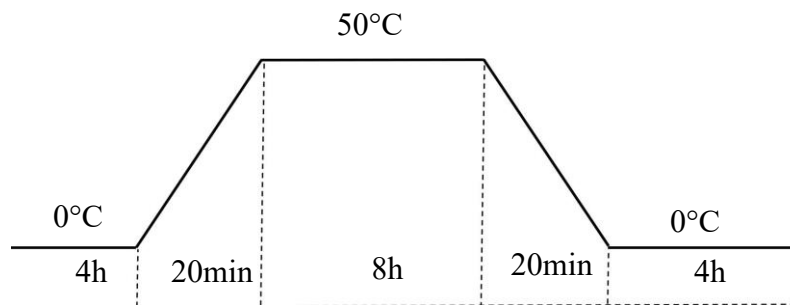


Figure 4.7.9 Heat cycling program.

### 4.7.3 Preparing the samples for heat cycling test

To evaluate the impact of polymer-modified PCM concrete when employed as a building wall material, an enclosed prototype was constructed at laboratory scale. The prototype was structured in the following sequence, from interior to exterior: a 180 mm thick layer of PCM polymer-modified concrete for 200x200x180mm samples, the tile thickness was 7mm, and the concrete thickness was 23mm, accompanied by a 50mm thick layer of extruded polystyrene foam for 300x300x50mm dimensions. The configuration of the physical models and a cross-sectional view of the prototype are visually presented from Figure 4.7.10 and Figure 4.7.11. Within this prototype setup, a total of three thermocouples were employed. One thermocouple was positioned on the backside side of the sample, another was placed on the surface, and a third was inserted in the middle of the prototype box. The mid-sample thermocouples were utilized to facilitate comparisons with the various sides of the thermocouples. A total of 15 samples of this type were made, including four types of PCM and two types of tiles.

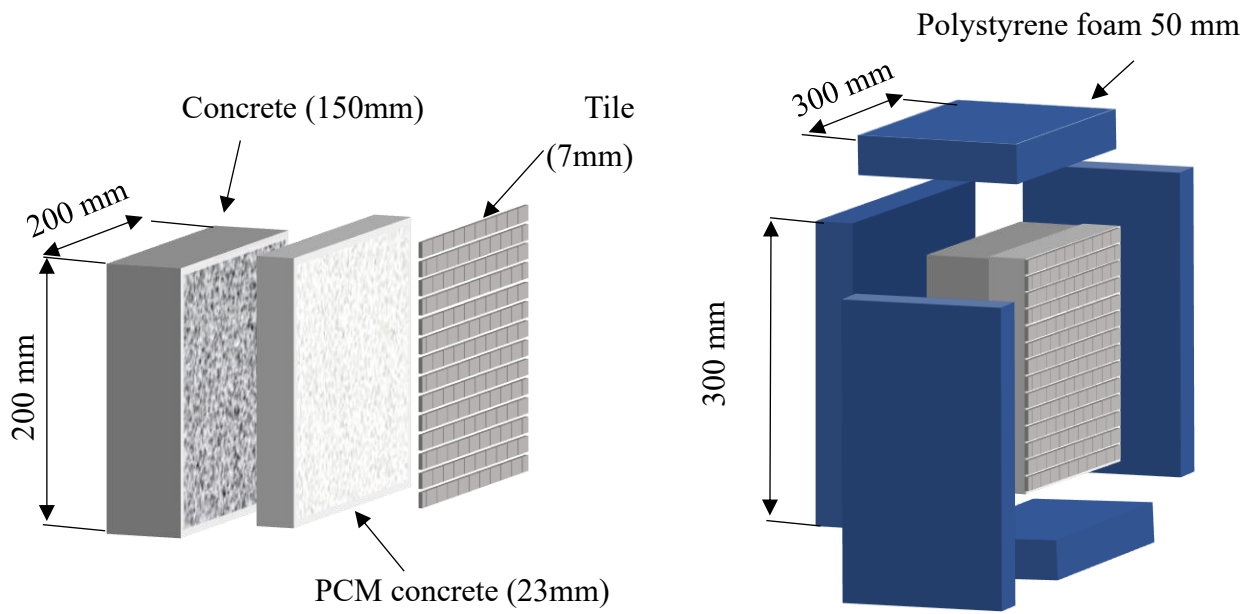


Figure 4.7.10 Preparation procedure of prototype setup.



Figure 4.7.11 Finished procedure.

#### 4.7.3.1 Heat cyclic test results of PCM6D with and without tile

The thermal performance of four types of polymers PCM concrete panels were assessed. Each PCM polymer panel was attached to black or white tiles, including a panel with no tile. A total of 15 samples of this type were created to test the temperature effects on different types of PCMs with tiles of different colors. Temperature measurements were taken at the surface, backside of the foam concrete, and the center of the prototype test room. The heat cycling conditions consisted of 24-hour cycles, with heating and cooling rates lasting for 8 hours at 2.5°C per minute. The temperature range during the heat cycling ranged between 10°C and 50°C, chosen based on the melting and freezing ranges of the PCMs.

Figures 4.7.12 to 4.7.14 depict the heat cyclic analysis of different types of concrete with PCM6D. The surface temperature of all samples increased dramatically up to 40°C at the beginning of the heating process, gradually reaching 50°C in about 3 hours. Meanwhile, the backside of the sample panels showed a melting process, there was minimal differentiation between No-PCM sample and those with PCM within the 0-30°C range. Subsequently, the temperature of all the samples gradually increased up to 50°C. Inside the prototype, the behavior was similar to all the panels during the heating process. On the contrary, during the cooling process, the surface temperature dropped dramatically from 50°C to 20°C. Over the following 3 hours, the temperature gradually decreased to 15°C. On the backside of the all the sample panel, the concretes initiated freezing and began releasing heat when the temperature reached the 0-30°C range. All the samples exhibited a similar temperature behavior, compared with samples with No-PCM and No-tile. Inside the prototype, all the samples exhibited uniform behavior with sample panels with white, black, and No-tile during the cooling process.

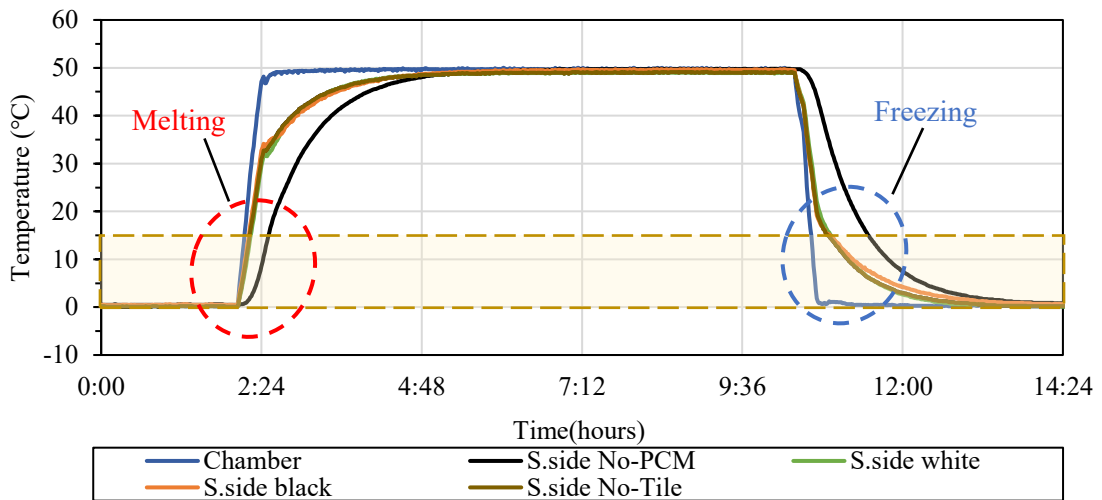


Figure 4.7.12 Heat cyclic analysis of different types of PCM6D on surface side of prototype.

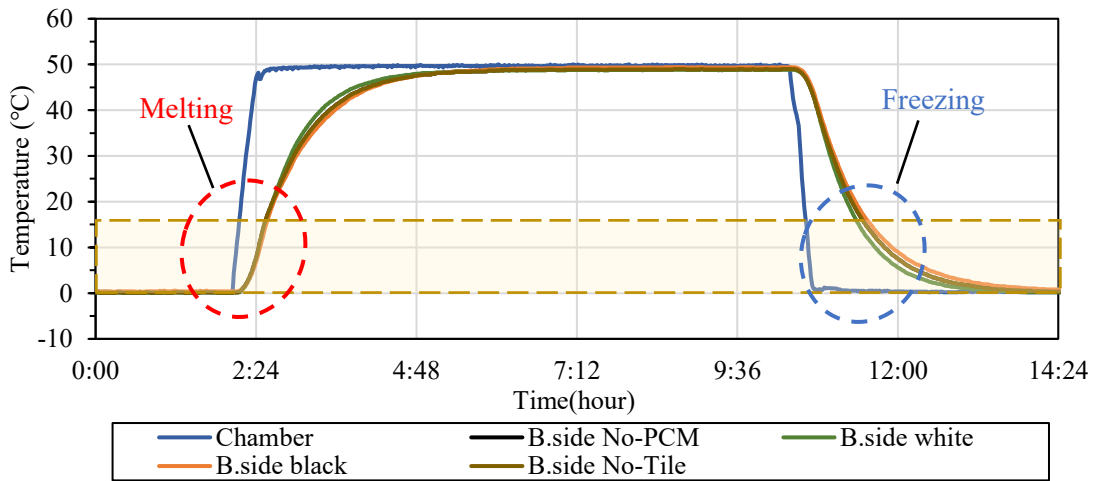


Figure 4.7.13 Heat cyclic analysis of different types of PCM6D on backside of prototype.

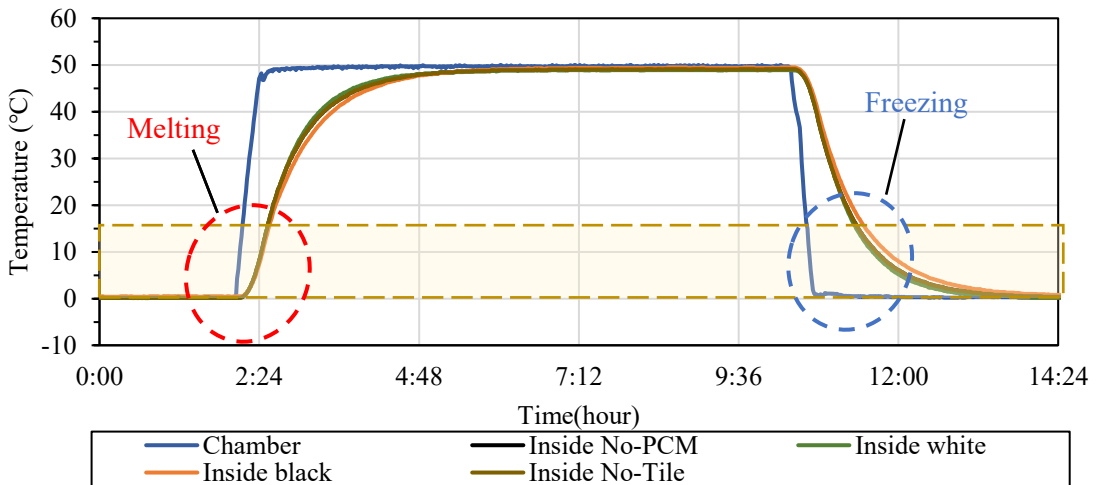


Figure 4.7.14 Heat cyclic analysis of different types of PCM6D on inside of prototype.



#### 4.7.3.2 Heat cyclic test results of PCM18D with and without tile

Figures 4.7.15 to 4.7.17 show the heat cyclic analysis of different types of concrete with PCM18D. The surface temperature of all the sample panels increased up to 20°C at the beginning of the heating process. A delay of about 30 minutes was observed for sample panels with No-tile and black tile compared to sample panels with white tile and No-PCM. Subsequently, the temperature gradually increased up to 50°C in about 3 hours. On the backside of the panels, as the temperature increased from 10°C to 30°C, all the sample panels began to melt and absorb heat, showing a delay of approximately 1 hour compared to No-PCM. As for the sample with white tile, temperature delay was around 16 minutes compared to No-PCM. After completing the melting process, the temperature gradually increased up to 47°C in about 7 hours. Inside the prototype, as the temperature increased from 10°C to 30°C, all the sample panels began to melt and absorb heat, maintaining the room temperature for around 10 minutes. After the melting process, the temperature gradually increased to 50°C in about 3 hours. Contrarily, during the cooling process, the surface temperature dropped dramatically from 50°C to 30°C. Over the following 3 hours, the temperature gradually decreased to 10°C. The sample with white showed similar behavior compared with No-PCM. The samples with black tile and No-tile exactly same behavior and maintained the temperature for around 30 min. On the backside of all the sample panels, as the temperature fell from 30°C to 10°C, all sample panels initiated freezing and releasing heat. The temperatures of the samples with black tile and No-tile were delayed for approximately 1 hour compared to No-PCM, which decreased more rapidly. For the sample with white tile, temperature delay of around 20 minutes was observed. Inside the prototype, negligible temperature difference was observed between panels No-PCM and all the sample panels with tile and No-tile.

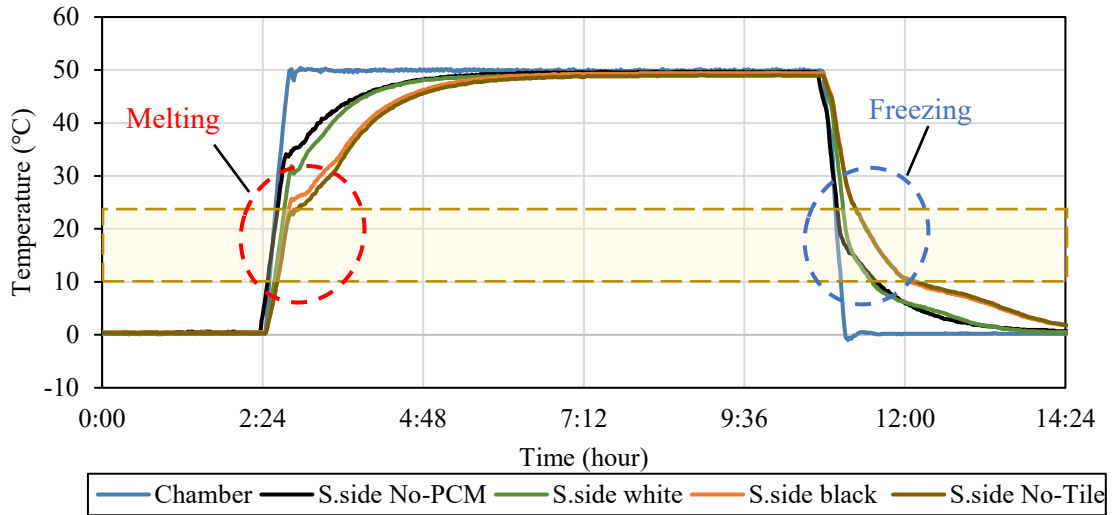


Figure 4.7.15 Heat cyclic analysis of different types of PCM18D on surface of prototype.

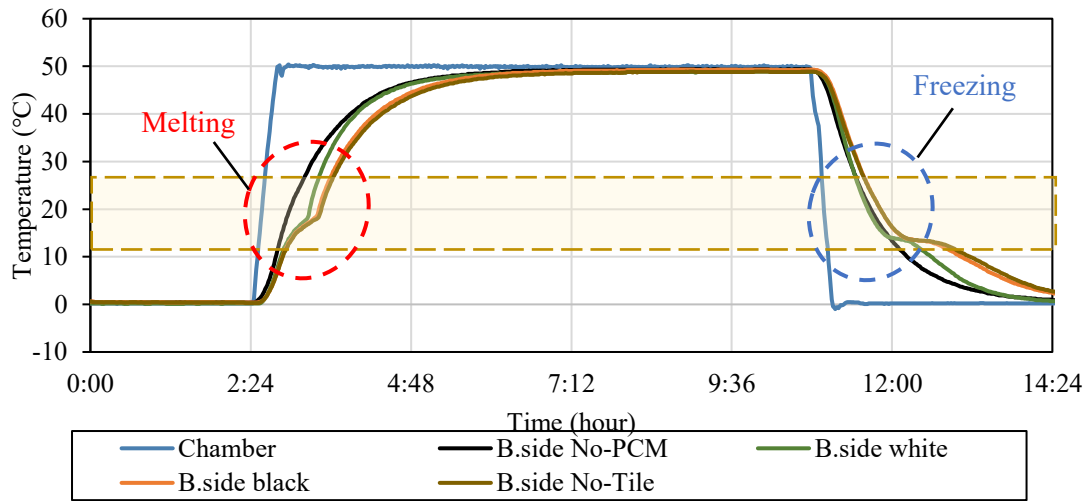


Figure 4.7.16 Heat cyclic analysis of different types of PCM18D on backside of prototype.

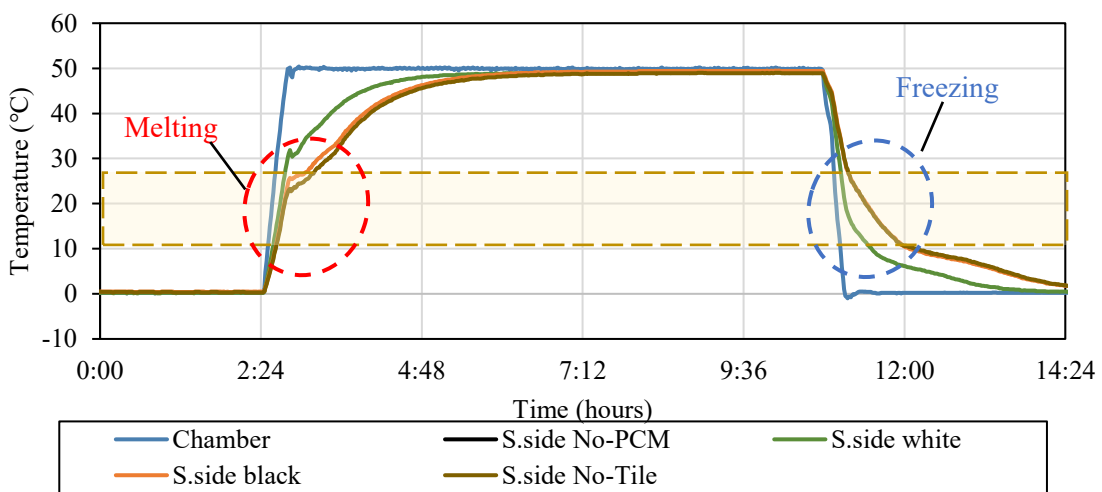


Figure 4.7.17 Heat cyclic analysis of different types of PCM18D on inside of prototype.

#### 4.7.3.3 Heat cyclic test results of PCM28D with and without tile

Figures 4.7.18 to 4.7.20 show the heat cyclic analysis of different types of concrete with PCM28D. The surface temperature of all the sample panels increased up to 20°C at the beginning of the heating process. When comparing the temperature gradients of all the sample panels, it was observed that the sample panel with white tile exhibited the longest temperature delay, which was approximately 1 hour. The sample panel with black tile showed a delay of around 28 minutes, while the panels with no tiles had a delay of 10 minutes. Subsequently, the temperature gradually increased up to 50°C in about 3 hours. On the backside of the panels, as the temperature increased from 20°C to 30°C, all the sample panels began to melt and absorb heat, showing a delay of approximately from 20 minutes and 1 hour compared to panels with No-PCM. The sample panels with white and black tiles exhibited the longest temperature delay in this regard. After completing the melting process, the temperature gradually increased up to 47°C in about 7 hours. Inside the prototype, as the temperature increased from 20°C to 30°C, all the sample panels began to melt and absorb heat, maintaining the room temperature for around 30 minutes to 1 hour. After the melting process, the temperature gradually increased to 50°C in about 3 hours. Contrarily, during the cooling process, the surface temperature dropped dramatically from 50°C to 30°C. The samples with white and black tiles as well as No-tile were released heat and maintained their temperature for around 36, 47 and 7 minutes respectively. Over the following 3 hours, the temperature gradually decreased to 10°C. The sample with No-tile showed similar behavior compared with No-PCM panels during the phase changing range. It released heat and maintained the room temperature for around 30 min. On the backside of all the sample panels, as the temperature fell from 30°C to 10°C, all sample panels initiated freezing and releasing heat. The sample panels with white and black tiles showed similar behavior with a delay of approximately 1 hour compared to No-PCM, which decreased more rapidly. As for the sample panel with No tile, there was a 30-minute delay in temperature change. Inside the prototype, negligible temperature difference was observed between panels No-PCM and all the sample panels with tile and No-tile.

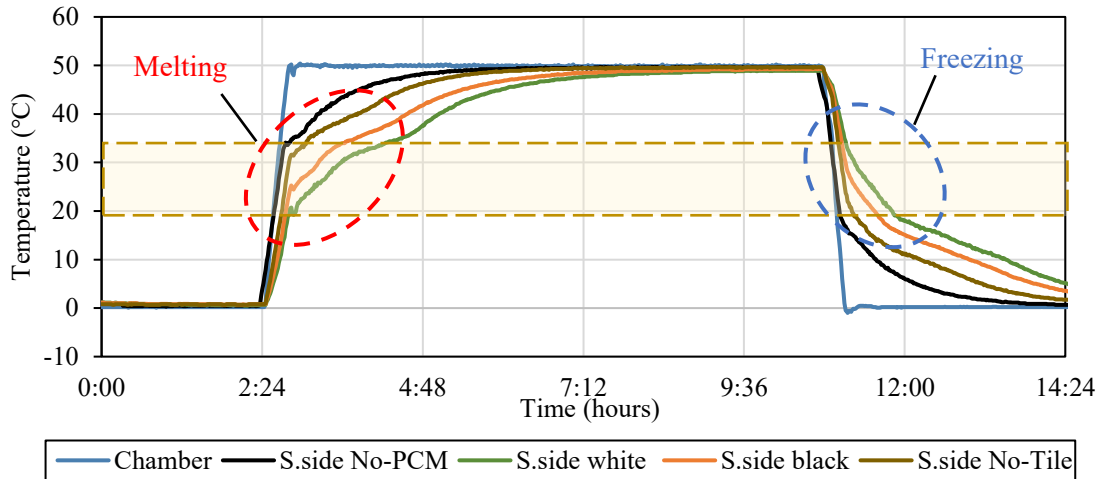


Figure 4.7.18 Heat cyclic analysis of different types of PCM28D on surface side of prototype.

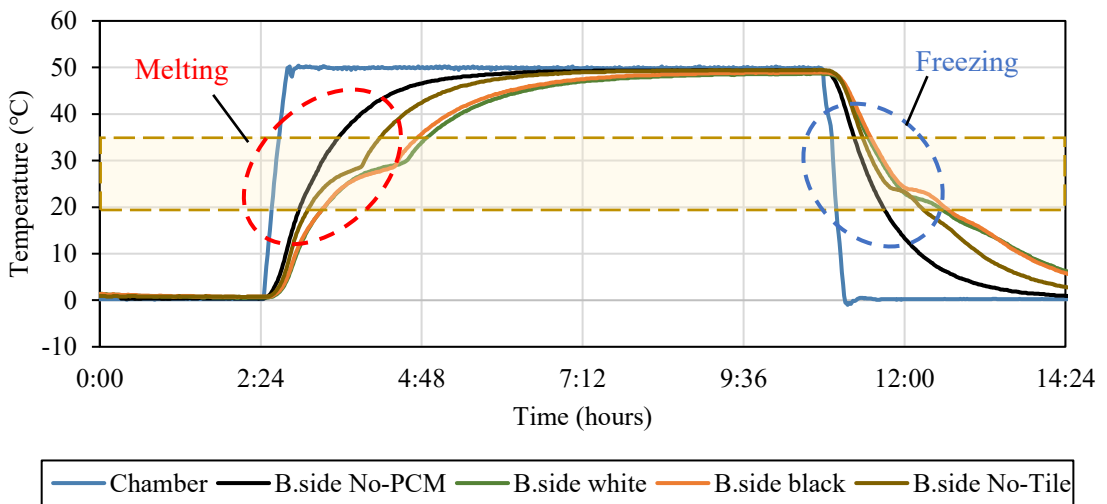


Figure 4.7.19 Heat cyclic analysis of different types of PCM28D on inside of prototype.

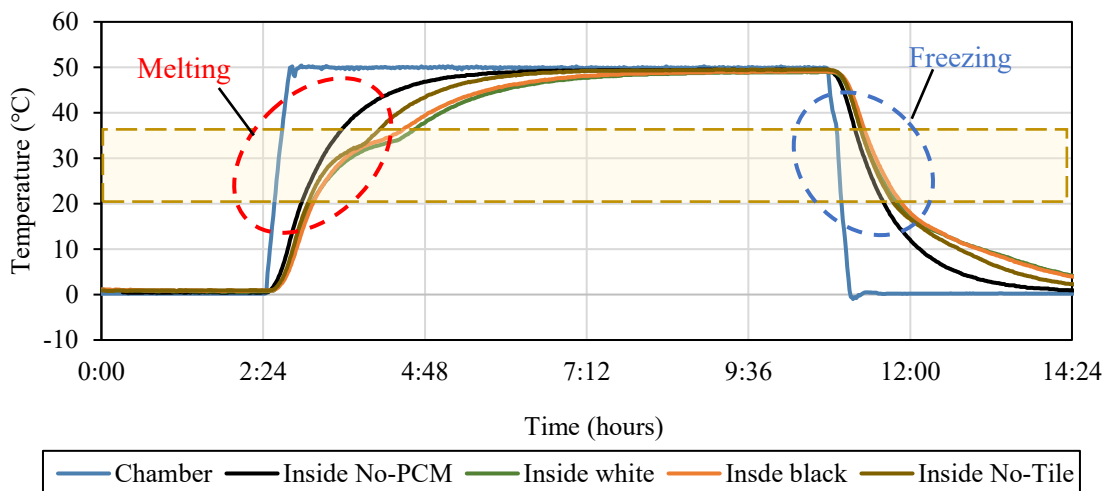


Figure 4.7.20 Heat cyclic analysis of different types of PCM28D on backside of prototype.

#### 4.7.3.4 Heat cyclic test results of PCM43D with and without tile

Figures 4.7.21 to 4.7.23 show the heat cyclic analysis of different types of concrete with PCM43D. The surface temperature of all samples increased dramatically up to 40°C at the beginning of the heating process, gradually reaching 50°C in about 3 hours, and meanwhile, the sample panels with No tile, black and white tile started to absorb the heat and maintained the temperature for around 3 to 4 hours as compared to No-PCM panel. The sample panel with black tile exhibited the longest delay in temperature increase. As for the backside of the sample panels, it showed similar results as the surface side. The melting process started, maintaining the temperature for approximately 4 hours within the 30-50°C range. Notably, samples panels with all the sample panels exhibited a clear melting curve compared to the sample with sample panel with No-PCM concrete. Subsequently, the temperature of all the samples gradually increased up to 50°C. However, No-PCM panel experienced a more dramatic increase. Inside the prototype, the samples with black tile showed the maintaining temperature longer time as compared with other sample panels.

On the contrary, during the cooling process, the surface temperature dropped dramatically from 50°C to 20°C. Over the following 3 hours, the temperature gradually decreased to 15°C. On the backside of all the sample panels, the concrete started to freeze and release heat as the temperature dropped within the range of 50-20°C. All the sample panels exhibited similar temperature behavior and maintained temperatures for around 20 minutes within this range, compared to the samples with No-PCM. Inside the prototype, all the samples followed a similar trend to the backside of the sample panels, whether they had white, black, or No tiles, during the cooling process. Among them, the sample with a black tile was the most effective at releasing heat.

One notable trend observed in the tests is that the presence of PCMs enhances the ability of the polymer-modified concrete to absorb, store, and release heat during heating and cooling cycles. The specific type of PCM and its melting and freezing temperature range play a crucial role in determining the extent of this impact. Samples with PCM28D and PCM43D exhibited particularly effective heat-absorption characteristics during heating, as well as sustained heat release during cooling, owing to their phase change temperature ranges.

Furthermore, the color of the tiles used in conjunction with the PCM concrete samples was found to influence their thermal behavior. Samples with black tiles demonstrated more effective heat absorption and release capabilities than those with white tiles or no tiles, highlighting the importance of considering the color of the surface when designing structures with PCM-enhanced concrete.

Overall, these heat cyclic tests underline the potential of PCM-enhanced concrete as a solution for managing temperature fluctuations in various applications, such as applying precast concrete in buildings. By selecting the appropriate PCM type and considering the color of the surface materials, it is possible to optimize the thermal performance of concrete structures, thereby reducing excessive heat and improving energy efficiency.

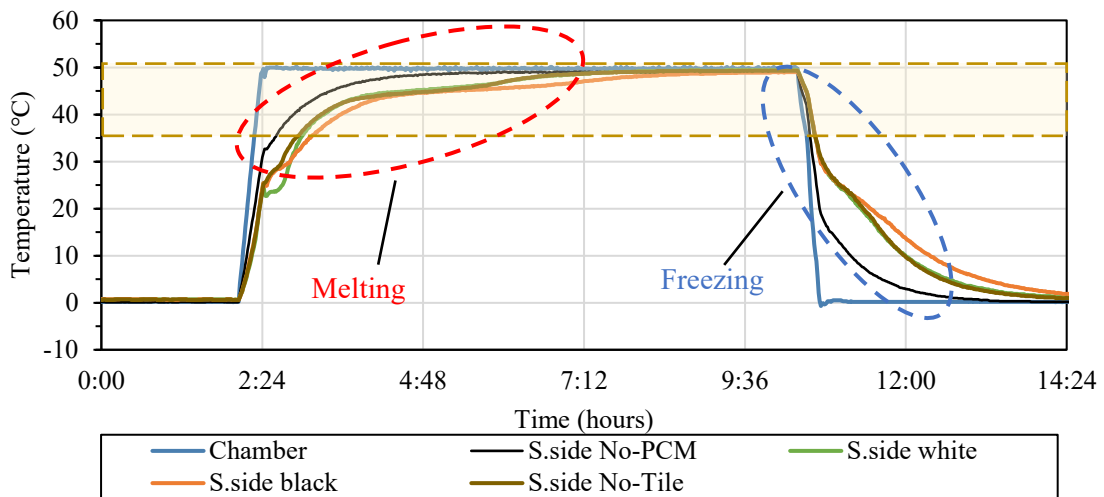
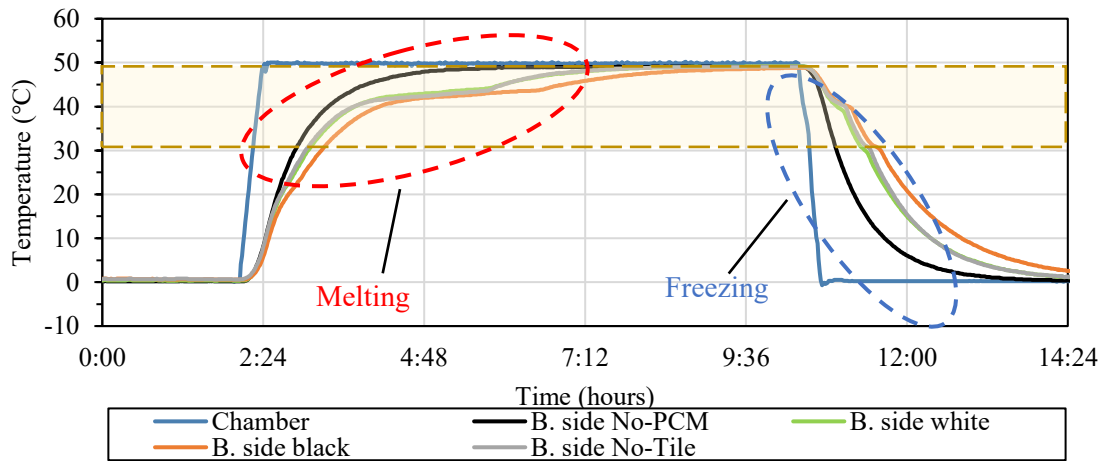


Figure 4.7.21 Heat cyclic analysis of different types of PCM28D on surface side of prototype.



4.1.1 Figure 4.7.22 Heat cyclic analysis of different types of PCM43D on backside of prototype.

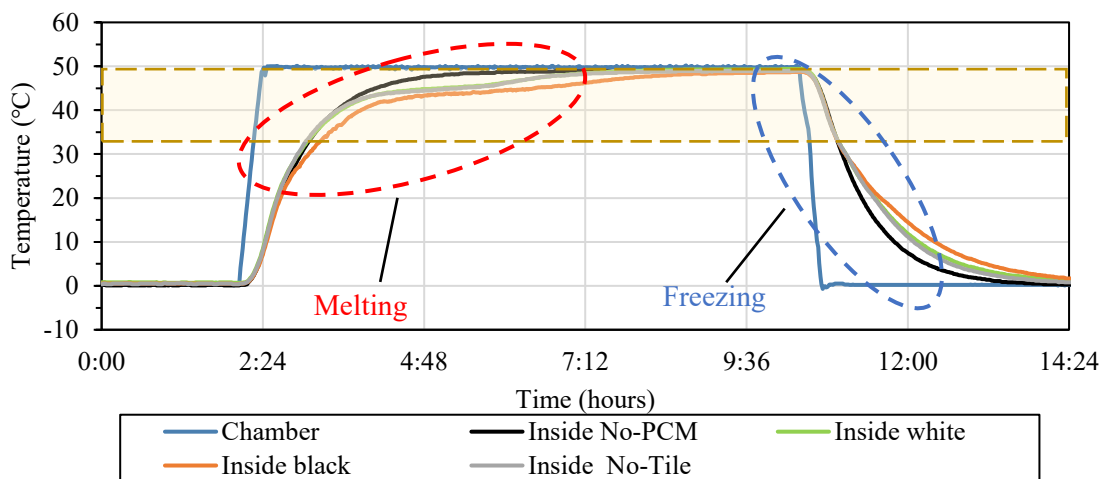


Figure 4.7.23 Heat cyclic analysis of different types of PCM43D on inside of prototype.

#### 4.7.4 Thermal expansion test

The purpose of thermal expansion test was to measure the strain and temperature changes caused by thermal deformation. This was achieved by irradiating the tile surface of the sample with a 500W incandescent lamp, simulating solar radiation. Temperature readings were taken at three points on the surface, the back surface, and within the sample, and recorded using a TDS-630. Strain measurements were obtained using a strain gauge (PL-60). The TDS-630 was employed for data recording, as in the case of temperature measurements. The experimental setup and test program are illustrated in the Figure 4.7.24 and Figure 4.7.25 below. The measurements were conducted in a constant temperature room with a room temperature set at 10°C. The test program consisted of three cycles, each comprising 3 hours of irradiation followed by 5 hours with the lamp off. This cycle was repeated three times for each test sample.

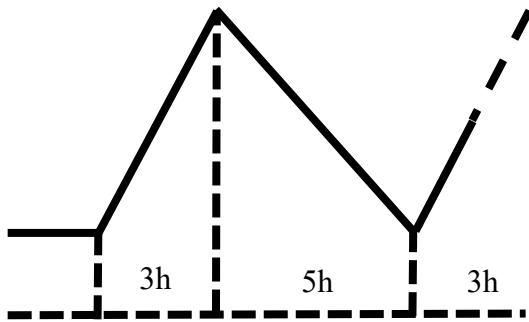


Figure 4.7.24 Test program of lamp heating test.

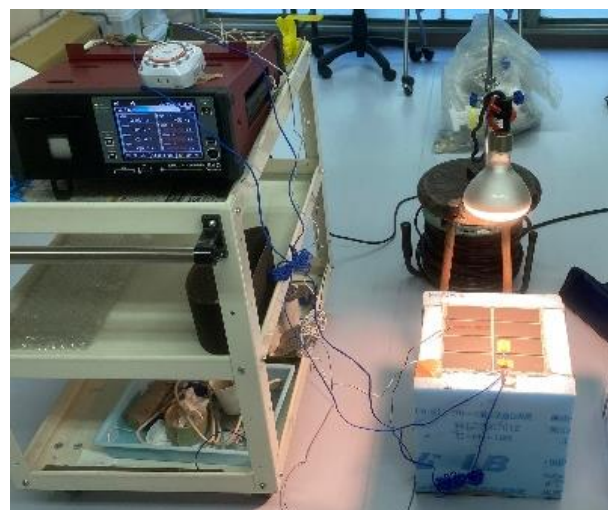
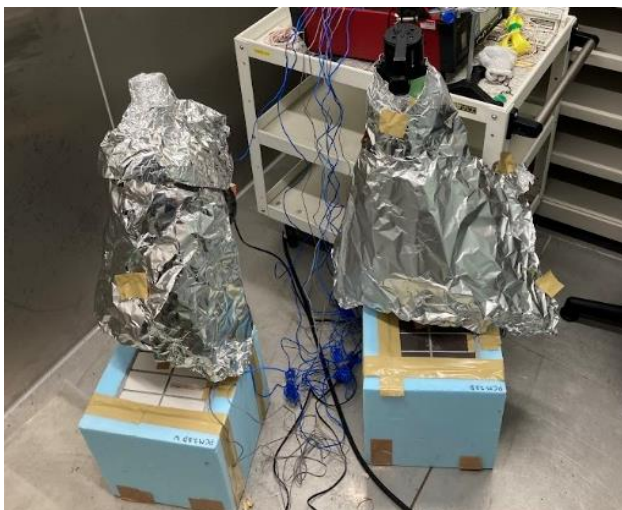


Figure 4.7.25 Experimental setup.

#### 4.7.4.1 Results of thermal expansion test

The lamp irradiation test results have revealed several important trends and phenomena related to the thermal behavior of two tile types and the impact of phase change materials (PCMs) in the context of this study.

As shown from Figure 4.7.26 to Figure 4.7.30, No-PCM specimens led to a significant increase in maximum temperature, reaching approximately 90°C, which is the highest among all the test specimens. Regarding strain gauge measurements, the sample panel exhibited shrinkage on the surface side, while it showed expansion on the backside. The black tile exhibited higher thermal shrinkage, around 50%, and a higher expansion percentage, around 87%, compared to the white tile, indicating that the white tile displayed thermal resistance.

In Figure 4.7.31 and Figure 4.7.35, PCM6D exhibited behavior similar to No-PCM. In terms of strain gauge measurements, the sample panel displayed shrinkage on the surface side and expansion on the backside. The black tile exhibited higher thermal shrinkage, around 18%, and a higher expansion percentage, around 62%, compared to the white tile.

As shown in Figure 4.7.36 and Figure 4.7.40, PCM18D achieved a maximum temperature of nearly 90°C, even with white tiles. However, strain measurements revealed that white tile specimens experienced shrinkage on both the surface side (S.side) and the backside (B.side). The black tile exhibited higher thermal shrinkage, around 16%, and a higher expansion percentage, around 83%, compared to the white tile.

In Figure 4.7.41 and Figure 4.7.45, PCM28D showed less thermal shrinkage and expansion on the back and surface sides of the panel. The black tile exhibited higher thermal shrinkage, around 58%, and a higher expansion percentage, around 71%, compared to the white tile. Comparing with sample panel with No PCM, the sample with PCM28D showed 50% lower thermal expansion, indicating that PCM may help reduce thermal expansion.

In Figure 4.7.46 and Figure 4.7.50, PCM43D exhibited distinct temperature behavior attributed to its phase change properties, with a phase change range occurring at higher temperatures than the other PCMs. This resulted in more noticeable temperature fluctuations. The strain measurements confirmed this behavior, showing surface contraction and back surface expansion for both specimens. The white tile exhibited higher thermal shrinkage, around 47%, and a higher expansion percentage, around 50% higher. These results might need to be reconfirmed through further experiments.

In conclusion, a consistent trend is observed where the maximum temperature of white tiles tends to be lower than that of black tiles during the lamp irradiation test. This color-based temperature variation is a key finding, indicating that tile color significantly contributes to the reduction of thermal expansion and thermal variation. Black tiles, known for their heat-absorbing properties, exhibit higher maximum temperatures.



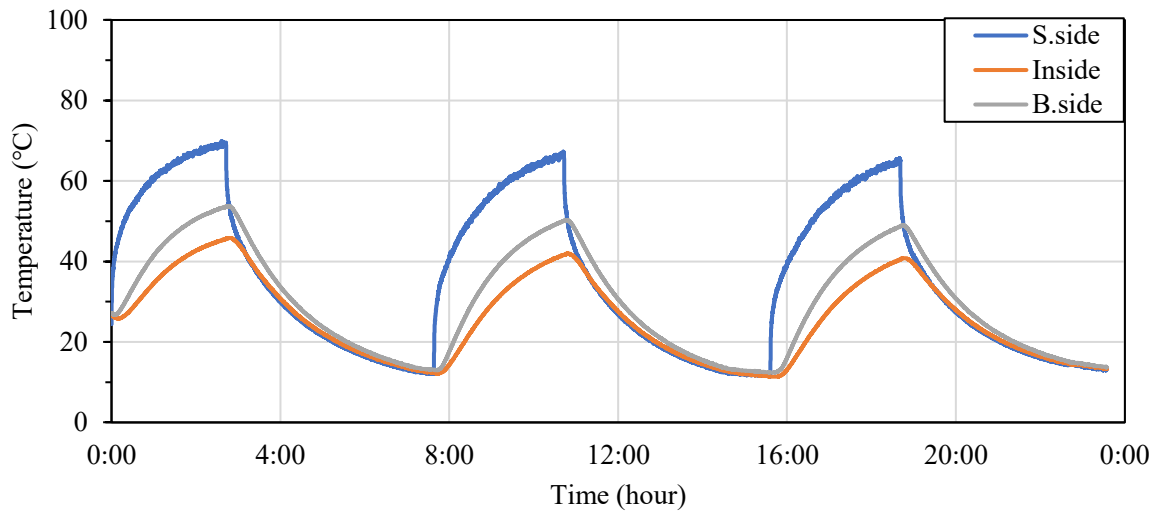


Figure 4.7.26 Thermal expansion analysis of No-PCM with white tile.

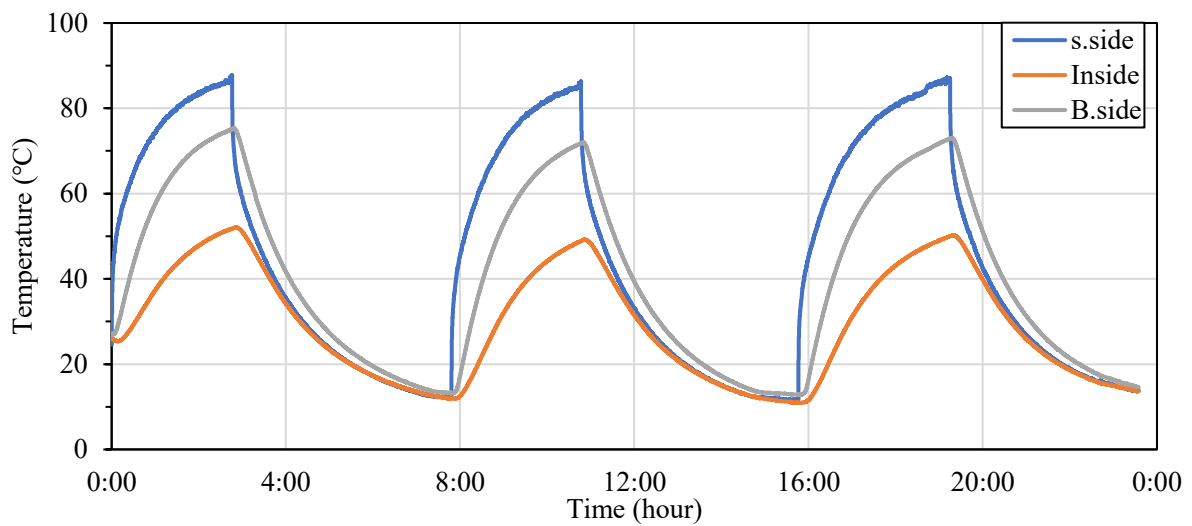


Figure 4.7.27 Thermal expansion analysis of No-PCM with black tile.

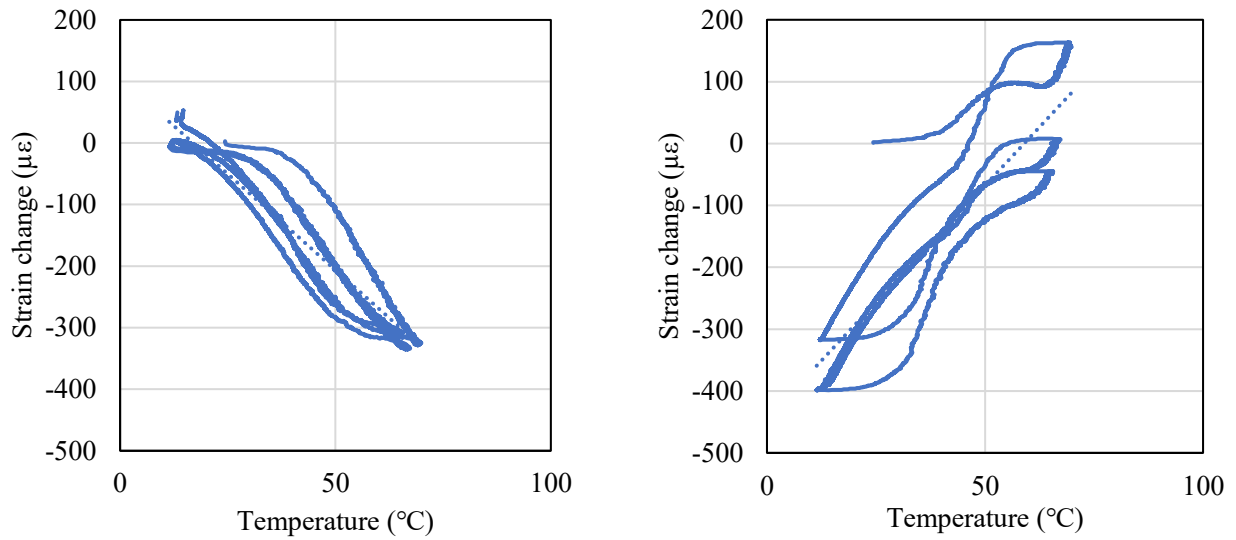


Figure 4.7.28 Strain measurement test on sample No-PCM with white tile ( L:S.side R:B.side).

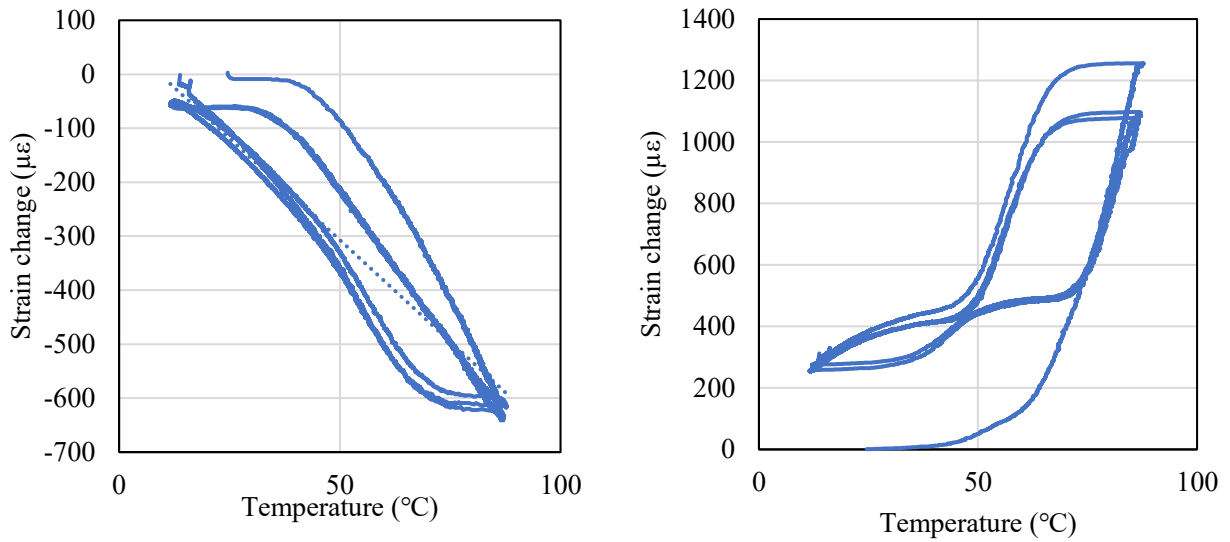


Figure 4.7.29 Strain measurement test on sample No-PCM with black tile L:S.side R:B.side).

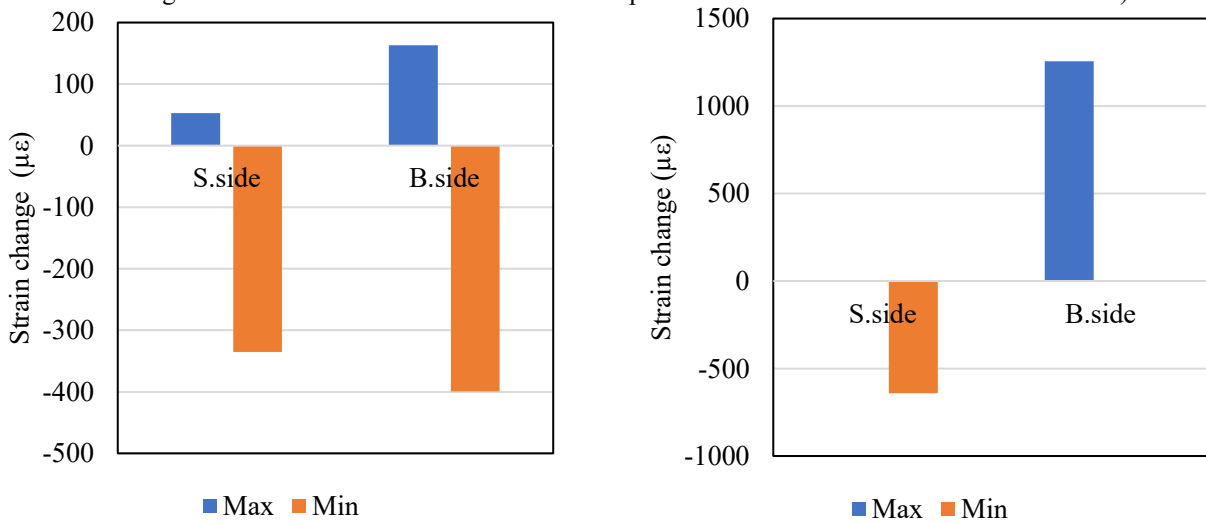


Figure 4.7.30 The results of max and min strain measurement test (No-PCM L: White tile R:Black tile).

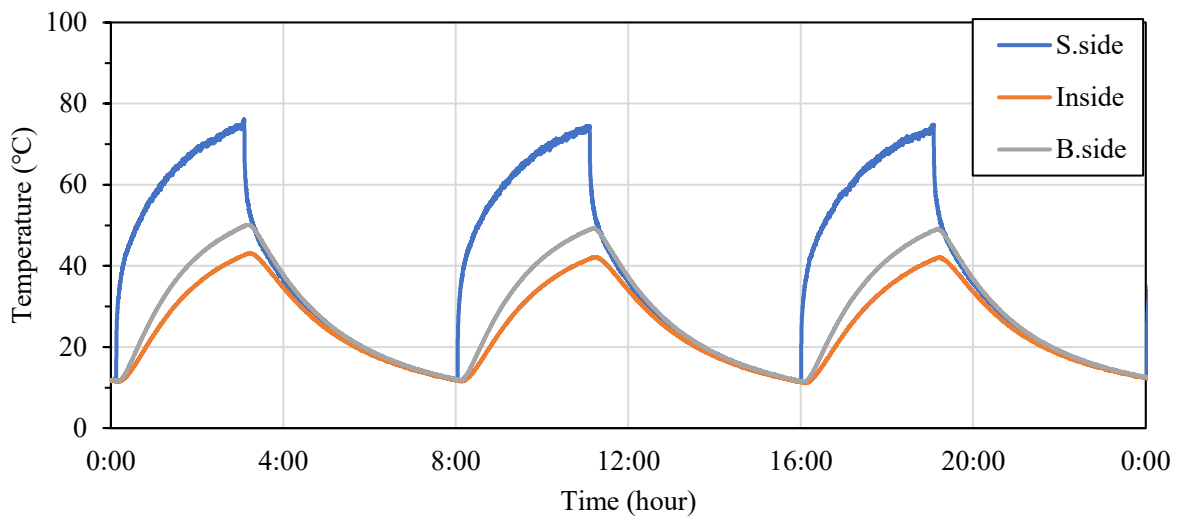


Figure 4.7.31 Thermal expansion analysis of PCM6D with white tile.

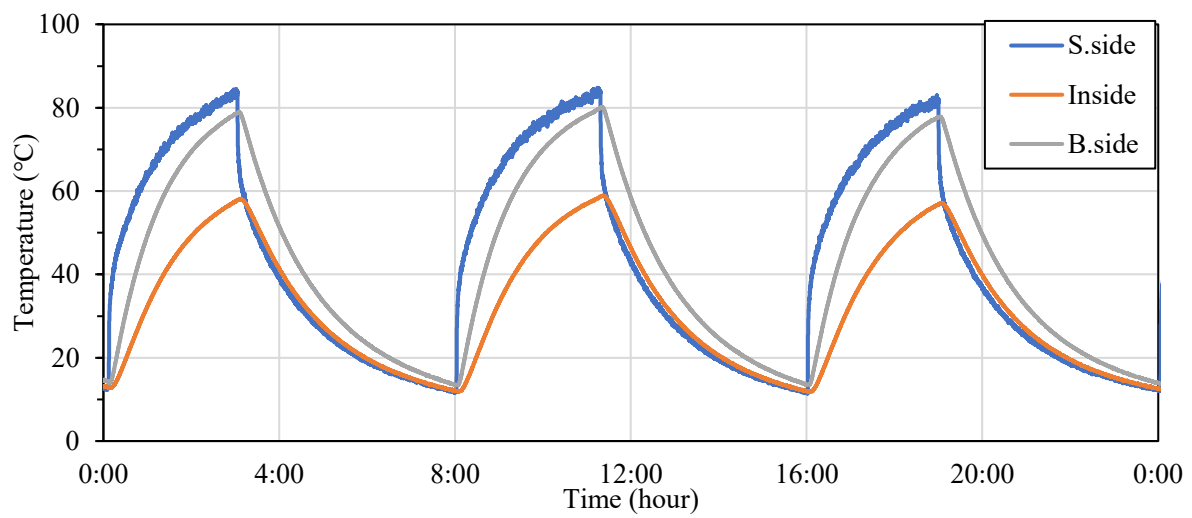


Figure 4.7.32 Thermal expansion analysis of PCM6D with black tile.

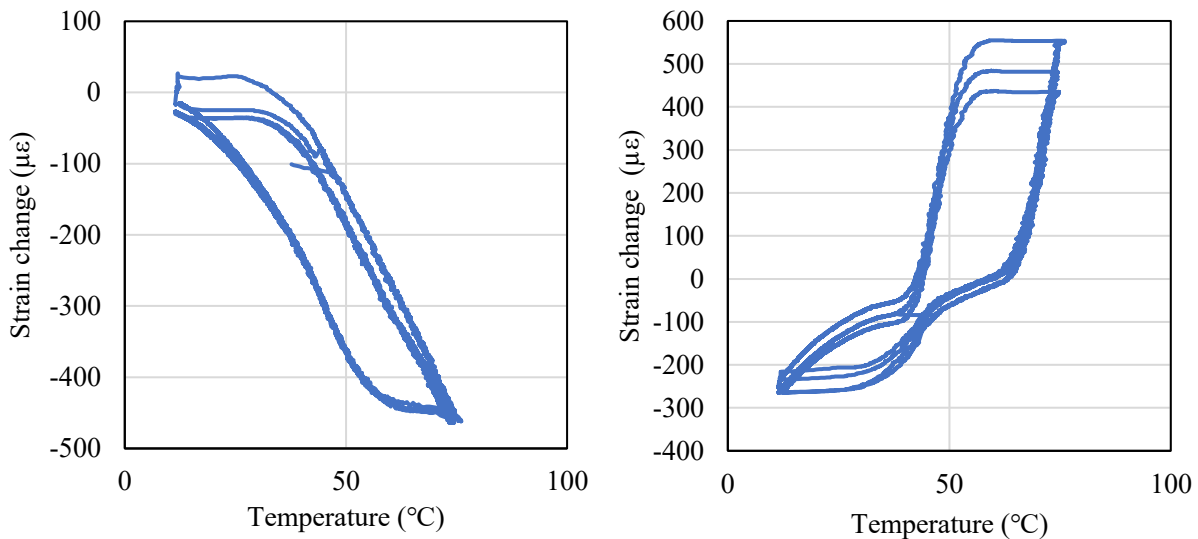


Figure 4.7.33 Strain measurement test on sample PCM6D with white tile L:S.side R:B.side).

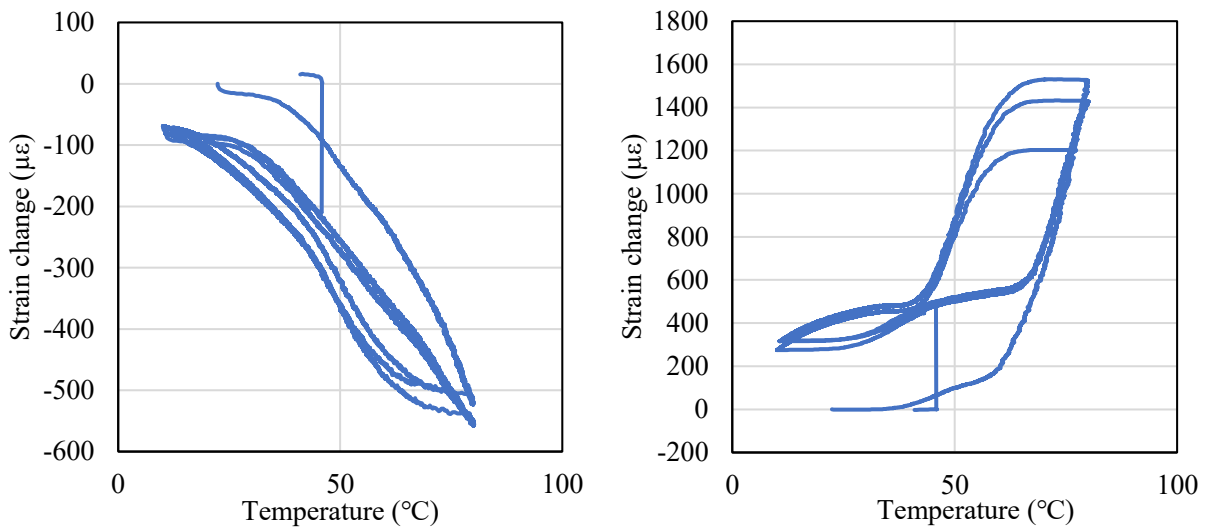


Figure 4.7.34 Strain measurement test on sample PCM6D with black tile L:S.side R:B.side).

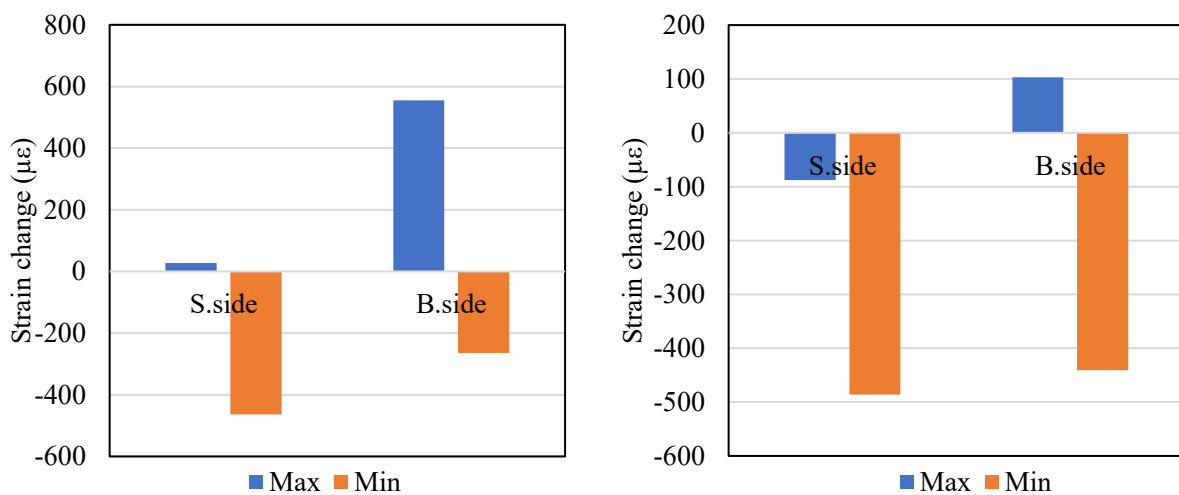


Figure 4.7.35 The results of max and min strain measurement test (PCM6D L: White tile R: Black tile).

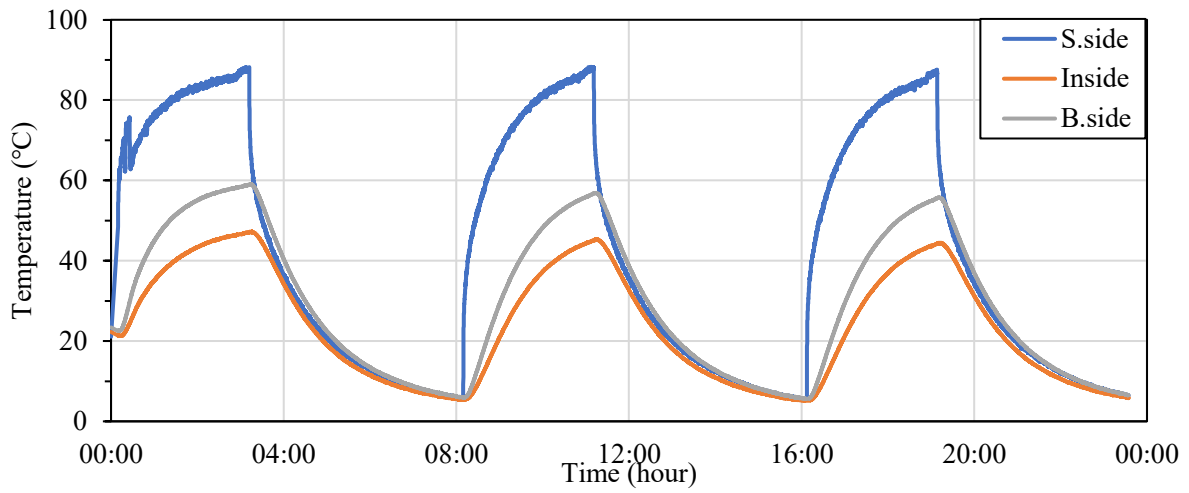


Figure 4.7.36 Thermal expansion analysis of PCM18D with white tile.

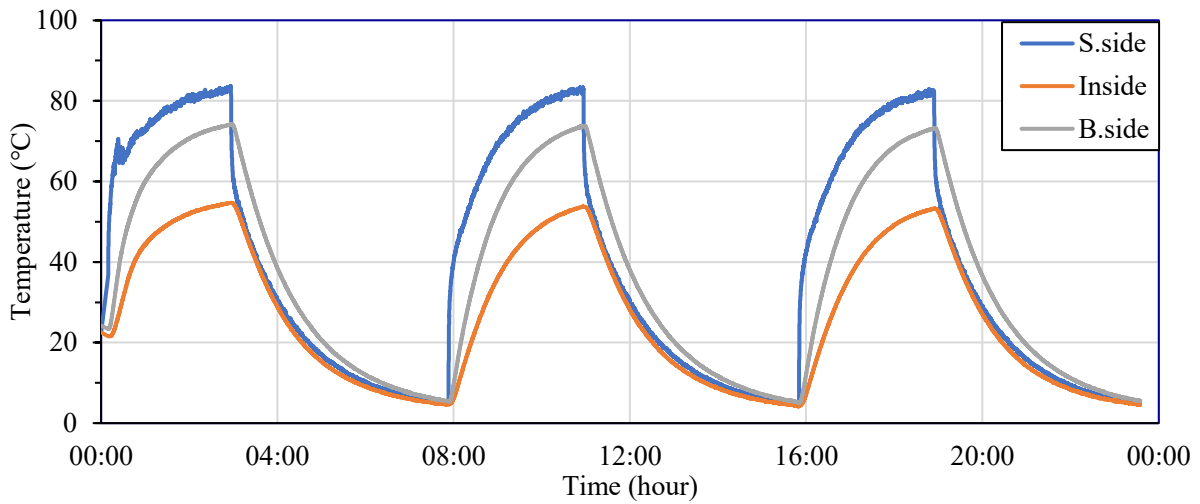


Figure 4.7.37 Thermal expansion analysis of PCM18D with black tile.

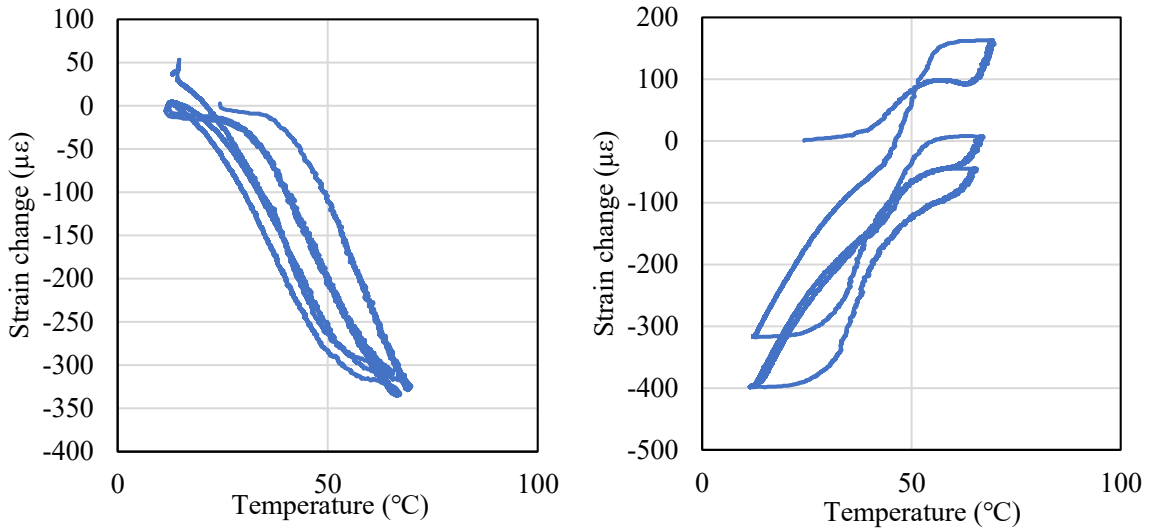


Figure 4.7.38 Strain measurement test on sample PCM18D with white tile (L:S.side R: B.side).

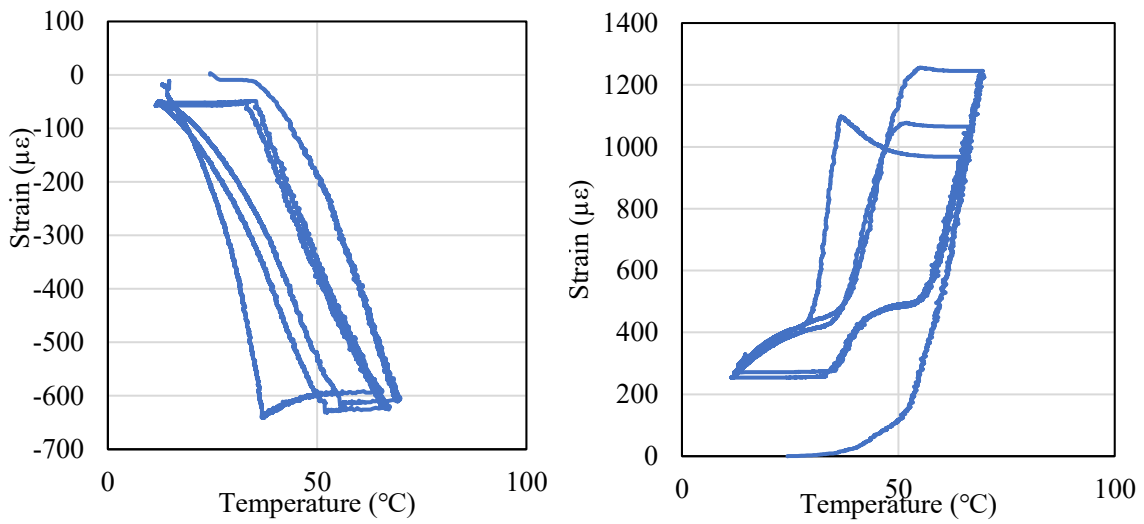


Figure 4.7.39 Strain measurement test on sample PCM18D with black tile (L:S.side R: B.side).

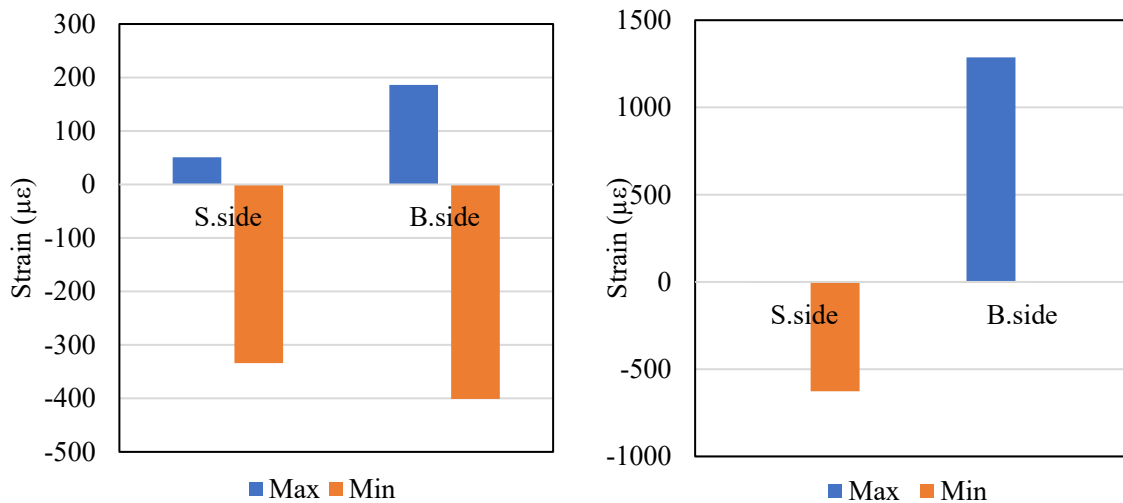


Figure 4.7.40 The results of max and min strain measurement test (PCM18D L: White tile R: Black tile).

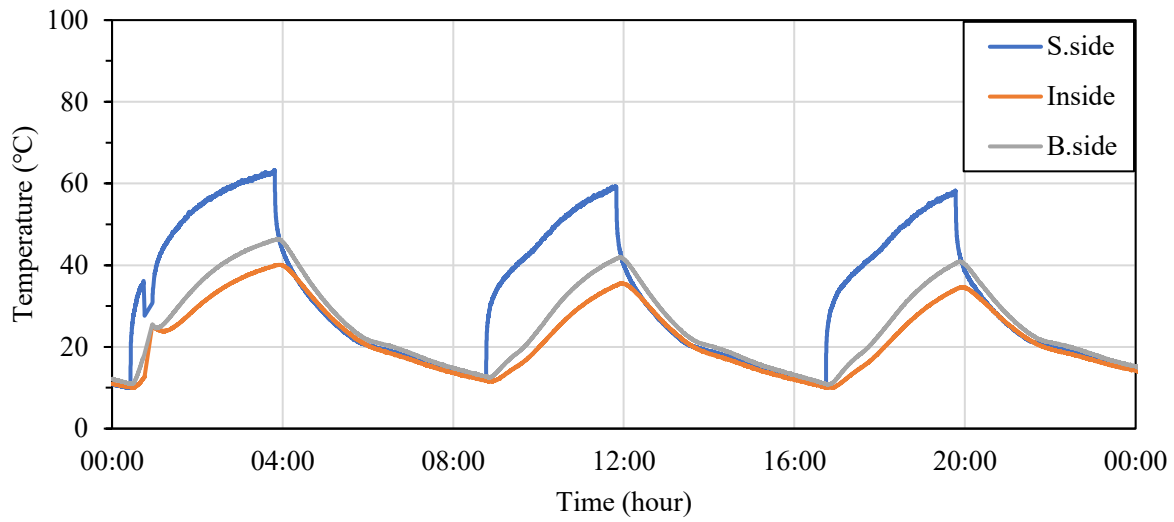


Figure 4.7.41 Thermal expansion analysis of PCM28D with white tile.

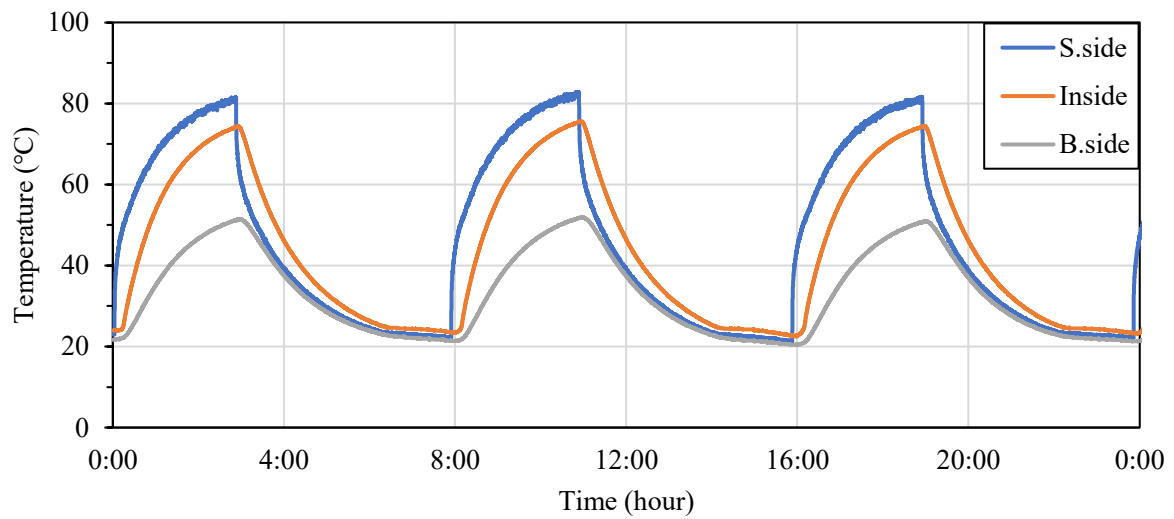


Figure 4.7.42 Thermal expansion analysis of PCM28D with black tile.

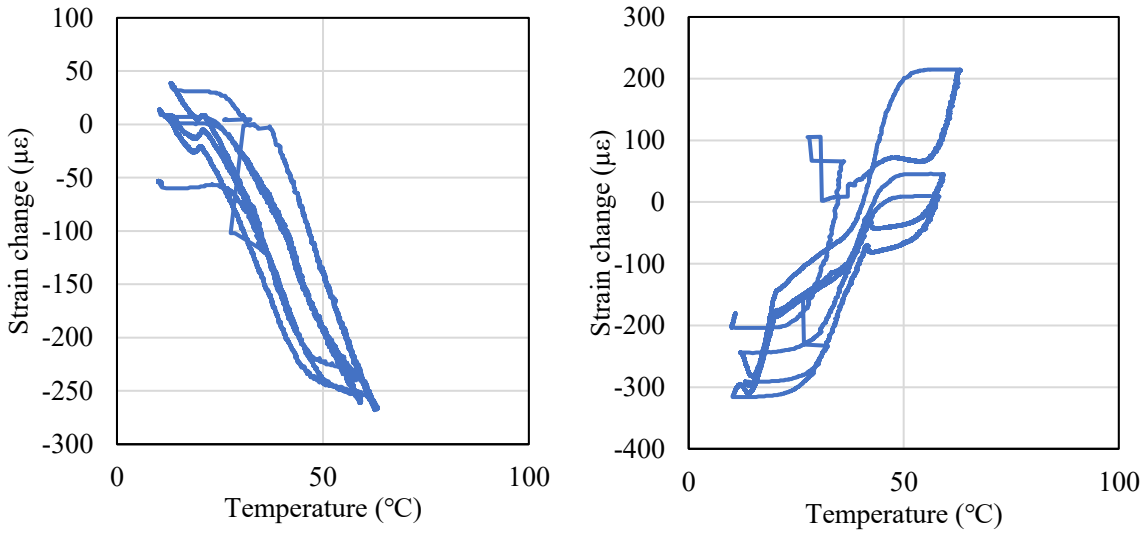


Figure 4.7.43 Strain measurement test on sample PCM28D with white tile ( L:S.side R:B.side).

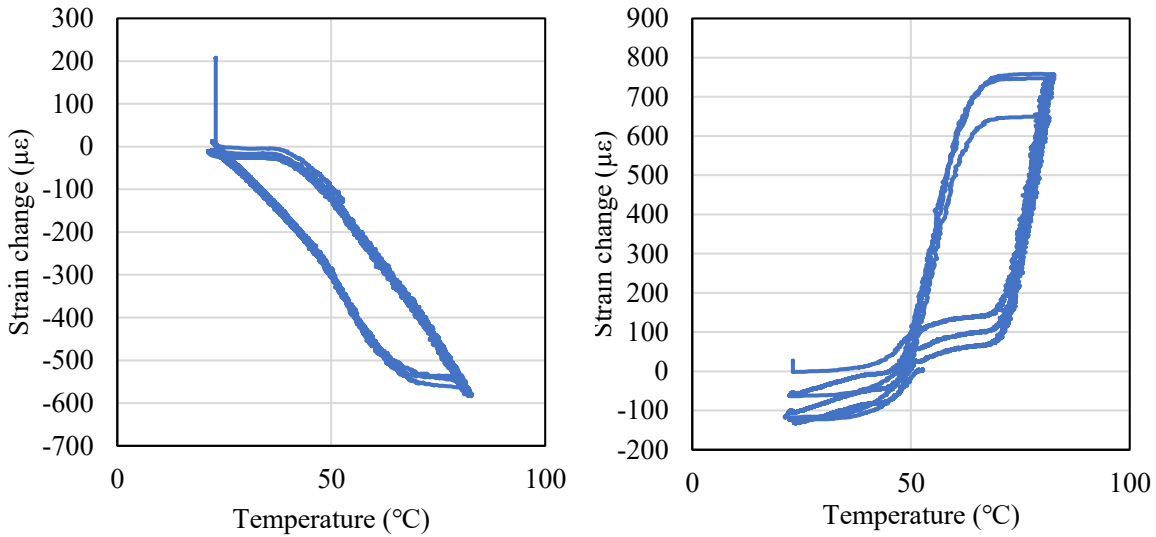


Figure 4.7.44 Strain measurement test on sample PCM28D with black tile ( L:S.side R:B.side).

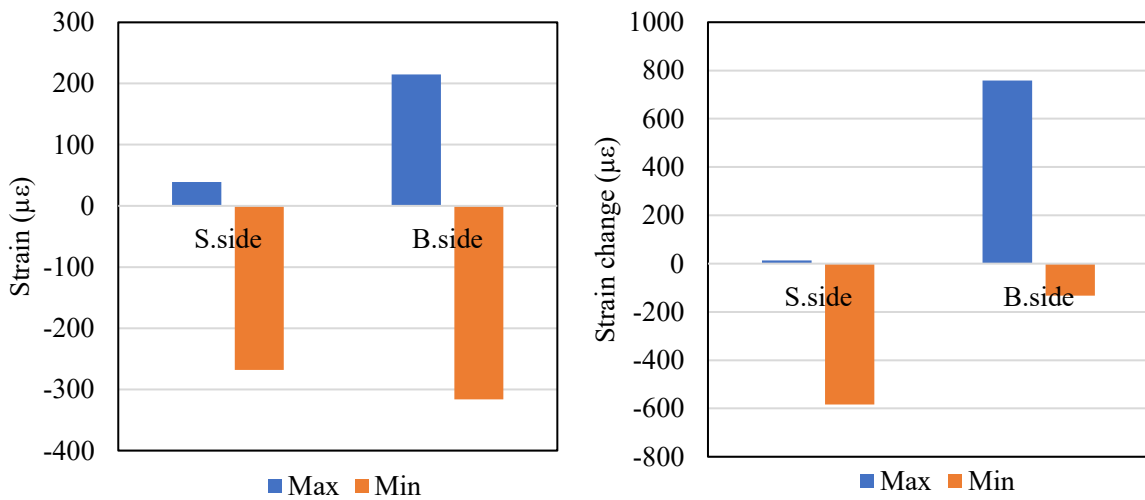


Figure 4.7.45 The results of max and min strain measurement test (PCM28D L: White tile R: Black tile).



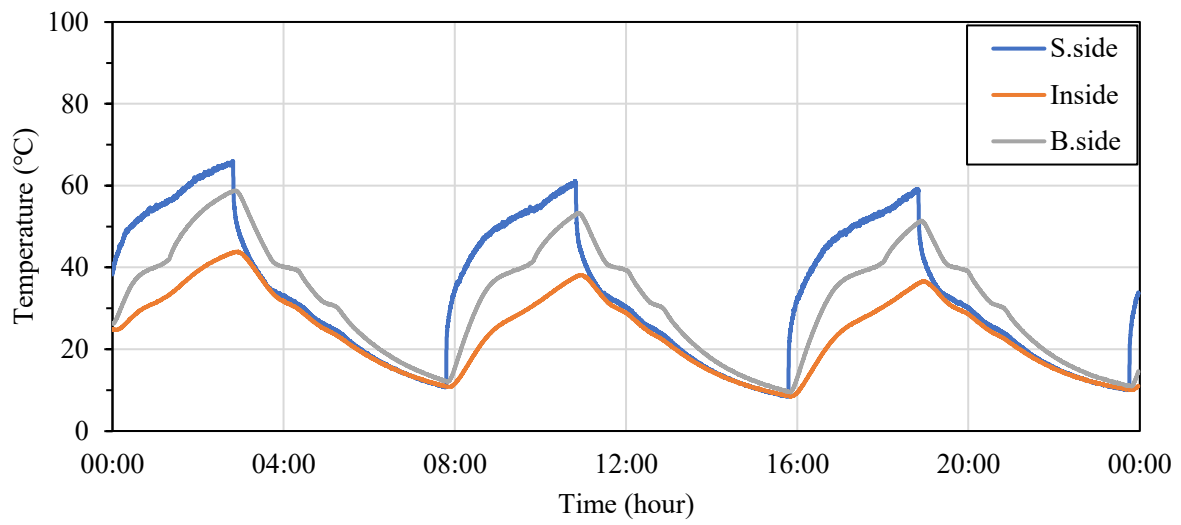


Figure 4.7.46 Thermal expansion analysis of PCM43D with white tile.

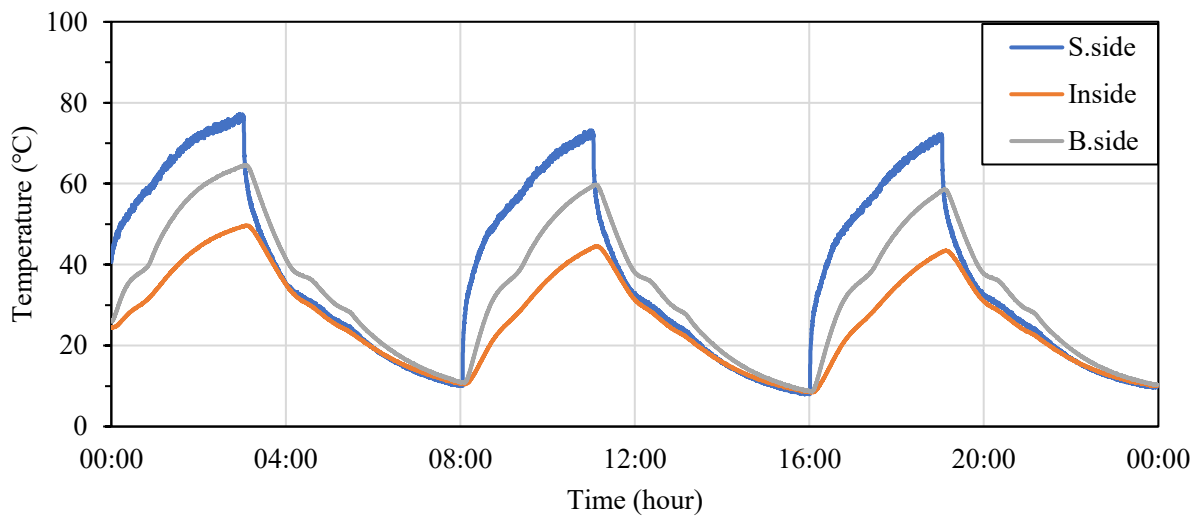


Figure 4.7.47 Thermal expansion analysis of PCM43D with black tile.

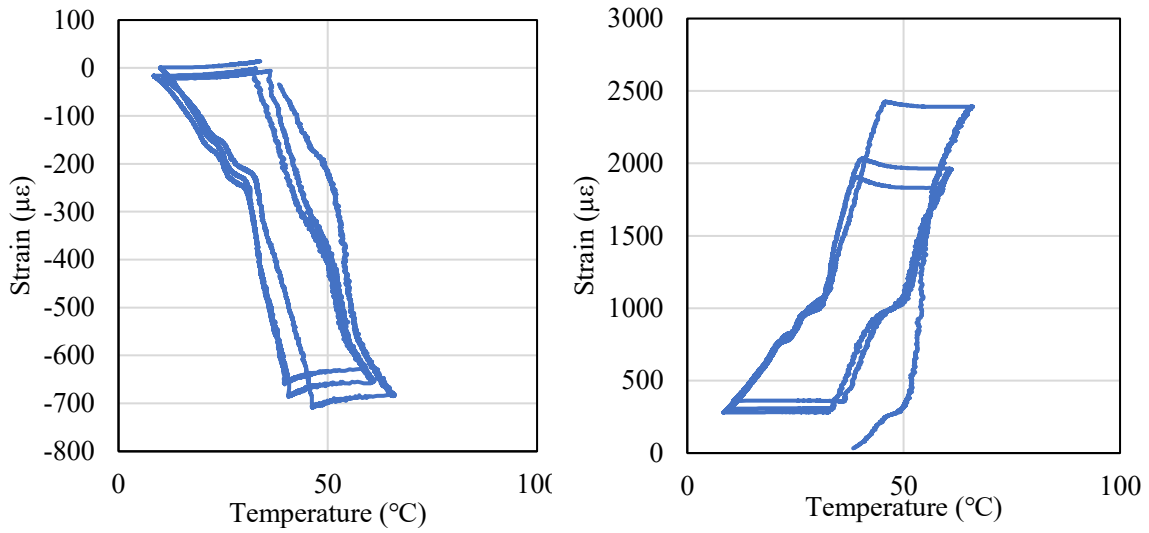


Figure 4.7.48 Strain measurement test on sample PCM43D with white tile (L:S.side R: B.side).

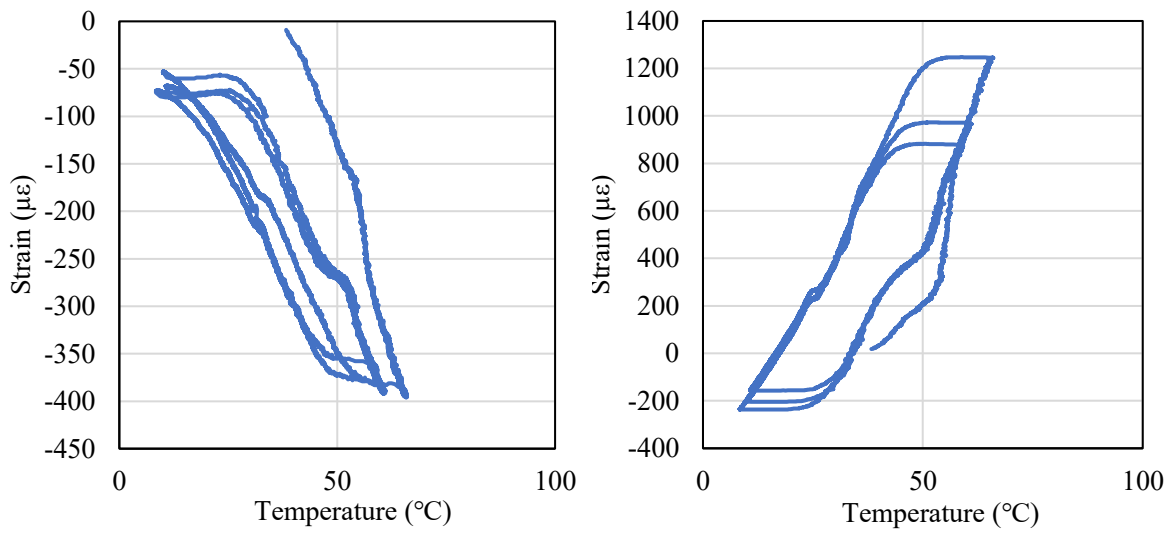


Figure 4.7.49 Strain measurement test on sample PCM43D with black tile (L:S.side R: B.side).

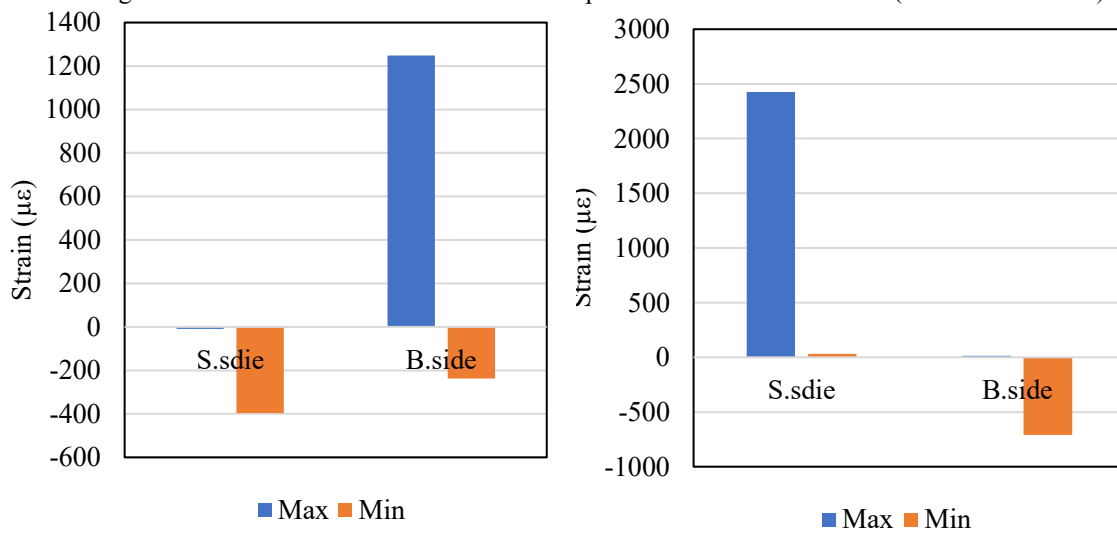


Figure 4.7.50 The results of max and min strain measurement test (PCM43D L: White tile R: Black tile).

#### 4.7.5 Thermal conductivity test

The impact of different types of polymers modified concrete, both with and without PCMs, on thermal conductivity was evaluated on day 28 of the study. In Figure 4.7.51, the thermal conductivity values are presented for PCM6D, PCM18D, PCM28D, and PCM43D polymer-modified concretes, all of which contained PCMs at a 30% substitution level.

Comparing these values to the reference concrete, it is evident that the addition of PCMs leads to increased thermal conductivity in the composite materials. The percentage increases in thermal conductivity for the composite concretes were as follows: 7.2% for PCM6D, 19.6% for PCM18D, 24% for PCM28D, and 17% for PCM43D, respectively.

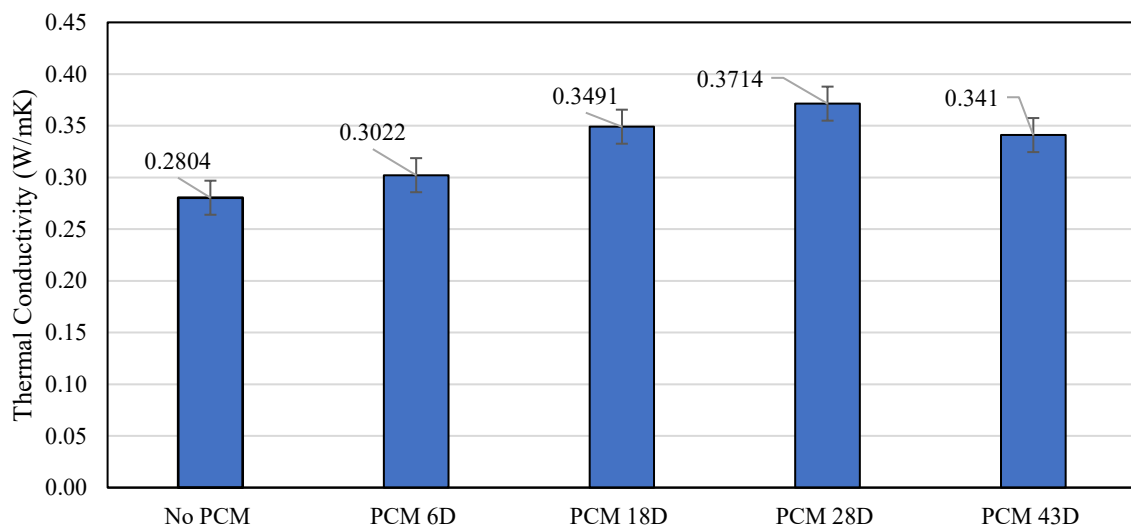


Figure 4.7.51 Thermal conductivity results on polymer-modified concrete.

## 4.8 CONCLUSIONS

This chapter is dedicated to finding solutions for reducing excessive heat in precast concrete structures and enhancing their overall quality and durability. To address these challenges, we employed polymer-modified concrete, recognizing several advantages associated with this choice. Polymer-modified concrete was chosen for its capacity to enhance bonding strength, adhesive forces, and overall construction durability.

We conducted trial tests on five different polymer types to determine the optimal mix composition and the polymer specifically suitable for polymer-modified concrete. Each trial carefully analyzed and adjusted flow tests, water-cement ratios, and polymer-cement ratios to find the optimal mix composition meeting the requirements. As a result, PAE-LDM6880 was selected due to its ability to meet requirements and enhance concrete strength as a characteristic of the polymer. The study on polymer-modified concretes with PCMs can be divided into five sections:

The initial section examines mechanical aspects, including the compressive strength of polymer-modified concretes with various PCM types. The density test revealed a substantial reduction in density of PCM-modified concretes at the 1-day stage due to the addition of PCMs. Although there was an initial decrease in strength with PCM introduction, all three concrete types exhibited significant improvements in compressive strength from day 7 to day 28. In the bonding test, it is noteworthy that all the samples demonstrated high bonding strength, ranging from 0.8 to 2 MPa, surpassing the specified requirement of 0.4 MPa. This indicates that the samples consistently met and even exceeded the required bonding strength, ensuring the reliability.

The second section focuses on specific enthalpy estimation and phase change temperature for blended PCM concretes. It analyzes the influence of different heating/cooling rates on the thermal behavior of polymer-modified concrete with PCMs, specifically regarding specific enthalpy and specific heat capacity. PCM43D displayed the highest  $\Delta h$  of 21.89 J/g and 21.56 J/g for the first and second peaks, respectively, among all the polymer-modified PCMs.

The third section is dedicated to thermal conductivity testing. The addition of PCMs resulted in increased thermal conductivity in the composite materials, with varying percentage increases depending on the PCM type.

In the fourth section, the study focuses on the heat cycle test, revealing that samples containing PCM28D and PCM43D displayed notably efficient heat-absorption characteristics during the heating phase. Moreover, they exhibited sustained heat release during the cooling phase, attributed to their specific phase change temperature ranges. The highest temperature maintenance was observed in PCM43D, with a delay of approximately 4 hours. Furthermore, the color of the tiles used in

conjunction with the PCM concrete samples was found to exert an influence on their thermal behavior. Samples with black tiles demonstrated superior heat absorption and release capabilities compared to those with white tiles or no tiles.

In summary, the PCM polymer-modified concrete meets the requirements, based on the results of mechanical property tests, cyclic tests simulating changes above normal ambient temperature and intense solar radiation, and thermal property tests, which showed that the PCM exhibited a temperature regulating function. Therefore, PCM is effective for use in the PC tile wall panel construction method.

#### 4.9 REFERENCES

- [1] M. Doğan and A. Bideci, “Effect of Styrene Butadiene Copolymer (SBR) admixture on high strength concrete,” *Constr Build Mater*, vol. 112, pp. 378–385, Jun. 2016, doi: 10.1016/J.CONBUILDMAT.2016.02.204.
- [2] Y. Ohama, “Polymer-based admixtures,” *Cem Concr Compos*, vol. 20, no. 2–3, pp. 189–212, Jan. 1998, doi: 10.1016/S0958-9465(97)00065-6.
- [3] G. Barluenga and F. Hernández-Olivares, “SBR latex modified mortar rheology and mechanical behaviour,” *Cem Concr Res*, vol. 34, no. 3, pp. 527–535, Mar. 2004, doi: 10.1016/J.CEMCONRES.2003.09.006.
- [4] M. H. F. Medeiros, P. Helene, and S. Selmo, “Influence of EVA and acrylate polymers on some mechanical properties of cementitious repair mortars,” *Constr Build Mater*, vol. 23, no. 7, pp. 2527–2533, Jul. 2009, doi: 10.1016/J.CONBUILDMAT.2009.02.021.
- [5] K. C. Jung, I. T. Roh, and S. H. Chang, “Stress analysis of runway repaired using compliant polymer concretes with consideration of cure shrinkage,” *Compos Struct*, vol. 119, pp. 13–23, Jan. 2015, doi: 10.1016/j.compstruct.2014.08.026.
- [6] E. Vincke *et al.*, “Influence of polymer addition on biogenic sulfuric acid attack of concrete,” *Int Biodeterior Biodegradation*, vol. 49, no. 4, pp. 283–292, Jun. 2002, doi: 10.1016/S0964-8305(02)00055-0.
- [7] P. I. Abdulrahman and D. K. Bzeni, “Bond strength evaluation of polymer modified cement mortar incorporated with polypropylene fibers,” *Case Studies in Construction Materials*, vol. 17, Dec. 2022, doi: 10.1016/j.cscm.2022.e01387.
- [8] Y. , I. J. , M. H. , and K. K. , Ohama, *Rubber Chemistry and Technology* , vol. 37(3). 1964.
- [9] F. Ascione, N. Bianco, R. F. De Masi, M. Mastellone, and G. Peter Vanoli, “Phase Change Materials for Reducing Cooling Energy Demand and Improving Indoor Comfort: A Step-by-Step Retrofit of a Mediterranean Educational Building,” *Energies 2019, Vol. 12, Page 3661*, vol. 12, no. 19, p. 3661, Sep. 2019, doi: 10.3390/EN12193661.
- [10] Z. Wang *et al.*, “Thermal storage performance of building envelopes for nearly-zero energy

- buildings during cooling season in Western China: An experimental study,” *Build Environ*, vol. 194, p. 107709, May 2021, doi: 10.1016/J.BUILDENV.2021.107709.
- [11] G. Evola, L. Marletta, and F. Sicurella, “A methodology for investigating the effectiveness of PCM wallboards for summer thermal comfort in buildings,” *Build Environ*, vol. 59, pp. 517–527, Jan. 2013, doi: 10.1016/J.BUILDENV.2012.09.021.
- [12] S. Ramakrishnan, X. Wang, J. Sanjayan, and J. Wilson, “Thermal performance of buildings integrated with phase change materials to reduce heat stress risks during extreme heatwave events,” *Appl Energy*, vol. 194, pp. 410–421, May 2017, doi: 10.1016/J.APENERGY.2016.04.084.
- [13] X. Kong, S. Lu, J. Huang, Z. Cai, and S. Wei, “Experimental research on the use of phase change materials in perforated brick rooms for cooling storage,” *Energy Build*, vol. 62, pp. 597–604, Jul. 2013, doi: 10.1016/J.ENBUILD.2013.03.048.
- [14] N. Zhu, F. Liu, P. Liu, P. Hu, and M. Wu, “Energy saving potential of a novel phase change material wallboard in typical climate regions of China,” *Energy Build*, vol. 128, pp. 360–369, Sep. 2016, doi: 10.1016/J.ENBUILD.2016.06.093.
- [15] J. Lei, J. Yang, and E. H. Yang, “Energy performance of building envelopes integrated with phase change materials for cooling load reduction in tropical Singapore,” *Appl Energy*, vol. 162, pp. 207–217, Jan. 2016, doi: 10.1016/J.APENERGY.2015.10.031.
- [16] J. Lei, K. Kumarasamy, K. T. Zingre, J. Yang, M. P. Wan, and E. H. Yang, “Cool colored coating and phase change materials as complementary cooling strategies for building cooling load reduction in tropics,” *Appl Energy*, vol. 190, pp. 57–63, Mar. 2017, doi: 10.1016/J.APENERGY.2016.12.114.
- [17] E. M. Alawadhi, “Thermal analysis of a building brick containing phase change material,” *Energy Build*, vol. 40, no. 3, pp. 351–357, Jan. 2008, doi: 10.1016/J.ENBUILD.2007.03.001.
- [18] “Microtek.” Accessed: Sep. 18, 2023. [Online]. Available: <https://www.microteklabs.com/>
- [19] JIS A 1173, “Method of test for slump of polymer-modified mortar”.
- [20] S. O. Y. Kan, “Mix proportioning and properties of polymer-modified concretes and mortars,” Collage of Engineering, Nihon University , Koriyama , 1983.
- [21] JIS A 1172, “Method of test for strength of polymer-modified mortar”.
- [22] R. Shadnia, L. Zhang, and P. Li, “Experimental study of geopolymer mortar with incorporated PCM,” *Constr Build Mater*, vol. 84, pp. 95–102, Jun. 2015, doi: 10.1016/j.conbuildmat.2015.03.066.
- [23] L. Haurie, S. Serrano, M. Bosch, A. I. Fernandez, and L. F. Cabeza, “Single layer mortars with microencapsulated PCM: Study of physical and thermal properties, and fire behaviour,” *Energy Build*, vol. 111, pp. 393–400, Jan. 2016, doi: 10.1016/j.enbuild.2015.11.028.
- [24] P. E. Bat-Erdene and S. Pareek, “Experimental Study on the Development of Fly Ash Foam Concrete Containing Phase Change Materials (PCMs),” *Materials*, vol. 15, no. 23, Dec. 2022, doi: 10.3390/ma15238428.

- [25] R. Illampas, I. Rigopoulos, and I. Ioannou, "Influence of microencapsulated Phase Change Materials (PCMs) on the properties of polymer modified cementitious repair mortar," *Journal of Building Engineering*, vol. 40, Aug. 2021, doi: 10.1016/j.job.2021.102328.
- [26] JIS A 5557, "Method of test for adhesion of polymer-modified mortar".
- [27] P. Ismael Abdulrahman and D. Khidhir Bzeni, "Bond strength evaluation of polymer modified cement mortar incorporated with polypropylene fibers," 2022, doi: 10.1016/j.cscm.2022.e01387.

# **CHAPTER 5**

**ULTRA LIGHT WEIGHT PCM FOAM CONCRETE**

**ENERGY (NRG) FOAM**



## 5.1 EXPERIMENTAL OVERVIEW

This chapter is to develop an ultra-lightweight foam concrete integrated with PCM. The initial section investigates mechanical aspects including dry bulk density and wet density as the target value of the NRG-foam concrete. The second section is dedicated to develop a design model for engineering implementation and upscaling of NRG-foam mixtures. The final section provides the conclusion of the chapter, summarizing the key findings and insights.

## 5.2 RESEARCH BACKGROUND

The samples of the phase change material (PCM) modified mineral insulation material examined in this research work are so-called energy (NRG) foam. This is being developed at the Institute of Construction and Building Materials (WiB) of TU Darmstadt University. The main concepts are to increase the insulating effect and the energy storage capacity of the NRG foam. To achieve improved insulation property, the strategy involves reducing thermal conductivity of foam concrete.

Foamed concrete, a lightweight concrete characterized by significantly reduced density, high porosity, and low thermal conductivity [1], [2], [3], [4], holds promise for enhancing insulation. In comparison to commonly used materials such as extruded polystyrene XPS board, which has an insulation K-value between 0.040 and 0.024 W/m.K [5], foam concrete presents an alternative [6]. In general, thermal property of foam concrete depends on density, pore size distribution and pore volume. Typically produced with varying densities ranging from 400 to 1600 kg/m<sup>3</sup>, foam concrete exhibits low thermal conductivity (0.389 to 0.734 W/m.K) [7], [8], [9].

Furthermore, there is potential to achieve a thermal conductivity comparable to extruded polystyrene XPS board by producing ultra-lightweight foam concrete with densities between 180 to 260 kg/m<sup>3</sup>. However, there is limited research on materials with densities lower than 400 kg/m<sup>3</sup>.

Regarding to increase energy storage potential, phase change materials (PCMs) has been initiated as a promising approach due to their remarkable ability to store and release thermal energy [10]. Integrating the concept of cementitious material with PCMs holds promise for creating lightweight cementitious cellular composites with favorable mechanical and thermal properties. However, previous studies have demonstrated that that the addition of PCMs [11], [12] leads to a reduction in compressive strength and workability of cementitious composites [13], [14].

Despite potential drawbacks, the incorporation of PCMs is expected to be advantageous in ultra-light weight concrete due to the inherently low thermal conductivity of PCM itself. This addition is expected to contribute to the reduction of thermal conductivity in the composite material, consequently enhancing thermal insulation properties.

The aim of the research is to develop an ultra-lightweight foam concrete integrated with PCM within a density range of between 180 to 260 kg/m<sup>3</sup> and to establish a design model for engineering implementation and upscaling of NRG-foam mixtures.

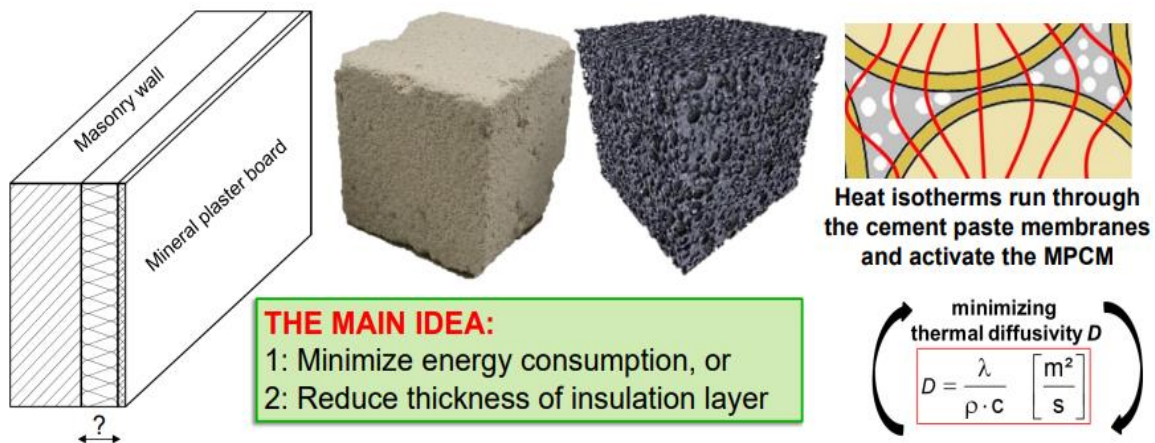


Figure 5.1.1 The main idea of NRG foam [15]

### 5.2.1 Objective

- To investigate the ultra-lightweight foam concrete density ranges (180–260 kg/m<sup>3</sup>) to study the effects of density. More specifically, to define the dry bulk density and wet density as the target value of the NRG-foam concrete,
- To study the effects of different amounts of PCM in NRG-foam with different density ranges,
- To determine mechanical behavior of NRG-foam with different density ranges,
- To determine the ribbon thickness of NRG-foam for all mix design of NRG-foam by defining the porosity of the NRG-foam concrete as the target value,
- To evaluate the thermal behavior of the phase change materials incorporated into NRG-foam concrete.

### 5.2.2 Mix design

In this experiment, 12 different PCM foam concrete mixtures with dry densities, ranging between 180 kg/m<sup>3</sup> and 260 kg/m<sup>3</sup>, were considered.

Table 5-1 Mix designs of the NRG foam.

	180 kg/m <sup>3</sup>	200 kg/m <sup>3</sup>	220 kg/m <sup>3</sup>	240 kg/m <sup>3</sup>	260 kg/m <sup>3</sup>
<b>Reference</b>	✓	✓	✓	✓	✓
<b>PCM-5%</b>	✓	✓	-	-	-
<b>PCM-10%</b>	✓	✓	✓	✓	
<b>PCM-20%</b>	-	-	X	X	X

### 5.2.3 Production of foam concrete

The foam concrete samples were prepared using the pre-forming method. The first step in this method was to prepare the paste. Thus, PCM and cement with metakaolin was mixed until a homogeneous appearance was achieved. Next, the obtained binder was mixed with water for 120 seconds, followed by the superplasticizer and mixed for another 60 seconds. The stabilizer was added to the mixture for 90 seconds. Finally, the hardening accelerator was added prior to the continued mixing procedure until a homogenous paste was obtained.

The second step was to produce the foam. It was produced using the Gertec foam generator, a compact device for the continuous production of foam. The parameters controlling the produced foam were the water flow, compressed air flow and foaming agent concentration. The performed experimental tests showed that the foam with a given density can be obtained with different generator settings. In the conducted tests, foam with a density of 70 kg/m<sup>3</sup> was produced under the settings of 40 dm<sup>3</sup>/min (40 L/min) of compressed air and 3 dm<sup>3</sup>/min (3 L/min) of water. The concentration of the foaming agent was 2% of the water volume. The foam was produced concurrently with the control of the assumed density. Afterwards, the foam was gradually added to the cement paste and successively mixed until a homogeneous mixture was obtained. After homogeneously mixing, the volume and wet density of all the mixtures were determined. Finally, the foam concrete was poured into molds, which were completely sealed using silicone to avoid leakage. The molds were 100 × 100 × 500 mm, 40 × 40 × 160 mm and 150 × 150 × 150 mm, mainly for the mechanical and thermal tests.

#### 5.2.4 Experimental findings

In this experiment, 12 different PCM foam concrete mixtures with dry densities, ranging between 180 kg/m<sup>3</sup> and 260 kg/m<sup>3</sup>, were considered. Since NRG-foam with PCM is a highly sensitive material; thus, all mixtures were carefully measured and their wet density and volume were recorded respectively to ensure their target dry density and target volume were reached. As for the Reference and PCM 5% samples with different densities, there were no problems with mix composition as the foam was stable for every mixture (Figure 5.1.2). And no volume loss was observed.

As for the NRG-foam with 10% PCM, the molds were completely sealed in advance to prevent any collapse of the foam in mixture. The foam structure of the paste of all the compositions, mixed according to this mix design, collapsed even in the homogeneous mixture. It should be noted that there were two possible reasons that might have caused the foam structure of the paste to collapse or the volume of the paste in foam to decrease. The first reason was related to the accelerator. After the paste was mixed with the foam, the hardening accelerator was usually implemented to speed up the hardening process and porous structure formation. However, the collapse of the paste in foam structure could be caused by the insufficient amount of hardening accelerator. To address this issue of foam collapse in mixtures containing NRG foam with 10% PCM, we decided to increase the amount of accelerator by 10%. As a result, all the paste in foam structures for all the mixtures remained stable after one day (Figure 5.1.3). The second reason was that Nextek24 PCM may cause the decrease in the volume of the foam. Previous studies said that Nextek 24D had the most favorable properties with respect to processing and the core of Nextek 24D consists of a phase change material of kerosene, coated with melamine. However, our research showed that adding 10% of PCM into the mixture caused volume loss of around 10% in the foam. As shown in figures 5.1.2 and table 5-2, the initial volume of all the mixtures was 15L. After adding the PCM 10% into the mixture, its volume decreased to 14L which was not considerably high-volume loss.

As for the NRG foam with 20% PCM, the compositions were mixed according to the same mix design. But during the mixing process, mixtures were so dry that it was nearly impossible to mix after 20% of Nextek24 PCMs was added. Because the increase in the PCM content of the mixtures leads to an increase in the amount of water needed for their preparation. Even when the superplasticizer was added into the mixture, it still required large amounts of superplasticizer to achieve desired flowability of mixture, which could compromise the foam structure's stability. Another reason was that Nextek24 PCM caused the decrease in the volume of the foam. The experiments revealed that incorporating 20% PCM into the mixture resulted in a volume loss of approximately 20-30% in the foam.

To solve this problem, it can be suggested that the amount of foam should be increased. Controlling the wet density by increasing the amount of foam in the mixture may help compensate for the volume loss caused by the Nextek24 PCM. This adjustment allows for a more favorable environment for mixing the PCM and other components effectively.













Figure 5.1.2 The mixtures of NRG foam with Nextek24 PCM with 10% collapsed foam structure.

















Figure 5.1.3 The mixtures of NRG foam with Nextek24 PCM with 10% after increasing accelerator.



Table 5-2 The results of volume measurement for reference NRG-foam samples.

NRG-Foam	Mass to produce 15L	Volume of NRG foam	Hardening
R180	15L		
R200	15L		
R220	15L		
R240	15L		
R260	15L		

NRG-Foam	Mass to produce 15L	Volume of NRG foam	Hardening
PCM-5% 180	15L		
PCM-5% 200	14.5L		
PCM-10% 180	14L		
PCM-10% 200	14L		

NRG-Foam	Mass to produce 15L	Volume of NRG foam	Hardening
PCM-10% 220	13.6L		
PCM-10% 240	14L		
PCM-10% 260	14L		



**5.2.5 Density test**

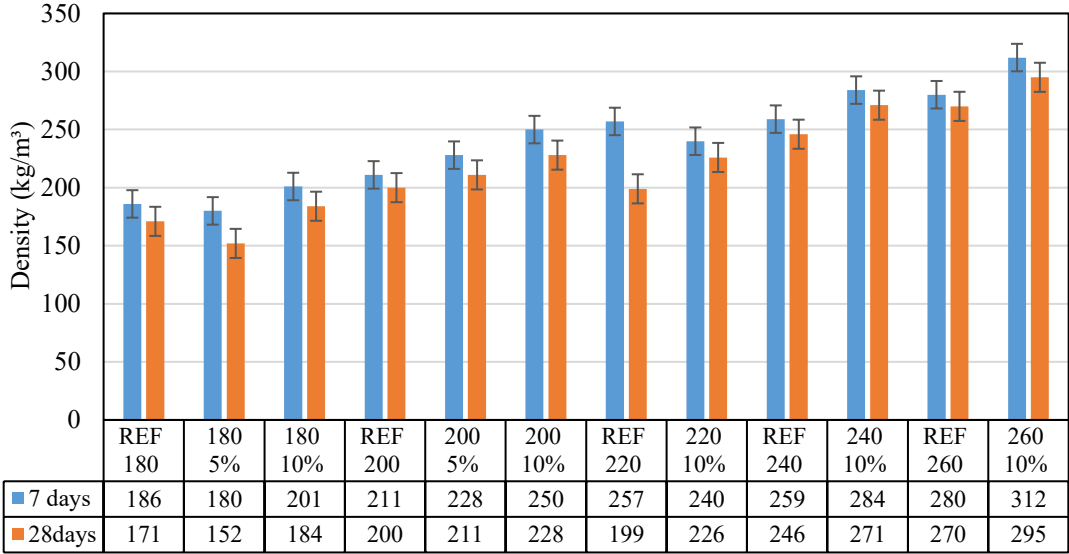


Figure 5.1.4 Density results of NRG foam concretes.

**5.2.5.1 Results of the density test**

The primary characteristics that define foam concrete density are stability and consistency. The outcomes of the density tests are provided from table 5-3 to table 5-8. Stability, in the context of foamed concrete, refers to the ratio of the initial (fresh) density to the final (hardened) density. Conversely, consistency relates to the ratio between fresh density and the target density, which is determined by the quantity of foam introduced into the foam concrete mixture. In general, the density of foam concrete is influenced by both stability and consistency factors, both of which have a direct impact on the material's strength. The test results demonstrate that all mix compositions containing PCM exhibited comparable levels of consistency and stability, closely aligning with the intended target densities. Our results show that all the PCM mix compositions had similar consistency and stability that were close to the target densities.

Figure 5.1.4 shows the results of NRG foam concretes with and without PCM, was tested. Density measurements were taken at 7 days and 28 days. The density of all samples was carefully adjusted by adding foam to achieve low-density foamed concrete.

When comparing the initial density with the density after 28 days, it was observed that all samples experienced weight loss. For the REF samples, the weight loss was approximately 8% after 28 days. In the case of NRG foam with PCM-5%, the weight loss was around 12%. Meanwhile, for NRG foam with PCM-10%, the weight loss averaged around 7% as shown.

Table 5-3 7 days density test of NRG foam samples with No-PCM.

(Density control)							
Mix Designation	Sample	Curing period (d)	Density of foam (kg/m <sup>3</sup> )	Fresh density (kg/m <sup>3</sup> )	Dry density (kg/m <sup>3</sup> )	Consistency (%)	Stability (%)
<b>R180</b>	4x4x16	7	72	206	199	1,1	1,0
					200	1,1	1,0
					245	1,1	0,8
	15x15x15				219	1,1	0,9
	10x10x50				197	1,1	1,0
<b>R200</b>	4x4x16	7	71	211	275	1,1	0,8
					194	1,1	1,1
					192	1,1	1,1
	15x15x15				222	1,1	1,0
	10x10x50				180	1,1	1,2
<b>R220</b>	4x4x16	7	70	231	216	1,1	1,1
					220	1,1	1,0
					220	1,1	1,0
	15x15x15				236	1,1	1,0
	10x10x50				221	1,1	1,0
<b>R240</b>	4x4x16	7	73	280	279	1,2	1,0
					271	1,2	1,0
					271	1,2	1,0
	15x15x15				255	1,2	1,1
	10x10x50				243	1,2	1,2
<b>R260</b>	4x4x16	7	72	318	278	1,2	1,1
					281	1,1	1,1
					282	1,1	1,1
	15x15x15				302	1,2	1,1
	10x10x50				315	1,2	1,0

Table 5-4 28 days density test of NRG foam samples with No-PCM.

(Density control)								
Mix Designation	Sample	Curing period (d)	Density of foam (kg/m <sup>3</sup> )	Fresh density (kg/m <sup>3</sup> )	Dry density (kg/m <sup>3</sup> )	Consistency (%)	Stability (%)	
<b>R180</b>	4x4x16	28	72	206	231	1.1	0.9	
					186	1.1	1.1	
					186	1.1	1.1	
	15x15x15				207	1.1	1.0	
	10x10x50				182	1.1	1.1	
	4x4x16				184	1.1	1.1	
<b>R200</b>	4x4x16	28	71	211	184	1.1	1.1	
					266	1.1	0.8	
					203	1.1	1.0	
	15x15x15				166	1.1	1.3	
	10x10x50				259	1.1	0.9	
	4x4x16				259	1.1	0.9	
<b>R220</b>	4x4x16	28	70	231	252	1.1	0.9	
					227	1.1	1.0	
					15x15x15	199	1.1	1.2
	10x10x50				261	1.1	1.0	
	4x4x16				266	1.1	1.0	
	4x4x16				251	1.1	0.0	
<b>R240</b>	4x4x16	7	73	259	235	1.1	1.1	
					15x15x15	229	1.1	1.1
					10x10x50	278	1.0	1.0
	4x4x16				281	1.1	1.0	
	4x4x16				282	1.1	1.0	
	4x4x16				302	1.2	0.9	
<b>R260</b>	15x15x15	7	72	270	315	1.2	0.9	
	10x10x50							

Table 5-5 7 days density test of NRG foam samples with 5% PCM.

(Density control)							
Mix Designation	Sample	Curing period (d)	Density of foam (kg/m <sup>3</sup> )	Fresh density (kg/m <sup>3</sup> )	Dry density (kg/m <sup>3</sup> )	Consistency (%)	Stability (%)
<b>180 PCM-5%</b>	4x4x16	7	72	208	180	1.2	1.2
					180	1.2	1.2
					180	1.2	1.2
	15x15x15				196	1.2	1.1
	10x10x50				184	1.2	1.1
	4x4x16				230	1.2	1.1
<b>200 PCM-5%</b>	4x4x16	7	72	243	223	1.2	1.1
					230	1.2	1.1
					219	1.2	1.1
	15x15x15				207	1.2	1.2
	10x10x50				207	1.2	1.2
	4x4x16				207	1.2	1.2

Table 5-6 28 days density test of NRG foam samples with 5% PCM.

(Density control)							
Mix Designation	Sample	Curing period (d)	Density of foam (kg/m <sup>3</sup> )	Fresh density (kg/m <sup>3</sup> )	Dry density (kg/m <sup>3</sup> )	Consistency (%)	Stability (%)
<b>180 PCM-5%</b>	4x4x16	28	72	208	152	1.2	1.4
					153	1.2	1.4
					151	1.2	1.4
	15x15x15				181	1.2	1.2
	10x10x50				175	1.2	1.2
	4x4x16				217	1.2	1.1
<b>200 PCM-5%</b>	4x4x16	28	72	243	209	1.2	1.2
					209	1.2	1.2
					216	1.2	1.1
	15x15x15				206	1.2	1.2
	10x10x50				206	1.2	1.2
	4x4x16				206	1.2	1.2

Table 5-7 7 days density test of NRG foam samples with 10% PCM.

(Density control)								
Mix Designation	Sample	Curing period (d)	Density of foam (kg/m <sup>3</sup> )	Fresh density (kg/m <sup>3</sup> )	Dry density (kg/m <sup>3</sup> )	Consistency (%)	Stability (%)	
<b>180 PCM-10%</b>	4x4x16	7	74	264	194	1.5	1.0	
					203	1.5	1.2	
					207	1.5	1.0	
	15x15x15				246	1.5	1.3	
					10x10x50	237	1.5	1.1
<b>200 PCM-10%</b>	4x4x16	7	73	233		270	1.2	1.2
					227	1.2	1.1	
					254	1.2	1.1	
	15x15x15				210	1.2	0.9	
					10x10x50	230	1.2	1.0
<b>220 PCM-10%</b>	4x4x16	7	73	252		236	1.1	1.1
					245	1.1	1.0	
					238	1.1	1.1	
	15x15x15				301	1.1	0.8	
					10x10x50	262	1.1	1.0
<b>240 PCM-10%</b>	4x4x16	7	73	310		285	1.3	1.1
					281	1.3	1.1	
					285	1.3	1.1	
	15x15x15				307	1.3	1.0	
					10x10x50	289	1.3	1.1
<b>260 PCM-10%</b>	4x4x16	7	73	320		350	1.2	0.9
					294	1.2	1.1	
					293	1.2	1.1	
	15x15x15				320	1.2	1.0	
					10x10x50	298	1.2	1.1

Table 5-8 28 days density test of NRG foam samples with 10% PCM.

(Density control)							
Mix Designation	Sample	Curing period (d)	Density of foam (kg/m <sup>3</sup> )	Fresh density (kg/m <sup>3</sup> )	Dry density (kg/m <sup>3</sup> )	Consistency (%)	Stability (%)
<b>180 PCM-10%</b>	4x4x16	28	74	264	180	1.5	1.5
					184	1.5	1.4
					188	1.5	1.4
	15x15x15				219	1.5	1.2
	10x10x50				206	1.5	1.3
	4x4x16				230	1.2	1.0
<b>200 PCM-10%</b>	4x4x16	28	73	233	207	1.2	1.1
					246	1.2	0.9
					210	1.2	1.1
	15x15x15				226	1.2	1.0
	10x10x50				223	1.1	1.1
	4x4x16				231	1.1	1.1
<b>220 PCM-10%</b>	4x4x16	28	73	252	223	1.1	1.1
					292	1.1	0.9
					232	1.1	1.1
	15x15x15				297	1.3	1.0
	10x10x50				270	1.3	1.1
	4x4x16				285	1.3	1.1
<b>240 PCM-10%</b>	4x4x16	28	73	310	305	1.3	1.0
					286	1.3	1.1
					274	1.8	1.2
	15x15x15				334	1.2	1.0
	10x10x50				276	1.2	1.2
	4x4x16				312	1.2	1.0
<b>260 PCM-10%</b>	4x4x16	28	73	320	291	1.2	1.1
					312	1.2	1.0
					291	1.2	1.1
	15x15x15				276	1.2	1.2
	10x10x50				274	1.8	1.2
	4x4x16				334	1.2	1.0

### 5.2.6 Compressive strength test

Compressive strength testing was conducted on cubic specimens measuring  $100 \times 100 \times 100 \text{ mm}^3$  (Figure 5.1.5). These cubic samples were produced directly from molds of the same dimensions and also from larger molds ( $300 \times 300 \times 100 \text{ mm}^3$ ) after a cutting process. All specimens remained in the molds for 24 hours before being demolded and left to cure for 28 days at a temperature of  $20^\circ\text{C}$  and 60% relative humidity. These strength tests are conducted using a certified testing device connected to a computer, allowing for the adjustment and modification of test conditions which is shown in the Figure 5.1.5. The strength of the specimens is determined at an age of 28 days.



Figure 5.1.5 Compressive strength test of NRG foam.

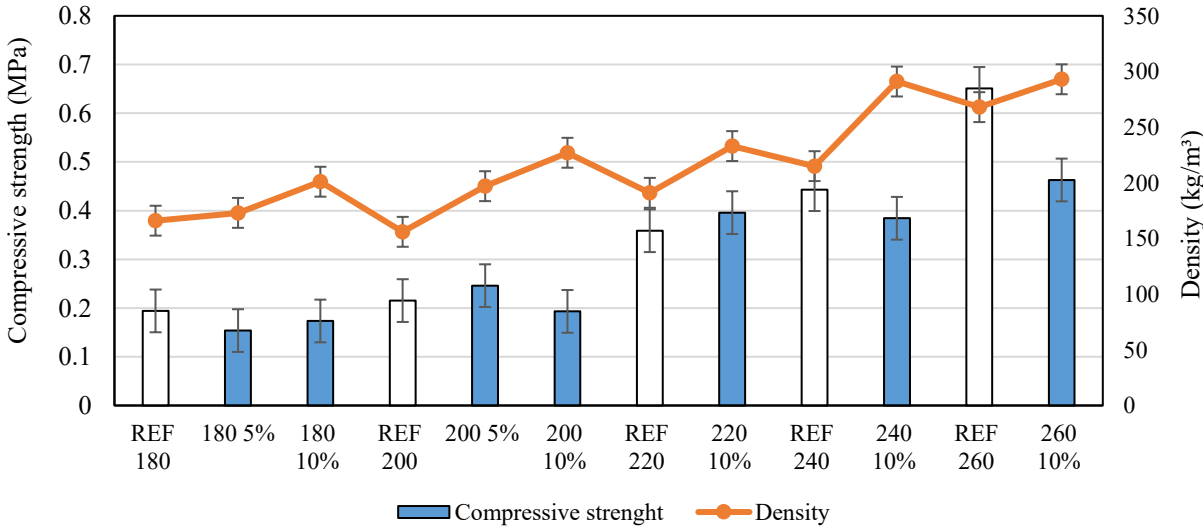


Figure 5.1.6 Compressive strength test results.

### 5.2.6.1 Results of compressive strength test

The results of the compressive strength tests were compared based on the variable components used in the production of reference NRG foam, as showed in Figures 5.1.6. In general, trend in the compressive strength showed decrease in strength with increasing PCM volume fraction and higher w/c ratio. For example, the highest compressive strength observed at 0.6 MPa in REF 260 and addition 10% PCM, compressive strength reduced by 30%. As for the lowest compressive strength found at 180-5% at 0.15 MPa which reduced by 21% as compare with reference sample. The compressive strength values for samples with PCM ranged approximately between 0.15 MPa and 0.4 MPa. For comparison, the compressive strength of thermal insulation materials such as glass wool and XPS panels approximately between 0.2 and 0.3 MPa [16], [17]. Therefore, the observed strength values for samples with PCM seem acceptable for insulation materials.

### 5.2.7 Thermal conductivity experiment

Adhesive tape is used to encircle the test specimens, preventing the occurrence of cracks due to NRG foam shrinkage. This tape serves a dual purpose: crack prevention and securing the test specimens together. After being removed from the climate chamber, the test specimens undergo weighing and are subsequently enveloped in foil. Specialized adhesive tape is used to affix thermocouples on both sides of the specimens. The test specimens are then fully covered with the thermocouples, and contact mats are inserted into the Heat Flow Meter (HFM), as depicted in Figure 5.1.7.

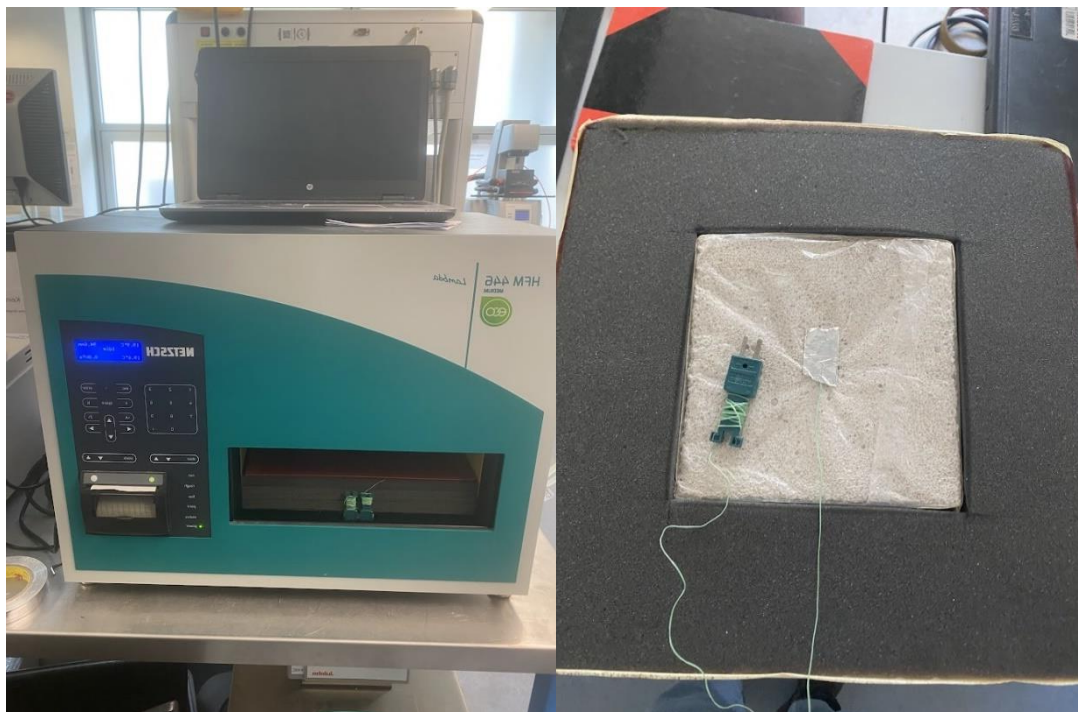


Figure 5.1.7 Thermal conductivity machine (left) and test specimen wrapped in foil with a thermocouple glued on (right).



### 5.2.7.1 Results of thermal conductivity

The thermal conductivity is measured at four different temperatures in the range from 0°C to 40°C, as this temperature range reflects the temperature range for the use of thermal insulation material. The thermal conductivity test involved determining the thermal properties of samples with dry densities ranging from 180 kg/m<sup>3</sup> to 260 kg/m<sup>3</sup>. Among these, the samples with a density of 260 kg/m<sup>3</sup>, both with and without PCMs, exhibited the highest thermal conductivity values, within the range of 0.06 to 0.07 W/m.K. Notably, the sample with 260 PCM-10% demonstrated the highest thermal conductivity, attributed to its higher density of 293 kg/m<sup>3</sup> compared to the sample without PCM at 268 kg/m<sup>3</sup>.

Conversely, the samples with the lowest thermal conductivity were those with a density of 180 kg/m<sup>3</sup>, with and without PCMs. Their thermal conductivity values ranged from 0.05 to 0.06 W/m.K. The sample with 180 PCM-5% recorded the lowest thermal conductivity, and this was associated with its lower density of 151 kg/m<sup>3</sup> compared to the sample without PCM at 183 kg/m<sup>3</sup>.

It is clear that a decrease in the density of foam concrete is associated with a reduction in thermal conductivity. Additionally, the presence of an independent cell foam structure was observed to impede heat loss from pores, potentially contributing to lower conductivity values, consistent with conclusions from prior studies [18], [19]. As for the impact of PCMs, their contribution was not explicitly demonstrated. This lack of clarity may be attributed to the adjustment of density through the incorporation of additional foam, leading to an increase in the density of samples containing PCMs. Notably, the thermal conductivity values of NRG foam with and without PCM were higher than those of commercial insulation materials.

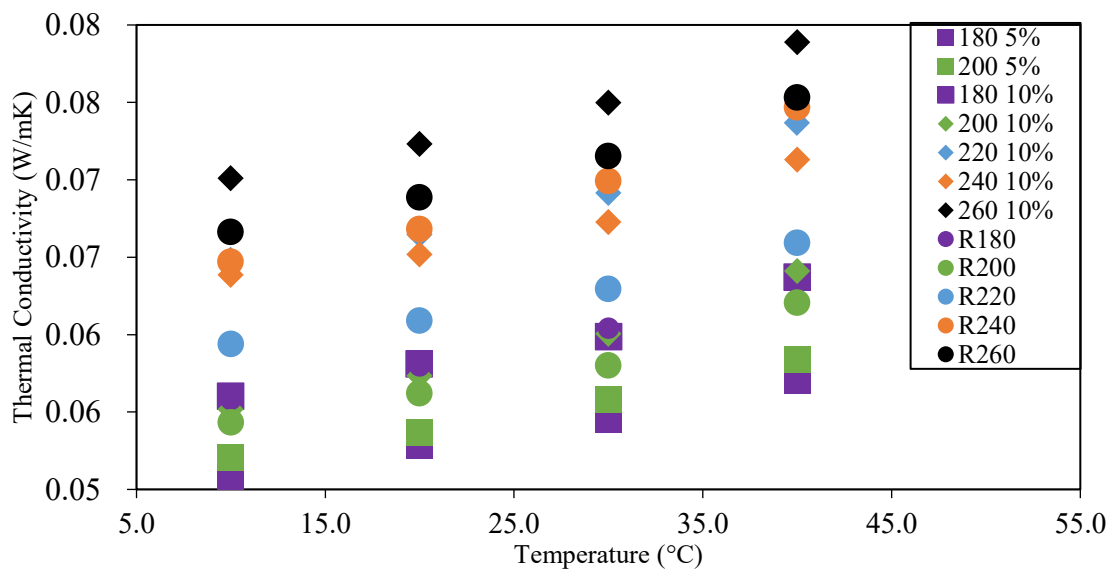


Figure 5.1.8 Results of thermal conductivity of NRG foam.

## 5.2.8 Mixture design tool for upscale

For the upscale of the NRG-Foam mixtures to the industrial scale, a design tool was created. The NRG-Foam mixture design tool is based on the definition of a target value. In this context, two different approaches are followed in the project. Approach No. 1 defines the dry bulk density of the insulation material as the target value, and Approach No. 2 defines the porosity of the insulation material as the target value. In addition to the target value definition, an intermediate constraint must be fulfilled. The intermediate constraint is defined by the volume ratio between PCM volume and binder paste volume. This must mathematically correspond to the desired PCM volume ratio. The cement mass and the PCM mass are taken as variables. Figure 5.1.9 and Figure 5.1.10 show calculation tables of an example mixture design.

NRG-Foam	MPCM volume of paste (Vol.-%)	20					Volume PCM Constraints for Solver
Mass in		1 m <sup>3</sup>	Ratio V.-%	Volume % V.-%	density kg/m <sup>3</sup>	Volume in 1 m <sup>3</sup>	20,000
Cement	<b>Cement, CEM I 52.5 R</b>						
Type:	107,29 kg		75	27,41%	3100	0,0346 m <sup>3</sup>	
Binder	<b>Centriit NC II MC (synth. Metakaolin)</b>						
Type:	16,73		25	9,14%	1450	0,0115 m <sup>3</sup>	
<b>Total binder content</b>	<b>124,01</b>						
MPCM	<b>Nextek 24D</b>	19,70 kg		20%	780	0,02525 m <sup>3</sup>	
Additive	<b>Hardening accelerator Trocurin BE</b>	2,48 kg		2%	1300	0,0019 m <sup>3</sup>	
Additive	<b>Superplasticizer Powerflow 3189*</b>	0,62 kg		0,46%	1060	0,0006 m <sup>3</sup>	
Additive	<b>Stabilizer Centrament Stabi 508</b>	3,584 kg		2,18%	1300	0,0028 m <sup>3</sup>	
<b>Water (for w/b)</b>		49,61 kg		39%	1000	0,0496 m <sup>3</sup>	
Paste in foam without PCM						0,1010 m <sup>3</sup>	
<b>Paste in foam with PCM</b>		200,00 kg		13%		<b>0,1263 m<sup>3</sup></b>	
<b>Foam (w/b) (2.0% foam agent)</b>		61,16 kg		87%	<b>70</b>	<b>0,8737 m<sup>3</sup></b>	
<b>Water (total)</b>		109,55				0,1095	
w/b designed	<b>0,40</b>	w/b ist-value:	0,4				
w/b (total)	0,89						
calculated density <sub>paste_wet</sub>	1584,1 kg/m <sup>3</sup>						
Calculated density <sub>foam_wet</sub>	261,16 kg/m <sup>3</sup>						
calculated density <sub>paste_solid (w/b)</sub>	200,00 kg/m <sup>3</sup>						
<b>Dry density corrected</b>	<b>200,00 kg/m<sup>3</sup></b>						
<b>input-parameter</b>							
target value / input in Solver							

Figure 5.1.9 Calculation sheet of the NRG-Foam mix design using the example of 20 volume percent PCM and a dry bulk density of 200 kg/m<sup>3</sup> → Target value is the dry bulk density.

NRG-Foam		MPCM volume of paste (Vol.-%)	20				Volume PCM Constraints for Solver
		Mass in	Ratio	Volume %	density	Volume in	20,000
		1 m <sup>3</sup>	V.-%	V.-%	kg/m <sup>3</sup>	1 m <sup>3</sup>	
Cement	<b>Cement, CEM I 52.5 R</b>						
Type:		107,29 kg	75	27,41%	3100	0,0346 m <sup>3</sup>	
Binder	<b>Centrilit NC II MC (synth. Metakaolin)</b>						
Type:		16,73 kg	25	9,14%	1450	0,0115 m <sup>3</sup>	
<b>Total binder content</b>		124,01 kg					
MPCM	<b>Nextek 24D</b>						
		19,70 kg		20%	780	0,02525 m <sup>3</sup>	
Additive	<b>Hardening accelerator Trocurin BE</b>						
		2,48 kg		2%	1300	0,0019 m <sup>3</sup>	
Additive	<b>Superplasticizer Powerflow 3189*</b>						
		0,62 kg		0,46%	1060	0,0006 m <sup>3</sup>	
Additive	<b>Stabilizer Centrament Stabi 508</b>						
		3,584 kg		2,18%	1300	0,0028 m <sup>3</sup>	
<b>Water (for w/b)</b>		49,61 kg		39%	1000	0,0496 m <sup>3</sup>	
Paste in foam without PCM						0,1010 m <sup>3</sup>	
<b>Paste in foam with PCM</b>		200,00 kg		13%		0,1263 m <sup>3</sup>	
<b>Foam (w/b) (2.0% foam agent)</b>		61,16 kg		87%	70	0,8737 m <sup>3</sup>	
<b>Water (total)</b>		109,55 kg				0,1095 m <sup>3</sup>	
w/b designed		0,40	w/b list-value:			0,4	
w/b (total)		0,89					
calculated density <sub>paste_wet</sub>		1584,1 kg/m <sup>3</sup>					
calculated density <sub>foam_wet</sub>		261,16 kg/m <sup>3</sup>					
calculated density <sub>paste_solid (w/b)</sub>		200,00 kg/m <sup>3</sup>					
<b>Dry density corrected</b>		200,00 kg/m <sup>3</sup>					
input-parameter							
target value / input in Solver							

Figure 5.1.10 Calculation sheet of the NRG-Foam mix design using the example of 20 volume percent PCM and a dry bulk density of 200 kg/m<sup>3</sup> → Target value is the porosity.

To find the solution, the generalized reduced gradient (GRG) method with mixed restrictions is used for the mixture design tool. That is, the problem is reduced to unrestricted minimization on pieces of boundary manifolds of the admissible set. Thus, all approximations are admissible. A change of the boundary manifold is based on the optimality constraints. The GRG method determines the relative change in a target cell in the form of convergence.

The achieved convergence is indicated by a fractional number between 0 and 1. A larger number of decimal places in a given number indicates a lower convergence. The smaller the convergence, the more accurate the result and the larger the number of iteration steps and the longer the time needed to find the solution. In the NRG-Foam mixture design tool, the differential for estimating difference parts of the objective and constraint functions is according to a central approach.

Figure 5.1.11 shows a flowchart for the GRG solution approach of the mixture design tool to visualize the method.

Based on the mixture design tool, the NRG foam porosity can be calculated as a function of the corresponding bulk density and PCM volume content in the binder paste, depending on Approach 1 or Approach 2. The results for the PCM contents 0 vol.% - 40 vol.% are shown in Figure 5.1.12.

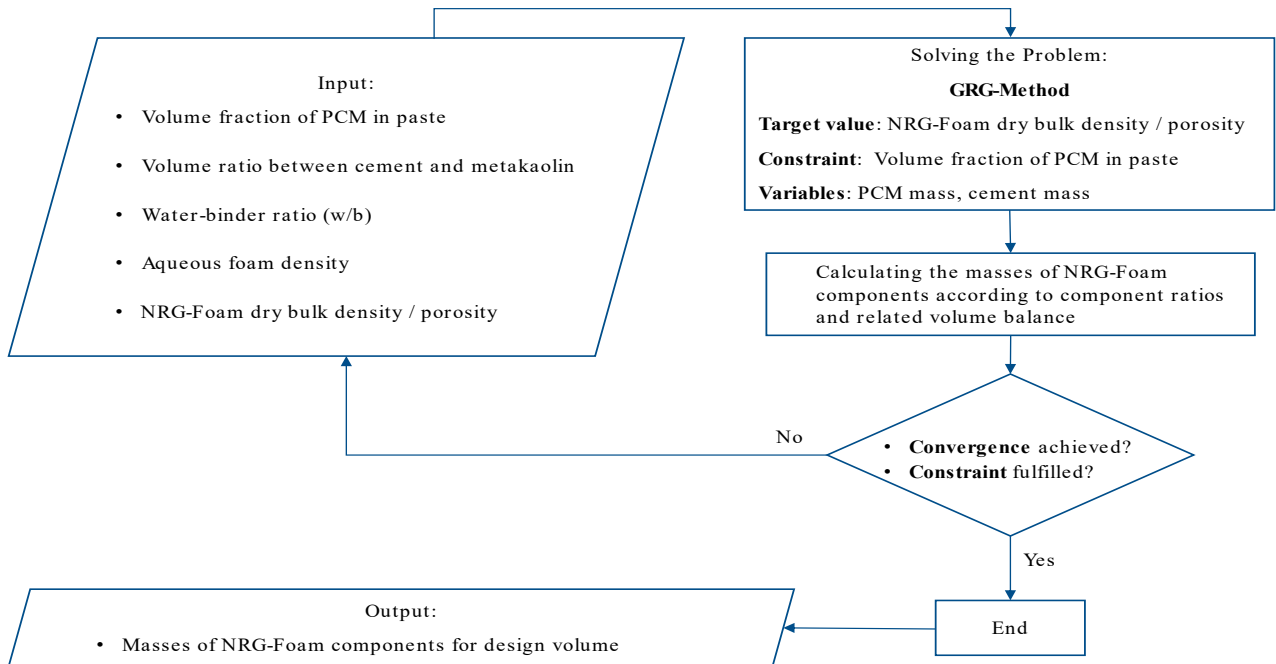


Figure 5.1.11 Flowchart for the GRG solution approach of the mixture design tool.

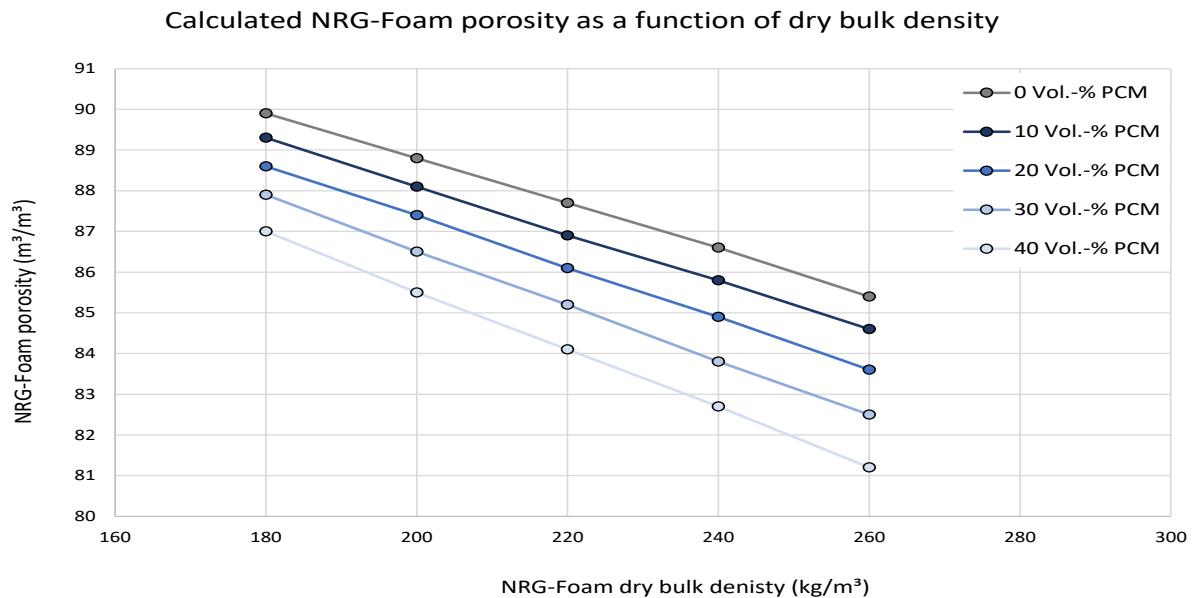


Figure 5.1.12 Calculated NRG-Foam porosity as a function of dry bulk density.

### 5.2.9 Approach for an engineering design model for NRG-Foam

For the engineering implementation and upscaling of NRG-Foam mixtures, a design model approach was developed, which can be coupled with the mixture design tool mentioned in Section 5.2.8.

The model approach describes a limit function of the NRG-Foam stability as a function of the PCM volume fraction in the binder paste. For this purpose, a distinction is firstly made between the two material phases, the NRG-Paste and the NRG-Foam. In order to ensure sufficient NRG-Paste stability, the PCMs must be distributed with a safe average particle distance and coated with an appropriate binder paste layer. In this context, the approach of the so-called “*ribbon thickness*” according to [2] is applied (see Figure 5.1.13).

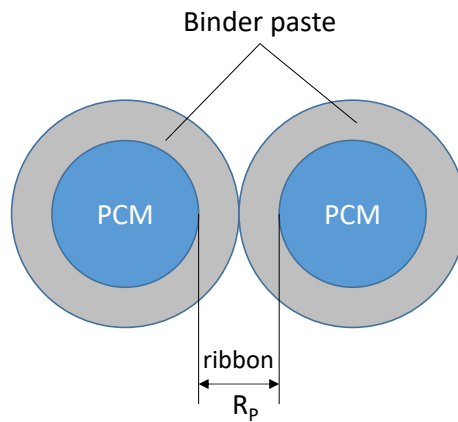


Figure 5.1.13 Schematic representation of the average particle spacing of the PCM particles in the binder glue as ribbon thickness  $R_p$ .

NRG-Paste is considered as a material composite consisting of binder paste and PCM particles. The PCM particles are distributed in the NRG-Paste according to their particle size distribution with a safe average particle distance and a certain volume ratio to the binder paste. Here, the  $R_p$  value is the ribbon thickness,  $V_P$  is the volume of binder paste, and  $S_{PCM}$  is the surface area of all PCM particles as a function of particle size distribution and volume ratio in NRG-Paste. To determine the mean distance between two PCM particles, the total binder volume is smeared out onto the surface of the PCM particles. For a single PCM particle, the thickness of a paste layer around this particle results in  $V_P/S_{PCM}$ . In order to determine the mean particle distance,  $V_P$  must be considered twice. This results in the Equation 3:

$$R_p = \frac{2V_P}{S_{PCM}} \quad (5-1).$$

The ribbon thickness highly depends on the particle size distribution of the used PCM microcapsules. The particle size distribution for the Nextek 24D PCM used in the NRG-STORAGE project as reference PCM is shown in Figure 5.1.14.

By considering the volume of microencapsulated PCM per cubic meter of NRG-Paste, the total particle surface  $S_{PCM}$  can be calculated as a function of the particle size distribution. By dividing the double volume of binder glue  $2V_P$  present in one cubic meter of NRG-Paste mixture by the particle surface, the ribbon thickness of the NRG-Paste  $R_P$  is obtained. On this basis,  $R_P$  of the NRG-Paste blends for the Nextek 24D PCM was calculated as a function of different possible PCM volume contents and visualized in Figure 5.1.15.

To describe the average foam structure of NRG-Foam and the associated foam stability, the “ribbon thickness” approach can be applied by analogy. Here, the material composite NRG-Foam is described as a two-component system consisting of NRG-Paste (binder skeleton) and air voids. The ribbon thickness in this context represents the average distance of the air voids and implicitly the average material thickness of the binder skeleton (see Figure 5.1.16).

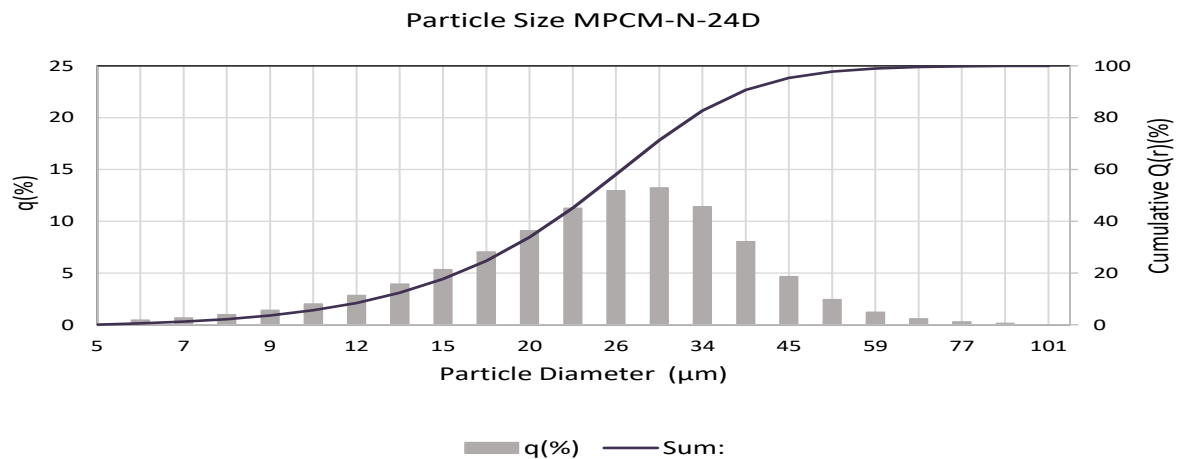


Figure 5.1.14 Particle size distribution of encapsulated Nextek 24D PCM.

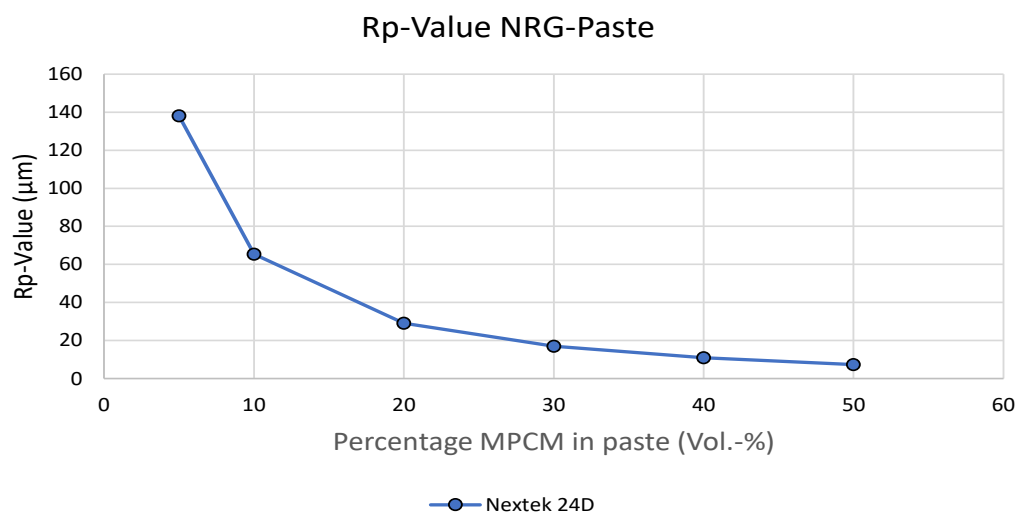


Figure 5.1.15 Rp-Value of microencapsulated PCM from Nextek 24D as function of PCM percentage in NRG-Paste.

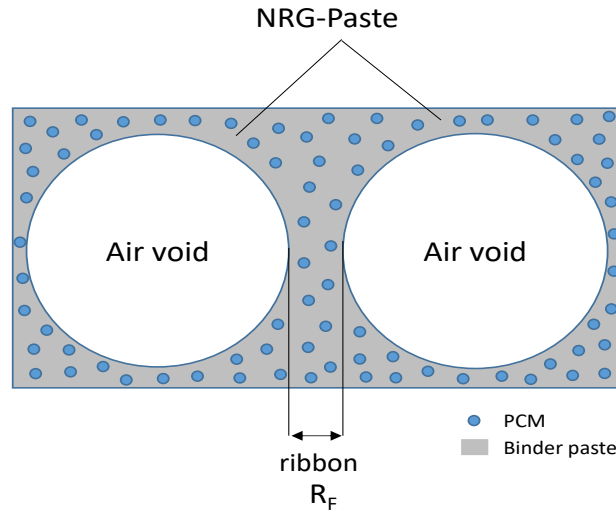


Figure 5.1.16 Schematic representation of the average distance of air bubbles in the NRG-Paste as *ribbon thickness*  
 $R_F$

Here  $R_F$  is the ribbon thickness of NRG-Foam,  $V_{NRGP}$  the volume of the NRG-Paste binder and  $S_{Air}$  the surface area of all air voids as a function of the air void size distribution and the volume fraction in NRG-Foam composite. In order to determine the mean air void distance,  $V_{NRGP}$  must be considered twice. This results in the Equation 4:

$$R_F = \frac{2V_{NRGP}}{S_{Air}} \quad (5-2).$$

To determine the air void distribution of the NRG-Foam composite, 3D  $\mu$ XCT scans were performed on NRG-Foam specimens with different bulk densities between  $180 \text{ kg/m}^3$  and  $220 \text{ kg/m}^3$ . This showed that the air void distribution of all investigated bulk densities was approximately identical. Accordingly, a simplified average air void distribution was transferred to all foam mixtures. The mean pore size distribution and an example of a 3D  $\mu$ XCT scan can be seen in Figure 5.1.17. It should be noted that this experiment was conducted in laboratory at NIMS with the help of Prof Tsuchiya Koichi.

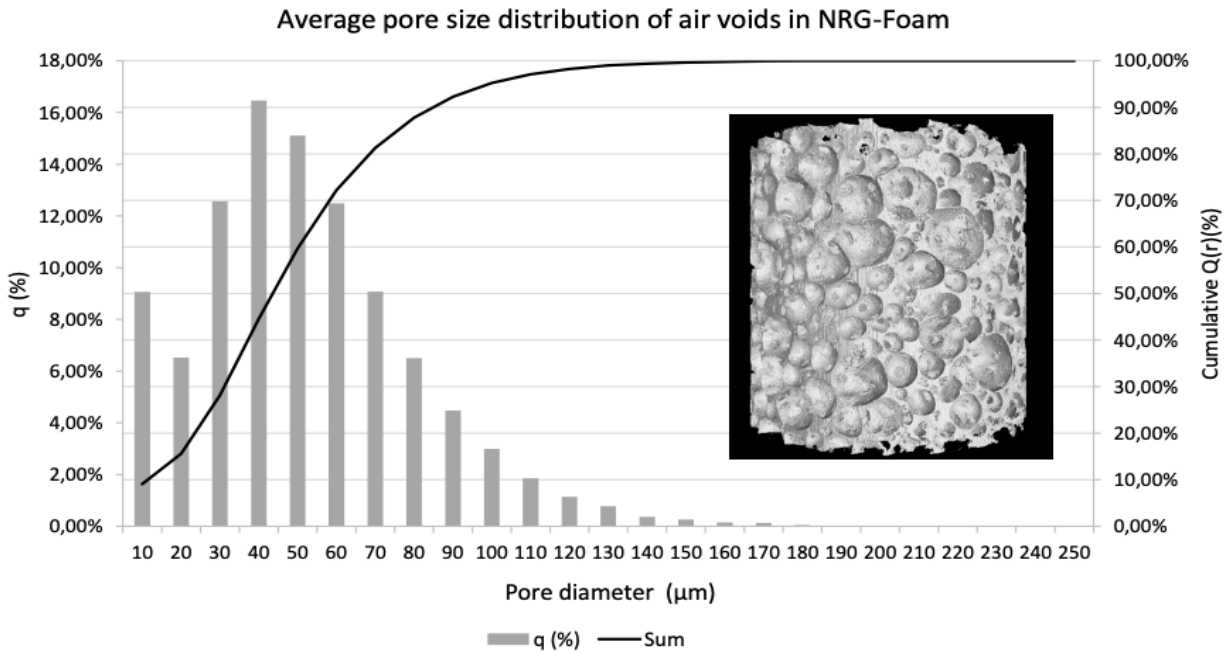


Figure 5.1.17 Average pore size distribution of NRG-Foam based on 3D  $\mu$ XCT scans[20].

Considering the porosity of the NRG-Foam and the corresponding volume of air per cubic meter of NRG-Foam, the total surface area of the air voids  $S_{Air}$  can be calculated as a function of the pore size distribution. Dividing twice the volume of NRG-Paste binder  $2V_{NRGP}$  present in one cubic meter of NRG-Foam mixture by the air void surface area, the ribbon thickness of NRG-Foam  $R_F$  can be obtained. On this basis,  $R_F$  of NRG-Foam mixtures was calculated as a function of different possible porosities, and it is shown in Figure 5.1.18.

In order to determine the above-mentioned limiting function for NRG-Foam stability as a function of the PCM volume fraction in the binder paste (NRG-Paste), the ribbon thickness of the NRG-Paste  $R_P$  is linked with the ribbon thickness of the NRG-Foam  $R_F$ . The linkage is based on empirically obtained test data on foam stability in the fresh state (no foam decay in the fresh state) and general applicability (sufficient strength for the production of insulation boards) which have been done according to the new mixing design tool mentioned in Section 5.2.8. The stability depends on the PCM volume fraction in the NRG-Paste and the foam porosity of the NRG-Foam. From the tests it can be seen that NRG-Pastes with PCM volume contents  $> 40\%$  by volume cannot be processed and that NRG-Foam with a porosity  $> 92\%$  cannot be used because the foam is too fragile to produce insulation boards. Furthermore, it can be seen from test series that the higher the PCM volume fraction in the NRG-Paste, the lower the porosity in NRG-Foam must be for the foam to be applicable as an insulation board. This results in the foam technology relationships shown in Table 5-9.



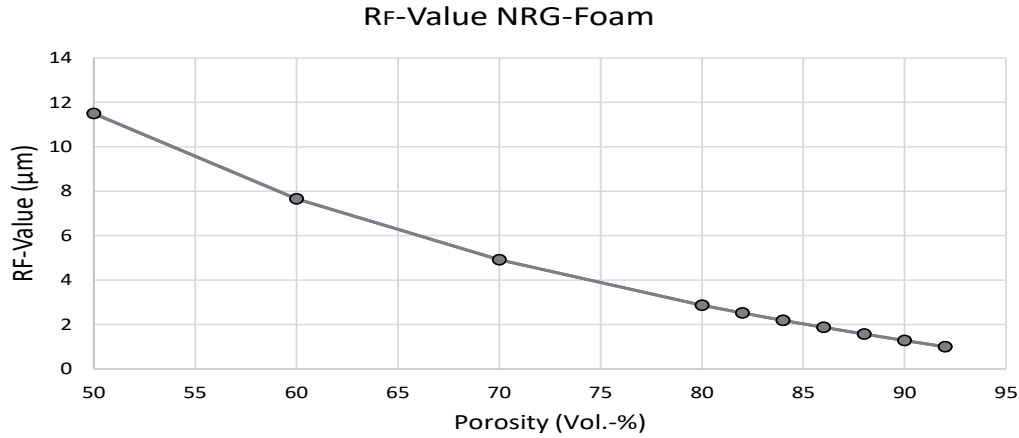


Figure 5.1.18 RF-Value of NRG-Foam as a function of NRG-Foam porosity.

Table 5-9 Relationship between  $R_P$ -value and  $R_F$ -value.

Vol.-% PCM in NRG-Paste	$R_P$	Porstity (%) of NRG-Foam	$R_F$
5	138.07	92	1
10	65.4	88	1.57
20	29.07	86	1.87
30	16.96	80	2.87
40	10.9	60	7.66

The relationship between  $R_P$  and  $R_F$  can now be used to visualize the ribbon thickness of the NRG-Foam  $R_F$  as a function of the ribbon thickness of the NRG-Paste  $R_P$ . The curve can be represented by an exponential function of the following form (Equation 5):

$$f(x) = A_1 \cdot e^{(-x/t1)} + A_2 \cdot e^{(-x/t2)} + y_0 \quad (5-3).$$

It can be clearly seen from this function that as the PCM volume fraction in the NRG-Paste increases, the  $R_P$  value decreases and, correspondingly, the porosity in the NRG-Foam decreases and the  $R_F$  value increases (see Figure 5.1.19).

Using this determined limit function for NRG-Foam stability as a function of the PCM volume fraction in the binder paste  $R_F = f(R_P)$ , a just functional NRG-Foam mixture with an associated limiting porosity respectively limiting bulk density can be determined with the input of a desired PCM volume fraction in the binder paste. If the bulk density of a mixture with a given PCM volume fraction is increased compared to the calculated limiting bulk density, it can be assumed that the design works. However, if the bulk density is reduced in comparison to the limiting bulk density determined in the model, there is no evidence that the design will work.

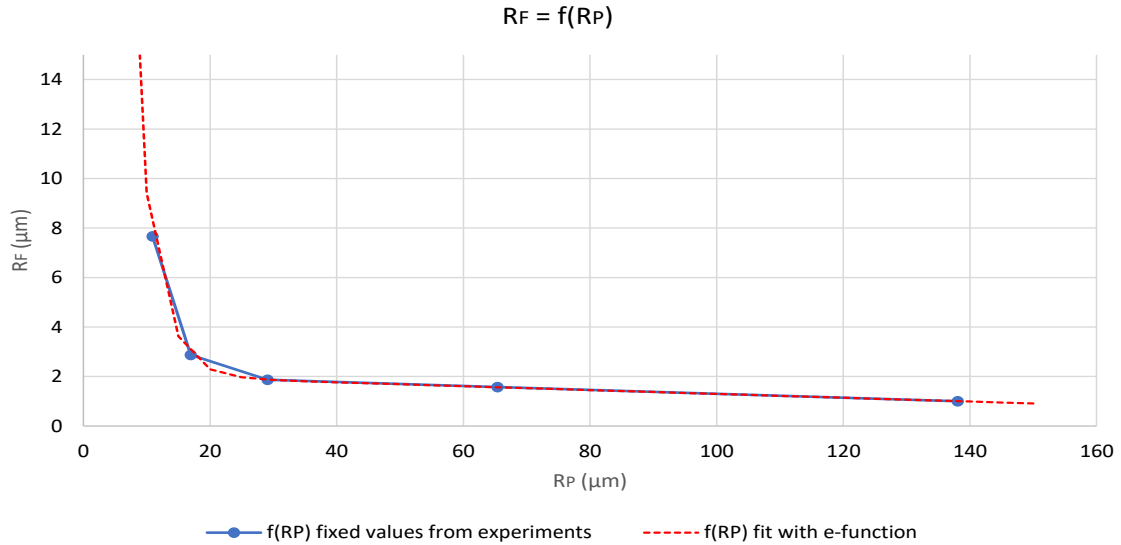


Figure 5.1.19 Ribbon thickness of the NRG-Foam  $R_F$  as a function of the ribbon thickness of the NRG-Paste  $R_P$ .

The approach can be made consistent throughout, starting with the mixing design tool, the associated NRG-Foam porosities, and the ribbon thickness approach  $R_F = f(R_P)$  based on empirically determined values which are designed according to this mixing design tool. The following Figure 5.1.20 shows the consistent relationship of the NRG-Foam limiting porosities or limiting bulk densities with the ribbon thickness approach as an approach for an engineering NRG-Foam design model. As an example, the input desired PCM contents of 10 % and 20 % by binder paste volume and the resulting limiting bulk densities are shown.

After the respective limiting bulk density for the corresponding PCM volume fraction has been determined, the necessary masses of the NRG-Foam components for a selected production volume can be calculated with the help of the mixing design tool from Section 5.2.8. If adjustments are made in the design, this approach can lead to an iterative solution.

Later in the project, the engineering design model will be automated in a computer-based design program and extended to material target parameters, such as strength and insulation performance. This will result in further limit functions. The most stringent requirement of a specific NRG-Foam application then becomes decisive. All limit functions will be validated with further measurement results in the course of the project.

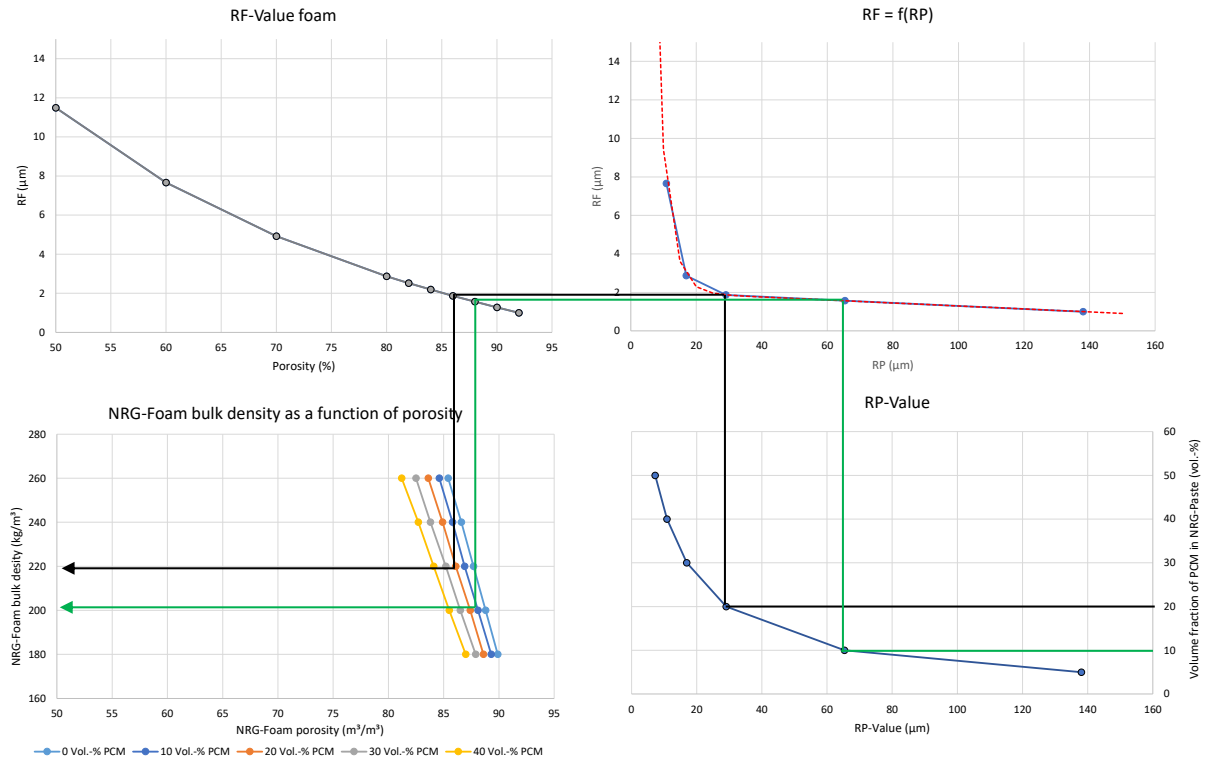


Figure 5.1.20 Approach for an engineering design model based on the limiting function for NRG-Foam stability  $R_F = f(R_P)$ .

### 5.3 CONCLUSIONS

Ultra-lightweight PCM Foam Concrete (NRG Foam), explores the innovative field of ultra-lightweight PCM foam concrete, NRG Foam, in collaboration with the Technical University of Darmstadt, Germany. The main purpose of NRG foam is to increase thermal insulation and thermal energy storage capacity. The objective of this research is twofold. First, to develop an ultra-lightweight concrete foam integrated with PCM. The material properties of NRG foam concrete were analyzed in detail. Key parameters include foam porosity and ribbon thickness. The findings are as follows

In this experiment, 12 different PCM foam concrete mixtures with dry densities, ranging between 180 kg/m<sup>3</sup> and 260 kg/m<sup>3</sup>, were considered. Since NRG-foam with PCM is a highly sensitive material; thus, all mixtures were carefully measured and their wet density and volume were recorded respectively to ensure their target dry density and target volume were reached. As for the Reference and PCM 5% samples with different densities, there were no problems with mix composition as the foam was stable for every mixture. A clear relationship between density and strength was confirmed, indicating that compressive strength increases with higher density, regardless of the specific composition of the foam concrete. Consequently, the observed strength values for samples with PCM seem acceptable for insulation materials.

As for the thermal conductivity test, a reduction in the density of foam concrete was found to be associated with a reduction in thermal conductivity. Notably, the thermal conductivity values of NRG foam with and without PCM were higher than those of commercial insulation materials.

An empirical model that establishes a clear relationship between foam porosity (RP) and ribbon thickness (RF), where  $RF = f(RP)$ . This model optimizes the thermal insulation and energy storage capacity of NRG foam.

### 5.4 REFERENCES

- [1] M. R. Ahmad, B. Chen, and S. Farasat Ali Shah, "Investigate the influence of expanded clay aggregate and silica fume on the properties of lightweight concrete," *Constr Build Mater*, vol. 220, pp. 253–266, Sep. 2019, doi: 10.1016/J.CONBUILDMAT.2019.05.171.
- [2] O. Gencel *et al.*, "Foam Concrete Produced with Recycled Concrete Powder and Phase Change Materials," *Sustainability (Switzerland)*, vol. 14, no. 12, Jun. 2022, doi: 10.3390/su14127458.
- [3] O. Gencel *et al.*, "Lightweight foam concrete containing expanded perlite and glass sand: Physico-mechanical, durability, and insulation properties," *Constr Build Mater*, vol. 320, p. 126187, Feb. 2022, doi: 10.1016/J.CONBUILDMAT.2021.126187.

- [4] Q. S. Khan, M. N. Sheikh, T. J. McCarthy, M. Robati, and M. Allen, “Experimental investigation on foam concrete without and with recycled glass powder: A sustainable solution for future construction,” *Constr Build Mater*, vol. 201, pp. 369–379, Mar. 2019, doi: 10.1016/J.CONBUILDMAT.2018.12.178.
- [5] M. Aksit, C. Zhao, B. Klose, K. Kreger, H. W. Schmidt, and V. Altstädt, “Extruded polystyrene foams with enhanced insulation and mechanical properties by a benzene-trisamide-based additive,” *Polymers (Basel)*, vol. 11, no. 2, Feb. 2019, doi: 10.3390/polym11020268.
- [6] J. Gołaszewski *et al.*, “Effect of Foaming Agent, Binder and Density on the Compressive Strength and Thermal Conductivity of Ultra-Light Foam Concrete,” *Buildings*, vol. 12, no. 8, Aug. 2022, doi: 10.3390/buildings12081176.
- [7] K. Ramamurthy, E. K. Kunhanandan Nambiar, G. Indu, and S. Ranjani, “A classification of studies on properties of foam concrete,” *Cem Concr Compos*, vol. 31, pp. 388–396, 2009, doi: 10.1016/j.cemconcomp.2009.04.006.
- [8] L. Chica and A. Alzate, “Cellular concrete review: New trends for application in construction,” *Constr Build Mater*, vol. 200, pp. 637–647, Mar. 2019, doi: 10.1016/J.CONBUILDMAT.2018.12.136.
- [9] Y. H. M. Amran, N. Farzadnia, and A. A. A. Ali, “Properties and applications of foamed concrete; a review,” *Constr Build Mater*, vol. 101, pp. 990–1005, Dec. 2015, doi: 10.1016/J.CONBUILDMAT.2015.10.112.
- [10] P. E. Bat-Erdene, S. Pareek, E. Koenders, C. Mankel, M. Löher, and P. Xiao, “Evaluation of the Thermal Performance of Fly Ash Foam Concrete Containing Phase Change Materials (PCMs),” *Buildings*, vol. 13, no. 10, Oct. 2023, doi: 10.3390/buildings13102481.
- [11] M. Hunger, A. G. Entrop, I. Mandilaras, H. J. H. Brouwers, and M. Founti, “The behavior of self-compacting concrete containing micro-encapsulated Phase Change Materials,” *Cem Concr Compos*, vol. 31, no. 10, pp. 731–743, Nov. 2009, doi: 10.1016/J.CEMCONCOMP.2009.08.002.
- [12] F. Kuznik, J. Virgone, and J. Noel, “Optimization of a phase change material wallboard for building use,” *Appl Therm Eng*, vol. 28, no. 11–12, pp. 1291–1298, Aug. 2008, doi: 10.1016/J.APPLTHERMALENG.2007.10.012.
- [13] S. Cunha, M. Lima, and J. B. Aguiar, “Influence of adding phase change materials on the physical and mechanical properties of cement mortars,” *Constr Build Mater*, vol. 127, pp. 1–10, Nov. 2016, doi: 10.1016/J.CONBUILDMAT.2016.09.119.
- [14] A. Jayalath *et al.*, “Properties of cementitious mortar and concrete containing micro-encapsulated phase change materials,” *Constr Build Mater*, vol. 120, pp. 408–417, Sep. 2016, doi: 10.1016/J.CONBUILDMAT.2016.05.116.
- [15] A. Caggiano, C. Mankel, and E. Koenders, “Reviewing theoretical and numerical models for PCM-embedded cementitious composites,” *Buildings*, vol. 9, no. 1. MDPI AG, Dec. 21, 2018.

doi: 10.3390/buildings9010003.

- [16] “Mechanical Properties of Glass Wool.” Accessed: Jan. 18, 2024. [Online]. Available: <https://www.huameiworld.com/news/mechanical-properties-of-glass-wool.html>
- [17] “XPS Extruded Polystyrene Foam (Styrofoam) .” Accessed: Jan. 18, 2024. [Online]. Available: <https://www.easycomposites.eu/xps-extruded-polystyrene-foam>
- [18] L. Qiao *et al.*, “Design of monolithic closed-cell polymer foams via controlled gas-foaming for high-performance solar-driven interfacial evaporation †,” 2021, doi: 10.1039/d1ta01032h.
- [19] O. Gencel *et al.*, “Foam Concrete Produced with Recycled Concrete Powder and Phase Change Materials,” *Sustainability* 2022, *Vol. 14, Page 7458*, vol. 14, no. 12, p. 7458, Jun. 2022, doi: 10.3390/SU14127458.
- [20] S. M. Md Suman Mia, Yuya Takahashi, Tetsuya Ishida, and Koichi Tsuchiya, “Thermal and Mechanical Properties of Porous Cementitious Composites Using Phase-Change Materials with Different Microstructures,” *The 4th International Conference On Green Civil and Environmental Engineering*, 2023.

**CHAPTER 6**  
**NUMERICAL SIMULATION ANALYSIS OF PCM**  
**CONCRETE**

## 6.1 SIMULATION OVERVIEW

Numerical Simulation Analysis of PCM Concrete, a comprehensive numerical simulation analysis was conducted to investigate the energy efficiency of PCM concrete. The main objectives of this chapter are to validate the experimental data with numerical calculations and to establish a predictive model for the energy efficiency of concrete. To achieve these goals, a one-dimensional model was meticulously developed based on empirical insights gained from studies of heat transfer in PCM concrete. Heat conduction in the concrete was calculated using the heat conduction equation based on Fourier's law.

### 6.1.1 Introduction

The analysis of heat transfer in building materials, particularly Phase Change Materials (PCMs), presents unique challenges due to their thermochemical properties and operational complexity. In recent years, researchers have increasingly turned to numerical methods to investigate the energy efficiency of PCMs [1], [2], [3]. These methods typically involve formulating and solving heat transfer equations to model the behavior of phase change materials. For example, Ramakrishnan et al. [4] conducted a comprehensive evaluation of the thermal performance of cementitious composites incorporating phase change materials. Their study involved a combination of experimental assessments and numerical simulations. Additionally, Karthikeyan et al. [5] conducted a study on a cylinder storage tank filled with paraffin encapsulated spherical containers to analyze heat transfer during the phase change process. Their methodology incorporated an enthalpy formulation in mathematical models to accurately represent the phase change behavior of paraffin across different temperature ranges. The fully explicit finite difference method was then employed to solve these models. The results obtained from these mathematical models were validated against experimental data, ensuring their accuracy and reliability.

In this research, the study of heat conduction in PCM concrete was conducted using the heat conduction equation based on Fourier's law. Additionally, the mechanism of heat transfer through vibration was explored, where energy is transferred from regions of higher temperature to lower temperature. In solids, the movement of atoms results in tiny vibrations known as phonons, acting as carriers of energy. Phonons are crucial for heat transfer, facilitating the movement of energy through the material's structure [6]. The main objectives of this chapter are to validate the experimental data with numerical calculations and to establish a predictive model for the energy efficiency of concrete. To achieve these goals, a one-dimensional model was meticulously developed based on empirical insights gained from studies of heat transfer in PCM concrete.



## 6.1.2 Establishing a simulation model for temperature evolution

### 6.1.2.1 Simulation domain

As shown in Figure 6.1.1, a semi two-dimensional model was developed based on the experimental testing conditions of "Heat cyclic analysis" experiment in chapter 2. From chapter 2, the box used in the experiment is constructed by six sides, of which five sides are made from polystyrene foam material with a much lower thermal conductivity compared to concrete side. Therefore, we assume that the cubic box exchanges heat with the external environment-chamber (green part in Figure 6.1.1) only through the concrete side. From left to right, the figure was divided into a solid region including concrete and phase change materials, and inner gas region. The solid phase is composed of two types of very small blocks: the concrete matrix and a certain quantity of randomly distributed phase change material (PCM). Each block represents a part of the concrete matrix or a part of PCM, marked by gray and blue colors respectively. The internal gas space is treated as a homogeneous gas phase. This model primarily investigates the conduction behavior of heat in solid materials containing different phases with phase change materials. Therefore, it is assumed that the box directly transfers heat with the chamber through the surface, in an efficiency 1, which does not influence by the convection situation or contacting areas. Therefore, only the solid region is considered as the simulation domain in this model, where the points A, B, and C are corresponded to the temperature recording points in the experiment. The temperature at point A is considered to be the chamber temperature and the temperature at point B is regarded as the temperature evolution recorded by the backside thermocouple in the experiment.

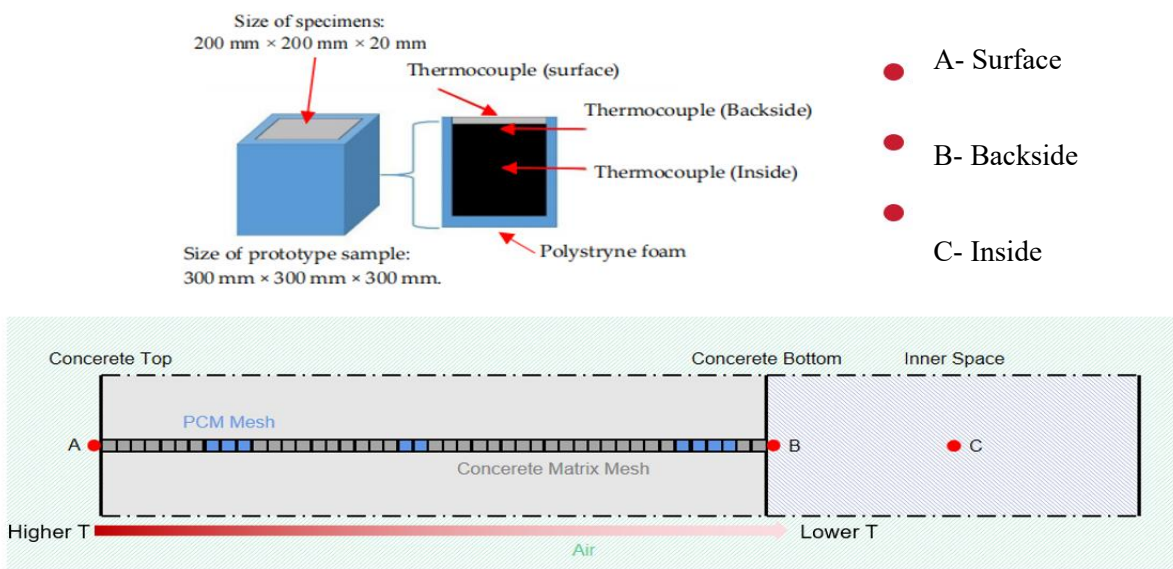


Figure 6.1.1 Schematic of the heat evolution model and parameter definitions on DSC model.

### 6.1.2.2 Parameterization

The parameters involved in the model and their physical significance are shown in Table 1. The "Initial parameters" are input as defining parameters for the entire system before the simulation starts and remain unchanged throughout the loops, regardless of the different blocks. The "Intermediate parameters" are redefined each time when a new block is checked within a loop.

Table 6-1 Inputs Parameters for Simulation Process

Initial parameters	$T_0$	Temperature of point A
	$MF_{PCM}$	The mass fraction of the PCM material.
	$PSD_{PCM}$	The size distribution of the PCM material.
	$MZ_{PCM}$	The melting zone of of the PCM material.
Intermediate parameters	$T_i$	Temperature of the blocks between point A and B
	$x_i$	The position of the blocks (point A as 0)
	$\alpha_i$	The degree of melting in the PCM material (0 for liquid, 1 for solid and any number in between for percentage of melting).
	$dT_i$	The temperature difference between adjacent blocks.
	$\langle C_i \rangle$	Coefficient group
$C_i$	During each heat transfer, a random coefficient is selected from the $\langle C_i \rangle$ according to probability $Pc$	
Output parameters	$T_{end}$	Temperature of point B

$$\alpha_i = \frac{T_i}{MZ_{PCM}} \quad \text{Equation 6-1}$$

$$dT_i = T_{i+1} - T_i \quad \text{Equation 6-2}$$

$$Pc = \left( \frac{\log space(T_{i+1} - T_i, a, b)}{\sum \log space(T_{i+1} - T_i, a, b)} \right)^c \quad \text{Equation 6-3}$$

$$\langle C_i \rangle = \ln^{m-|T_i - T_{i+1}|} space(d, e, b) \quad \text{Equation 6-4}$$

$$C_i = r(\langle C_i \rangle, 1, t, Pc) \quad \text{Equation 6-5}$$

$$T_{i+1} = T_i(1 + C_i) \quad \text{Equation 6-6}$$

The  $a$ ,  $b$ ,  $c$ ,  $d$  and  $e$  in these formulas are constant parameters, which vary according to different experimental materials (composition of concrete, type of PCM, particle distribution, etc.), but remain unchanged throughout a complete simulation process. Logspace represents the construction of  $b$  values distributed proportionally on a logarithmic scale, ranging from  $T_{i+1}-T_i$  to  $a$ . Linspace represents the construction of  $b$  values distributed proportionally on an exponential scale, ranging from  $d$  to  $e$ . The  $r$  function represents the random selection of a value from  $\langle C_i \rangle$ , weighted by the probability  $P_c$ .

### 6.1.3 Model simulation overview

The simulation consists of  $n$  cycles, with each cycle occurring as described below: The temperature is uniformly distributed at an initial value  $T_0$  on the concrete surface based on the chamber starting temperature and its heating rate (Point A in the experiment). Subsequently, heat determined by temperature is transferred to the next adjacent blocks in sequence. During the cooling process, the transfer of heat can be considered as a negative value. The heat transfer to subsequent blocks  $i+1$  is influenced by the block's properties and the temperature difference with the previous block. This dictates the heat transfer coefficient  $C_i$  between blocks. The transfer continues until it reaches the end block (Point B in the experiment). The simulation persists until the  $T_0$  reaches its maximum, shown in Figure 6.1.2. After each cycle,  $T_0$  is updated according to the increase or decrease in the chamber temperature in the experimental data. The numbers of cycles can be adjusted based on actual needs. A greater number of cycles will result in more detailed heating and cooling curves, but it will also increase the simulation time and the computational load. In our research, the whole process is simulated in Software Matlab 2023a.

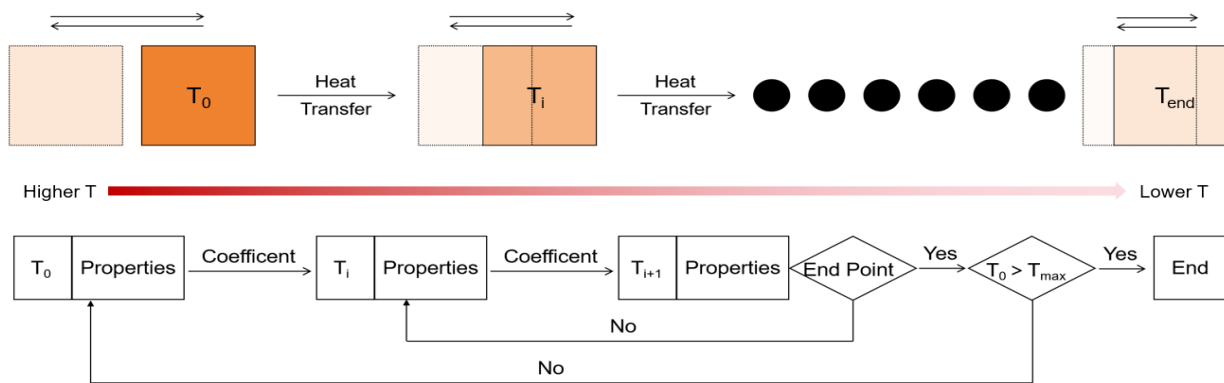


Figure 6.1.2 Schematic of the basic model and parameter definitions heat evolution model

### 6.1.3.1 Simulation Domain for heat transfer model

Having established the aforementioned theory and basic model, we refined the model for the heat evolution experiments [7], [8]. A semi three-dimensional model was constructed based on the experimental testing conditions. The sample within the holder is partitioned into numerous small cylindrical shapes. Each cylinder comprises a certain number of blocks corresponding to the concrete matrix and randomly distributed PCM (Phase Change Material). Initially, the entire sample within the holder shares a consistent starting temperature. Over time, the temperature at the bottom part rises, transmitting heat to samples situated higher up, shown in figure 6.1.3.

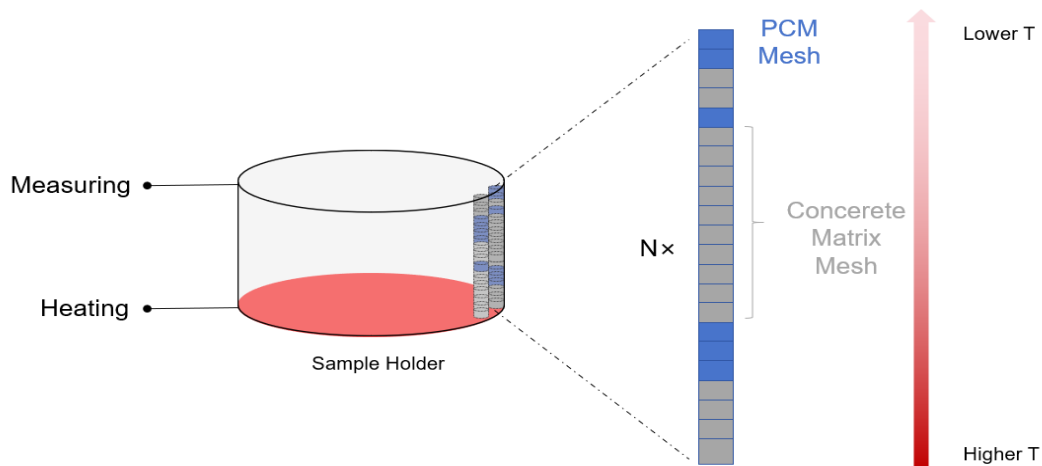


Figure 6.1.3 Schematic of the heat transfer model and parameter definitions.

### 6.1.3.2 Parameterization

In the heat transfer model, the various parameters have the same significance as in the temperature model. The constant parameters a, b, c, d may need adjustment, which is conducted through validation. To compensate for the omission of various heat conduction directions, appropriate adjustments were made to the upper and lower bounds of the coefficient group. To convert temperature transfer into heat transfer, Fourier's law was employed. According Fourier's law[9]

$$q = -k\nabla T$$

Equation 6-7

With k as the Thermal conductivity factor. In this model, since the temperature difference between two adjacent blocks in each cycle is very small, it can be considered in a differential form, therefore

$$dq = -k(T_{i+1} - T_i)$$

Equation 6-8

$$q = -k \sum_i (T_{i+1} - T_i) \text{ Equation 6-9}$$

### 6.1.3.3 Model simulation overview

The heat conduction mechanism in this refined model remains consistent with the heat transfer model, however, the transfer of heat from starting block to end block (as shown in Figure 6.1.2) will be executed N times in each cycle, as the distribution of PCM in every cylindrical shape is different. Moreover, only the upward heat conduction, from the bottom to the top, is considered effective. Transfers in other directions are disregarded.

### 6.1.4 Model validation and heat evolution model

Based on the constructed model, a thermal cyclic simulation was conducted for concrete containing various amounts of PCM6D and the results were compared with existing experimental findings, as shown in Figure 6.1.4. The simulation time is from 4:18 AM to 10:28 PM. For ease of description, the horizontal axis is converted to minutes, and 4:18 AM is set as 0 minutes. The constant parameters were first validated based on experimental data with a PCM content of 30%, with a set to -5, b to 60, and c to 6. In the concrete matrix block, d is consistently -0.55. In the PCM block, d is -0.5 in the solid state and -0.4 in other states, e is set to -1, and m is set to 3. Subsequently, these data were retained and used to predict the simulation results for other concentrations.

In the figure, focusing from left to right on the initial cooling phase, the simulated results align well with the experimental data, showing that concrete with a higher concentration of PCM6D experiences a more modest temperature drop over the same duration. In the model, the thermal conductivity coefficient of PCM is lower than that of the concrete matrix, leading to a slower heat transfer rate in samples with higher PCM content.

When it comes to the heating phase, it is divided into three segments:

1. Pre-phase Change Heating: Both experimental and simulation results depict a rapid heating rate with no significant variation among the samples. The thermal conductivities of the samples differ but not prominently during this phase.

2. Phase Change: A noticeable slowing in the heating rate occurs as PCM content increases. This deceleration is attributed to a portion of the heat being consumed for latent heat during the PCM phase transition (22-28°C). Consequently, there's a notable reduction in the effective thermal conductivity coefficient during this phase, which is reflected as a plateau or slowed heating rate in the curve. At this stage, there was a slight deviation between the simulation results and the experimental results. There are two possible reasons: one is that the constant parameters a, b, c, d, etc., which are treated

as constants, should actually be functions of the block's characteristics or even time; the second is the inherent issue with time in the simulation method itself. Which is due to the model's assumption that each simulation step (or time increment) is consistent, whereas, in reality, each heat transfer event might not happen at regular intervals. This issue can be addressed by introducing a time-adjustment equation for each PCM content level, but to maintain clarity in this analysis, this adjustment was omitted.

3. Post-phase Change Heating: The heating rate for all samples post phase change is slower compared to the initial phase. This slowdown is influenced by two main factors. Firstly, the temperature difference between the sample blocks and the surrounding chamber  $T_0 - T_i$  narrows, equalizing the probability of heat transfer between adjacent blocks. Secondly, as heat continues to transfer, the temperature difference between neighboring blocks  $T_{i+1} - T_i$  diminishes, leading to a corresponding drop in the thermal conductivity coefficient. This manifests as a gradual increase in the curve. Notably, for samples with lower PCM content, there's a significant discrepancy between simulation and experimental results in the high-temperature zone. The reason for this deviation is also due to the treatment of parameters as constants and the inconsistency in the handling of time.

The subsequent cooling phase mirrors the heating segment but in reverse, exhibiting a progressive decline in temperature. Noteworthy is the pronounced plateau during PCM phase transition, mainly because the system's block temperatures are closer to the chamber's ( $T_0 - T_i$ ), reducing the blocks' vibration probability (i.e., the effective thermal conductivity). After a sufficient duration, all samples equilibrate to the ambient temperature.

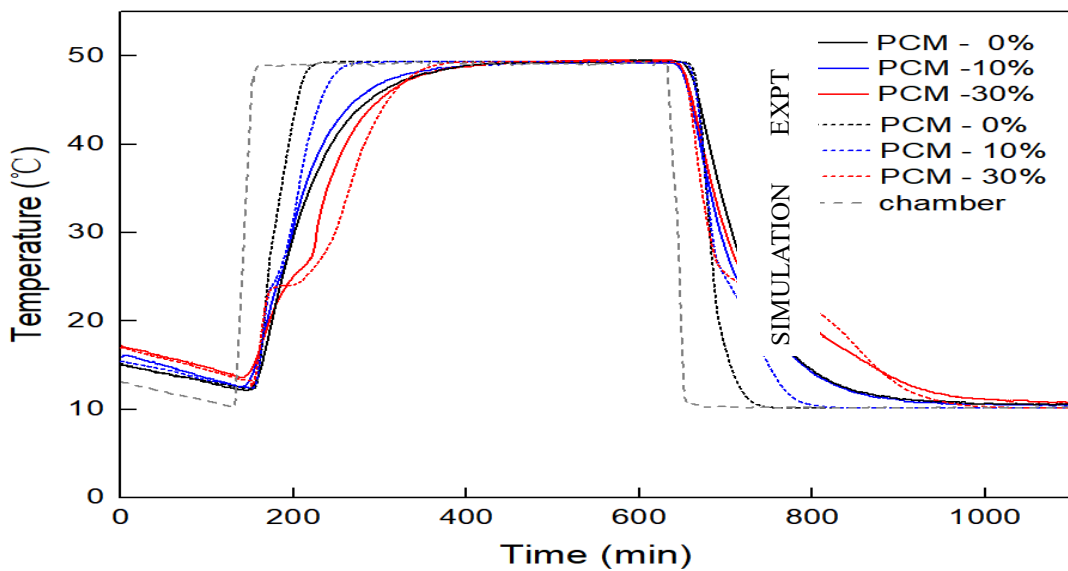
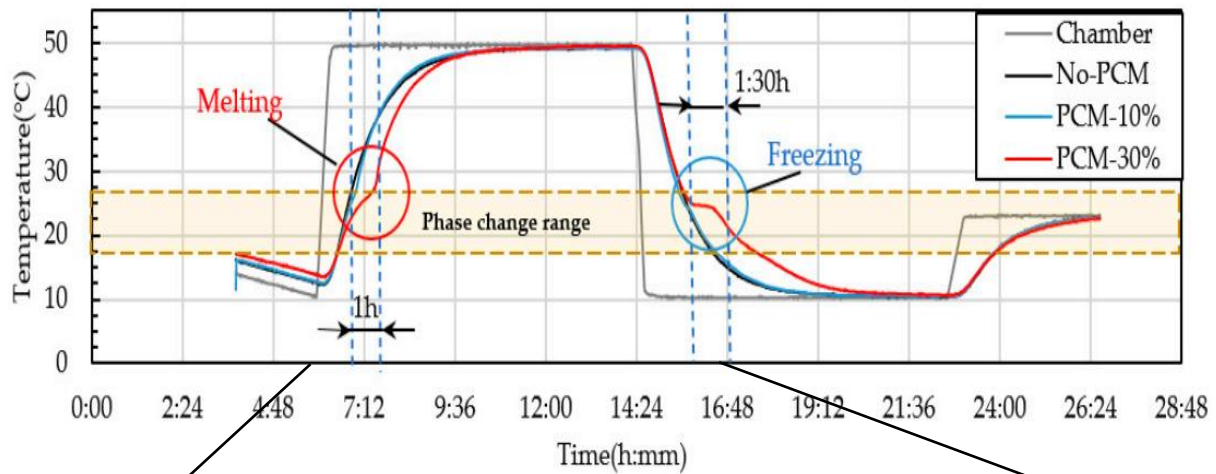


Figure 6.1.4 Heat cyclic results for different amounts of PCM6D (solid line represents experimental testing, dashed line represents simulation results).

The results presented above validate the reliability of this model for simulating and theoretically explaining the effects of varying PCM6D content. Subsequently, simulations were conducted for samples containing 30% of different types of PCM, and the outcomes were compared with existing experimental data, as depicted in Figure 6.1.5.

Initially analyzing the 28D sample, its simulation within one cycle mirrors the trends seen with the 6D sample. However, the entire heating and cooling rates are slower for 28D compared to 6D, and the plateau during phase transition (24-28°C) is more pronounced. Model analysis reveals that the coefficient value for 28D is generally lower than that of 6D. Given that the concrete matrix's

contribution to the coefficient remains fairly consistent, this suggests that the thermal conductivity of 28D PCM is inferior (or its thermal output performance is superior).

Next, considering the 18D sample, its temperature change curve is notably distinct, resembling samples with lower PCM content. This can be attributed to the phase transition temperature range of 18D PCM being lower (below 15°C), and the chamber temperature rises from 10°C to 50°C before cooling. Consequently, the temperature variation interval for PCM18D is barely evident under these conditions. In the model, the coefficient of PCM Blocks remains virtually unchanged throughout the process. Notably, the cooling phase scarcely shows any phase transition. During heating, the temperature difference between the Blocks and the chamber (ambient) is significant, thus invoking a greater coefficient impact. However, during cooling, due to the minor temperature difference between the concrete matrix and PCM Blocks with the chamber, the vibration probability of the Blocks is limited, resulting in almost no significant coefficient variations.

Conversely, for the 43D PCM sample, its phase transition occurs at higher temperatures (above 42°C), and there's a longer duration where a significant temperature difference exists between the Blocks and the chamber ( $T_0 - T_i$ ). Moreover, with the inherent temperature ( $T_i$ ) of the Blocks being high, the vibration probability is amplified, thereby granting more opportunities for the coefficient to come into play. This effect profoundly influences the entire system. It can be observed that 43D takes a considerable duration to reach the chamber's equilibrium temperature, with its phase transition spanning the entire high-temperature range.

In conclusion, the reactions of different types of PCM to temperature variations within a fixed temperature range differ significantly. Thus, choosing the appropriate PCM is crucial, depending on the specific application environment.



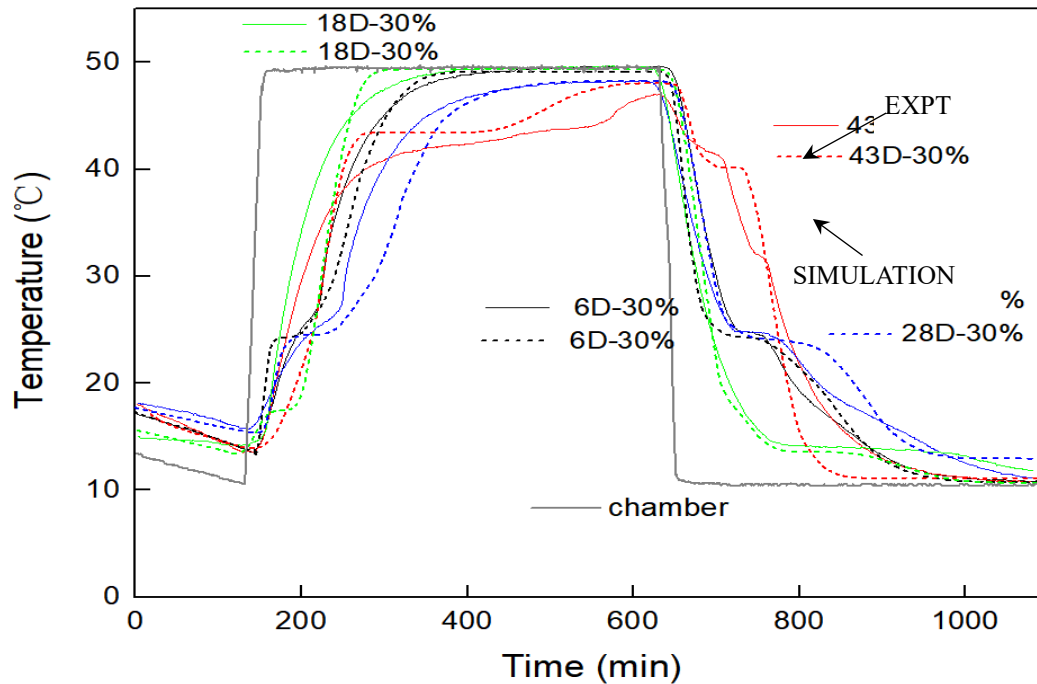


Figure 6.1.5 Heat cyclic results for different types of PCM-30% (solid line represents experimental testing, dashed line represents simulation results).

Through simulations of samples with different amounts of the same type of PCM and those with the same amount but different types of PCM, the outcomes demonstrated high consistency with experimental results. Moreover, the parameterized explanations provided by the model offer a coherent interpretation of the observed differences. Thus, relying on this model, we ventured into predictions in two main aspects.

Firstly, we explored a scenario not easily achievable in practical experiments – varying the particle size distribution of PCM. In completed experiments, the particle size of PCM6D spanned between 15-30 micrometers. We expanded our predictions to include particle sizes ranging from 7.5-15 micrometers and 30-60 micrometers, the results of which are presented in Figure 6.1.6.

At a glance, variations in particle size do not significantly influence the temperature curve, particularly in the cooling phase. However, in the heating phase, the smaller-sized PCM6D particles manifest a more noticeable plateau. This can be attributed to the implication that smaller particle sizes suggest a more homogeneous distribution. Within the model, this means that the Blocks representing PCM are more likely to be adjacent to those symbolizing the concrete matrix. Especially within the phase transition temperature range of PCM, there's a considerable difference in the coefficients between these two entities. Therefore, with smaller particle sizes, there's an extended duration required for the completion of heat transfer during the phase transition.

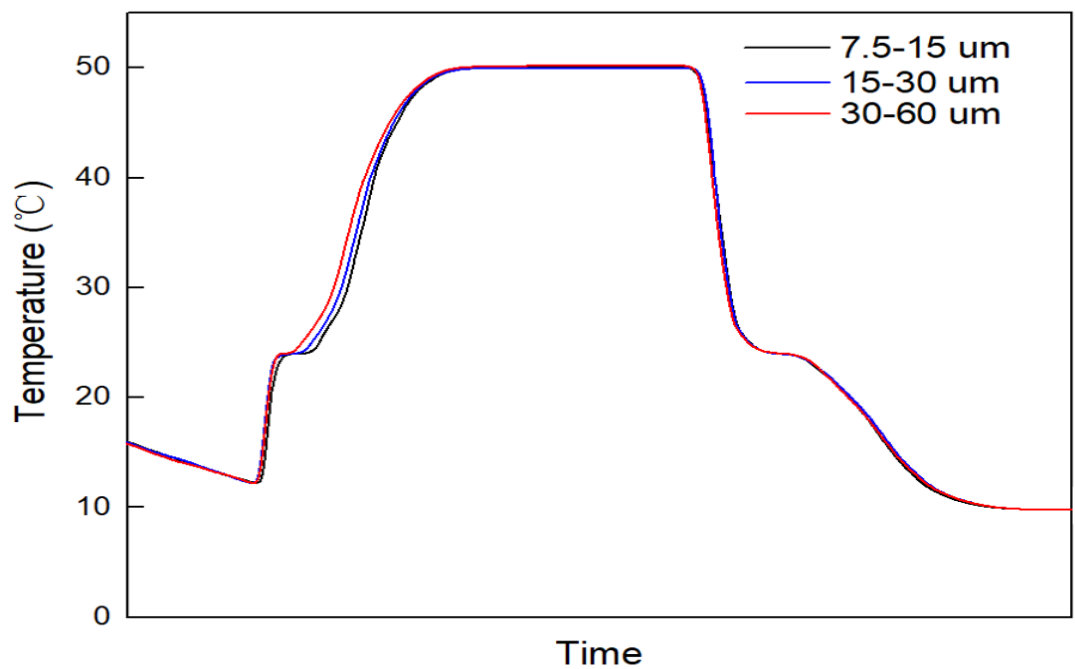


Figure 6.1.6 Heat cyclic prediction results for PCM6D-30% with varying particle sizes.

Subsequently, we projected predictions for concentrations of PCM6D not observed in the experiments: 20%, 25%, 35%, and 40%. It is evident that with the increment of PCM content, there isn't a significant difference during the initial cooling phase. The disparity in the first segment of the heating phase (prior to phase transition temperature) is also minimal. In the second segment (within the phase transition temperature range), due to the increased number of Blocks representing higher PCM content, the coefficient undergoes noticeable variation with temperature. As a result, a pronounced plateau phase is manifested. In the third segment (post phase transition temperature), samples with higher PCM content exhibit a slower rate of temperature rise. This is attributed to the overall lower coefficient influenced by the dominance of PCM-representative Blocks.

The cooling curve features mirror those of the heating curve, but it's worth noting that when PCM content is excessively high, the sample temperature might not return to its minimum value within a

cycle. Therefore, in general, the choice of PCM content is crucial for different application environments. If the content is too low, its temperature-buffering effect is not distinct; if it's too high, the sample might not effectively release the energy stored within, potentially compromising usage stability.

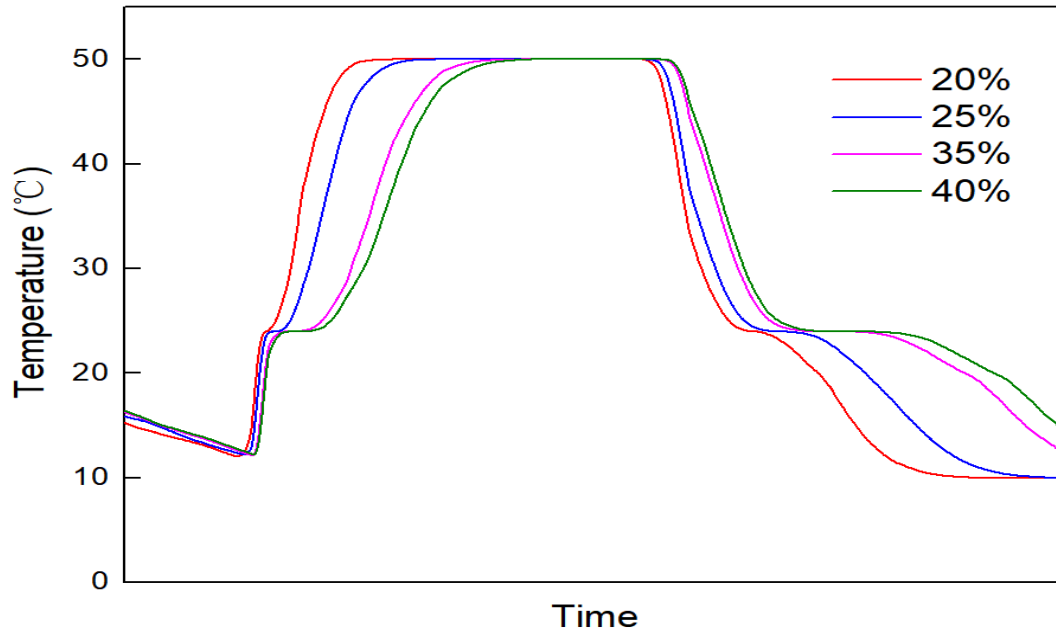


Figure 6.1.7 Heat cyclic prediction results for different amounts of PCM6D.

The basic model was subsequently refined to address the heat flow issue in DSC (Differential Scanning Calorimetry). Considering that samples in DSC typically undergo processes like grinding and compression, their microstructure and material parameters actually change. Without readjusting the model parameters, the results aren't suitable for quantitative analysis. Here, we only present the simulation results for the 18DPCM-30% sample at three different heating rates (1, 5, and 10°C per minute) and compare them with experimental findings, as shown in Figure 6.1.7.

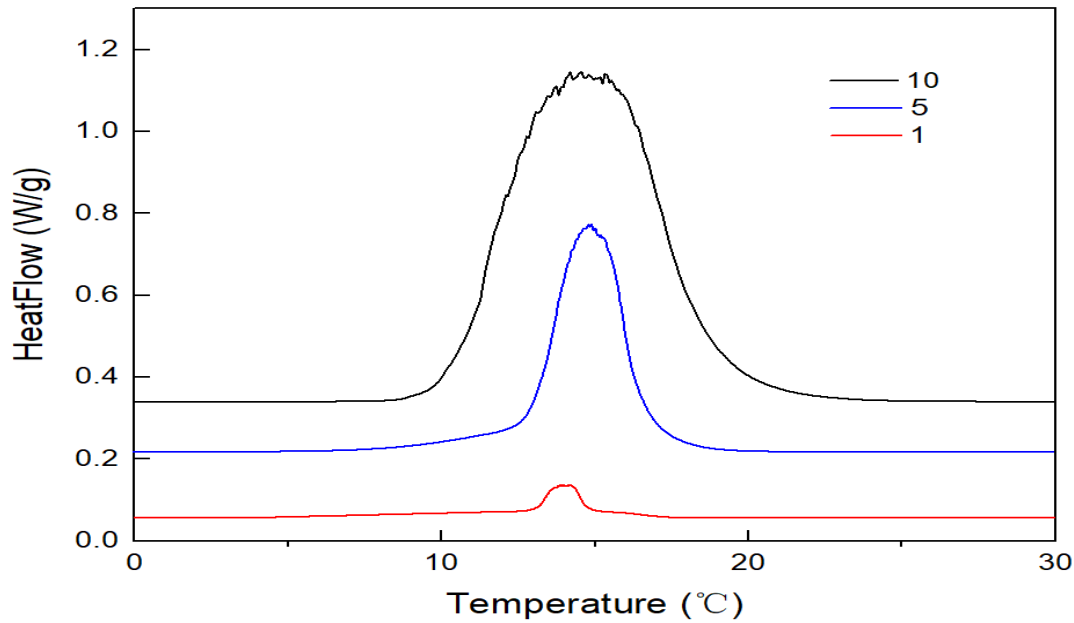


Figure 6.1.8 Simulation results of DSC for PCM18D-30% at three different heating rates.

It is observed that, outside the phase transition temperature and its vicinity (outside the 10-20°C range), the heat flow curve demonstrates a gradual increasing trend. In model terms, the temperature difference between blocks within a single cylindrical form (as illustrated in Figure 3) under this scenario is relatively minor. Hence, the calorific compensation provided by the DSC heating system to maintain the temperature increase is also minimal. However, within the phase transition range, as the PCM's coefficient gradually reduces, there comes a moment when the temperature difference between Blocks inside the cylinder becomes significant. The DSC heating system then needs to provide more compensation. This is reflected in Figure 8 as a pronounced peak around the phase transition temperature and its neighboring range.

For faster heating rates, it's clear that both the peak's area and height increase. Furthermore, the position of the peak slightly shifts towards a higher temperature with increasing heating rate. This is because the quicker change in environmental temperature leads to a larger temperature difference  $(T_0 - T_i)$  between the Blocks and their environment. As a result, the coefficient becomes more influential, broadening the phase transition plateau. This causes a certain lag in the heat compensation.

While the refined DSC model isn't yet suitable for quantitative analysis without redefining the basic model's parameters, its preliminary simulation results align quite well with experimental findings. This suggests that the basic model's underlying theory is generally applicable and is immensely helpful in studying the thermal performance of both PCM-added and pure concrete materials.

## 6.2 CONCLUSIONS

Numerical Simulation Analysis of PCM Concrete, a comprehensive numerical simulation analysis was conducted to investigate the energy efficiency of PCM concrete. The main objectives of this chapter are to validate the experimental data with numerical calculations and to establish a predictive model for the energy efficiency of concrete.

The results of the numerical simulations were compared closely with the experimental data, and it was found that there was a remarkable consistency between the two. The validated numerical approach was then extended to explore the behavior of PCM foam concrete. The validated numerical approach was then extended to predict the behavior of PCM foam concrete.

Numerical simulations revealed that PCM plays a crucial role in effectively mitigating prototype room temperature fluctuations in various PCM foam concretes. This entire simulation process was extended to include the use of the PCM in a variety of PCM form concrete. It is noteworthy that the entire simulation process was performed in-depth using Matlab 2023a software. The results are promising for advancing the understanding and prediction of energy efficiency in PCM concrete systems.

## 6.3 REFERENCES

- [1] P. Tittlein *et al.*, “Simulation of the thermal and energy behaviour of a composite material containing encapsulated-PCM: Influence of the thermodynamical modelling,” 2014, doi: 10.1016/j.apenergy.2014.11.055.
- [2] N. Essid, A. Eddhahak, and J. Neji, “Experimental and numerical analysis of the energy efficiency of PCM concrete wallboards under different thermal scenarios Experimental and numerical analysis of the energy efficiency of PCM concrete wallboards under different thermal scenarios Experimental and numerical analysis of the energy efficiency of PCM concrete wallboards under different thermal scenarios,” *Journal of Building Engineering*, p. 45, 2022, doi: 10.1016/j.jobbe.2021.103547i.
- [3] D. Li, Y. Zheng, C. Liu, and G. Wu, “Numerical analysis on thermal performance of roof contained PCM of a single residential building,” *Energy Convers Manag*, vol. 100, pp. 147–156, Aug. 2015, doi: 10.1016/J.ENCONMAN.2015.05.014.
- [4] S. Ramakrishnan, X. Wang, J. Sanjayan, and J. Wilson, “Thermal performance assessment of phase change material integrated cementitious composites in buildings: Experimental and numerical approach,” *Appl Energy*, vol. 207, pp. 654–664, Dec. 2017, doi:

10.1016/J.APENERGY.2017.05.144.

- [5] S. Karthikeyan and R. Velraj, “Numerical investigation of packed bed storage unit filled with PCM encapsulated spherical containers – A comparison between various mathematical models,” *International Journal of Thermal Sciences*, vol. 60, pp. 153–160, Oct. 2012, doi: 10.1016/J.IJTHERMALSCI.2012.05.010.
- [6] “N.W. Ashcroft and N.D. Mermin, ‘*Solid State Physics*’, Saunders College Publishing, New York, 1976, Chap 2, 3.” Accessed: Feb. 06, 2024. [Online]. Available: <https://www.sciepub.com/reference/120196>
- [7] P. E. Bat-Erdene, S. Pareek, E. Koenders, C. Mankel, M. Löher, and P. Xiao, “Evaluation of the Thermal Performance of Fly Ash Foam Concrete Containing Phase Change Materials (PCMs),” *Buildings*, vol. 13, no. 10, Oct. 2023, doi: 10.3390/buildings13102481.
- [8] P. E. Bat-Erdene and S. Pareek, “Experimental Study on the Development of Fly Ash Foam Concrete Containing Phase Change Materials (PCMs),” *Materials*, vol. 15, no. 23, Dec. 2022, doi: 10.3390/ma15238428.
- [9] R. Rajagopal, “Fourier’s Law of Heat Conduction,” 2007.

**CHAPTER 7**  
**ENERGY ANALYSIS SUMULATION OF BUILDINGS**  
**WITH PCM**

## 7.1 SIMULATION OVERVIEW

In this chapter, energy simulation analysis conducted on PCM foam concrete using experimental results data including the enthalpy change, thermal conductivity, and density of PCM concrete measured in the above-mentioned DSC tests, thermal cycle tests, and mechanical properties tests. This is structured into three sections. Initial section describes with the necessary input for simulation in Energy plus such as general input as run period, schedules and parameters of materials. The second discusses simulation results. The discussion focuses on four key parameters: outside temperature, room temperature, heating load, and cooling load. This assessment is based on comparing temperature fluctuations between wall materials and PCM foam concrete. The final section presents the chapter's conclusion. It should be noted that this simulation was tested with the help of Yuki Osanai, President of OFactory.

### 7.1.1 Introduction

The usage of energy in constructions has become a demanding concern according to rising living standards and the increasing demand for heating and cooling. The International Energy Agency [1] reported that the construction field already occupied over one third of world energy usage, so this proportion is rising up even further in the next 50 years, particularly in residential buildings[2]. Therefore, there is an urgent need to air conditioning and heating load in constructions and enhance their energy efficiency.

Multiple options to minimize the heating and cooling loads in buildings were exposed [3], [4], [5]. One of the promising solutions to this growing issue is the integration of renewable energy sources into the construction field. By using solar thermal energy, for example, it is possible to decrease heating and cooling energy demands. In this regard, the incorporation of phase change materials (PCMs) has been initiated as a promising approach due to their remarkable ability to reserve and radiate that thermal energy. A phase transition process of PCMs, which involves melting and solidifying states, allows them operate as a heating and cooling system. When an ambient room degree reaches, the PCM accumulate energy before transitioning from a solid to a liquid state, and when the temperature drops, it solidifies, releasing the stored energy back into our environment [6]. It is said that this process makes it possible to create and maintain an acceptable thermal comfort in residential buildings.

Within the building sector, the integration of PCMs' phase change properties offers various applications such as incorporating these materials into walls, roofs and floors to regulate indoor temperatures effectively [7], [8]. Recently, researchers have been dedicated to utilization of PCM in plasterboard as an insulation material and light weight concrete. For example, research conducted by Yuka Kusama et al [9]. examined the use of plasterboard containing microcapsule PCM (mPCM) and gel PCM. Their analysis demonstrated that the average heat transfer coefficients in rooms with mPCM



and gelPCM were 10% and 5% lower, respectively, compared to rooms with traditional PB walls. Furthermore, the mPCM room exhibited a notable reduction in heating load, estimated at around 35%. Kumar et al. [10] conducted an energy performance analysis using EnergyPlus software. They successfully integrated PCM with melting temperature 24°C into building wall in India climate conditions. As a results-maintained temperature throughout the year, eliminating the need for external heating or cooling sources.

The purpose of this simulation is to the understanding of the phase change phenomena in foam concrete and explore the potential to enhance indoor comfort and reducing cooling and heating energy demand.

### 7.1.2 Model establishment

Energy Plus, the software used in the test, is a program created for the purpose of providing energy simulations of the entire building to engineers, architects, and researchers, and can model such energy consumption as heating load, cooling load, ventilation, illumination, and water usage. In this test, since the air conditioning load is focused, the flow of heat energy to the calculation model which mimics the architecture shown in Figure 7.1.1 and Figure 7.1.2 was simulated, and the outside temperature, indoor temperature, and heating and cooling load were numerically simulated, and it was utilized for the comparison examination of the temperature change on the time axis. By changing the thermal conductivity, specific heat, and density of internal building members, it is possible to compare and study thermal comfort of any material.

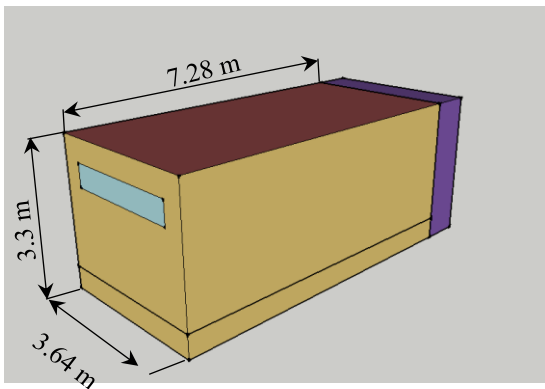


Figure 7.1.1: Calculation model northwest side.

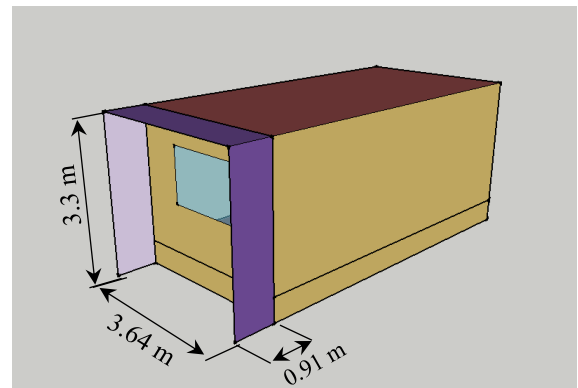


Figure 7.1.2 Calculation model southeast side.

### 7.1.3 Environment

The environment which is set when the comparative examination is carried out in this test is described in this paragraph. There are two settings added: simulation environment and wall material.

This study utilizes weather data from the one of the Tokyo Metropolitan Government in Fiscal 2018 published by Japan Metropolitan Agency for energy calculations. The climate of the Tokyo region is characterized by its temperate nature, featuring a Pacific Ocean side climate, as shown in Figure 7.1.3 [11]. Winters tend to be cold, while summers are hot. Figure 7.1.4 presents the annual average temperature and precipitation data for Tokyo [12]. The calculations specifically focus on the cold weather in January and the hot weather in August. In addition, Figure 7.1.5 and 7.1.6 shows the average air temperature and solar radiation in both January and August.

Detailed temperature changes are analyzed in January and August, when heating and cooling loads are large.



Figure 7.1.3: Location of the house [11]. Source: Energy Plus screenshot.

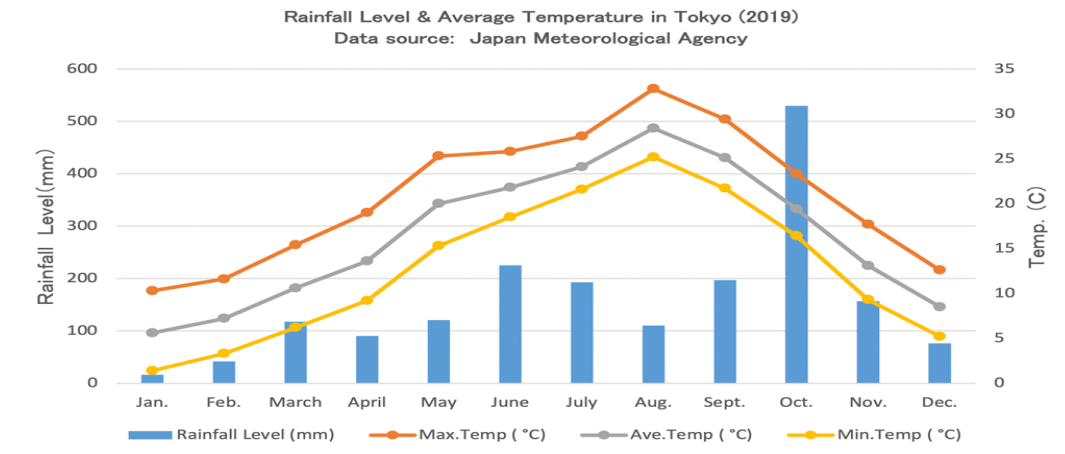


Figure 7.1.4: Annual temperature in Tokyo (2019) [12]

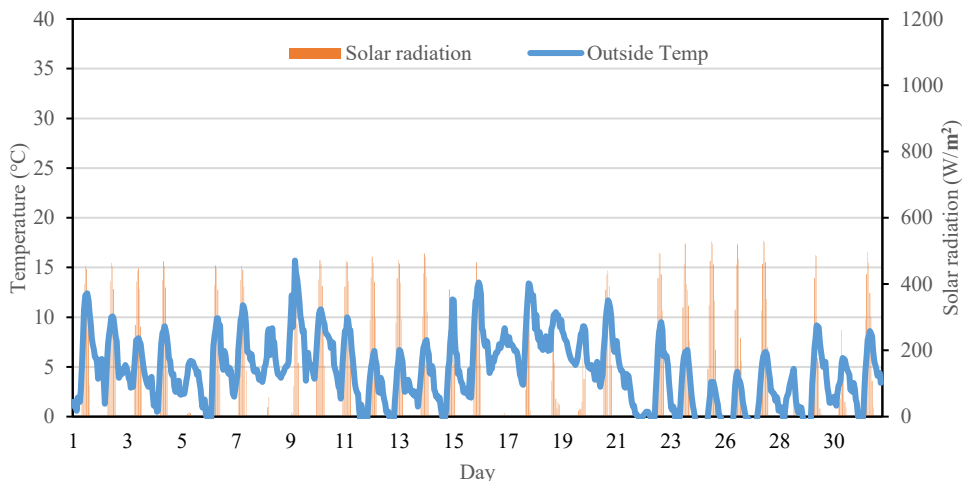


Figure 7.1.5: January weather in Tokyo involves considerations of both temperature and solar radiation.

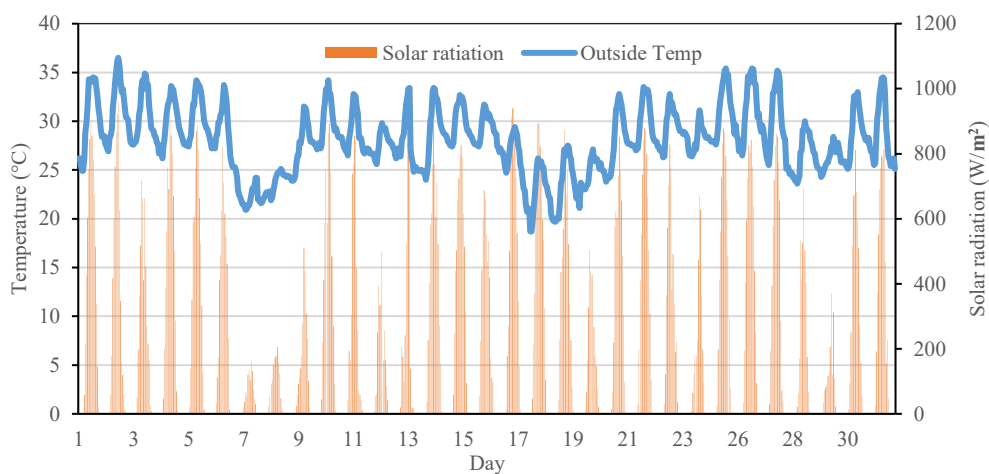
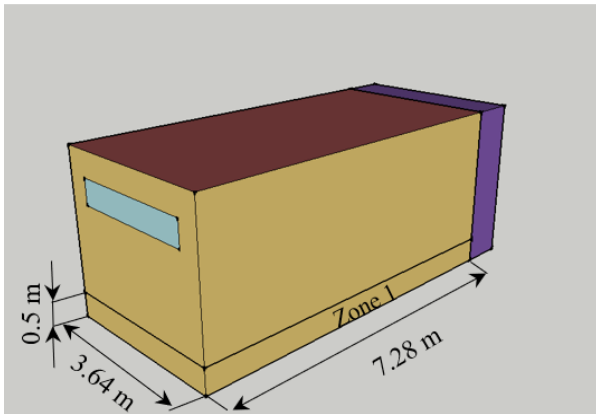


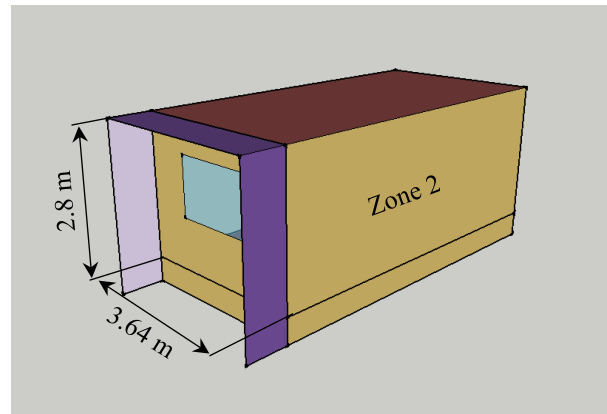
Figure 7.1.6: August weather in Tokyo involves considerations of both temperature and solar radiation.

### 7.1.4 Description of the zones

This house is composed by two different zones named: basement, living room, Figure 7. In order to reduce the time of each simulation, several simplifications have been considered, for example: connect different rooms in one zone and consider that the house is isolated.



(a) Zone 1



(b) Zone 2

Figure 7.1.7: Description of the zones (a) Zone 1: Basement (b) Zone 2: Living room.

Field	Units	Obj1	Obj2	Obj3	Obj4	Obj5	Obj6	Obj7	Obj8	Obj9	Obj10	Obj11	Obj12
Name		Surface 1	Surface 2	Surface 3	Surface 4	Surface 5	Surface 6	Surface 10	Surface 11	Surface 12	Surface 7	Surface 8	Surface 9
Surface Type		Floor	Wall	Wall	Wall	Ceiling	Wall	Wall	Wall	Wall	Floor	Roof	Wall
Construction Name		base_bot	base_wall	base_wall	base_wall	base_surface	base_wall	Exterior Wall	Exterior Wall	Exterior Wall	1F_Floor	Exterior Roof	Exterior Wall
Zone Name		Thermal Zone 1	Thermal Zone 1	Thermal Zone 1	Thermal Zone 1	Thermal Zone 1	Thermal Zone 1	Thermal Zone 2	Thermal Zone 2	Thermal Zone 2	Thermal Zone 2	Thermal Zone 2	Thermal Zone 2
Outside Boundary Condition		Ground	Outdoors	Outdoors	Outdoors	Surface	Outdoors	Outdoors	Outdoors	Outdoors	Surface	Outdoors	Outdoors
Outside Boundary Condition Object						Surface 7					Surface 5		
Sun Exposure		NoSun	SunExposed	SunExposed	SunExposed	NoSun	SunExposed	SunExposed	SunExposed	SunExposed	NoSun	SunExposed	SunExposed
Wind Exposure		NoWind	WindExposed	WindExposed	WindExposed	NoWind	WindExposed	WindExposed	WindExposed	WindExposed	NoWind	WindExposed	WindExposed
View Factor to Ground													
Number of Vertices													
Vertex 1 X-coordinate	m	3.64	0	3.64	3.64	3.64	0	0	3.64	0	3.64	3.64	3.64
Vertex 1 Y-coordinate	m	7.28	0	7.28	0	0	7.28	0	0	7.28	7.28	0	7.28
Vertex 1 Z-coordinate	m	0	0.5	0.5	0.5	0.5	2.8	2.8	2.8	0	2.8	2.8	2.8
Vertex 2 X-coordinate	m	3.64	0	3.64	3.64	3.64	0	0	3.64	0	3.64	3.64	3.64
Vertex 2 Y-coordinate	m	0	0	7.28	0	7.28	7.28	0	7.28	0	7.28	0	7.28
Vertex 2 Z-coordinate	m	0	0	0	0	0.5	0	0	0	0	2.8	0	2.8
Vertex 3 X-coordinate	m	0	3.64	0	3.64	0	0	3.64	3.64	0	0	0	0
Vertex 3 Y-coordinate	m	0	0	7.28	7.28	7.28	0	0	7.28	0	0	7.28	7.28
Vertex 3 Z-coordinate	m	0	0	0	0	0.5	0	0	0	0	0	2.8	0
Vertex 4 X-coordinate	m	0	3.64	0	3.64	0	0	3.64	3.64	0	0	0	0
Vertex 4 Y-coordinate	m	7.28	0	7.28	7.28	0	0	0	7.28	0	7.28	0	7.28
Vertex 4 Z-coordinate	m	0	0.5	0.5	0.5	0.5	2.8	2.8	2.8	0	2.8	2.8	2.8

Figure 7.1.8: Description of the zones. Source: Energy Plus

### 7.1.5 Simulation parameters

The material input simulation specifications detail the composition of three key building elements: the wall, ceiling surface, and floor. The wall is a three-layer structure with exterior structural plywood, 100 mm of glass wool, and a 12 mm PCM board. The ceiling surface consists of four layers, including asphalt roofing, structural plywood, 200 mm of glass wool insulation, and 9 mm of gypsum board. The floor is composed of three layers, featuring 100 mm of glass wool, 15 mm of structural plywood, and a 15 mm thick flooring material. Specifications on architecture are shown in Table.7-1 and Table. 7-2.

Table 7-1 Simulation parameters.

<b>Building orientation</b>		<b>South</b>
<b>Building shape</b>		Width 3.64m, depth 7.28m, height 2.8m
<b>Shelter shape</b>		Width 3.64m, depth 0.91m, distance from the ground 3.3m
<b>East sleeve wall shape</b>		Depth 0.91m, height 3.3m, distance from west side wall 3.3m
<b>West sleeve wall shape</b>		Depth 0.91m, height 3.3m, distance from west side wall 0m
<b>South opening</b>		Width 2.73m, height 0.5m
<b>North opening</b>		Width 1.82m, height 1.17m
<b>Opening specifications</b>	Thermal Permeability [W / m <sup>2</sup> K]	1.3
	Solar heat transmittance	66.80%
<b>Wall specifications</b>	1st layer (outside)	Structural plywood 15 mm
	2nd layer	Glass wool 32K 100 mm
	3rd layer (inside)	PCM board (Gypsum board) 12 mm
<b>Ceiling surface specifications</b>	1st layer (outside)	Asphalt roofing 5 mm
	2nd layer	Structural plywood 15 mm
	3rd layer	Glass wool 32K 200 mm
	4th layer (inside)	Gypsum board 9 mm
<b>Floor specifications</b>	1st layer (outside)	Glass wool 32K 100 mm
	2nd layer	Structural plywood 15 mm
	3rd layer (inside)	Flooring 15 mm
<b>Heating set temperature</b>		20°C
<b>Cooling set temperature</b>		27°C

Table 7-2 Characteristic of the structure materials of the calculation model.

Name	Glass wool_32K	Plywood for the structure	Flooring	Plasterboard	Asphalt roofing
<b>Roughness</b>	Medium	Medium	Medium	Medium	Medium
	Smooth	Smooth	Smooth	Smooth	Rough
<b>Thickness [m]</b>	0.1	0.015	0.015	0.009	0.005
<b>Conductivity [W/m-K]</b>	0.038	0.15	0.15	0.14	0.11
<b>Density [kg/m<sup>3</sup>]</b>	16	550	550	1110	1000
<b>Specific Heat [J/kg-K]</b>	840	1300	1300	1130	920
<b>Thermal Absorptance</b>	0.9	0.9	0.9	0.9	0.85
<b>Solar Absorptance</b>	0.7	0.7	0.7	0.5	0.85

### 7.1.6 General input as run period and schedules

#### 7.1.6.1 Run period of simulation

The characteristics of this object depend on the particular case under study. In general, the simulation will cover a one-year period from January 1 to December 31, as show in Figure 7.1.9.

Field	Units	Obj1
Name		Annual
Begin Month		1
Begin Day of Month		1
Begin Year		12
End Month		31
End Day of Month		0
End Year		0
Day of Week for Start Day		No
Use Weather File Holidays and Special Days		No
Use Weather File Daylight Saving Period		No
Apply Weekend Holiday Rule		No
Use Weather File Rain Indicators		2
Use Weather File Snow Indicators		

Figure 7.1.9. Object: Run period. Source: Energy plus.

### 7.1.6.2 Schedule of simulation

We employed typical household schedules for the simulation. Obj4, representing heating, is active until June 30th at 24:00, maintaining a temperature of 20°C. Starting from August 31st, the set temperature is adjusted to 1°C to avoid running the heating system. From September 1st to December 31st, the temperature is maintained at 20°C.

For cooling (Obj 5), the set point is set to 50°C throughout the day until February 28th, avoiding the activation of cooling system. From March 1st to November 30th, the temperature is set at 27°C. Subsequently, the operating schedule continues until February 28th at 50°C. Detailed operating schedules are illustrated in Figure 7.1.10.

Field	Units	Obj1	Obj2	Obj3	Obj4	Obj5
Name		Always Off	Always On	night_vent	Heating Setpoints	Cooling Setpoints
Schedule Type Limits Name		Fraction	Fraction	Fraction	Temperature	Temperature
Field 1	varies	Through: 12/31	Through: 12/31	Through: 03/31	Through: 6/30	Through: 2/28
Field 2	varies	For: AllDays	For: AllDays	For: AllDays	For: AllDays	For: AllDays
Field 3	varies	Until: 24:00	Until: 24:00	Until: 24:00	Until: 24:00	Until: 24:00
Field 4	varies	0	1	0	20	50
Field 5	varies			Through: 06/30	Through: 8/31	Through: 11/30
Field 6	varies			For: AllDays	For: AllDays	For: AllDays
Field 7	varies			Until: 24:00	Until: 24:00	Until: 24:00
Field 8	varies			1	1	27
Field 9	varies			Through: 09/30	Through: 12/31	Through: 12/31
Field 10	varies			For: AllDays	For: AllDays	For: AllDays
Field 11	varies			Until: 07:00	Until: 24:00	Until: 24:00
Field 12	varies			1	20	50
Field 13	varies			Until: 17:00		
Field 14	varies			0		
Field 15	varies			Until: 24:00		
Field 16	varies			1		
Field 17	varies			Through: 10/31		
Field 18	varies			For: AllDays		
Field 19	varies			Until: 24:00		
Field 20	varies			1		
Field 21	varies			Through: 12/31		
Field 22	varies			For: AllDays		
Field 23	varies			Until: 24:00		
Field 24	varies			0		

Figure 7.1.10. Occupancy schedule. Source: Energy plus schedule database.

For zone 1, the ventilation frequency is set to 5 times per hour according to the set point schedule settings in this model. As for zone 2, the ventilation frequency is set to 0.5 times per hour, as shown in Figure 7.1.11.

Field	Units	Obj1	Obj2
Name		Vant A	Vant B
Zone or ZoneList Name		Thermal Zone 1	Thermal Zone 2
Schedule Name		Always On	Always On
Design Flow Rate Calculation Method		AirChanges/Hour	AirChanges/Hour
Design Flow Rate	m3/s		
Flow per Zone Floor Area	m3/s-m2		
Flow per Exterior Surface Area	m3/s-m2		
Air Changes per Hour	1/hr	5	0.5
Constant Term Coefficient			
Temperature Term Coefficient			
Velocity Term Coefficient			
Velocity Squared Term Coefficient			

Figure 7.1.11. Ventilation schedule. Source: Energy plus schedule database.

### 7.1.7 Conduction through the wall

The most basic time series solution is the response factor equation which relates the flux at one surface of an element to an infinite series of temperature histories at both sides as shown by Equation 7-1:

$$q''_{ko}(t) = \sum_{j=0}^{\infty} X_j T_{o,t-j\delta} - \sum_{j=0}^{\infty} Y_j T_{i,t-j\delta}$$

Equation 7-1

where  $q''$  is heat flux,  $T$  is temperature,  $i$  signifies the inside of the building element,  $o$  signifies the outside of the building element,  $t$  represents the current time step, and  $X$  and  $Y$  are the response factors. While in most cases the terms in the series decay fairly rapidly, the infinite number of terms needed for an exact response factor solution makes it less than desirable. Fortunately, the similarity of higher order terms can be used to replace them with flux history terms. The new solution contains elements that are called conduction transfer functions (CTFs). The basic form of a conduction transfer function solution is shown by the following equation 7-2:

$$q''_{ki}(t) = -Z_o T_{i,t} - \sum_{j=1}^{nz} Z_j T_{i,t-j\delta} + Y_o T_{o,t} + \sum_{j=1}^{nz} Y_j T_{o,t-j\delta} + \sum_{j=1}^{nq} \Phi_j q''_{ki,t-j\delta}$$

Equation 7-2

for the inside heat flux, and

$$q''_{ko}(t) = -Y_o T_{i,t} - \sum_{j=1}^{nz} Y_j T_{i,t-j\delta} + X_o T_{o,t} + \sum_{j=1}^{nz} X_j T_{o,t-j\delta} + \sum_{j=1}^{nq} \Phi_j q''_{ko,t-j\delta}$$

Equation 7-3

for the outside heat flux ( $q'' = q/A$ )

where:

$X_j$  = Outside CTF coefficient,  $j = 0, 1, \dots, nz$ .

$Y_j$  = Cross CTF coefficient,  $j = 0, 1, \dots, nz$ .

$Z_j$  = Inside CTF coefficient,  $j = 0, 1, \dots, nz$ .

$\Phi_j$  = Flux CTF coefficient,  $j = 1, 2, \dots, nq$ .

$T_i$  = Inside face temperature

$T_o$  = Outside face temperature

$q''_{ko}$  = Conduction heat flux on outside face

$q''_{ki}$  = Conduction heat flux on inside face

The basis for the zone and air system integration is to formulate energy and moisture balances for the zone air and solve the resulting ordinary differential equations using a predictor-corrector



approach. The formulation of the solution scheme starts with a heat balance on the zone air.

$$C_z \frac{dT_z}{dt} = \sum_{i=1}^{N_{sl}} \dot{Q}_i + \sum_{i=1}^{N_{surfaces}} h_i A_i (T_{si} - T_z) + \sum_{i=1}^{N_{zones}} \dot{m}_i C_p (T_{zi} - T_z) + \dot{m}_{inf} C_p (T_\infty - T_z) + \dot{Q}_{sys}$$

Equation 7-4

Where:

$$\sum_{i=1}^{N_{sl}} \dot{Q}_i = \text{sum of the convective internal loads}$$

$$\sum_{i=1}^{N_{surfaces}} h_i A_i (T_{si} - T_z) = \text{convective heat transfer from the zone surfaces}$$

$$\dot{m}_{inf} C_p (T_\infty - T_z) = \text{heat transfer due to infiltration of outside air}$$

$$\sum_{i=1}^{N_{zones}} \dot{m}_i C_p (T_{zi} - T_z) = \text{heat transfer due to interzone air mixing}$$

$$\dot{Q}_{sys} = \text{air systems output}$$

$$C_z \frac{dT_z}{dt} = \text{energy stored in zone air}$$

$$C_z = \rho_{air} C_p C_T$$

$$\rho_{air} = \text{zone air density}$$

$$C_p = \text{zone air specific heat}$$

$C_T = \text{sensible heat capacity multiplier (Detailed description is provided below)}$  If the air capacitance is neglected, the steady-state system output must be:

$$-\dot{Q}_{sys} = \sum_{i=1}^{N_{sl}} \dot{Q}_i + \sum_{i=1}^{N_{surfaces}} h_i A_i (T_{si} - T_z) + \sum_{i=1}^{N_{zones}} \dot{m}_i C_p (T_{zi} - T_z) + \dot{m}_{inf} C_p (T_\infty - T_z)$$

Equation 7-5

Air systems provide hot or cold air to the zones to meet heating or cooling loads. The system energy provided to the zone,  $Q_{sys}$ , can thus be formulated from the difference between the supply air enthalpy and the enthalpy of the air leaving the zone as shown in Equation 7-5.

$$\dot{Q}_{sys} = \dot{m}_{sys} C_p (T_{sup} - T_z)$$

Equation 7-6

This equation assumes that the zone supply air mass flow rate is exactly equal to the sum of the air flow rates leaving the zone through the system return air plenum and being exhausted directly from the zone. Both air streams exit the zone at the zone mean air temperature. The result of substituting Equation 2.3 for  $Q_{sys}$  in the heat balance Equation 2.1 is shown in Equation 7-6.

$$C_z \frac{dT_z}{dt} = \sum_{i=1}^{N_{sl}} \dot{Q}_i + \sum_{i=1}^{N_{surfaces}} h_i A_i (T_{si} - T_z) + \sum_{i=1}^{N_{zones}} \dot{m}_i C_p (T_{zi} - T_z) + \dot{m}_{inf} C_p (T_\infty - T_z) + \dot{m}_{sys} C_p (T_{sup} - T_z)$$

Equation 7-7

### 7.1.8 Setting up wall materials

In this test, two different temperature ranges of microencapsulated phase change materials (PCMs): PCM6D and PCM18D were chosen based on the experimental results. Notably, PCM6D-30% and PCM18D-30% exceed the strength of the ALC panel in the compressive strength and the high-capacity heat storage of PCM is the maximum. To set up PCM simulations, the temperature of Tokyo was taken into consideration and No-PCM and gypsum board were used as the main materials for the comparative examination of PCM heating and cooling efficiency. Physical properties of PCM concrete are detailed in Table 7-3 to 7-6.

Table 7-3 Thermal conductivity of PCM concrete.

Name of the samples	Temperature range (°C)	Thermal conductivity (W/m. K)	
		Upper	Lower
No-PCM	020~°C	0.3648	0.3766
PCM6D-30%	020~°C	0.1693	0.1709
PCM18D-30%	10~30°C	0.1646	0.1661

Table 7-4 Density of concrete PCM concrete.

Name of sample	Density [kg/m <sup>3</sup> ]
No-PCM	1008
PCM6D-30%	730
PCM18D-30%	826

Table 7-5 Phase change behavior of PCM concrete.

No soul	PCM concrete Melting range		Melting peak	Melting enthalpy	Specific heat capacity		Crystallized enthalpy
	T <sub>i</sub> (°C)	T <sub>f</sub> (°C)	T <sub>m</sub> (°C)	$\Delta H_{\text{fusion}}$ (J/g)	C <sub>p</sub> (J/g)°C		$\Delta H_{\text{cryst}}$ (J/g)
PCM6D 30%	-	16.84	6.86	22.89	2.1630	24.47	
	13.35						
PCM18D 30%	-	30.40	16.84	39.93	3.8410	40.69	
	12.86						

### 7.1.8.1 Specific heat capacity of PCM

The specific heat capacity is referred to the amount of energy required to raise the temperature of 1 gram of substance by 1°C or 1K with units quoted as (J/g°C). Also designed as Cp, specific heat capacity can be quantitatively measured using a DSC as it is obtained at constant pressure.

The schematic DSC, specific heat capacity plots are shown from Figure 7.1.12 to 7.1.14, while detailed numerical values are presented in Table 7-6 to Table 7-8.

Table 7-6 Specific Heat of No-PCM.

Temp (°C)	Specific Heat (J/(g°C))	Temp (°C)	Specific Heat (J/(g°C))
5	0.93	25	1.03
10	0.96	30	1.06
15	0.98	35	1.10
20	1.00	40	1.15

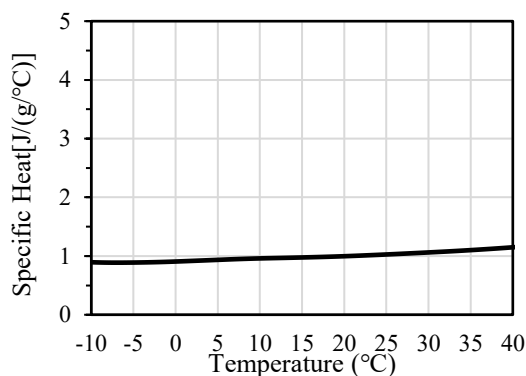


Figure 7.1.12 Specific heat of No-PCM.

Table 7-7 Specific Heat of 6D.

Temp (°C)	Specific Heat (J/(g°C))	Temp (°C)	Specific Heat (J/(g°C))
5	2.1	25	2.7
10	2.0	30	2.6
15	1.8	35	1.8
20	1.9	40	1.4

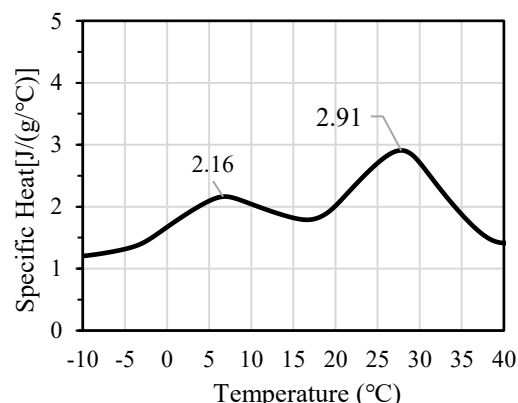


Figure 7.1.13 Specific heat of PCM6D.

Table 7-8 Specific Heat of 18D.

Temp (°C)	Specific Heat (J/(g°C))	Temp (°C)	Specific Heat (J/(g°C))
5	1.6	25	1.8
10	2.4	30	1.2
15	3.5	35	1.2
20	3.2	40	1.3

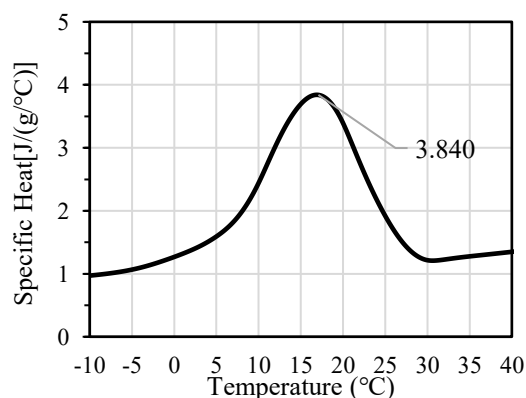


Figure 7.1.14 Specific heat of PCM18D.

### 7.1.8.2 Enthalpy of PCM

The specific enthalpy measurements, conducted within a temperature range of -25 to 60°C, allow us to understand the phase transition behavior of these materials. The specific enthalpy is assumed to be zero at -20 °C, enabling the analysis of changes in enthalpy.

For PCM6D (Figure 7.1.15 and Figure 7.1.16), the phase transition range, characterized by substantial changes in enthalpy, occurs from 6 to 16 °C. Within this phase transition range, PCM6D exhibits a specific enthalpy of 120 J/g, indicating its significant capacity for absorption. Additionally, it releases capacity is 102 J/g of thermal energy during this phase transition.

For PCM18D (Figure 7.1.17 and Figure 7.1.18), the phase transition range, characterized by substantial changes in enthalpy, occurs from 6 to 16 °C. Within this phase transition range, PCM6D exhibits a specific enthalpy of 120 J/g, indicating its significant capacity for absorption. Additionally, it releases capacity is 102 J/g of thermal energy during this phase transition.

Figure 7.1.19 and Figure 7.1.20 show settings utilized in EnergyPlus for a PCM simulation.

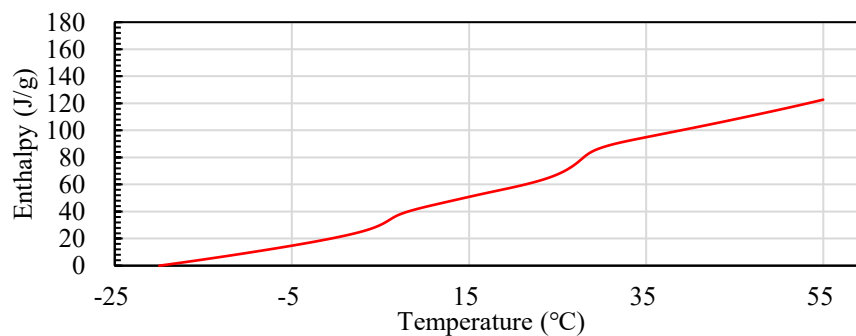


Figure 7.1.15 Enthalpy of PCM6D (Heating).

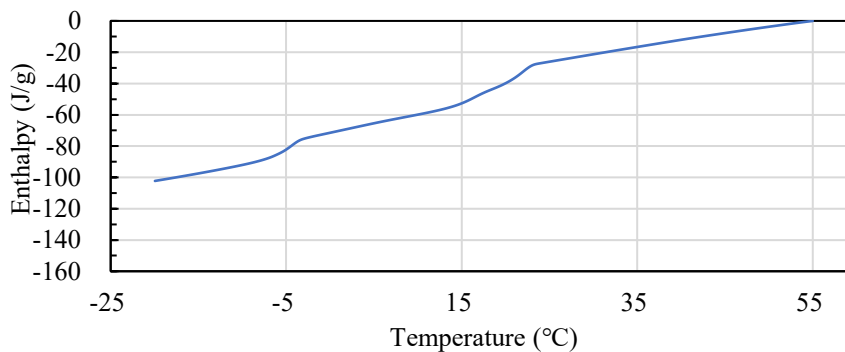


Figure 7.1.16 Enthalpy of PCM6D (Cooling).

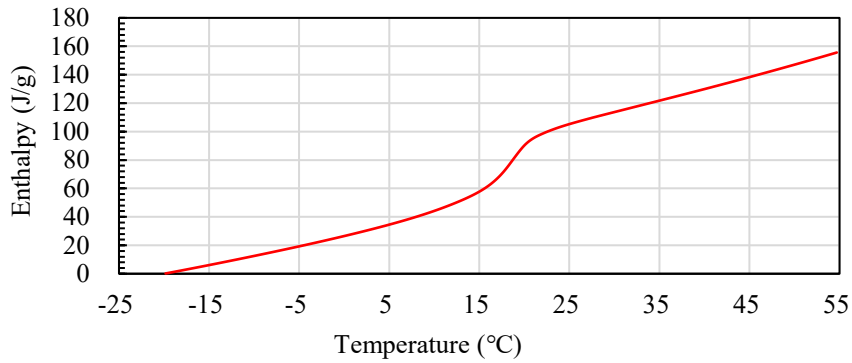


Figure 7.1.17 Enthalpy of PCM18D (Heating).

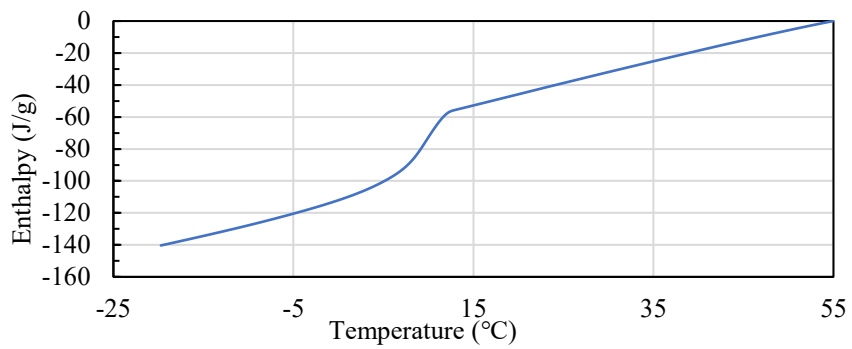


Figure 7.1.18 Enthalpy of PCM18D (Cooling).

Field	Units	Obj1
Name		PCM_boait
Temperature Coefficient for Thermal Conductivity	W/m-K2	
Temperature 1	C	-20
Enthalpy 1	J/kg	0
Temperature 2	C	0.01
Enthalpy 2	J/kg	20842.02315
Temperature 3	C	6.15
Enthalpy 3	J/kg	34375.12481
Temperature 4	C	10.17
Enthalpy 4	J/kg	43609.42096
Temperature 5	C	19.91
Enthalpy 5	J/kg	57842.4507
Temperature 6	C	28.23
Enthalpy 6	J/kg	81548.28086
Temperature 7	C	33.22
Enthalpy 7	J/kg	92617.78435
Temperature 8	C	54.98
Enthalpy 8	J/kg	122712.2387
Temperature 9	C	100
Enthalpy 9	J/kg	184950

Field	Units	Obj1
Name		PCM_boait
Temperature Coefficient for Thermal Conductivity	W/m-K2	
Temperature 1	C	-20
Enthalpy 1	J/kg	0
Temperature 2	C	0.01
Enthalpy 2	J/kg	26512.58913
Temperature 3	C	5.5
Enthalpy 3	J/kg	35406.56671
Temperature 4	C	13.03
Enthalpy 4	J/kg	51617.12812
Temperature 5	C	19.92
Enthalpy 5	J/kg	89663.02921
Temperature 6	C	25.7
Enthalpy 6	J/kg	106548.6192
Temperature 7	C	30.11
Enthalpy 7	J/kg	113906.2097
Temperature 8	C	54.89
Enthalpy 8	J/kg	155999.4226
Temperature 9	C	100
Enthalpy 9	J/kg	232645

Figure 7.1.19 Enthalpy of PCM6D. Source: Energy plus. Figure 7.1.20 Enthalpy of PCM18D. Source: Energy Plus.

## 7.2 TEST RESULTS

The test results of this chapter are described in two points: temperature change and heating and cooling load.

### 7.2.1 Comparative results in indoor temperature without heating and cooling load

On the result of the comparative examination under the above-mentioned setting conditions, the comparison of the temperature change for various materials, including gypsum, No-PCM, PCM6D and PCM18D, are shown from Figure 7.2.1 to 7.2.8. These figures show the temperature variations during periods of January and August when the heating and cooling is not used.

To obtain a comprehensive understanding of the temperature differences between materials, a comparative analysis was performed. The results of this comparison are shown in Figures 7.2.9 through 7.2.16 to provide a visual evaluation of the temperature variations of the specified materials.

Across all materials, indoor temperatures were generally higher than external temperatures. However, in PCM concrete, the indoor temperature closely approached the external temperature, resulting in a smaller temperature change amplitude. When comparing gypsum and No-PCM, as shown in Figure 7.2.10 and Figure 7.2.11, no significant differences were observed in January and August. This can be explained as these two materials has similar material properties such as density and heat capacity.

Comparing No-PCM with PCM6D, PCM6D exhibited lower temperature variation, with a difference of 2-4°C in both January and August (Figure 7.2.11 and Figure 7.2.12). Similarly, when comparing PCM6D with PCM18D, PCM18D demonstrated results lower than PCM6D, with a temperature difference of 1-3°C in both January and August, as shown in Figure 7.2.15 and Figure 7.2.16.

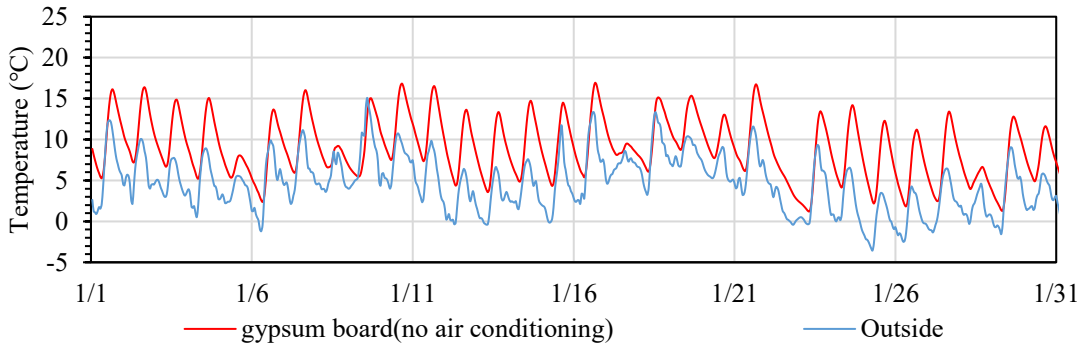


Figure 7.2.1 Indoor simulation of the gypsum wall in January.

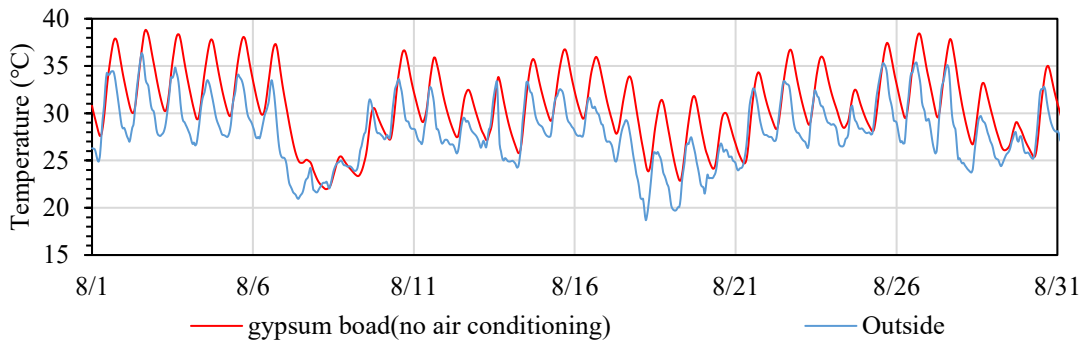


Figure 7.2.2 Indoor simulation of the gypsum wall in August.

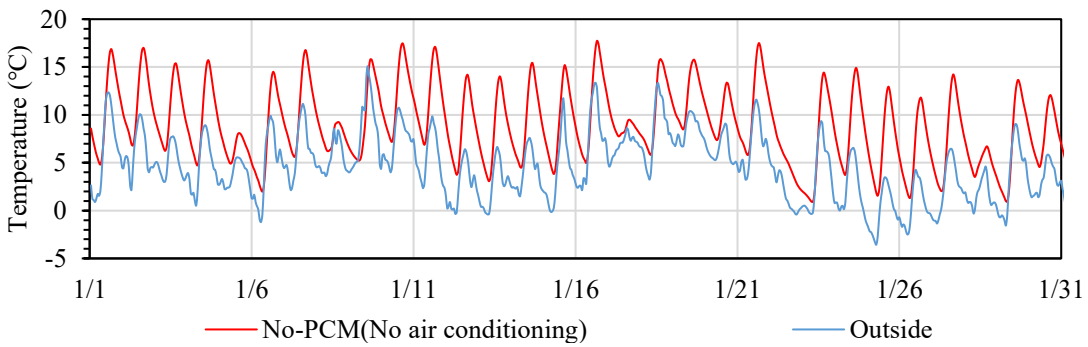


Figure 7.2.3 Indoor simulation of the No-PCM wall in January.

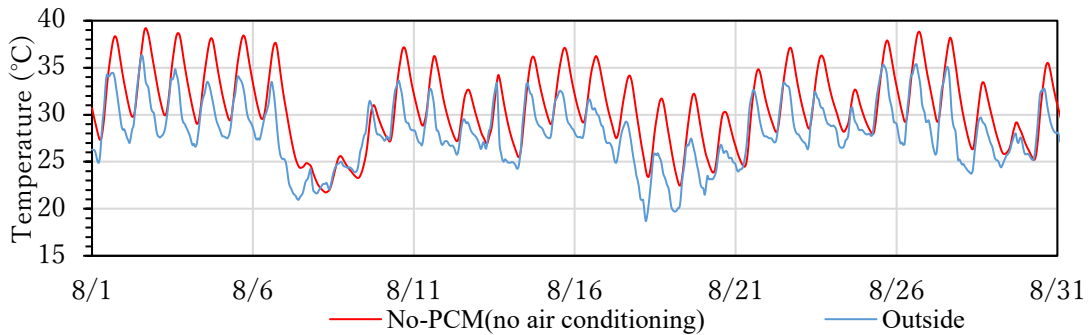


Figure 7.2.4 Indoor simulation of the No-PCM wall in August.

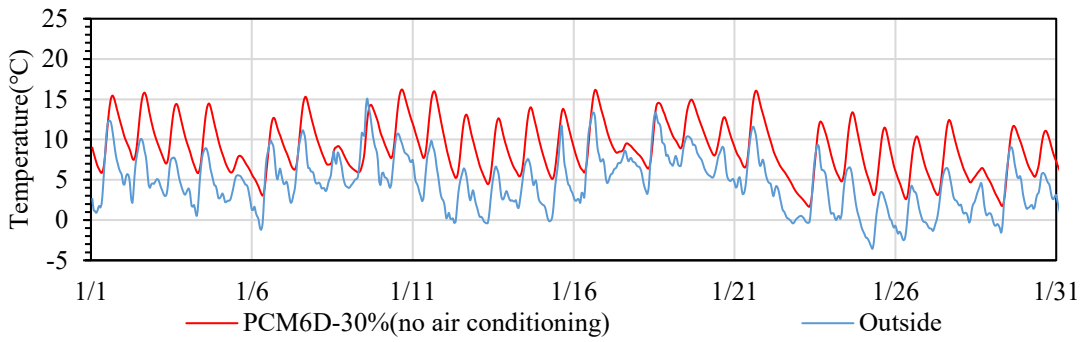


Figure 7.2.5 Indoor simulation of the PCM6D-30% wall in January.

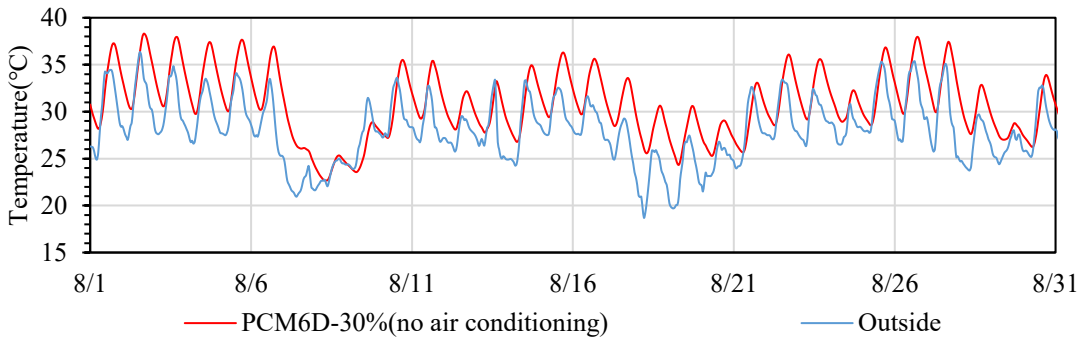


Figure 7.2.6 Indoor simulation of the PCM6D-30% wall in August.

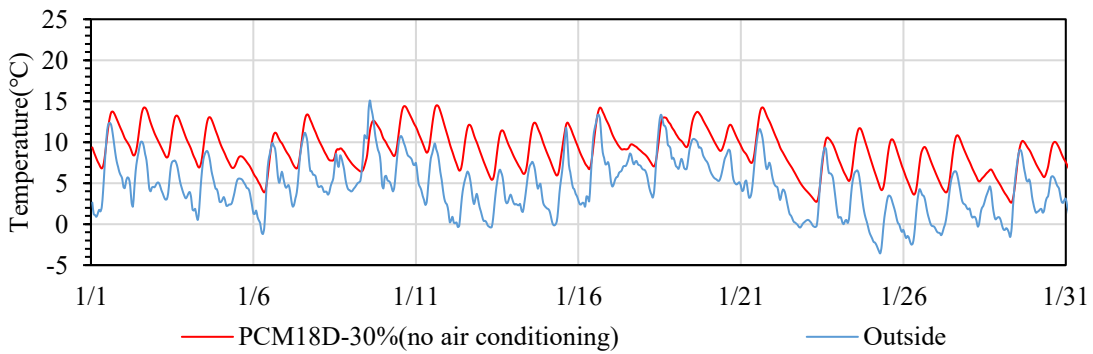


Figure 7.2.7 Indoor simulation of the PCM18D-30% wall in January.

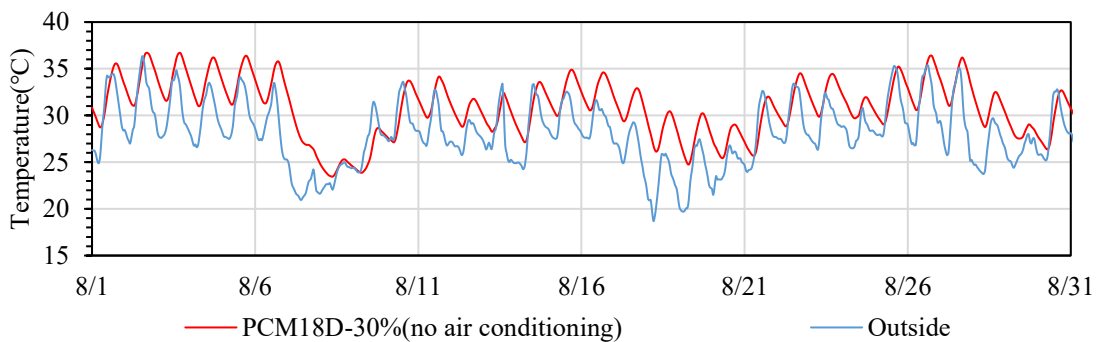


Figure 7.2.8 Indoor simulation of the PCM18D-30% wall in August.



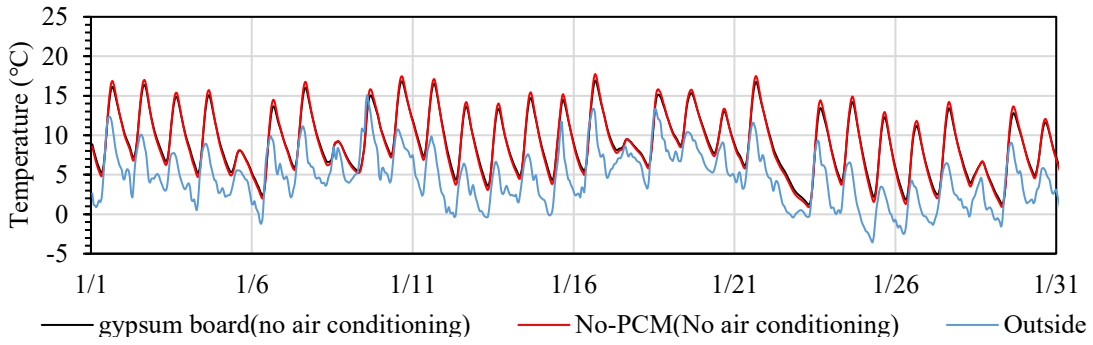


Figure 7.2.9 Indoor simulation comparison of gypsum wall and No-PCM wall in January.

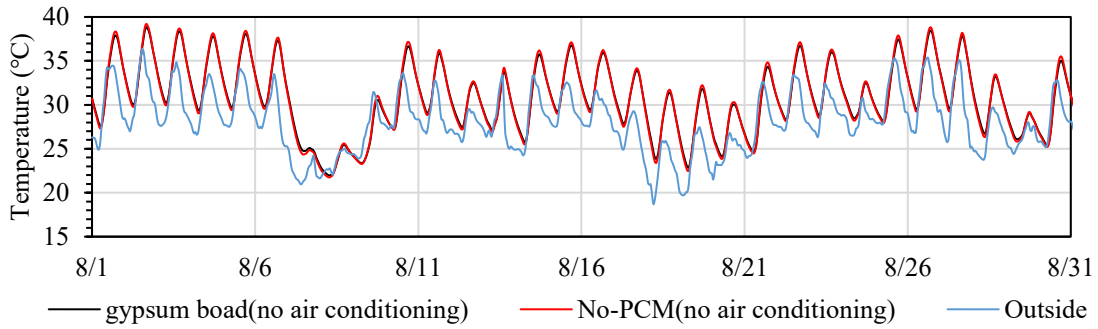


Figure 7.2.10 Indoor simulation comparison of gypsum wall and No-PCM wall in August.

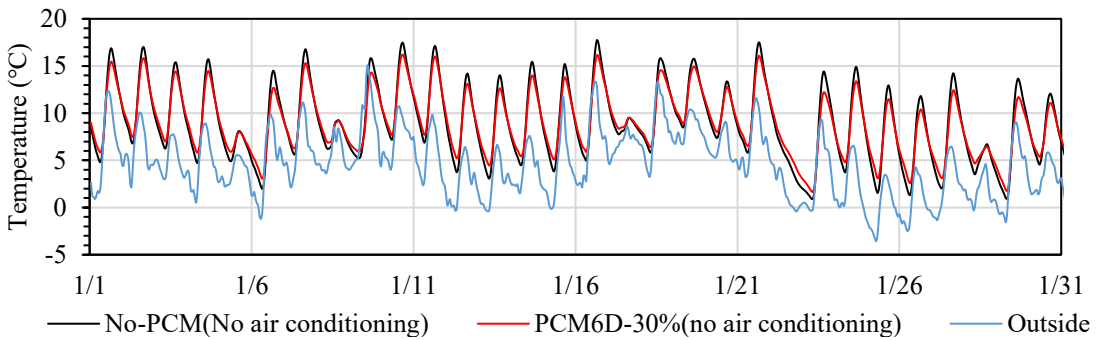


Figure 7.2.11 Indoor simulation comparison of No-PCM wall and PCM6D-30% wall in January.

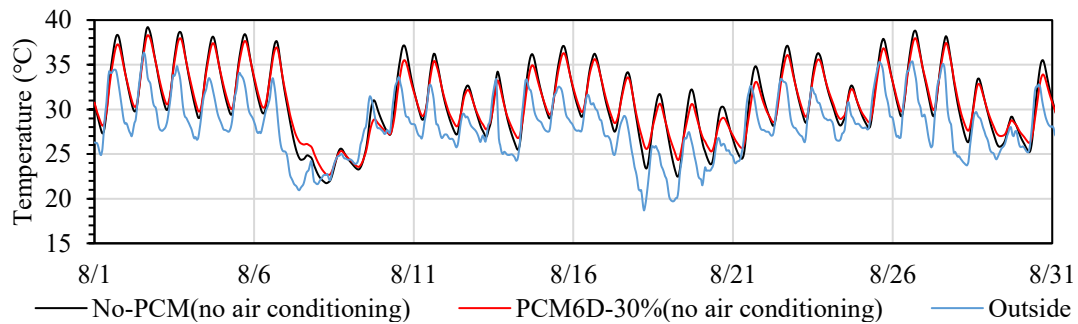


Figure 7.2.12 Indoor simulation comparison of No-PCM wall and PCM6D-30% wall in August.

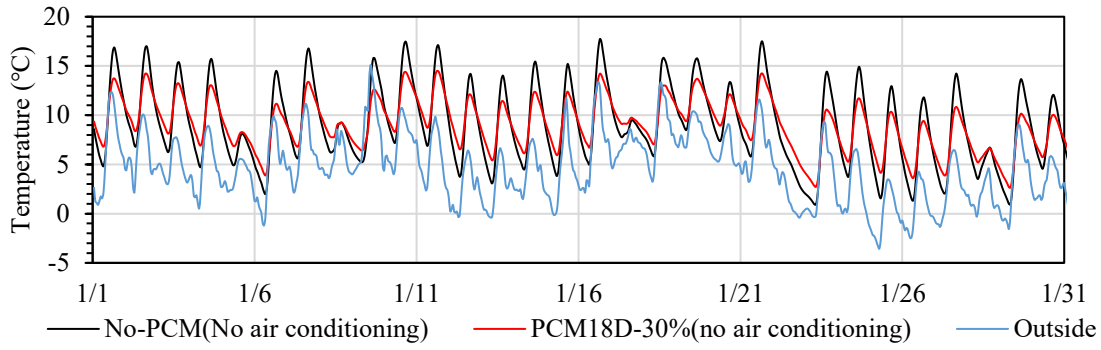


Figure 7.2.13 Indoor simulation comparison of No-PCM wall and PCM18D-30% wall in January.

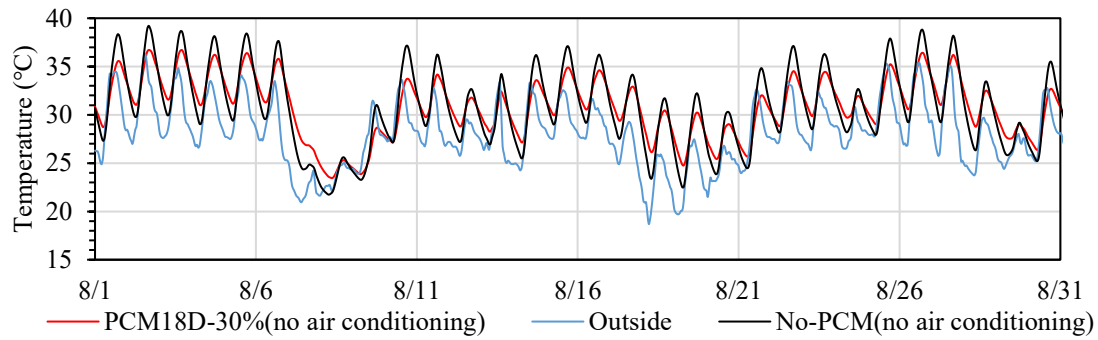


Figure 7.2.14 Indoor simulation comparison of No-PCM wall and PCM18D-30% wall in August.

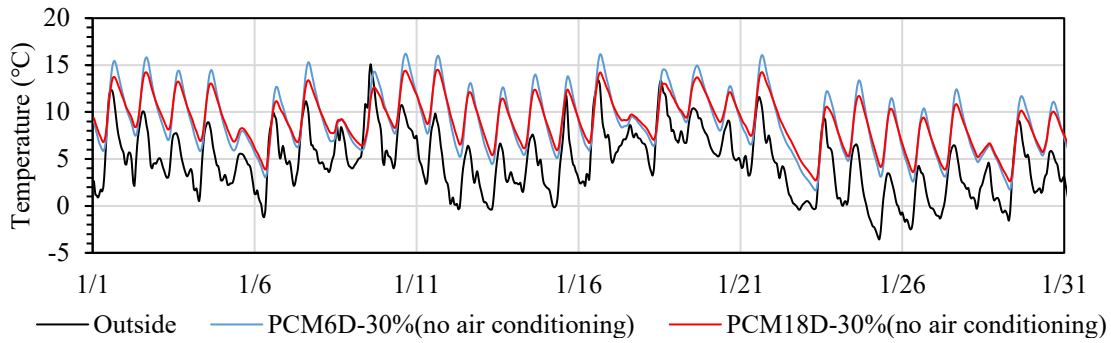


Figure 7.2.15 Indoor simulation comparison of PCM6D-30% wall and PCM18D-30% wall in January.

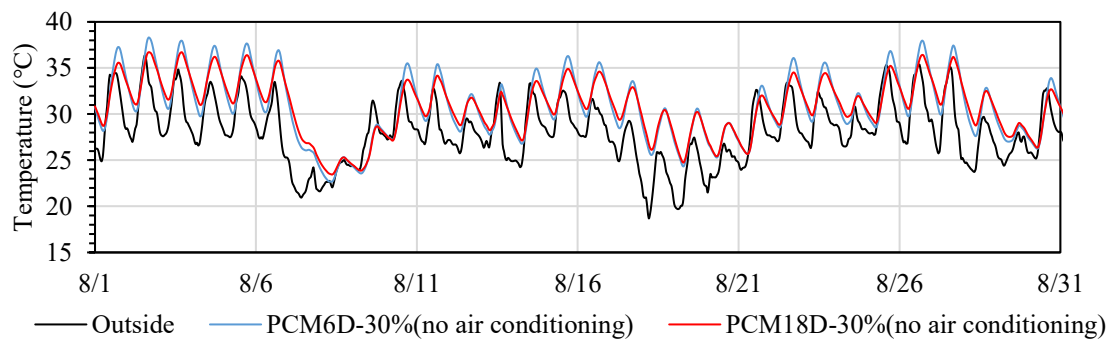


Figure 7.2.16 Indoor simulation comparison of PCM6D-30% wall and PCM18D-30% wall in August.

### 7.2.2 Comparative results in indoor temperature with heating and cooling load

The comparison results of the temperature change for various materials, including gypsum, No-PCM, PCM6D and PCM18D, are shown from Figure 7.2.17 to 7.2.32. These figures show the temperature variations during the periods of January and August with heating and cooling load. Since the heating load is applied in January and cooling load in August, the temperature change was set between 20°C and 27°C degrees respectively as the border line. In that case, the fluctuation shown represents that an extra heating load is applied, and the air conditioning load increases.

When comparing gypsum and No-PCM, as shown in Figure 7.2.25 and Figure 7.2.26, no significant differences were observed in January and August under the heating and cooling load. On some days under heating and cooling loads, the room temperature is higher during the winter months than set temperatures during the day. This phenomenon can be explained as during the winter months, it is might depended on material properties and solar radiation penetrating into room. For example, gypsum and No-PCM have similar properties in terms of density and heat capacity. As a result, temperature trends observed in rooms with gypsum and No-PCM materials could be similar. In contrast, on some days under heating and cooling loads, the room temperature is lower during the summer on some days than set temperatures during the day. This can be explained as during certain days of summer, external weather conditions, such as cooler temperatures or reduced solar radiation, may contribute to the lower indoor temperatures compared to the set values.

In comparison to PCM6D and PCM18D, PCM18D demonstrated results lower temperature fluctuations and effectively maintained room temperature, especially in January (Figure 7.2.31). While there was a slight difference observed in August, as shown in Figure 7.2.32, PCM18D consistently demonstrated better temperature stability. This enhanced performance can be attributed to the capability of PCM to absorb and store energy from the indoor air, thereby maintaining temperature fluctuations more effectively. Furthermore, another factor to decrease in heat load is PCM18D's higher heat capacity compared to PCM6D and No-PCM. The higher heat capacity of PCM18D allows it to absorb and release more energy per unit volume or mass, making it more effective in regulating temperature.

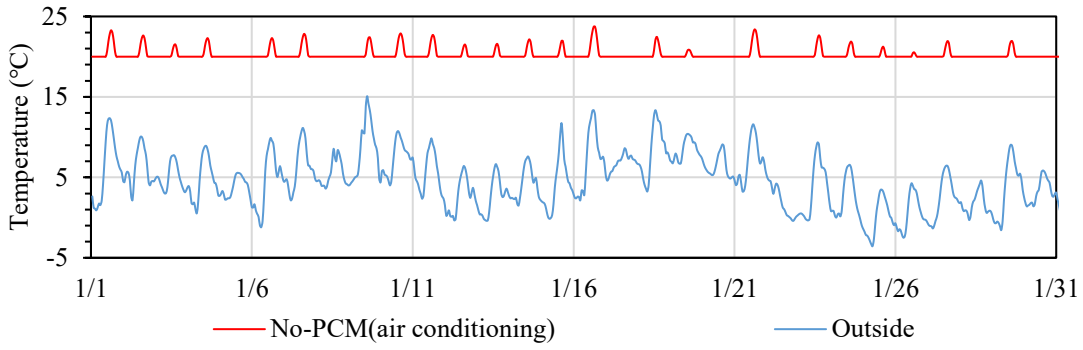


Figure 7.2.17 Indoor simulation with the air conditioning of the gypsum wall in January.

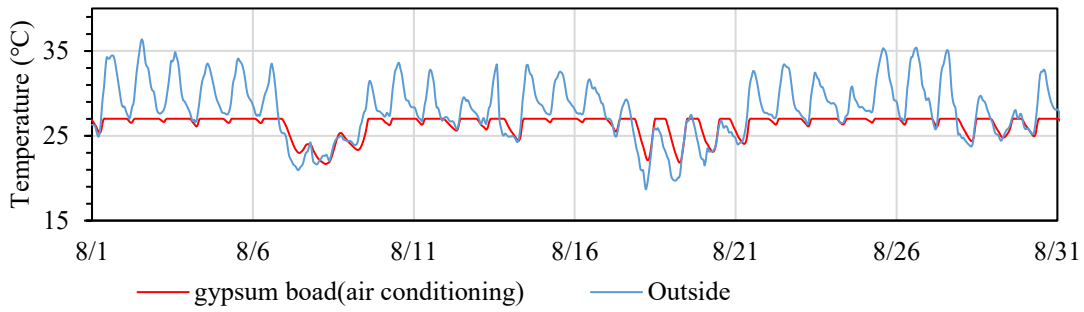


Figure 7.2.18 Indoor simulation with the air conditioning of the gypsum wall in August.

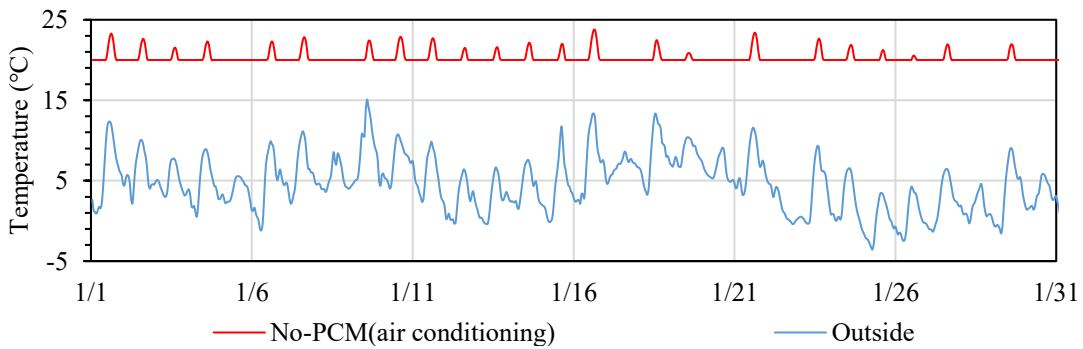


Figure 7.2.19 Indoor simulation with the air conditioning of No-PCM wall in January.

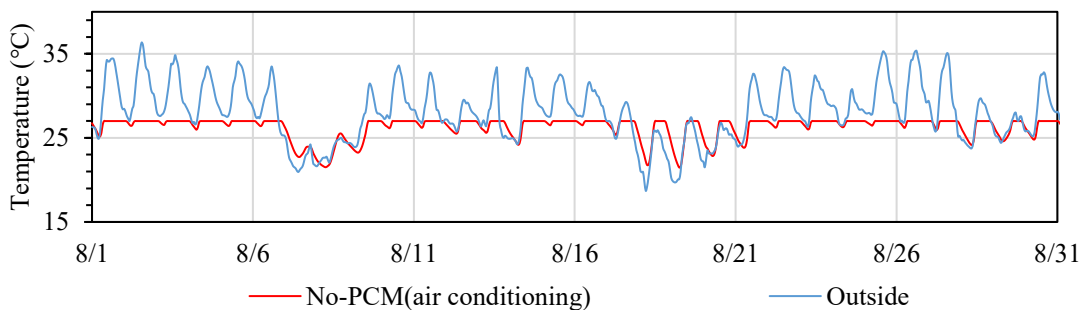


Figure 7.2.20 Indoor simulation with the air conditioning of No-PCM wall in August.

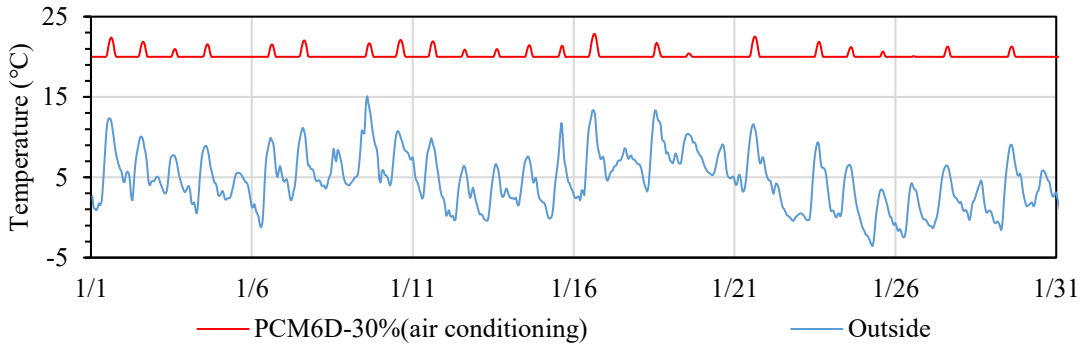


Figure 7.2.21 Indoor simulation with the air conditioning of PCM6D-30% wall in January.

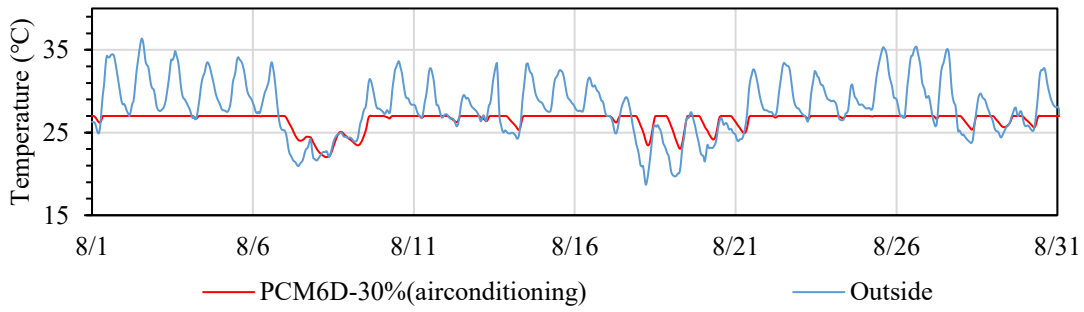


Figure 7.2.22 Indoor simulation with the air conditioning of PCM6D-30% wall in August.

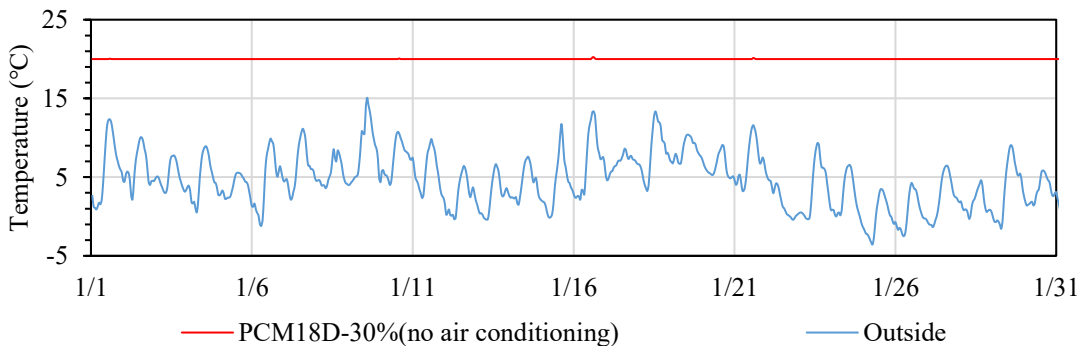


Figure 7.2.23 Indoor simulation with the air conditioning of PCM18D-30% wall in January.

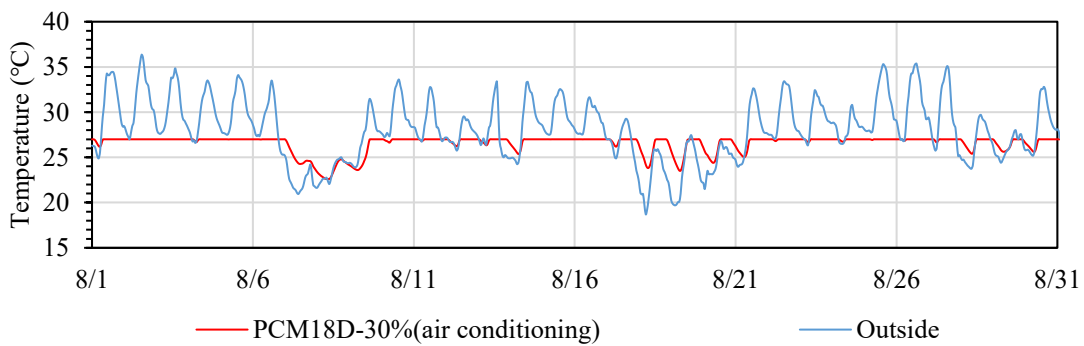


Figure 7.2.24 Indoor simulation with the air conditioning of PCM18D-30% wall in August.

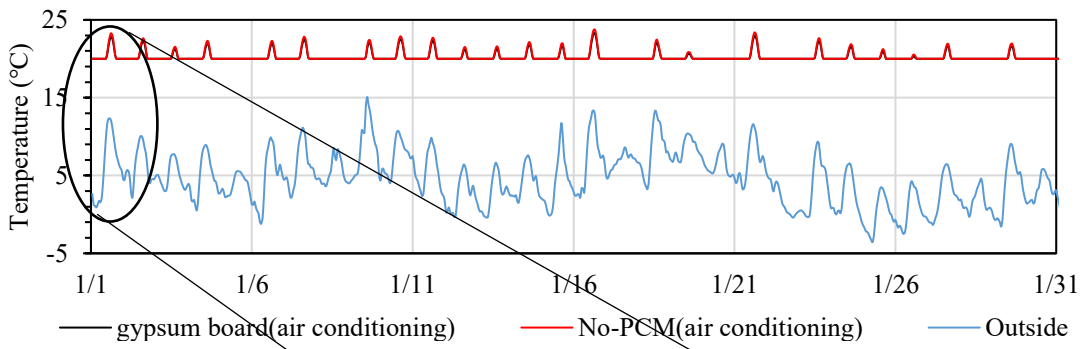


Figure 7.2.25 Indoor simulation comparison with the air conditioning of gypsum and No-PCM in January.

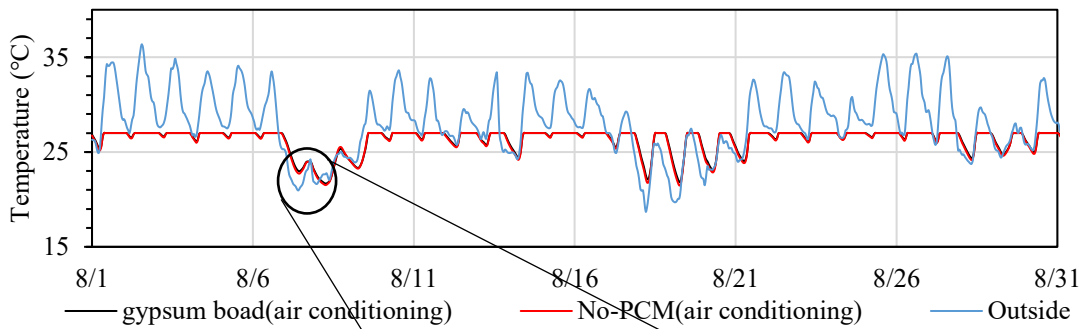
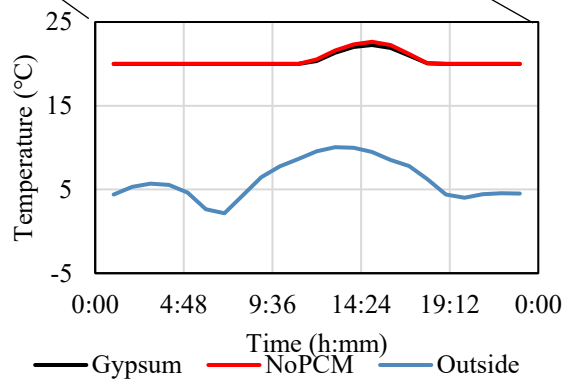
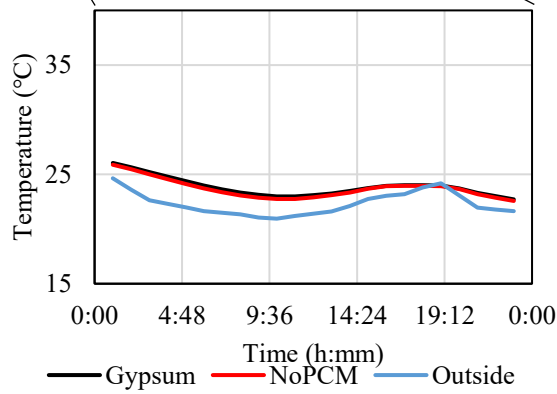


Figure 7.2.26 Indoor simulation comparison with the air conditioning of gypsum and No-PCM in August.



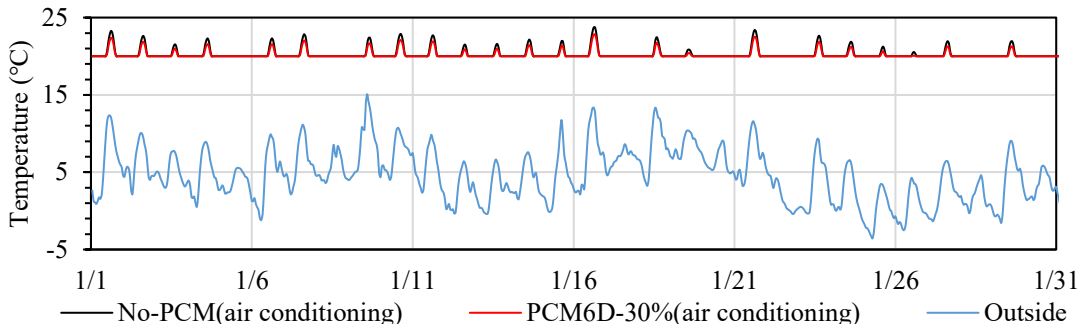


Figure 7.2.27 Indoor simulation comparison with the air conditioning of PCM6D-30% and No-PCM January.

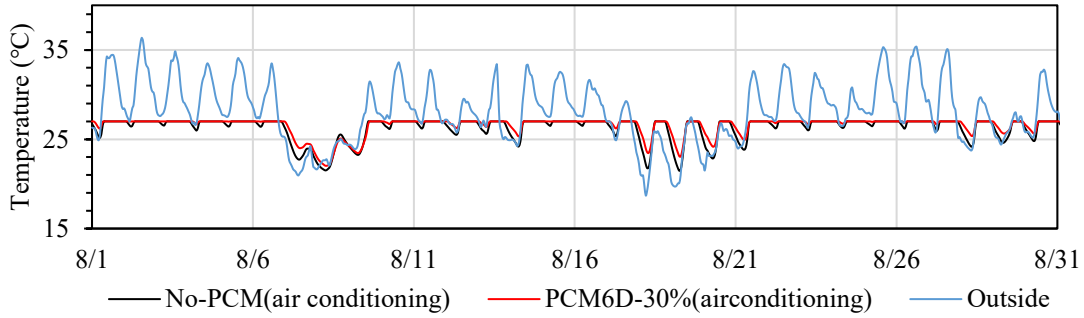


Figure 7.2.28 Indoor simulation comparison with the air conditioning of PCM6D-30% and No-PCM August.

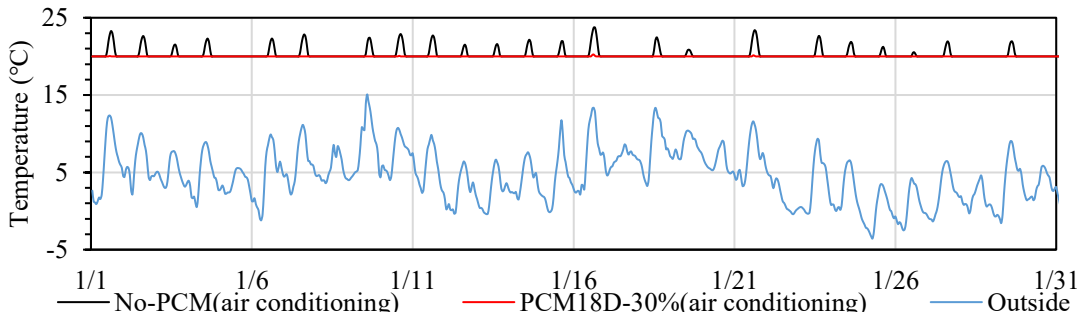


Figure 7.2.29 Indoor simulation comparison with the air conditioning of PCM18D-30% and No-PCM January.

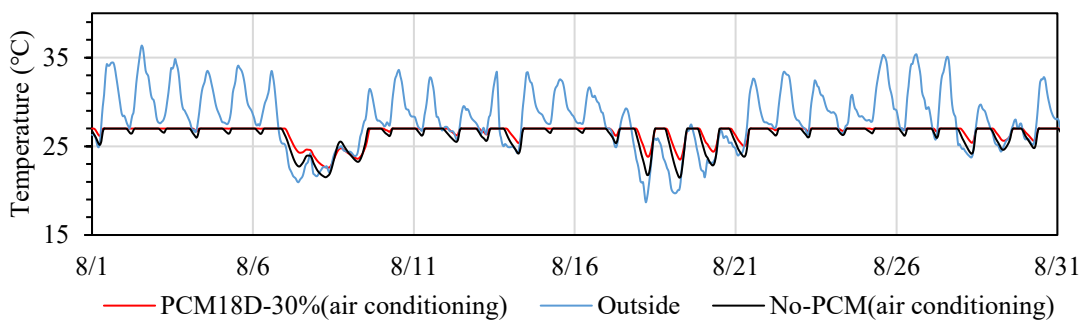


Figure 7.2.30 Indoor simulation comparison with the air conditioning of PCM18D-30% and No-PCM in August.

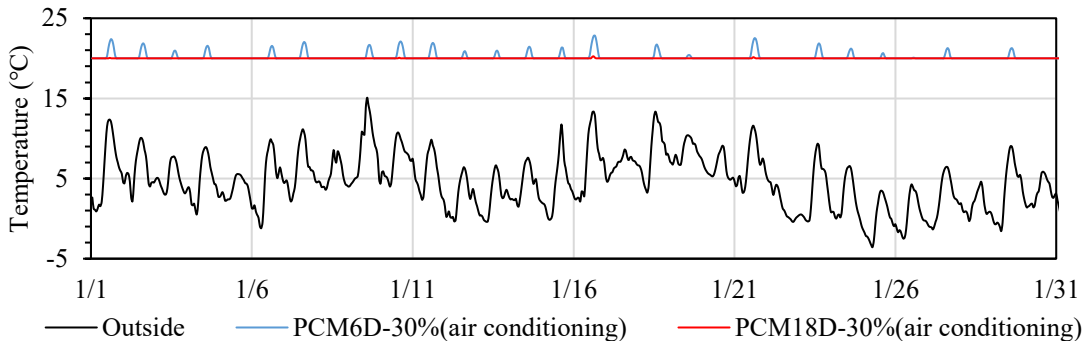


Figure 7.2.31 Indoor simulation comparison with the air conditioning of PCM6D-30% & PCM18D-30% in January.

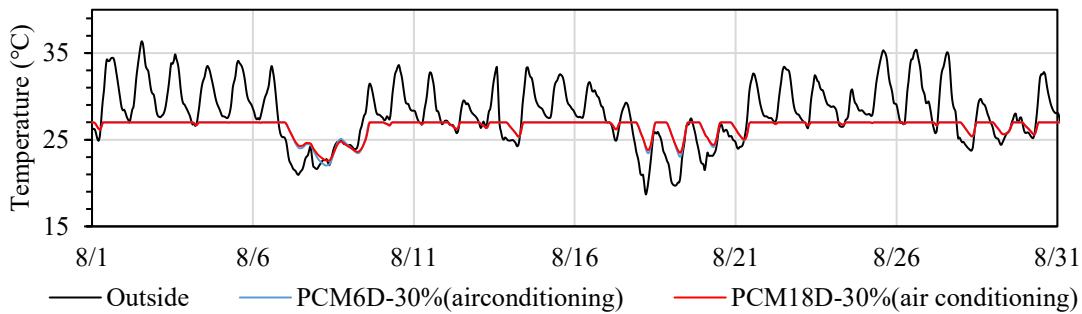


Figure 7.2.32 Indoor simulation comparison with the air conditioning of PCM6D-30% & PCM18D-30% in August.

### 7.2.3 Heating and cooling loads

The results of the day-to-day heating and cooling load were calculated based on the change in temperature and the comparison for each material is Figures from 7.2.33 to 7.2.48.

In the Figure 7.2.41 and Figure 7.2.42, comparison results of gypsum and No-PCM are shown, it is hardly possible to recognize the difference in the heating and cooling load.

As for the PCM concrete, the heating load of PCM6D was almost no different from that of No-PCM, but in the cooling load, the difference was sufficient for the cooling load as shown in Figure 7.2.43 and Figure 7.2.44. Further analysis in Figures 7.2.47 and 7.2.48 demonstrates that PCM18D exhibits noticeable differences in both heating and cooling loads compared to PCM6D. This indicates that variations in PCM composition play a crucial role in influencing heating and cooling loads, with PCM18D-30% showing enhanced performance in regulating temperature fluctuations.



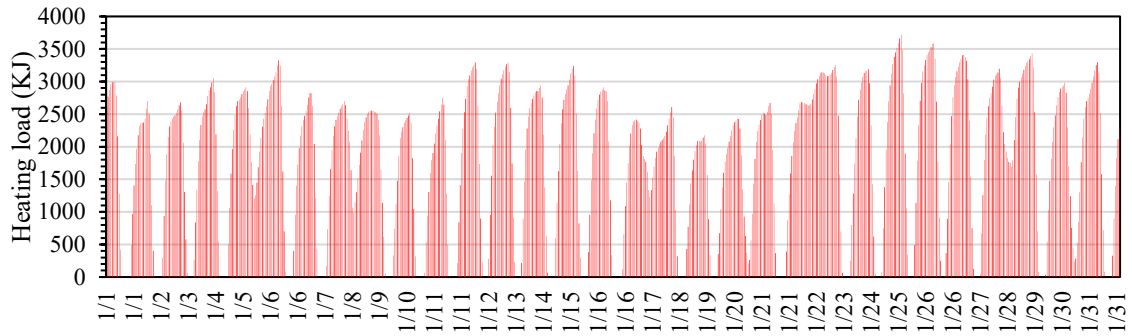


Figure 7.2.33 Air-conditioning load of the gypsum wall building in January.

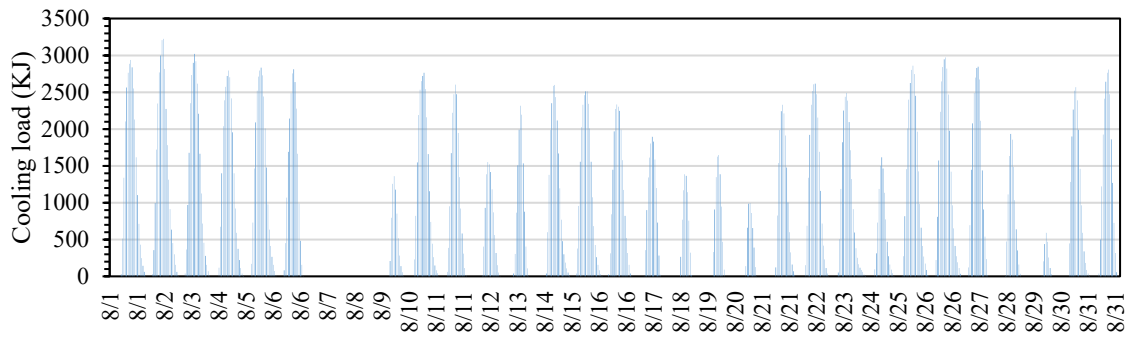


Figure 7.2.34 Air-conditioning load of the gypsum wall building in August.

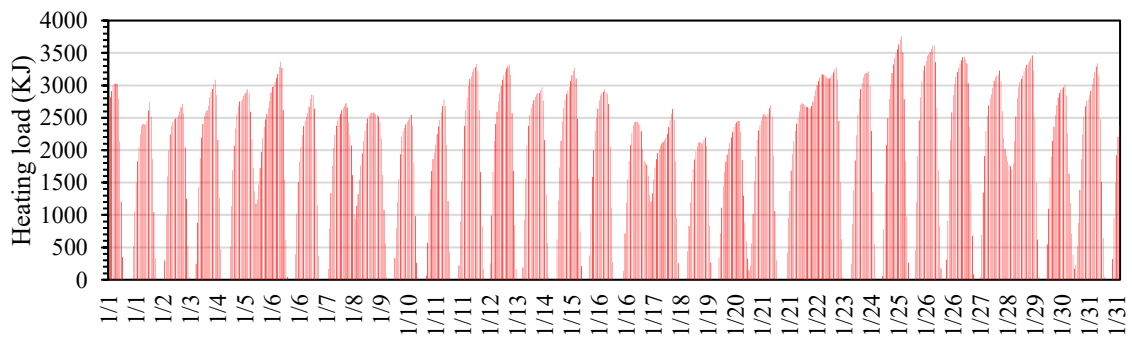


Figure 7.2.35 Air-conditioning load of the No-PCM wall building in January.

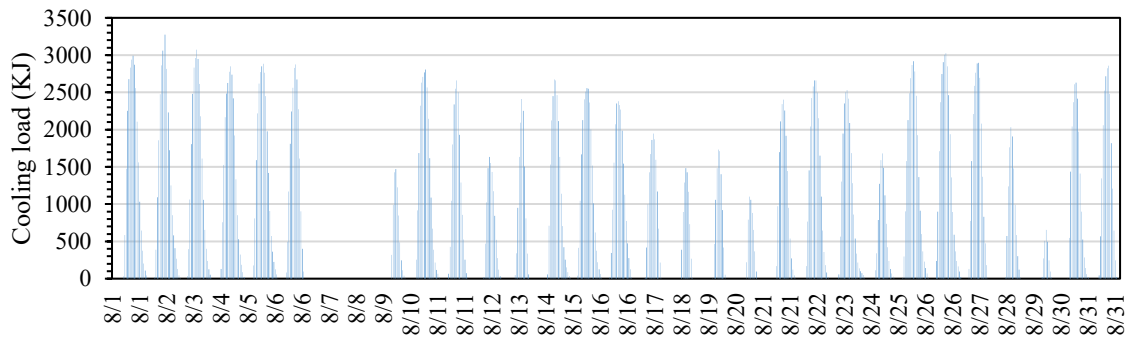


Figure 7.2.36 Air-conditioning load of the No-PCM wall building in August.

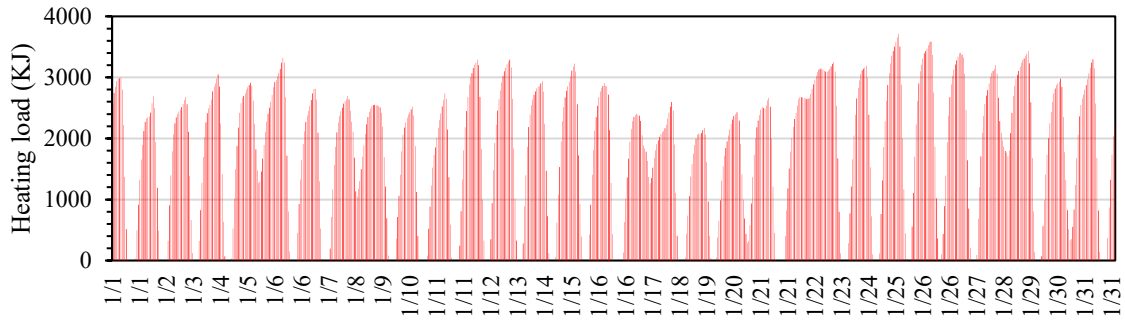


Figure 7.2.37 Air-conditioning load of the PCM6D-30% wall building in January.

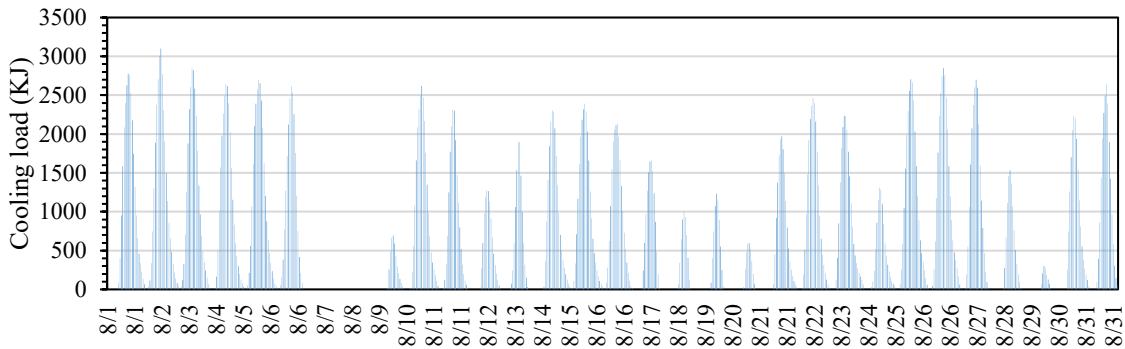


Figure 7.2.38 Air-conditioning load of the PCM6D-30% wall building in August.

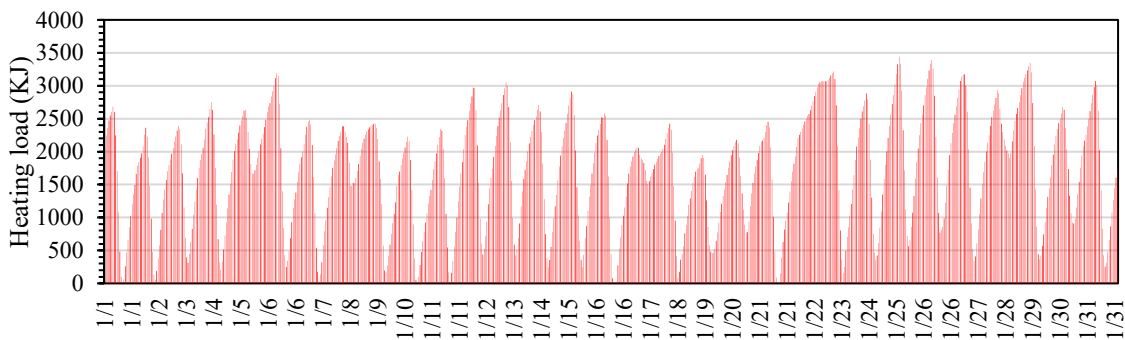


Figure 7.2.39 Air-conditioning load of the PCM18D-30% wall building in January.

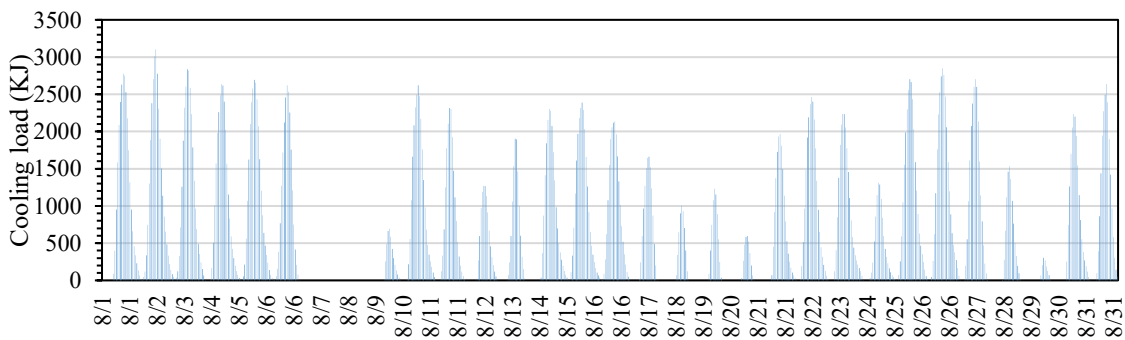


Figure 7.2.40 Air-conditioning load of the PCM18D-30% wall building in August.

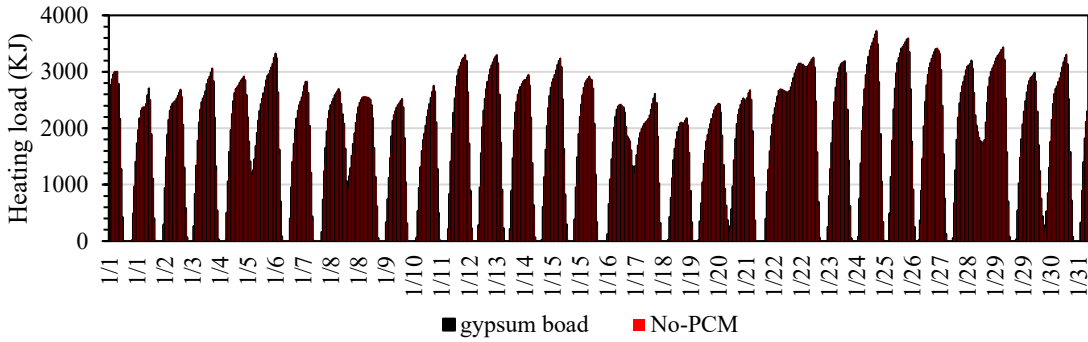


Figure 7.2.41 Air-conditioning load of gypsum wall building and No-PCM wall building in January.

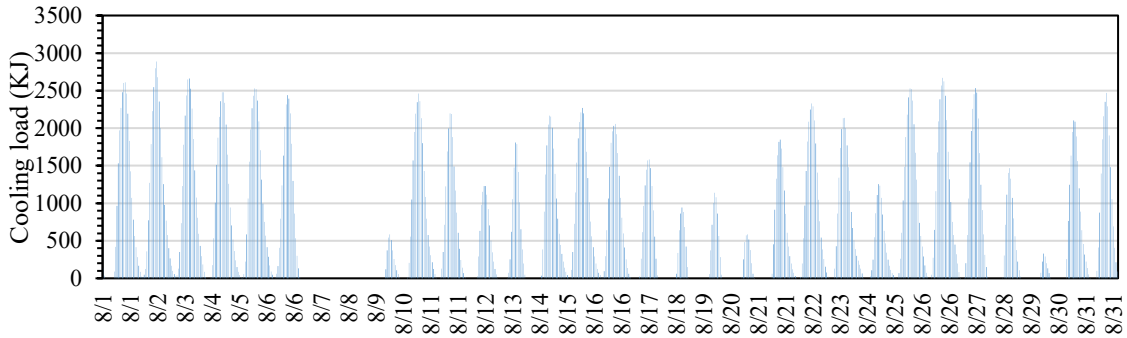


Figure 7.2.42 Air-conditioning load of gypsum wall building and No-PCM wall building in August.

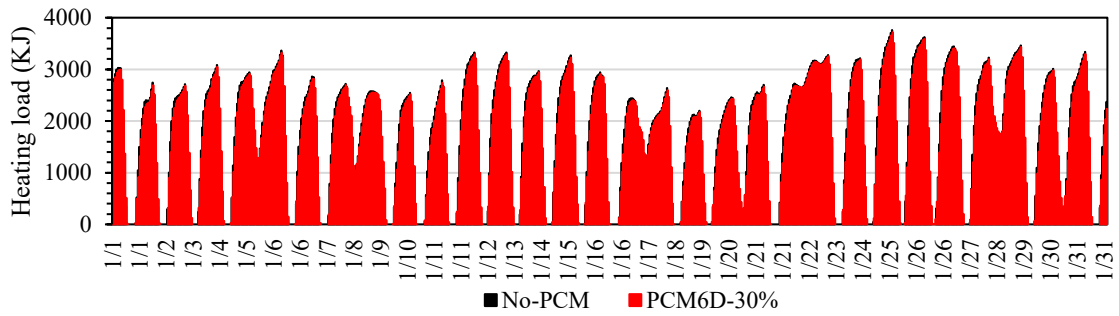


Figure 7.2.43 Air-conditioning load of No-PCM wall building and PCM6D-30% wall building in January.

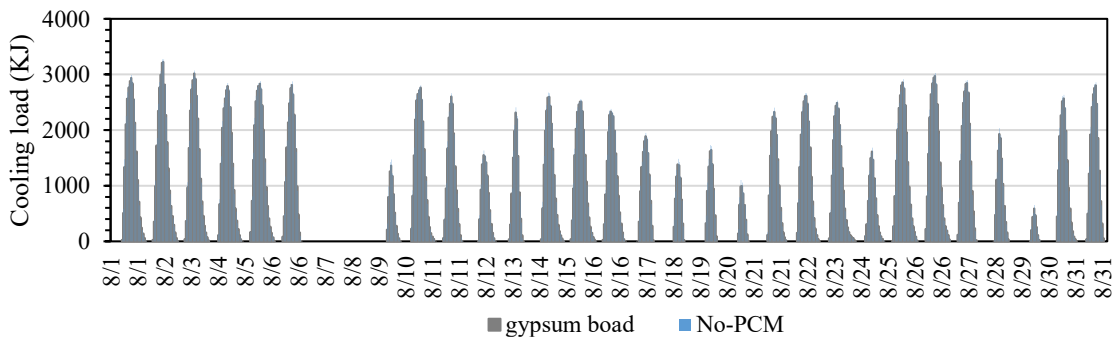


Figure 7.2.44 Air-conditioning load of No-PCM wall building and PCM6D-30% wall building in August.

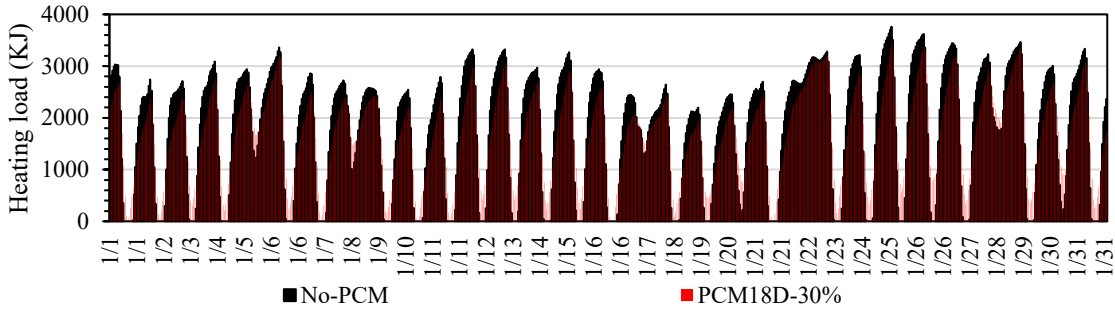


Figure 7.2.45 Air-conditioning load of No-PCM wall building and PCM18D-30% wall building January.

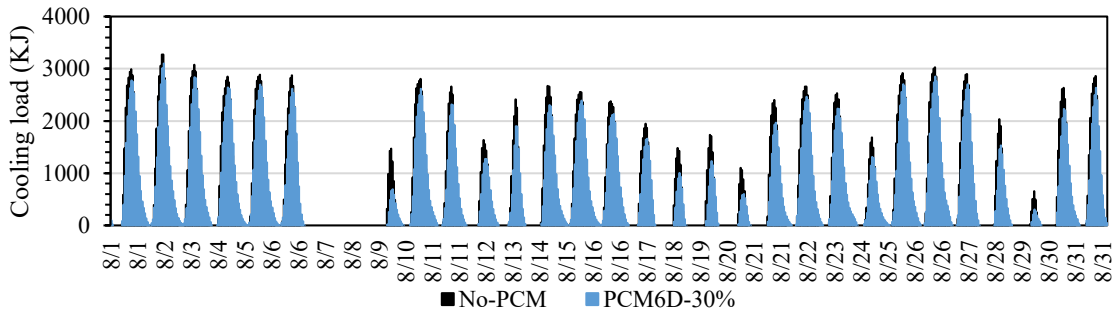


Figure 7.2.46 Air-conditioning load of No-PCM wall building and PCM18D-30% wall building in August.

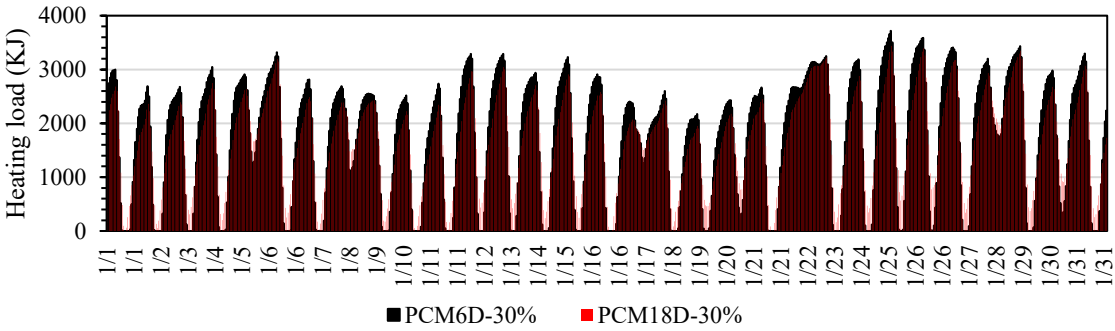


Figure 7.2.47 Air-conditioning load of PCM6D-30% wall building and PCM18D-30% wall building in January.

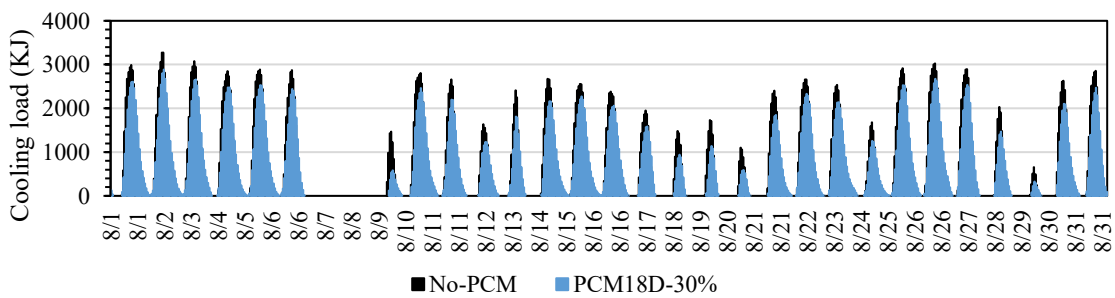


Figure 7.2.48 Air-conditioning load of PCM6D-30% wall building and PCM18D-30% wall building in August

### 7.2.4 Monthly heating and cooling loads

The graph below shows monthly heating and cooling loads throughout the year and the comparison results for each material.

In the material comparison which did not contain PCM, the one with low air conditioning load was gypsum board, but the difference was about 2.4% for the heating load and about 4.8% for the cooling load. As for the PCM concrete, PCM6D-30% had about 1.6% reduction in heating load and about 13% reduction in cooling load compared with No-PCM, and gypsum board was less burdened in heating load. On the other hand, in PCM18D-30%, the heating load was reduced by about 11% and the cooling load by about 20%, indicating a significant load reduction.

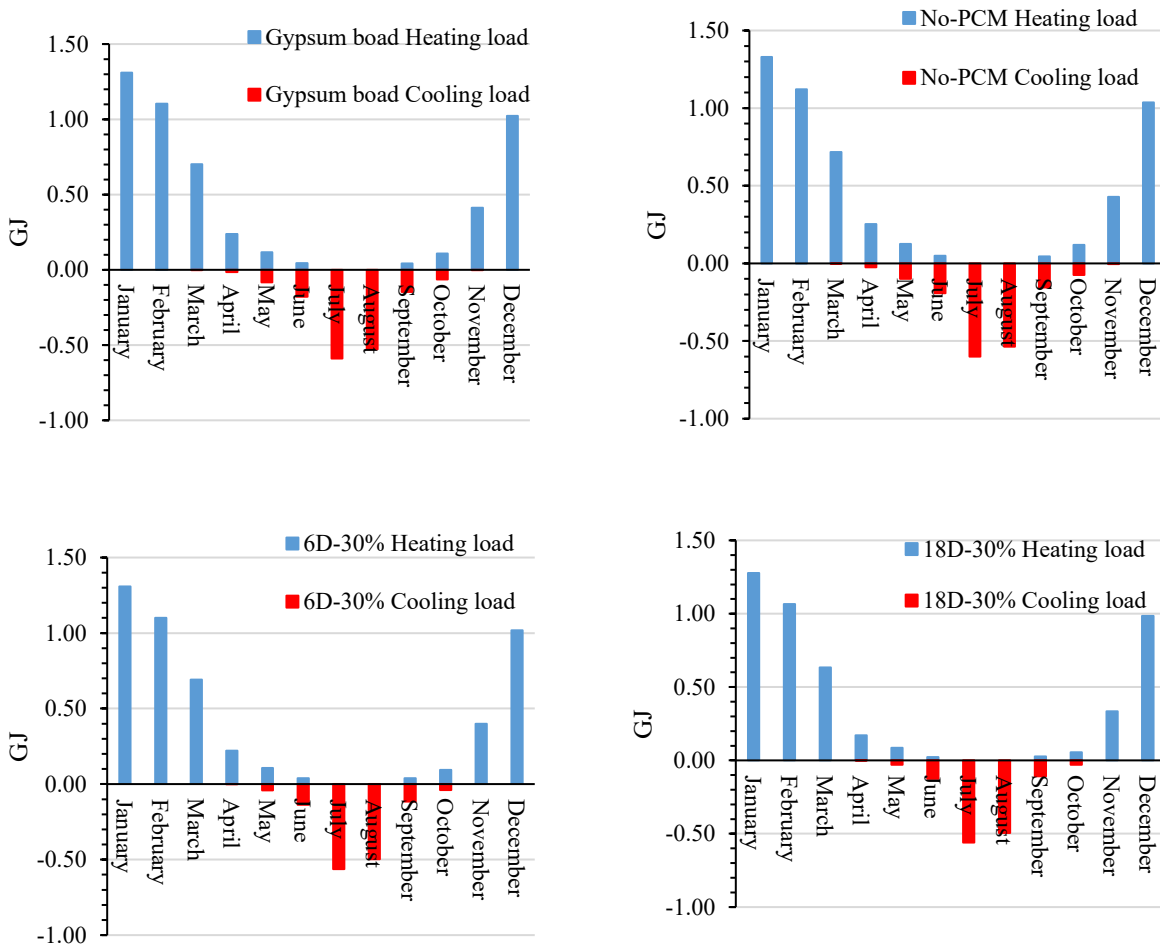
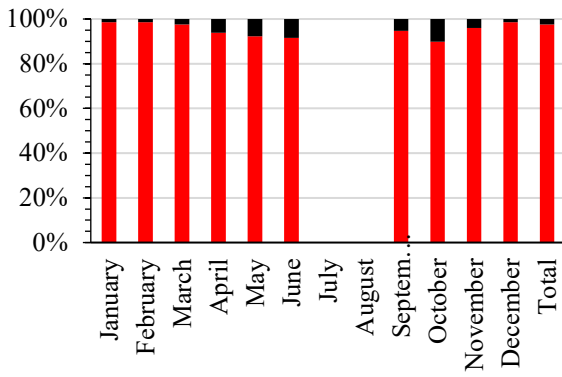
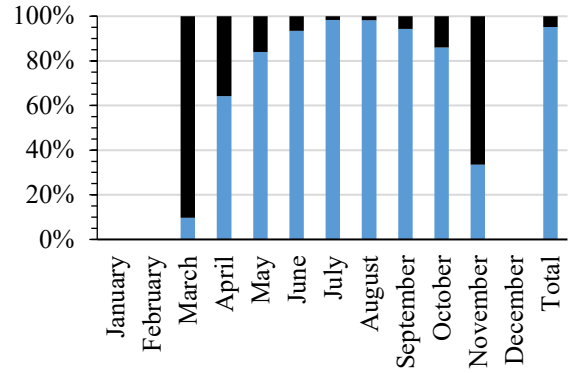


Figure 7.2.49 Monthly division air-conditioning load.

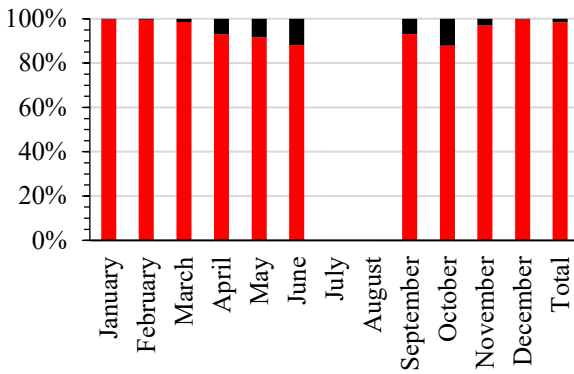


(a) Heating load

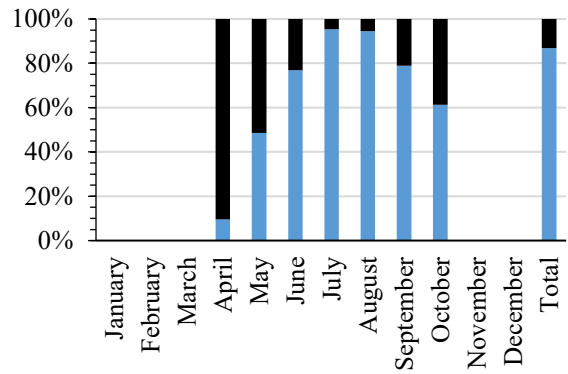


(b) Cooling load

Figure 7.2.50 Air-conditioning load percentage of PCM6D-10% in No-PCM standard.

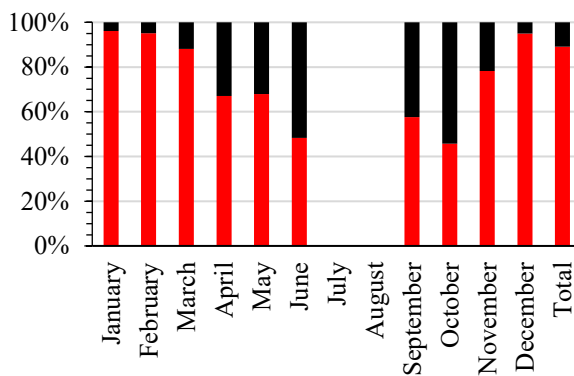


(a) Heating load

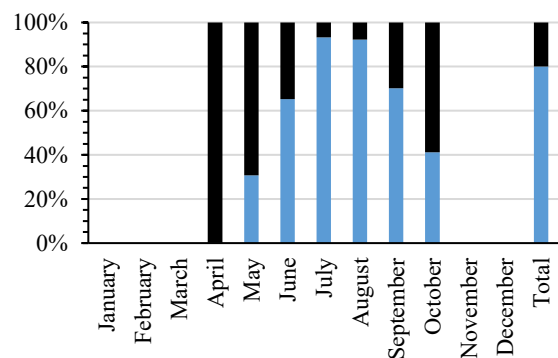


(b) Cooling load

Figure 7.2.51 Air-conditioning load percentage of PCM6D-20% in No-PCM standard.



(a) Heating load



(b) Cooling load

Figure 7.2.52 Air-conditioning load percentage of PCM6D-30% in No-PCM standard.

### 7.3 CONCLUSIONS

Energy Plus software was used for energy analysis simulations. PCM was incorporated to a residential building in Tokyo under the winter and summer seasons.

The comparison between gypsum and No-PCM materials revealed no significant differences in room temperature trends during January and August under heating and cooling loads.

Regarding PCM materials, PCM18D exhibited less temperature fluctuation and better temperature stability, especially in January. The performance of PCM18D can be attributed to its ability to absorb and store energy from indoor air and effectively maintained temperature fluctuations.

From the results of this study, PCM concrete showed a promising solution for achieving significant reductions in heating and cooling loads in residential houses. The test results indicate that PCM implementation can lead to load reductions of approximately 10-20%.

### 7.4 REFERENCES

- [1] “IEA (2022), Buildings, IEA, Paris.” Accessed: Jun. 08, 2023. [Online]. Available: <https://www.iea.org/topics/buildings>, License: CC BY 4.0
- [2] “World Energy Outlook 2022”, Accessed: May 25, 2023. [Online]. Available: [www.iea.org/t&c/](https://www.iea.org/t&c/)
- [3] C. Far and H. Far, “Improving energy efficiency of existing residential buildings using effective thermal retrofit of building envelope,” *Indoor and Built Environment*, vol. 28, no. 6, pp. 744–760, Jul. 2019, doi: 10.1177/1420326X18794010/ASSET/IMAGES/LARGE/10.1177\_1420326X18794010-FIG11.JPEG.
- [4] P. Lotfabadi and P. Hançer, “A Comparative Study of Traditional and Contemporary Building Envelope Construction Techniques in Terms of Thermal Comfort and Energy Efficiency in Hot and Humid Climates,” *Sustainability 2019, Vol. 11, Page 3582*, vol. 11, no. 13, p. 3582, Jun. 2019, doi: 10.3390/SU11133582.
- [5] V. J. L. Gan, I. M. C. Lo, J. Ma, K. T. Tse, J. C. P. Cheng, and C. M. Chan, “Simulation optimisation towards energy efficient green buildings: Current status and future trends,” *J Clean Prod*, vol. 254, p. 120012, May 2020, doi: 10.1016/J.JCLEPRO.2020.120012.
- [6] D. W. Hawes, D. Feldman, and D. Banu, “Latent heat storage in building materials Objectives of research in thermal storage building materials,” 1993.

- [7] P. K. S. Rathore and S. K. Shukla, “Potential of macroencapsulated PCM for thermal energy storage in buildings: A comprehensive review,” *Constr Build Mater*, vol. 225, pp. 723–744, Nov. 2019, doi: 10.1016/J.CONBUILDMAT.2019.07.221.
- [8] L. Royon, L. Karim, and A. Bontemps, “Thermal energy storage and release of a new component with PCM for integration in floors for thermal management of buildings,” *Energy Build*, vol. 63, pp. 29–35, Aug. 2013, doi: 10.1016/J.ENBUILD.2013.03.042.
- [9] Y. Kusama and Y. Ishidoya, “Effects of construction position of PCM layer on energy conservation and environmental improvement,” *AIJ Journal of Technology and Design*, vol. 22, no. 52, pp. 1027–1030, Oct. 2016, doi: 10.3130/aijt.22.1027.
- [10] S. Kumar, R. Sheeja, A. J. S. Jospher, G. Sai Krishnan, Chandrasekar, and A. Aroulraj, “Energy-saving potential of a passive cooling system for thermal energy management of a residential building in Jaipur City, India,” in *Materials Today: Proceedings*, Elsevier Ltd, 2020, pp. 1471–1477. doi: 10.1016/j.matpr.2020.09.301.
- [11] “Kantō region in Japan .” Accessed: Jan. 20, 2024. [Online]. Available: [https://en.wikipedia.org/wiki/Kant%C5%8D\\_region](https://en.wikipedia.org/wiki/Kant%C5%8D_region)
- [12] “Rainfall Level & Average Temperature in Tokyo (2019).” Accessed: Jan. 20, 2024. [Online]. Available: <https://www.alljapanrelocation.com/destination-guides/tokyo/climate-weather/>



**CHAPTER 8**  
**CONCLUDING REMARKS**

## **8.1 CONCLUDING REMARKS**

This thesis mainly focuses on the development of sustainable and energy-efficient building materials by incorporating phase change materials (PCMs) into concrete structures. The research involves a comprehensive investigation of both the PCM and various types of PCM-concrete through a combination of experimental and simulation techniques. As a results, PCM concrete offer a promising solution by efficiently storing and releasing thermal energy, reducing heating and cooling loads. This approach contributes to sustainability in construction, demonstrating a capacity to mitigate excessive heat on external wall. This innovative approach can create and maintain a comfortable thermal environment while significantly reducing energy consumption.

This thesis concludes with seven key sets of conclusions, providing comprehensive insights into the implications and potential application of the research.

### **8.1.1 Conclusions of chapter 2**

This research explored the impact of incorporating phase change materials (PCMs) into foam concrete, focusing on both mechanical and thermal properties. Here are the key findings:

The initial section explored the mechanical aspects, as the amount of PCM increased, the foam volume also increased, which led to a decrease in compressive strength. However, even with a reduction in strength, the compressive strength remained sufficient for applications like ALC panels.

The use of a special OM mixer was crucial in maintaining the integrity of the microcapsule PCMs during the mixing process. This prevented the formation of typical cracks in the PCMs within the concrete, preserving their energy storage potential.

The third section focused on thermal behavior of PCM foam concrete. Three tests were conducted to evaluate the thermal behavior of PCM foam concrete. The DSC test confirmed that all types of PCM foam concrete melted and froze within the expected temperature ranges, and energy storage capacity increased with the amount of PCM. The thermal conductivity test revealed that increasing the thermal conductivity of the composite material is advisable for improved performance. The thermocycle analysis demonstrated that PCM foam concrete effectively maintained temperatures within a certain range, with PCM43D exhibiting the longest temperature delay of approximately 8 hours.

In conclusion, PCM foam concrete offers several beneficial characteristics, including enhanced thermal performance and latent heat storage. The results suggest that PCMs have the potential to reduce indoor temperature fluctuations, contributing to energy savings and improved thermal comfort in buildings.

### 8.1.2 Conclusions of chapter 3:

This chapter focused on addressing the specific question of how to enhance energy storage capacity (TES) of concrete. Three different types of concretes with blended PCM have been studied to evaluate mechanical aspect and thermal characterization. It can be divided into 4 sections.

The initial section explored the mechanical aspects, including the compressive strength and density of concretes with blended PCMs. It was observed that the addition of PCMs significantly impacted the density of ND and NC concretes, resulting in a substantial reduction at the 3-day. While there was an initial decrease in compressive strength when PCMs were introduced, all three types of concrete demonstrated significant improvements in compressive strength from day 7 to day 28.

The second section focused on specific enthalpy estimation and phase change temperature for blended PCM concretes. Different heating/cooling rates and their influence on thermal behavior were analyzed. NC exhibited the highest  $\Delta h$ , latent heat capacity, and specific heat capacity among the three concrete types, indicating its superior thermal performance.

In the third section, thermal conductivity tests were conducted, revealing that increasing PCM substitution led to reduced thermal conductivity. ND exhibited improved thermal conductivity compared to FC and NC, emphasizing the importance of thermal conductivity in maximizing the latent heat storage efficiency of PCMs.

The fourth section included a heat cycle test with a laboratory-scale prototype. NC and ND concretes demonstrated delayed temperature changes, maintaining temperatures within the phase-changing range. NC exhibited the highest temperature maintenance, with a delay of around 3 hours and 30 minutes.

The findings suggest that PCMs have the potential to enhance thermal performance in specific applications. It was observed that while FC had a higher energy heat storage capacity based on DSC analysis, the heat cyclic analysis yielded the lowest results, highlighting the significance of thermal conductivity in heat transfer. Therefore, a balance between thermal conductivity and energy storage capacity is essential for optimizing energy storage capacity, particularly in blended PCMs. Expanding the melting and freezing temperature range could be a suitable approach for enhancing energy storage capacity in such systems.

### **8.1.3 Conclusions of chapter 4:**

In conclusion, this chapter focused on addressing excessive heat in precast concrete structures and enhancing their quality and durability through the use of polymer-modified concrete. It can be divided into 4 sections

The initial section explored the mechanical aspects, the addition of PCMs led to an initial reduction in density and compressive strength, but significant improvements were observed from day 7 to day 28. Bonding strength surpassed specified requirements, ensuring reliability.

The second section focused on specific enthalpy estimation and phase change temperature for blended PCM concretes. The specific enthalpy and phase change temperature of polymer-modified concretes with PCMs were examined. PCM43D exhibited the highest specific enthalpy, indicating efficient thermal regulation.

In the third section, the addition of PCMs increased thermal conductivity to varying degrees, depending on the PCM type used.

The fourth section included a heat cycle test with a laboratory-scale prototype. PCM28D and PCM43D demonstrated efficient heat absorption during the heating phase and sustained heat release during cooling, with the highest temperature maintenance observed in PCM43D. The color of tiles influenced thermal behavior, with black tiles proving superior.

In summary, the study confirmed that PCM polymer cement concrete meets project requirements. It exhibited desirable mechanical properties and efficient thermal regulation, making it suitable for managing temperature changes due to intense solar radiation. Therefore, PCM can effectively enhance the quality and durability of precast concrete structures while addressing excessive heat.

### **8.1.4 Conclusions of chapter 5:**

Ultra-lightweight PCM Foam Concrete (NRG Foam), explores the innovative field of ultra-lightweight PCM foam concrete, NRG Foam, in collaboration with the Technical University of Darmstadt, Germany. The main purpose of NRG foam is to increase thermal insulation and thermal energy storage capacity. The objective of this research is twofold. First, to develop an ultra-lightweight concrete foam integrated with PCM. The material properties of NRG foam concrete were analyzed in detail. Key parameters include foam porosity and ribbon thickness. The findings are as follows:

In this experiment, 12 different PCM foam concrete mixtures with dry densities, ranging between 180 kg/m<sup>3</sup> and 260 kg/m<sup>3</sup>, were considered. Since NRG-foam with PCM is a highly sensitive material; thus, all mixtures were carefully measured and their wet density and volume were recorded respectively to ensure their target dry density and target volume were reached. As for the Reference and PCM 5% samples with different densities, there were no problems with mix composition as the foam was stable for every mixture. A clear relationship between density and strength was confirmed, indicating that compressive strength increases with higher density, regardless of the specific composition of the foam concrete.

An empirical model that establishes a clear relationship between foam porosity (RP) and ribbon thickness (RF), where  $RF = f(RP)$ . This model optimizes the thermal insulation and energy storage capacity of NRG foam.

### **8.1.5 Conclusions of chapter 6:**

This chapter conducted a comprehensive numerical simulation analysis to evaluate the energy efficiency of PCM concrete. The primary objectives were to validate experimental data using numerical calculations and to establish a predictive model for concrete's energy efficiency.

The results of the numerical simulations were in close agreement with the experimental data, demonstrating remarkable consistency between the two. This validated numerical approach was extended to predict the behavior of PCM foamed concrete.

The numerical simulations showcased the significant role of PCM in effectively stabilizing room temperature fluctuations in various PCM foam concretes. The entire simulation process, performed in-depth using Matlab 2023a software, offers promising insights into advancing our understanding and predictive capabilities related to energy efficiency in PCM concrete systems.

### **8.1.6 Conclusions of chapter 7:**

Energy Plus software was used for energy analysis simulations. PCM was incorporated to a residential building in Tokyo under the winter and summer seasons.

The comparison between gypsum and No-PCM materials revealed no significant differences in room temperature trends during January and August under heating and cooling loads.

Regarding PCM materials, PCM18D exhibited less temperature fluctuation and better temperature stability, especially in January. The performance of PCM18D can be attributed to its ability to absorb and store energy from indoor air and effectively maintained temperature fluctuations.

From the results of this study, PCM concrete showed a promising solution for achieving significant reductions in heating and cooling loads in residential houses. The test results indicate that PCM implementation can lead to load reductions of approximately 10-20%.

## **8.2 RECOMMENDATIONS FOR FUTURE WORK**

Several considerations should be addressed in future research endeavors. Initially, the study involved small-scale prototypes conducted within a climatic chamber to evaluate the energy storage capacity of different concrete types integrated with various phase change materials (PCMs). While these experiments provided valuable insights, it is imperative for future investigations to incorporate 3D heat transfer simulations within the chamber environment. This entails considering heat radiation and convection through computational fluid dynamics (CFD) simulation analysis, enabling a more comprehensive exploration based on both experimental and simulation data. This approach facilitates an in-depth examination from nano and microscale perspectives, allowing for the simulation of the optimal amount of PCM and the ideal wall thickness.

Secondly, in continuation of the small-scale test conducted on PCM concrete, additional experimental studies are essential to ensure the proper application of PCM foam concrete in large-scale, real building environments.

Thirdly, the cost of PCMs presents a challenge for widespread PCM applications. Therefore, future studies should also focus on developing strategies to make PCM applications more cost-effective and affordable, promoting their practical use in various construction scenarios.

RESEARCH AND DEVELOPMENT OF CONCRETE  
CONTAINING PHASE CHANGE MATERIALS (PCM)  
相変化材料 (P C M) 混合コンクリートに関する研究開発

(論文の内容の要旨)

バ ト エ ル デ ネ  
B a t - E r d e n e

プ レ ブ エ ル デ ネ  
P U R E V - E R D E N E

(和文 4000 字)

この研究は、主に持続可能で省エネルギー住宅の開発に焦点を当てたもので、全 8 章から構成されている。

第 1 章「序論」では、PCM とそのセメント構造への統合について紹介する。

生活水準の向上と冷暖房需要の増加により、建築部門のエネルギー消費は重大な関心事となっている。国際エネルギー機関 (IEA) の報告によると、建築部門のエネルギー消費量はすでに全体の 30% を超えており、今後 50 年間で特に住宅においてこの割合はさらに上昇すると予想されている。そのため、建物の冷暖房負荷を減らし、エネルギー効率を高めることが急務となっている。

建物の冷暖房負荷を最小限に抑えるために、様々な解決策が導入されている。この増大する問題に対する有望な解決策のひとつが、再生可能エネルギー源の建築部門への統合である。例えば、太陽熱エネルギーを利用することで冷暖房エネルギー需要を減少させることが可能である。これを達成するために、熱エネルギーを貯蔵・放出する顕著な能力を持つ PCM の導入が有望なアプローチとして考えられている。PCM の相転移プロセスは融解と凝固の状態を含み、PCM が冷暖房システムとして機能することを可能にする。周囲の温度が上昇すると、PCM はエネルギーを吸収して固体から液体へと相転移し、温度が下がると固化して蓄積されたエネルギーを周囲に放出する。このプロセスにより、住宅建築において室温を維持し許容可能な熱的快適性を生み出すことが可能になると言われている。

建築分野では、PCM の特性を統合することでこれらの材料を壁、屋根、床に組み込んで室温を効果的に調整するなど、様々な応用が可能になる。PCM の統合によく使われる 2 つの方法は直接含浸法とマイクロカプセル化である。1 つ目の直接含浸法は、多孔質骨材に PCM を吸収させるものであるが、PCM の漏れや蓄熱能力の低下につながる可能性がある。2 つ目の方法であるマイクロカプセル化は、PCM を保護殻で覆うことでこの問題に対処し、加熱・冷却サイクル中もその特性を維持する。しかし、PCM のマイクロカプセル化にはコンクリートの練混ぜ中に摩擦等により割れるという重大な欠点がある。保護殻は機械的剛性が限られたポリマーで構成されるため、内部の PCM が損傷する可能性がある。このような損傷は実質的なエネルギー損失につながる。



第2章「PCMを含むフライアッシュフォームコンクリート」では、主にコンクリート構造物にPCMを適用する際に直面する課題について幅広く取り上げた。主な目標は、相変化温度範囲の異なる数種類のPCMを、損傷やエネルギー損失なしに使用する革新的なフライアッシュフォームコンクリートを開発することであった。これを達成するために、本研究ではフライアッシュフォームコンクリートの基本的な材料特性と熱挙動を分析し以下の結果を得た。

- (1) OMミキサーという特殊な練混ぜ機を使用することで、マイクロカプセル化されたPCMは、コンクリートマトリックス内でひび割れを生じたり損傷を受けたりすることなく、その構造的完全性を維持できることが立証された。
- (2) PCMは室内温度の変動を低減し、建物のエネルギー節約と熱的快適性の可能性を示すことが明らかになった。

第3章「PCMによるコンクリートのエネルギー貯蔵能力の強化」では、PCMフォームコンクリートの省エネの可能性を確認する先行研究を進展させる。PCMを組込んだコンクリートのエネルギー貯蔵能力を高めることに焦点を当て、2方向からのアプローチを紹介する。第一のアプローチは、PCMコンクリートの熱伝導率を高め、相変化過程における熱伝達を促進することである。フォームコンクリート、普通コンクリート、超重量コンクリートなど、様々なタイプのコンクリートについて熱伝導率と蓄熱能力を分析した。第二のアプローチは、対応可能な温度帯を拡張するために、各種PCMの混合物をコンクリートに組み込むことである。本研究では、エネルギー貯蔵能力に重点を置き、材料特性と熱挙動に焦点を当てている。

- (1) 2種類のPCMを普通コンクリートと組合わせた場合、混合PCMフォームコンクリートとは対照的に、熱伝導率が19%増加することが示された。
- (2) 同様の比較において、蓄熱容量が34%増加することが示された。

第4章「PCMのプレキャストコンクリート壁パネルへの応用」では、プレキャストコンクリート工場との共同研究について述べる。この研究の主眼は、外断熱PCa工法を採用した集合住宅に見

られる重大な問題への対処にある。外気温の変化や日射に起因する外壁のひび割れや異音が報告されている。根本的な問題は、タイル、外壁材、基礎構造間の膨張率の温度差によって発生する応力に関連している。

プレキャストコンクリート工場は、これらの問題に対処するため外壁温度の過昇を防ぐこと、接着強度が 0.4MPa を超えるようにすること、構造内の PCM の形状完全性を保つことなど、正確な基準を設けた。これらの要件を満たすため、本研究では接着強度とその他の機械的特性を高めることに焦点を当てた。

これらの課題を克服するために、本研究ではポリマーセメントモルタルを使用した。構造物の接着強度とその接着力を高めることができるとともに、温度過昇に関する問題に対応するため、ポリマーセメントコンクリートに PCM を組み込むことを検討し、以下の知見を得た。

- (1) PCM を添加した場合でも、モルタルにポリマーを添加することにより機械的強度が大幅に向上し、前述の要件を満たした。
- (2) PCM を添加したモルタルは、特に熱的性能の向上と温度過昇の抑制に関して有利な特性を示した。

第 5 章 「超軽量 PCM エネルギー (NRG) フォームコンクリート」では、ドイツのダルムシュタット工科大学との共同研究を通じて、超軽量 PCM フォームコンクリート「NRG フォーム」の革新的な分野を探る。NRG フォームとは、ダルムシュタット工科大学で開発中の特殊 PCM (改質鉱物断熱材) であり、その主な利点は、断熱性能と熱エネルギーの貯蔵能力を高めることにある。この研究の目的は 2 つある。第一に、PCM と一体化した超軽量フォームコンクリートを開発すること。第二に、実際の用途で NRG フォーム混合物の実装とスケーリングを成功させるための実用的な工学設計モデルを作成し、NRG フォームコンクリートの材料特性と熱挙動を詳細に分析することである。主なパラメータには、発泡体の空隙率とリボンの厚さが含まれる。これにより得られた知見を以下に示す。

- (1) 発泡体の空隙率 (RP) とリボンの厚さ (RF) の間に  $RF = f(RP)$  という明確な関係を確立する経験的モデルの定式化に成功した。このモデルは、NRG フォームの断熱性とエネルギー

一貯蔵能力を最適化するものである。

第6章「PCM コンクリートの数値シミュレーション解析」では、PCM コンクリートのエネルギー効率を調査するため、包括的な数値シミュレーション解析を実施した。本章の主な目的は、数値計算によって実験データを検証し、コンクリートのエネルギー効率に関する予測モデルを確立することである。これらの目標を達成するため、PCM コンクリートにおける熱伝導の研究から得られた実験に基づき、1次元モデルを開発した。コンクリート内の熱伝導は、フーリエの法則に基づく熱伝導方程式を用いて計算した。これにより得られた知見を以下に示す。

- (1) 数値シミュレーションを実行し、その結果を実験データと綿密に比較した結果、両者の間に顕著な整合性があることが明らかになった。その後、検証された数値的アプローチをPCM 発泡コンクリートの挙動を探るために拡張した。
- (2) 数値シミュレーションにより、様々なPCM フォームコンクリートにおいて室温変動を効果的に緩和する上で、PCM が極めて重要な役割を果たすことが明らかになった。このシミュレーションプロセス全体が、Matlab 2023a ソフトウェアを使って綿密に実行されたことは注目に値する。この成果は、PCM コンクリートシステムにおけるエネルギー効率の理解と予測を進める上で有望である。

第7章「PCM を適用した住宅のエネルギー解析シミュレーション」では、PCM コンクリートに関するエネルギー分析シミュレーションの詳細な検討を行う。建築材料としてのPCM コンクリートの統合に関するエネルギー効率と費用対効果の評価を掘り下げている。これらの複雑なエネルギー分析を行うために、本研究では高度なエネルギー・シミュレーション・プログラム・ソフトウェアである「EnergyPlus」を活用した。このツールは、建物内の熱エネルギー動態を綿密に比較・精査するために使用される。この評価は主に、従来の壁材とPCM フォームコンクリートの温度変化を比較することに主眼を置いている。これらのエネルギー分析シミュレーションから同時に得られた以下の結果は洞察に富んでいる。

- (1) 住宅におけるPCM 利用の有効性として、気候がPCM 材料の相変化温度と密接に一致する

地域では、特定の気候帯と本質的に結びついていることを示した。しかし、使用する PCM の種類を気候帯に合わせて適切に調整すれば、シミュレーション結果に基づき、冷暖房エネルギー負荷の約 20～30%の削減が達成可能である。

第 8 章では、本研究の結果を総括し、今後の挑戦的な展望を示した。

本論文では、PCM が室内温度の変動を最小限に抑え、省エネルギー性能と建物の快適性を改善できることを示した。本研究の成果は、PCM コンクリートを用いた住宅のエネルギー効率の高さを明らかにし、将来の持続可能な建築材料の研究に貢献するものである。

# 研究業績一覧

日本大学大学院工学研究科 博士後期課程 建築学専攻  
学生番号 202121 (氏名) Bat-Erdene PUREV-ERDENE

## 審査論文

### A. 基本論文

1) Purev-Erdene Bat-Erdene and S. Pareek, “Experimental Study on the Development of Fly Ash Foam Concrete Containing Phase Change Materials (PCMs)”, *Materials*, 15, 8428, 2022.11.

### B. 学会誌及びこれに準ずるもの

1) Purev-Erdene Bat-Erdene, S. Pareek, E. Koenders, C. Mankel, M. Löher and P. Xiao, “Evaluation of the Thermal Performance of Fly Ash Foam Concrete Containing Phase Change Materials (PCMs)”, *Buildings*, 13, 2481, 2023.9.

2) Purev-Erdene Bat-Erdene, S. Pareek, S. Danzandorj and S. Sambuunjam, “A Review of Phase Change Materials in Concrete for a Sustainable Built Concrete”, *Proceedings of International Conference on Construction and Innovation-2019*, pp.108-112, Ulaanabaatar, Mongolia, 2019. 9.

3) Sunjidmaa Sambuunjam, S. Pareek, S. Danzandorj and P.-E. Bat-Erdene, “A Study on Fiber Reinforced Geopolymer Mortars”, *Proceedings of International Conference on Construction and Innovation-2019*, pp.113-116, Ulaanabaatar, Mongolia. 2019. 9.

### C. 日本大学工学部紀要及びこれに準ずるもの

1)無し

### D. 学会の大会, 支部大会などの口頭発表

1) Purev-Erdene Bat-Erdene, S. Pareek, S. Danzandorj, S. Sambuunjam and R. Thombare, “Use of Fly Ash in Production of Foamglass”, *Proceedings of EUROCOALASH 2019 conference*, University of Dundee, pp.218-225, Dundee, Scotland, UK 2019.6.

2) Sunjidmaa Sambuunjam, S. Pareek, S. Danzandorj, R. Thombare and P.-E. Bat-Erdene, “Study on Utilization of Fly Ash in Production of Light Aggregate”, *Proceedings of EUROCOALASH 2019 conference*, University of Dundee, pp.195-206, Dundee, Scotland, UK, 2019.6.

## その他

無し

## Acknowledgements

I am pleased to get this opportunity to express my sincere gratitude and indebtedness to individuals who have supported and surrounding me throughout my journey.

I would to express my heartfelt thankfulness to my supervisor **Prof. Sanjay PAREEK**, Dr.Eng, RC Structures & Materials Lab, Department of Architecture, College of Engineering, Nihon University, for the undefining support and immeasurable guidance throughout this journey. His unsurpassed knowledge and international networking in Materials Engineering Science, which have enriched this work beyond measure. Without his support this thesis would not have been possible.

I would like to thank all of my reviewers, **Prof. Yukio Hamada** and **Prof. Urabe Tomoyoshi** of Nihon University and **Prof. Daisuke Ogura** of Kyoto University and **Prof. Tetsuya Ishida** of Tokyo University. The valuable comments that I had received from them aided in enhancing the quality of my research and enriching my thesis.

I would also like to give special thanks to **Prof. Eddie Koenders** from TU Darmstadt University of Science and Technology for providing me the opportunity to study in his institute and his PhD students **Löher Maximillian** and **Peng Xiao** for their contributions to the numerical analysis of heat transfer model.

I am always grateful to the laboratory members of the same college of Nihon University. Especially, I would like to thank all assistant undergraduate students **Mr. Suzuki AKEMI**, **Mr. Nozue Kazuki** and **Mr. Yuto Kimura** who have contributed to research work and started this thesis from zero. I should also mention a cooperated person whose name is **Mr. Yuki Osanai**, President of O-Factory, helped for marking the simulation of heat analysis part.

I would like to acknowledge the financial support of the Rotary Yoneyama and Rinri association, the way of granting a scholarship my doctoral degree is to be achieved. I would like to express my grateful to **Mr. Junichi Kokubun** for his continuous support throughout my PhD journey. Additionally, I am truly grateful to Nihon University for granting me great opportunity to study abroad which has broadened my opened my eyes and significantly contributed to my academic journey.

Finally, I would like to expressing my heartfelt gratitude to my family especially to my mother, **Ms. Batdemberel Sunjidmaa**, for always being there and believing in me. I would not have reached where I am today without unwavering support and encouragement.